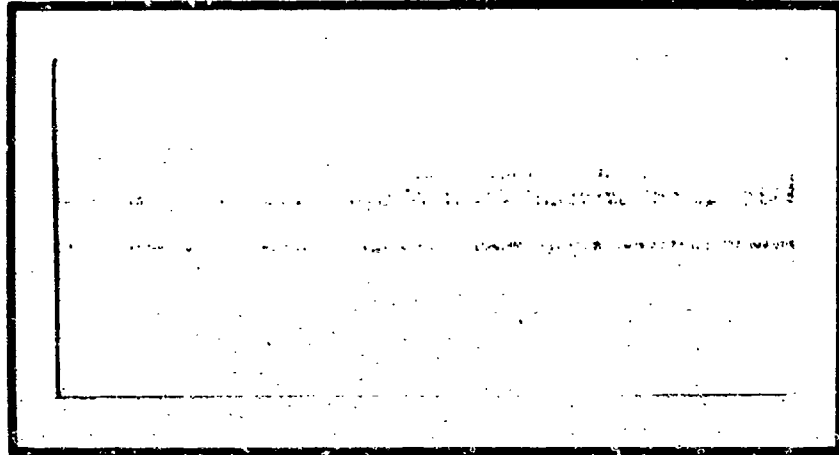


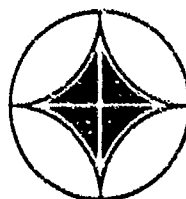
DTIC FILE COPY

AFOSR-TX- 87-1825

AD-A189 791



DTIC  
ELECTE  
JAN 07 1989  
S D  
CH



APPLIED  
RESEARCH  
ASSOCIATES, INC.

Engineering and Applied Science

DISTRIBUTION STATEMENT A  
Approved for public release;

87 12 29 080

## REPORT DOCUMENTATION PAGE

Form Approved  
OMB No. 0704-0188

1a. REPORT SECURITY CLASSIFICATION UNCLASSIFIED		1b. RESTRICTIVE MARKINGS None	
2a. SECURITY CLASSIFICATION AUTHORITY N/A since unclassified		3. DISTRIBUTION/AVAILABILITY OF REPORT Approved for Public Release; Distribution Unlimited	
2b. DECLASSIFICATION/DOWNGRADING SCHEDULE N/A since unclassified		5. MONITORING ORGANIZATION REPORT NUMBER(S) <b>AFOSR-TR-87-1825</b>	
4. PERFORMING ORGANIZATION REPORT NUMBER(S) 5967-87		7a. NAME OF MONITORING ORGANIZATION AFOSR/NA	
6a. NAME OF PERFORMING ORGANIZATION Applied Research Associates, Inc	6b. OFFICE SYMBOL (if applicable) NA	7b. ADDRESS (City, State, and ZIP Code) Bldg. 410 Bolling AFB, DC 20332-6448	
8a. NAME OF FUNDING/SPONSORING ORGANIZATION AFOSR	8b. OFFICE SYMBOL (if applicable) NA	9. PROCUREMENT INSTRUMENT IDENTIFICATION NUMBER F49620-85-C-0102	
8c. ADDRESS (City, State, and ZIP Code) Bldg. 410 Bolling AFB, DC 20332-6448		10. SOURCE OF FUNDING NUMBERS	
		PROGRAM ELEMENT NO. 6.1102F	PROJECT NO. 2302
		TASK NO. C1	WORK UNIT ACCESSION NO.

11. TITLE (include Security Classification) (U) Experimental and Theoretical Response of Multiphase Porous Media to Dynamic Loads: Annual Report 2

12. PERSONAL AUTHOR(S)  
Kim, Kwang J., Blouin, Scott E., Timian, David A.13a. TYPE OF REPORT  
Annual13b. TIME COVERED  
FROM 860701 TO 87063014. DATE OF REPORT (Year, Month, Day)  
87092415. PAGE COUNT  
30816. SUPPLEMENTARY NOTATION  
N/A

17. COSATI CODES			18. SUBJECT TERMS (Continue on reverse if necessary and identify by block number)
FIELD	GROUP	SUB-GROUP	

19. ABSTRACT (Continue on reverse if necessary and identify by block number)

This report summarizes results of a combined theoretical and experimental investigation of wave propagation and liquefaction from high intensity dynamic loading of saturated porous media. This work presents results obtained during the second year of a three year research effort. Theoretical derivations describing undrained hydrostatic and uniaxial strain loadings were obtained and incorporated into a numerical code (NKOCF) which models the two-phase undrained response of saturated soils and rocks. Numerical calculations of the response of saturated rock and soil compare very well with laboratory data in which both the soil and rock are liquefied during the unload portion of the cycle. Theoretical and numerical solutions for the speed and damping of waves of the first and second kind in fully coupled two-phase media are also presented. Parameter studies of the influence of frequency and variations in material properties on wavespeed and damping are performed.

Experimental work includes a study of the undrained response of saturated soils and rocks to uniaxial loadings, liquefaction of these materials during the unloading, and subsequent

20. DISTRIBUTION/AVAILABILITY OF ABSTRACT <input checked="" type="checkbox"/> UNCLASSIFIED/UNLIMITED <input type="checkbox"/> SAME AS RPT <input type="checkbox"/> OTHER		21. ABSTRACT SECURITY CLASSIFICATION UNCLASSIFIED	
22a. NAME OF RESPONSIBLE INDIVIDUAL Wen C. Boyce		22b. TELEPHONE (include Area Code) (202) 767-6963	22c. OFFICE SYMBOL AFOSR/NA

## 19. Abstract (cont.)

consolidation during undrained reloading. An experimental study of the influence of  $\sigma'$  level and stress path on grain damage of carbonate sands was performed which showed the influence of increasing shear stress on the microscopic grain damage. Finally an experimental study of fluid friction was performed which confirmed Biot's theoretical work for circular and flat ducts and which developed empirical constants describing  $f$  in the transitional and turbulent regimes. The influence of fluid inertia and acceleration sensitive friction terms on pressure gradients were also investigated.

EXPERIMENTAL AND THEORETICAL RESPONSE  
OF MULTIPHASE POROUS MEDIA  
TO DYNAMIC LOADS

ANNUAL REPORT 2

24 September 1987

DTIC  
ELECTE  
JAN 07 1988  
H

Prepared for

Air Force Office of Scientific Research  
Bolling Air Force Base  
Washington, DC 20332-6448

Under Contract No. F49620-85-C-0102

Prepared by

Kwang J. Kim  
Scott E. Blouin  
David A Timian

Applied Research Associates, Inc.  
New England Division  
South Royalton, Vermont 05068

Accession For	
NTIS GRA&I	<input checked="" type="checkbox"/>
DTIC TAB	<input type="checkbox"/>
Unannounced	<input type="checkbox"/>
Justification	
By	
Distribution/	
Availability Codes	
Dist	Avail and/or Special
A-1	



DISTRIBUTION STATEMENT A

Approved for public release



## TABLE OF CONTENTS

Section	Page
1 Overview and Summary. . . . .	1
2 Theoretical Treatment of Undrained Uniaxial and Hydrostatic Loadings. . . . .	5
3 Treatment of Undrained Uniaxial Loading . . . . .	21
4 Theoretical Analysis of Wave Propagation in Saturated Porous Media. . . . .	51
5 Numerical Analysis of Wave Propagation in Saturated Porous Media. . . . .	77
6 Liquefaction and Consolidation Under Uniaxial Strain Loadings. . . . .	145
7 Grain Damage as a Function of Stress Path and Magnitude . . . . .	181
8 Laboratory Investigation of Fluid Flow Through Porous Media . . .	251
9 List of References. . . . .	283
 Appendix	
A Listing of Program NKOCF. . . . .	285
B Example Problem Using Program NKOCF . . . . .	295
C Listing of Program TWAVE. . . . .	301
D Calculation of Equivalent Coefficient of Permeability for a Flat Duct . . . . .	307



## SECTION 1

### OVERVIEW AND SUMMARY

#### 1.1 INTRODUCTION

This report describes research performed during the second year of a three year investigation of wave propagation and related effects in multiphase porous media. The research effort is comprised of both a theoretical and an experimental program which compliment and support one another. This combined approach has proved valuable in identifying and analyzing phenomena governing the propagation of high intensity stress waves in saturated porous media and other related phenomena including liquefaction and post-liquefaction processes such as consolidation. The report is organized into four chapters (Sections 2 through 5) covering progress in theoretical analysis and implementation of analytic techniques into computational algorithms, and three chapters (Sections 6 through 8) describing experimental results and analyses. An overview and summary of these seven chapters is provided in the following subsection.

#### 1.2 CHAPTER OVERVIEW AND SUMMARY

Sections 2 and 3 contain a theoretical and numerical two-phase analysis of undrained uniaxial strain and hydrostatic loadings of porous saturated materials. Uniaxial strain loadings closely duplicate explosion-induced airblast loadings on the ground surface as well as direct coupled loadings along a spherically divergent wavefront at early times. Uniaxial loadings are thus the most generally applicable loadings for the study of explosive effects. Section 2 discusses the advantage of the multiphase analysis from both the theoretical and experimental standpoints, and develops the theoretical constitutive equations for undrained loading of a fully coupled elastoplastic skeleton with compressible grains and pore water. Specific examples of hydrostatic and uniaxial loadings are shown which demonstrate the interrelationships between effective stress, pore pressure and total stress and which demonstrate liquefaction early in the unload cycle resulting from the hysteretic nature of the material skeleton.

Section 3 describes the development of the numerical code NKOCP which uses the theoretical equations of Section 2 in incremental form to model the uniaxial and hydrostatic undrained response of actual soils and rock. The code incorporates nonlinear elastic response of the solid grains, nonlinear compressibility of the pore water and nonlinear plastic response of the porous skeleton into a fully coupled two phase material model. Skeleton response characteristics from laboratory tests can be input directly into the code to insure accurate depiction of the actual material response. The use of NKOCP is described and a listing of the code and an example problem are provided.

Sections 4 and 5 contain theoretical and numerical treatments of wave propagation and damping in saturated porous media. In Section 4, a closed form solution for wave propagation velocity and damping in fully saturated porous media is derived for a fully coupled model with compressible solid grains and pore water. This solution demonstrates existence of two types of compression waves, termed waves of the first and second kinds. It also provides a means of benchmarking and verifying multiphase code calculations and a means of planning and guiding a further investigation of these two types of waves using our finite element two phase codes.

The general theoretical solution for the wavespeeds and damping are incorporated into the numerical code TWAVE, described in Section 4 and listed in APPENDIX C. TWAVE is used in Section 5 in a parametric study of the influence of excitation frequency and variations in material properties on propagation velocity and damping. Compressional wave velocity for waves of the first kind is shown to vary as a function of the frequency-permeability product, with a zone where wavespeed transitions from a lower bound value to a higher bound value with increasing values of the product. Damping is seen to be a maximum where the rate of change in wavespeed is greatest. Waves of the second kind also show a transition in wavespeed from near zero at low values of the frequency-permeability product to an upper bound value at higher values of the product. The results of this parametric study will be used in the coming year to identify and study phenomena controlling damping and wavespeed for both types of waves.

Descriptions of the experimental apparatus and results are contained in Sections 6 through 8. Section 6 shows the results of undrained uniaxial strain loading of saturated limestone and uncemented silt-sand-gravel mixtures. Both materials show liquefaction early in the unload portion of the cycle predicted by the theoretical model developed in Sections 2 and 3. Comparisons are shown between the laboratory data and calculations of the undrained response made with NKOCF using completely independent measures of skeleton response and grain and pore water compressibility. There is excellent overall correlation with the laboratory data and the computed undrained material response.

Section 7 describes an experimental study of grain damage during various types of loading to delineate similarities and differences in response of granular materials on the microscopic level between various shear loadings and purely compressional loadings. Grain damage was found to vary substantially with variation in mean stress, but has a relatively minor dependence on the level of shear stress. A method for quantitatively describing both the amount and severity of grain damage is developed. The stress strain response of all materials tested in this study is included for use in future analysis in which the plastic work will be correlated with the grain damage.

Section 8 describes experimental apparatus and results being used to investigate and characterize fluid friction in saturated porous media. Our generalized model for fluid friction is described, which includes frictional energy dissipation in the laminar, transitional and turbulent flow regimes. In this phase of the study, Biot's theoretical work, which was restricted to the laminar flow regime, is verified experimentally in both circular and flat ducts. Empirical coefficients are obtained which model the fluid friction behavior in the transitional and turbulent flow regimes as well. Preliminary tests are also documented showing the influence of fluid inertia and Biot's acceleration sensitive dissipation term on the pore pressure gradient during nonsteady state flow.



## SECTION 2

### THEORETICAL TREATMENT OF UNDRAINED UNIAXIAL AND HYDROSTATIC LOADINGS

#### 2.1 INTRODUCTION

In order to model the undrained response of saturated porous soils and rocks to high intensity dynamic loadings, it is often advantageous to combine the skeleton properties with the properties of the pore fluid and solid grains using two phase constitutive relationships. Specific advantages of this approach are:

- it avoids the experimental difficulties of achieving 100% saturation and avoids the inaccuracies in measuring effective stress by differencing total stress and pore pressure data. The latter inaccuracies arise because effective stresses are often very small relative to the total stresses and pore pressures.
- it permits computation of reliable material response characteristics in high pressure regimes which are extremely difficult to achieve in the laboratory but which are important in the study of explosive effects or other high energy applications.

Another application of the two phase theoretical model is in the interpretation and understanding of laboratory data from undrained load-unload testing of saturated soils and rocks. As is described in Section 6, we liquefied both porous soil and rock in undrained uniaxial strain tests. The two phase theoretical model was very useful in interpretation of these test data, and allowed us to identify some unexpected aspects of pore pressure and effective stress response. This new insight into two phase response resulted in revision of some of our earlier work based on a more elementary two phase model. It also increases our understanding of blast liquefaction phenomena which have been observed in large scale field tests (Blouin and Shinn, 1983).

## 2.2 IDEALIZED RESPONSE OF FULLY-COUPLED SATURATED MATERIALS TO UNDRAINED HYDROSTATIC AND UNIAXIAL STRAIN LOADINGS.

Fragaszy and Voss (1986) observed liquefaction of saturated sands during the unloading portion of undrained hydrostatic tests. Kim, Blouin and Timian (1986) reported preliminary test results showing liquefaction of saturated soils and rocks during the unloading portion of undrained uniaxial strain tests. Their results are updated and completed in Section 6 of this report. The liquefaction phenomena during a single load-unload cycle in which stresses are either completely or predominantly compressive rather than shear can be explained by two phase analysis which considers the inelastic, hysteretic nature of the soil or rock skeleton (Rischbieter et al., 1977, Blouin and Kim 1983). While the overall liquefaction response could be explained by simple decoupled two phase models, subtleties in the pore water and skeleton response were incorrectly described by these models. In order to more fully understand the liquefaction data presented in Section 6, we extended this earlier work through the use of a fully coupled two phase model.

## 2.3 HYDROSTATIC RESPONSE

The hydrostatic and uniaxial strain response of saturated porous materials is described by Blouin and Kim (1984). The three governing equations describing the hydrostatic response are the effective stress law expressed as

$$p = p' + \pi \quad (2-1)$$

the relationship between volume strain and pore pressure and effective stress given by

$$\epsilon_v = \frac{p'}{K_s} + \frac{\pi}{K_g} \quad (2-2)$$

and the bulk undrained stress-strain relationship given by

$$p = K_f \epsilon_v \quad (2-3)$$



where

- $p$  = total pressure
- $p'$  = effective pressure
- $\pi$  = pore pressure
- $\epsilon_v$  = volume strain
- $K_s$  = bulk modulus of skeleton
- $K_g$  = bulk modulus of solid grains
- $K_f$  = fully coupled undrained bulk modulus of saturated two phase material

$K_f$  is given by

$$K_f = K_m + K_s - \frac{K_m K_s}{K_g} + K_m K_s \left[ \frac{K_m + K_s - \frac{K_m K_s}{K_g} - K_g}{K_g^2 - K_m K_s} \right] \quad (2-4)$$

where  $K_m$  is the bulk modulus of the solid grain-pore water mixture given by

$$K_m = \frac{K_g K_w}{K_w + n(K_g - K_w)} \quad (2-5)$$

with

- $K_w$  = bulk modulus of pore water
- $n$  = porosity

Eliminating the effective pressure from Equation 2-1 and 2-2 yields

$$p = \pi \left( 1 - \frac{K_s}{K_g} \right) + K_s \epsilon_v \quad (2-6)$$

Substitution of Equation 2-6 into 2-3 yields the pore pressure as a function of the volumetric strain as

$$\pi = \frac{(K_f - K_s)}{\left(1 - \frac{K_s}{K_g}\right)} \epsilon_v \quad (2-7)$$

Eliminating the pore pressure from Equations 2-1 and 2-2 gives

$$p = p' \left(1 - \frac{K_g}{K_s}\right) + K_g \epsilon_v \quad (2-8)$$

Substitution of Equation 2-8 into Equation 2-3 gives the effective pressure as a function of the volumetric strain as

$$p' = \frac{(K_g - K_f)}{\left(\frac{K_g}{K_s} - 1\right)} \epsilon_v \quad (2-9)$$

For purposes of an idealized simple model, the pore water and solid grains may be assumed linear-elastic, and the skeleton response can be described by a bilinear approximation as shown in Figure 2.1 with a loading modulus  $K_{sl}$  and an unloading modulus  $K_{su}$ . For a given maximum volume strain,  $\epsilon_{vmax}$ , the corresponding maximum effective pressure is calculated from Equation 2-9 as

$$p'_{max} = \frac{(K_g - K_{fsl})}{\left(\frac{K_g}{K_{sl}} - 1\right)} \epsilon_{vmax} \quad (2-10)$$

where  $K_{fsl}$  is computed from Equation 2-4 using  $K_s = K_{sl}$ . During unloading the effective pressure is expressed as

$$p' = p'_{\max} - \frac{(K_g - K_{fu})}{\left(\frac{K_g}{K_{su}} - 1\right)} (\epsilon_{v\max} - \epsilon_v) \quad (2-11)$$

If, during undrained unloading, the effective pressure drops to zero, a state of liquefaction occurs. For a load-unload cycle beginning with no pressure on the saturated material, the volume strain at the onset of liquefaction,  $\epsilon_{vliq}$ , can be calculated from Equation 2-11 with  $p'$  set to zero as

$$\epsilon_{vliq} = \epsilon_{v\max} - \frac{\left(\frac{K_g}{K_{su}} - 1\right)}{(K_g - K_{fu})} p'_{\max} \quad (2-12)$$

Substituting Equation 2-10 into 2-12 yields the strain at the onset of liquefaction as a function of the peak strain

$$\epsilon_{vliq} = \left[ 1 - \frac{(K_g - K_{fL}) \left(\frac{K_g}{K_{su}} - 1\right)}{(K_g - K_{fu}) \left(\frac{K_g}{K_{sL}} - 1\right)} \right] \epsilon_{v\max} \quad (2-13)$$

To illustrate the behavior of a saturated material in hydrostatic undrained loading a simple numerical example is presented in Figure 2.2. The following values which roughly approximate the properties of a porous limestone, were used in calculating the total pressure, effective pressure and pore pressure load-unload cycles shown in this Figure.

$$\begin{aligned} K_g &= 5.0 \times 10^6 \text{ psi} \\ K_{sL} &= 0.5 \times 10^6 \text{ psi} \\ K_{su} &= 2.0 \times 10^6 \text{ psi} \\ K_w &= 0.3 \times 10^6 \text{ psi} \\ n &= 0.1 \end{aligned}$$

From Equations 2-5 and 2-4 the following values of the mixture modulus,  $K_m$ , and the undrained loading and unloading modulus of the bulk mixture,  $K_{fL}$  and  $K_{fU}$ , were computed .

$$K_m = 1.948 \times 10^6 \text{ psi}$$

$$K_{fL} = 2.142 \times 10^6 \text{ psi}$$

$$K_{fU} = 2.831 \times 10^6 \text{ psi}$$

Assuming a maximum volume strain of 3%, values of peak total pressure, pore pressure and effective pressure from Equations 2-3, 2-7 and 2-9 respectively were computed.

$$p_{\max} = 64,260 \text{ psi}$$

$$\pi_{\max} = 54,720 \text{ psi}$$

$$p'_{\max} = 9,540 \text{ psi}$$

During unloading, because of the hysteretic nature of the skeleton, the material liquefies at a strain computed from Equation 2-13 of

$$\epsilon_{vliq} = 2.341\%$$

Using the values computed above, the load-unload response of the idealized saturated porous material is plotted in Figure 2.2 in terms of total pressure, pore pressure and effective pressure versus volume strain. The first significant feature of this plot is that liquefaction occurs at a strain of 2.34% as the effective pressure between the grains falls to zero. Liquefaction as a result of the hysteretic skeleton is clearly illustrated here. The skeleton hysteresis also results in hysteresis in the bulk material and apparent hysteresis in the pore water. Note that the apparent hysteresis in the pore water is negative, i.e. there is an apparent net energy gain in the pore water during the load-unload cycle. This apparent energy gain is due to rapid expansion of the solid grains during unloading which results from the rapid drop in effective pressure in the skeleton. As the solid grains expand they cause a less rapid decrease in pore pressure down to the point of liquefaction. Once liquefaction is reached, the pore pressure unloads at a rate governed by the bulk modulus of the solid grain-pore water mixture,  $K_m$ .

The hysteresis in the total pressure load-unload cycle represents the actual energy lost by the bulk material during the cycle. The bulk material loads up along a slope given by the loading bulk modulus,  $K_{fL}$ , and unloads down

a slope given by the unloading bulk modulus,  $K_{fu}$ , until the point of liquefaction is reached. From there, the material is a dense fluid and unloads down the slope given by the mixture modulus,  $K_m$ . Note that the area (energy dissipation) within this cycle is considerably less than the area within the effective pressure cycle. The area within the effective pressure cycle represents both the nonrecoverable energy dissipated by the skeleton as heat, and the recoverable energy associated with the elastic compression and expansion of the solid grains. This recoverable portion of the energy equals the area within the pore pressure cycle; thus, the total area within the effective pressure cycle equals the sum of the areas within the total pressure and pore pressure cycles.

## 2.4 UNIAXIAL STRAIN RESPONSE

The uniaxial loading is representative of the strain path under airblast loadings as well as the early time strain path from spherical explosive charges. For uniaxial loadings Blouin and Kim (1984) present derivations which parallel those of the previous subsection for hydrostatic loadings. The three governing equations for the uniaxial response include the effective stress law,

$$\sigma_a = \sigma_a' + \pi \quad (2-14)$$

the relationship between volume strain, effective stress and pore pressure,

$$e_v = \frac{\sigma_a'}{M_s} + \frac{K_s}{K_g M_s} \pi \quad (2-15)$$

and the constrained undrained stress-strain relationship,

$$\sigma_a = M_f e_v \quad (2-16)$$

where

- $\sigma_a$  = total axial stress
- $\sigma_a'$  = effective axial stress
- $M_s$  = constrained modulus of skeleton
- $M_f$  = fully coupled undrained constrained modulus of saturated two phase material

$M_f$  is given by

$$M_f = K_f + M_s - K_s \quad (2-17)$$

Eliminating the effective axial stress from Equations 2-14 and 2-15 yields

$$\sigma_a = \pi \left( 1 - \frac{K_s}{K_g} \right) + M_s \epsilon_v \quad (2-18)$$

Substitution of Equation 2-18 into Equation 2-16 gives

$$\pi = \frac{(M_f - M_s)}{\left( 1 - \frac{K_s}{K_g} \right)} \epsilon_v \quad (2-19)$$

Note that substitution of Equation 2-17 into 2-19 yields Equation 2-7. Thus, the pore pressure response in uniaxial loading is identical to that in hydrostatic loading.

Eliminating the pore pressure from Equations 2-14 and 2-15 gives

$$\sigma_a = \sigma_a' \left( 1 - \frac{K_g}{K_s} \right) + \frac{K_g M_s}{K_s} \epsilon_v \quad (2-20)$$

Substitution of Equation 2-20 into 2-16 gives

$$\sigma_a' = \frac{\left( \frac{K_g M_s}{K_s} - M_f \right)}{\left( \frac{K_g}{K_s} - 1 \right)} \epsilon_v \quad (2-21)$$

Because radial stresses are generally less than axial stresses in uniaxial loading, an additional expression for effective radial stress as a function of volume strain must be developed. In their development of

governing equations for undrained uniaxial loading, Blouin and Kim (1984) give effective radial stress,  $\sigma_r'$ , as

$$\sigma_r' = K_0 \sigma_a' - \frac{(1 - 2\nu)}{(1 - \nu)} \frac{K_s}{K_g} \pi \quad (2-22)$$

where the coefficient of horizontal earth pressure,  $K_0$ , is given by

$$K_0 = \frac{\nu}{1 - \nu} \quad (2-23)$$

and  $\nu$  is Poisson's ratio.

Substitution of Equations 2-19 and 2-21 into 2-22 yields

$$\sigma_r' = \frac{1}{(1-\nu)(K_g-K_s)} [\nu M_s K_g + M_s K_s (1 - 2\nu) - M_f K_s (1 - \nu)] \epsilon_v \quad (2-24)$$

In order to develop a simple idealized model for uniaxial loading we assume the same bilinear model described in Figure 2-1 for the hydrostatic loading with the constrained skeleton modulus given by the elastic relationship

$$M_s = \frac{3(1 - \nu)}{(1 + \nu)} K_s \quad (2-25)$$

Assuming Poisson's ratio to be a constant during both loading and unloading, the appropriate constrained loading and unloading moduli,  $M_{sl}$  and  $M_{su}$  respectively, can be computed from the hydrostatic moduli using Equation 2-25.

For a given maximum axial or volumetric strain,  $\epsilon_{vmax}$ , the corresponding maximum effective axial stress,  $\sigma'_{amax}$ , the maximum effective radial stress,  $\sigma'_{rmax}$ , the maximum pore pressure,  $\pi_{max}$ , and the maximum total axial stress,  $\sigma_{amax}$  are computed using Equations 2-21, 2-24, 2-19 and 2-14 respectively and the appropriate values of loading moduli  $M_{fl}$ ,  $M_{sl}$  and  $K_{sl}$ . Similarly, the effective axial and effective radial stresses during unloading, the pore pressure during unloading and the total axial stress during unloading can be

expressed using the above respective equations and the corresponding unloading moduli,  $M_{fu}$ ,  $M_{su}$  and  $K_{su}$ .

In order to compute the point of liquefaction during the uniaxial loading,  $\epsilon_{vliq}$ , the skeletal conditions at the point of liquefaction must be defined. During undrained unloading the effective radial stress and effective axial stress do not generally tend to reach zero at the same strain. However, as soon as any one of the principal effective stresses drops to zero the skeleton enters in an unconfined state and is assumed to be unable to support skeletal stresses in the other principal stress orientations. Thus, we define the point of liquefaction in undrained uniaxial unloading as the point where any principal effective stress first drops to zero. Generally, the radial effective stress will reach zero before the axial stress. Using a parallel development to that for Equation 2-13 for the hydrostatic loading, the volume strain at the onset of liquefaction during uniaxial unloading can be computed by:

- (1) expressing the peak effective radial stress in terms of peak strain and the appropriate loading moduli according to Equation 2-24;
- (2) expressing effective radial stress during unloading in terms of the volume strain ( $\epsilon_{vmax} - \epsilon_v$ ) and the appropriate unloading moduli using the expression for  $\sigma'_{rmax}$  from (1) above in the same manner used to obtain Equation 2-11;
- (3) Solving the above expression for the volume strain at liquefaction,  $\epsilon_{vliq}$ , by setting the effective radial stress to zero, thus obtaining:

$$\epsilon_{vliq} = \left[ 1 - \frac{(K_g - K_{su})}{(K_g - K_{sl})} \frac{(\nu M_{sl} K_g + M_{sl} K_{sl} (1 - 2\nu) - M_{fl} K_{sl} (1 - \nu))}{(\nu M_{su} K_g + M_{su} K_{su} (1 - 2\nu) - M_{fu} K_{su} (1 - \nu))} \right] \epsilon_{vmax} \quad (2-26)$$



For a fluid, where radial stress equals axial stress (no shear stresses), Poisson's ratio is 0.5 and  $M_s$  equals  $K_s$  according to Equation 2-25; Equation 2-26 then degenerates to Equation 2-13 for hydrostatic loadings.

To illustrate the behavior of a saturated material in uniaxial undrained loading a numerical example is shown in Figure 2.3 using the same material parameters as used in the hydrostatic loading of Figure 2.2. The only additional parameter needed is Poisson's ratio which is taken as

$$\nu = 0.2$$

From Equations 2-25 and 2-17 the constrained loading and unloading moduli of the skeleton and bulk saturated material are computed as

$$M_{sl} = 1.0 \times 10^6 \text{ psi}$$

$$M_{su} = 4.0 \times 10^6 \text{ psi}$$

$$M_{fl} = 2.642 \times 10^6 \text{ psi}$$

$$M_{fu} = 4.831 \times 10^6 \text{ psi}$$

Assuming a peak axial volume strain of 3%, values of peak total axial stress, pore pressure, and effective axial and radial stress were computed from Equations 2-16, 2-19, 2-21 and 2-24 respectively as

$$\sigma_{amax} = 79,260 \text{ psi}$$

$$p_{max} = 54,730 \text{ psi}$$

$$\sigma'_{amax} = 24,530 \text{ psi}$$

$$\sigma'_{rmax} = 2,030 \text{ psi}$$

The hysteretic nature of the skeleton results in liquefaction once the radial effective stress drops to zero at a strain given by Equation 2-26 of

$$\epsilon_{vliq} = 2.546\%$$

Using the values computed above, the load-unload response of the idealized saturated porous material is plotted in Figure 2.3 in terms of total axial stress, pore pressure, and effective axial and radial stresses as functions of

volume strain. The overall behavior during the uniaxial loading is similar to that during the hydrostatic loading, but with several significant differences.

- During unload, liquefaction is assumed to occur when the radial effective stress drops to zero. Since the axial effective stress has not yet reached zero, an instability results. In this figure we have assumed a strain controlled condition, so the instability causes a sudden drop to zero in the axial effective stress. This drop in effective stress results in a sudden drop in total stress and a sudden increase in pore pressure, until pressure equilibrium is achieved in the liquefied soil water mixture. The sudden pore pressure increase is due to the expansion of the solid grains caused by the sudden drop in effective stress. The sudden drop in total stress is due to the sudden loss of axial effective stress in the material skeleton. The drop in effective stress equals the sum of the increase in pore pressure plus the decrease in total stress, according to the effective stress law.
- The actual energy loss during the uniaxial load-unload cycle (represented by the hysteresis in the total axial stress cycle) is approximately four times that experienced in the hydrostatic loading to the same peak volume strain. This is also reflected by the higher hysteresis in the effective axial stress cycle as compared to the effective pressure cycle in the hydrostatic loading.
- The pore pressure response during the loading and initial portion of the unloading is identical in the uniaxial and hydrostatic loadings. At the onset of liquefaction, however, the pore pressure suddenly increases during the uniaxial unloading.

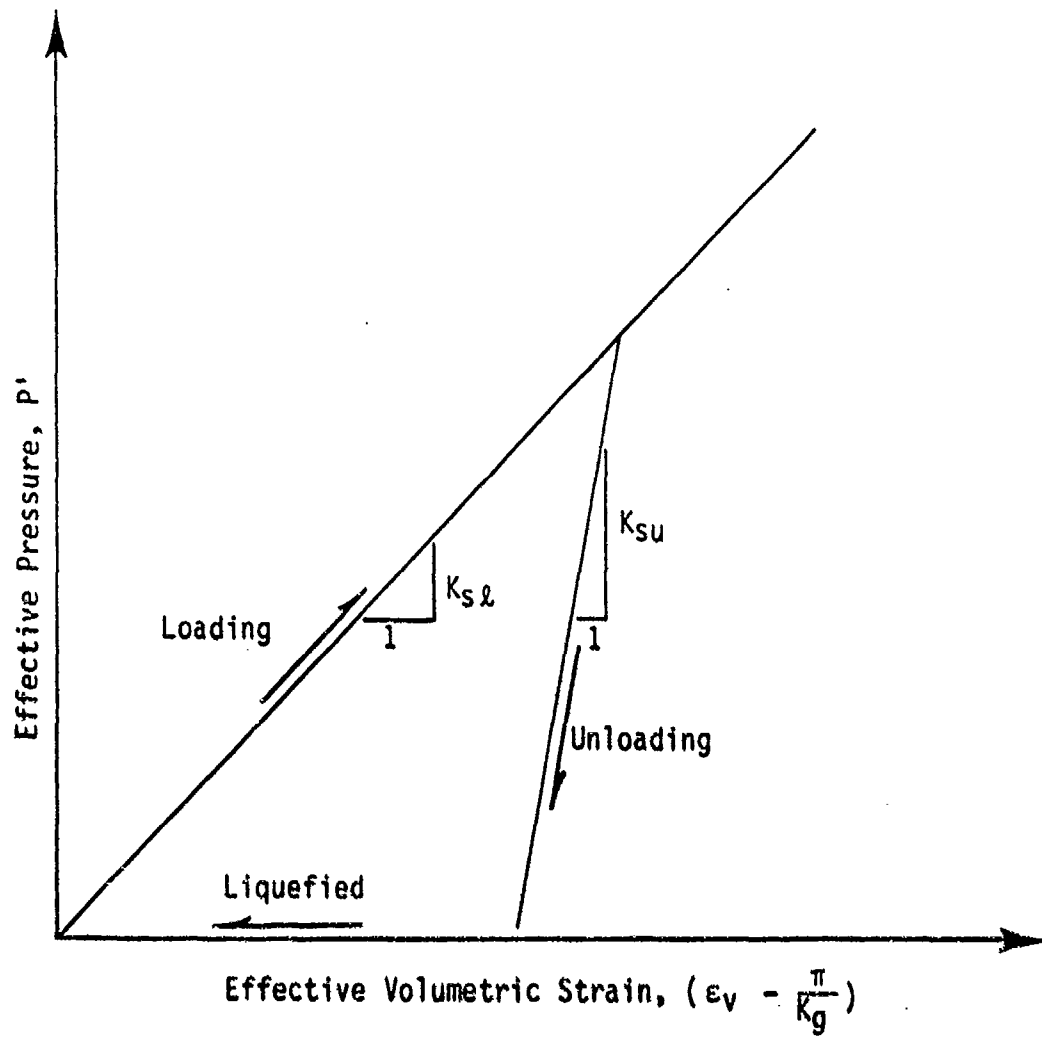


Figure 2.1. Idealized simple bilinear skeleton model.

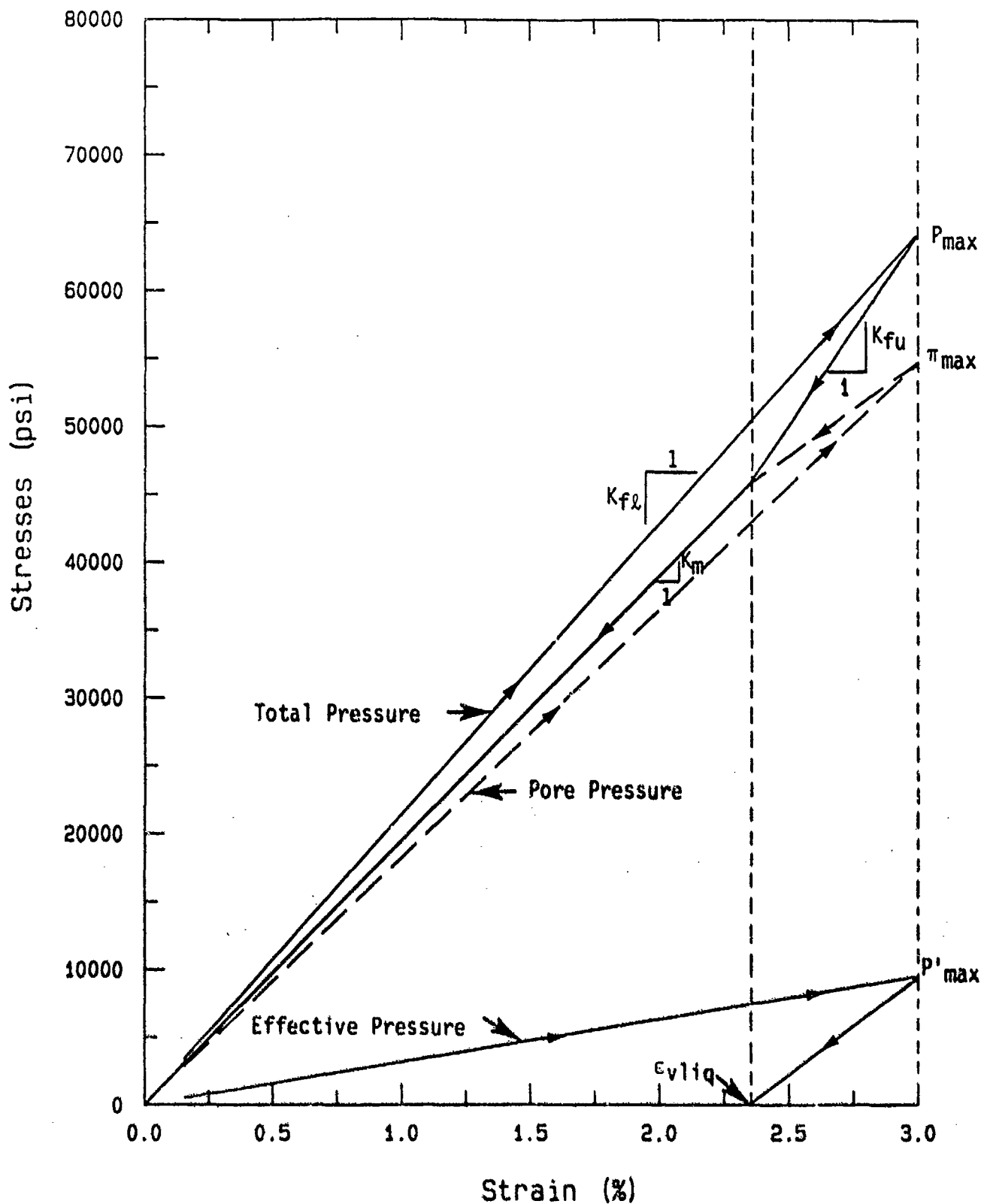


Figure 2.2. Undrained hydrostatic load-unload response of idealized saturated porous material.

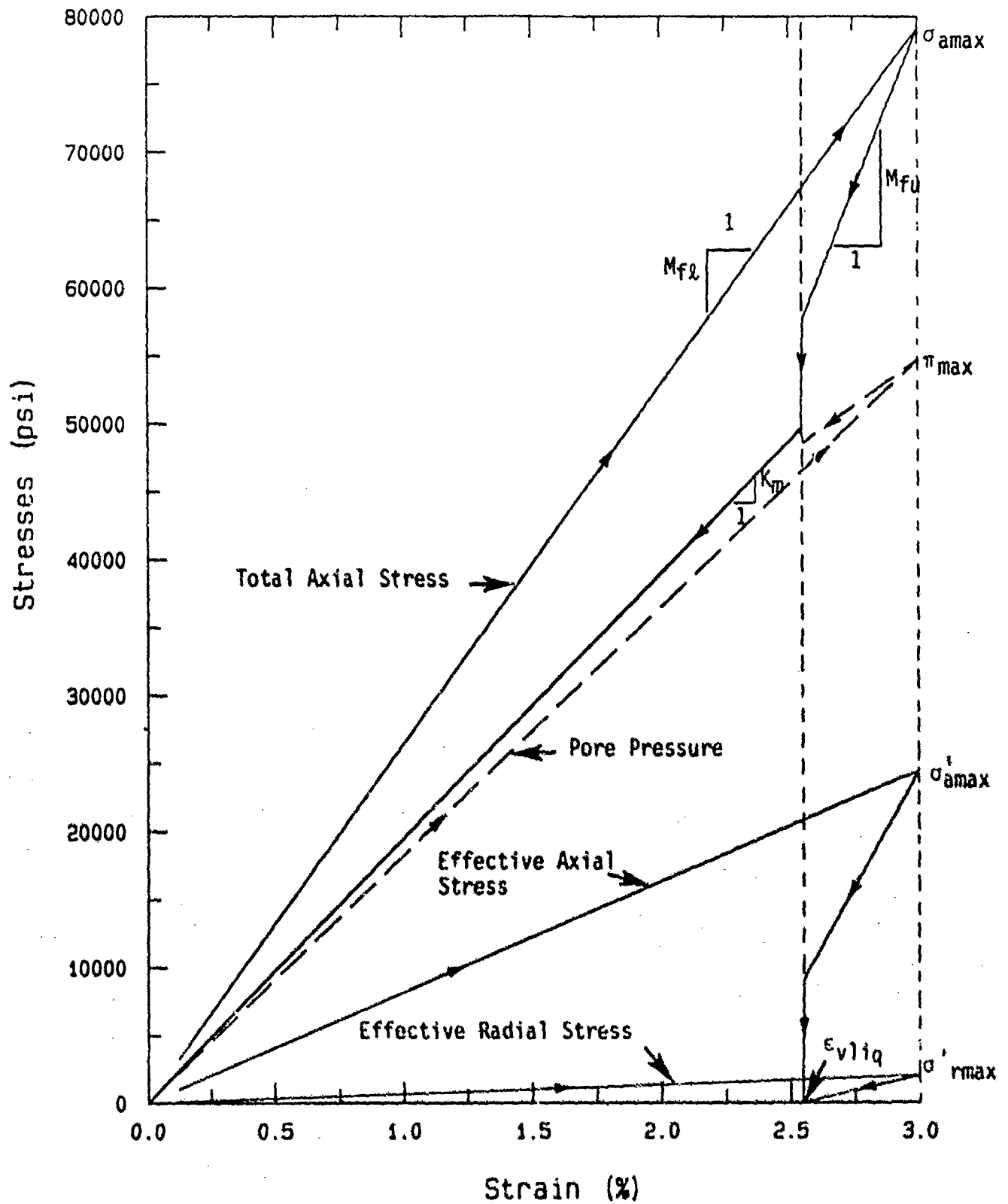


Figure 2.3. Undrained uniaxial strain load-unload response of idealized saturated porous material.



## SECTION 3

### NUMERICAL TREATMENT OF UNDRAINED UNIAXIAL LOADING

#### 3.1 INTRODUCTION

As discussed in the introduction to Section 2, there are advantages in modeling the undrained response of saturated porous materials based on the properties of their individual components. Section 2 provides the theoretical basis for modeling both the undrained hydrostatic and uniaxial response using linear approximations of the pore water and solid grain response and bilinear approximations of the skeleton response. In reality, none of the components of saturated porous soils and rocks are linear, particularly at the stresses of interest in modeling explosive loadings. Basically, all of the constitutive relationships developed in section 2 can be applied in incremental form using numerical techniques to model the actual nonlinear behavior of real earth materials in undrained loadings. This section describes the development of numerical techniques for modeling undrained uniaxial strain load-unload behavior of saturated porous materials and presents demonstration calculations. The numerical model incorporates nonlinear elastic response of the solid grains and pore water and nonlinear plastic response of the porous skeleton. Hydrostatic loadings, as discussed in Section 2, can be treated as a special case of uniaxial loadings where the constrained moduli equal the bulk moduli and Poisson's ratio is 0.5.

#### 3.2 CONSTITUTIVE MODEL FOR DRAINED POROUS SKELETON

The drained uniaxial loading response of a porous rock or soil skeleton is generally unique for a given material and can be established experimentally. The loading response can be digitized and input as part of the skeleton model for each particular material. The unloading behavior has been shown (Blouin, Martin and McIntosh, 1984) to be a function of the peak axial stress. Thus, skeleton unloading must be modeled using analytic formulations that describe the unloading response as a function of previous maximum stress.

Figure 3.1 shows a typical uniaxial load-unload response for a soil skeleton. The skeleton is strongly hysteretic, with the unload curve initially dropping steeply, but breaking back toward the stress axis at low axial stress, in what is often described as the unloading hook. In dynamic problems it is usually important to model the unloading hook, because a large percentage of the response time is spent on this portion of the unload curve, and it thus has a strong influence on late-time displacements. It will also have a strong influence on the onset of liquefaction during undrained unloading. The maximum strain at the peak axial stress,  $\sigma'_p$ , is comprised of an elastic or recoverable component,  $\epsilon'_e$ , and a plastic or permanent component,  $\epsilon'_p$ .

An expanded view of the schematic unloading response is shown in Figure 3.2. The unloading is approximated by a bilinear unload having an initial unload modulus,  $M_{ui}$ , and an approximation to the unloading hook of  $M_{uh}$ . The break point between the two slopes is chosen so that the energy dissipation in the approximation equals that lost in the actual load-unload cycle. This is achieved by adjusting the break so that the two shaded areas of Figure 3.2 are equal. The fraction,  $r$ , defines the break point between the linear unloading approximations. As a mathematical convenience, we introduce the apparent unloading modulus,  $M_{ua}$ .

The initial unloading modulus,  $M_{ui}$ , can generally be expressed as an exponential function of the peak axial stress (Merkle and Dass, 1985). It is represented by

$$M_{ui} = a_3 \sigma'_p{}^{a_4} \quad (3-1)$$

Figure 3.3, from Blouin, Martin and McIntosh (1984) shows a fit to initial unloading moduli of Enewetak beach sand given by

$$M_{ui} = 347 \sigma'_p{}^{(0.65)} \quad (3-2)$$

where  $M_{ui}$  and  $\sigma'_p$  are measured in ksi.



Analysis of the same Enewetak data set shows that the recoverable strain,  $\epsilon'_e$ , is also an exponential function of the peak stress given by

$$\epsilon'_e = a_1 \sigma'_p a_2 \quad (3-3)$$

Figure 3.4 shows the fit to the Enewetak sand data which is given by

$$\epsilon'_e = 0.031 \sigma'_p (0.45) \quad (3-4)$$

where strain is expressed in percent and stress in psi.

Finally, the break point between the two linear unload approximations, expressed as the fraction,  $r$ , is approximately constant, as demonstrated in Figure 3.5 for the Enewetak beach sand. An average  $r$  value of 15.2% was obtained.

From geometric analysis of Figure 3.2, an expression for the hook modulus,  $M_{uh}$ , can be derived which is given as

$$M_{uh} = \frac{r M_{ua}}{(1 - (1 - r) \frac{M_{ua}}{M_{ui}})} \quad (3-5)$$

where the apparent unloading modulus is given by

$$M_{ua} = \frac{\sigma'_p}{\epsilon'_e} \quad (3-6)$$

All the values on the right side of Equation 3-5 are defined in the previous equations.

### 3.3 CONSTITUTIVE MODEL FOR WATER

Kim, Blouin and Timian (1986) presented a composite table for the pressure volume response of fresh water and sea water at pressures from 0 to 800 kbars. For calculational purposes the tangent bulk modulus is expressed

as a function of pressure by fitting the modulus data at a temperature of 20°C for the fresh water and 25° for the sea water.

$$\text{Sea Water: } K_W = 0.00034283\pi^2 + 6.1839\pi + 23806.6 \quad (3.7a)$$

$$\text{Fresh Water: } K_W = 0.00031775\pi^2 + 6.2713\pi + 21746.9 \quad (3.7b)$$

for  $\pi \leq 10,000$  bars

$$\text{Sea Water: } K_W = 9.55\pi + 24758. \quad (3.8a)$$

$$\text{Fresh Water: } K_W = 9.49\pi + 21920. \quad (3.8b)$$

for  $10,000 < \pi \leq 100,000$  bars

$$\text{Sea Water: } K_W = 0.00000291\pi^2 + 3.365\pi + 614918. \quad (3.9a)$$

$$\text{Fresh Water: } K_W = 0.00000685\pi^2 + 1.337\pi + 768348. \quad (3.9b)$$

for  $\pi > 100,000$  bars

where  $\pi$  and  $K_W$  are expressed in terms of bars.

Figure 3.6 parts a through c, show the fits to the fresh water data.

### 3.4 CONSTITUTIVE MODEL FOR SOLID GRAINS

In order to realistically model the nonlinear response of the solid grains to both the applied pore pressure and effective stress, analytic expressions for the deformation of solids at high pressure are required. High pressure data for many rocks and minerals show a linear relationship between loading wave velocity and particle velocity (e.g. Allen, 1967). Loading wave velocity,  $c_L$ , can be expressed as

$$c_L = c_0 + S v_p \quad (3-10)$$

where  $c_0$  = the initial wave velocity at relatively low pressure  
 $v_p$  = peak particle velocity

S = experimentally determined constant relating  $c_L$  to  $v_p$  (generally about equal to 1.5 for most dense rocks and minerals).

Conservation of mass and momentum on either side of the wavefront yield the familiar relationships (e.g. Chou and Hopkins, 1972).

$$\sigma_p = \rho_0 c_L v_p \quad (3-11)$$

and

$$M = \rho_0 c_L^2 \quad (3-12)$$

where

$\sigma_p$  = peak axial stress

$\rho_0$  = initial material density

M = constrained secant modulus defined as

$$M = \frac{\sigma_p}{\epsilon_p} \quad (3-13)$$

where

$\epsilon_p$  = peak axial strain corresponding to the peak stress  $\sigma_p$

Substitution of Equation 3-10 into 3-11 gives

$$\sigma_p = \rho_0 c_0 v_p + \rho_0 S v_p^2 \quad (3-14)$$

and solving for peak particle velocity as a function of peak stress yields

$$v_p = \frac{f(\sigma_p)}{2\rho_0 S} \quad (3-15)$$

where

$$f(\sigma_p) = (\rho_0^2 c_0^2 + 4\rho_0 S \sigma_p)^{\frac{1}{2}} - \rho_0 c_0 \quad (3-16)$$

Substitution of Equation 3-15 into 3-12 gives

$$M = F(\sigma_p) \quad (3-17)$$

where

$$F(\sigma_p) = \rho_0 c_0^2 + c_0 f(\sigma) + \frac{f^2(\sigma)}{4\rho_0} \quad (3-18)$$

The constrained tangent modulus,  $M_t$ , used in the numerical model is defined as the slope of the stress strain curve by

$$M_t = \frac{d\sigma}{d\epsilon} \quad (3-19)$$

Equating 3-17 and 3-13 and solving for  $\epsilon_p$  yields

$$\epsilon_p = \frac{\sigma_p}{F(\sigma_p)} \quad (3-20)$$

Differentiating Equation 3-20 with respect to  $\sigma_p$  and inverting gives the constrained tangent modulus as

$$M_t = \frac{F^2(\sigma_p)}{F(\sigma_p) - \sigma_p F'(\sigma_p)} \quad (3-21)$$

Differentiating Equations 3-18 and 3-16 with respect to  $\sigma_p$  yields

$$F'(\sigma_p) = c_0 f'(\sigma_p) + \frac{f(\sigma_p) f'(\sigma_p)}{2\rho_0} \quad (3-22)$$

and

$$f'(\sigma_p) = \frac{2\rho_0 S}{(\rho_0^2 c_0^2 + 4\rho_0 S \sigma_p)^{1/2}} \quad (3-23)$$

Equations 3-15 through 3-23 can be used to define the high pressure constrained stress strain and modulus relationships for the solid grains. A numerical example is shown in Figure 3.7 using the following material parameters:

$$\rho_0 = 5.14 \text{ lb-S}^2/\text{ft}^4 \text{ (2650 kg/m}^3\text{)}$$

$$c_0 = 16735 \text{ ft/s (5100 m/s)}$$

$$S = 1.5$$

Substituting  $c_0$  into Equation 3-12 gives an initial secant modulus of

$$M = 10 \times 10^6 \text{ psi (690 kbars)}$$

As explained in Section 2, the volumetric relationships for the solid grains should be specified in terms of the bulk modulus,  $K_g$ , rather than in terms of the constrained modulus. At high pressures, the shear strength of the grain materials becomes insignificant compared to the applied stress and the materials tend to behave like fluids. At these pressures, the bulk tangent modulus equals the constrained tangent modulus with Poisson's ratio equal to 0.5. Beneath some threshold stress,  $P_b$ , Poisson's ratio begins to decrease from 0.5 at  $P_b$  to an initial value of Poisson's ratio,  $\nu_0$ , at a low value of mean stress. We have used the simple relationship depicted in Figure 3.8 to approximate the influence of mean stress on Poisson's ratio and the ratio of bulk modulus to constrained modulus,  $g(p)$  is related as

$$K_g = g(p)M_t$$

(3-24)

where  $g(p)$  is defined as

$$g(p) = \frac{2}{3} \frac{(1 - 2\nu_o)}{(1 - \nu_o)} \frac{p}{p_b} + \frac{(1 + \nu_o)}{3(1 - \nu_o)}$$

(3-25)

for  $p < p_b$ .

For  $p \geq p_b$ ,

$$g(p) = 1$$

(3-26)

Poisson's ratio can be computed as a function of the modulus ratio,  $g(p)$ , at a given pressure as

$$\nu = \frac{3g(p) - 1}{1 + 3g(p)}$$

(3-27)

Figure 3.8 shows both the modulus ratio and Poisson's ratio plotted as a function of pressure for typical solid grains having an initial Poisson's ratio of 0.2 and a threshold pressure,  $p_b$ , of 5 kbars.

### 3.5 MODELING PRELOAD CONDITIONS

Dynamic undrained loadings of in situ saturated materials do not start from a condition of zero stress because, except right near the surface, the materials are under some initial in situ stress conditions. The effective vertical stress will equal the stress imposed by the buoyant weight of the overburden, though this may be modified by local tectonic stress conditions.

The pore pressure will normally be a function of the water table depth, which will also affect the buoyant overburden load and effective stresses. Thus, initial in situ effective stress and pore pressure conditions are infinitely variable relative to one another and must be treated as mutually independent. In order to compute the undrained response to uniaxial strain loadings of in situ material, a methodology has been developed to account for the influence of the in situ stresses and pore pressures on the in situ material response.

It is helpful to use a laboratory test procedure analogy to develop the governing in situ stress-strain relationships. We can establish three sample states:

1. The virgin stress-free (unstrained) state prior to application of any effective stress or pore pressure; we assume a total volume of the saturated sample,  $\bar{V}_0$ , of unity;

$$\bar{V}_0 = 1 \quad (3-28)$$

The corresponding porosity,  $\bar{n}_0$ , is defined as

$$\bar{n}_0 = \frac{\bar{V}_0 - V_{go}}{\bar{V}_0} = 1 - \frac{V_{go}}{\bar{V}_0} \quad (3-29)$$

where  $V_{go}$  = volume of solid grains in the virgin unstrained state.

Equation 3-29 can be rewritten to give the grain fraction in terms of porosity as

$$\boxed{\frac{V_{go}}{\bar{V}_0} = 1 - \bar{n}_0} \quad (3-30)$$

2. The in situ stress state, where the in situ effective stresses and pore pressures are either known or can be defined. The in situ stresses and pore pressures are governed by the depth of overburden and depth of the water table. The notation for the in situ state is

$\pi_i$  = in situ pore pressure  
 $\sigma'_i$  = in situ effective vertical (axial) stress  
 $V_{wi}$  = volume of pore water in the in situ stress condition

3. A set of hypothetical parameters which preserve the in situ material mass in the zero stress condition. In addition to  $V_{go}$ , we have

$V_{wo}$  = volume of pore water in the in situ material, but at zero pore pressure

Define the total volume of in situ material in the zero stress condition,  $V_o$ , as

$$V_o = V_{go} + V_{wo} \quad (3-31)$$

Define the ratio of  $V_{wo}$  to  $V_o$  as a fictitious porosity,  $n_o$ , according to

$$n_o = \frac{V_{wo}}{V_o} \quad (3-32)$$

The parameters in this third state are defined for mathematical convenience. Since the pore pressure and the effective stress in the in situ condition are specified independently, the volumes of in situ material when taken to the zero stress state do not generally constitute a compatible saturated material. The volume of zero stress pore water will generally be too small or too large to fill the available pore space.

Equation 2-15 can be rewritten in incremental form as

$$d\bar{\epsilon} = \frac{d\sigma'}{M_s} + \frac{3K_s}{M_s} \frac{d\pi}{3K_g} \quad (3-33)$$

where the modulus values represent the tangent moduli at the stress level of interest and the total strain increment  $d\bar{\epsilon}$  is in terms of the virgin state.



The final term  $d\pi/3K_g$  represents the axial component of strain created by the pore water compression of the solid grains. It can be expressed as

$$d\bar{\epsilon}_{g\pi} = \frac{d\pi}{K_g} \quad (3-34)$$

where  $\epsilon_{g\pi}$  is the volumetric strain of the solid grains due to the pore water pressure.

The term  $3K_s/M_s$  represents the apparent softening of the skeleton due to the fact that the uniform decrease in grain volume generated by the pore pressure must be redistributed as an axial volume decrease in the uniaxial loading. The term  $d\sigma'/M_s$  is the component of strain due to the effective stress and can be expressed as

$$d\bar{\epsilon}' = \frac{d\sigma'}{M_s} \quad (3-35)$$

Using Equations 3-34, 3-35 and 2-25, Equation 3-33 can be rewritten in terms of incremental strain as

$$d\bar{\epsilon} = d\bar{\epsilon}' + \frac{(1 + \nu)}{3(1 - \nu)} d\epsilon_{g\pi} \quad (3-36)$$

To obtain the total strain at the in situ stress state, we integrate Equation 3-36 to give

$$\bar{\epsilon}_i = \epsilon_i' + \frac{(1 + \nu)}{3(1 - \nu)} \epsilon_{g\pi i} \quad (3-37)$$

where the terms  $\epsilon_i'$  and  $\epsilon_{g\pi i}$  represent integrations of the nonlinear strain relationships with respect to stress.

The total strain in the in situ condition is defined as

$$\bar{\epsilon}_i = 1 - \frac{V_i}{V_0} \quad (3-38)$$

and the ratio of the in situ total volume to the initial volume in the virgin state is obtained by combining Equations 3-37 and 3-38 to give

$$\frac{V_i}{V_0} = 1 - \epsilon'_i - \frac{(1 + \nu)}{3(1 - \nu)} \epsilon_{gi} \quad (3-39)$$

The total strain in the solid grains in the in situ condition,  $\epsilon_{gi}$ , is defined as

$$\epsilon_{gi} = 1 - \frac{V_{gi}}{V_{go}} \quad (3-40)$$

where  $V_{gi}$  = the in situ grain volume

This strain is a function of the pressure on the grains,  $p_{gi}$ , which is given by

$$p_{gi} = \frac{p'_i}{1 - n_i} + \pi_i \quad (3-41)$$

where  $n_i$  = in situ porosity  
 $p'_i$  = effective mean stress in the porous skeleton  
 $p'_i/(1-n_i)$  = pressure on the solid grains due to effective stresses in the skeleton.

The effective mean stress in the skeleton can be determined from

$$p'_i = 1/3 (\sigma'_i + 2\sigma'_{r,i}) \quad (3-42)$$

where  $\sigma'_{r,i}$  = the in situ radial effective stress

From equations 2-22, 2-23 and 3-42 we obtain

$$p'_i = \frac{(1 + \nu)}{3(1 - \nu)} \sigma'_i - \frac{2(1 - 2\nu)}{3(1 - \nu)} \frac{K_g}{K_g} \pi_i \quad (3-43)$$

where the bulk moduli values are the secant moduli at the in situ stress level.

The total strain in the grains in the in situ condition can now be obtained by using the total pressure on the grains from Equation 3-41 to compute the strain from the grain properties described in Section 3.4. The volume of the grains in the in situ state relative to the volume in the virgin state is obtained by rewriting Equation 3-40,

$$\frac{V_{gi}}{V_{go}} = 1 - \epsilon_{gi} \quad (3-44)$$

Finally, the volume strain in the pore water in the in situ state is given as

$$\epsilon_{wi} = 1 - \frac{V_{wi}}{V_{wo}} \quad (3-45)$$

and can be directly obtained from the pressure volume relationships for water described in subsection 3.3. Equation 3.45 is rewritten as

$$\frac{V_{wi}}{V_{wo}} = 1 - \epsilon_{wi} \quad (3-46)$$

The total compressed volume of material in the in situ state is given by

$$V_i = V_{gi} + V_{wi} \quad (3-47)$$

The calculational procedure used to compute the initial in situ state is outlined below.

1. Let the virgin volume,  $\bar{V}_0$ , equal unity using Equation 3-28.

2. Compute the solid grain volume,  $V_{g0}$ , from Equation 3-30.
3. Compute the solid grain volume under the in situ stress conditions,  $V_{gi}$ , from Equation 3-44.
4. Compute the total in situ volume from Equation 3-39.
5. Compute the in situ pore water volume from Equation 3-47.
6. Compute the in situ pore water volume at zero pressure,  $V_{w0}$ , from Equation 3-46.
7. Compute the total volume of in situ material in the zero stress state,  $V_0$ , from Equation 3-31.
8. Compute the fictitious porosity,  $n_0$ , from Equation 3-32.
9. Compute the in situ porosity,  $n_i$ , from

$$n_i = \frac{V_{wi}}{V_i} \quad (3-48)$$

10. Compute the in situ volume strain,  $\bar{\epsilon}_i$ , from Equation 3-38.

### 3.6 NUMERICAL MODELING OF UNIAXIAL UNDRAINED RESPONSE

#### 3.6.1 Computational Algorithm NKOCF

In order to realistically predict the response of saturated porous materials to undrained loadings, the nonlinear response characteristics of the individual components must be accurately modeled. This requires an incremental numerical technique which can incorporate all important behavioral characteristics of the solid grains, pore water and most importantly the material skeleton. The algorithm NKOCF fully describes the load-unload response of fully saturated porous materials in uniaxial strain conditions. NKOCF uses the fully coupled material model described by Kim, Blouin and Timian (1986). It can also be used to simulate hydrostatic loadings by substituting the bulk

moduli for the constrained moduli, and setting Poisson's ratio to 0.5. NKOCP is an advanced version of KOCP, described by Kim, Blouin and Timian (1986) with the added capabilities of:

- modeling the response of materials starting from an arbitrary specified in situ stress condition;
- modeling the unloading response including liquefaction.

This improved algorithm incorporates the unloading model for the skeleton described in subsection 3.2, the solid grain model described in 3.4 and the preload capabilities described in 3.5. Details of the computational procedures are described by Kim, Blouin, and Timian (1986), Section 5.

### 3.6.2 NKOCP User's Manual

NKOCP, listed in Appendix A, uses input from Tapes 55 and 8. Tape 55 includes:

- the digitized skeleton stress-strain loading response (usually obtained from drained laboratory tests),
- parameters describing the drained skeleton unloading characteristics,
- in situ parameters
- solid grain properties
- general input/output control parameters

Tape 8 contains a table of  $K_0$  vs. effective vertical strain pairs. The compressibility of the pore water from subsection 3.3 is built in. All inputs are in free format.

### DESCRIPTION OF INPUT FILES

#### TAPE 55

### Card 1 - General Parameters

NF, NW, EMAX, NDIV, NDIVU, NDIVM, LPRINT

NF = 0 pressure in psi  
= 1 pressure in bars  
= 2 pressure in psi with constant water modulus,  $K_w$ , of  $0.3 \times 10^6$  psi and constant solid grain modulus,  $K_g$ , of  $5 \times 10^6$  psi.

NW = 0 fresh water  
= 1 sea water

EMAX = Maximum total strain at the start of unload

NDIV = Number of interpolation divisions between each consecutive data point on the loading stress-strain curve

NDIVU = Number of equal strain decrements between  $\epsilon'_p$  and EMAX used to compute unloading prior to liquefaction

NDIVM = Number of equal strain decrements between 0 and the point of liquefaction used to compute unloading following liquefaction

LPRINT = Output printing interval, e.g. for LPRINT = 10 every tenth computed point will be output.

### Card 2 - In Situ Characteristics

PF, SE, V, POR

PF = In situ pore water pressure

SE = In situ effective vertical stress

V = Poisson's ratio of in situ skeleton

POR = Virgin porosity prior to any loading.

Card 3 - Skeleton Unloading Characteristics

A1, A2, A3, A4, R, XKOI, XKOH

A1, A2 = Recoverable unloading strain parameters from Equation 3-3

A3, A4 = Parameters for initial unloading constrained modulus from Equation 3-1

R = Stress fraction at the break point of the two unloading slopes described in Figure 3.2

XKOI = Value of  $K_0$  during the initial unloading

XKOH = Value of  $K_0$  during unload along the second (hook) portion of the bilinear unloading slope

Card 4 - Solid Grain Properties

R0, C0, GVO, SS, PB

R0 = Initial grain density,  $\text{lb-s}^2/\text{in}^4$

C0 = Initial wavespeed,  $\text{in/s}$

GVO = Poisson's ratio at low stress from Figure 3.8

SS = Slope of propagation velocity to particle velocity relationship, S

PB = Threshold pressure, psi, where the tangent constrained modulus becomes equal to the tangent bulk modulus from Figure 3.8

Card 5 - Digitized Virgin Skeleton Loading Stress-Strain Response

NPOINT

$\epsilon'_1, \sigma'_1$	}	NPOINT cards with effective vertical strain and stress pairs
$\epsilon'_2, \sigma'_2$		
- -		
- -		
$\epsilon'_n, \sigma'_n$		

TAPE 8

Card 1 -  $K_0$  Values for Skeleton During Loading

NKO

$\epsilon'_1, K_{01}$	}	NK0 cards with effective vertical strain and $K_0$ pairs, e.g. between $\epsilon'_1$ and $\epsilon'_2$ the value $K_{02}$ is used
$\epsilon'_2, K_{02}$		
- -		
- -		
$\epsilon'_n, K_{0n}$		

DESCRIPTION OF OUTPUT FILES

Output is on three tapes, 6, 3, and 66. Tapes 6 and 3 contain load-unload response prior to liquefaction. Tape 66 contains the response following liquefaction.



# TAPE 6

$\epsilon, \sigma'_v, \pi, \sigma, LF$


$\epsilon$  = Total volume strain (%)

$\sigma'_v$  = Effective vertical stress

$\pi$  = Pore water pressure

$\sigma$  = Total vertical stress

LF = 0 indicates stress state on virgin loading curve

= 1 indicates stress state on the initial unloading curve

= 2 indicates stress state on the hook portion of the unloading curve

= 4 indicates stress state post liquefaction, mixture response

# TAPE 3

$\epsilon, \sigma'_h, \sigma_h, M_f, n$


$\epsilon$  = Total volume strain (%)

$\sigma'_h$  = Effective horizontal stress

$\sigma_h$  = Total horizontal stress

$M_f$  = Fully coupled constrained tangent modulus

$n$  = Current porosity

$\epsilon, \pi, K_m, n$


$\epsilon$  = Total volume strain (%)

$\pi$  = Pore water pressure

$K_m$  = Undrained tangent mixture modulus

$n$  = Current porosity

### 3.6.3 Example Problem

An example problem is documented in Appendix B. This example problem duplicates the sample problem described in Section 2.4. Appendix B includes Table B.1 for the listings of input files, Table B.2 for the listings of output files, and Figure B.1 for the load-unload response of the example problem.

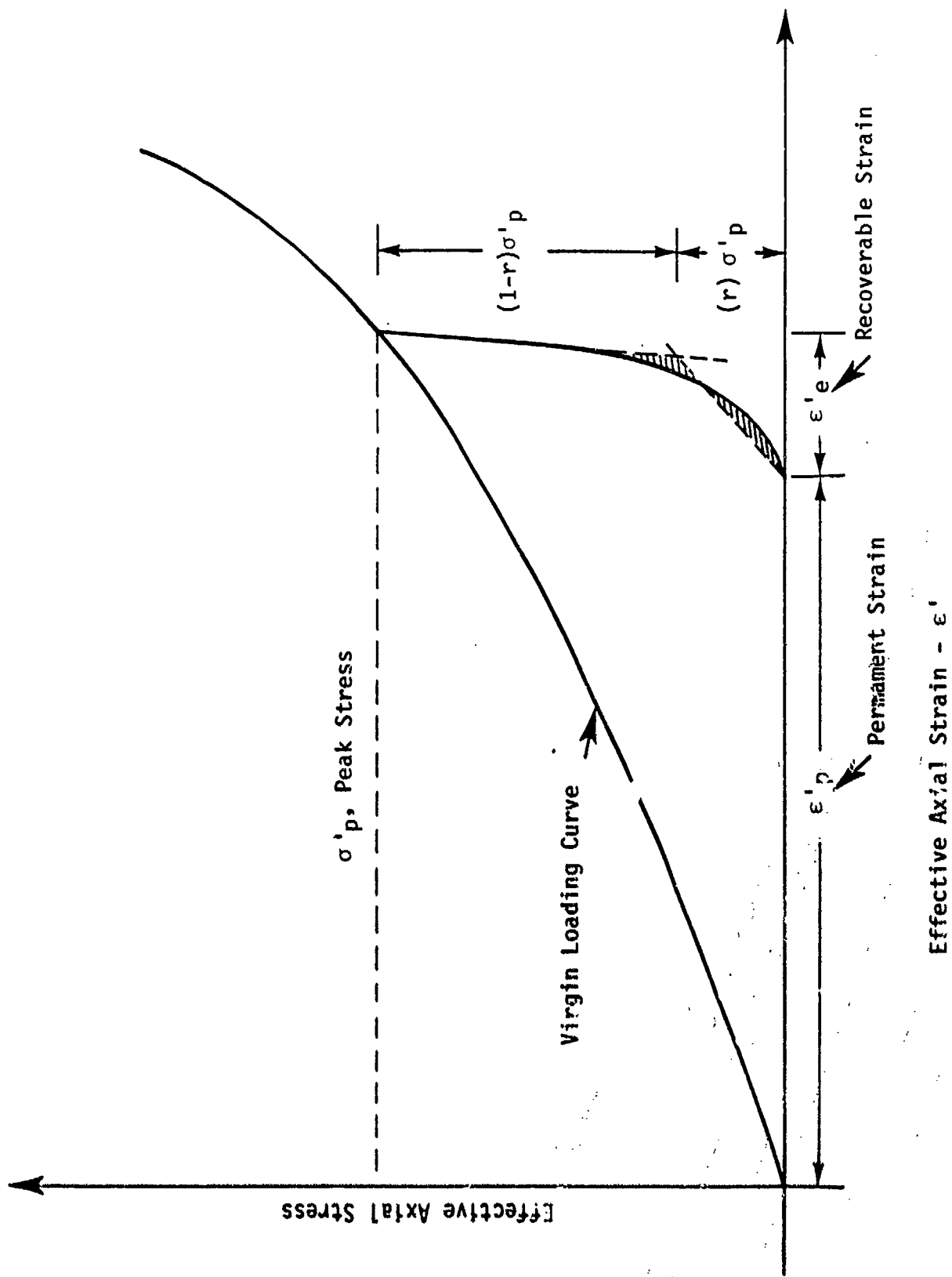


Figure 3.1. Schematic skeleton stress-strain behavior during drained uniaxial strain loading.

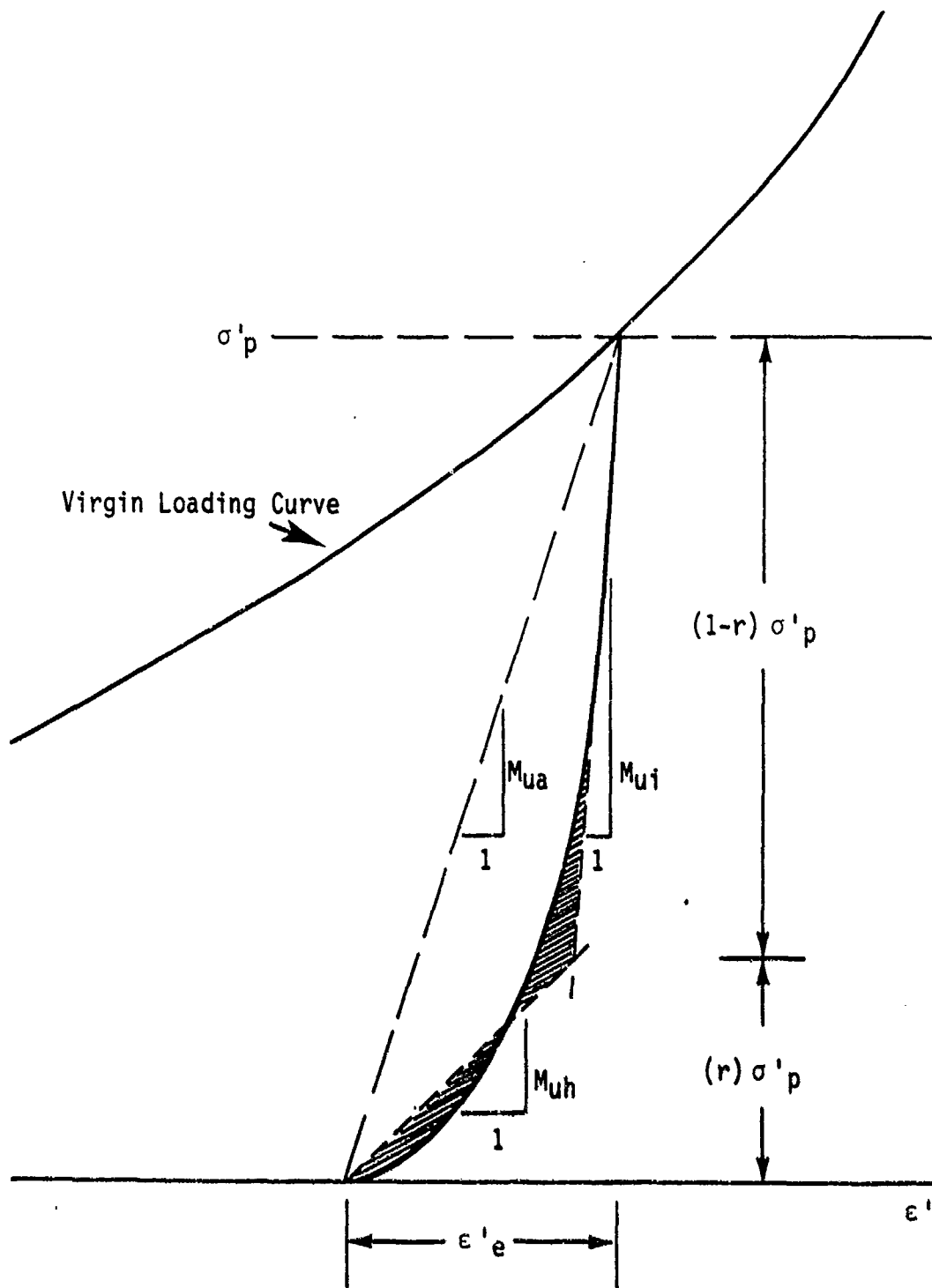


Figure 3.2. Variable bilinear approximation of constrained unloading.

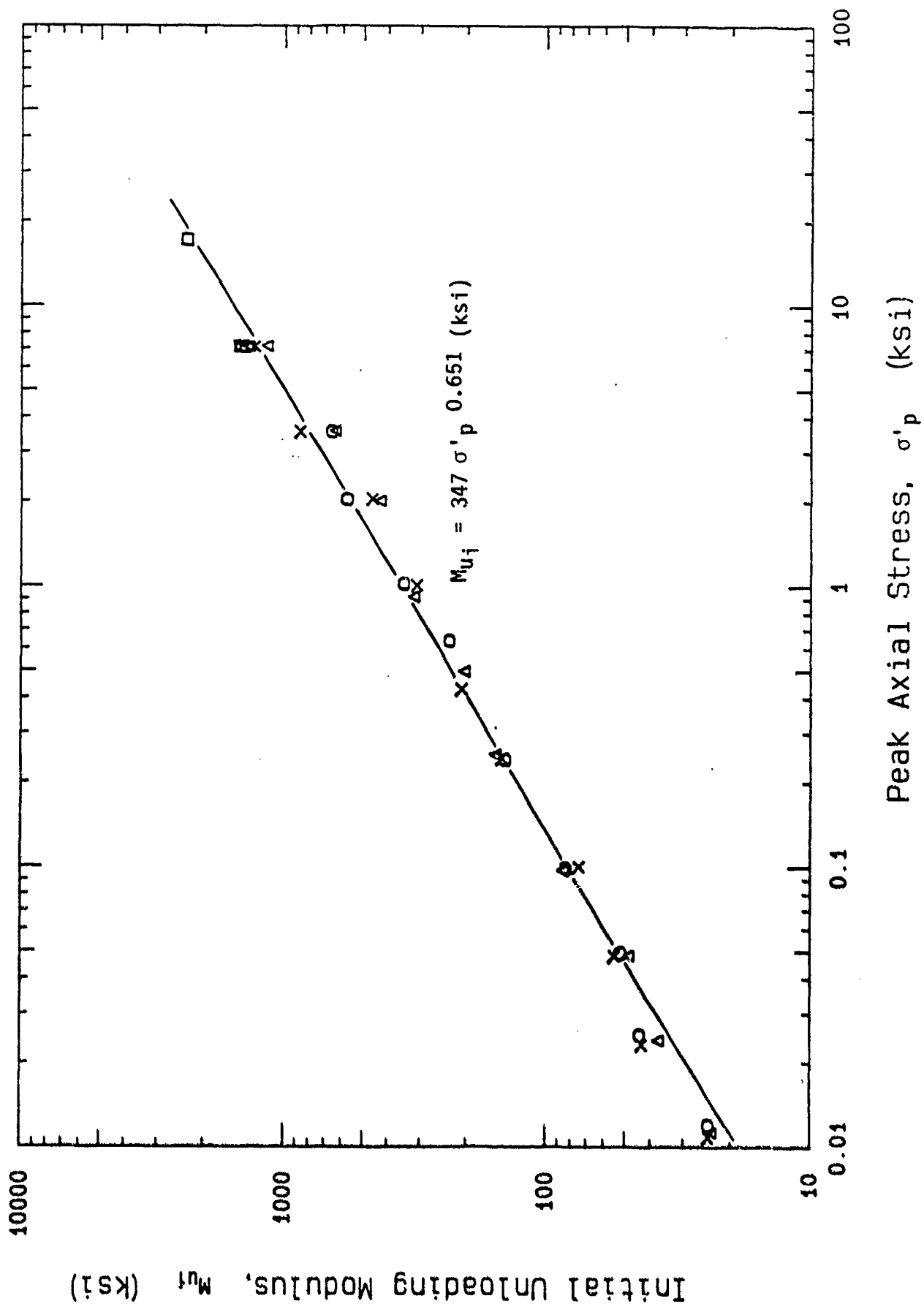


Figure 3.3. Initial constrained unloading modulus, Enewetak beach sand.

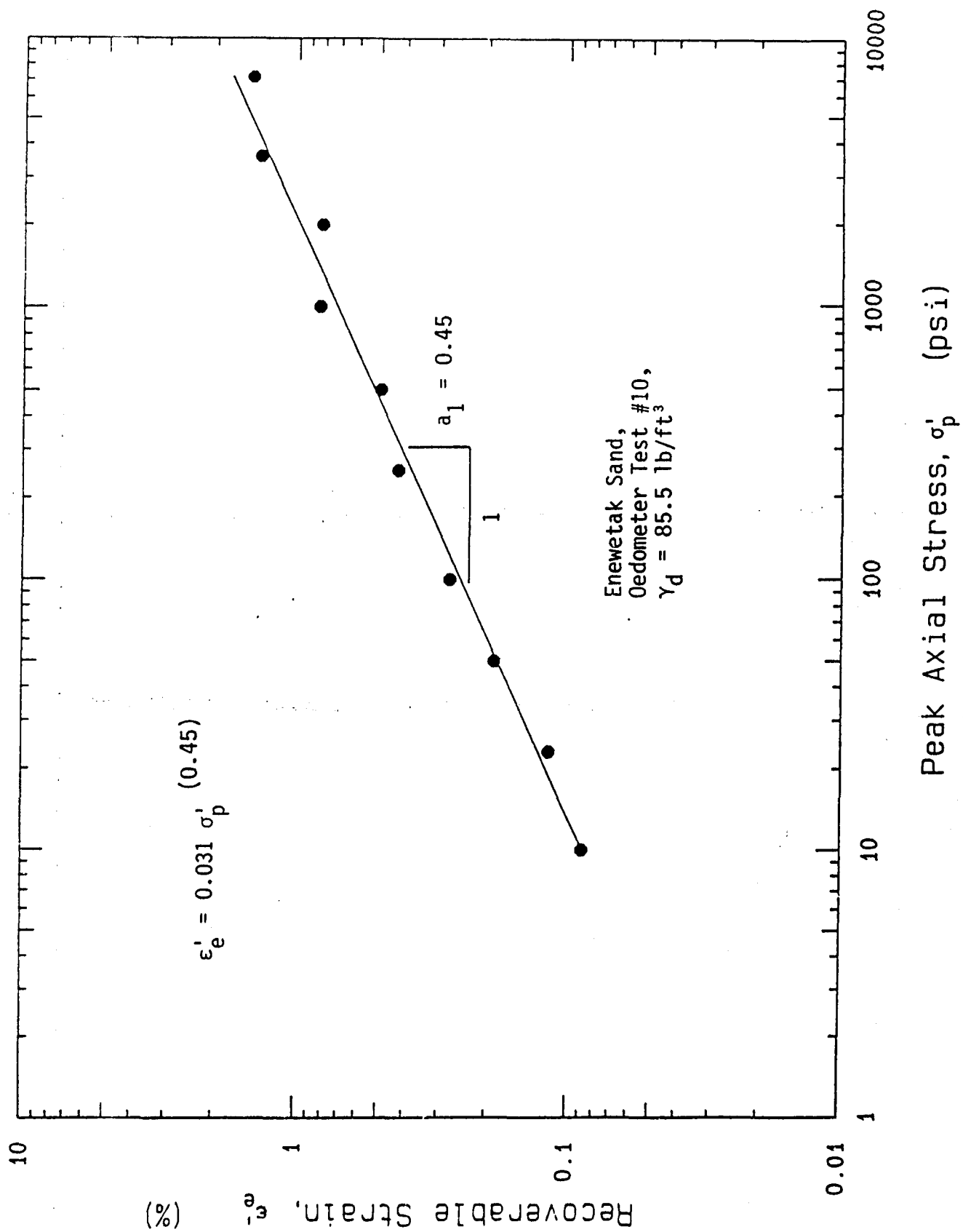


Figure 3.4. Recoverable strain as a function of peak stress for Enewetak beach sand.

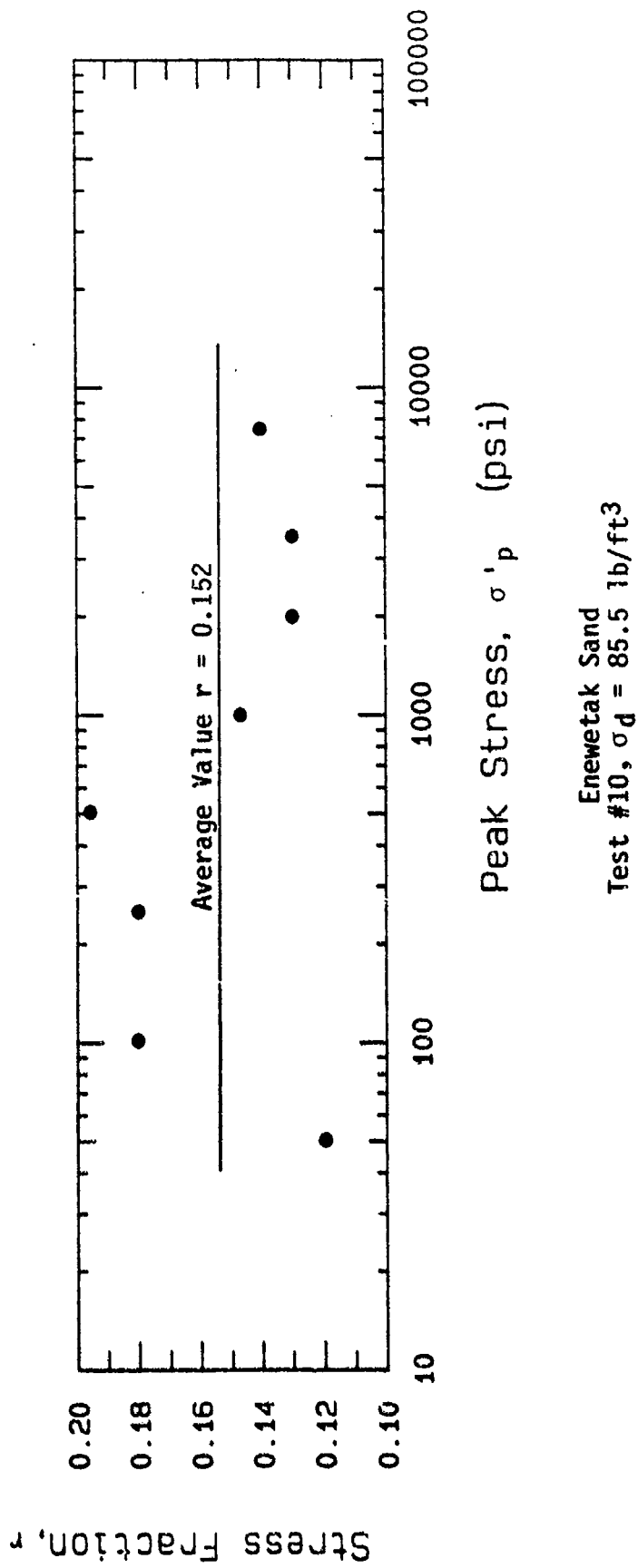


Figure 3.5. Stress fraction,  $r$ , vs peak stress for Enewetak beach sand.

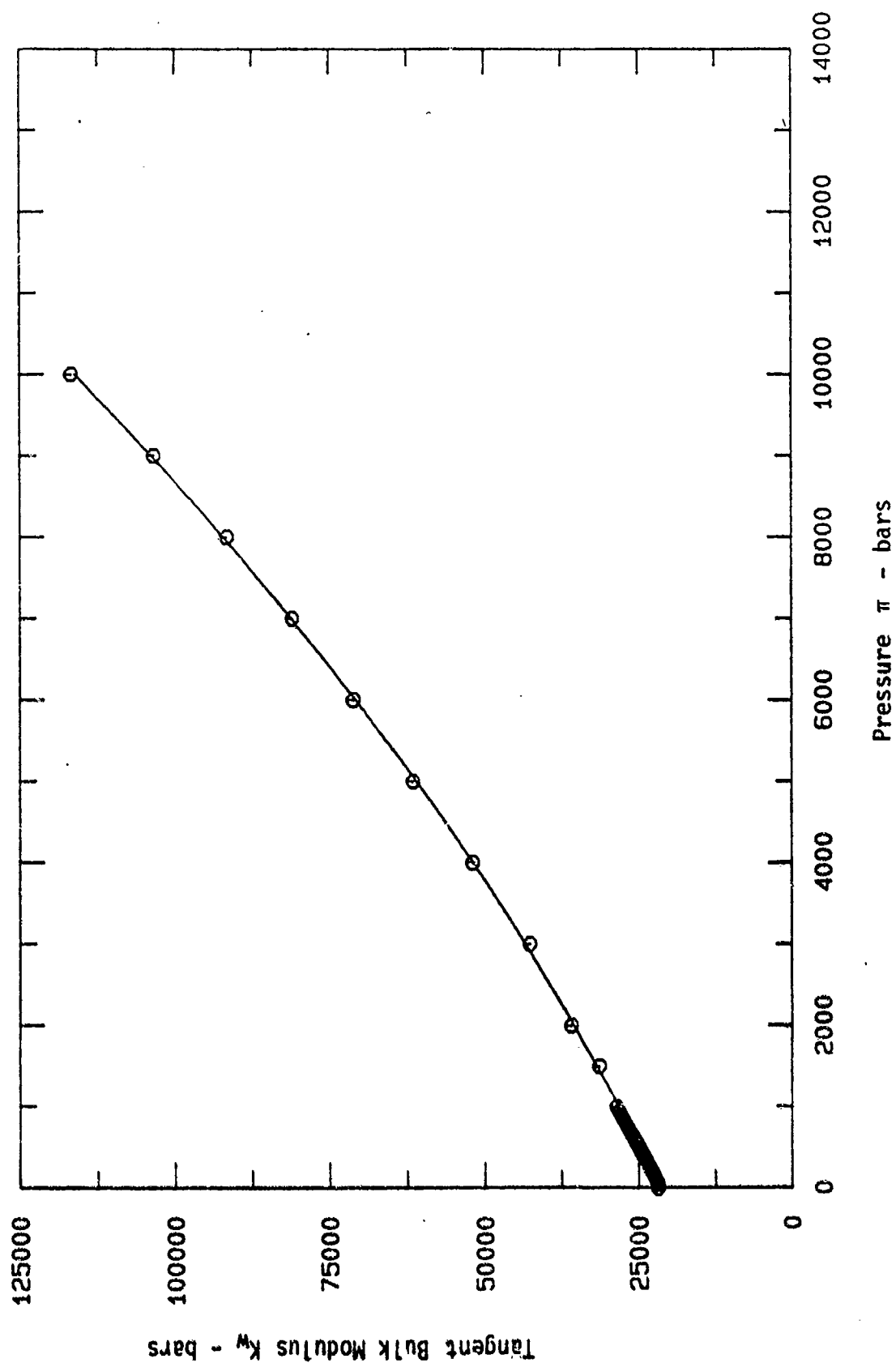


Figure 3.6a. Tangent bulk modulus of fresh water to 10 Kbars.



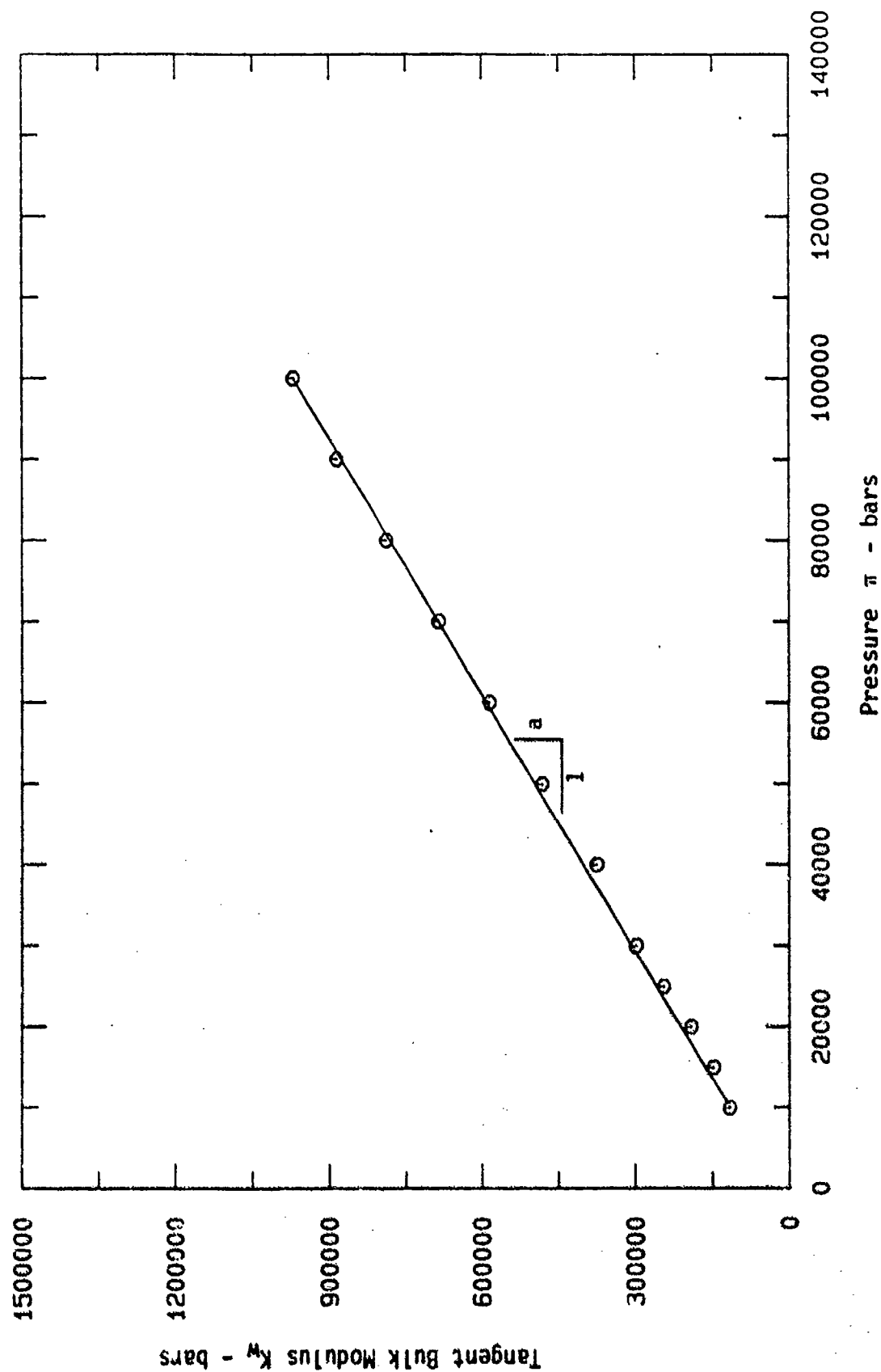


Figure 3.6b. Tangent bulk modulus of fresh water, 10 to 100 Kbars.

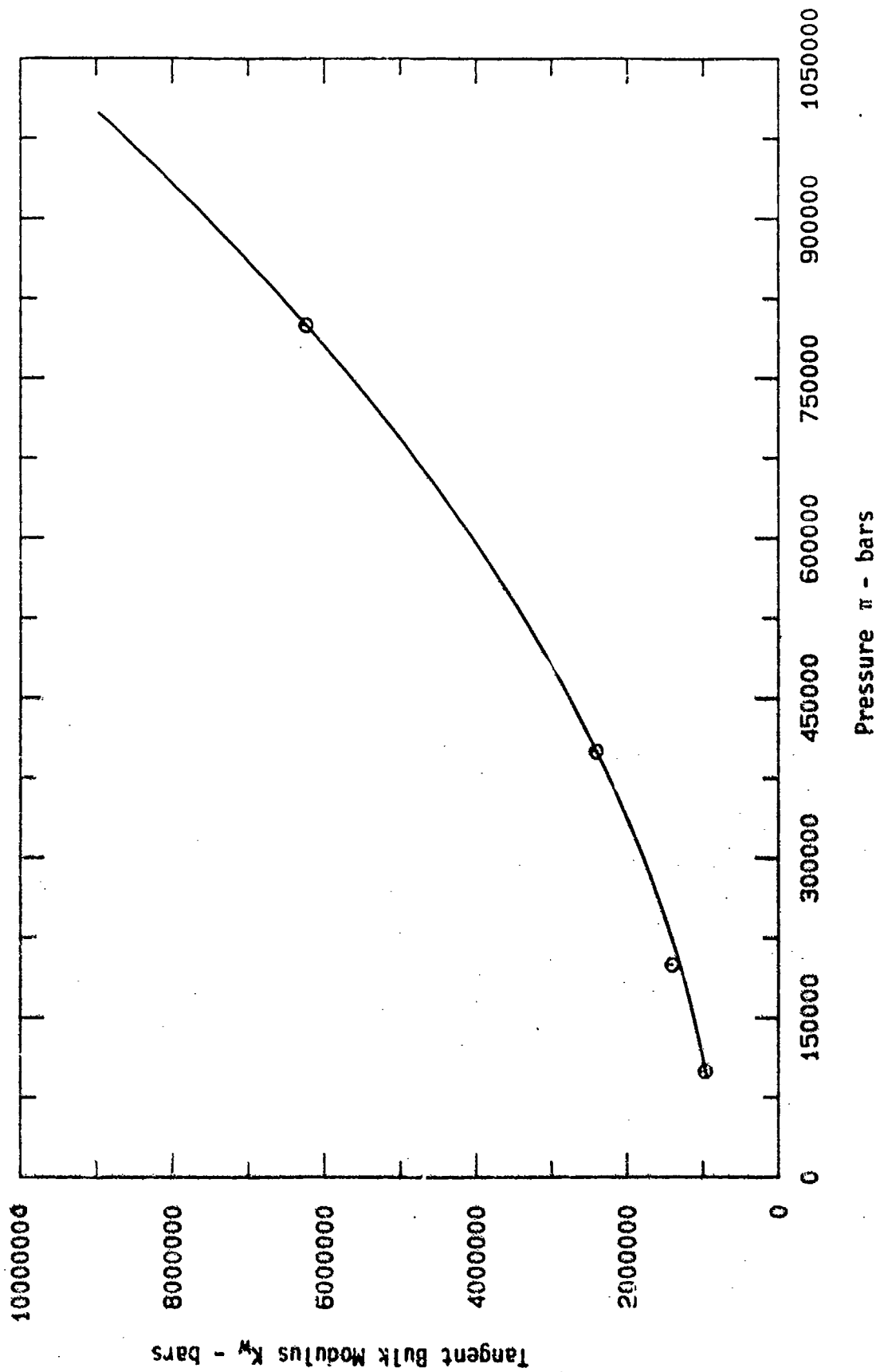


Figure 3.6c. Tangent bulk modulus of fresh water greater than 100 Kbars.

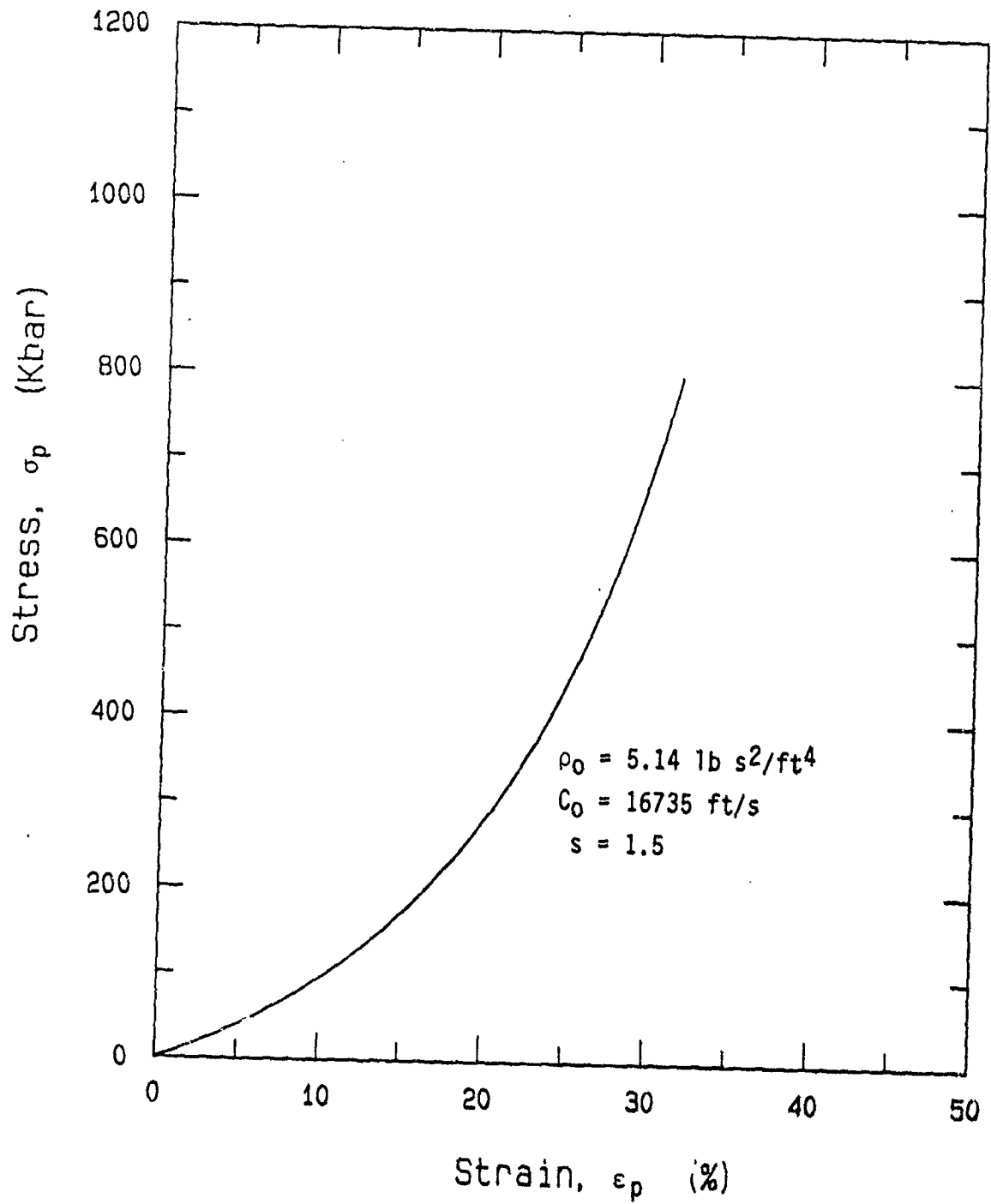


Figure 3.7. Computed uniaxial stress-strain relationship for typical solid grains.

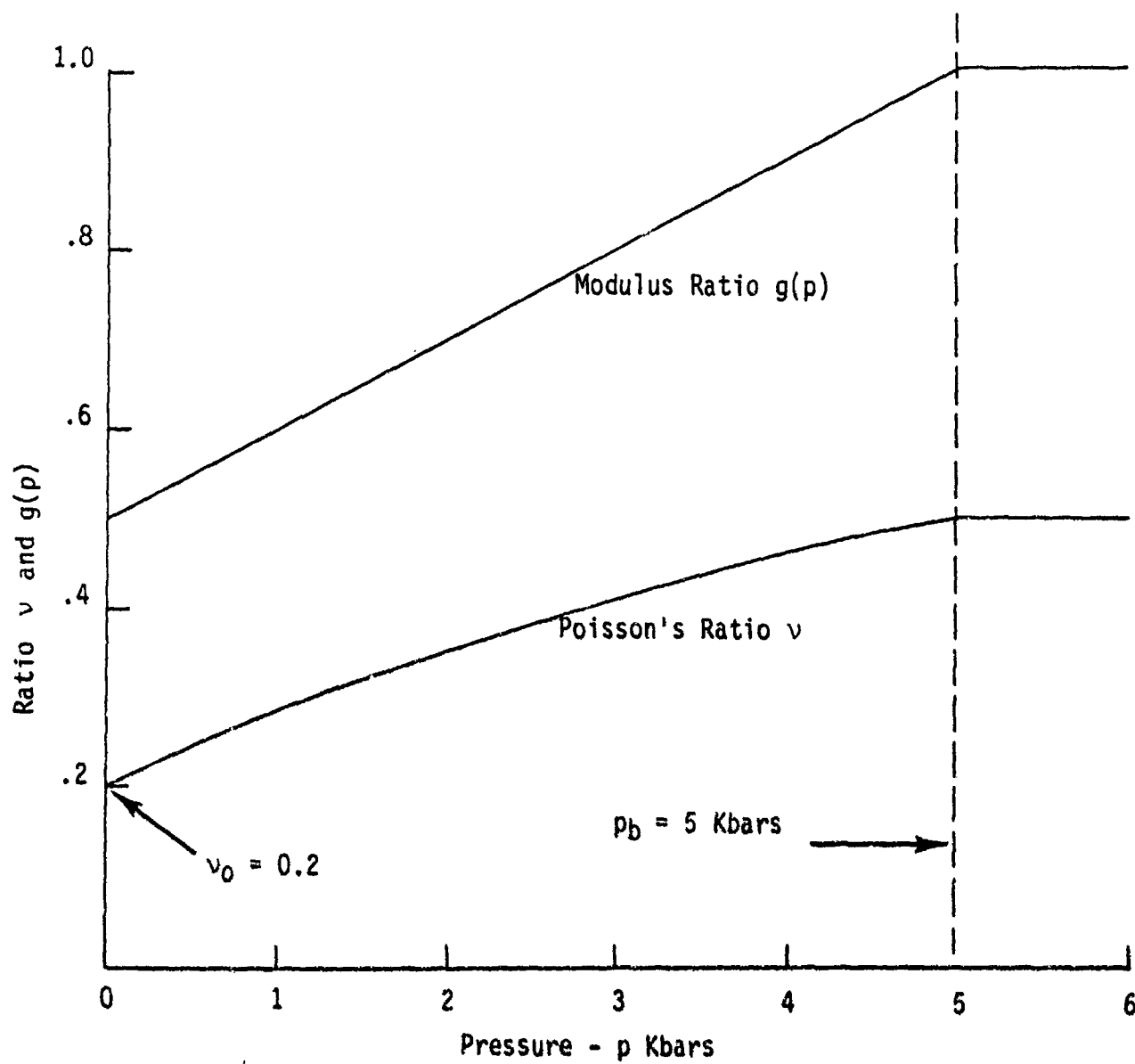


Figure 3.8. Poisson's ratio and modulus ratio  $g(p)$  as a function of pressure for solid grains.

## SECTION 4

### THEORETICAL ANALYSIS OF WAVE PROPAGATION IN SATURATED POROUS MEDIA

#### 4.1 INTRODUCTION

The fully coupled field equations presented by Kim, Blouin and Timian, 1986, Section 7, were used to derive an analytical closed-form solution for wave propagation velocity in fully saturated porous media. This solution is highly versatile in that it considers compression of the solid grains, compression of the pore water, deformation of the porous skeleton, and spatial damping and can be used to compute wavespeeds of the first and second kind and damping coefficients in various geologic materials. This solution provides a means of verifying the multiphase code calculations and also provides a means of analyzing the influence of material property variations on wavespeed and attenuation. Subsections 4.2 and 4.3 describe the development of the closed form solution for the wavespeeds of the first and second kind.

#### 4.2 GENERAL RELATIONSHIPS

The behavior of saturated porous media can be described by two equations of motion and two supplementary equations. The first supplementary equation is that for continuity of flow and the second describes the effective stress law. The first equation of motion prescribes the motion of the bulk mixture and the second defines the motion of the pore fluid relative to the porous skeleton.

##### 4.2.1 Governing Equation for Bulk Mixture

The differential equation governing the bulk mixture is given by

$$\sigma_{ij,j} = (1 - n) \rho_g \ddot{u}_i + n \rho_f \ddot{u}_i \quad (4-1)$$

$\sigma_{ij,j}$  is the total stress gradient applied to an infinitesimal element of saturated material at some given time.  $\sigma_{ij,j}$  is expressed in tensor notation

and represents the stress gradient in each of 3 mutually perpendicular coordinates (e.g. see Mendelson, 1968). For instance, in the x direction,

$$\sigma_{xj,j} = \frac{\partial \sigma_{xx}}{\partial x} + \frac{\partial \sigma_{xy}}{\partial y} + \frac{\partial \sigma_{xz}}{\partial z} = (1 - n) \rho_g \ddot{u}_x + n \rho_f \ddot{U}_x \quad (4-2)$$

The term  $(1 - n)\rho_g$  is the mass of the soil skeleton per unit volume of saturated material, where  $n$  is the porosity and  $\rho_g$  is the mass density of the solid grains.  $u_i$  is the displacement of the skeleton in the  $i$  direction and  $\ddot{u}_i$  is the acceleration of the skeleton in the  $i$  direction. The term  $n \rho_f$  is the mass of the pore fluid per unit volume of saturated material where  $\rho_f$  is the mass density of the pore fluid.  $U_i$  is the absolute displacement of the pore fluid in the  $i$  direction and  $\ddot{U}_i$  is the absolute acceleration of the pore fluid in the  $i$  direction.

The bulk mass density of the saturated material,  $\rho$ , is given by

$$\rho = (1 - n)\rho_g + n \rho_f \quad (4-3)$$

Substitution of the value for  $(1 - n)\rho_g$  from Equation 4-3 into Equation 4-1 gives

$$\sigma_{ij,j} = (\rho - n \rho_f) \ddot{u}_i + n \rho_f \ddot{U}_i \quad (4-4)$$

A term  $w_i$  is introduced which is the apparent fluid displacement in the  $i$  direction relative to the soil skeleton and is given by

$$w_i = n(U_i - u_i) \quad (4-5)$$

In seepage problems,  $w_i$  is referred to as the discharge displacement. It describes the discharge of fluid through a soil mass of unit area. The discharge velocity, or apparent relative velocity,  $\dot{w}_i$ , between the soil particles and pore water is the velocity of water in a discharge duct of unit area needed to maintain the actual relative velocity in the porous soil of the same

unit area. The actual relative velocity between the skeleton and the pore water is given by  $\dot{w}_i/n$ . Finally,  $\ddot{w}_i$  is the apparent relative acceleration between the soil skeleton and pore water given by

$$\ddot{w}_i = n(\ddot{U}_i - \ddot{u}_i) \quad (4-6)$$

Equation 4-6 is an approximation of the actual relative acceleration because the porosity is not constant, as assumed here, but is in reality changing with time. This is just one of several simplifying assumptions made in the linear analysis which make this theoretical development tractable. Equation 4-4 can be expressed in terms of the apparent relative fluid acceleration as simply

$$\sigma_{ij,j} = \rho \ddot{u}_i + \rho_f \ddot{w}_i \quad (4-7)$$

#### 4.2.2 Governing Equation for Pore Fluid

The equation of motion governing the pore fluid is derived from Biot's work (1956). Biot expressed the pore pressure gradient,  $\pi_{,i}$ , as

$$\pi_{,i} = \rho_f \ddot{U}_i + D_i \quad (4-8)$$

where the pore pressure gradient is expressed in tensor notation. For example, the gradient in the x direction is given by

$$\pi_{,x} = \rho_f \ddot{U}_x + D_x \quad (4-9)$$

The term  $\rho_f \ddot{U}_i$  is the inertial force per unit volume of pore fluid.  $D_i$  represents the viscous friction force between the pore fluid and the soil skeleton per unit volume of pore fluid. Solving equation 4-6 for  $\ddot{U}_i$  and substituting into Equation 4-8 gives

$$\pi_{,i} = \frac{\rho_f}{n} \ddot{w}_i + \rho_f \ddot{u}_i + D_i \quad (4-10)$$

For dynamic laminar flow, Biot (1956) derived the exact expression for the viscous friction term,  $D_i$ , for both circular and flat ducts which is given by

$$D_i = \gamma_f \frac{F(\kappa)}{k} \dot{w}_i \quad (4-11)$$

where  $\gamma_f$  is the unit weight of pore fluid and  $F(\kappa)$  is the viscous friction correction factor, and  $k$  is the coefficient of permeability.  $F(\kappa)$  is a complex function given by

$$F(\kappa) = f_1(\kappa) + i f_2(\kappa) \quad (4-12)$$

The magnitudes of the real part,  $f_1(\kappa)$ , and imaginary part,  $f_2(\kappa)$  are plotted in Figure 4.1 as a function of the nondimensional parameter,  $\kappa$ , which is defined as

$$\kappa = \bar{r} \kappa_0 \quad (4-13)$$

where

$$\kappa_0 = \left( \left( \frac{8}{n} \right) \omega k \right)^{1/2} \quad (4-14)$$

In Equation 4-14,  $g$  is the gravitational acceleration,  $\omega$  is the excitation frequency, and the factor,  $\bar{r}$ , is the constant which is dependent on the shape of flow path. For Generalized Darcy's Flow (also called Poiseuille Flow),  $f_1(\kappa)$  and  $f_2(\kappa)$  are independent of  $\kappa$  and  $\bar{r} = 0$ . For the circular duct,  $\bar{r}$  is unity. And for the flat duct, the value of  $\bar{r}$  is approximately equal to  $\sqrt{2/3}$ .

For the purpose of simplifying expressions, we define a modified coefficient of permeability as

$$\bar{k} = \frac{k}{F(\kappa)} \quad (4-15)$$

Substituting Equation 4-15 into 4-11 gives

$$D_i = \frac{\gamma_f}{\bar{k}} \dot{w}_i \quad (4-16)$$



Note that as shown in Equation 4-12, that  $\bar{k}$  is a complex function of  $\kappa$ .

An approximate form of Equation 4-16 was developed by Kim and Blouin (1984) and is given by

$$D_i = \frac{\gamma_f}{\bar{k}} \dot{w}_i + \frac{\rho_f}{n} r \ddot{w}_i \quad (4-17)$$

where  $\gamma_f$  = unit weight of pore fluid  
 $r$  = empirical mass increment factor

The theoretical value of  $r$  is 1/3 for the circular duct and 1/5 for the flat duct. Equation 4-17 is a good approximation when the nondimensional parameter,  $\kappa$ , is less than 2.

For mathematical convenience, and to allow us to compare the exact and approximate solutions, both solutions are incorporated in a single expression for the fluid friction given by

$$D_i = \frac{\gamma_f}{\bar{k}} \dot{w}_i + \frac{\rho_f}{n} r \ddot{w}_i \quad (4-18)$$

In using Equation 4-18, it should be noted that for the approximate solution  $\bar{r} = 0$  and  $\bar{k} = k$ , and for the exact solution  $r = 0$  and  $\bar{k} = \bar{k}$ . Substitution of Equation 4-18 into Equation 4-10 gives

$$\pi_{,i} = \frac{\rho_f}{n} (1 + r) \dot{w}_i + \rho_f \ddot{u}_i + \frac{\gamma_f}{\bar{k}} w_i \quad (4-19)$$

#### 4.2.3 Continuity Equation of Flow

The continuity equation for pore fluid flow is derived from mass conservation relationships. The volumetric strain of the pore fluid,  $\epsilon_f$ , is given by

$$d\epsilon_f = - \frac{dp_f}{\rho_f} = c_f d\pi \quad (4-20)$$

where

$c_f$  = pore fluid compressibility

$\pi$  = pore fluid pressure

The volume strain of the solid grains,  $\epsilon_g$ , is given by

$$d\epsilon_g = - \frac{d\rho_g}{\rho_g} = c_g d\pi + \frac{c_g}{1-n} dp' \quad (4-21)$$

where

$c_g$  = bulk compressibility of solid grains

$p'$  = effective mean pressure

The dry density,  $\rho_d$ , is given by

$$\rho_d = \frac{m_g}{V_t} = (1 - n)\rho_g \quad (4-22)$$

where  $m_g$  is the mass of the solid grains in skeleton volume  $V_t$ . The change in dry density is given by

$$d\rho_d = -\rho_d d\epsilon_v \quad (4-23)$$

where  $\epsilon_v$  is the volumetric strain of the skeleton. Differentiating Equation 4-22 with respect to  $n$  and  $\rho_g$  gives

$$d\rho_d = (1 - n) d\rho_g - \rho_g dn \quad (4-24)$$

Equating 4-23 and 4-24 yields

$$d\epsilon_v = \frac{dn}{1-n} - \frac{d\rho_g}{\rho_g}$$

(4-25)

Conservation of mass for the pore fluid within a specified initial volume of saturated porous material is given by

$$n \rho_f V_t = n' \rho_f' V_t' \quad (4-26)$$

where, as illustrated in Figure 4.2, the terms to the left of the equal sign represent the fluid mass under the initial conditions and the terms to the right represent the same fluid mass under deformed conditions. Equation 4-26 may be expressed in infinitesimal incremental form as

$$n\rho_f V_t = (n + dn) (\rho_f + d\rho_f) (1 + d\epsilon_f) V_t \quad (4-27)$$

where

$\epsilon_f$  = volumetric diffusion of pore fluid as depicted in Figure 4.2.

Solving Equation 4-27 for  $d\epsilon_f$  and discarding second order terms yields

$$d\epsilon_f = -\frac{dn}{n} - \frac{d\rho_f}{\rho_f} \quad (4-28)$$

Equation 4-28 is combined with Equation 4-25 to yield

$$(1 - n)d\epsilon_v + nd\epsilon_f + (1 - n)\frac{d\rho_g}{\rho_g} + n\frac{d\rho_f}{\rho_f} = 0 \quad (4-29)$$

Combining Equations 4-20 and 4-21 with 4-29 gives

$$n(d\epsilon_f - d\epsilon_v) + d\epsilon_v - \frac{1}{K_m} d\pi - c_g dp' = 0 \quad (4-30)$$

where  $K_m$  is the bulk modulus of the solid/fluid mixture which is expressed by

$$K_m = \frac{1}{nc_f + (1 - n)c_g} \quad (4-31)$$

The change in effective mean pressure is given by

$$dp' = K_s (d\epsilon_v - c_g d\pi) \quad (4-32)$$

Substituting Equation 4-32 into 4-30 gives

$$n(d\epsilon_F - d\epsilon_V) + (1 - c_g K_S) d\epsilon_V + (c_g^2 K_S - \frac{1}{K_m}) d\pi = 0 \quad (4-33)$$

#### 4.2.4 Effective Stress Law

From Terzaghi's effective stress law, the change in total stress is expressed as the sum of the change in effective stress and the change in pore water pressure as

$$d\sigma_{ij} = d\sigma'_{ij} + \delta_{ij} d\pi \quad (4-34)$$

where

$\sigma_{ij}$  = total stress

$\sigma'_{ij}$  = effective stress

$\delta_{ij}$  = Kronecker's delta

$\delta_{ij} = 0$  if  $i \neq j$

$\delta_{ij} = 1$  if  $i = j$

### 4.3 PROPAGATION VELOCITY OF PLANE COMPRESSIONAL WAVES IN SATURATED ELASTIC POROUS MEDIA

Using the four general relationships derived in Section 4.2, equations for dynamic response to uniaxial strain loadings can be easily determined. These have broad general application to explosive loadings which typically generate planar or spherical compressional waves in saturated porous media.

#### 4.3.1 Governing Equations for Uniaxial Strain Loadings

For plane wave propagation in the vertical direction Equation 4-7 for the bulk mixture can be expressed as

$$\rho \frac{\partial \dot{u}_z}{\partial t} + \rho_f \frac{\partial \dot{w}_z}{\partial t} - \frac{\partial \sigma_z}{\partial z} = 0 \quad (4-35)$$

Likewise, Equation 4-19 governing motion of the pore fluid is expressed as

$$\rho_f \frac{\partial \dot{u}_z}{\partial t} + \frac{\gamma_f}{k} \dot{w}_z + \frac{\rho_f}{n} (1 + r) \frac{\partial \dot{w}_z}{\partial t} - \frac{\partial \pi}{\partial z} = 0 \quad (4-36)$$

The continuity equation of flow, Equation 4-33, can be differentiated with respect to time to give

$$n(\dot{\epsilon}_F - \dot{\epsilon}_V) + (1 - c_g K_S) \dot{\epsilon}_V + (c_g^2 K_S - \frac{1}{K_m}) \dot{\pi} = 0 \quad (4-37)$$

From Figure 4.2 it can be seen that the strain difference,  $\epsilon_F - \epsilon_V$ , represents the extent of the pore water diffusion relative to the solid skeleton. Thus, the apparent relative velocity of the pore water can be expressed as

$$n(\dot{\epsilon}_F - \dot{\epsilon}_V) = \frac{\partial \dot{w}_z}{\partial z} \quad (4-38)$$

The volumetric strain rate of the porous skeleton,  $\dot{\epsilon}_V$ , can be expressed as

$$\begin{aligned} \dot{\epsilon}_V &= \frac{\partial}{\partial t} \frac{\partial u_z}{\partial z} \\ &= \frac{\partial}{\partial z} \frac{\partial u_z}{\partial t} \\ &= \frac{\partial \dot{u}_z}{\partial z} \end{aligned} \quad (4-39)$$

Substituting Equations 4-38 and 4-39 into 4-37 gives

$$\frac{\partial \dot{w}_z}{\partial z} + (1 - c_g K_S) \frac{\partial \dot{u}_z}{\partial z} + c_g^2 K_S - \frac{1}{K_m} \frac{\partial \pi}{\partial t} = 0 \quad (4-40)$$

The effective stress law from Equation 4-34 can be expressed for uniaxial strain as

$$d\sigma_z = d\sigma_z' + d\pi \quad (4-41)$$

The effective vertical stress is a function of the vertical strain,  $\epsilon_z$ , and the pore fluid pressure,  $\pi$ , applied to the solid grains according to

$$d\sigma_z' = M_S (d\epsilon_z - c_g K_S d\pi) \quad (4-42)$$

where  $M_S$  is the constrained modulus of the porous skeleton (see Blouin and Kim, 1984). Substitution of Equation 4-42 into 4-41 yields

$$d\sigma_z = M_S d\epsilon_z + (1 - c_g K_S) d\pi \quad (4-43)$$

Differentiating Equation 4-43 with respect to time gives

$$\dot{\sigma}_z = M_S \dot{\epsilon}_z + (1 - c_g K_S) \dot{\pi} \quad (4-44)$$

For uniaxial strain

$$\dot{\epsilon}_z = \dot{\epsilon}_v \quad (4-45)$$

Combining Equations 4-39, 4-44, and 4-45 gives

$$M_S \frac{\partial \dot{u}_z}{\partial z} + (1 - c_g K_S) \frac{\partial \pi}{\partial t} - \frac{\partial \sigma_z}{\partial z} = 0 \quad (4-46)$$

#### 4.3.2 Wave Velocity for Harmonic Excitation

For vertically propagating, one dimensional oscillatory (sinusoidal) motion with the pore fluid and porous skeleton in phase. The response of the saturated porous medium may be expressed as

$$\dot{u}_z = \dot{u}_{z0} e^{\alpha z} e^{i\omega(t + \frac{z}{c})} \quad (4-47)$$

$$\dot{w}_z = \dot{w}_{z0} e^{\alpha z} e^{i\omega(t + \frac{z}{c})} \quad (4-48)$$

$$\pi = \pi_0 e^{\alpha z} e^{i\omega(t + \frac{z}{c})} \quad (4-49)$$

$$\sigma_z = \sigma_{z0} e^{\alpha z} e^{i\omega(t + \frac{z}{c})} \quad (4-50)$$

where  $c$  is the wave velocity and  $\alpha$  is the damping constant for a given excitation frequency  $\omega$ . For mathematical simplicity we define  $c'$  such that

$$\frac{1}{c'} = \frac{1}{c} - i\frac{\alpha}{\omega} \quad (4-51)$$

Substitution of Equation 4-51 into 4-47 through 4-50 yields

$$\dot{u}_z = \dot{u}_{z0} e^{i\omega(t + \frac{z}{c'})} \quad (4-52)$$

$$\dot{w}_z = \dot{w}_{z0} e^{i\omega(t + \frac{z}{c'})} \quad (4-53)$$

$$\pi = \pi_0 e^{i\omega(t + \frac{z}{c'})} \quad (4-54)$$

$$\sigma_z = \sigma_{z0} e^{i\omega(t + \frac{z}{c'})} \quad (4-55)$$

Differentiating Equations 4-52 through 4-55 with respect to time yields

$$\frac{\partial \dot{u}_z}{\partial t} = i \omega \dot{u}_z \quad (4-56)$$

$$\frac{\partial \dot{w}_z}{\partial t} = i \omega \dot{w}_z \quad (4-57)$$

$$\frac{\partial \pi}{\partial t} = i \omega \pi \quad (4-58)$$

$$\frac{\partial \sigma_z}{\partial t} = i \omega \sigma_z \quad (4-59)$$

Differentiating Equations 4-52 through 4-55 with respect to  $z$  yields

$$\frac{\partial \dot{u}_z}{\partial z} = \frac{i\omega}{c'} \dot{u}_z \quad (4-60)$$

$$\frac{\partial \dot{w}_z}{\partial z} = \frac{i\omega}{c'} \dot{w}_z \quad (4-61)$$

$$\frac{\partial \pi}{\partial z} = \frac{i\omega}{c'} \pi \quad (4-62)$$

$$\frac{\partial \sigma_z}{\partial z} = \frac{i\omega}{c'} \sigma_z \quad (4-63)$$

Substituting the differential Equations 4-56 through 4-63 into the governing equations for the uniaxial strain loadings, 4-35, 4-36, 4-40 and 4-46 yields



$$\begin{bmatrix} \rho & \rho_f & 0 & -\frac{1}{c'} \\ \rho_f & \frac{\gamma_f}{i\omega K} + \frac{\rho_f}{n} (1+r) & -\frac{1}{c'} & 0 \\ \frac{(1 - c_g K_S)}{c'} & \frac{1}{c'} & -\left(\frac{1}{K_m} - c_g^2 K_S\right) & 0 \\ \frac{M_S}{c'} & 0 & 1 - c_g K_S & -1 \end{bmatrix} \begin{Bmatrix} \dot{u}_z \\ \dot{w}_z \\ \pi \\ \sigma_z \end{Bmatrix} = \begin{Bmatrix} 0 \\ 0 \\ 0 \\ 0 \end{Bmatrix} \quad (4-64)$$

Equation 4-64 can be solved by setting the determinant of the matrix to zero. A modest amount of algebraic manipulations yields

$$a^4 (c')^4 - b^2 (c')^2 + 1 = 0 \quad (4-65)$$

where

$$a^4 = \frac{b_1 + b_2 i}{M_S} \quad (4-66)$$

$$b^2 = \frac{-b_3 + b_4 i}{M_S} \quad (4-67)$$

and

$$b_1 = \bar{b}_1 - \bar{b}_2 f_2(\kappa) \quad (4-68)$$

$$b_2 = \bar{b}_2 f_1(\kappa) \quad (4-69)$$

$$b_3 = \bar{b}_3 + \bar{b}_4 f_2(\kappa) \quad (4-70)$$

$$b_4 = \bar{b}_4 f_1(\kappa) \quad (4-71)$$

and

$$\bar{b}_1 = \rho a_2 a_3 - \rho_f^2 a_3 \quad (4-72)$$

$$\bar{b}_2 = \rho a_1 a_3 \quad (4-73)$$

$$\bar{b}_3 = 2 \rho_f a_4 - a_2 a_4^2 - a_2 a_3 M_s - \rho \quad (4-74)$$

$$\bar{b}_4 = a_1 a_4^2 + a_1 a_3 M_s \quad (4-75)$$

and

$$a_1 = - \frac{\gamma_f}{k\omega} \quad (4-76)$$

$$a_2 = \frac{\rho_f}{n} (1 + r) \quad (4-77)$$

$$a_3 = \frac{1}{K_m} - c_g^2 K_s \quad (4-78)$$

$$a_4 = 1 - c_g K_s \quad (4-79)$$

The solution of Equation 4-65 is given by

$$(c')^2 = \frac{b^2 \pm (b^4 - 4a^4)^{1/2}}{2a^4} \quad (4-80)$$

Equation 4-80 can be decomposed into real and imaginary parts,

$$(c')^2 = d_3 + id_4 \quad (4-81)$$

and the solution for  $c'$  is of the form

$$c' = d_1 + id_2 \quad (4-82)$$

where  $d_1$  and  $d_2$  are related to  $d_3$  and  $d_4$  as follows:

$$d_1 = \frac{1}{\sqrt{2}} [(d_3^2 + d_4^2)^{1/2} + d_3]^{1/2} \quad (4-83)$$

$$d_2 = -\frac{1}{\sqrt{2}} [(d_3^2 + d_4^2)^{\frac{1}{2}} - d_3]^{\frac{1}{2}} \quad (4-84)$$

Solving Equations 4-51 and 4-82 for the wavespeed,  $c$ , and the damping constant,  $\alpha$ , yields the following:

$$c = d_1 + \frac{d_2^2}{d_1} \quad (4-85)$$

$$\alpha = \frac{d_2}{d_1} \frac{\omega}{c} \quad (4-86)$$

Because of the nature of the quadratic formula in Equation 4-80, two solutions are generated for each set of parameters. These two solutions are called waves of the first kind and waves of the second kind. The following subsection presents two verifications of the above equation.

#### 4.3.3 Wave Propagation Velocity for Special Cases

In this subsection plane wave propagation velocities are determined for three special cases:

- incompressible grains with generalized Darcy flow ( $r = 0$ ) and no damping ( $\alpha = 0$ );
- the product of the permeability and the excitation frequency approaches zero;
- the product of the permeability and the excitation frequency approaches infinity.

In the latter two cases, it will be demonstrated that the effect of permeability and excitation frequency on the wave velocity are equivalent and that low values of the product give the lower bound value of the wavespeed and that high values give the upper bound wavespeed.

#### 4.3.3.1 Incompressible Grains, Generalized Darcy Flow

For infinitely stiff grains,  $K_g \rightarrow \infty$  or  $C_g = 0$  and for generalized Darcy flow the mass increment factor,  $r$ , equals zero. The fluid friction is simply proportional to the relative fluid velocity and is independent of the excitation frequency. Equations 4-76 through 4-79 can be rewritten as

$$\varepsilon_1 = \frac{\gamma_f}{k\omega} \quad (4-87)$$

$$a_2 = \frac{\rho_f}{n} \quad (4-88)$$

$$a_3 = \frac{1}{K_m} \quad (4-89)$$

$$a_4 = 1 \quad (4-90)$$

Equations 4-68 through 4-71 yield

$$b_1 = (1 - n) \frac{\rho_f \rho_g}{K_f} \quad (4-91)$$

$$b_2 = - \frac{n\rho}{k\omega K_f} \quad (4-92)$$

$$b_3 = - \frac{(1-n)^2 K_f \rho_f + n(1-n) K_f \rho_g + n \rho_f M_s}{n K_f} \quad (4-93)$$

$$b_4 = \frac{K_f + nM_s}{k\omega K_f} \quad (4-94)$$

Substitution of Equations 4-91 and 4-92 into Equation 4-66 gives

$$a^4 = \frac{(1-n) \rho_g \rho_f}{M_s K_f} + \frac{n}{i\omega k} \frac{n\rho_f + (1-n)\rho_g}{K_f M_s} \quad (4-95)$$

Substitution of Equations 4-93 and 4-94 into Equation 4-67 gives

$$b^2 = \frac{n(1-n) \rho_g K_f + (1-n)^2 \rho_f K_f + n \rho_f M_s}{n M_s K_f} + \frac{n}{i\omega k} \left( \frac{K_f + n M_s}{n M_s K_f} \right) \quad (4-96)$$

Equations 4-95 and 4-96 are identical to equations derived by van der Kogel (1977) and serves as a check on an elementary application of our equations. Substitution of these equations into Equation 4-80 and 4-85 with  $\alpha = 0$  gives the wavespeeds of the first and second kinds for incompressible grains and generalized Darcy flow.

#### 4.3.3.2 Lower Bound Wavespeed

Whenever the permeability and/or the excitation frequency approach zero, there is no relative motion between the pore fluid and the porous skeleton and an undrained loading situation exists. Substitution of  $k\omega = 0$  into Equations 4-76 through 4-79 yields

$$a_1 = \omega \quad (4-97)$$

$$a_2 = \frac{\rho_f}{n} \quad (4-98)$$

$$a_3 = \frac{n}{K_f} + \frac{(1-n)}{K_g} - \frac{K_s}{K_g^2} \quad (4-99)$$

$$a_4 = 1 - \frac{K_s}{K_g} \quad (4-100)$$

Substitution of Equations 4-97 through 4-100 into Equation 4-68 through 4-71 result in no change in the expressions for  $b_1$  and  $b_3$ , but  $b_2$  and  $b_4$  are given

by

$$b_2 = \infty \quad (4-101)$$

$$b_4 = \infty \quad (4-102)$$

Substitution of  $b_1$  through  $b_4$  into Equations 4-66, 4-67, 4-65 and 4-85 gives

$$c^2 \left[ c^2 - \frac{a_4^2 + a_3 M_s}{\rho a_3} \right] = 0 \quad (4-103)$$

Solution of Equation 4-103 yields

$$\boxed{c^2 = 0} \quad (4-104)$$

and

$$\boxed{c^2 = \frac{a_4^2 + a_3 M_s}{\rho a_3}} \quad (4-105)$$

Equation 4-104 indicates that propagation velocity of waves of the second kind equals zero for the undrained case. Substitution of Equations 4-99 and 4-100 into Equation 4-105 yields

$$c^2 = \left( \frac{1}{\rho} \right) M_f \quad (4-106)$$

where  $M_f$  is the fully coupled undrained constrained modulus which is given by

$$M_f = K_m + M_s - \frac{K_m K_s}{K_g} + K_m K_s \left( \frac{K_m + K_s - \frac{K_m K_s}{K_g} - K_g}{K_g^2 - K_m K_s} \right) \quad (4-107)$$

This is identical to the fully coupled constrained modulus derived by Blouin and Kim (1984) for undrained uniaxial compression (see Section 2, Equation 2-17).

#### 4.3.3.3 Upper Bound Wavespeed

Whenever the permeability and/or excitation frequency approach infinity, Equations 4-69, 4-71 and 4-76 are given by

$$b_2 = 0 \quad (4-108)$$

$$b_4 = 0 \quad (4-109)$$

$$a_1 = 0 \quad (4-110)$$

The Equations for  $b_1$ ,  $b_3$ ,  $a_2$ ,  $a_3$  and  $a_4$  remain unchanged. Substitution of these expressions for  $a$ 's and  $b$ 's into Equation 4-65 and 4-85 gives

$$c^2 = -\frac{b_3}{2b_1} \pm \left( \frac{b_3^2}{4b_1^2} - \frac{M_s}{b_1} \right)^{1/2} \quad (4-111)$$

where the plus sign gives the velocity of waves of the first kind and the minus sign gives the velocity of waves of the second kind. The constants  $b_1$  and  $b_3$  in Equation 4-111 are given by

$$b_1 = \frac{\rho}{n} \rho_f \left[ \frac{n}{K_f} + \frac{1-n}{K_g} - \frac{K_s}{K_g^2} \right] \quad (4-112)$$

and

$$b_3 = - \left[ \rho - 2\rho_f \left( 1 - \frac{K_s}{K_g} \right) + \frac{\rho_f}{n} \left[ \left( 1 - \frac{K_s}{K_g} \right)^2 + M_s \left( \frac{n}{K_f} + \frac{1-n}{K_g} - \frac{K_s}{K_g^2} \right) \right] \right] \quad (4-113)$$

#### 4.4 Implementation Into Computational Algorithm

In order to fully utilize the analytic expression for wave velocity and damping derived in the previous subsection, the general solutions for the wavespeeds and damping given by Equations 4-85 and 4-86 have been coded into the program TWAVE, a listing of which is included in Appendix C. In Section 5 TWAVE is used to evaluate the influence of various parametric changes in material properties and excitation frequencies on wavespeed in two phase media.

##### 4.4.1 Computational Algorithm (TWAVE)

The TWAVE input is contained in an input file named "TAPE5" consisting of five "cards." As shown in Tables 4.1 and 4.2 the cards are arranged as follows:

Card 1, frequency option;

Card 2, excitation frequency;

Card 3, pore properties including porosity, permeability,  
mass increment factor, flow path constant;

Card 4, mass densities of the pore fluids and solid grains;

Card 5, bulk moduli of the pore fluid, solid grains and porous  
skeleton; constrained modulus of the porous skeleton.

The input values are in floating point format within the columns shown in Table 4.1. Any consistent set of units can be utilized.

Most of the input parameters listed in Table 4.2 are straightforward except for the frequency option, NF, the mass increment factor,  $r$ , and the flow path constant,  $\bar{r}$ .

- NF For any given set of properties the speed and damping of waves of the first kind vary as a function of frequency.



At the frequency where the wavespeed has the greatest variation, damping is at a maximum. The program computes and uses this approximate critical frequency and computes the corresponding wavespeed and damping when  $Nr = 1$ .

- $r$  The mass increment factor, as explained by Kim and Blouin, 1984, is a frequency dependent flow resistance term resulting from fluid friction. It is treated as an additional inertial mass term. For the simple extension of Darcy flow,  $r$  equals zero, which is termed generalized Darcy flow. In Biot's more rigorous theoretical treatment, based on laminar flow conditions, mass increment factors are introduced which are dependent on the pore geometry. For idealized pore geometries characterized by circular and flat ducts, the mass increment factors have values of  $1/3$  and  $1/5$ , respectively. Whenever the approximation using  $r$  is utilized, the flow path constant,  $\bar{r}$ , must be specified as zero.
- $\bar{r}$  The flow path constant,  $\bar{r}$ , represents Biot's exact expression for frequency dependent fluid friction in laminar flow. As with the approximate solution, values for Darcy flow and circular and flat ducts are specified. These values are 0, 1 and  $\sqrt{2/3}$ , respectively. Whenever the exact solution using  $\bar{r}$  is utilized, the approximation,  $r$ , must be set to zero.

Table 4.1. Summary of input parameters and FORTRAN equivalent.

Summary of Input Parameters

Card No. \ Column	1	5'6	10	11	20	21	30	31	40
1	NF								
2	$\omega$								
3	n			k		r		$\bar{r}$	
4	$\gamma_w$			g		S.G.f		S.G.g	
5	$K_f$			$K_g$		$K_s$		$M_s$	

FORTRAN Equivalent

Card No. \ Column	1	5'6	10	11	20	21	30	31	40
1	NF								
2	W								
3	POR			PER		R		RB	
4	GW			G		SGF		SGG	
5	BF			BG		BS		CS	

Table 4.2. Description of input parameters.

Card 1 - Frequency Options

NF = 0 Use given input frequency

NF = 1 Use internally computed approximate critical frequency  
(neglect input frequency)

Card 2 - Loading

$\omega$  = Frequency (rad/sec)

Card 3 - Pore Properties

n = Porosity

k = Permeability coefficient (ex. in/sec)

r = Mass increment factor (from Biot's 1961 paper)

r = 0 (generalized Darcy flow)

r = 1/5 (flat pore)

r = 1/3 (circular pore)

$\bar{r}$  = Flow path constant

$\bar{r}$  = 0 (generalized Darcy flow)

$\bar{r}$  =  $\sqrt{2/3}$  (flat pore)

$\bar{r}$  = 1 (circular pore)

Card 4 - Mass Densities

$\gamma_w$  = Unit weight of standard water (ex. 62.4/(12<sup>3</sup>) lb/in<sup>3</sup>)

g = Gravitational acceleration (ex. (32.2)(12) in/sec<sup>2</sup>)

S.G.<sub>f</sub> = Specific gravity pore fluid

S.G.<sub>g</sub> = Specific gravity of solid grain

Table 4.2. (concluded)

Card 5 - Moduli

$K_f$  = Bulk modulus of pore fluid

$K_g$  = Bulk modulus of solid grain

$K_s$  = Bulk modulus of porous skeleton

$M_s$  = Constrained modulus of porous skeleton

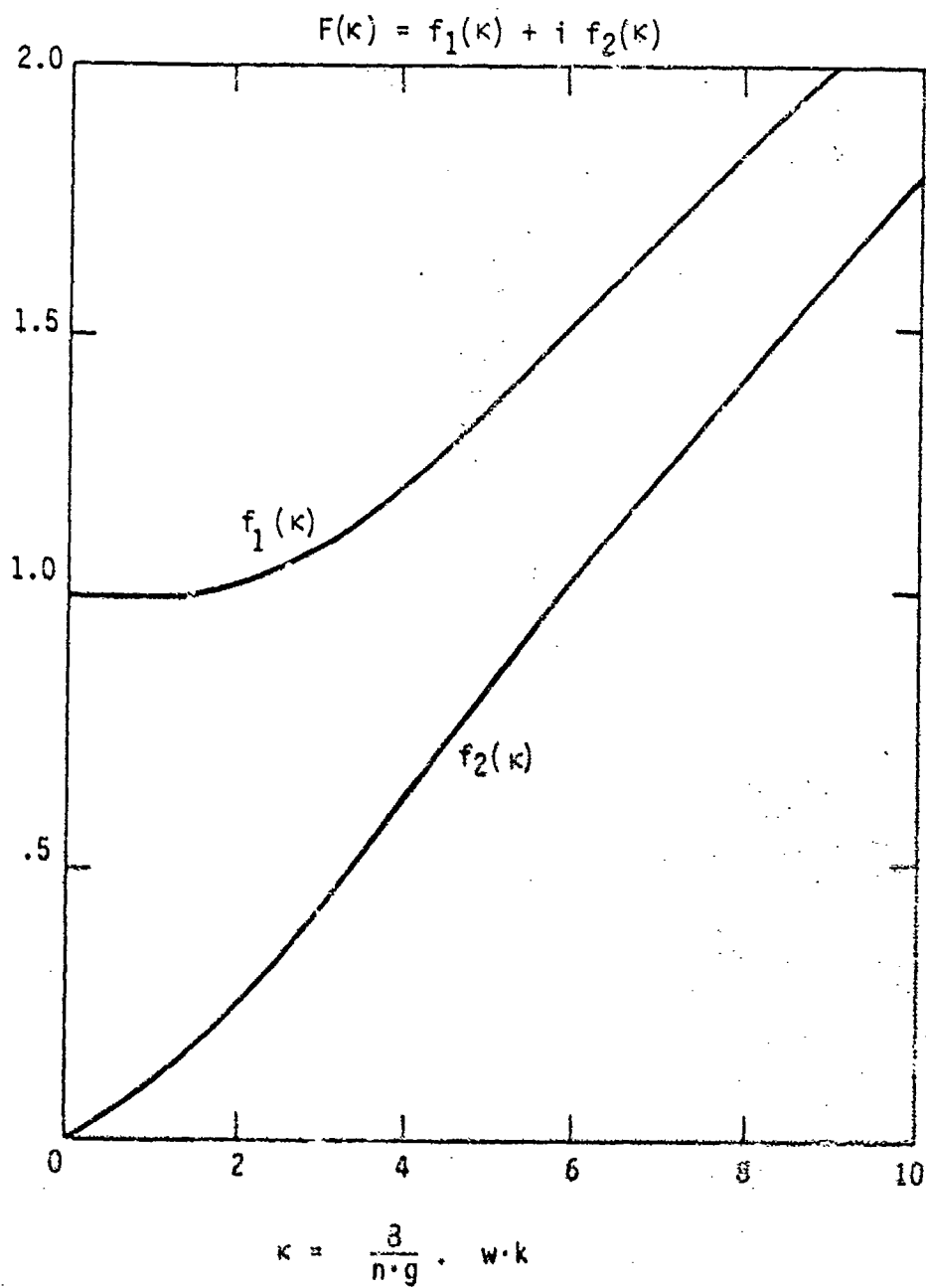


Figure 4.1. Viscous friction correction factor,  $F(\kappa)$ , as a function of  $\kappa$ .

# Conservation of Fluid Mass

$$n \rho_f V_t = n' \rho_f' V_t'$$

$V_t$  = apparent fluid volume before compression

$V_t' = (1 + \epsilon_f) V_t$ : apparent fluid volume after compression

$\epsilon_v$  = volumetric strain of porous skeleton

$\epsilon_f$  = volumetric diffusion of pore fluid

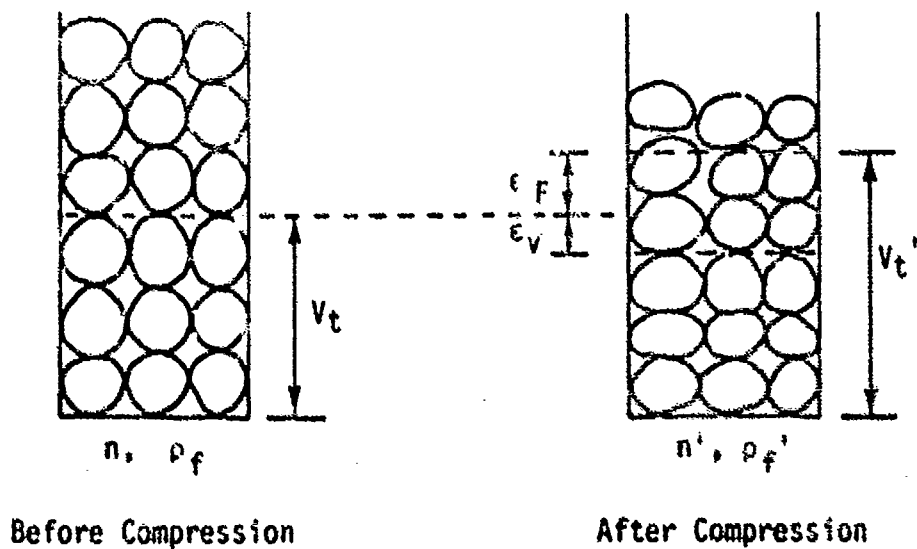


Figure 4.2. Schematic illustration of conservation of pore fluid mass in saturated porous materials.

## SECTION 5

### NUMERICAL ANALYSIS OF WAVE PROPAGATION IN SATURATED POROUS MEDIA

#### 5.1 INTRODUCTION

In this section the analytic closed form solution for wave velocity and damping in fully saturated elastic porous media, as implemented in TWAVE, is used to evaluate the influence of excitation frequency and systematic variations in material properties on the propagation velocity and damping. Important aspects of this parameter study are investigations of

- velocities and damping for waves of both the first and second kind and variation of velocity and damping as functions of the permeability-frequency product;
- the influence of pore shape and fluid friction on the wave propagation characteristics;
- The influence of water properties (sea water vs fresh water), porosity, and skeleton properties (Poisson's ratio, bulk modulus) on the wave propagation characteristics; and
- the adequacy of the approximate expression for fluid friction (used in the numerical model) as compared to the exact expression for fluid friction.

The overall results of this study provide the basis for quantitative evaluation and judgments regarding wave velocity characteristics and spatial attenuation in a broad variety of real earth materials. They are valuable guides to our basic understanding of wave propagation phenomena and to planning and analysis of the future numerical studies in this program.

## 5.2 INFLUENCE OF POROSITY AND SKELETON MODULUS ON WAVESPEED AND DAMPING

As described in Section 4, the expression of Equation 4-82 for the wavespeed in saturated porous media generates two solutions which are referred to as waves of the first and second kind. The wave of the first kind is the common compressional wave through the porous skeleton-fluid matrix with stresses distributed within the matrix in proportion to the properties of the components. The wave of the second kind is not well understood, but appears to be associated with a surge of pore fluid through the matrix. We plan on investigating the phenomena associated with waves of the second kind with the help of numerical simulations during the coming year.

In this subsection, TWAVE is used to generate plots of wavespeed and damping as a function of the frequency-permeability product for a variety of material properties chosen to envelop the properties of most porous saturated rocks and soils. The range of these parametric values are listed in Table 5.1.

The results of the parametric calculations are presented in the form of wavespeed and damping as a function of the product of frequency and permeability. Analysis of the solutions presented in Section 4 shows that the wavespeed and specific damping are a function of the frequency permeability product. As long as the product of the two doesn't change, there will be no change in either specific damping or wavespeed. Thus the product of the two parameters makes a convenient plotting reference.

The damping coefficient,  $\alpha$ , from Equations 4-47 through 4-50 is normalized by the excitation frequency,  $\omega$ , and is termed the specific damping. It is a measure of the rate of motion and stress attenuation per wavelength with increasing depth.

A set of parametric calculations using TWAVE was run on porous material saturated with fresh water. Skeleton modulus was varied by order of magnitude increments from 1,000 psi to 1,000,000 psi. Poisson's ratio of the skeleton was fixed at 0.3. Porosities of 0.2, 0.4 and 0.6 were computed. Values of flow path constant,  $r$ , for the exact solution of 0,  $\sqrt{2/3}$ , 1 and 2 were used.



The numerical data are organized in three groups, as shown in Table 5.2, according to the three different porosities. For each porosity four sets of wavespeed and damping plots are presented, one for each of the four skeleton moduli. Each Figure has plots of the four flow paths.

#### 5.2.1 Speed of Waves of the First Kind

- There is a wavespeed transition from lower to higher speed with increasing  $\omega k$ . The lower bound wavespeed, as discussed in Section 4.3.3.2, is identical to the wavespeed computed from the undrained constrained modulus using Equation 3-12. At the lower bound values of  $\omega k$  there is no significant relative motion between the pore water and the porous skeleton. Wavespeeds at higher values of  $\omega k$  approach an upper bound discussed in Section 4.3.3.3. The transition occurs over the 50 to 10,000 range, which for a typical sand porosity of 0.1 in/s corresponds to a frequency range of about 8 to 1,600 cycles per second.
- The wavespeed transition occurs more sharply for the pores having less fluid friction (minimum  $\bar{\Gamma}$ ).
- The wavespeed increases with increasing skeleton modulus but the magnitudes of the difference between the upper and lower bound wavespeeds do not vary consistently with increasing modulus.
- There appears to be little influence of porosity on the wavespeed increase for soft skeletons; but there is a large jump in wavespeed for high porosity materials with stiff skeletons and almost no jump in wavespeed for low porosity stiff materials.

#### 5.2.2 Speed of Waves of the Second Kind

- There is a wavespeed transition from near zero to an upper bound velocity with increasing values of  $\omega k$ . The lower bound approaches asymptotically to zero.

- The transition occurs more sharply for the pores having lower friction resistance, and it occurs at a somewhat lower  $\omega k$  than the transition for the waves of the first kind.
- The magnitude of the wavespeed jump increases with increasing skeleton stiffness.
- There is a relatively small influence of porosity on the wavespeed increase, compared to a strong influence of skeleton stiffness.

#### 5.2.3 Damping of Waves of the First Kind

- Specific damping shows a strong peak at the point of steepest increase in wavespeed.
- There is no damping at low values of  $\omega k$ , where there is no relative motion between the pore water and skeleton. At higher values of  $\omega k$  the damping appears to be decreasing toward zero.
- At the damping peak the pores with less frictional resistance have higher specific damping than those with higher frictional resistance. At higher values of  $\omega k$  this trend is reversed, and the higher frictional pores have the most damping. At low values of  $\omega k$  the damping in all cases is about the same.
- The specific damping is strongly influenced by the skeleton modulus, but as explained in Section 5.6.2 the damping drops to zero at certain modulus-porosity combinations.
- Porosity appears to have little influence on specific damping.

#### 5.2.4 Damping of Waves of the Second Kind

- Specific damping of waves of the second kind is extremely strong at low values of  $\omega k$  and drops exponentially toward zero at higher  $\omega k$  values. Damping is near zero at higher  $\omega k$  values. Damping is near zero once the wavespeeds approach their limiting upper bound, but as the wavespeeds

drop below the transition zone the damping becomes very strong. Thus, we speculate that it may be very difficult to detect waves of the second kind below their upper bound velocities. Note that the magnitudes of the specific damping plots are about three orders of magnitude higher than the corresponding plots for damping of waves of the first kind.

- There is almost no influence of the flow path factor,  $\bar{r}$ , on the specific damping.
- Increasing skeleton modulus significantly decreases the specific damping.
- Porosity has very little influence on the specific damping.

### 5.3 COMPARISON OF FRESH WATER AND SEA WATER

Since many porous materials are saturated with sea water, wave velocities and damping for a typical sand saturated with sea water were computed for comparison to similar material saturated with fresh water. For sand having properties listed in Table 5.2, with  $n = 0.4$  and  $k_s = 10,000$  psi, the series of computations shown in Figure 5.13 was generated using a bulk modulus for sea water of 350,000 psi. Comparison of these results to the corresponding plots for fresh water in Figure 5.6 shows that:

- wavespeeds for waves of the first kind are higher in the sea water saturated material because of the higher bulk modulus of the sea water and the correspondingly higher bulk modulus of the mixture;
- wavespeeds for waves of the second kind are not noticeably affected by the modulus of the pore water;
- specific damping of the first kind is lower in the sea water saturated material;
- however, specific damping for waves of the second kind is higher in the sea water saturated material.

The reasons for the last three observations are not well understood at this point.

#### 5.4 INFLUENCE ON POISSON'S RATIO ON VELOCITY AND DAMPING

The influence of Poisson's ratio of the skeleton was determined by computing the wavespeeds and damping for a typical saturated sand having the properties listed in Table 5.2 for  $n = 0.4$  and  $k_s = 10,000$  psi, but with Poisson's ratios of 0.2 and 0.4. As Equation 2-25 demonstrates, raising Poisson's ratio is equivalent to reducing the constrained skeleton modulus. The results, plotted in Figure 5.14 for  $\nu = 0.2$  and 5.15 for  $\nu = 0.4$ , can be compared to Figure 5.6 for  $\nu = 0.3$ . Variation in Poisson's ratio has only a slight effect on both velocity and specific damping.

- Wavespeed for both waves of the first and second kind are slightly higher with lower Poisson's ratio.
- Specific damping for both wave types is slightly lower with lower Poisson's ratio.

#### 5.5 COMPARISONS BETWEEN EXACT AND APPROXIMATE EXPRESSIONS FOR FLUID FRICTION

As explained in Section 4.4.1, the numerical codes TPDAP II and MPDAP use an approximation of  $r$  the frequency dependent fluid friction given by the mass increment factor, (Kim and Blouin, 1984). This approximation is necessary because the fluid friction term is frequency dependent and the frequency is not known beforehand. Hence, either an iterative scheme or an approximation such as the above must be employed. An iterative scheme would be too time consuming for most applications.

In order to check the adequacy of the mass increment approximation for fluid friction, we performed a suite of calculations on "standard" saturated material with properties shown in Table 5.2 with a porosity,  $n$ , of 0.4. The results are plotted in Figure 5.16 through 5.19 for values of skeleton modulus ranging from 1,000 psi to 1,000,000 psi. Each plot compares the exact expression for fluid friction in a circular duct ( $\bar{r} = 1$ ) with the approximate

expression ( $r = 1/3$ ). These are also compared to the generalized Darcy fluid friction approximation ( $r = \bar{r} = 0$ ). Conclusions determined from analysis of these plots include:

- The mass increment approximation gives an excellent representation of wavespeed and damping up to a critical value of  $\omega k$ , where the damping and the change in wavespeed are a maximum. At higher values of the frequency permeability product, the mass increment approximation becomes increasingly less accurate.
- For  $\omega k$  products above the critical value, the mass increment approximation underestimates the wavespeeds of both kinds of waves and underestimates the damping for waves of the first kind. Damping of waves of the second kind appears to be independent of the fluid friction term. The upper bound wavespeed is independent of the flow path constant,  $\bar{r}$ , and the wavespeeds converge to the Darcy flow case. However, in the approximation, the mass increment factor, as shown in Equation 4-19, is still carried at higher values of  $\omega k$ .

## 5.6. INFLUENCE OF POROSITY AND SKELETON MODULUS ON DAMPING AND WAVESPEED

Section 5.2 described the wavespeeds and specific damping as a function of the frequency-permeability product. In this section, we evaluate the wavespeeds and damping as a function of the skeleton bulk modulus. Material properties used for this study are the same as those listed in Table 5.2. For each porosity we evaluate the upper and lower bound wavespeeds which are independent of the flow path constants. In addition, we evaluate the values of the critical frequency-permeability product where the specific damping of waves of the first kind reaches a maximum. At this critical frequency-permeability, we compute velocities of waves of the first kind and specific damping of waves of both the first and second kind. Figures 5.20 through 5.22 show the results for  $n = 0.2$ ,  $n = 0.4$  and  $n = 0.6$ , respectively. Each figure includes plots for the four flow path constants listed in Table 5.2.

#### 5.6.1 Critical Frequency-Permeability

- Critical  $\omega_k$  shows a peak at higher skeleton bulk moduli ( $K_S > 100,000$  psi). The value of  $K_S$  where the peak occurs decreases as the porosity increases.
- The magnitudes of critical  $\omega_k$  increase with increasing porosity.
- However, the critical  $\omega_k$  values do not vary monotonically with variations in fluid friction. The lowest value of  $\omega_k$  is for an  $\bar{r}$  value of 1.0; values both above and below 1.0 produce higher values of the critical  $\omega_k$ .

#### 5.6.2 Maximum Specific Damping of Waves of the First Kind

- The specific damping curve has a saddle point, reaching zero damping at the skeleton bulk modulus where the critical  $\omega_k$  reaches its peak.
- The magnitude of specific damping increases with increasing porosity.
- The magnitude of specific damping increases with decreasing fluid friction (decreasing  $\bar{r}$ ).

#### 5.6.3 Specific Damping of Waves of the Second Kind at Critical $\omega_k$ .

- Specific damping at critical  $\omega_k$  decreases exponentially with increasing skeleton bulk modulus.
- The magnitude of specific damping decreases as the porosity increases.
- The magnitude of specific damping is lowest for material where the flow path constant,  $\bar{r}$ , is equal to 2.0.

#### 5.6.4 Velocities of Waves of the First Kind

- Up to a skeleton modulus  $K_S$ , of about 100,000 psi, wave velocities increase gradually with increasing modulus. Velocities are

higher in the materials having lower porosity. Around the value of  $K_s$  where the critical  $\omega k$  reaches its peak, wave velocities are increasing exponentially and converge to a single value where critical  $\omega k$  is a maximum.

- Both maximum and minimum wave velocities are the same at the point where the damping of waves of the first kind drops to zero.
- For the flow path constant  $\bar{r} = 2$ , the wave velocities at critical  $\omega k$  are approximately the average of the maximum and minimum values. For the other values of flow path constants ( $\bar{r} = 0, \sqrt{2/3}$ , and 1), the wave velocities at critical  $\omega k$  are slightly lower than the average of the maximum and minimum values.

#### 5.6.5 Maximum Velocities of Waves of the Second Kind

- Wave velocities, in general, increase as the skeleton bulk modulus increases and the magnitudes of the wave velocities are higher in the materials having higher porosity.
- The maximum wave velocity is not influenced by the fluid friction.

### 5.7 TPDAP II NUMERICAL CALCULATIONS

A series of 3 one-dimensional calculations of a vertically propagating planar compression wave were performed using the two phase finite element program TPDAP II. The input loading, as shown in Figure 5.23, was a short rise time triangular pulse with a peak stress of 5,000 psi and a positive phase duration of 10 msec. The loading pulse was applied to saturated sand having the properties listed in Figure 5.23. Snapshots of the pore water pressure profiles at four different times, from 10 to 40 msec, are shown in Figure 5.24. Three calculations are shown for assumed permeabilities of 0.001, 0.1 and 10 in/s.

The trends in these calculations are similar to those observed in the parametric calculations of the previous subsections. The wavespeed increases

substantially with increasing permeability. For the lowest permeability the velocity of the wavefront is about 5300 ft/s and for the highest permeability it is about 5900 ft/s. The wavespeed computed for this material according to the decoupled undrained modulus described by Blouin and Kim (1984) is about 5200 ft/s which agrees very well with the low permeability calculation.

There is a dramatic alteration of the wave shape for the intermediate permeability calculation. The wavefront is smeared and the amplitude is significantly attenuated relative to the calculations in the less permeable and more permeable materials. As discussed in the previous subsections, excess damping occurs in the transition region between the lower bound and upper bound wavespeeds.



Table 5.1. Material properties used in parameter study.

Fixed Constants:

<u>Density</u>	<u>Gravity Constant</u>	<u>Grain Bulk Modulus</u>	<u>Specific Gravity of Grains</u>
$\gamma_w = 62.4 \text{ lb/ft}^3$ ,	$g = 32.17 \text{ ft/sec}^2$ ,	$K_g = 5 \times 10^6 \text{ psi}$ ,	$\text{S.G.}_g = 2.67$

Flow Path Constant (exact expression for fluid friction):

$$\bar{r} = 0, \sqrt{2/3}, 1.0, 2.0$$

Mass Increment Factor (approximate expression for fluid friction):

$$r = 0, 1/5, 1/3, \text{ and } 1$$

Properties of Pore Fluid:

	<u>Fluid Bulk Modulus</u>		<u>Specific Gravity of Pore Fluid</u>
Fresh Water -	$K_f = 0.29 \times 10^6 \text{ psi}$	and	$\text{S.G.}_f = 1.0$
Sea Water -	$K_f = 0.35 \times 10^6 \text{ psi}$	and	$\text{S.G.}_f = 1.026$

Properties and Porous Skeleton:

Bulk Modulus -	$K_s = 1,000, 10,000, 100,000, 1,000,000 \text{ psi}$
Poisson's ratio -	$\nu = 0.2, 0.3, 0.4$

Porosities:

$$n = 0.2, 0.4, \text{ and } 0.6$$

Table 5.2. List of figures for influence of porosity and skeleton modulus on wavespeed and damping.

Skeleton Modulus :

	n = 0.2	n = 0.4	n = 0.5
$K_S = 1,000$	Fig. 5.1	Fig. 5.5	Fig. 5.9
$K_S = 10,000$	Fig. 5.2	Fig. 5.6	Fig. 5.10
$K_S = 100,000$	Fig. 5.3	Fig. 5.7	Fig. 5.11
$K_S = 1,000,000$	Fig. 5.4	Fig. 5.8	Fig. 5.12

Constants:

$K_f = 0.29 \times 10^6$  psi (Bulk Modulus of Pore Water)

$\nu = 0.3$  (Poisson's ratio)

$\bar{r} = 0, \sqrt{2/3}, 1, 2$  (Flow Path Constant)

# Wave Veloc. of First and Second Kind as a Function of Freq-Perm Product

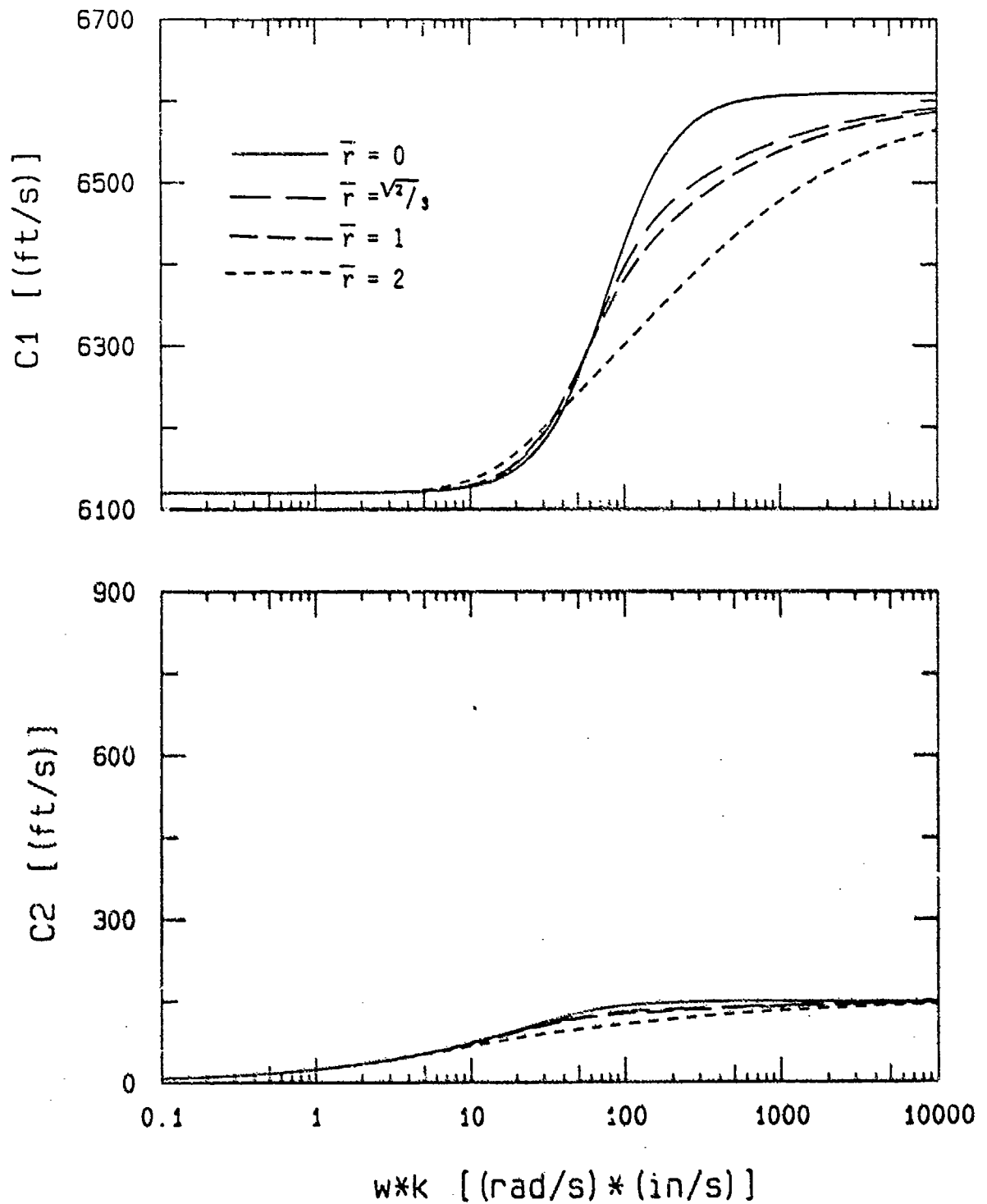


Figure 5.1a. Wave velocities,  $n = 0.2$  and  $K_s = 1,000$  psi.

# Specific Damping of First and Second Kind as a Function of Freq-Perm Product

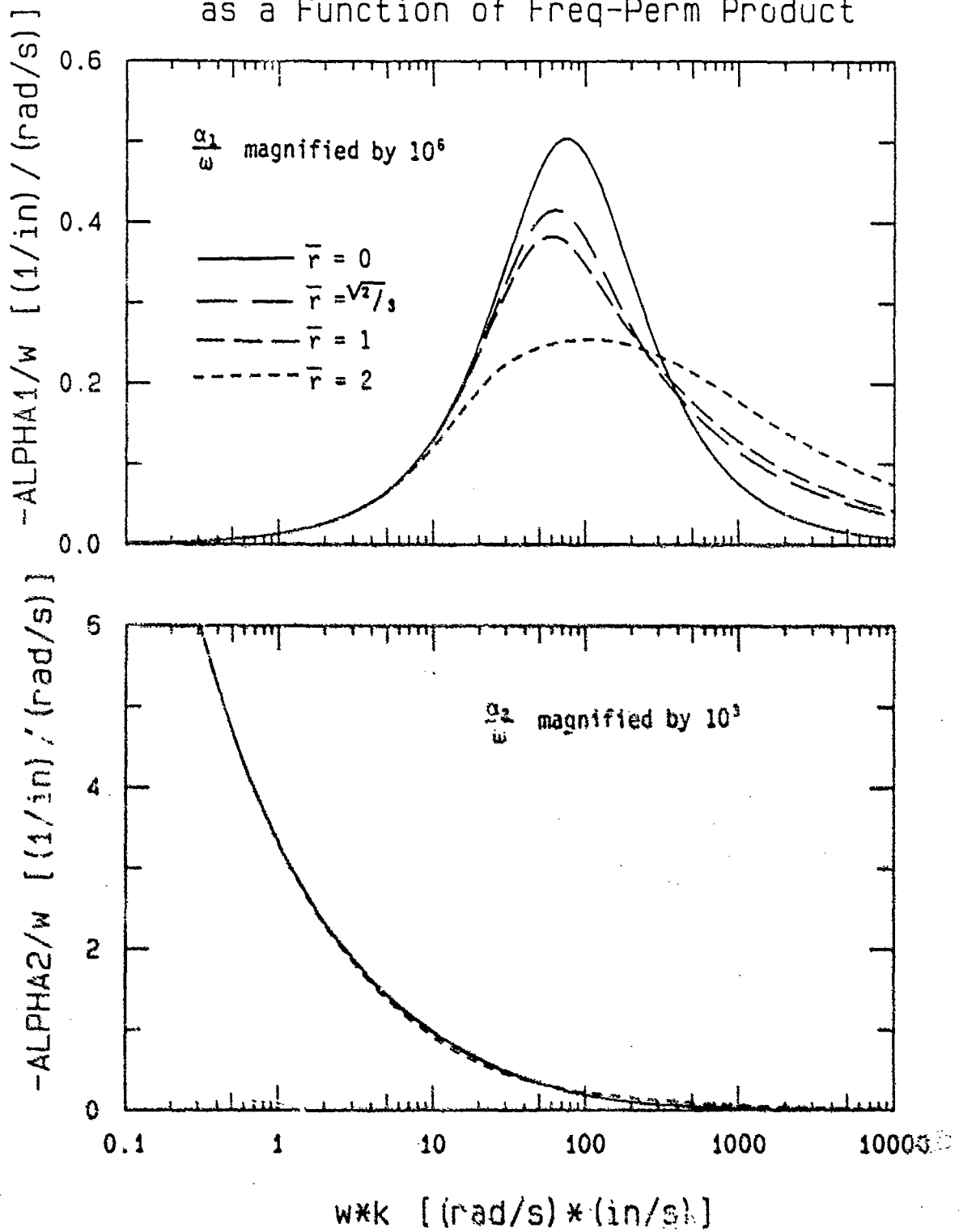


Figure 5.1b. Specific damping,  $n = 0.2$  and  $K_s = 1,000$  psi.

# Wave Veloc. of First and Second Kind as a Function of Freq-Perm Product

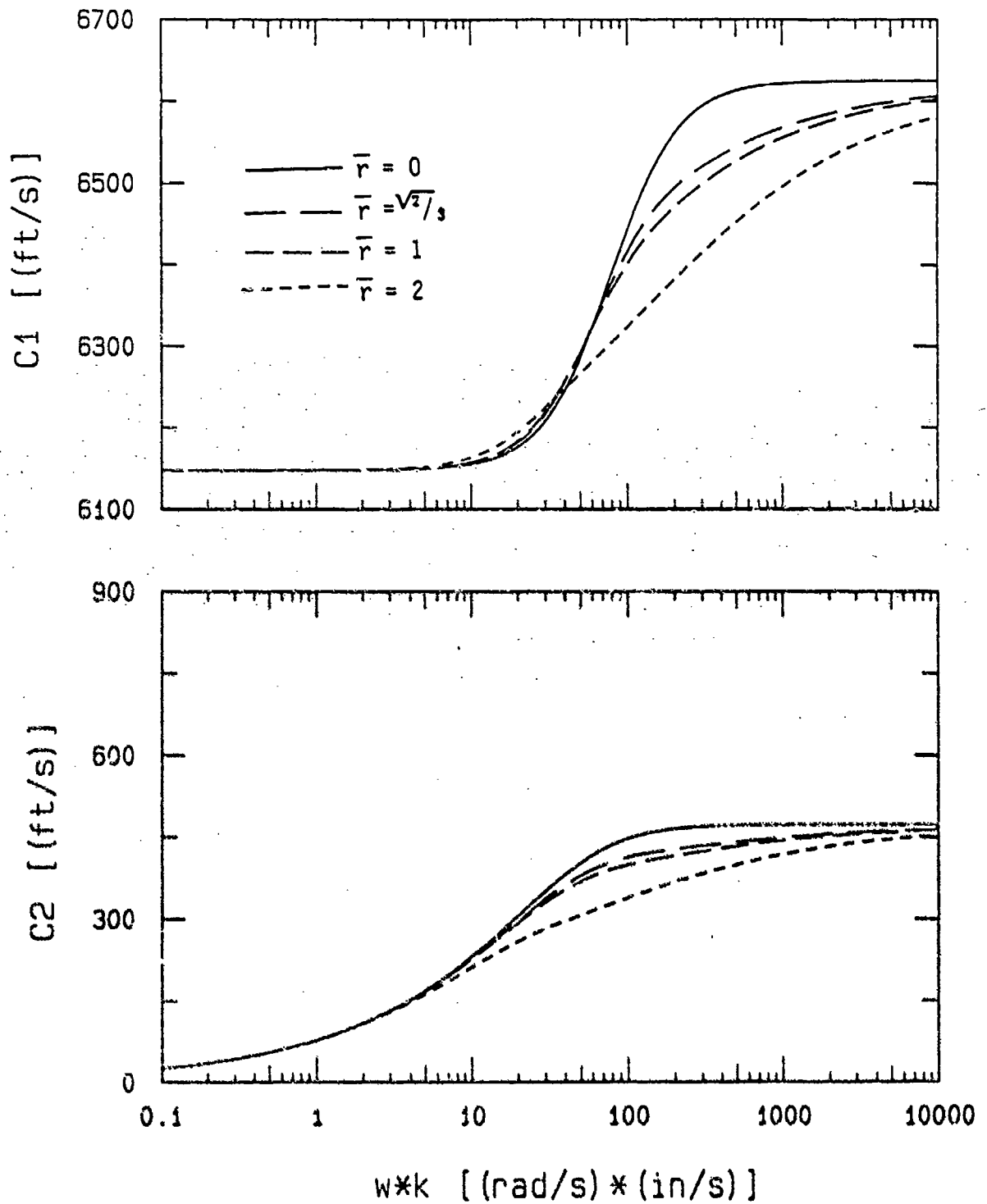


Figure 5.2a. Wave velocities,  $n = 0.2$  and  $K_s = 10,000$  psi.

# Specific Damping of First and Second Kind as a Function of Freq-Perm Product

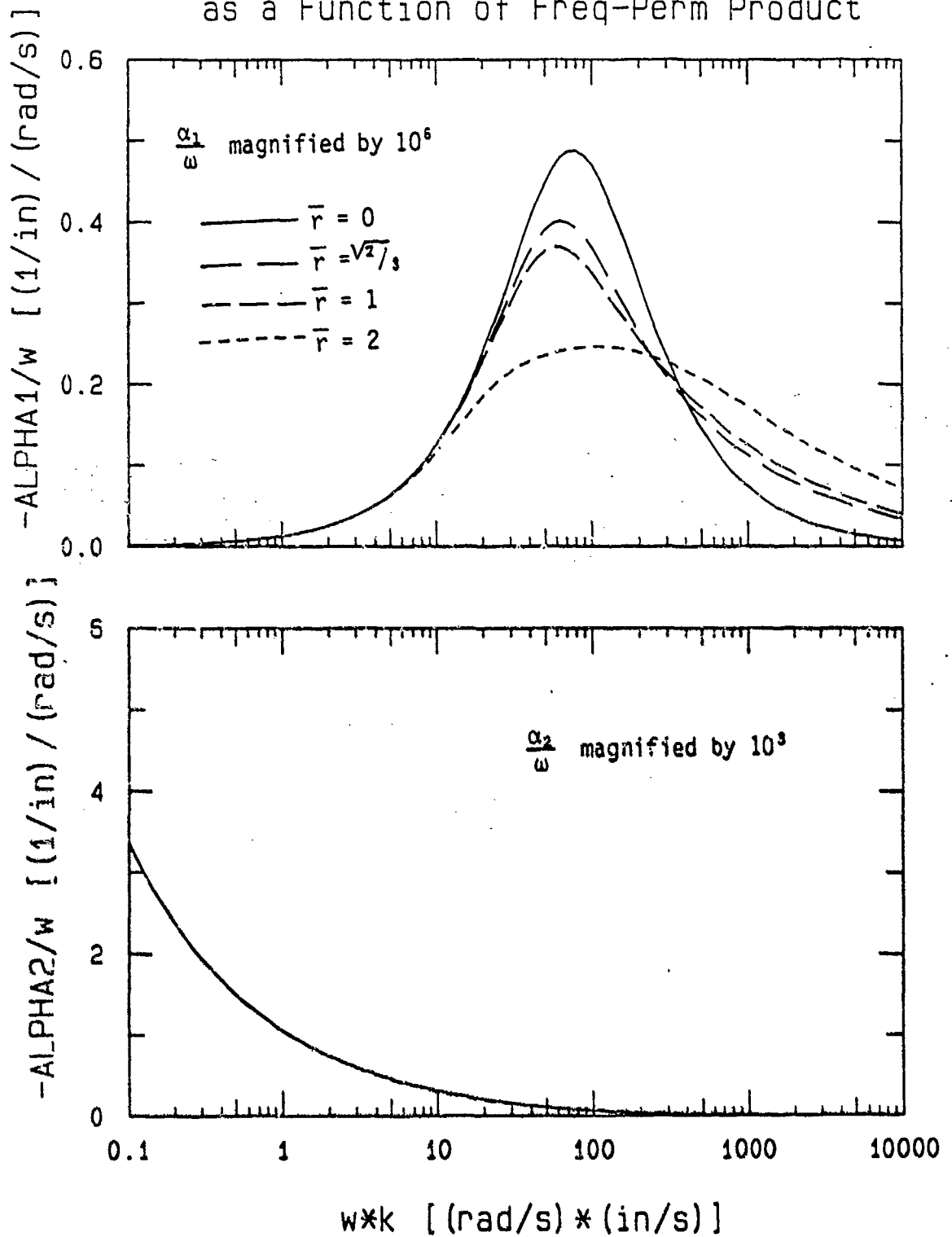


Figure 5.2b. Specific damping,  $n = 0.2$  and  $K_s = 10,000$  psi.

# Wave Veloc. of First and Second Kind as a Function of Freq-Perm Product

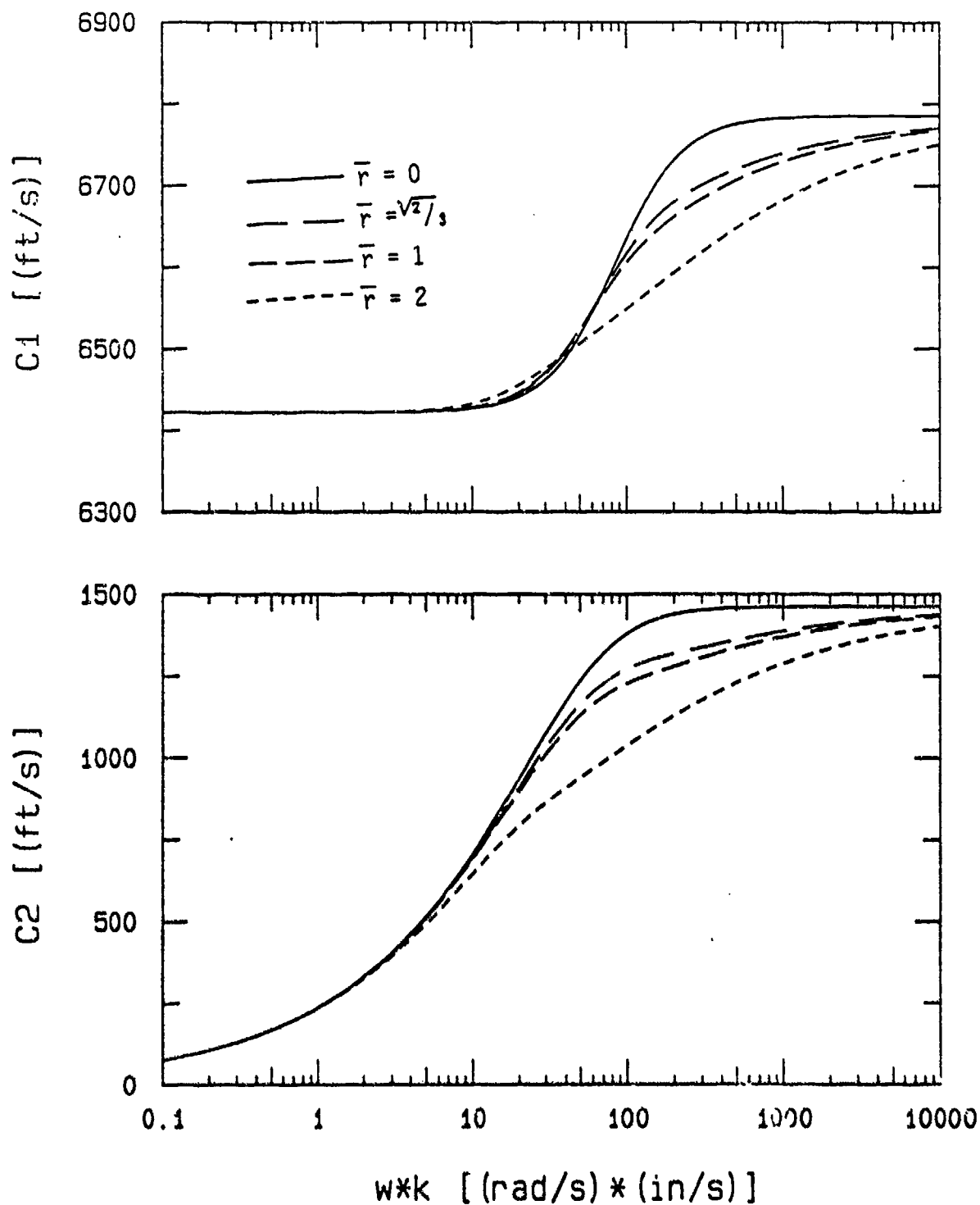


Figure 5.3a. Wave velocities,  $n = 0.2$  and  $K_s = 100,000$  psi.

# Specific Damping of First and Second Kind as a Function of Freq-Perm Product

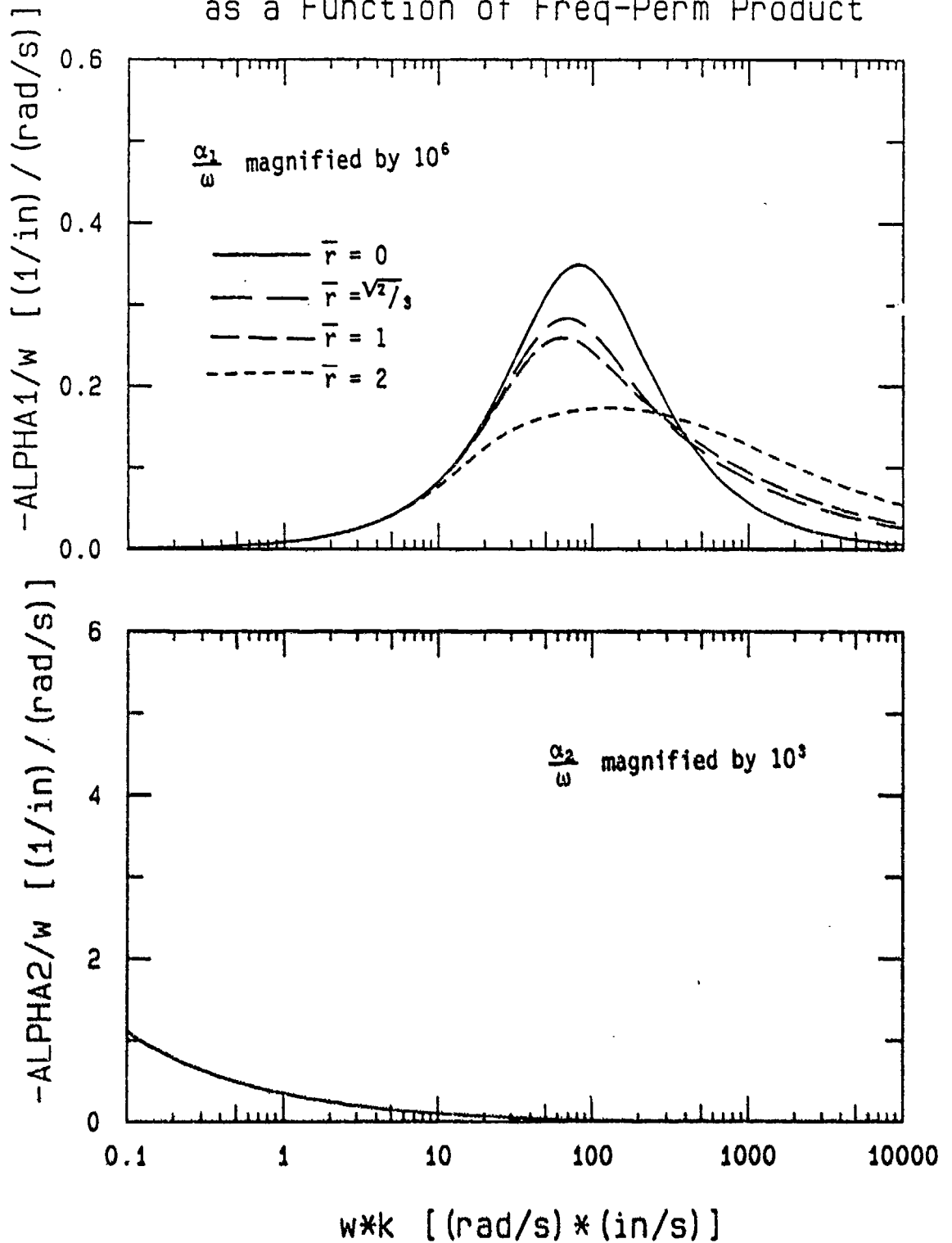


Figure 5.3b. Specific damping,  $n = 0.2$  and  $K_s = 100,000$  psi.



# Wave Veloc. of First and Second Kind as a Function of Freq-Perm Product

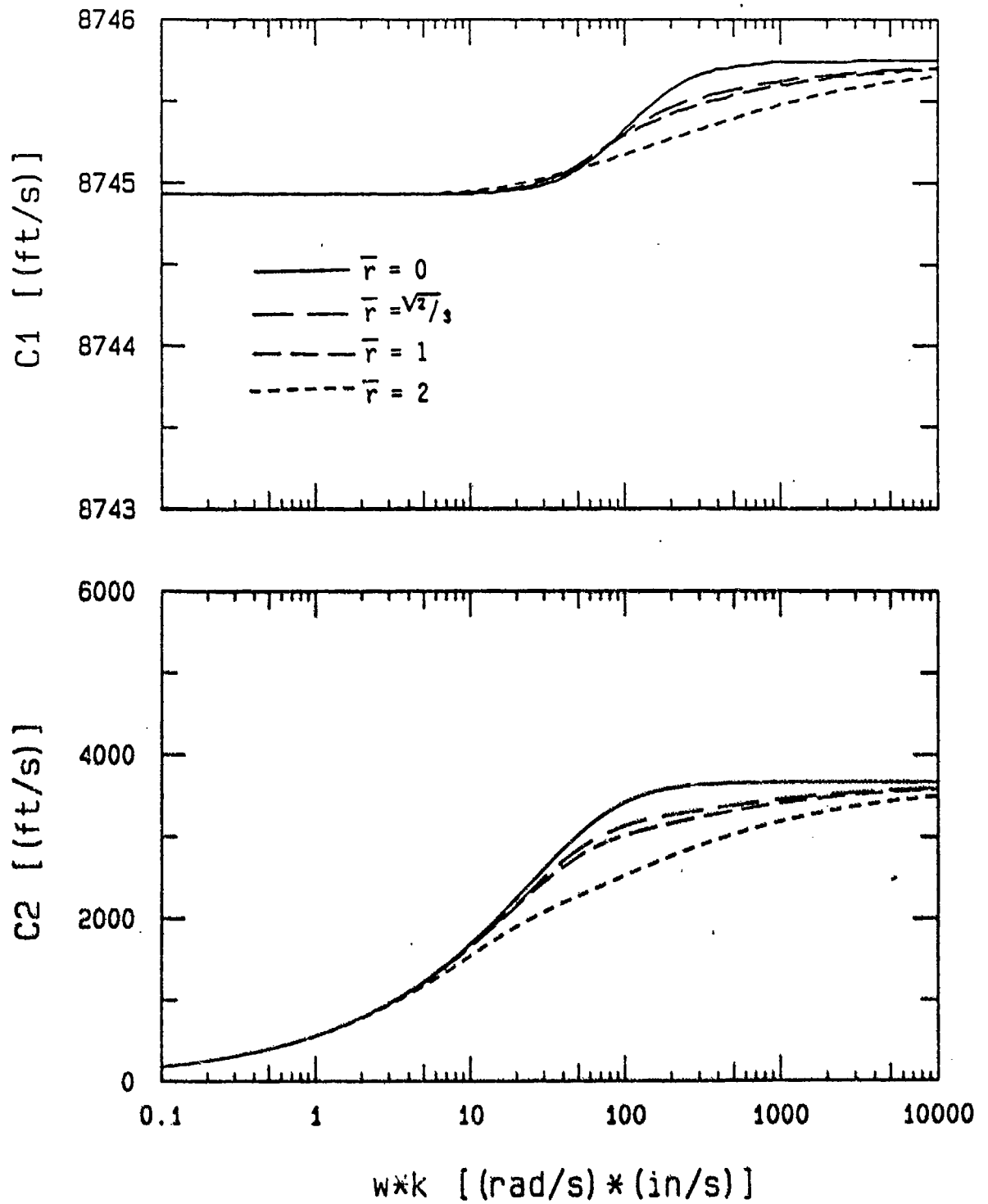


Figure 5.4a. Wave velocities,  $n = 0.2$  and  $K_s = 1,000,000$  psi.

# Specific Damping of First and Second Kind as a Function of Freq-Perm Product

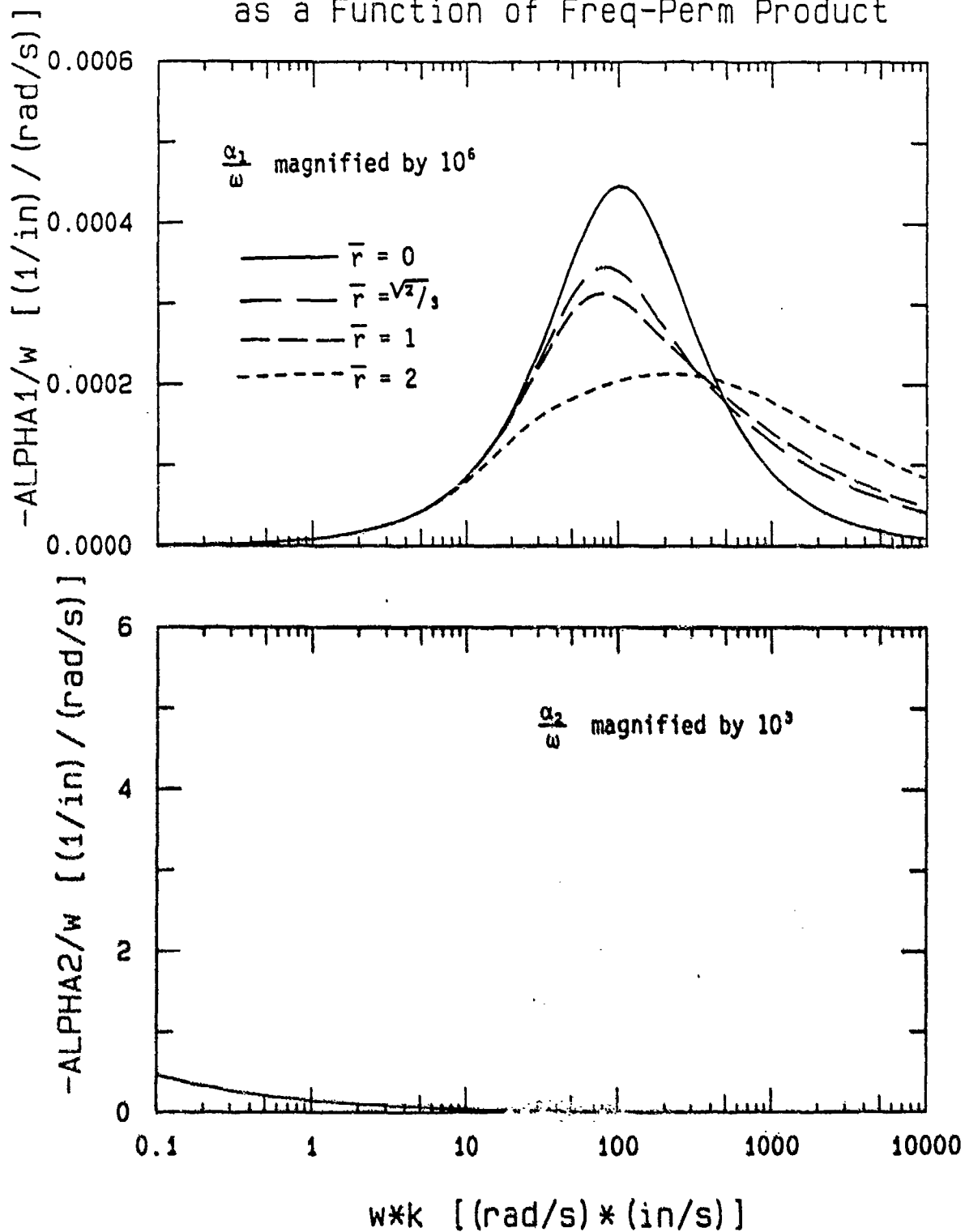


Figure 5.4b. Specific damping,  $n = 0.2$  and  $K_S = 1,000,000$  psi.

# Wave Veloc. of First and Second Kind as a Function of Freq-Perm Product

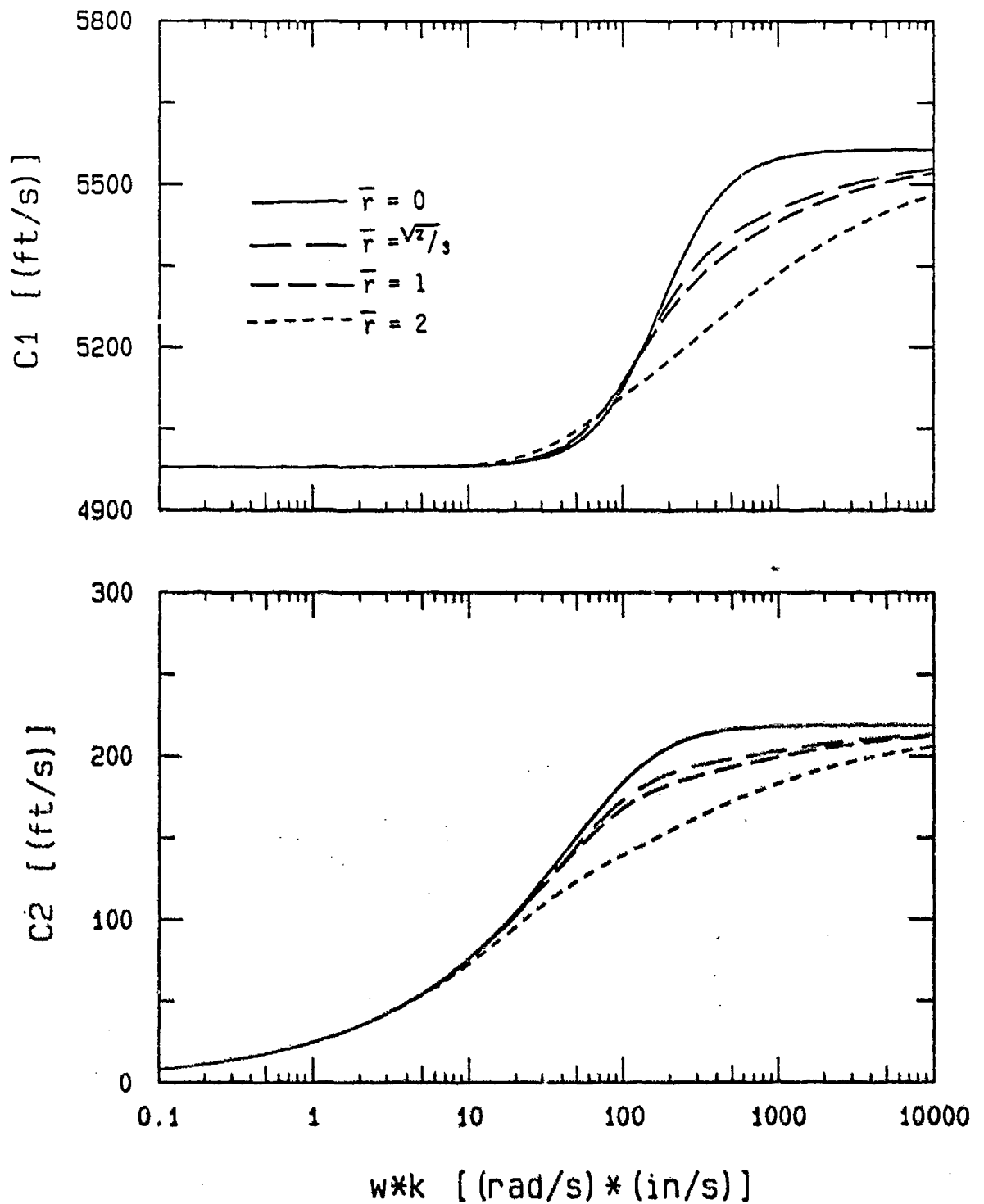


Figure 5.5a. Wave velocities,  $n = 0.4$  and  $K_s = 1,000$  psi.

# Specific Damping of First and Second Kind as a Function of Freq-Perm Product

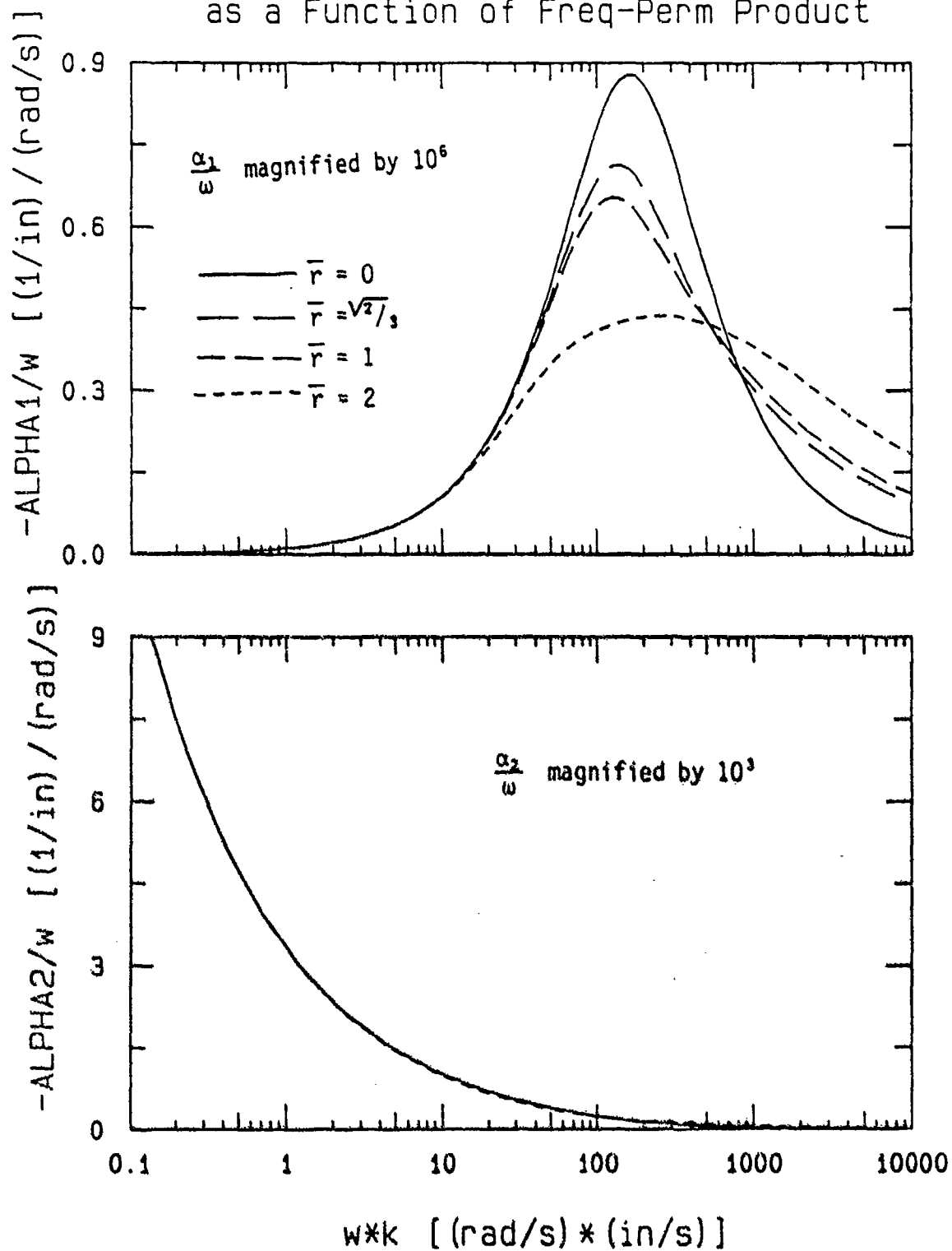


Figure 5.5b. Specific damping,  $n = 0.4$  and  $K_s = 1,000$  psi.

# Wave Veloc. of First and Second Kind as a Function of Freq-Perm Product

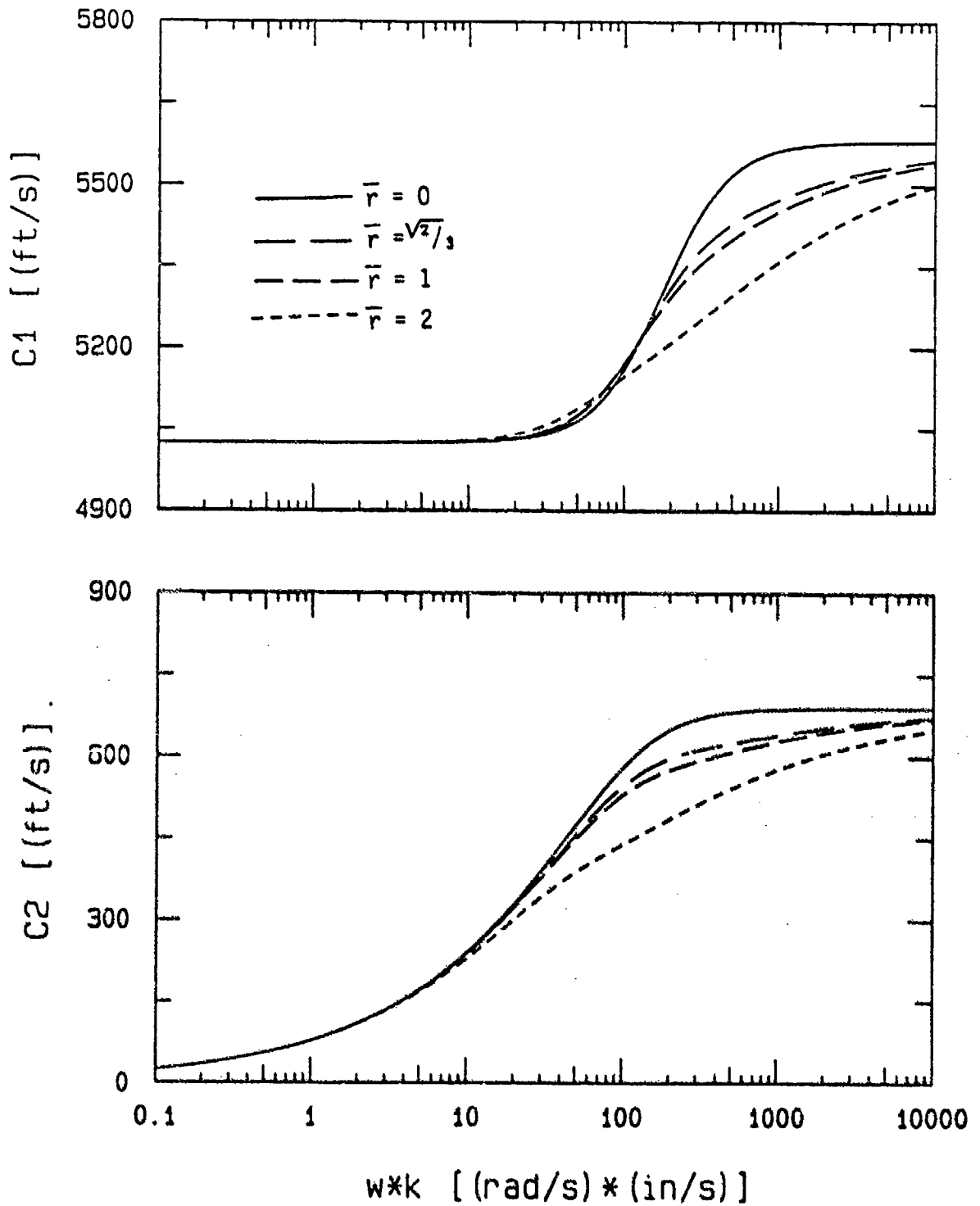


Figure 5.6a. Wave velocities,  $n = 0.4$  and  $K_s = 10,000$  psi.

# Specific Damping of First and Second Kind as a Function of Freq-Perm Product

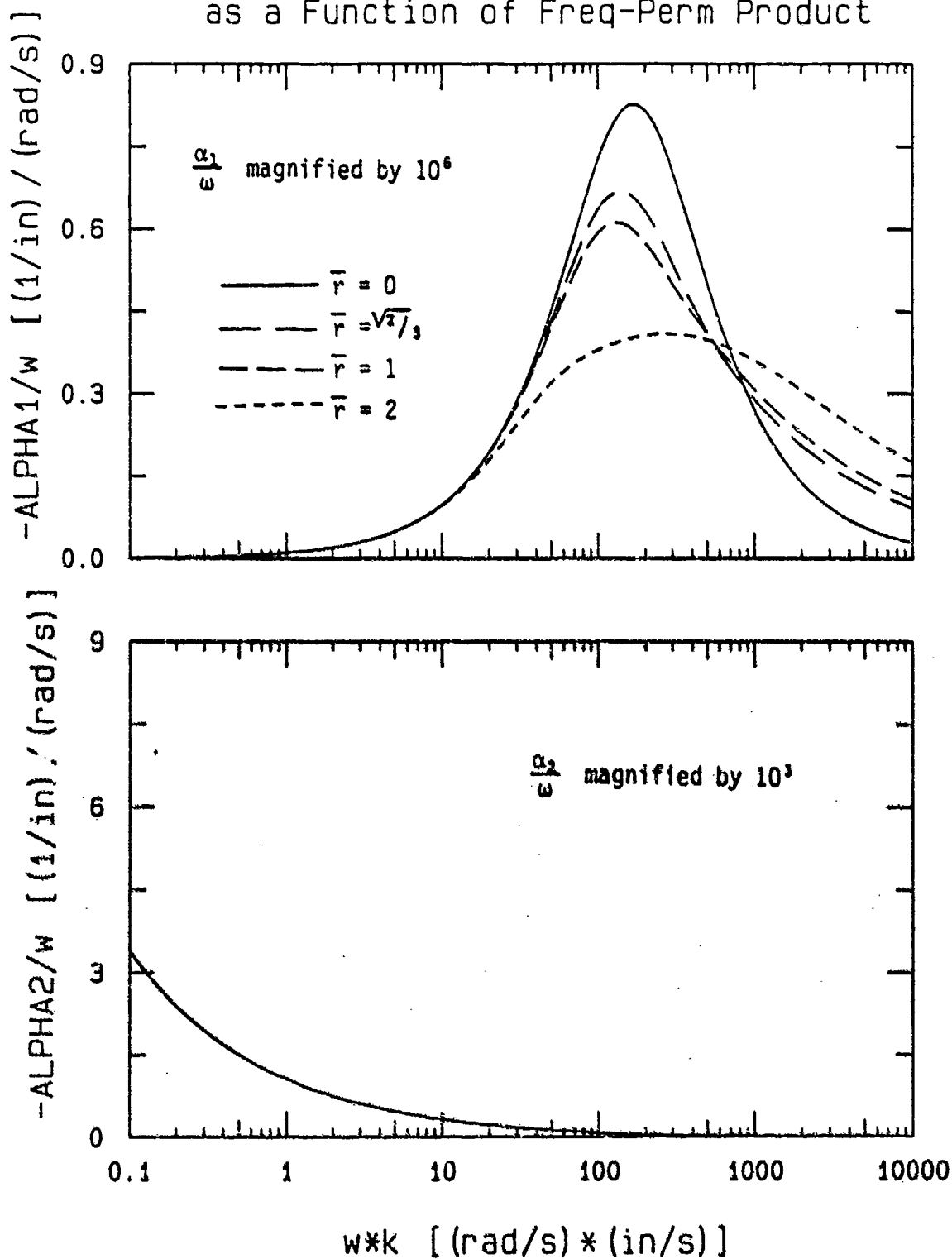


Figure 5.6b. Specific damping,  $n = 0.4$  and  $K_s = 10,000$  psi.

Wave Veloc. of First and Second Kind  
as a Function of Freq-Perm Product

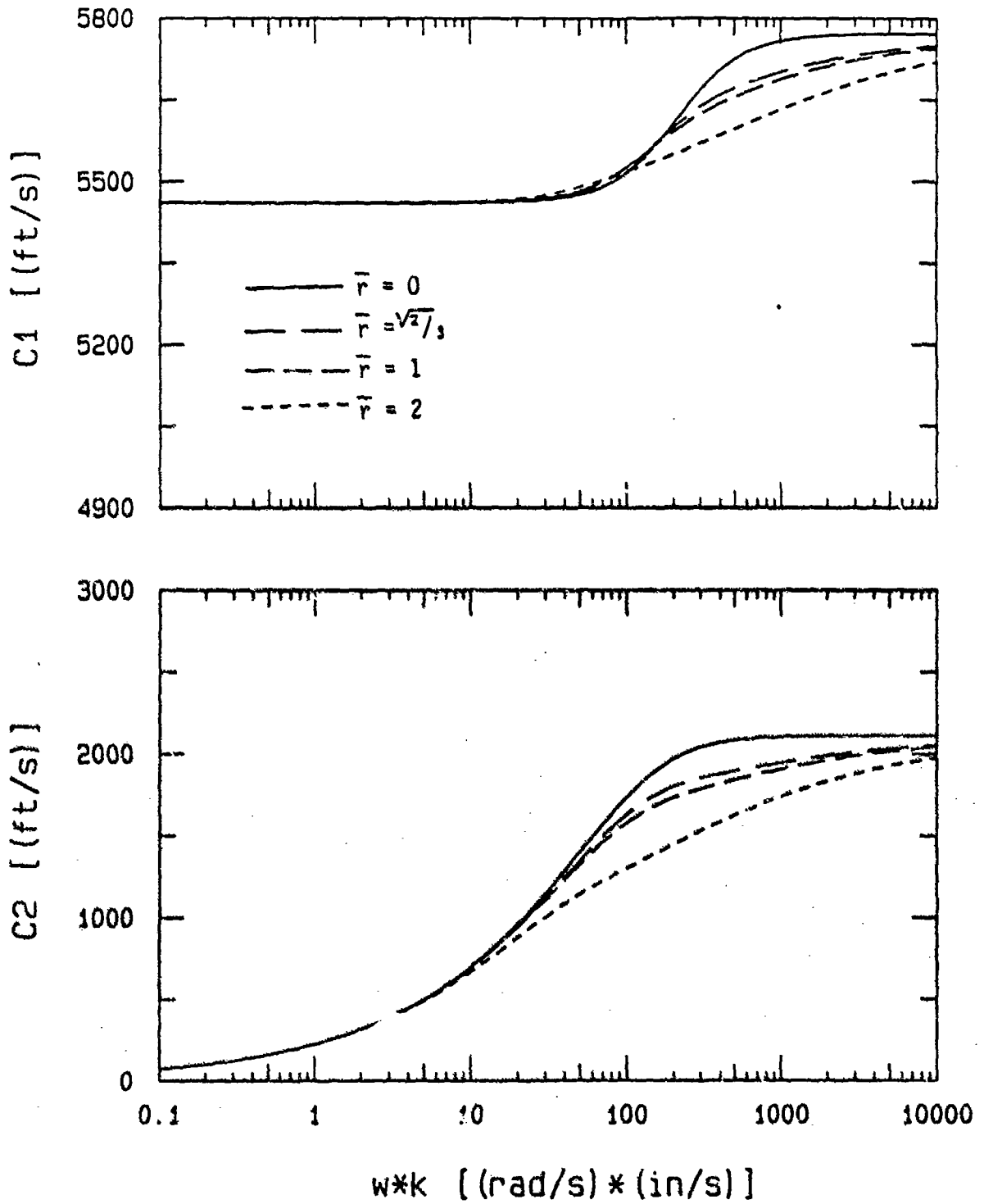


Figure 5.7a. Wave velocities,  $n = 0.4$  and  $K_s = 100,000$  psi.

# Specific Damping of First and Second Kind as a Function of Freq-Perm Product

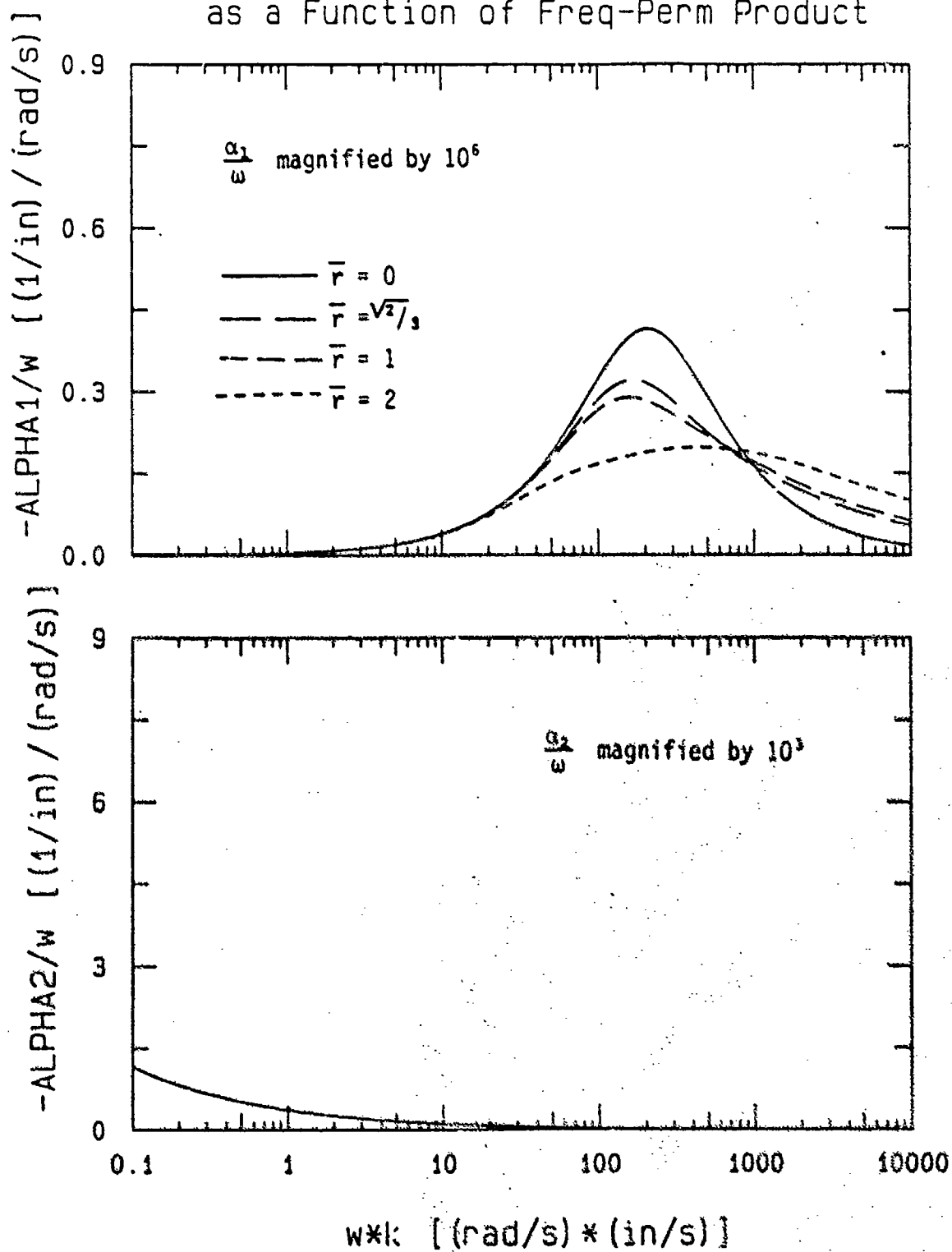


Figure 5.7b. Specific damping,  $n = 0.4$  and  $K_s = 100,000$  psi.



Wave Veloc. of First and Second Kind  
as a Function of Freq-Perm Product

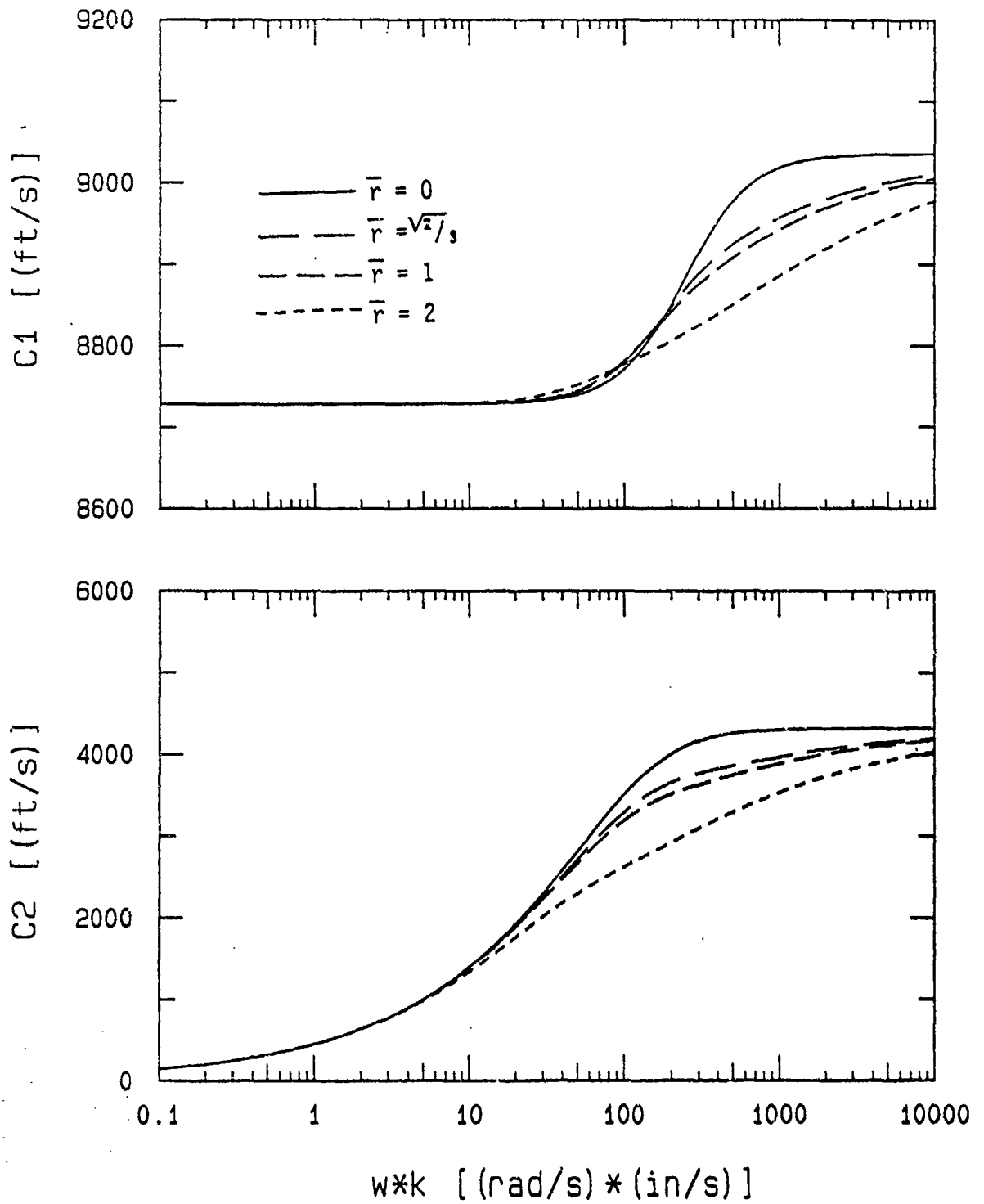


Figure 5.8a. Wave velocities,  $n = 0.4$  and  $K_s = 1,000,000$  psi.

# Specific Damping of First and Second Kind as a Function of Freq-Perm Product

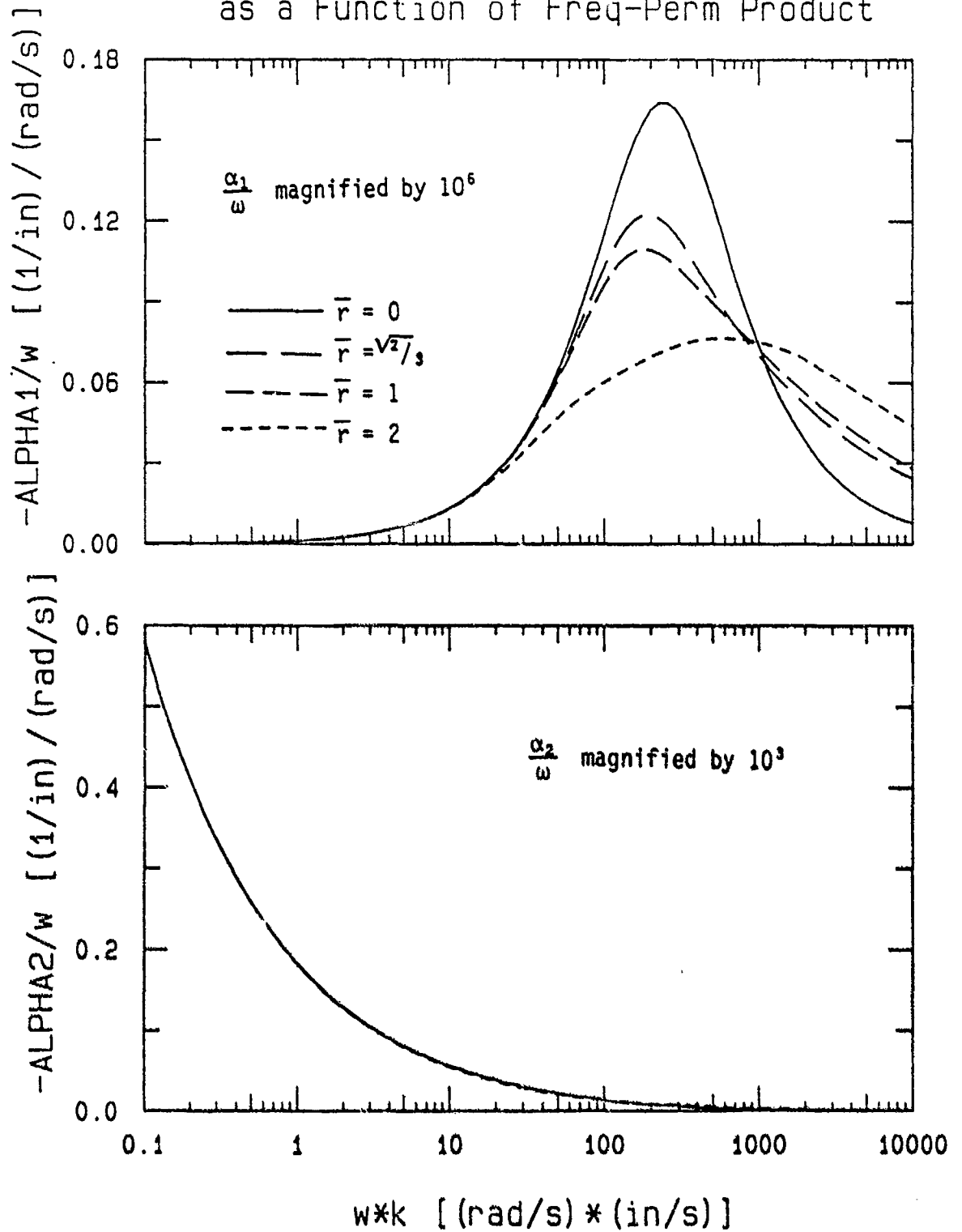


Figure 5.8b. Specific damping,  $n = 0.4$  and  $K_s = 1,000,000$  psi.

# Wave Veloc. of First and Second Kind as a Function of Freq-Perm Product

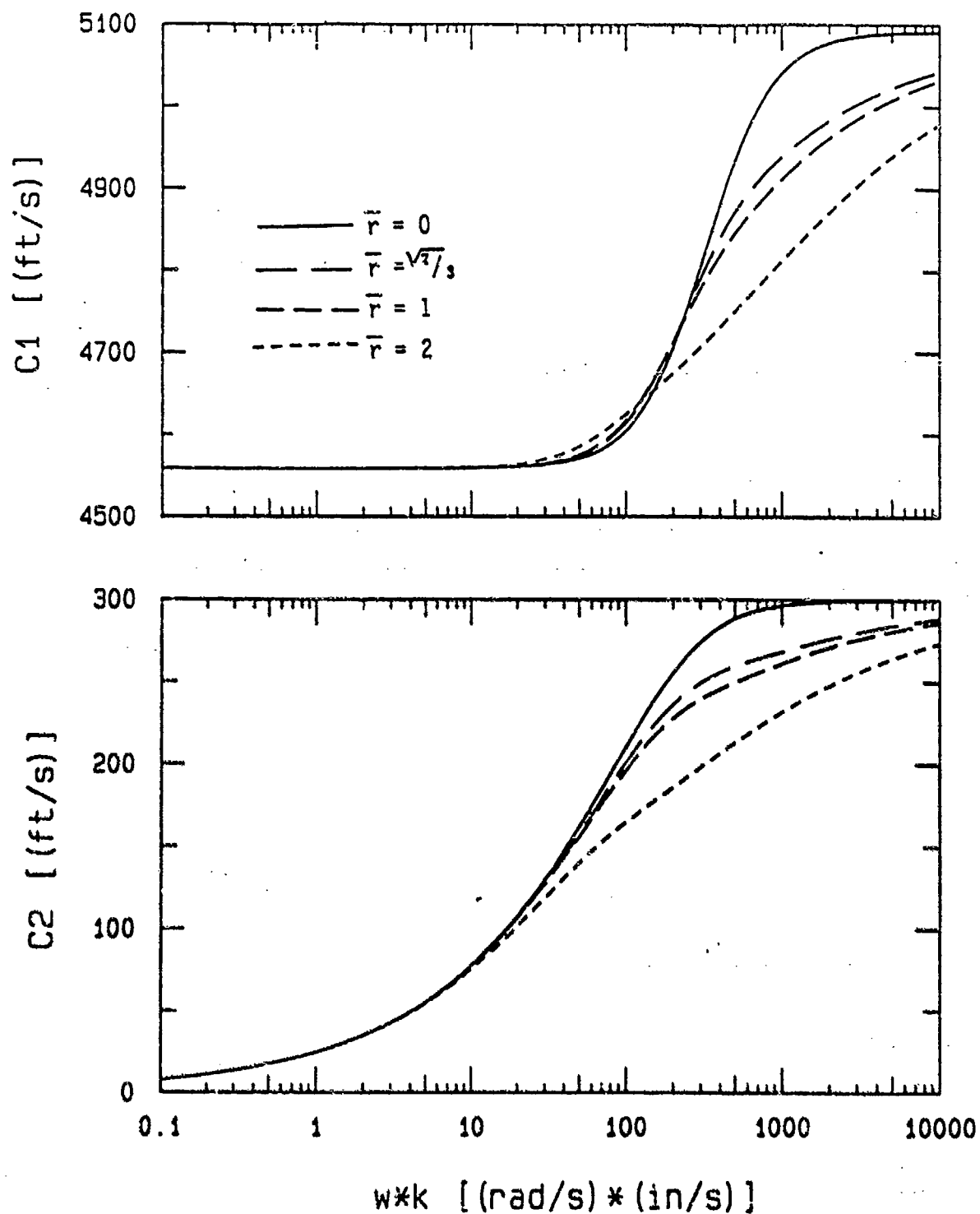


Figure 5.9a. Wave velocities in porous material saturated with fresh water;  $n = 0.6$ ,  $K_s = 1.000$  psi.

# Specific Damping of First and Second Kind as a Function of Freq-Perm Product

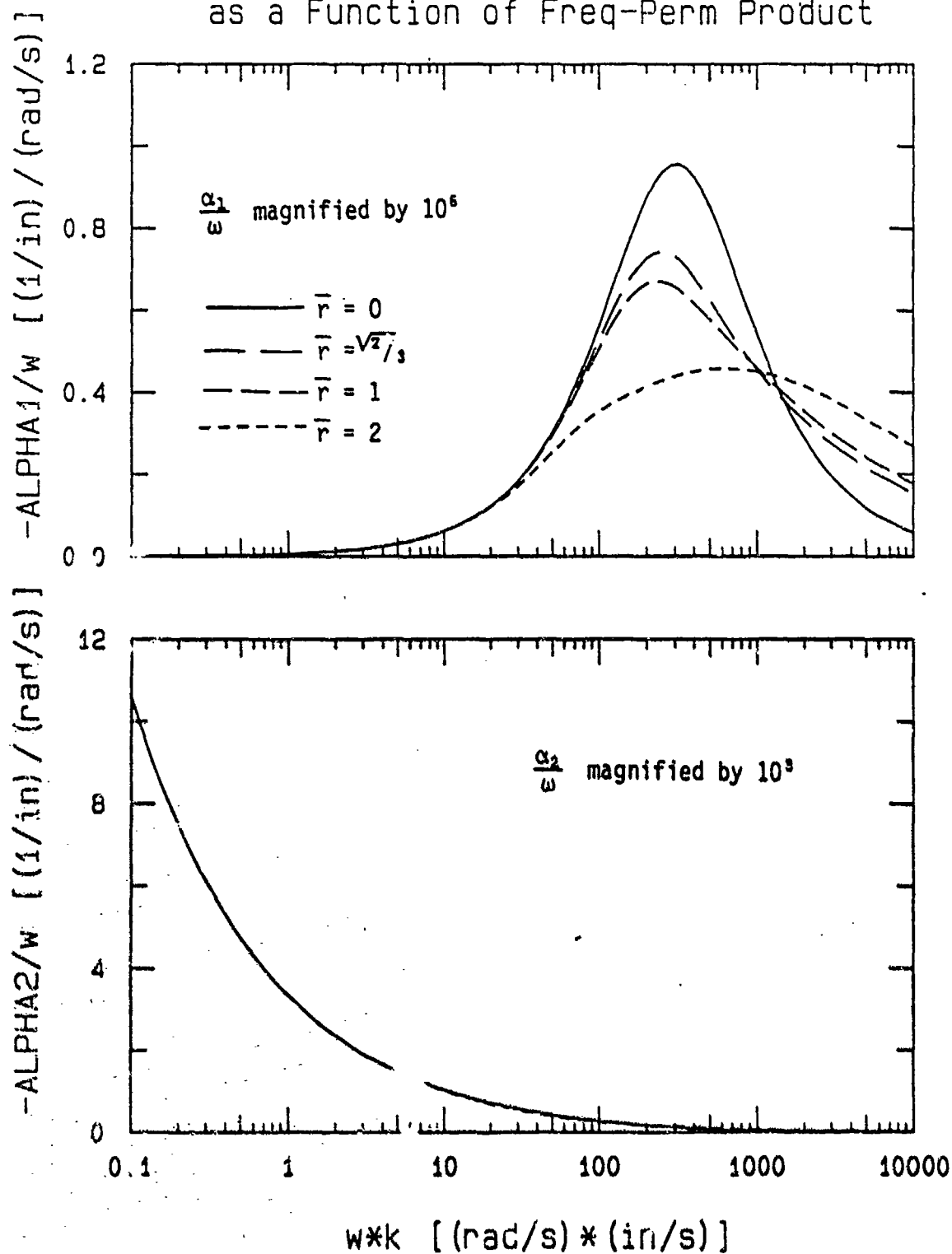


Figure 5.9b. Specific damping in porous material saturated with fresh water,  $n = 0.6$ ,  $K_s = 1,000$  psi.

# Wave Veloc. of First and Second Kind as a Function of Freq-Perm Product

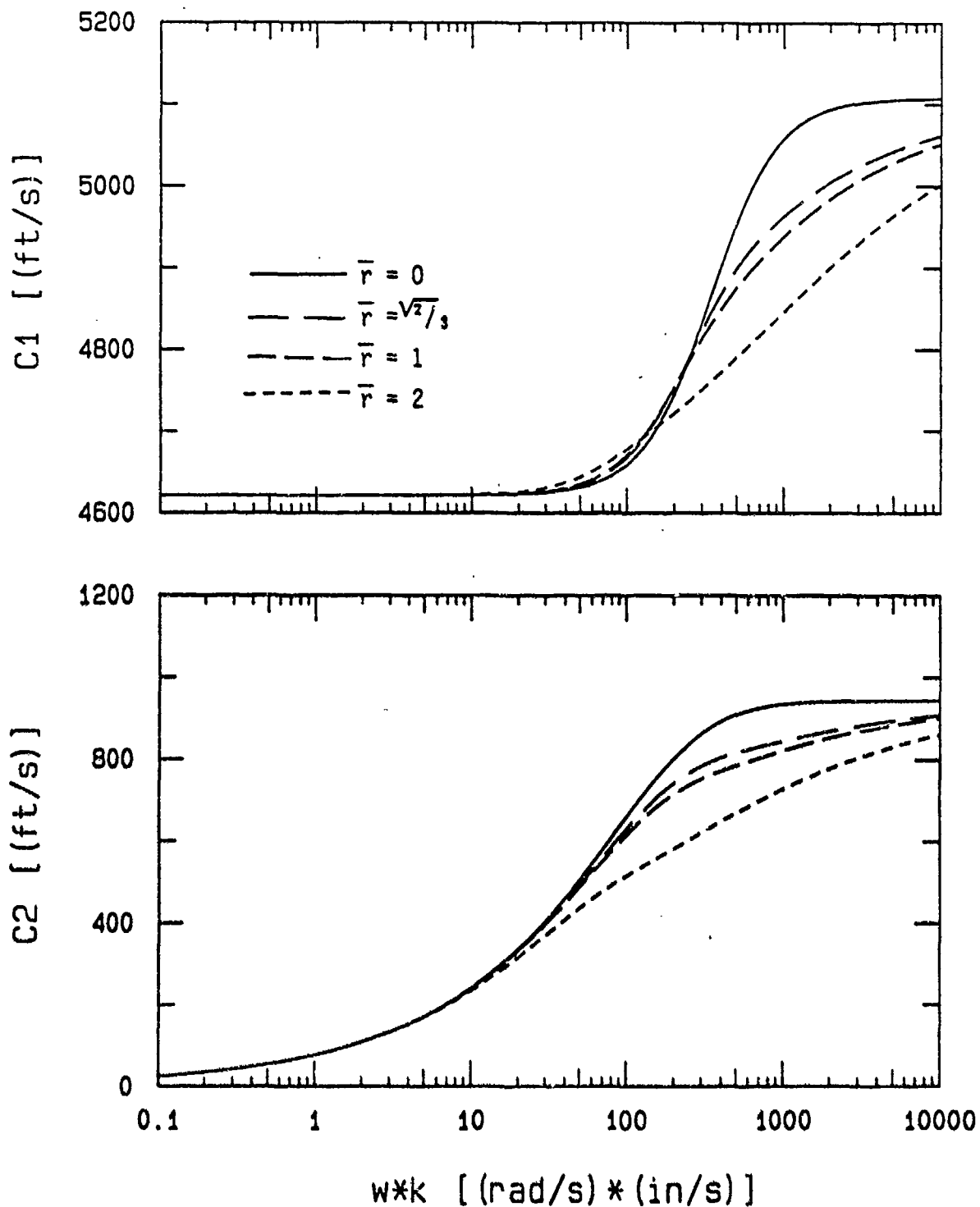


Figure 5.10a. Wave velocities in porous material saturated with fresh water,  $n = 0.6$ ,  $K_s = 10,000$  psi.

# Specific Damping of First and Second Kind as a Function of Freq-Perm Product

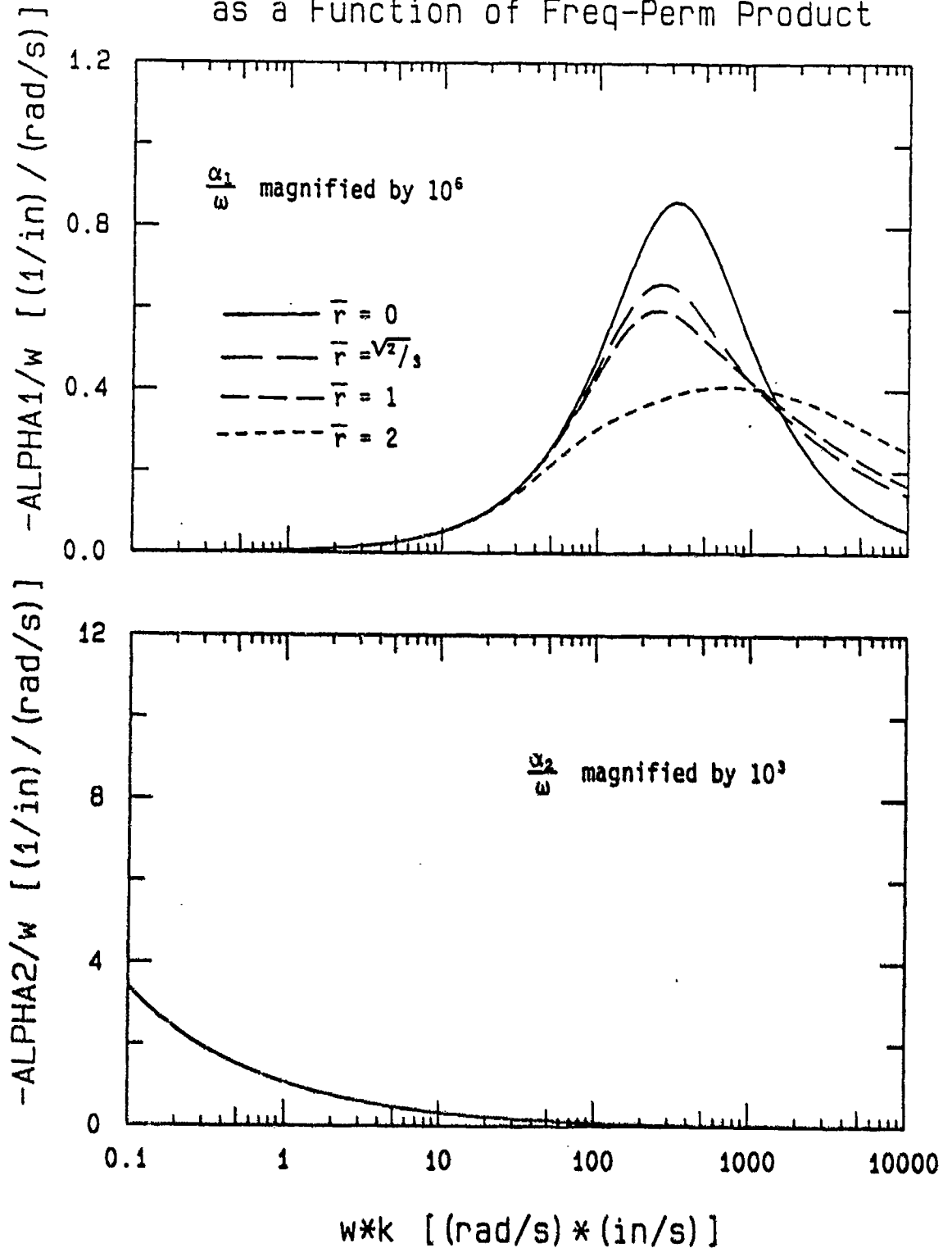


Figure 5.10b. Specific damping in porous material saturated with fresh water,  $n = 0.6$ ,  $K_s = 10,000$  psi.

Wave Veloc. of First and Second Kind  
as a Function of Freq-Perm Product

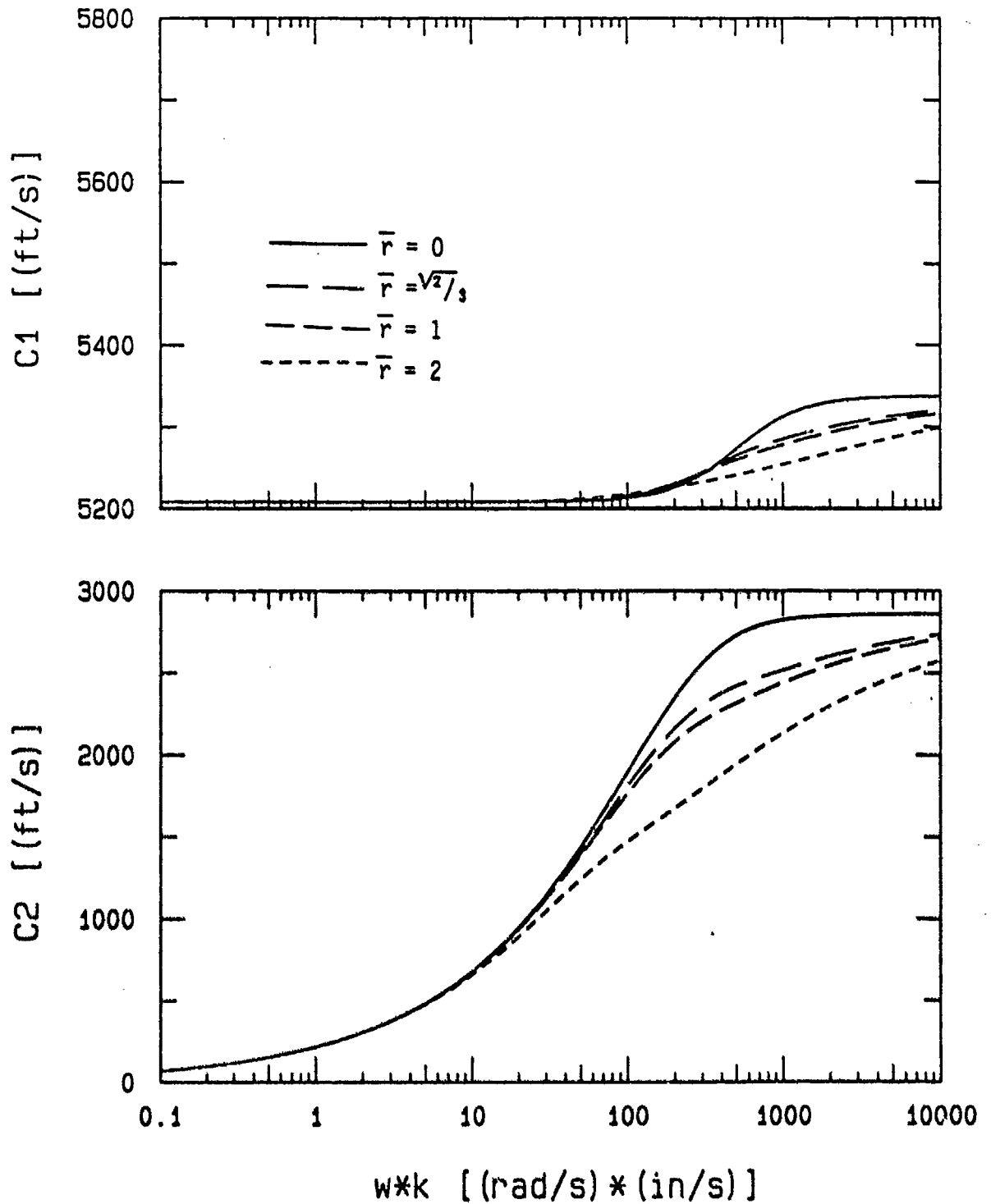


Figure 5.11a. Wave velocities in porous material saturated with fresh water,  $n = 0.6$ ,  $K_s = 100,000$  psi.

# Specific Damping of First and Second Kind as a Function of Freq-Perm Product

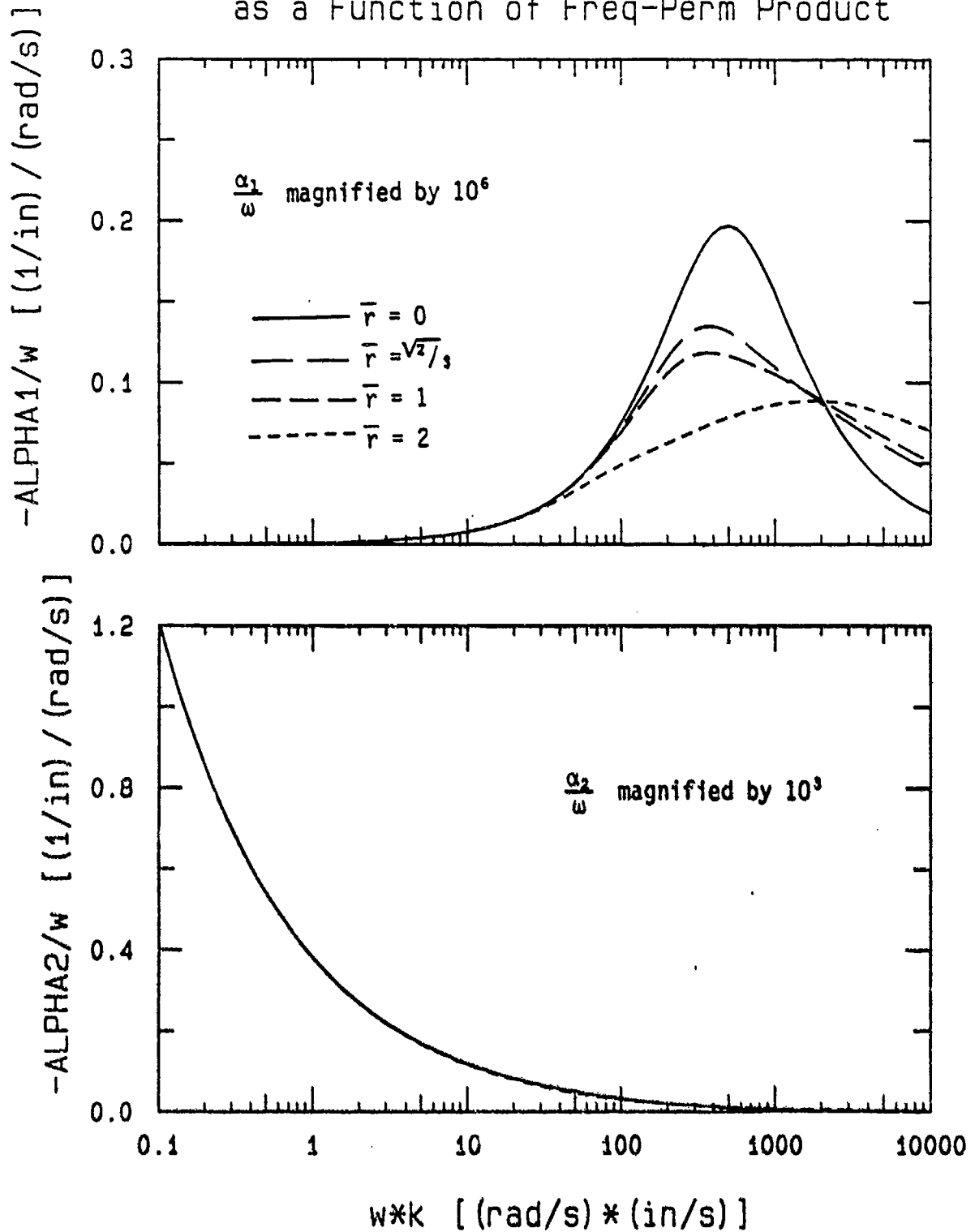


Figure 5.11b. Specific damping in porous material saturated with fresh water,  $n = 0.6$ ,  $K_s = 100,000$  psi.



# Wave Veloc. of First and Second Kind as a Function of Freq-Perm Product

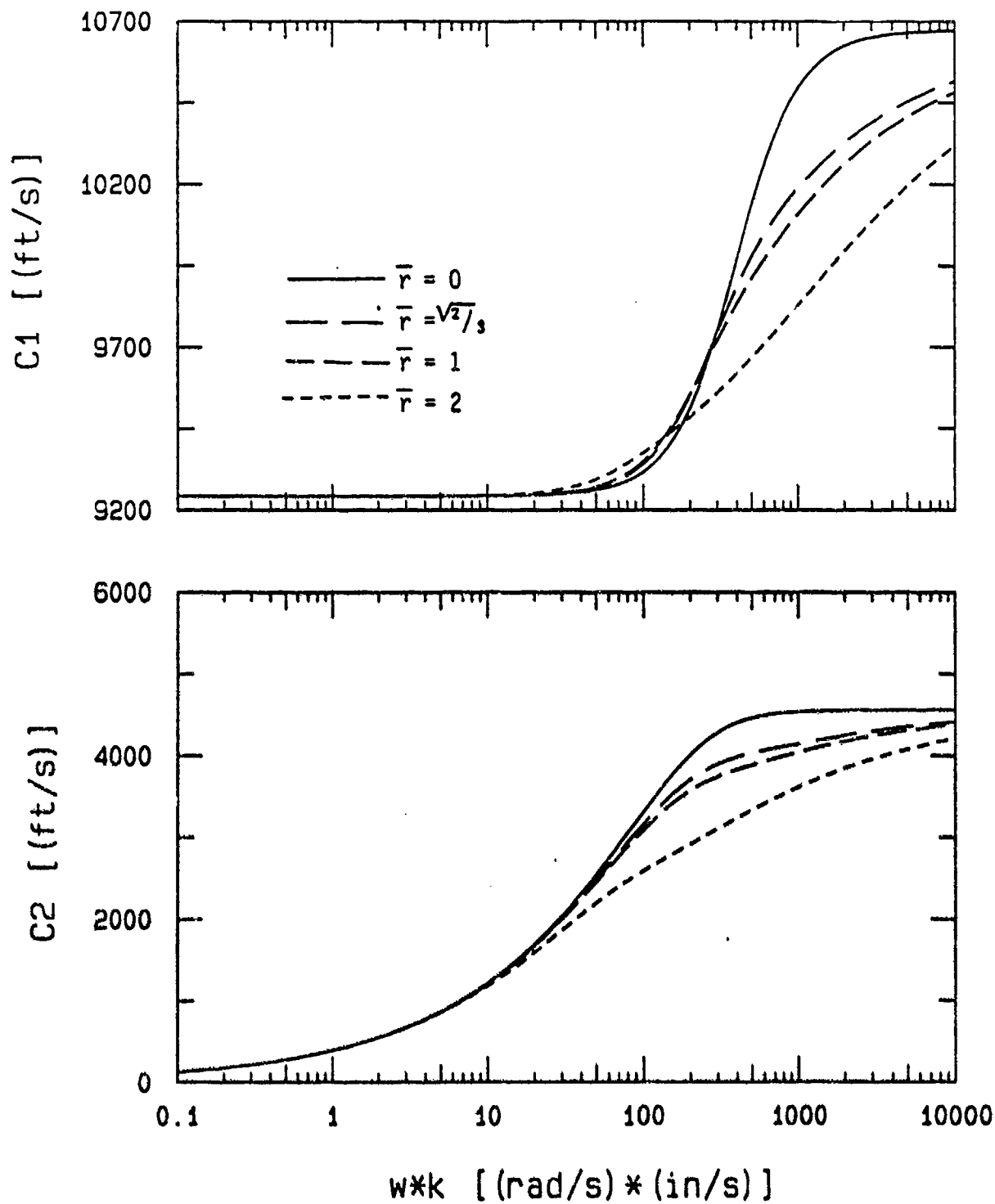


Figure 5.12a. Wave velocities in porous material saturated with fresh water,  $n = 0.6$ ,  $K_s = 1,000,000$  psi.

Specific Damping of First and Second Kind  
as a Function of Freq-Perm Product

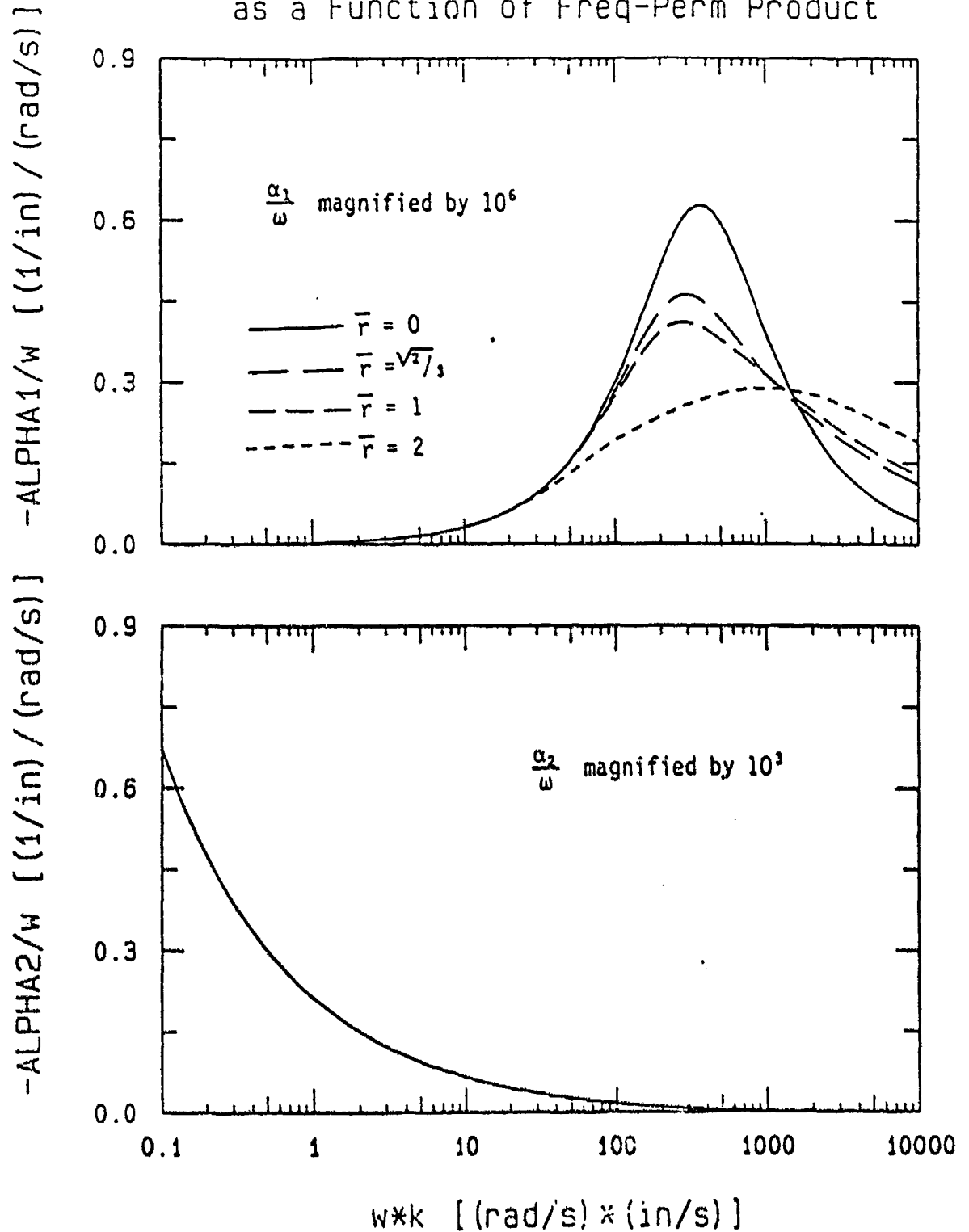


Figure 5.12b. Specific damping in porous material saturated with fresh water,  $n = 0.6$ ,  $K_s = 1,000,000$  psi.

# Wave Veloc. of First and Second Kind as a Function of Freq-Perm Product

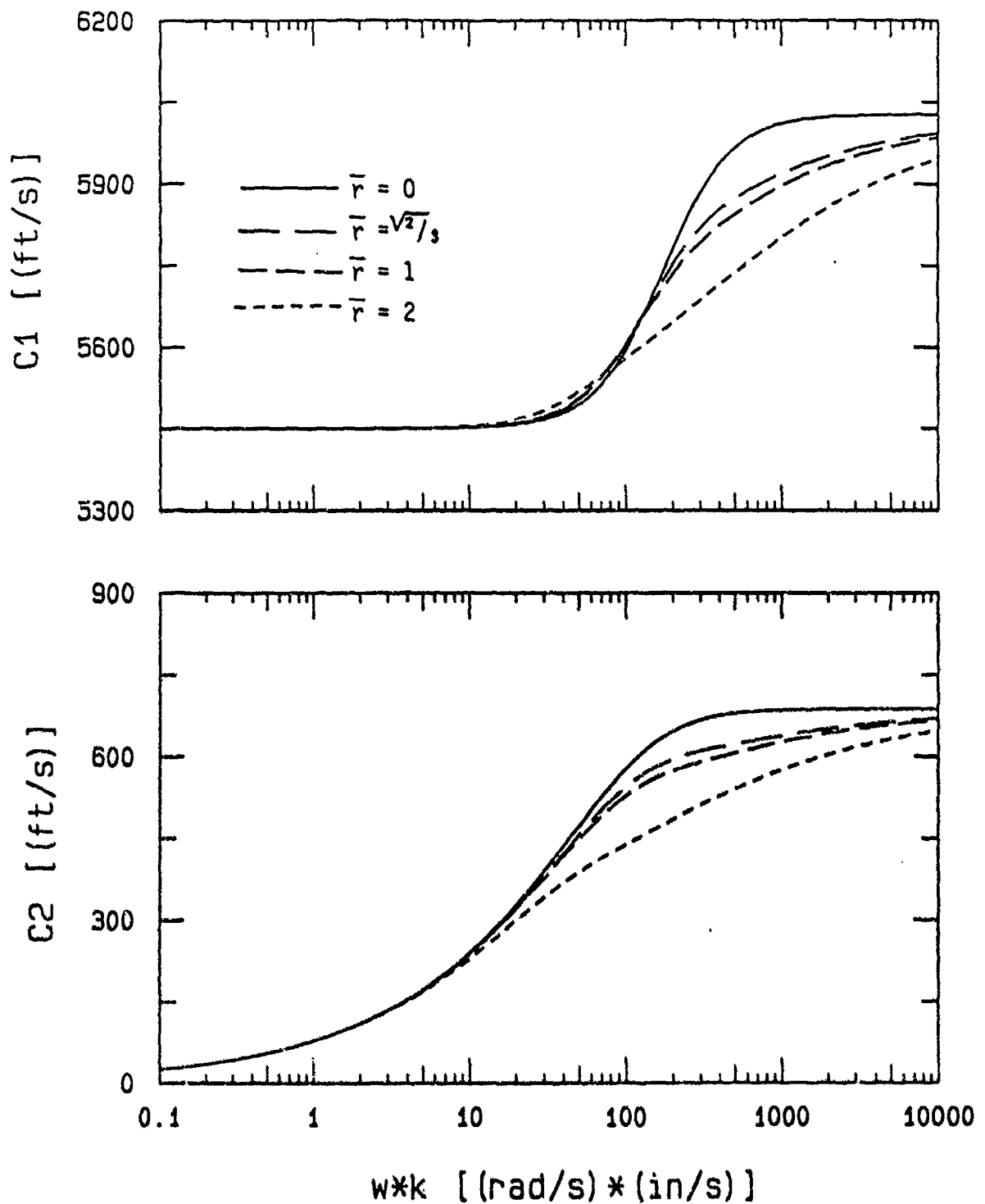


Figure 5.13a. Wave velocities in porous material saturated with sea water,  $r = 0.4$ ,  $K_s = 10,000$  psi.

# Specific Damping of First and Second Kind as a Function of Freq-Perm Product

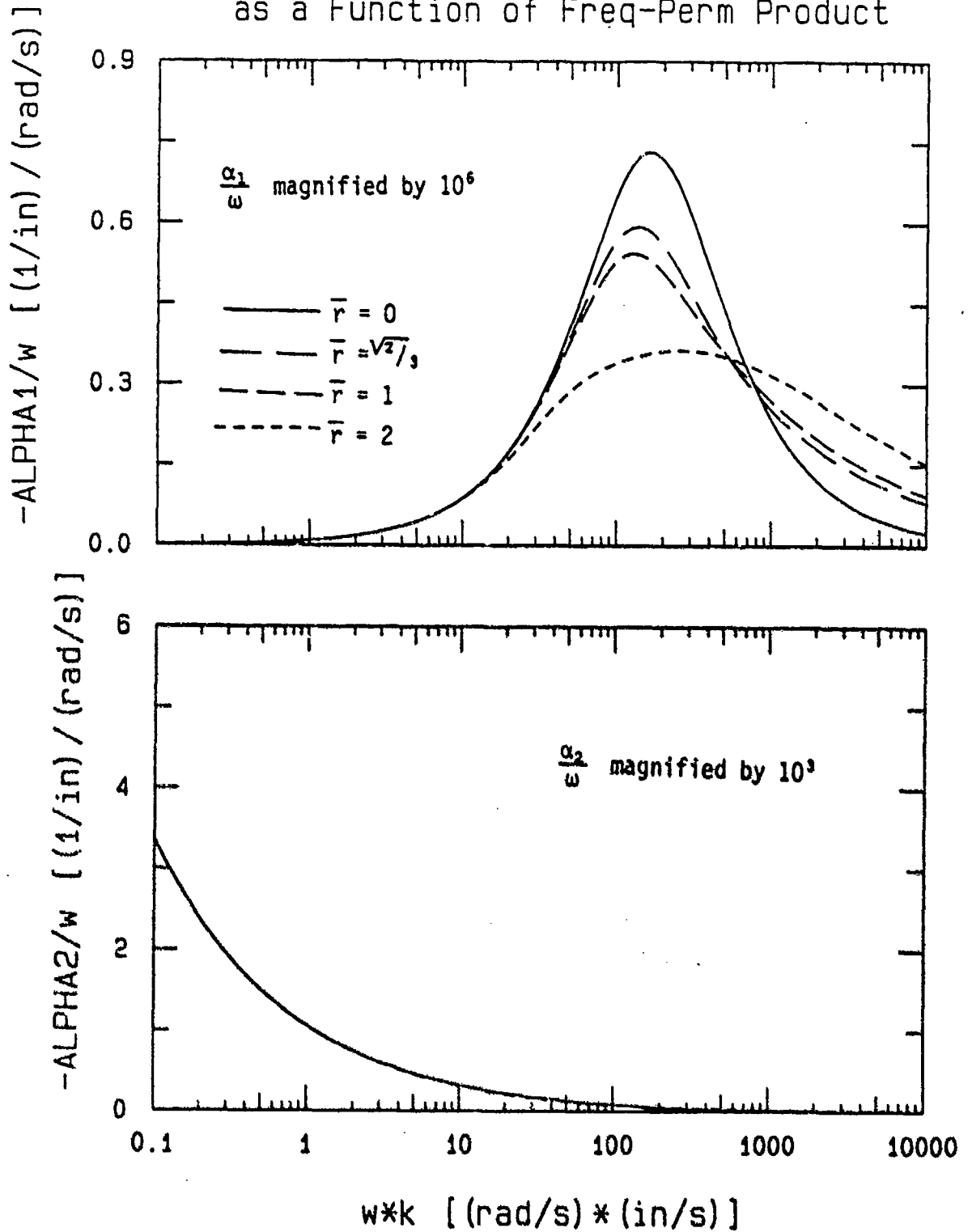


Figure 5.13b. Specific damping in porous material saturated with sea water,  $n = 0.4$ ,  $K_s = 10,000$  psi.

# Wave Veloc. of First and Second Kind as a Function of Freq-Perm Product

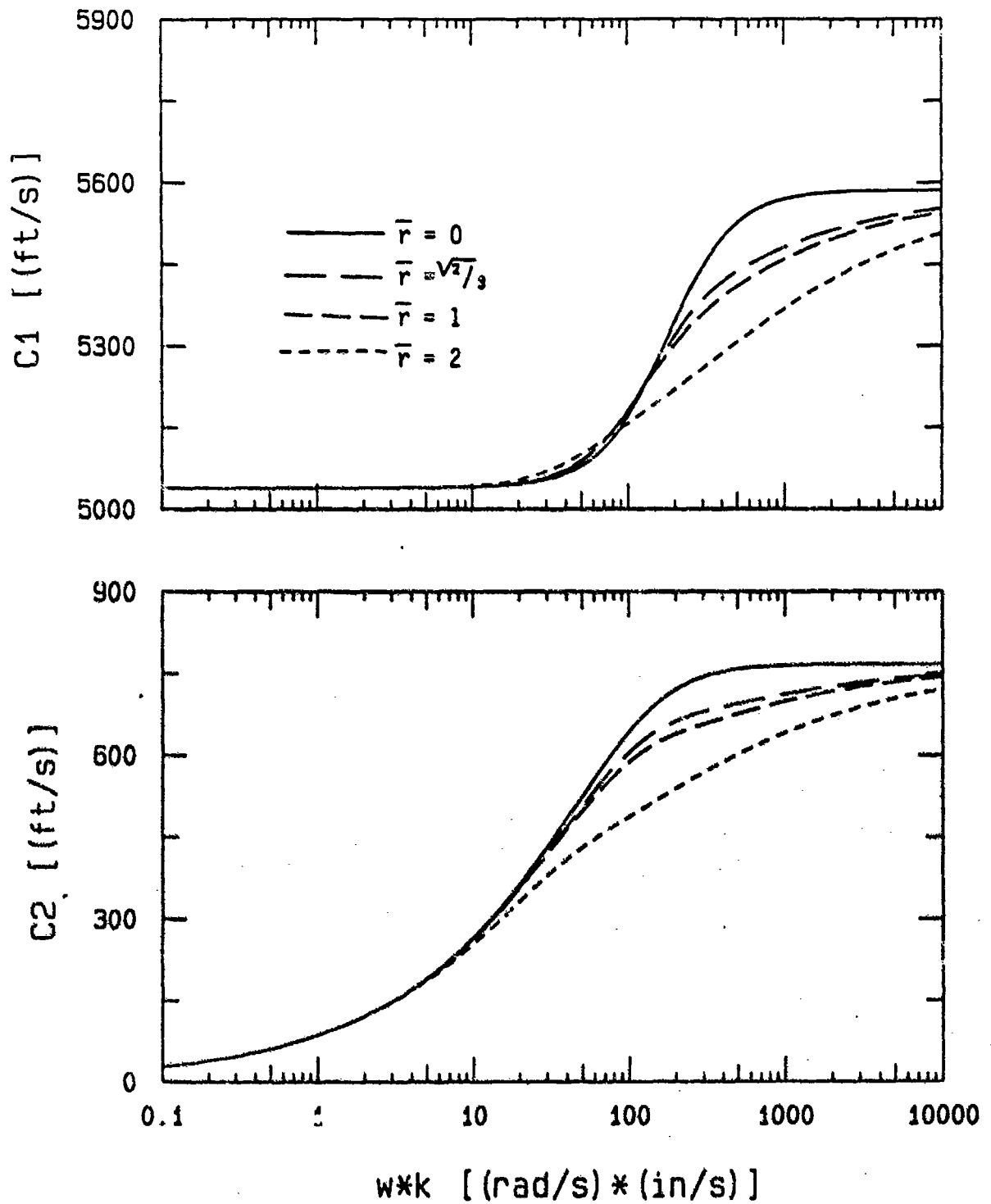


Figure 5.14a. Wave velocities with  $\nu = 0.2$  and  $n = 0.4$ ,  
 $K_s = 10,000$  psi.

# Specific Damping of First and Second Kind as a Function of Freq-Perm Product

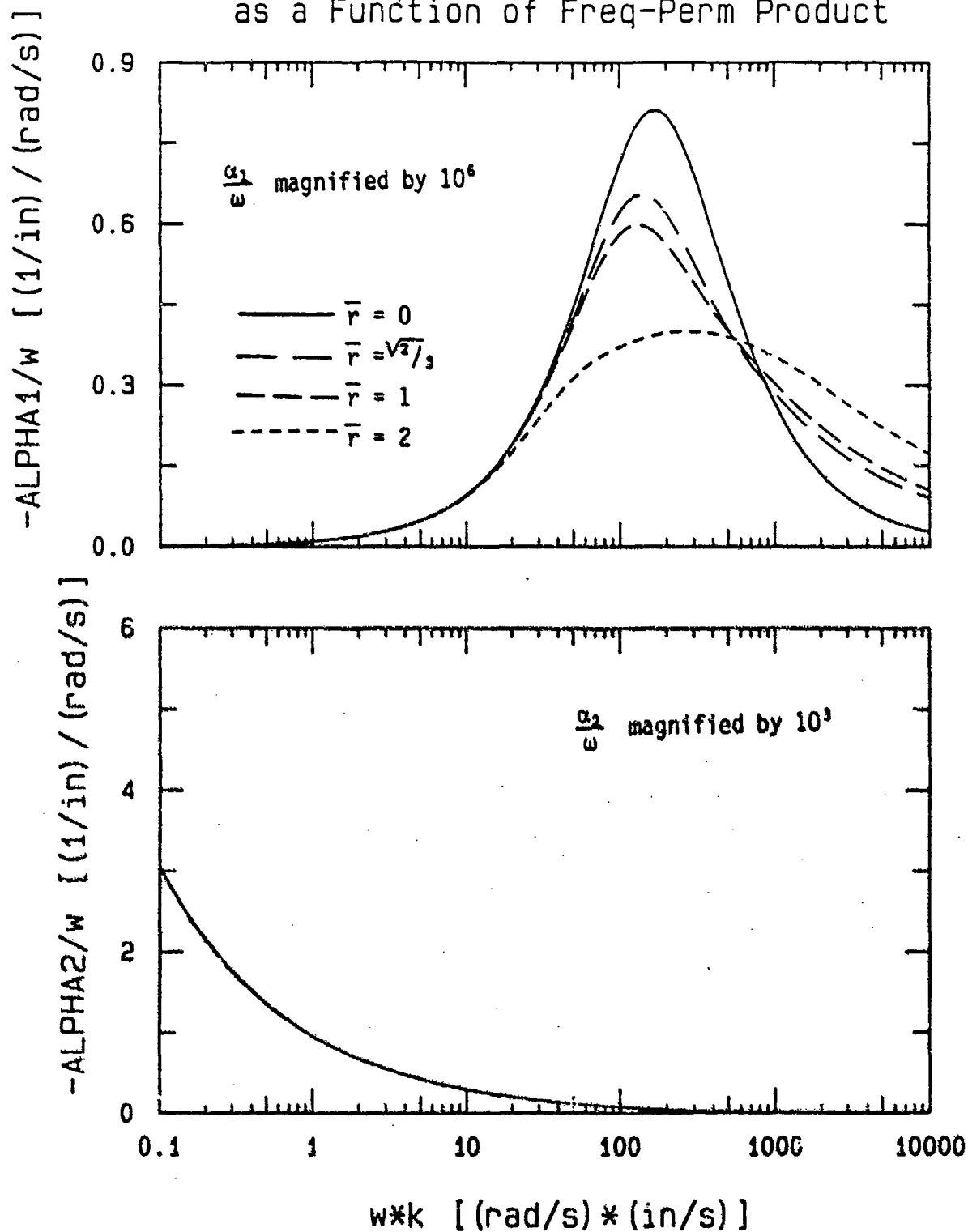


Figure 5.14b. Specific damping with  $\nu = 0.2$  and  $n = 0.4$ ,  $K_s = 10,000$  psi.

# Wave Veloc. of First and Second Kind as a Function of Freq-Perm Product

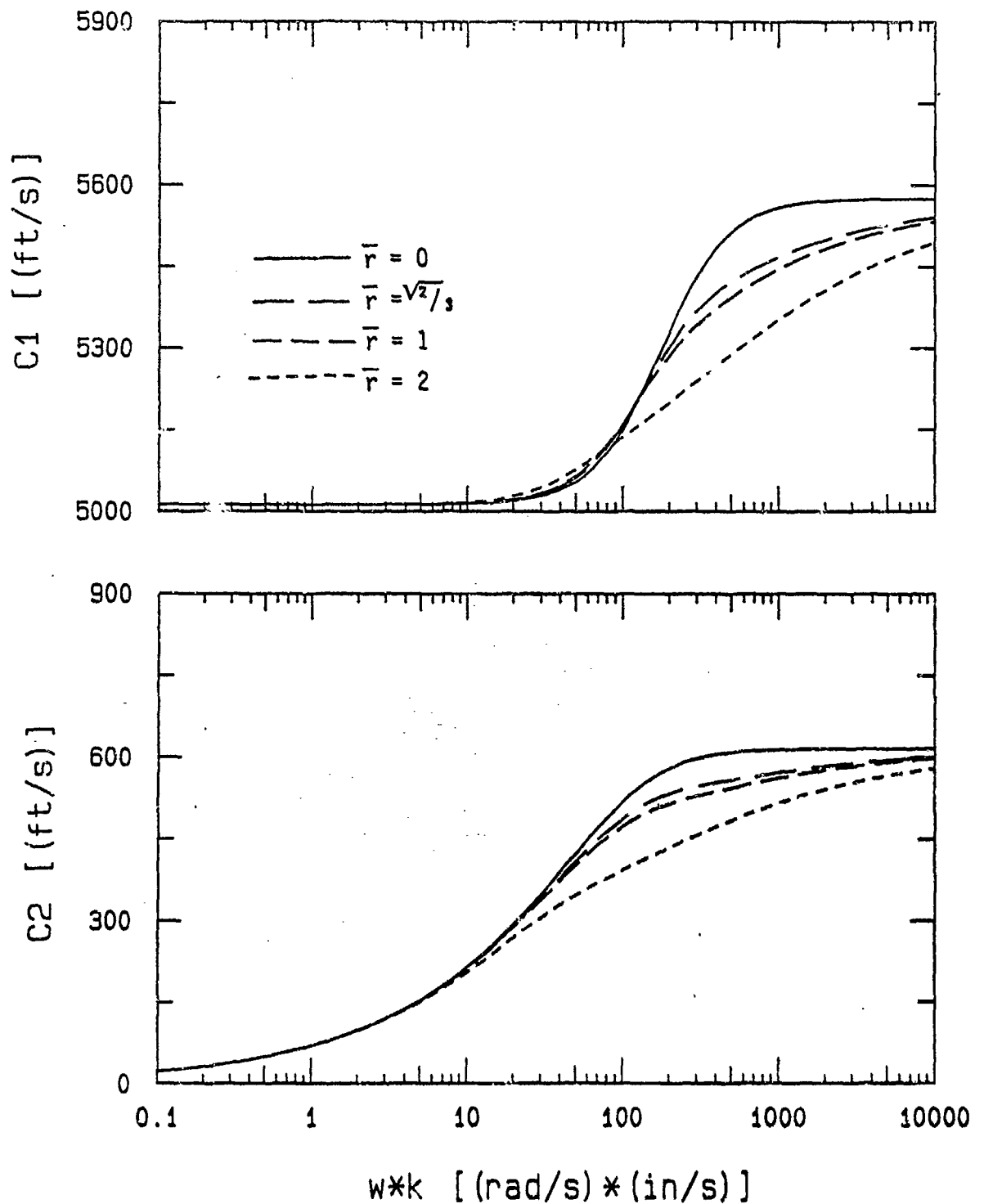


Figure 5.15a. Wave velocities with  $\nu = 0.4$  and  $n = 0.4$ ,  
 $K_s = 10,000$  psi.

Specific Damping of First and Second Kind  
as a Function of Freq-Perm Product

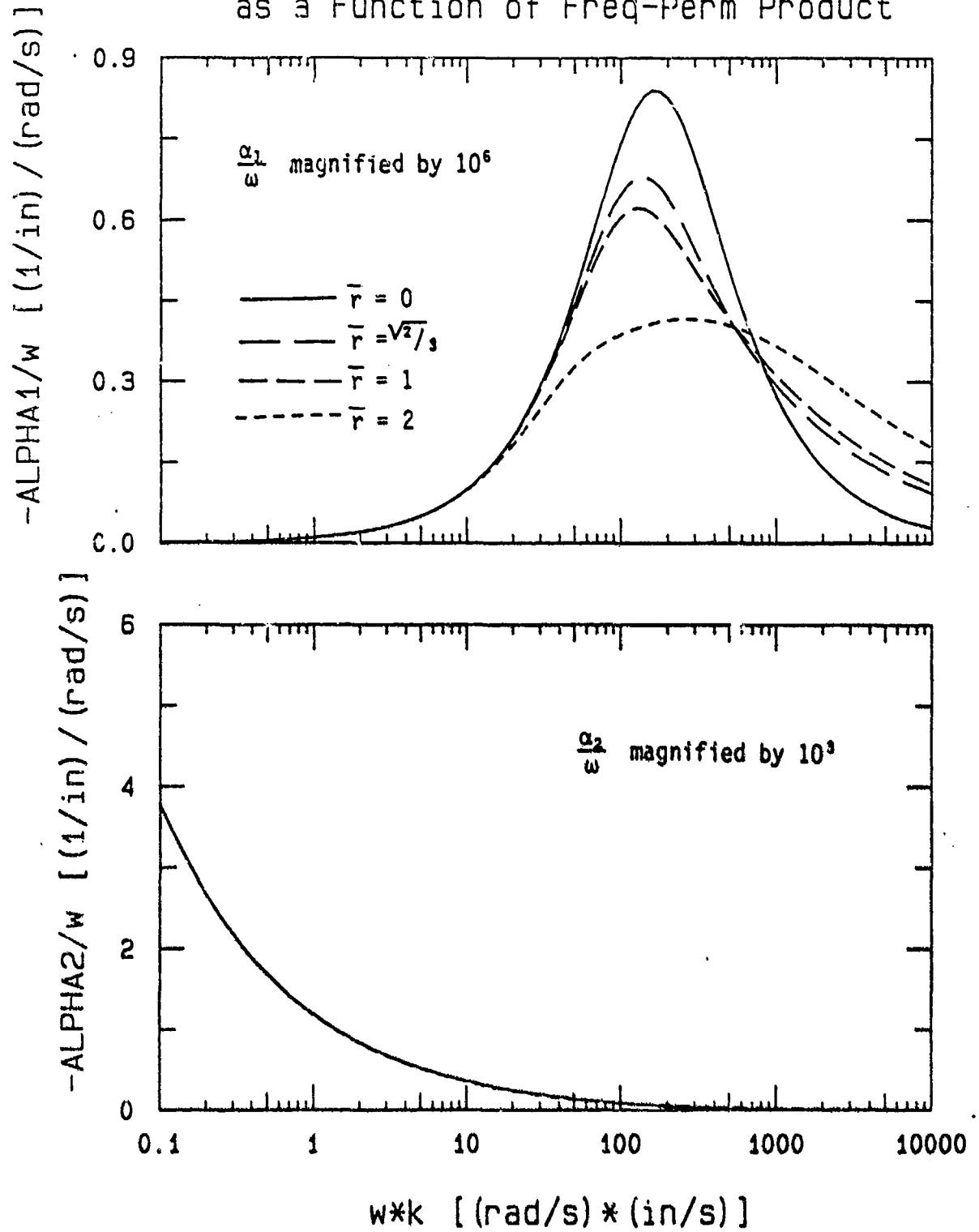


Figure 5.15b. Specific damping with  $\nu = 0.4$  and  $n = 0.4$ ,  
 $K_s = 10,000$  psi.



# Wave Veloc. of First and Second Kind as a Function of Freq-Perm Product

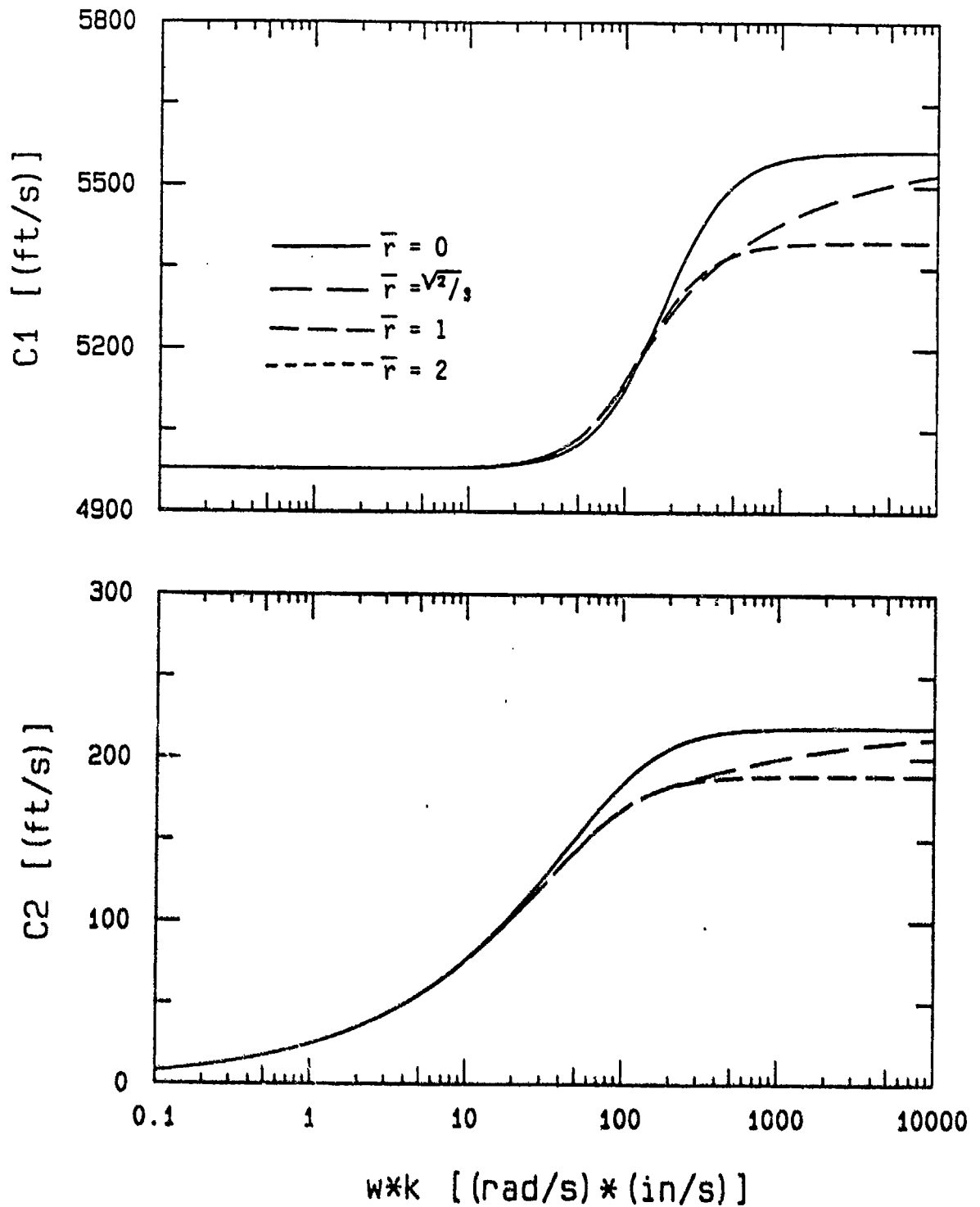


Figure 5.16a. Comparison of wavespeeds computed from approximate and exact expressions for fluid friction,  $n = 0.4$ ,  $K_s = 1,000$  psi.

# Specific Damping of First and Second Kind as a Function of Freq-Perm Product

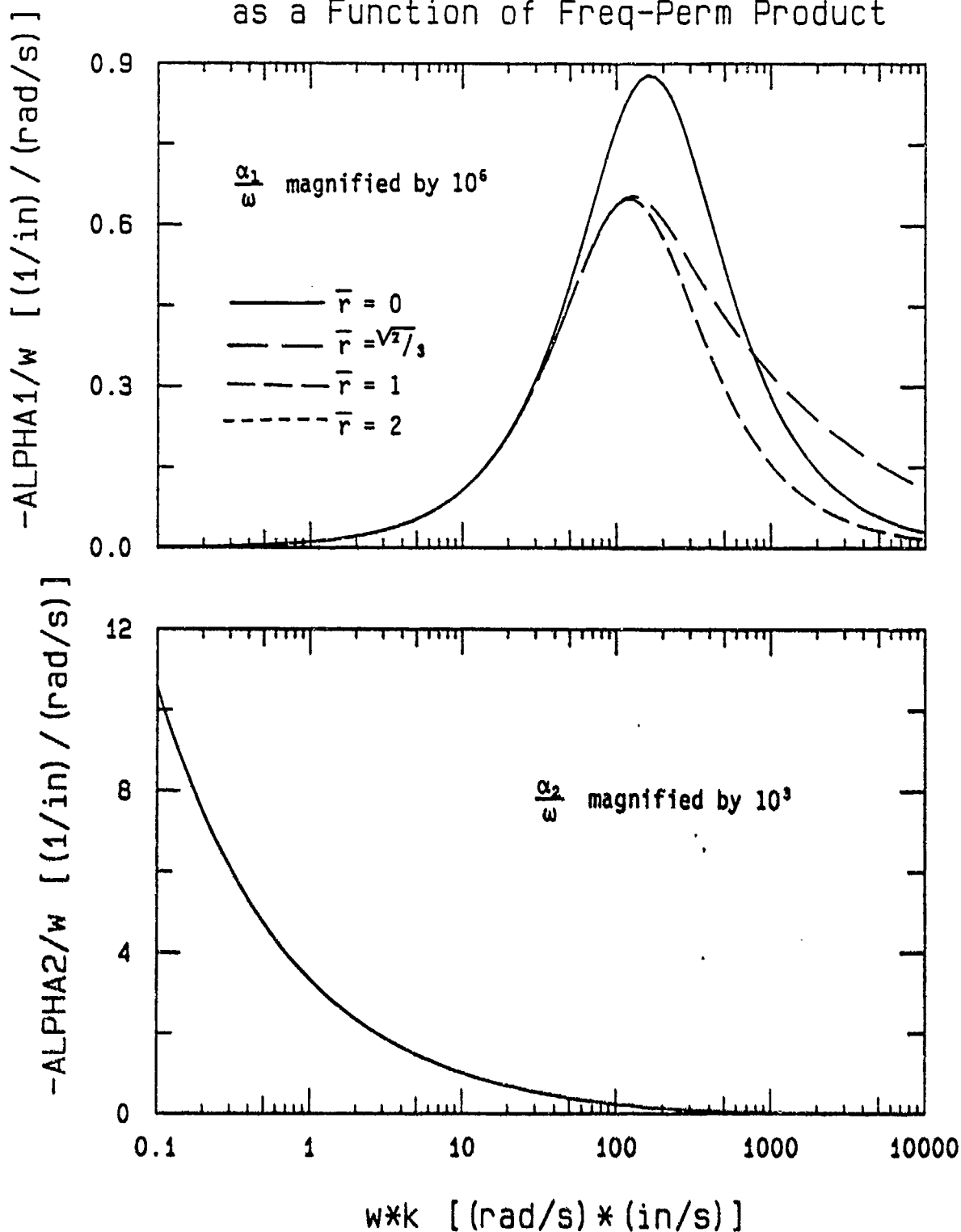


Figure 5.16b. Comparison of specific damping computed from approximate and exact expressions for fluid friction,  $n = 0.4$ ,  $K_s = 1,000$  psi.

Wave Veloc. of First and Second Kind  
as a Function of Freq-Perm Product

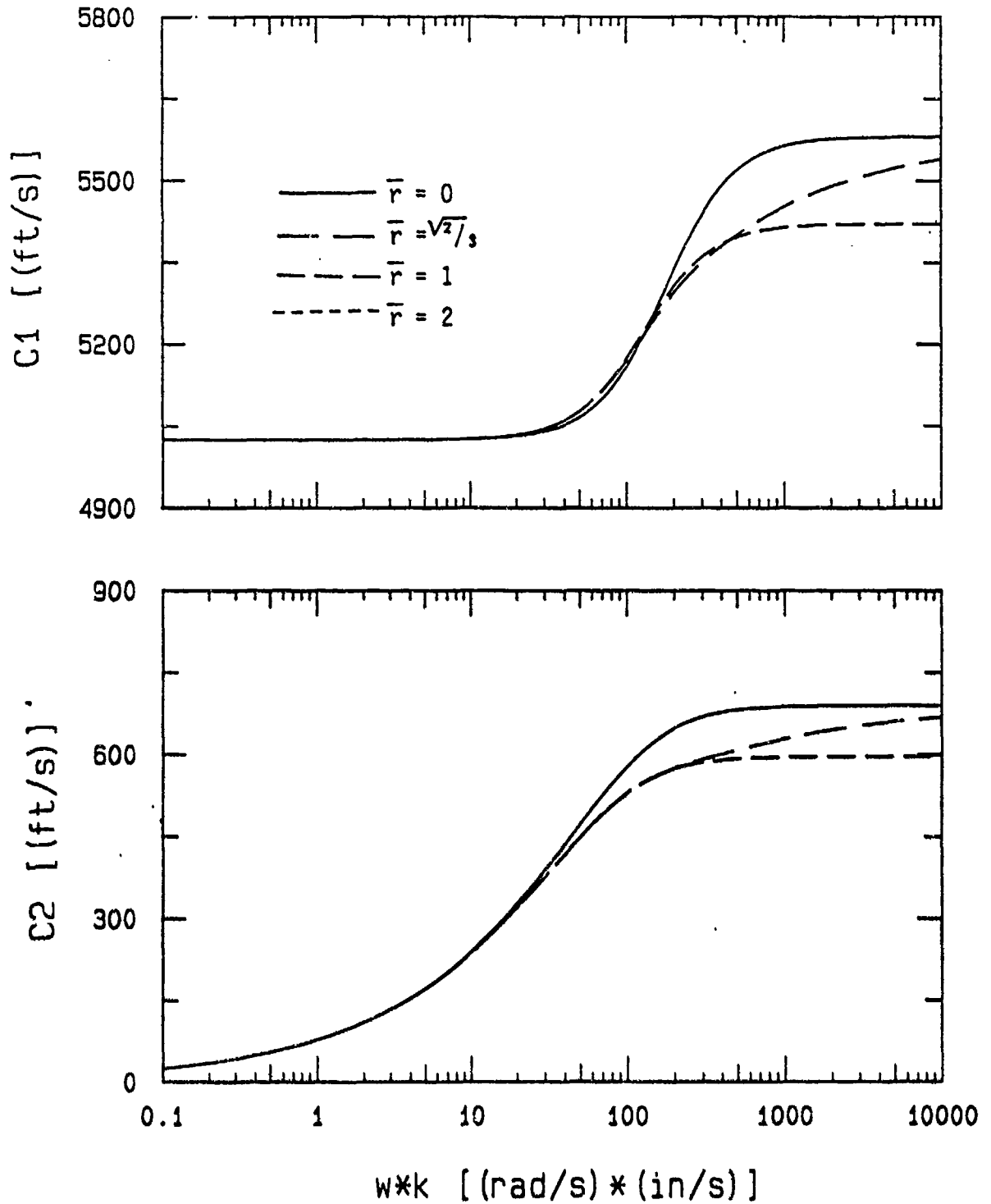


Figure 5.17a. Comparison of wavespeeds computed from approximate and exact expressions for fluid friction,  $n = 0.4$ ,  $K_s = 10,000$  psi.

# Specific Damping of First and Second Kind as a Function of Freq-Perm Product

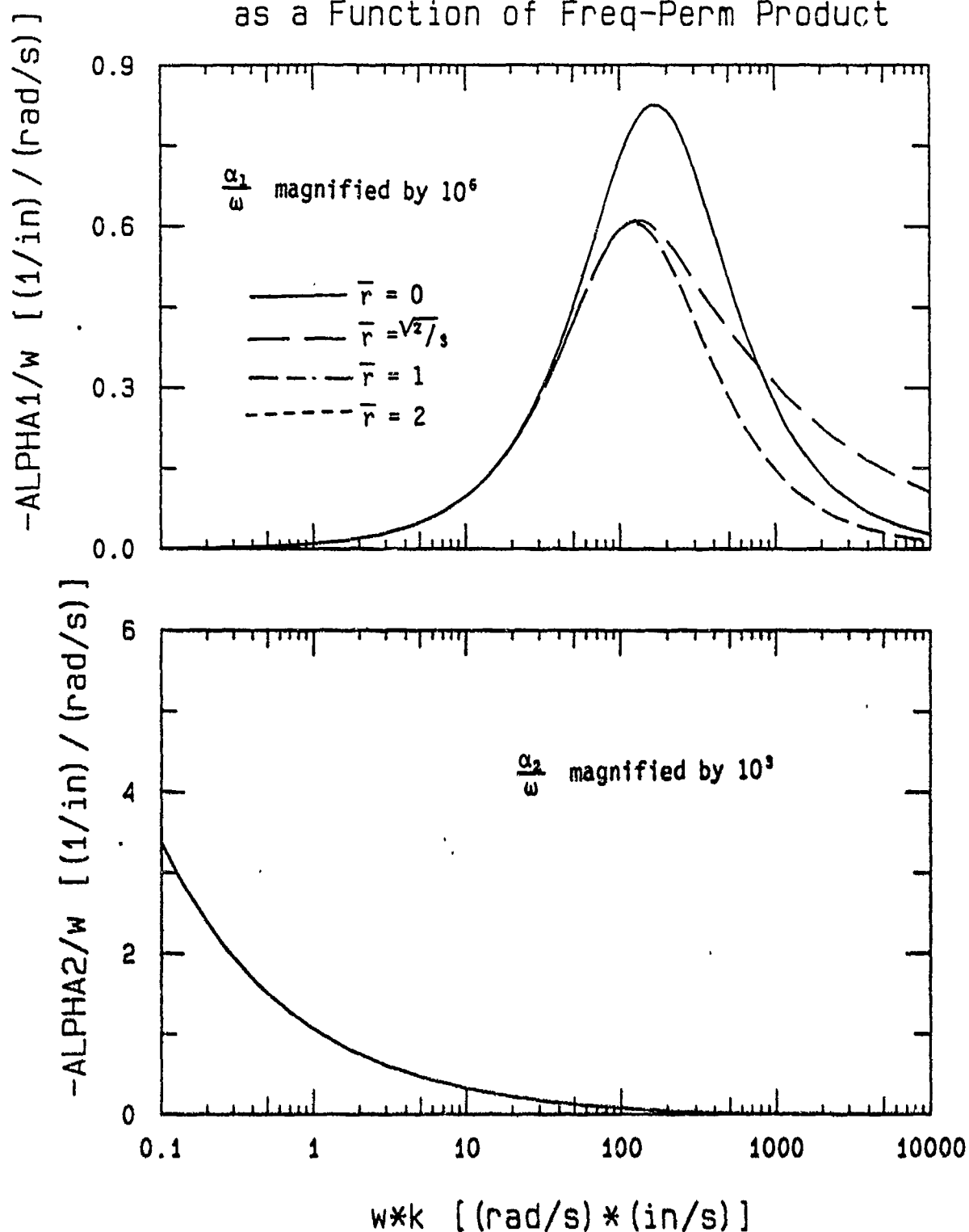


Figure 5.17b. Comparison of specific damping computed from approximate and exact expressions for fluid friction,  $n = 0.4$ ,  $K_s = 10,000$  psi.

# Wave Veloc. of First and Second Kind as a Function of Freq-Perm Product

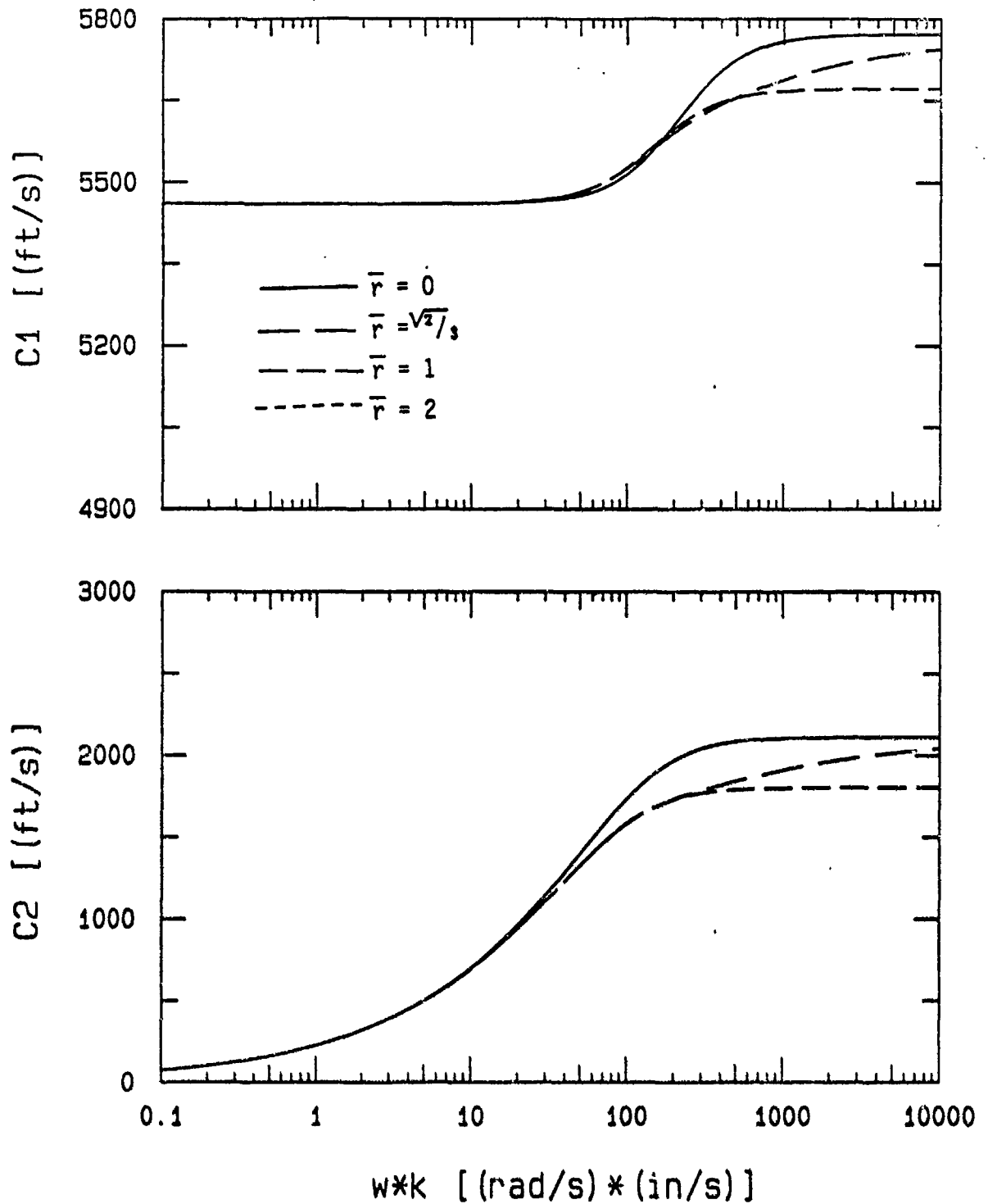


Figure 5.18a. Comparison of wavespeeds computed from approximate and exact expressions for fluid friction,  $n = 0.4$ ,  $K_s = 100,000$  psi.

# Specific Damping of First and Second Kind as a Function of Freq-Perm Product

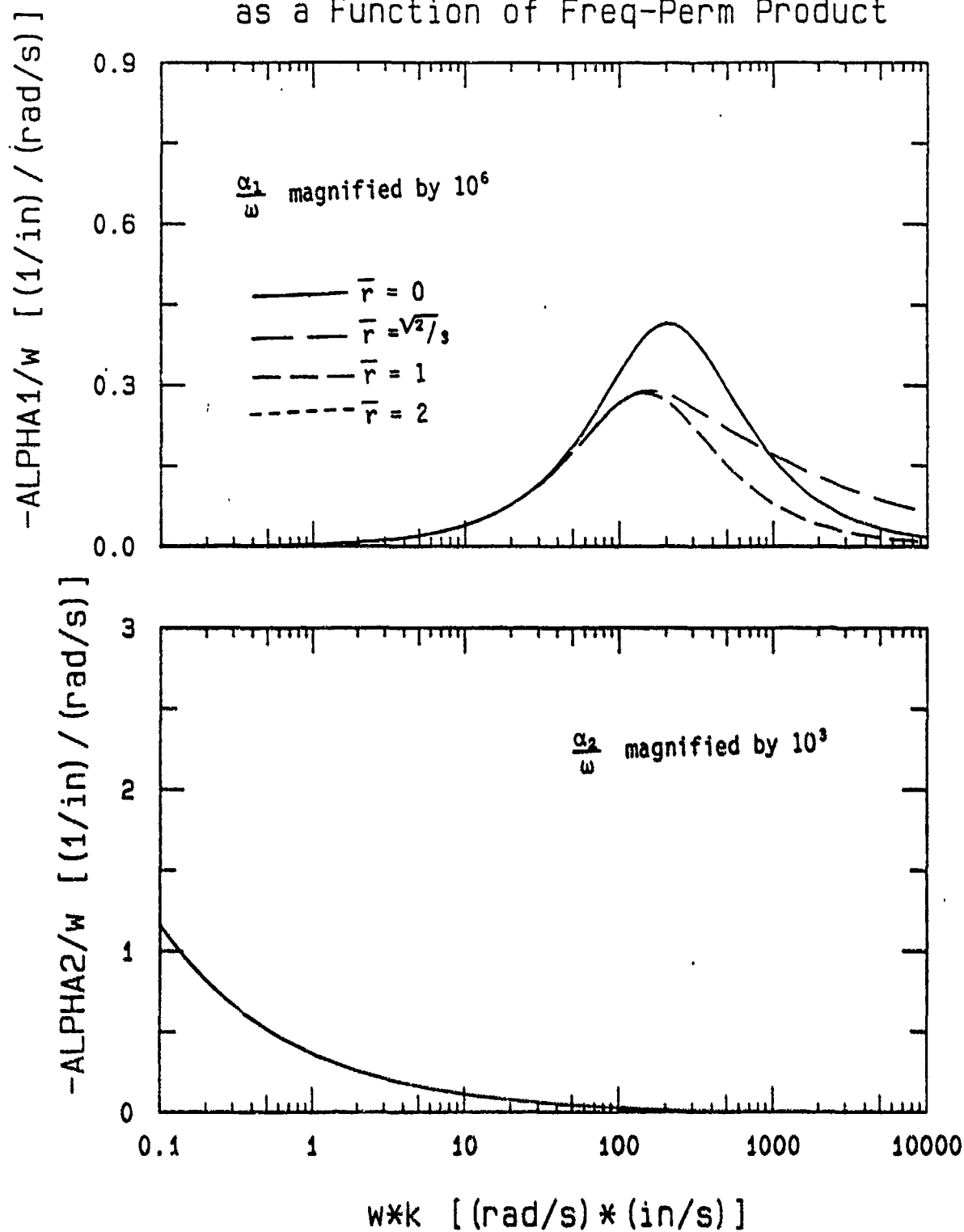


Figure 5.18b. Comparison of specific damping computed from approximate and exact expressions for fluid friction,  $n = 0.4$   
 $K_s = 100,000$  psi.

# Wave Veloc. of First and Second Kind as a Function of Freq-Perm Product

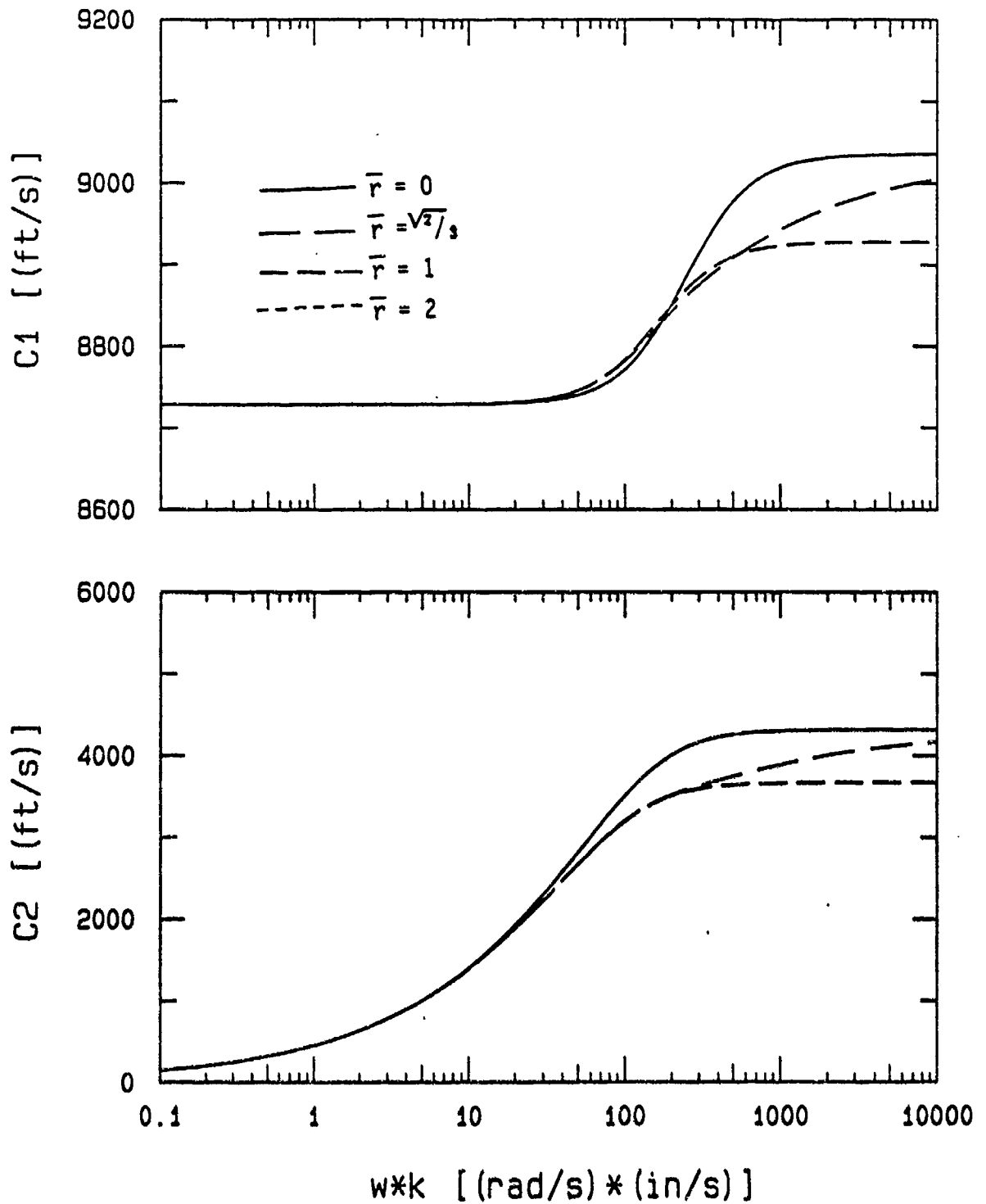


Figure 5.19a. Comparison of wavespeeds computed from approximate and exact expressions for fluid friction,  $n = 0.4$ ,  $K_s = 1,000,000$  psi.

Specific Damping of First and Second Kind  
as a Function of Freq-Perm Product

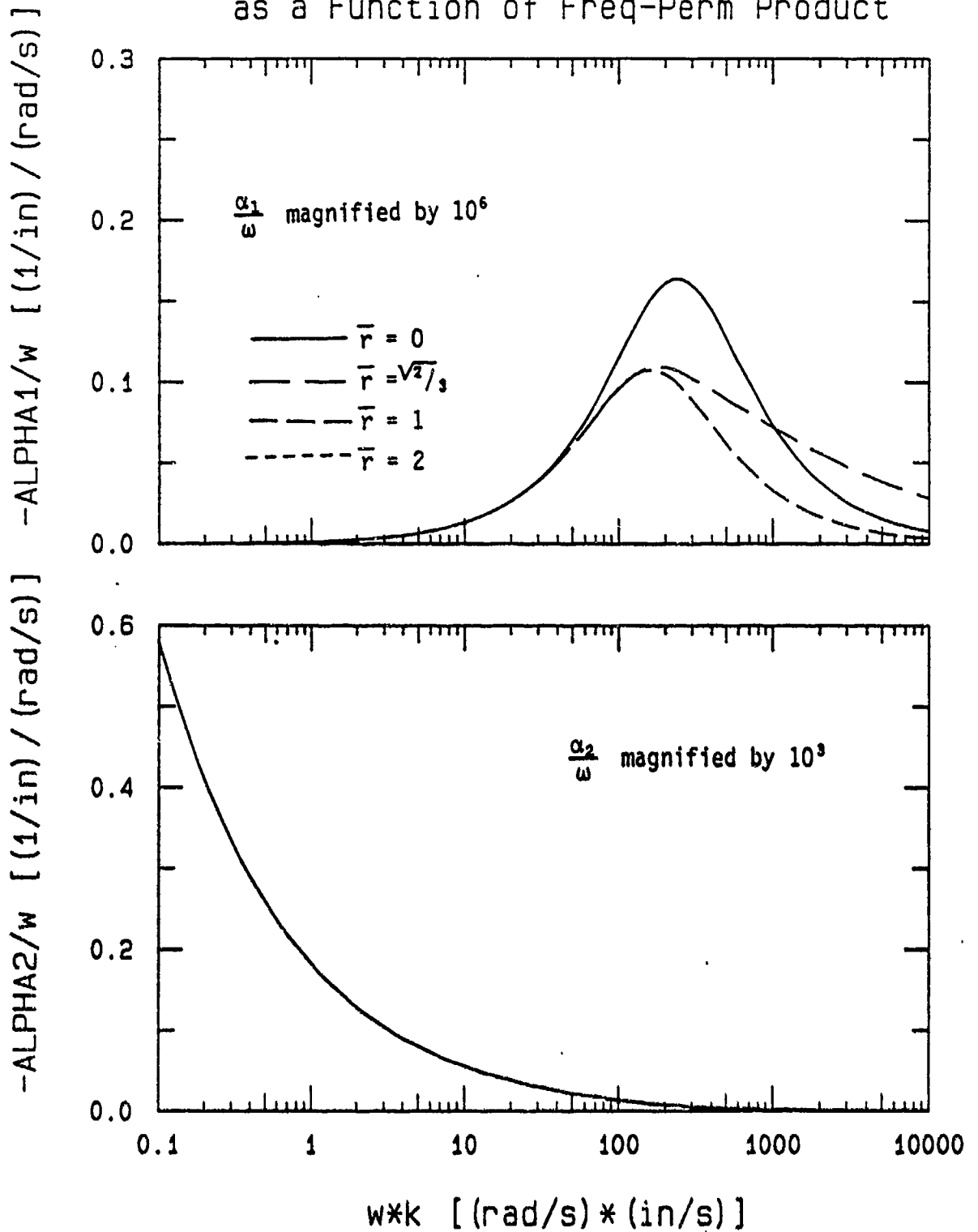


Figure 5.19b. Comparison of specific damping computed from approximate and exact expressions for fluid friction,  $n = 0.4$ ,  $K_s = 1,000,000$  psi.



Critical Frequency-Permeability Product as a  
Function of Skeleton Bulk Modulus

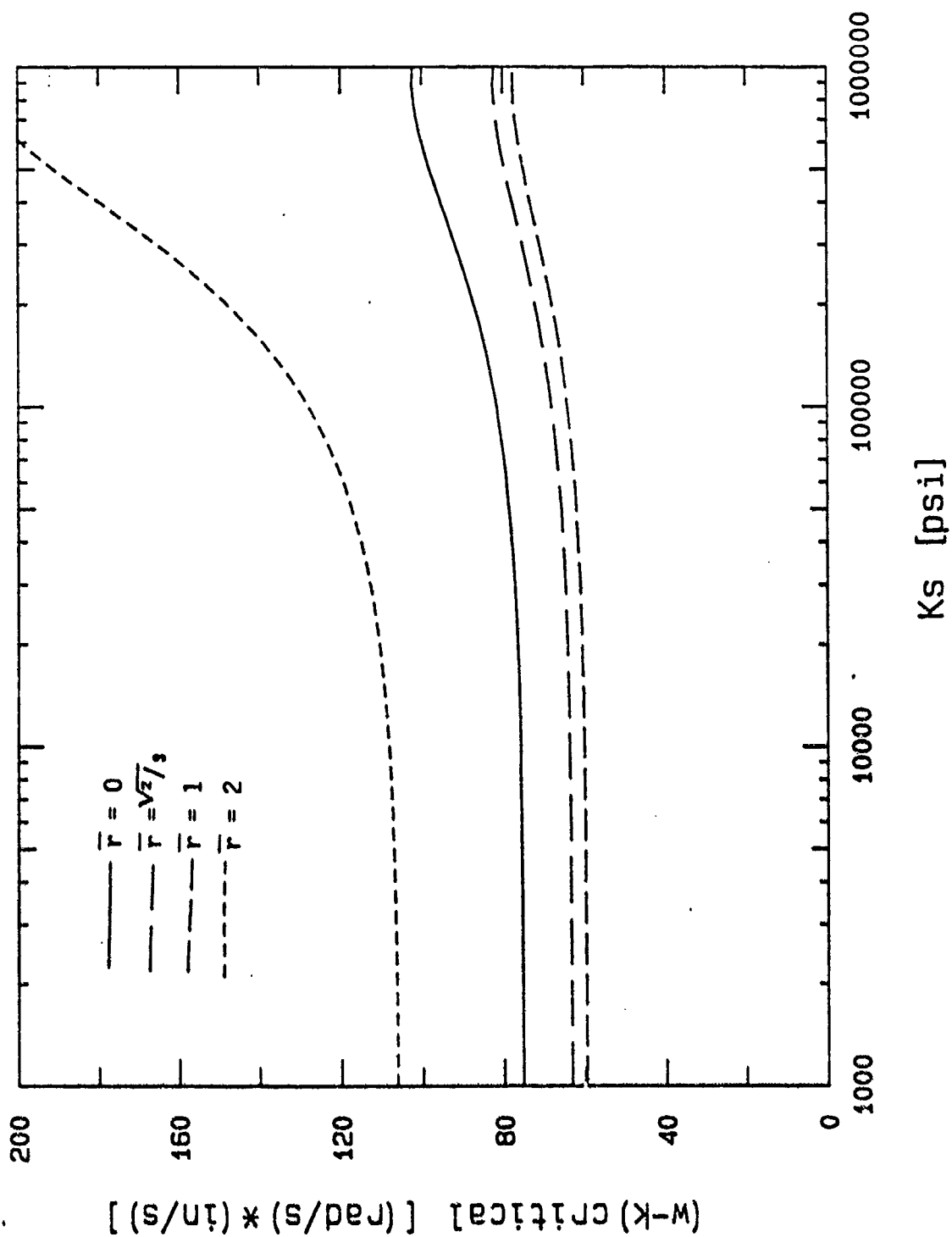


Figure 5.20a. Critical values of  $\omega k$ ,  $n = 0.2$ .

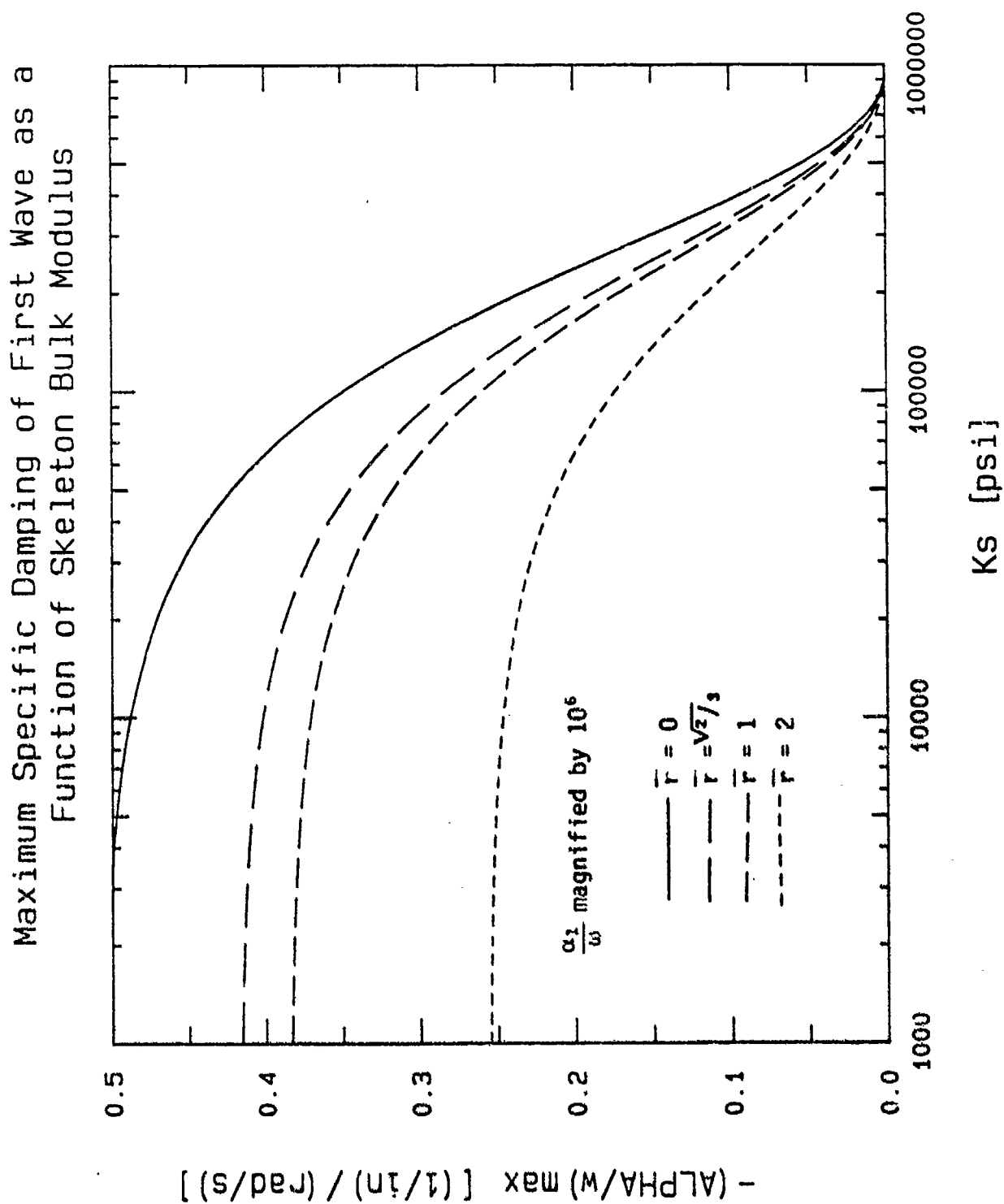


Figure 5.20b. Maximum specific damping of waves of the first kind,  $n = 0.2$ .

Specific Damping Constant of Second Wave at  
Critical  $\omega k$  as a Function of Skeleton Bulk Modulus

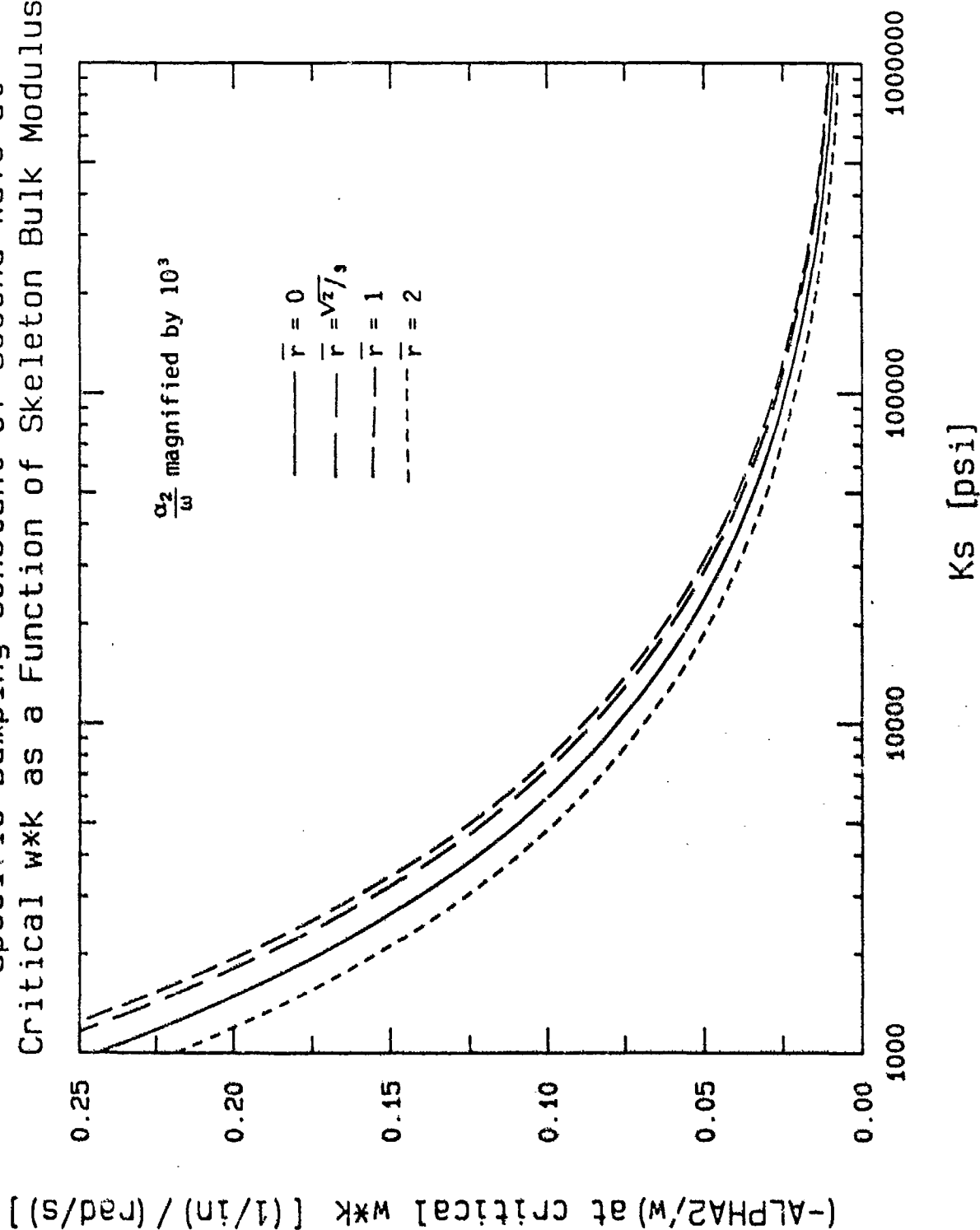


Figure 5.20c. Specific damping of waves of the second kind at critical  $\omega k$ ,  $n = 0.2$

# Wave Velocities of First Kind as a Function of Skeleton Bulk Modulus

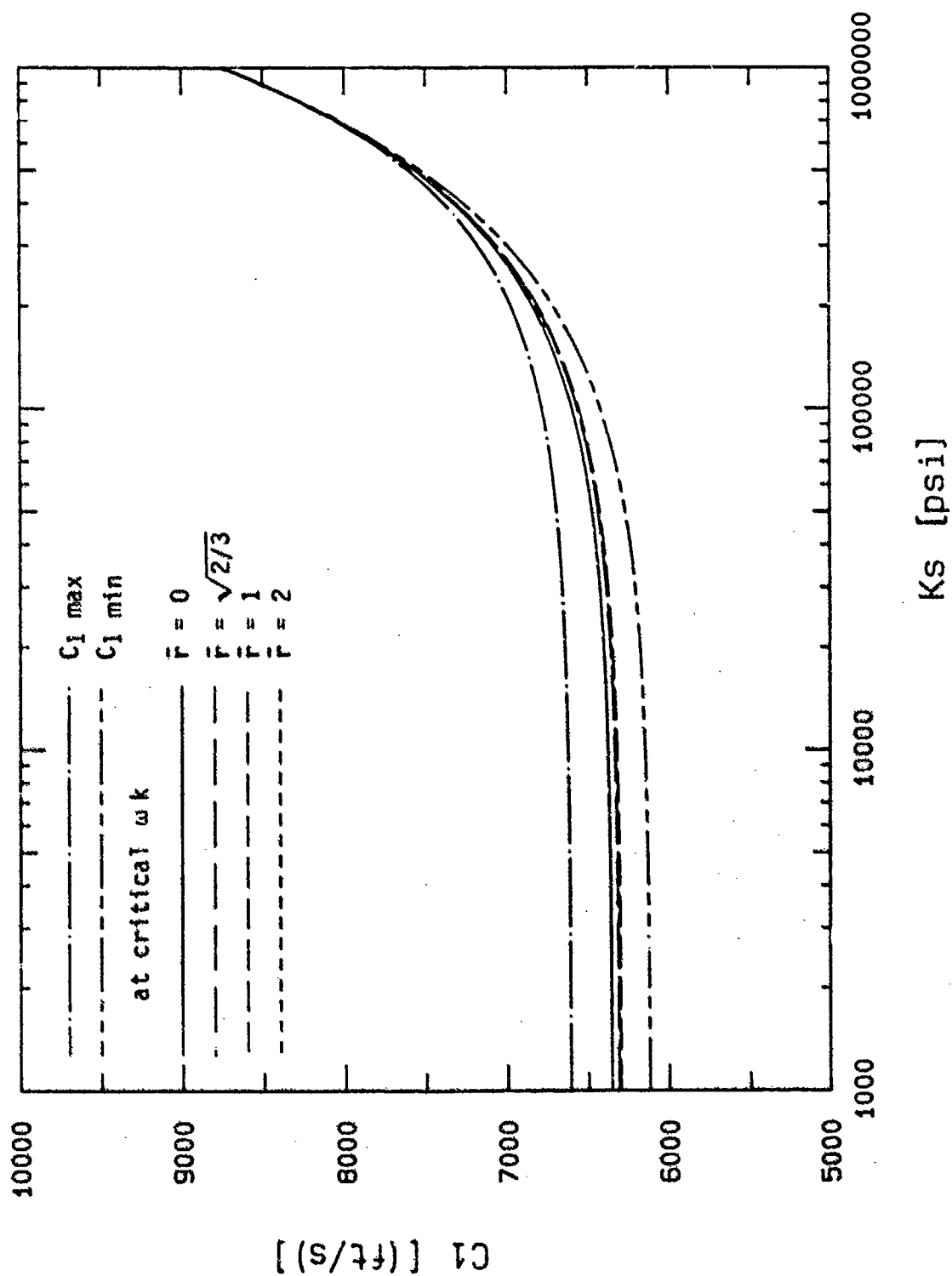


Figure 5.20d. Velocities of waves of the first kind,  $n = 0.2$ .

# Wave Velocities of Second Kind as a Function of Skeleton Bulk Modulus

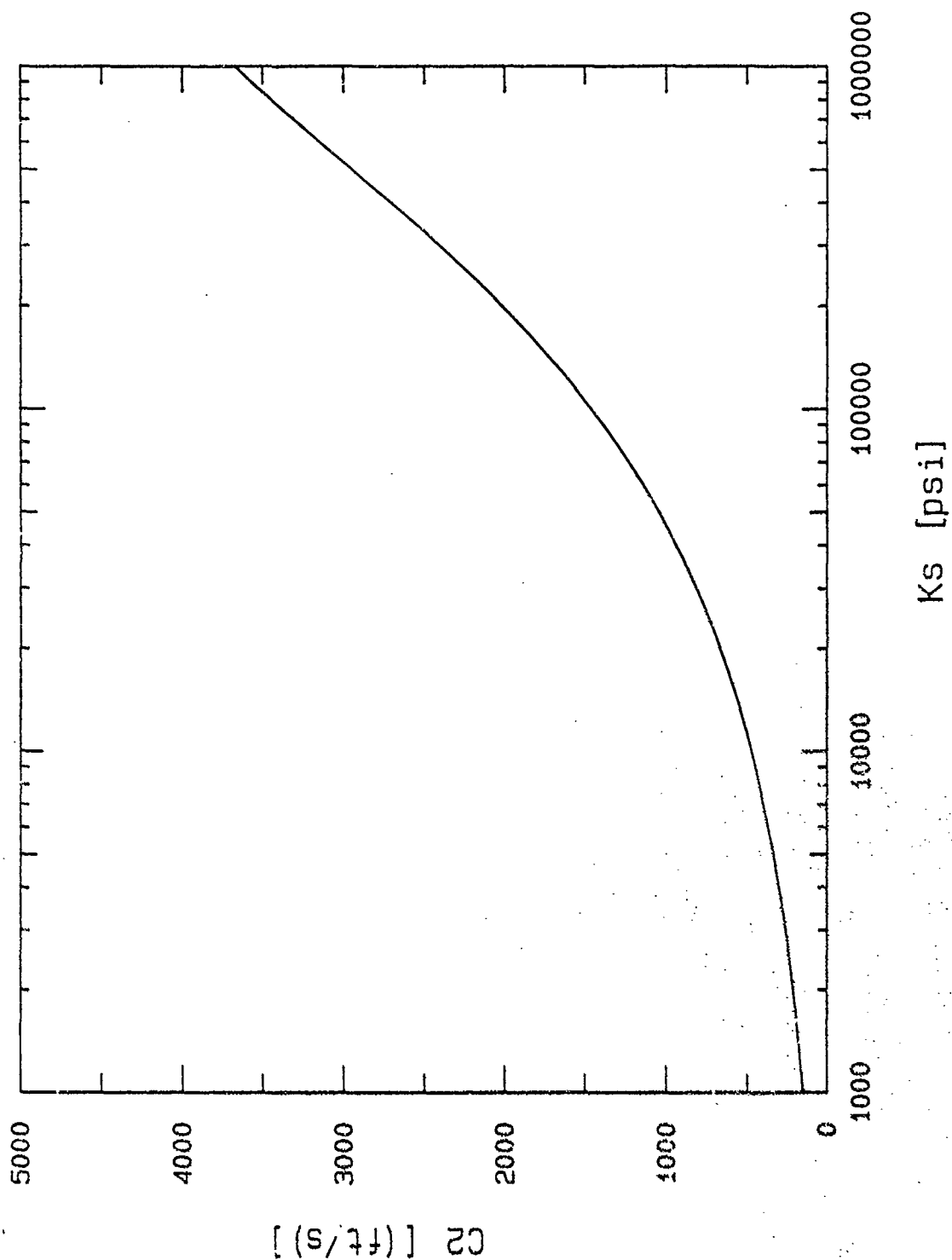


Figure 5.20e. Maximum velocities of waves of the second kind,  $n = 0.2$ .

Critical Frequency-Permeability Product as a  
Function of Skeleton Bulk Modulus

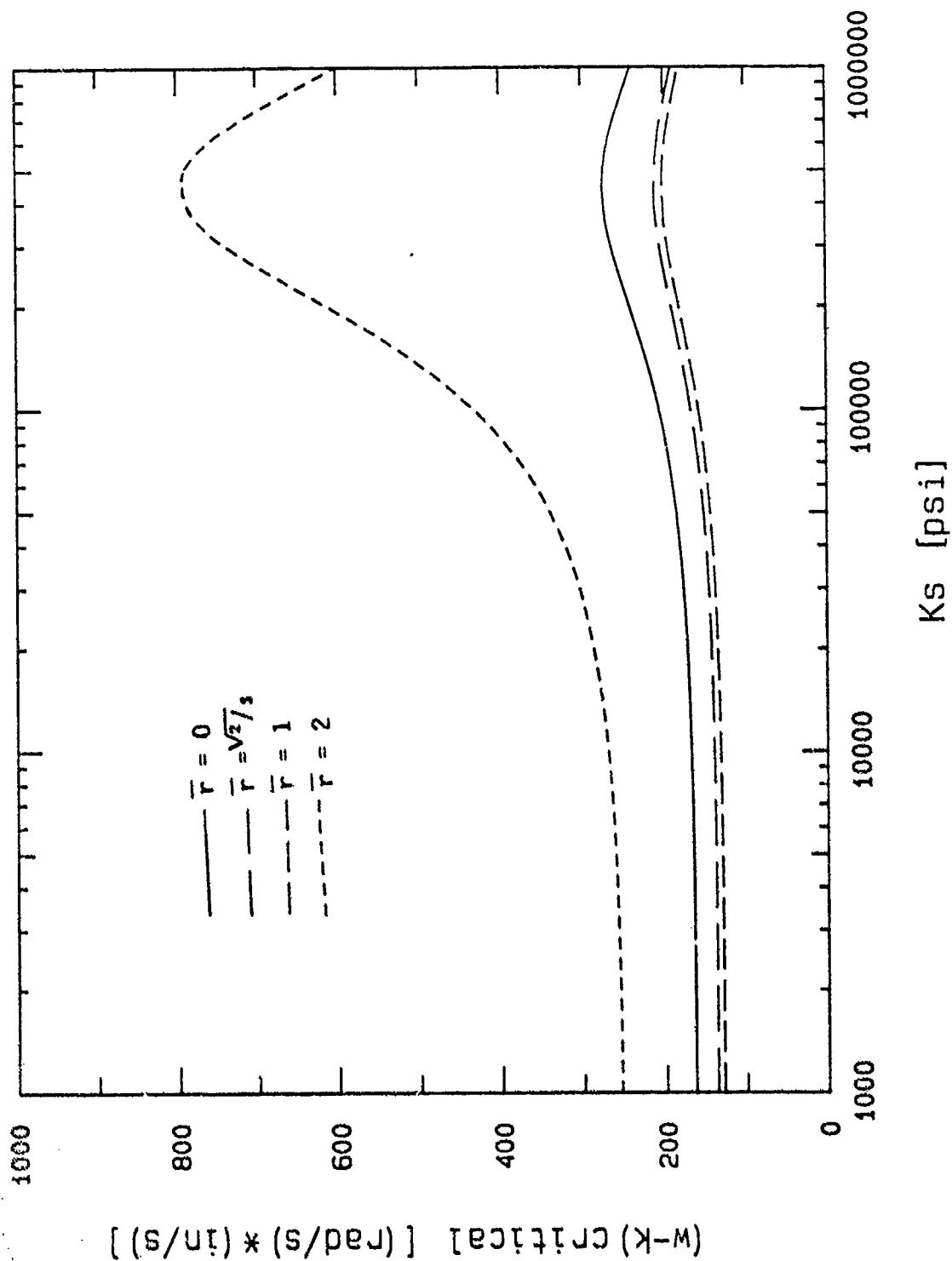


Figure 5.21a. Critical values of  $\omega k$ ,  $n = 0.4$ .

Maximum Specific Damping of First Wave as a  
Function of Skeleton Bulk Modulus

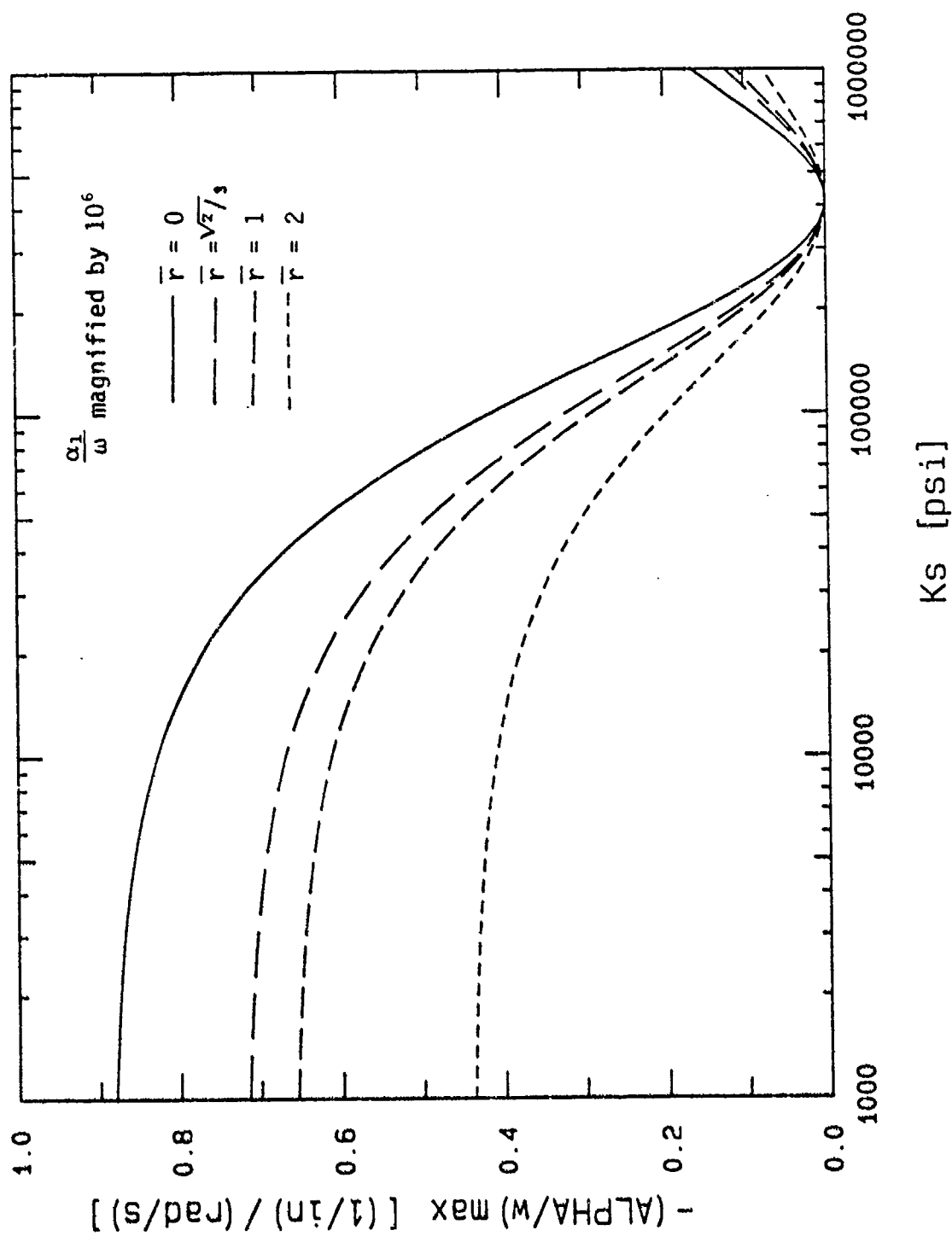


Figure 5.21b. Maximum specific damping of waves of the first kind,  $n = 0.4$ .

Specific Damping Constant of Second Wave at  
Critical  $\omega k$  as a Function of Skeleton Bulk Modulus

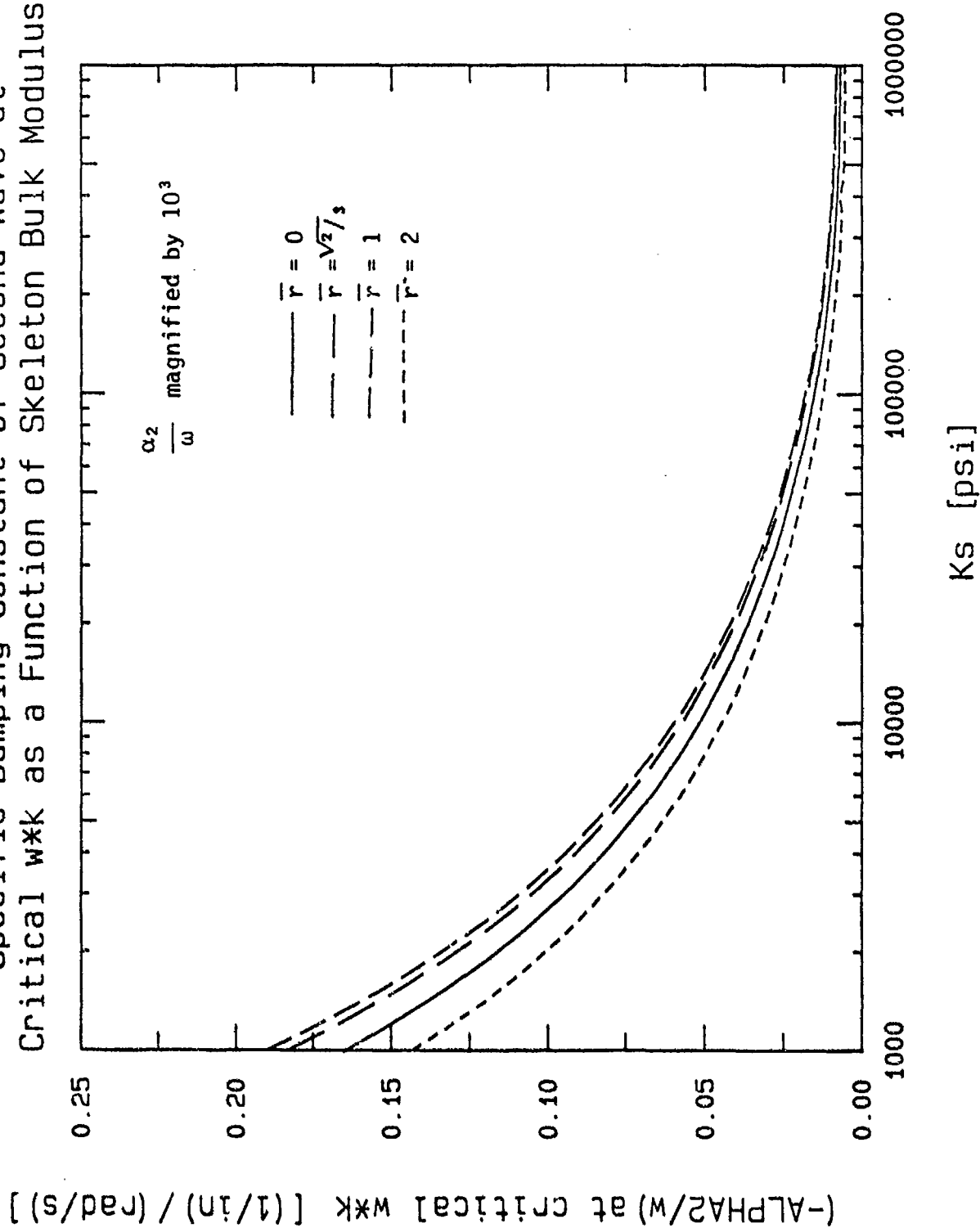


Figure 5.21c. Specific damping of waves of the second kind at critical  $\omega k$ ,  $n = 0.4$ .



# Wave Velocities of First Kind as a Function of Skeleton Bulk Modulus

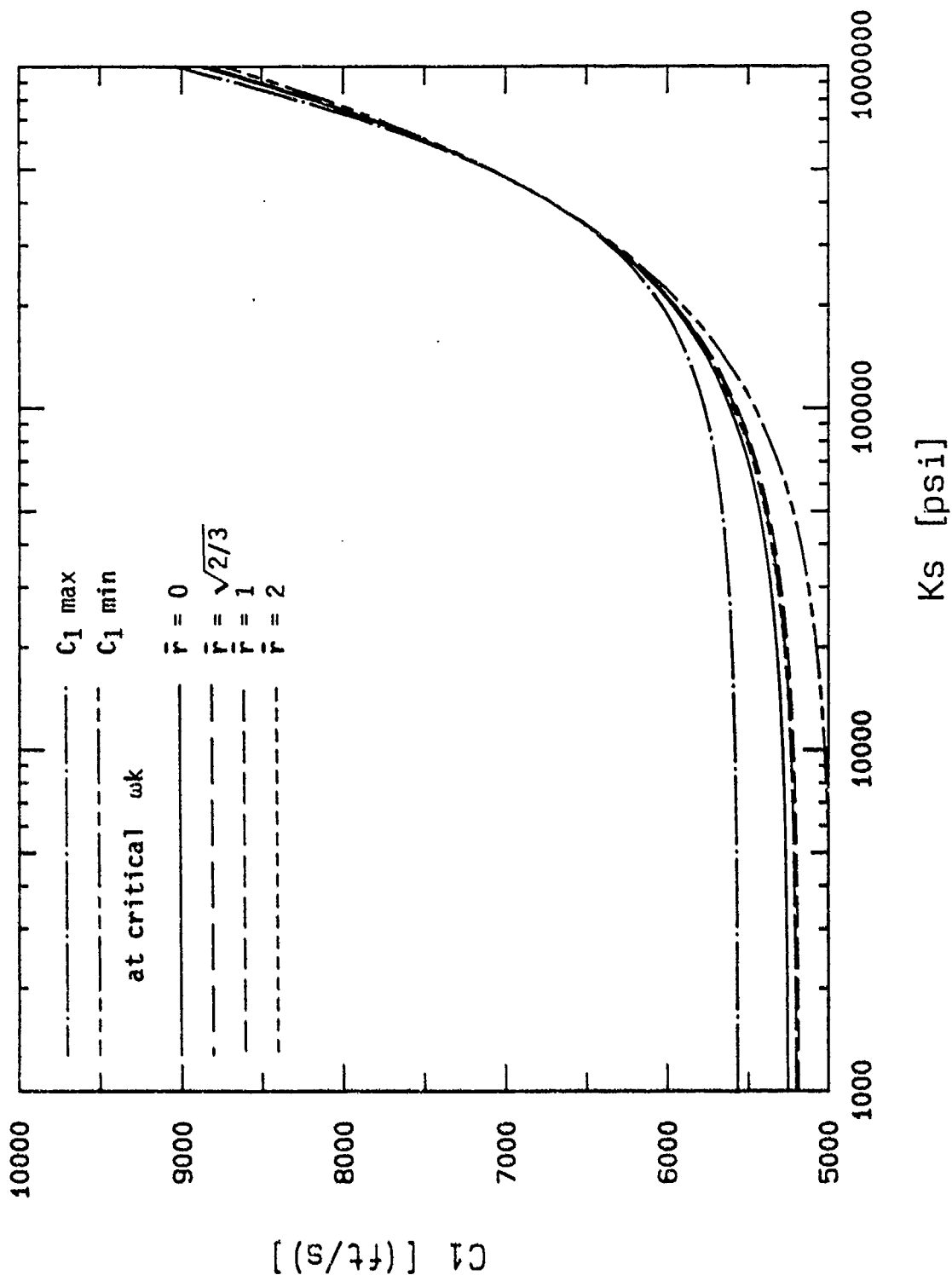


Figure 5.21d. Velocities of waves of the first kind,  $n = 0.04$ .

# Wave Velocities of Second Kind as a Function of Skeleton Bulk Modulus

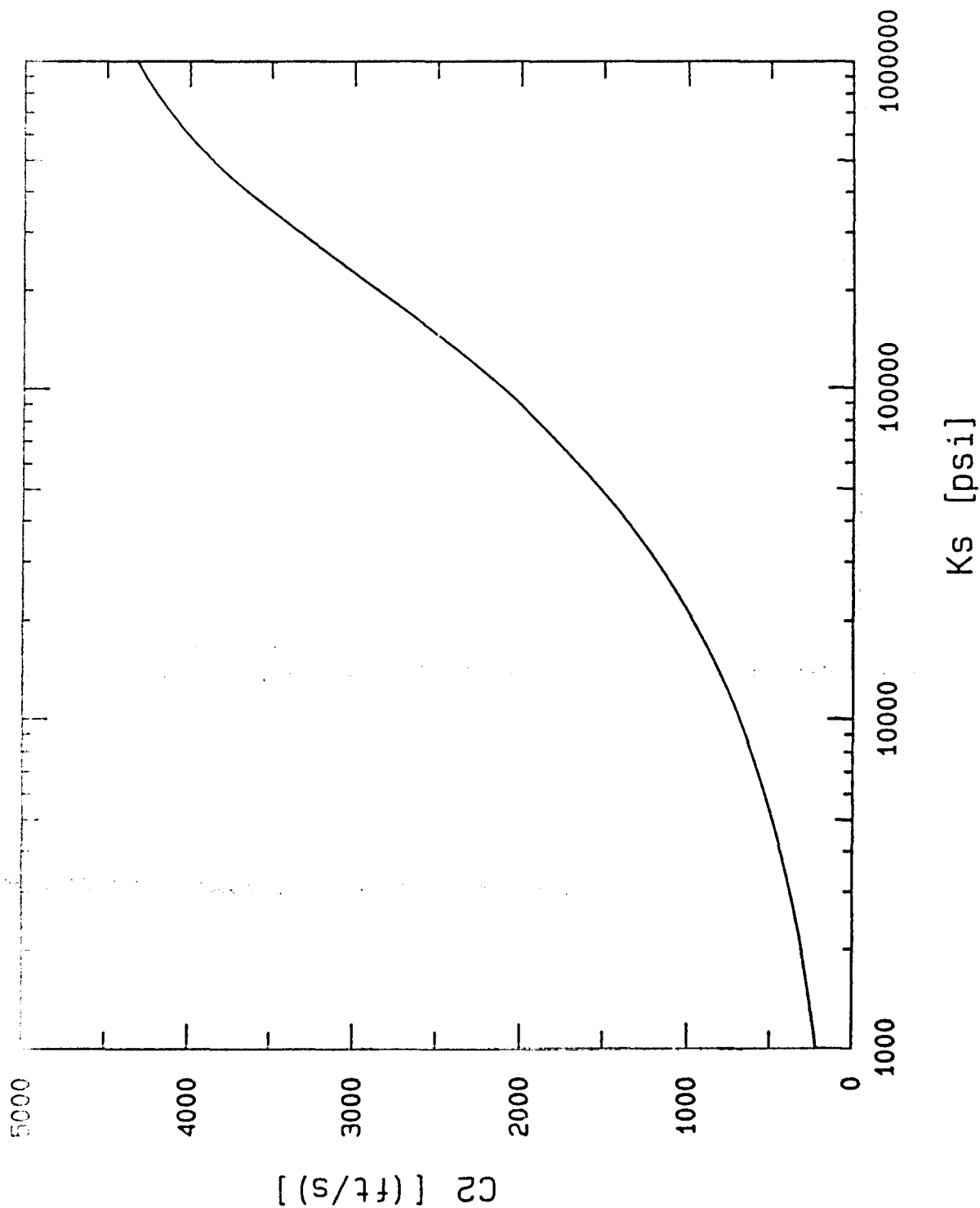


Figure 5.21e. Maximum velocities of waves of the second kind,  $n = 0.4$ .

Critical Frequency-Permeability Product as a  
Function of Skeleton Bulk Modulus

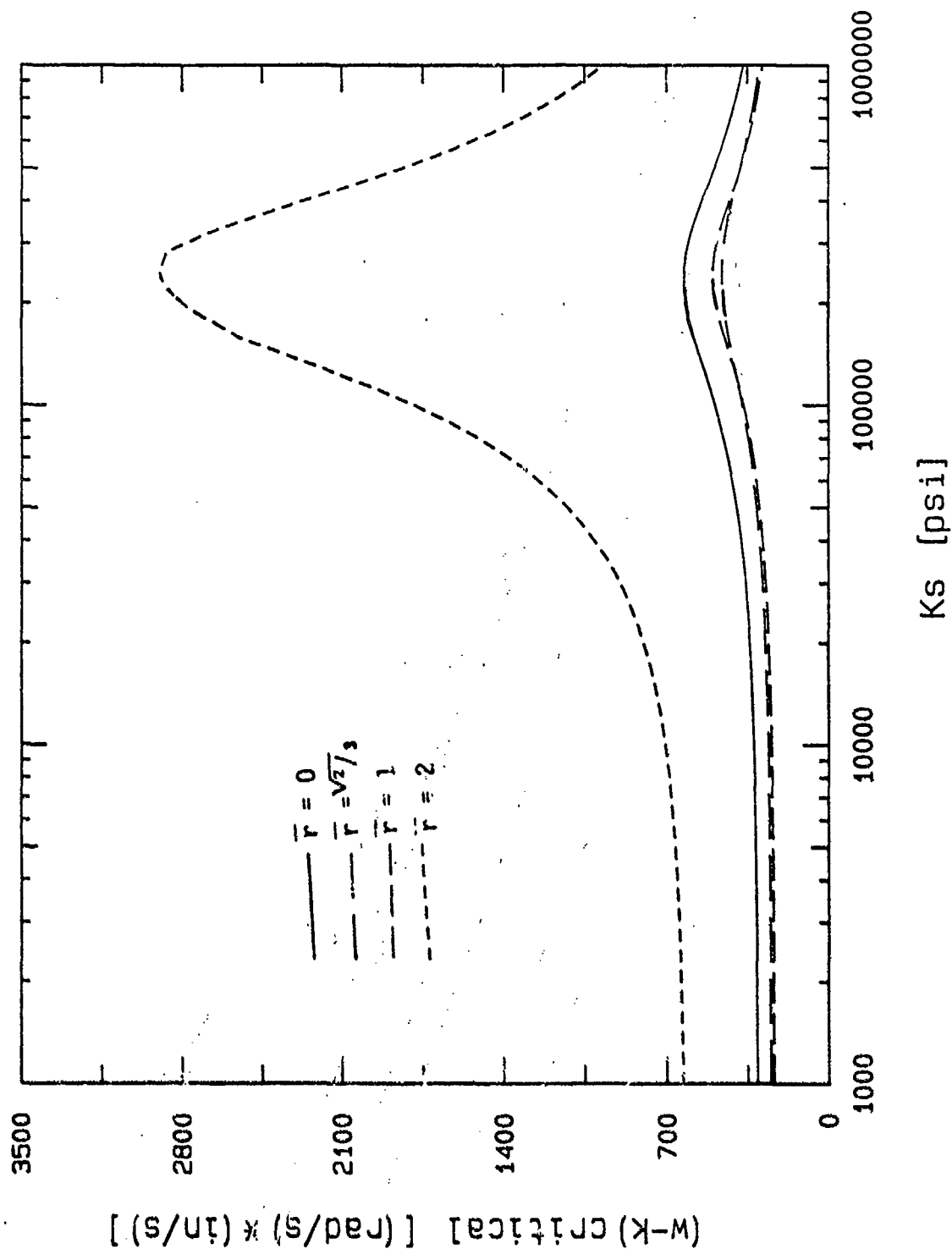


Figure 5.22a. Critical values of  $\omega k$ ,  $n = 0.6$ .

# Maximum Specific Damping of First Wave as a Function of Skeleton Bulk Modulus

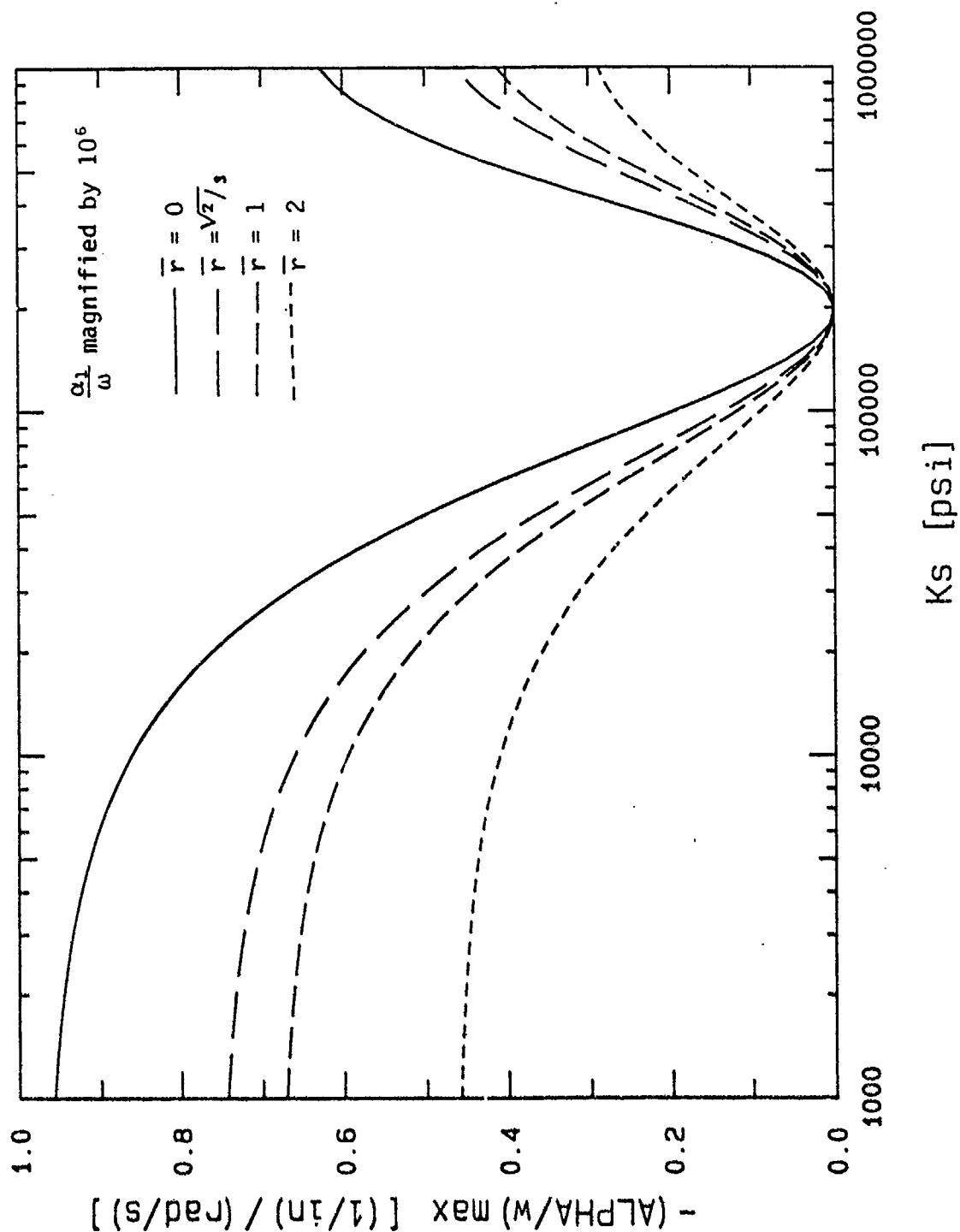


Figure 5.22b. Maximum specific damping of waves of the first kind,  $n = 0.6$ .

Specific Damping Constant of Second Wave at  
Critical  $wk$  as a Function of Skeleton Bulk Modulus

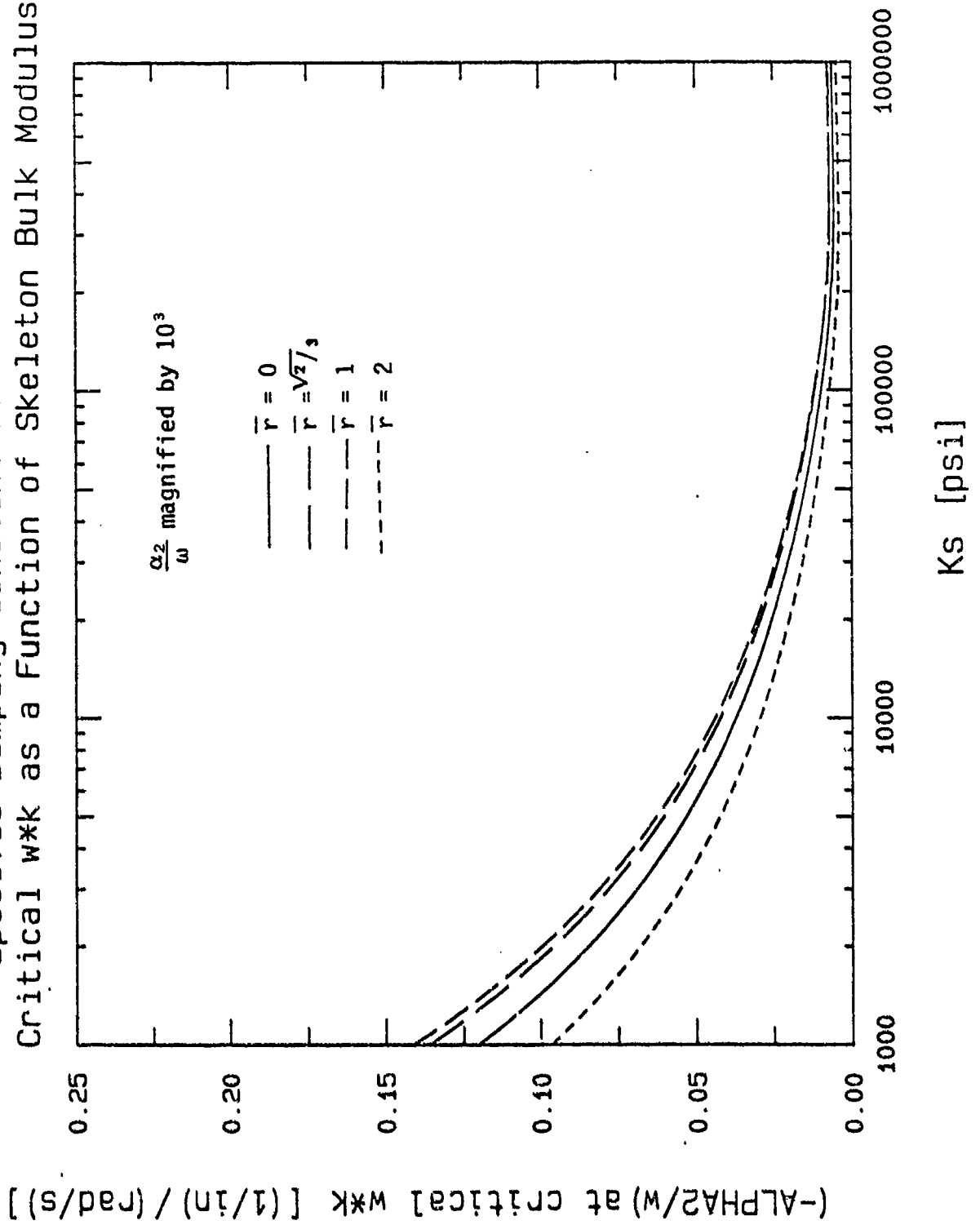


Figure 5.22c. Specific damping of waves of the second kind at critical  $\omega k$ ,  $n = 0.6$ .

# Wave Velocities of First Kind as a Function of Skeleton Bulk Modulus

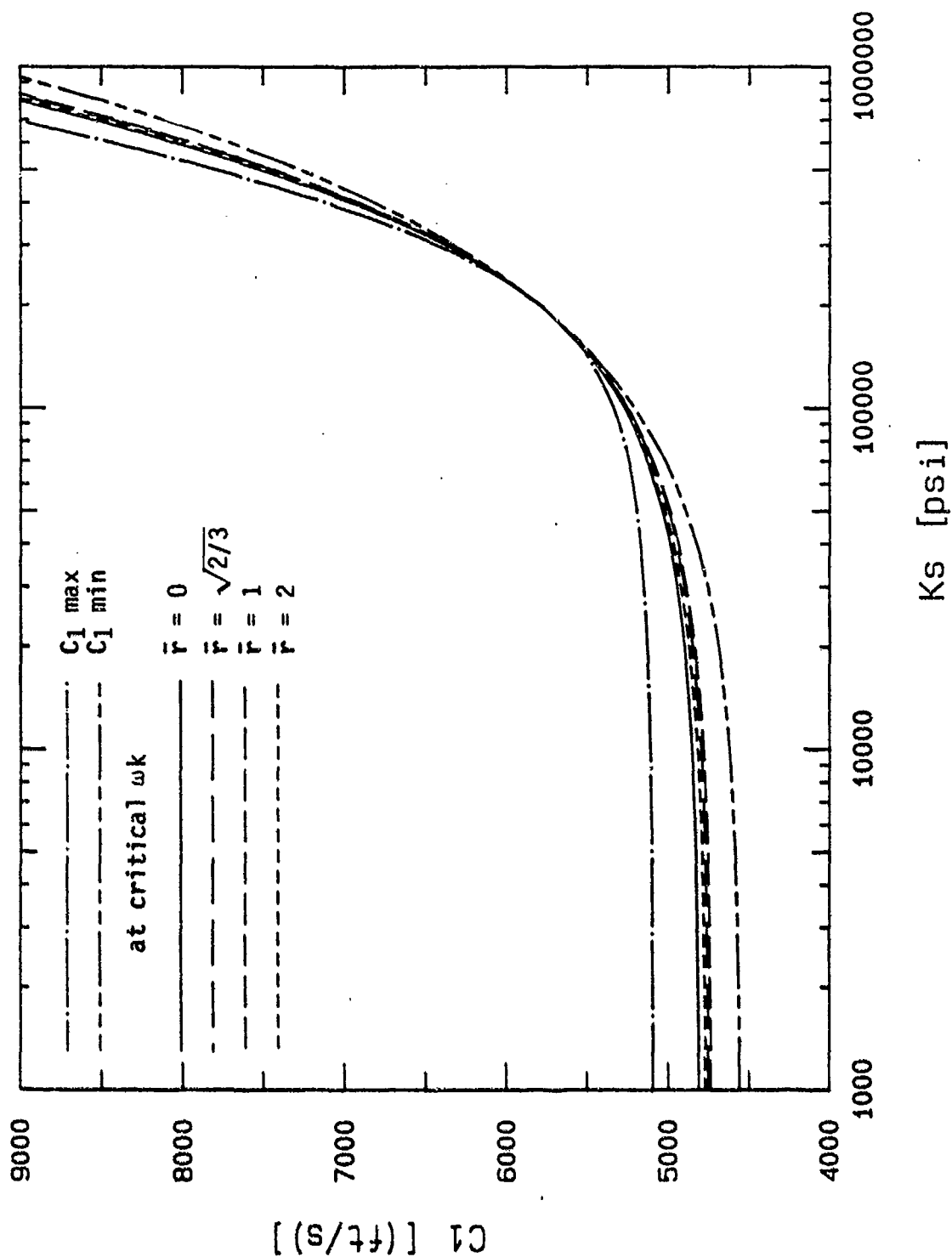


Figure 5.22d. Velocities of waves of the first kind,  $n = 0.04$ .

Wave Velocities of Second Kind as a  
Function of Skeleton Bulk Modulus

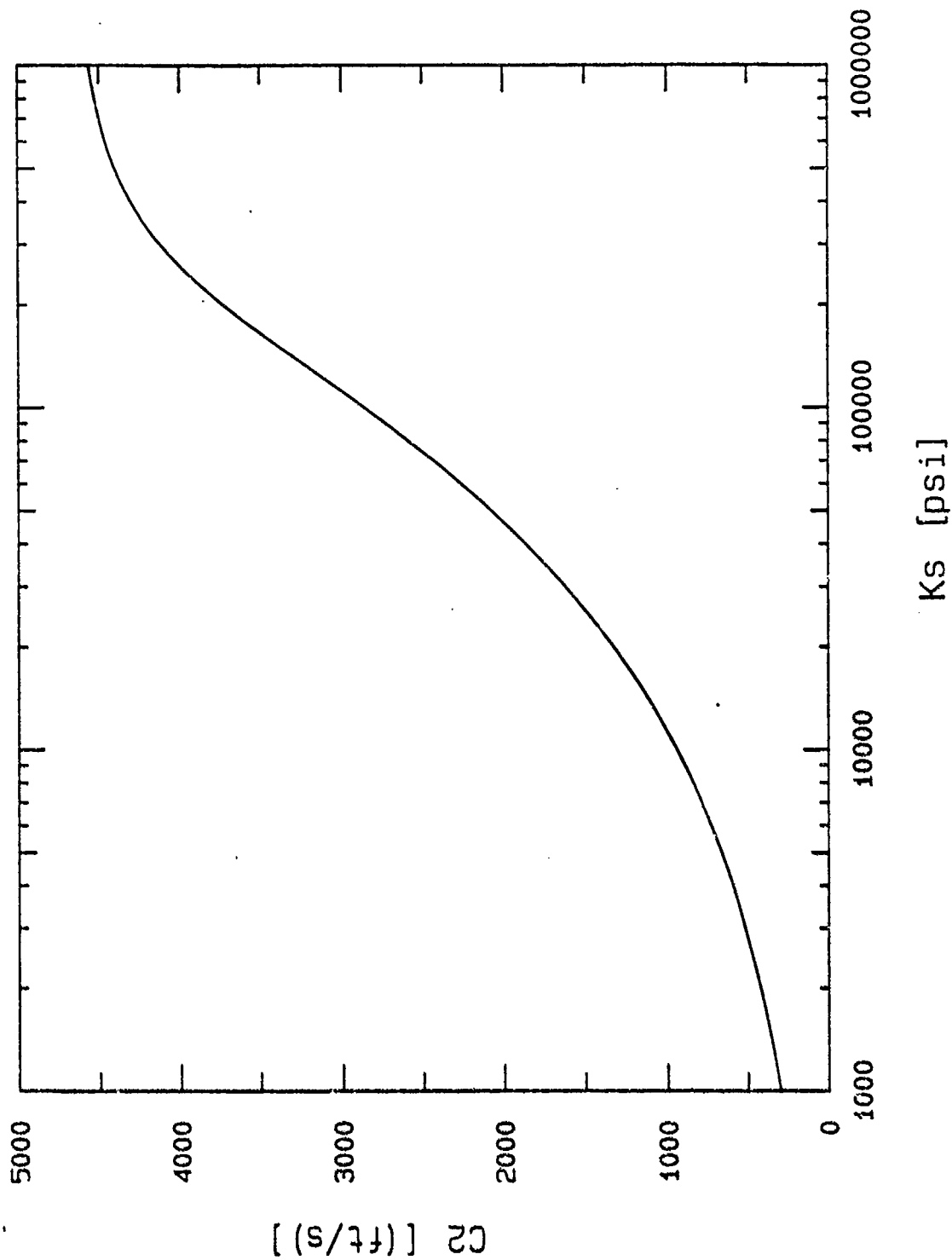
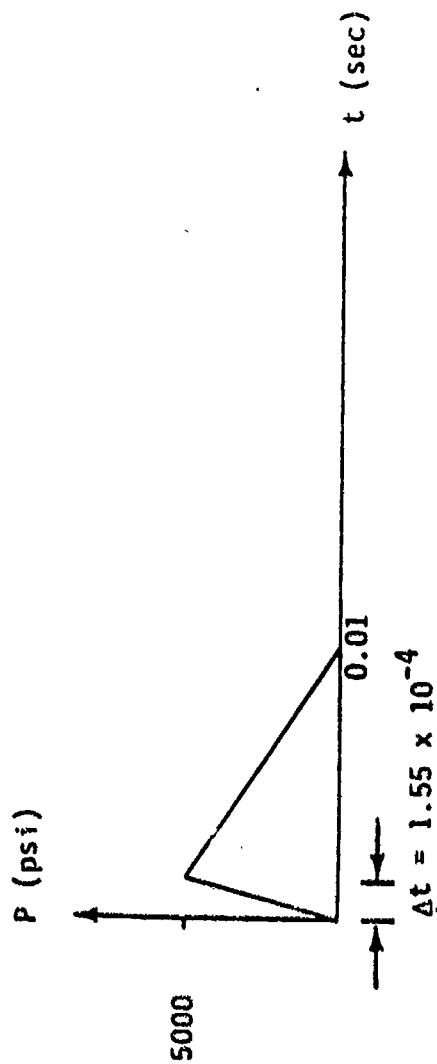


Figure 5.22e. Maximum velocities of waves of the second kind,  $n = 0.6$ .



#### ASSUMED MATERIAL PROPERTIES

Pore Water	
Bulk Modulus	$0.29 \times 10^6$ psi
Solid Grains	
Bulk Modulus	$5.0 \times 10^6$ psi
Specific Gravity	2.67
Solid Skeleton	
Bulk Modulus	3000 psi
Constrained Modulus	6000 psi
Poisson's Ratio	0.2
Porosity	0.35

Figure 5.23. Loading time history and material properties used in 1-D plane strain elastic wave propagation through two-phase medium.



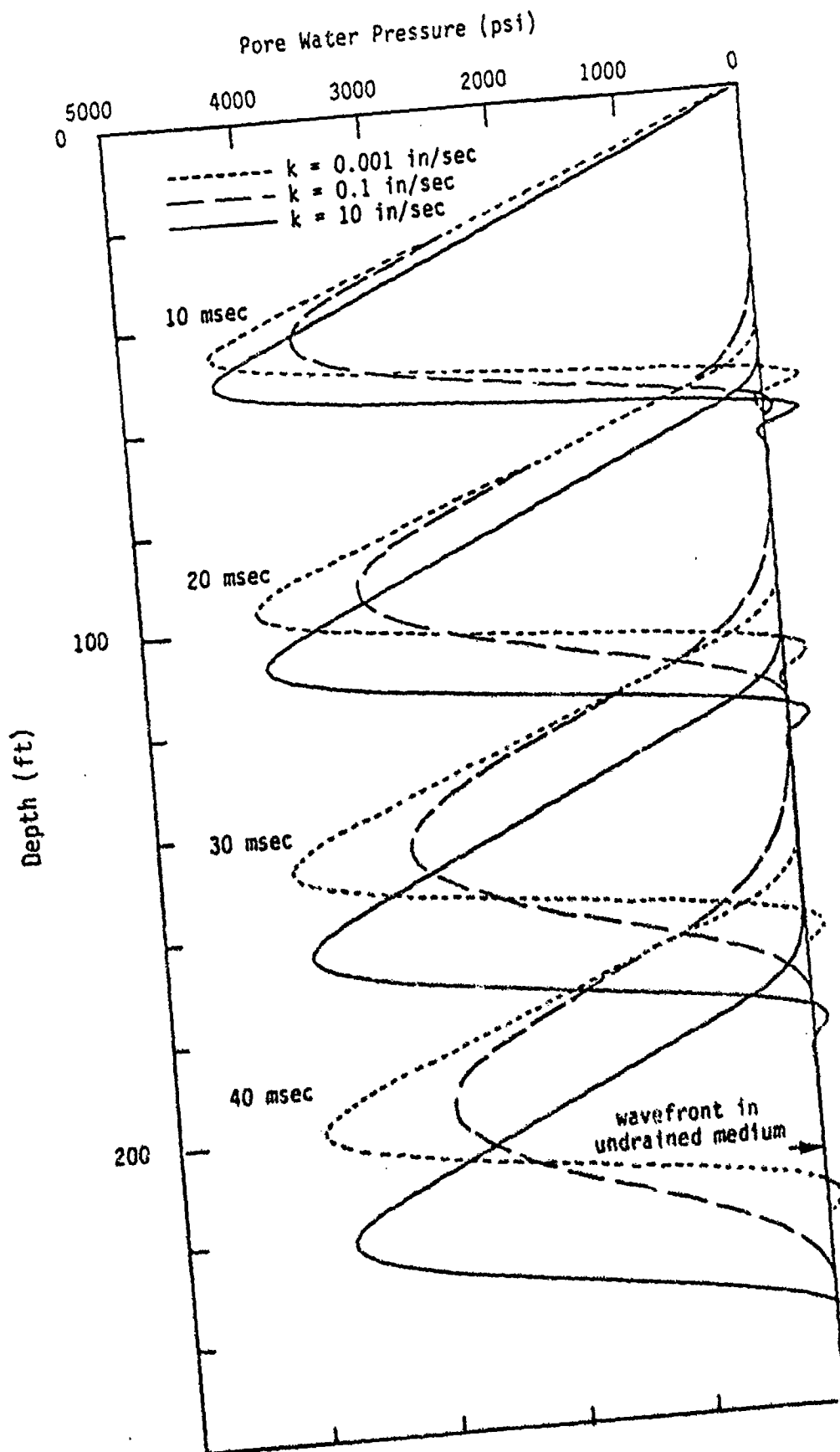


Figure 5.24. Profiles of pure water pressure at 10, 20, 30, and 40 msec, TPDAP II calculations.



## SECTION 6

### LIQUEFACTION AND CONSOLIDATION UNDER UNIAXIAL STRAIN LOADINGS

#### 6.1 INTRODUCTION

It is well established that both near surface and contained explosions in or on saturated porous soils cause extensive zones of liquefaction surrounding the detonation (Blouin and Shinn, 1983). The liquefaction, in turn, dramatically alters the late time ground motions and cratering processes. Following the onset of liquefaction, ground motions in the vicinity of the burst change suddenly from high frequency motions to very low frequency oscillatory motions having long durations. Immediately following formation of a crater or cavity by the dynamics of the explosion, liquefied material flows and/or slumps in to partially fill the excavation. Following the gravity controlled slumping and filling process, the zone of liquefied material gradually consolidates, with excess pore water working its way out to the ground surface. The consolidation process can take months, depending on the size of the explosion and the properties of the in situ soil. The combined liquefaction/gravity flow/consolidation process can drastically alter the size and shape of craters in saturated materials and has been a factor in misinterpretation of much cratering data. In the past, attempts have been made to relate final crater shapes and volumes directly to the explosion formation processes without regard to the late-time flow and consolidation processes.

In order to gain a quantitative understanding and validation of these processes a series of laboratory tests was performed which attempted to replicate important aspects of the in situ loading conditions. These tests, termed shock consolidation tests, utilized a uniaxial strain load/unload/consolidation cycle which was felt to be appropriate for modeling most important aspects of the in situ behavior. Materials tested included saturated beach sand, "undisturbed" silt-sand-gravel core samples, and weakly to strongly cemented porous limestone cores, all from Enewetak Atoll. These carbonate materials were furnished by the Defense Nuclear Agency from core taken in the vicinity

of the thermonuclear detonations KOA and OAK. Results of the shock consolidation tests are presented in this section and are compared to two phase calculations of the response of both a saturated rock and soil sample prepared using the code NKOCP described in Section 3.

## 6.2 TEST DESCRIPTION AND RESULTS

A series of 17 shock consolidation tests, listed in Table 6.1, was run on Enewetak beach sand, and silt-sand-gravel limestone and core specimens. As reported by Blouin, Kim and Timian (1986), a series of initial tests was attempted in a triaxial vessel, but as soon as the soil liquefied shortly into the unload cycle, it became impossible to control the unloading and consolidation portions of the test. Once liquefaction occurred, the sample behaved as a fluid and could support only hydrostatic pressure. During hydrostatic unloading it was impossible to control the radial deformation of the sample and maintain the uniaxial strain condition.

For this reason all testing was done in a rigid high pressure oedometer in which a nominal 1 in long by 4 in diameter cylindrical sample was loaded in uniaxial strain. The sample was constrained laterally by the cylindrical steel walls of the oedometer vessel and was loaded from the top by means of a rigid steel piston. High pressure seals between the top and the vessel walls prevented the escape of pore water. Following the initial undrained load-unload cycle, drainage was provided through a 1/16 in. line in the bottom of the vessel. Instrumentation consisted of a pore pressure gage attached to the drainage line, a linear displacement transducer to monitor piston displacement, and an external load cell to measure the total load applied to the piston by the load frame. A schematic section view of the oedometer device is shown in Figure 6.1.

Important steps in the testing procedure include the following:

1. Sample Saturation: In order to realistically simulate the in situ conditions, the samples must be completely saturated. If complete saturation isn't achieved, the undrained sample stiffness will be unrealistically low

and peak strains will be much greater than they should be. The samples are vacuum saturated with deaired sea water containing dissolved carbonates. Blouin and Timian (1986) showed that the absence of dissolved carbonates in the pore water results in significant reduction of cementation strength in cemented samples. Once vacuum saturation is complete, the samples are allowed to come to equilibrium under about 200 psi to 300 psi pore pressure. This assures that any remaining air in the samples is driven into solution in the pore water. An initial effective stress approximately equal to the pore pressure is also applied. This combination of initial pore pressures and effective stresses closely simulates the in situ condition of most of the core samples we tested.

2. Undrained Load-Unload: The samples are loaded and unloaded statically in an undrained condition. A peak axial stress on the order of 1 kbar is applied which insures sufficient strain to break down the cementation in all cemented materials. A correction must be applied to the axial deformation to account for the slight deformation in the piston seals, the rigid vessel, and the pore pressure gage and line. This correction was developed by measuring the total axial displacement for a sample of pure water as a function of pressure and then subtracting the portion of the displacement computed to be due to compression of the water. This excess displacement due to elastic deformations in the testing device is then subtracted from the axial displacement data from each test. This insures that the test specimens do not appear to be softer than they would be in their in situ condition.
3. Consolidation: Once each specimen is completely unloaded, the pore pressure line is opened and the sample is reloaded and allowed to gradually return to its initial effective stress. This consolidation process approximates the in situ process where the material is assumed to have been liquefied by the dynamic loading and was then reconsolidated under its original effective overburden stress.

Representative shock consolidation test data are presented in Figures 6.2 through 6.6. Figures 6.2 and 6.3 show data from saturated medium strength and

weak porous limestone samples, respectively, and Figures 6.4 through 6.6 show data from saturated uncemented soil samples. A series of three plots is shown for each test;

- total stress as a function of axial (volume) strain, obtained by dividing the measured total loads by the sample area;
- pore pressure as a function of axial (volume) strain, obtained from the pore pressure gage; and
- effective stress as a function of axial (volume) strain; obtained by subtracting the measured pore pressure from the total stress measurements at each strain increment.

We can use Figure 6.2, showing data from the low strength limestone, to illustrate the various steps in the testing procedure and the test results. Point "a" at the start of the undrained loading shows the initial conditions, i.e. effective stress of about 300 psi, pore pressure of about 300 psi and total stress of 600 psi. The sample is loaded undrained to point "c". At point "b", early in the undrained loading, the cementation in the skeleton breaks down. This is clearly shown by the effective stress response of Figure 6.2c. Prior to the breakdown of cementation, more than half of the total applied stress is carried by the limestone skeleton; but following the cementation breakdown only 5% of the additional applied stress is carried by the skeleton. The balance of the total applied stress is carried by the pore water.

From point "c", the undrained sample is unloaded to a state of zero stress at "e". As shown in Figure 6.2c, the skeleton is strongly hysteretic and unloads very rapidly until at "d" the effective stress drops to zero and a state of liquefaction is achieved. Note that at point "d" the overall volume strain is still 1.4% and the total stress is still over 11,000 psi. From point "d" to point "e" the sample is liquefied and the total stress equals the pore pressure. Also note that the hysteresis in the total stress curve is positive, i.e. energy is being dissipated, while the apparent hysteresis in the pore pressure load-unload cycle is negative as explained in Section 2.

At point "e" the pore pressure line is opened and shortly thereafter total stress is again applied and the sample is allowed to drain and consolidate until the effective stress reaches its pretest value at point "f". The strain during consolidation to the original effective stress is nearly 80% of the strain reached during the undrained loading. The residual strain following consolidation, normalized by the peak undrained strain, is plotted as a function of dry density in Figure 6.7. There is a trend in the data toward less residual strain with increasing dry density. However, for samples with dry densities of less than 100 lb/ft<sup>3</sup>, corresponding to porosities greater than 40% which are typical of the Enewetak materials, the average post loading subsidence is 85% of the peak strain reached in the undrained loadings. By computing the peak dynamic strain fields from the KOA and OAK detonations, this average consolidation can then be used to estimate the portions of the total crater volumes which might be attributed to post liquefaction consolidation.

The other data plots for the saturated limestone and soils of Figures 6.3 through 6.6 are similar in character to Figure 6.2, except that the soil skeletons carry much less of the total stress and don't show the early time breakdown of the cementation. All the shock consolidation samples, whether cemented or uncemented, showed very consistent and similar liquefaction behavior early in the unloading cycle. We feel this set of data is a good validation of the theoretical model developed in Sections 2 and 3.

### 6.3 COMPARISON OF COMPUTED AND MEASURED UNDRAINED UNIAXIAL RESPONSE.

The computational algorithm NKOCF, described in Section 3.6, was used to compute the uniaxial undrained response for a saturated limestone similar to that loaded in test A2A6 (see Table 6.1). The comparison between the computed response and the test data serves as a validation of the numerical techniques and, as described in Sections 2 and 3, gives us new insight into, and understanding of, the processes controlling the two phase response.

The inputs to NKOCF for the saturated limestone are listed in Table 6.2 and shown in Figure 6.8.

- The constitutive model for the uniaxial response of the porous skeleton consists of a trilinear fit to drained uniaxial data for porous Enewetak limestone having nearly the same porosity as sample A2A6. This data fit is shown in Figure 6.8 and consists of an initial stiff loading, until the cementation breaks at a strength of about 3,150 psi and a strain of 0.17%, followed by a much softer loading to strains of about 5%. Unloading follows the same slope as the initial cemented loading.
- The constitutive model for the sea water used to saturate the sample is that described in Section 3.3 which is incorporated into NKOCF as option NW = 1.
- The constitutive model for the solid grains is that described in Section 3.4 using initial constants listed in Table 6.2. These constants were computed from measured grain properties for the Enewetak materials described by Kim, Blouin and Timian (1986).

This model was loaded using NKOCF to a peak total strain of 1.587%, which corresponds to the peak strain in the experiment.

The comparison between the calculated response and the A2A6 test data is shown in Figure 6.9, parts a through c. The good agreement between the calculated response and test data is gratifying, particularly considering that the calculated response was developed from constitutive models for each of the components which were developed independently of the test data. Important features of the comparisons include:

- strong positive hysteresis in the total stress volume change cycle of Figure 6.9a, indicating that a substantial amount of energy is dissipated;
- apparent negative hysteresis in both the computed and measured pore pressure-volume strain cycles of Figure 6.9b. As described in the discussion of Section 2, this apparent negative hysteresis is a result of rapid expansion of the solid grains as the effective stress drops to



zero early in the unloading. The expansion of the grains compresses the pore water resulting in the apparent negative hysteresis;

- strongly hysteretic nature of the skeleton as evidenced by the effective stress-volume change comparison of Figure 6.9c;
- the unloading slope of the skeleton prior to liquefaction (Figure 6.9c) is significantly steeper in the calculation than in the data. The reason for this difference is the assumption in the numerical model that the sample liquefies as soon as the radial effective stresses drop to zero. In Section 2, once the radial effective stresses reach zero the skeleton was assumed to collapse with an immediate loss in axial effective stress. While this may be a valid model for granular soil, it does not appear to be valid for the porous limestone. An apparently better model would allow the axial effective stress to return to zero along a uniaxial unload path rather than drop precipitously once zero radial effective stress is reached. Additional investigation of details in the liquefaction mechanism and refinements to the model will be made during the coming year.

Figure 6.10 shows the calculated total and effective stress and pore pressure responses for the limestone combined in a single plot. Note that the relatively high pore pressures and low initial Poisson's ratio of the skeleton keep the radial effective stresses to a minimum. The low peak radial effective stress unloads very rapidly, according to the model assumptions discussed above, and causes liquefaction very early in the unloading cycle.

The final set of comparisons between calculated undrained uniaxial response and measured response is that shown in Figure 6.11 between test A4B6 and a saturated sand having constituent properties listed in Table 6.3. The skeleton properties are a fit to drained test data for a silty sand sample having a porosity close to that of sample A4B6. Sea water and grain properties are the same as those used in the limestone calculations. The comparisons between the test data and calculations are excellent. There are two major differences between the soil response and the limestone response discussed above:

- The absence of cementation in the soil sample results in much less of the total load being borne by the skeleton;
- Even though the skeleton is strongly hysteretic, the fact that the effective stresss are much less than in the limestone means that overall energy dissipation and hysteresis in the soil sample is much less than in the limestone. Thus, the hysteresis in the soil samples is minimal on the scale of the total stresses and pore pressures, making accurate measurements of total stress and pore pressure hysteresis very difficult for all the soil samples.

Table 6.1. Shock consolidation sample and test summary.

TEST ID	MATERIAL	HOLE ID/DEPTH (ft)	DRY DENSITY (lb/ft <sup>2</sup> )	POROSITY (%)	$\epsilon_r/\epsilon_p^*$
M31A6	Limestone	KAM2A/245.2	111.15	.359	.65
M31B6	Limestone	KAM2A/362.2	100.65	.42	.76
M28C6	Limestone	KAM2A/432.1	92.16	.469	.86
M27B6	Limestone	KAM2A/391.3	115.21	.336	.68
M28B6	Limestone	KAM2A/271.0	140.91	.188	.30
A2A6	Limestone	KAM2A/353.8	110.85	.361	.56
A4A6	S/S/G	OAM1 / 86.3	95.11	.452	.86
A4B6	S/S/G	OAM2 /259.8	103.05	.406	.84
M27A6	S/S/G	KAM2 / 59.0	95.31	.451	.79
M26B6	S/S/G	KAM2 / 33.5	103.22	.405	1.0
A2B6	S/S/G	OAM1 /284.9	100.61	.42	.80
M26A6	S/S/G	KAM2 / 11.5	89.41	.485	1.0
A3A6	S/S/G	OAR2 /827.4	95.14	.452	.88
A3B6	S/S/G	OAR2 /702.4	104.53	.398	.95
A3C6	S/S/G	OAR2 /472.8	100.18	.423	.83
M17A6	Beach Sand	Beach Sand	100.79	.419	.73
M17C6	Beach Sand	Beach Sand	103.9	.40	.68

\* $\epsilon_r/\epsilon_p$  is the ratio of residual strain,  $\epsilon_r$ , following drained consolidation, to the peak strain,  $\epsilon_p$ , attained during the initial undrained loading.

Table 6.2. Material properties used for the computation of undrained uniaxial strain load-unload response of saturated porous Enewetak limestone.

Drained Skeleton Properties:

Constrained loading modulus -  $M_{S1} = 1.86 \times 10^6$  psi for  $\epsilon_a' < .0017$   
 $M_{S1} = 64,000$  psi for  $.0017 \leq \epsilon_a = .05$

Constrained unloading modulus -  $M_{SU} = 1.86 \times 10^6$  psi

$K_0$  Values:

Loading -  $K_0 = 0.02$   $\nu = .0196$   $\epsilon_a' < 0.0017$   
 $K_0 = 0.74$   $\nu = .425$   $\epsilon_a' \geq 0.0017$

Unloading -  $K_0 = 0.74$   $\nu = .425$

Initial Porosity:  $n = 0.361$

Pore Water Property:

Used the properties of sea water described in Section 3.3.

Grain Properties:

Used the solid grain model described in Section 3.4 with the following properties:

Initial grain density -  $\rho_0 = 0.0002614$  lb-s<sup>2</sup>/in<sup>4</sup> (2.78 gr/cm<sup>3</sup>)

Initial wavespeed -  $C_0 = 12,658$  ft/s

Poisson's ratio at low stress -  $\nu_0 = 0.27$

Slope of propagation to particle velocity -  $S = 1.5$

Threshold pressure -  $P_b = 72,500$  psi

Table 6.3. Material properties used for the computation of undrained uniaxial strain load-unload response of saturated porous sand.

**Skeleton Properties:**

Initial porosity -	$n = 0.406$
Constrained loading modulus -	$M_{sl} = 14,200 \text{ psi}$
Constrained unloading modulus -	$M_{su} = 265,000 \text{ psi}$
Poisson's ratio -	$\nu = 0.32$

**Pore Water Properties:**

Used the properties of sea water described in Section 3.3.

**Grain Properties:**

Used the solid grain model described in Section 3.4 with the following properties:

Initial grain density -	$\rho_0 = 0.0002614 \text{ lb-s}^2/\text{in}^4 \text{ (2.78 gr/cm}^3\text{)}$
Initial wavespeed -	$C_0 = 12,658 \text{ ft/s}$
Poisson's ratio at low stress -	$\nu_0 = 0.27$
Slope of propagation to particle velocity -	$S = 1.5$
Threshold pressure -	$P_b = 72,500 \text{ psi}$

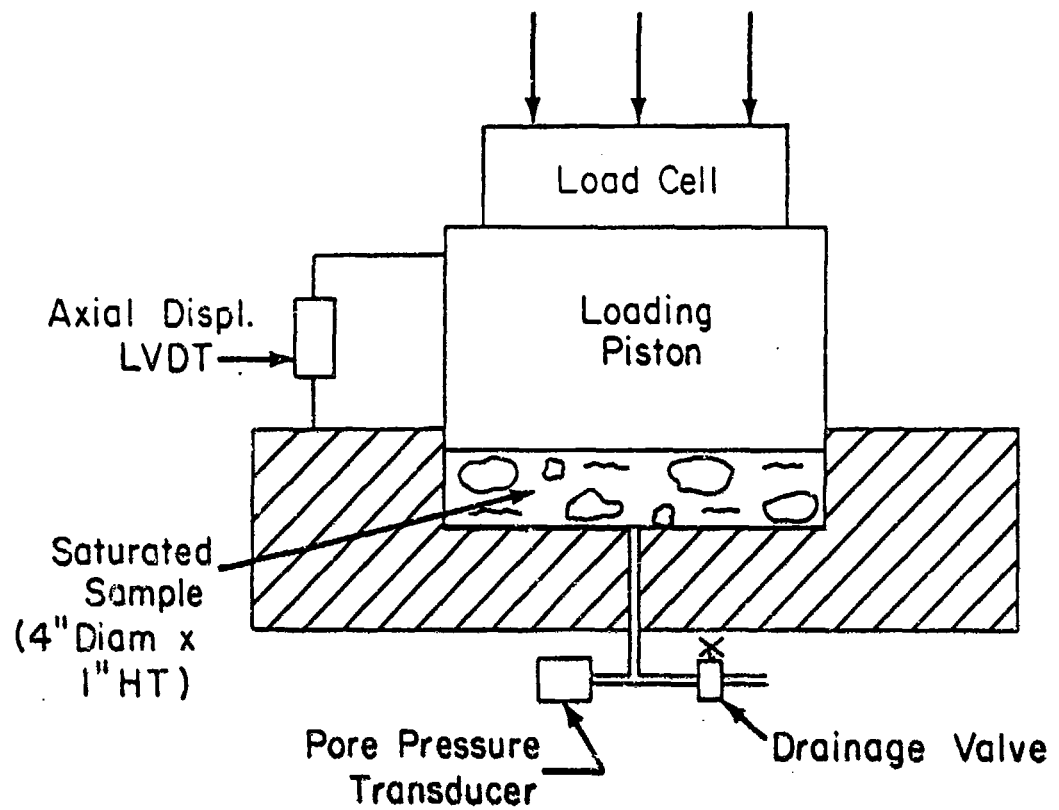


Figure 6.1. Schematic section view of rigid high pressure oedometer used for shock consolidation tests.

# Shock Consolidation (M31B6) KAM-2A Depth = 362.2 ft

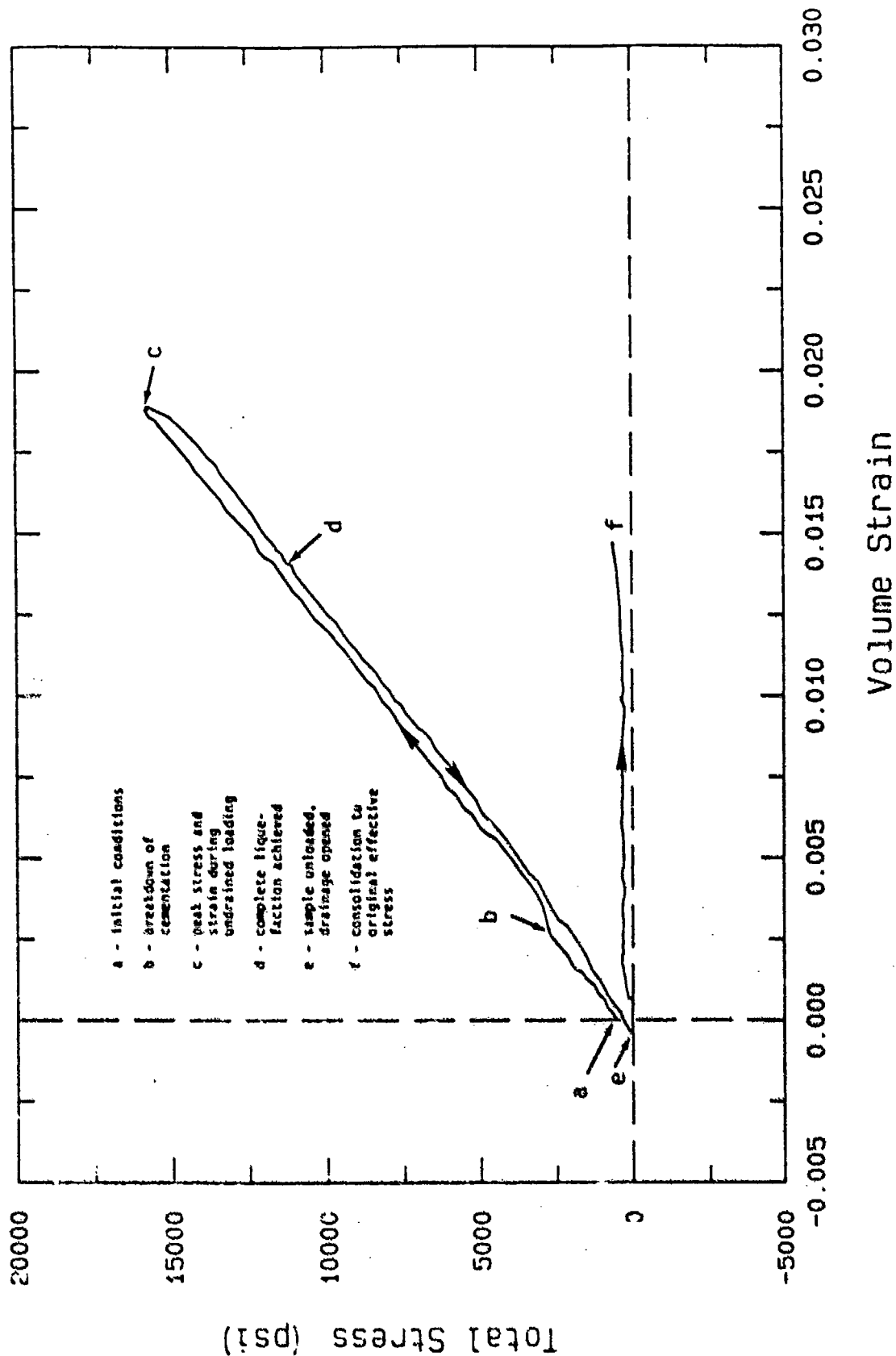


Figure 6.2a. Shock consolidation test M31B6 on low strength porous limestone; total stress response.

# Shock Consolidation (M31B6) KAM-2A Depth = 362.2 ft

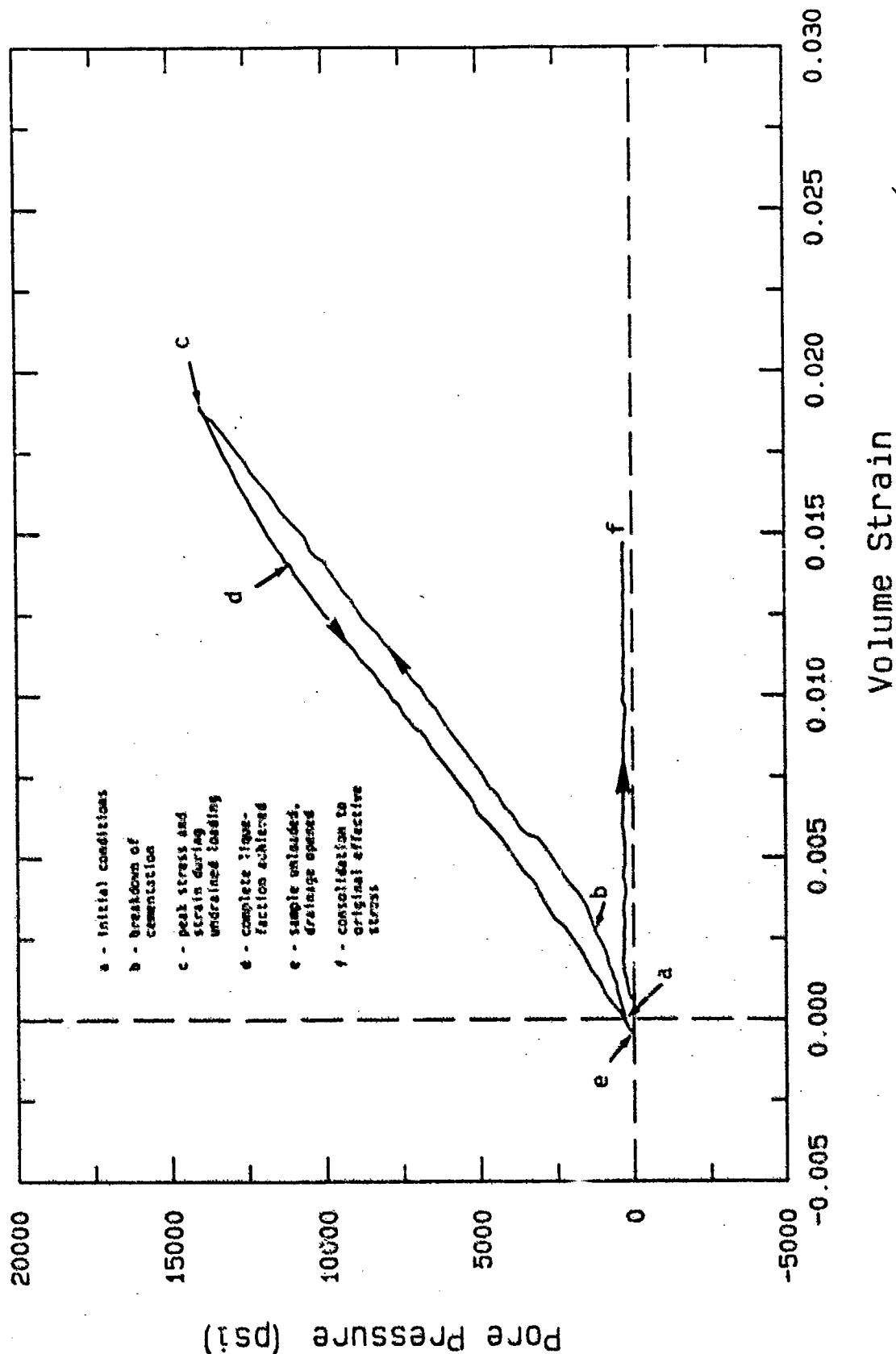


Figure 6.2b. Shock consolidation test M31B6 on low strength porous limestone; pore pressure response.



# Shock Consolidation (M31B6) KAM-2A Depth = 362.2 ft

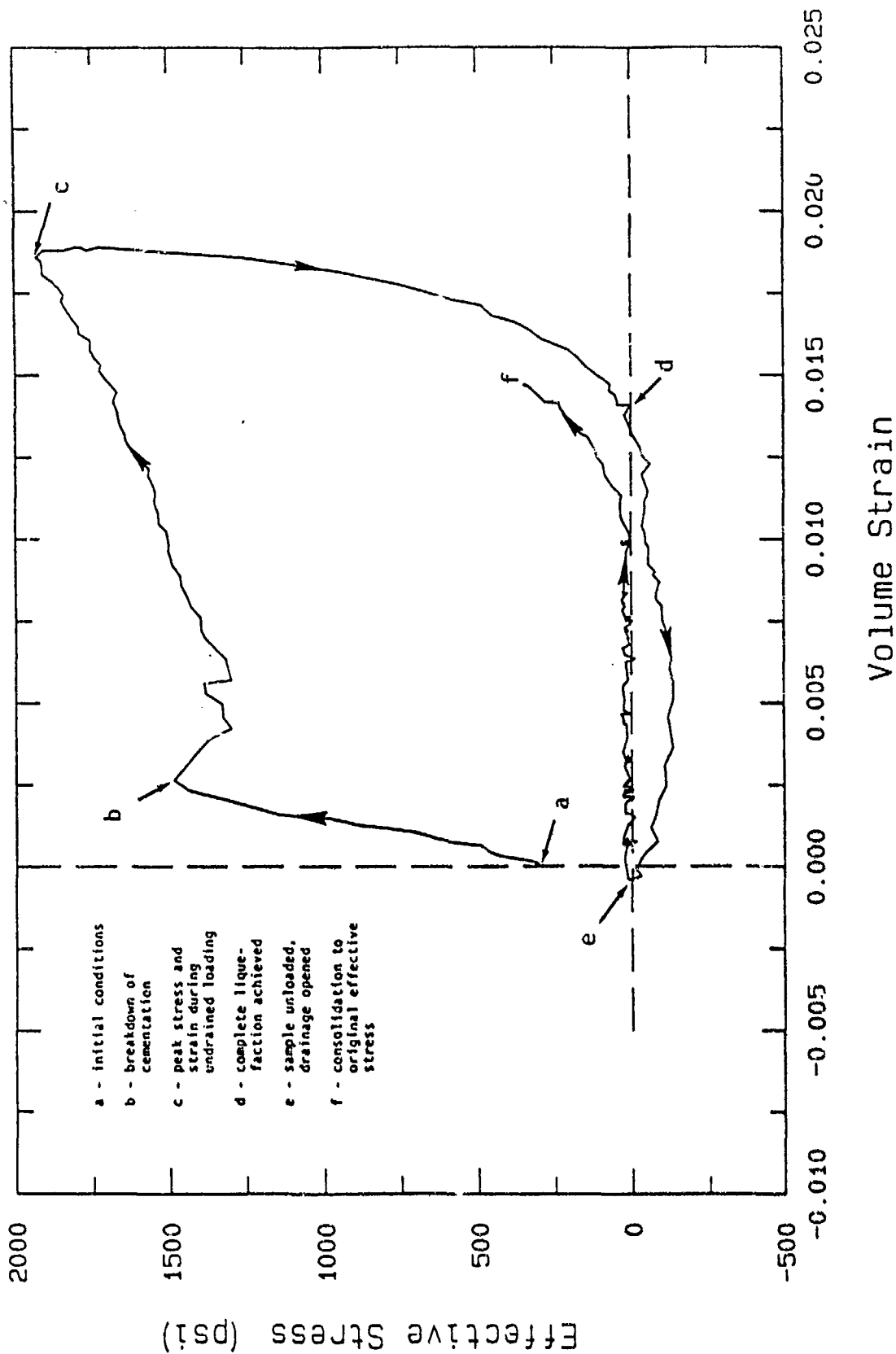


Figure 6.2c. Shock consolidation test M31B6 on low strength porous limestone; effective strength response.

Shock Consolidation (A2A6) KAM-2A  
Depth = 353.8 ft

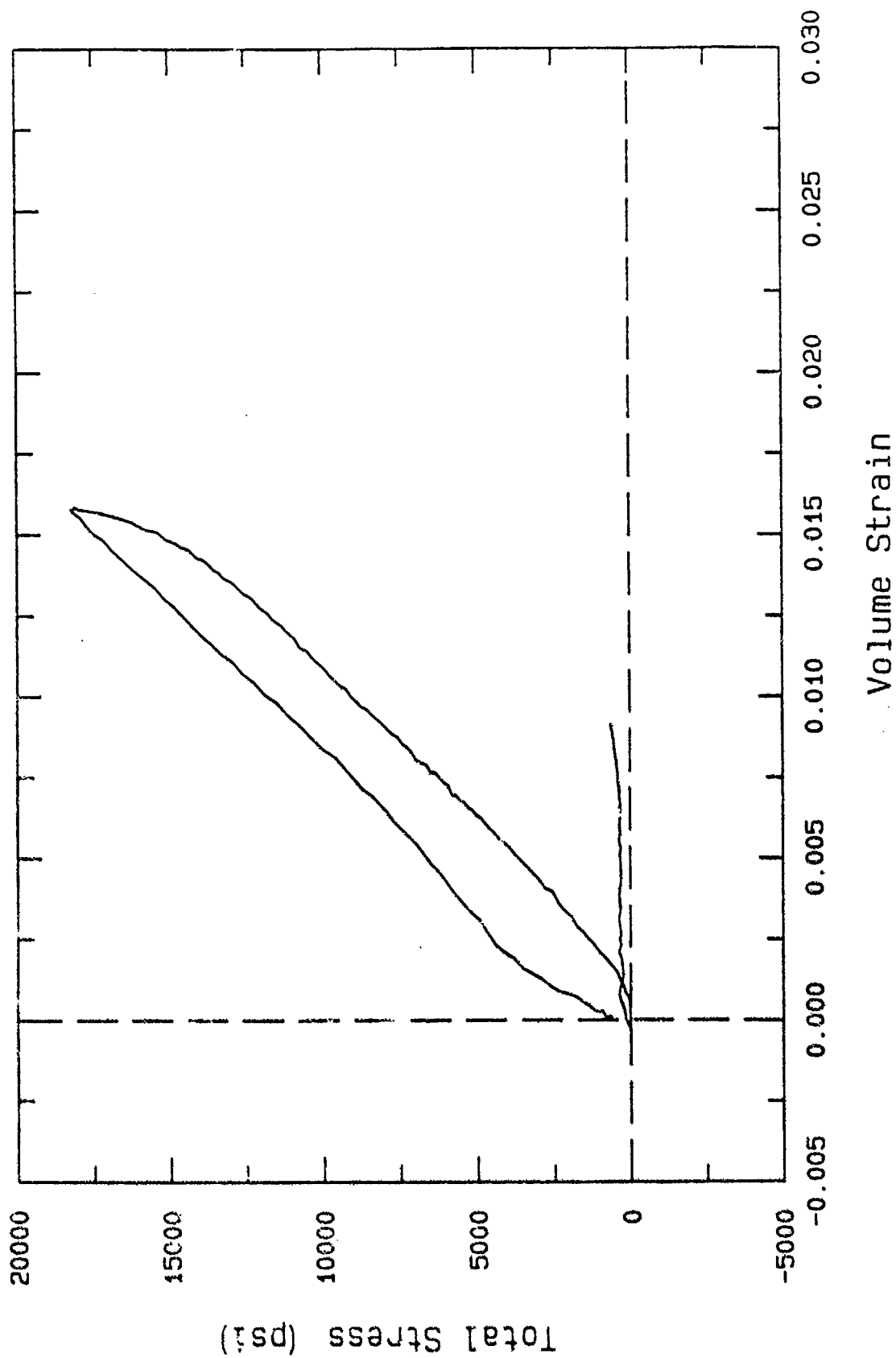


Figure 6.3a. Shock consolidation test A2A6 on medium strength porous limestone; total stress response.

Shock Consolidation (A2A6) KAM-2A

Depth = 353.8 ft

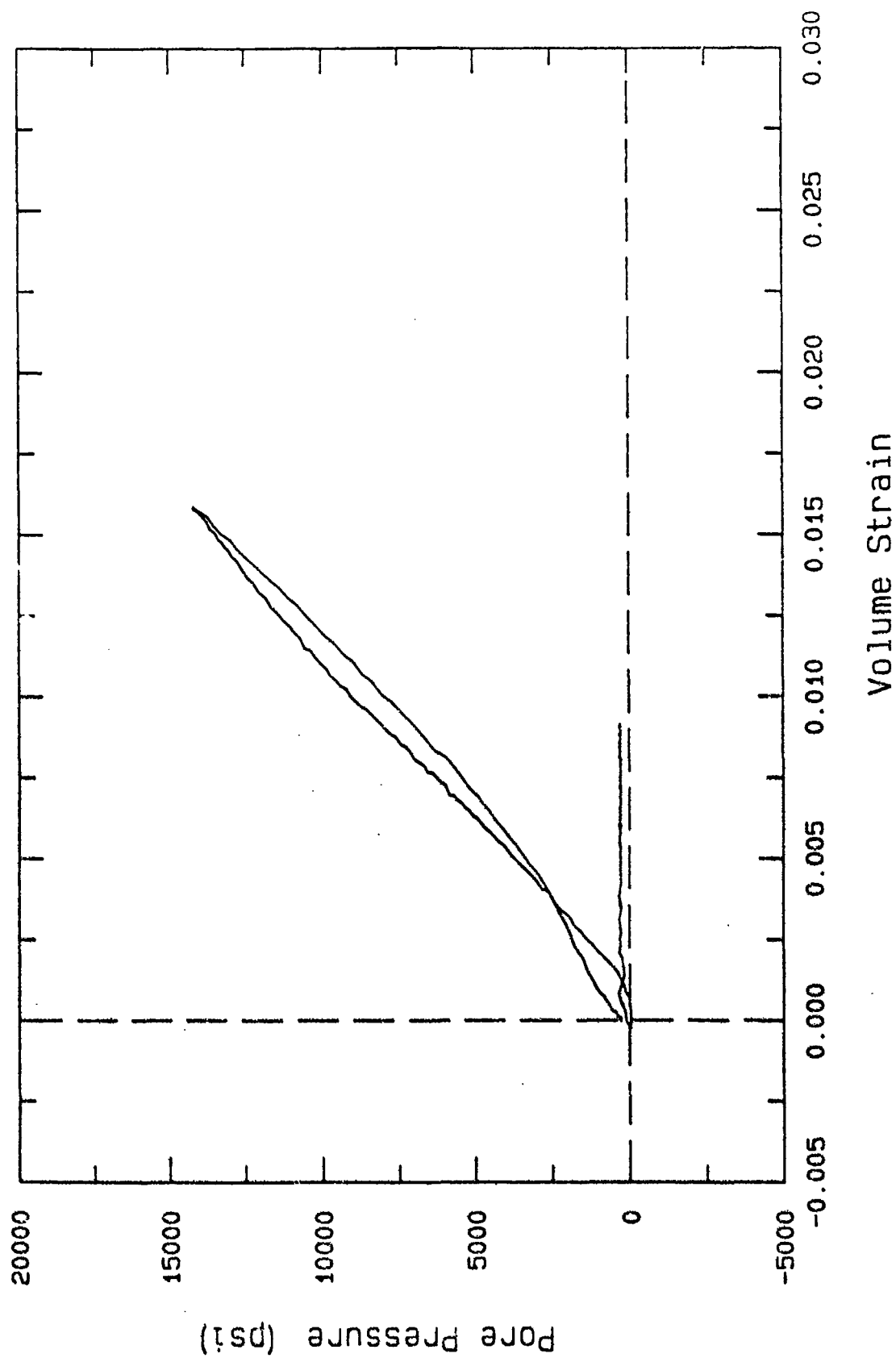


Figure 6.3b. Shock consolidation test A2A6 on medium strength porous limestone; pore pressure response.

Shock Consolidation (A2A6) KAM-2A  
Depth = 353.8 ft

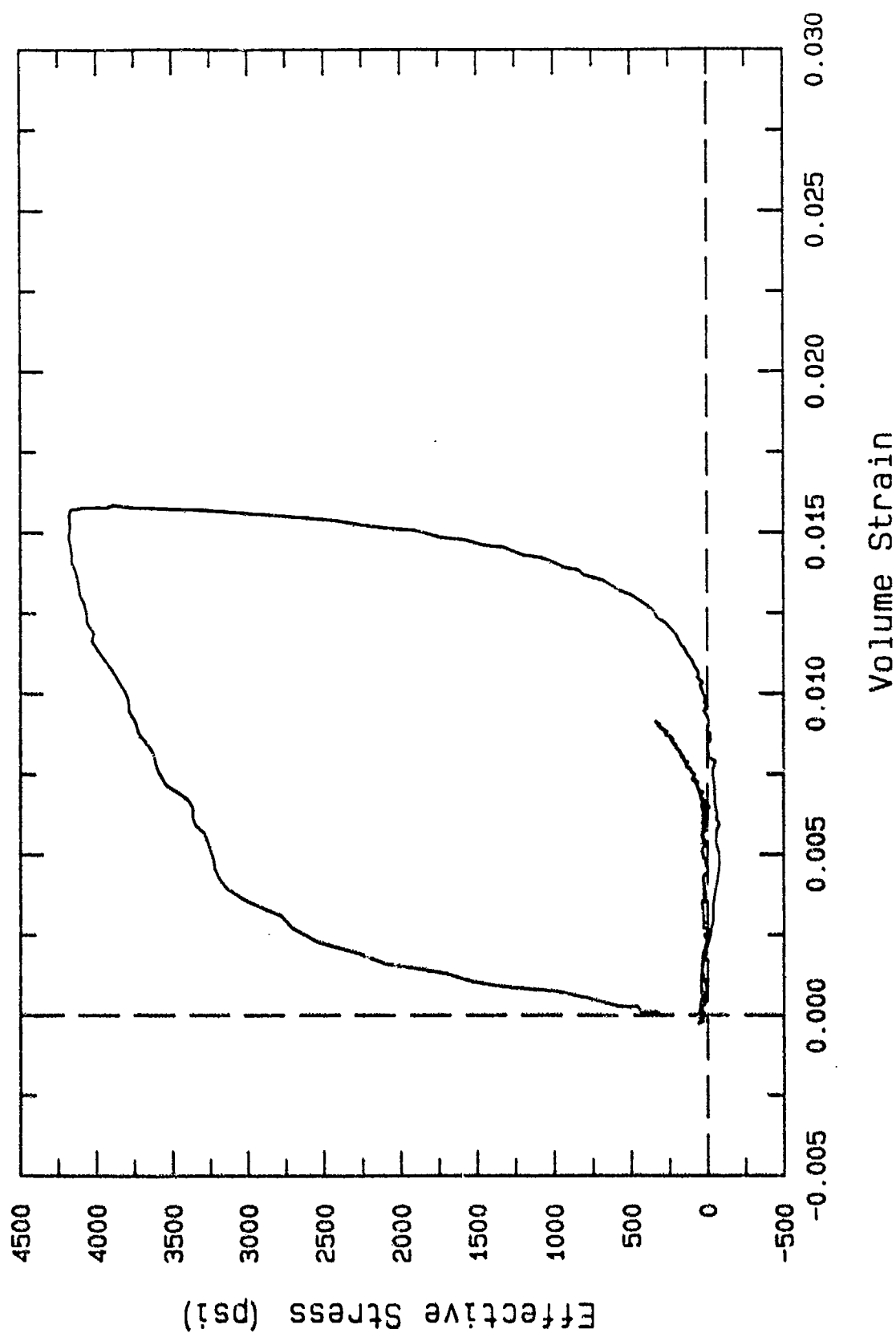


Figure 6.3c. Shock consolidation test A2A6 on medium strength porous limestone; effective stress response.

# Shock Consolidation (A4B6) OAM-2 Depth = 259.8 ft

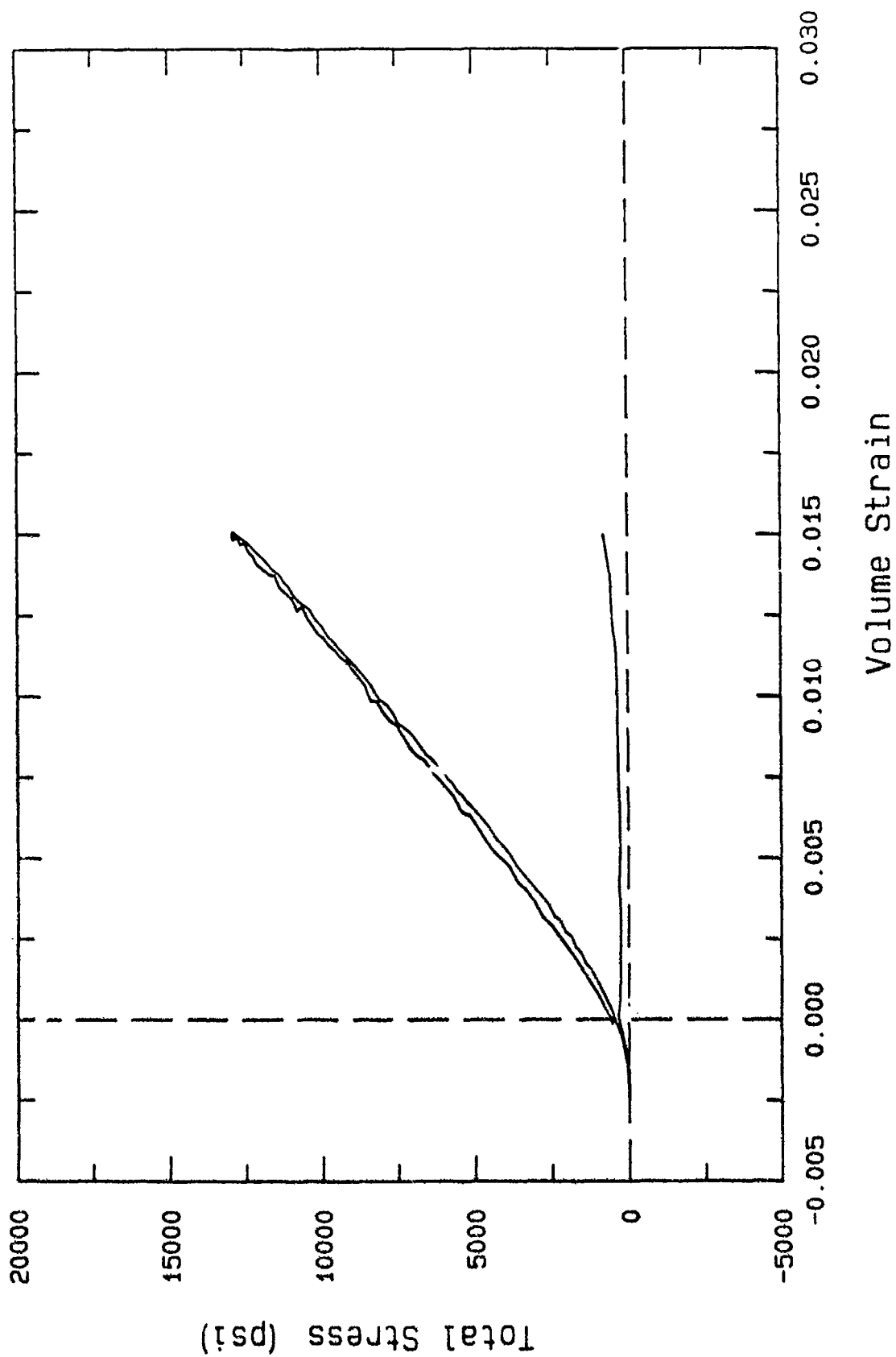


Figure 6.4a. Shock consolidation test A4B6 on uncemented silt, sand, gravel;  
total stress response.

Shock Consolidation (A4B6) 0AM-2  
Depth = 259.8 ft

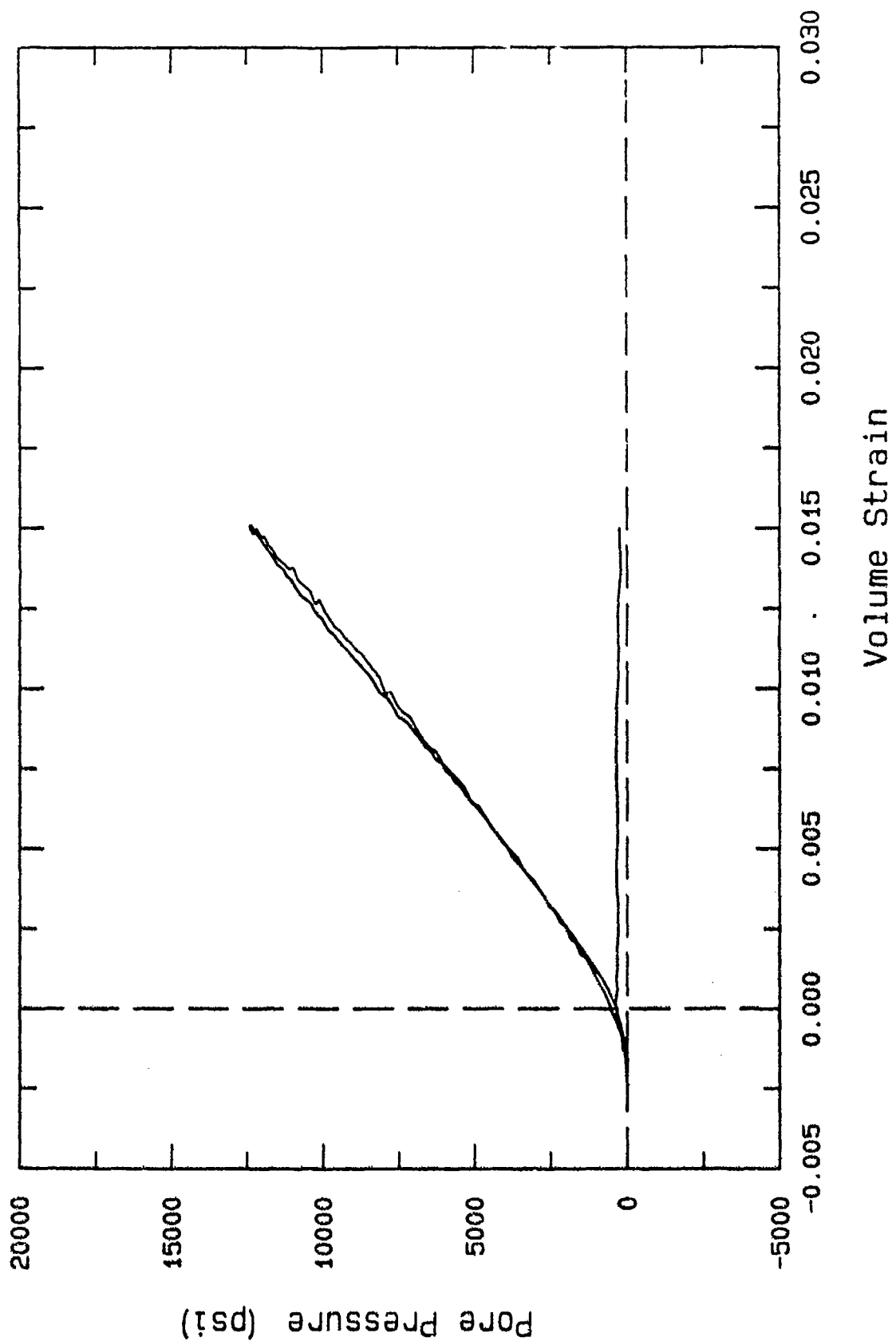


Figure 6.4b. Shock consolidation test A4B6 on uncemented silt, sand, gravel;  
pore pressure response.

Shock Consolidation (A4B6) OAM-2

Depth = 259.8 ft

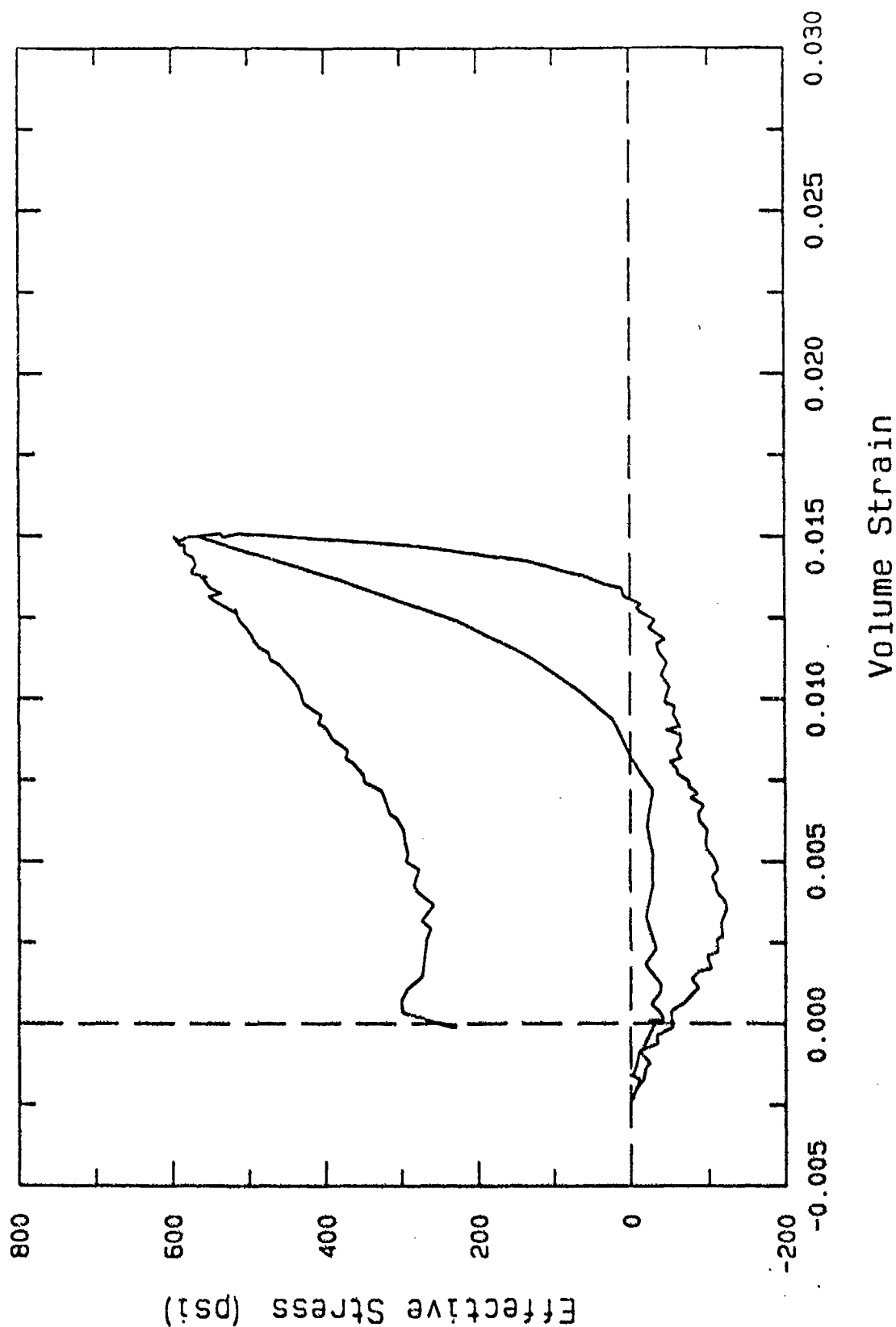


Figure 6.4c. Shock consolidation test A4B6 on uncemented silt, sand, gravel; effective stress response.

Shock Consolidation (A2B6) OAM-1  
Depth = 284.9 ft

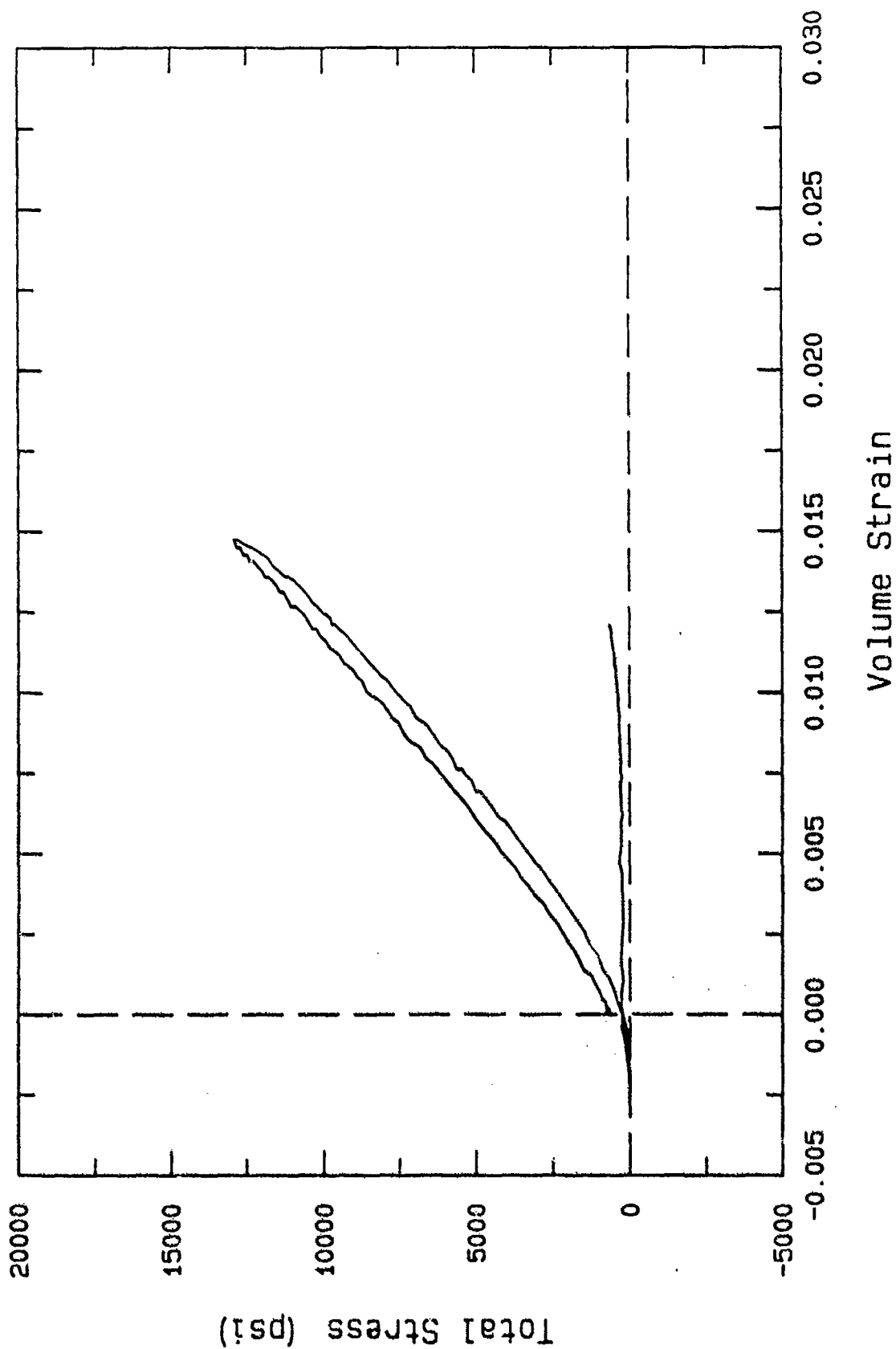


Figure 6.5a. Shock consolidation test A2B6 on uncemented silt, sand, gravel;  
total stress response.



# Shock Consolidation (A2B6) OAM-1 Depth = 284.9 ft

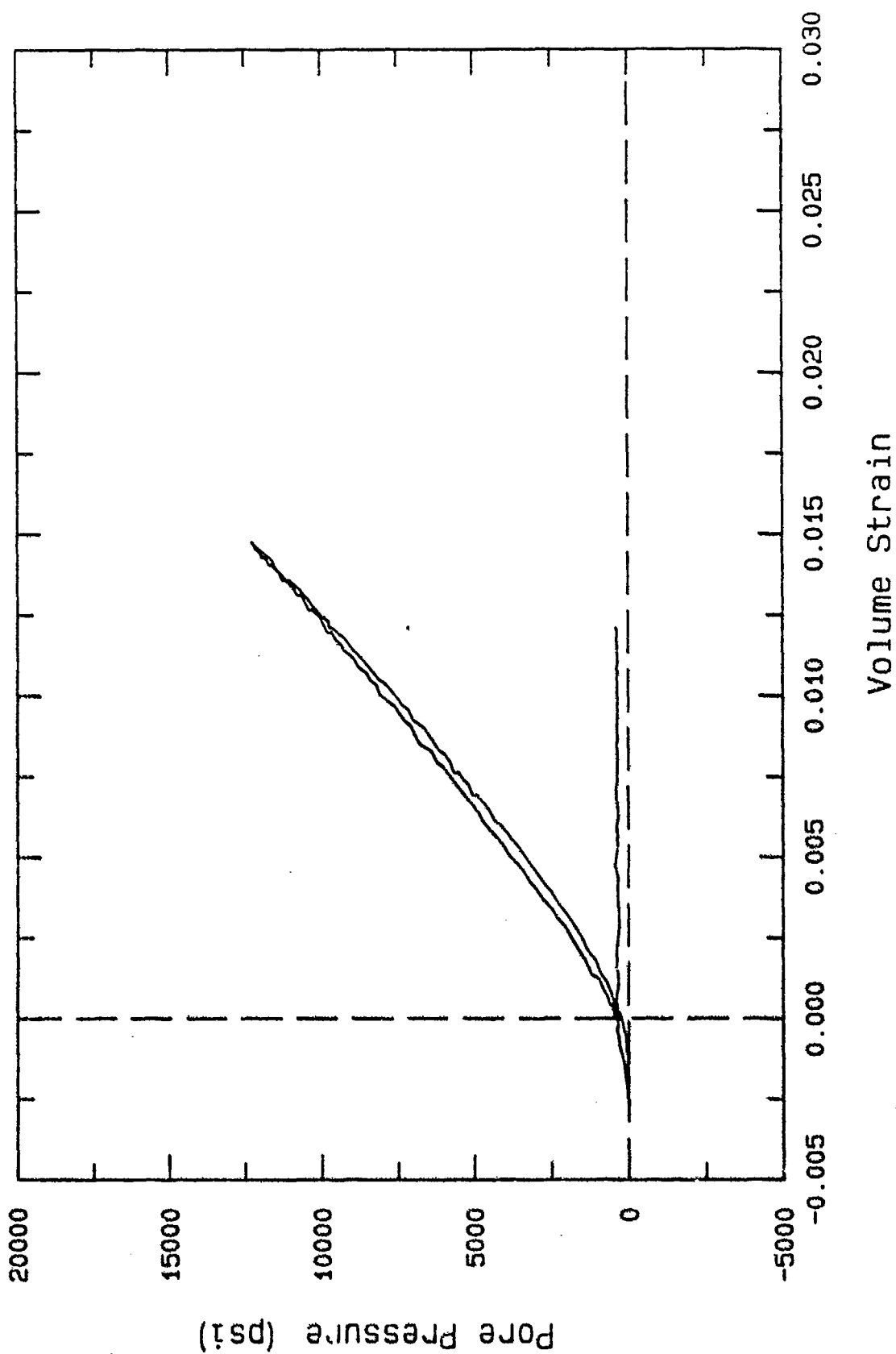


Figure 6.5b. Shock consolidation test A2B6 on uncemented silt, sand, gravel; pore pressure response.

Shock Consolidation (A2B6) OAM-1  
Depth = 284.9 ft

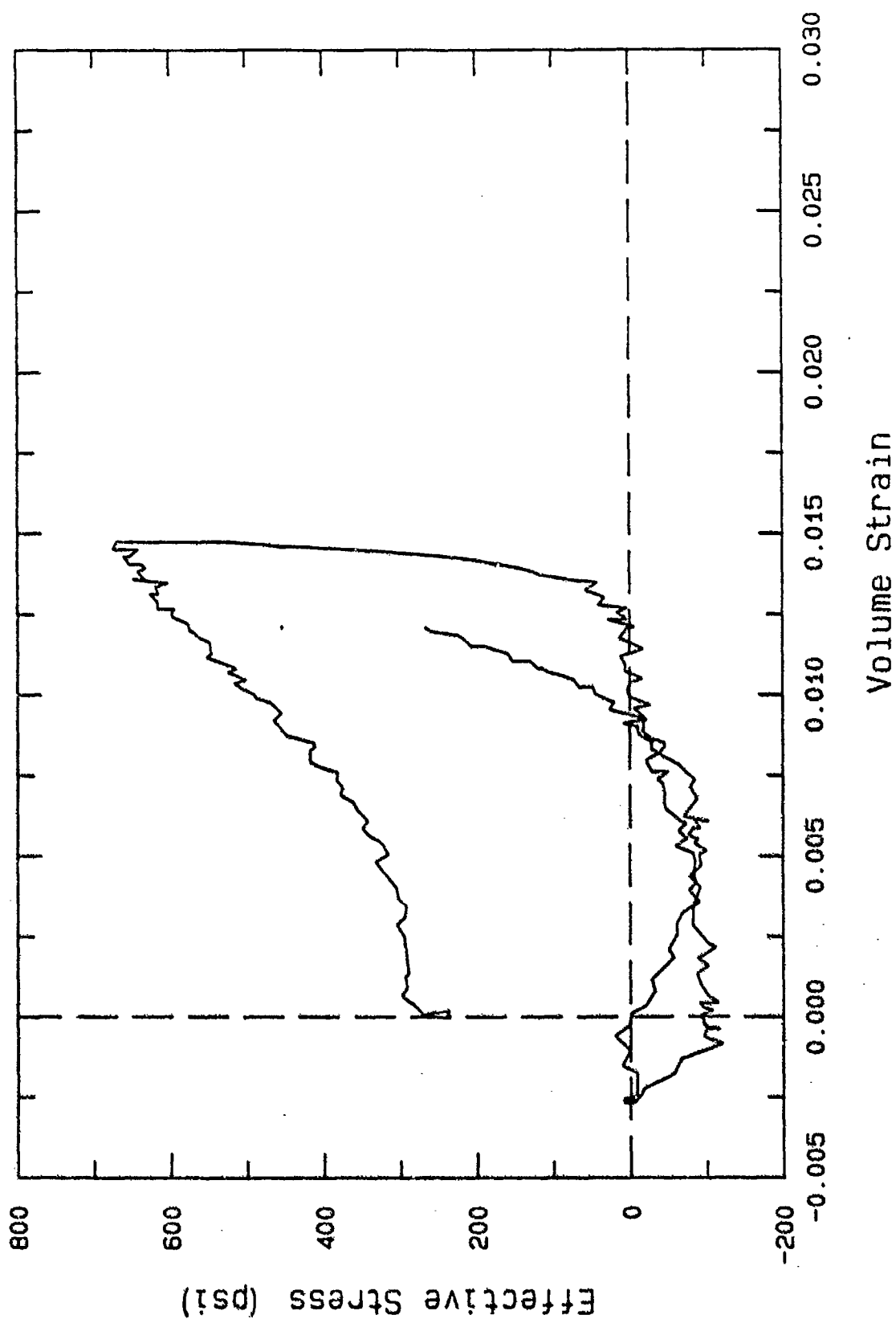


Figure 6.5c. Shock consolidation test A2B6 on uncemented silt, sand, gravel;  
effective stress response.

Shock Consolidation (M27A6) KAM-2  
Depth = 59.0-59.10 ft

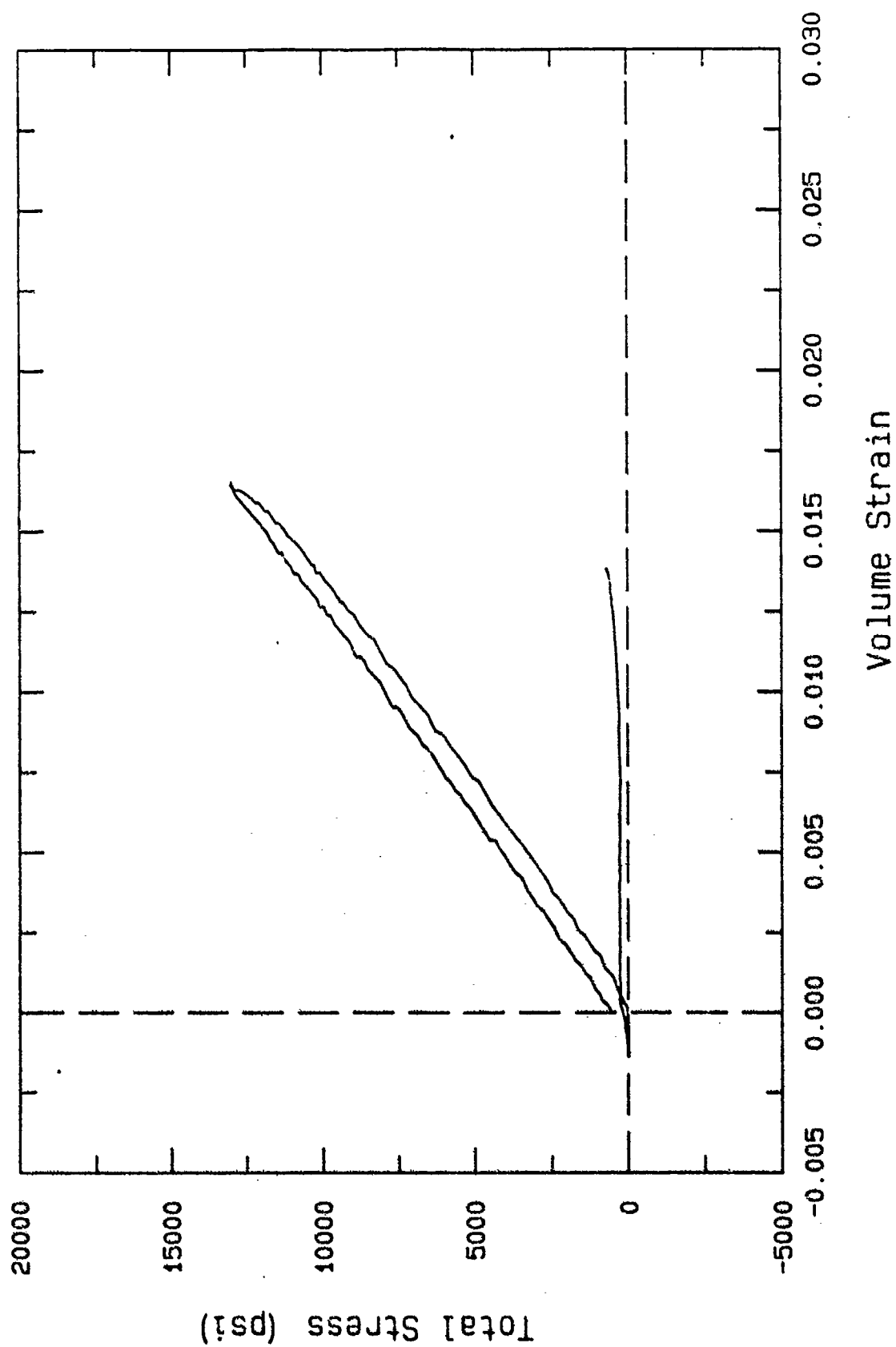


Figure 6.6a. Shock consolidation test M27A6 on uncemented silt, sand, gravel, total stress response.

Shock Consolidation (M27A6) KAM-2  
Depth = 59.0-59.10 ft

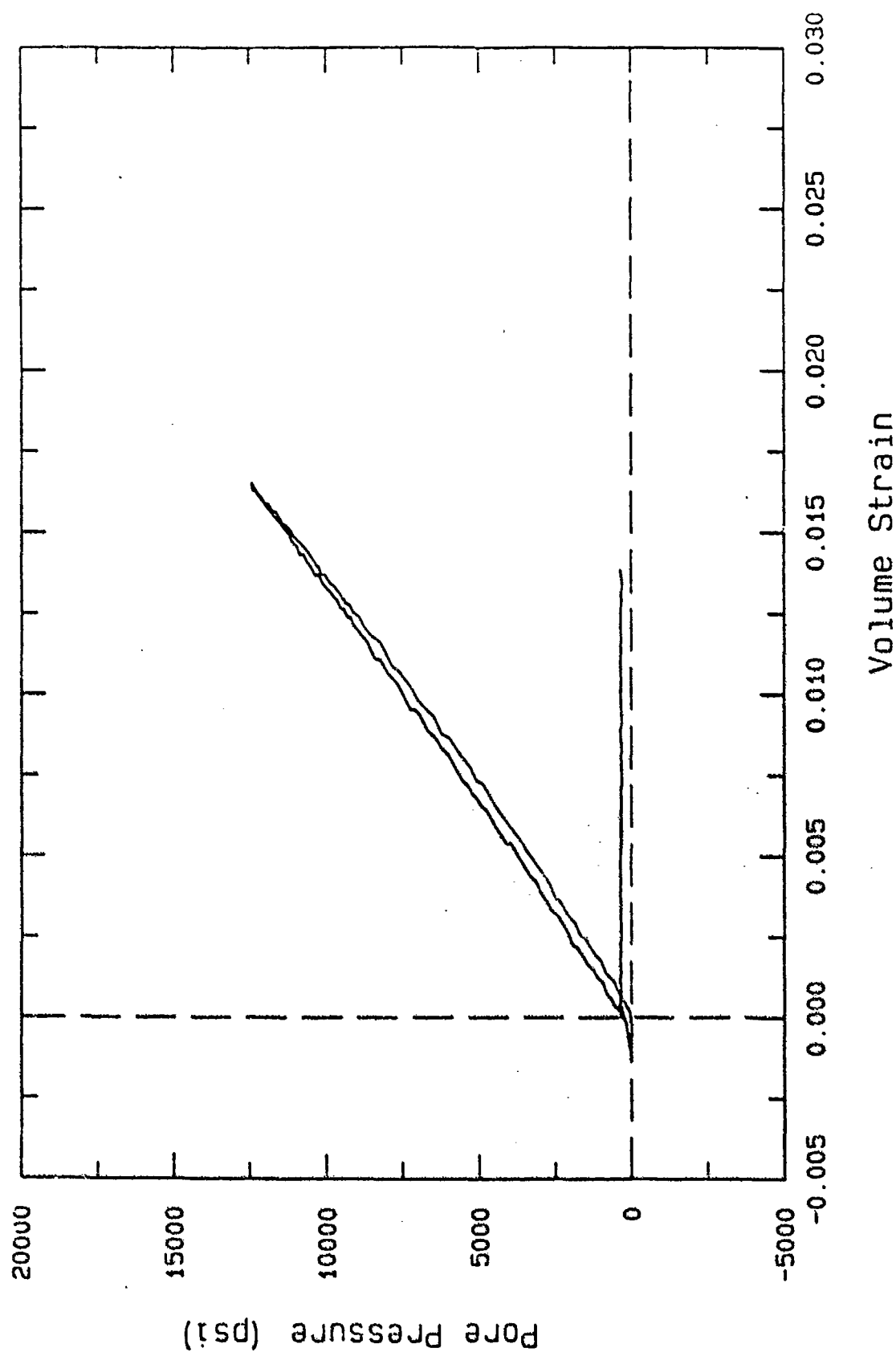


Figure 6.6b. Shock consolidation test M27A6 on uncemented silt, sand, gravel; pore pressure response.

Shock Consolidation (M27A6) KAM-2  
Depth = 59.0-59.10 ft

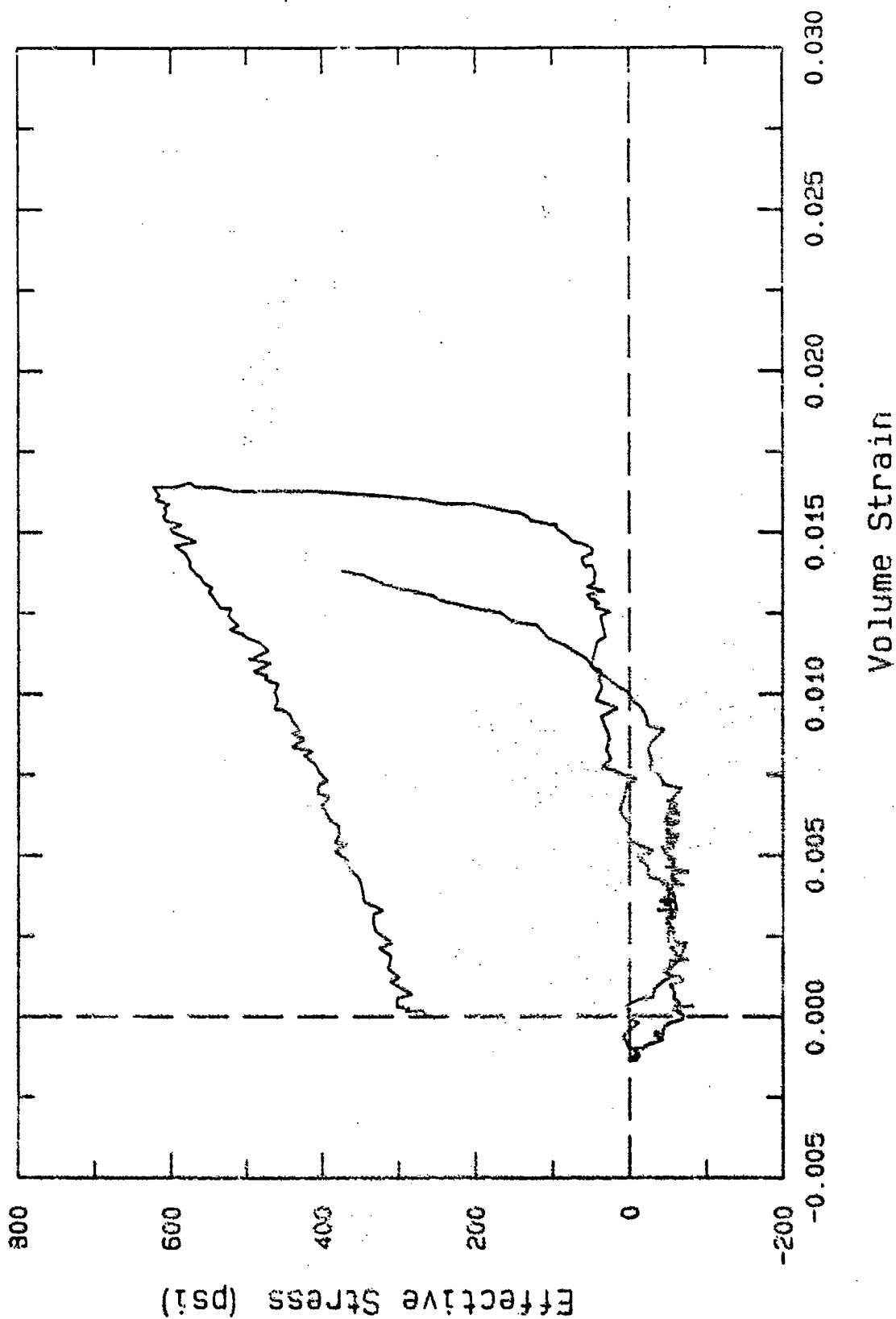


Figure 6.6c. Shock consolidation test M27A6 on uncemented silt, sand, gravel;  
effective stress response.

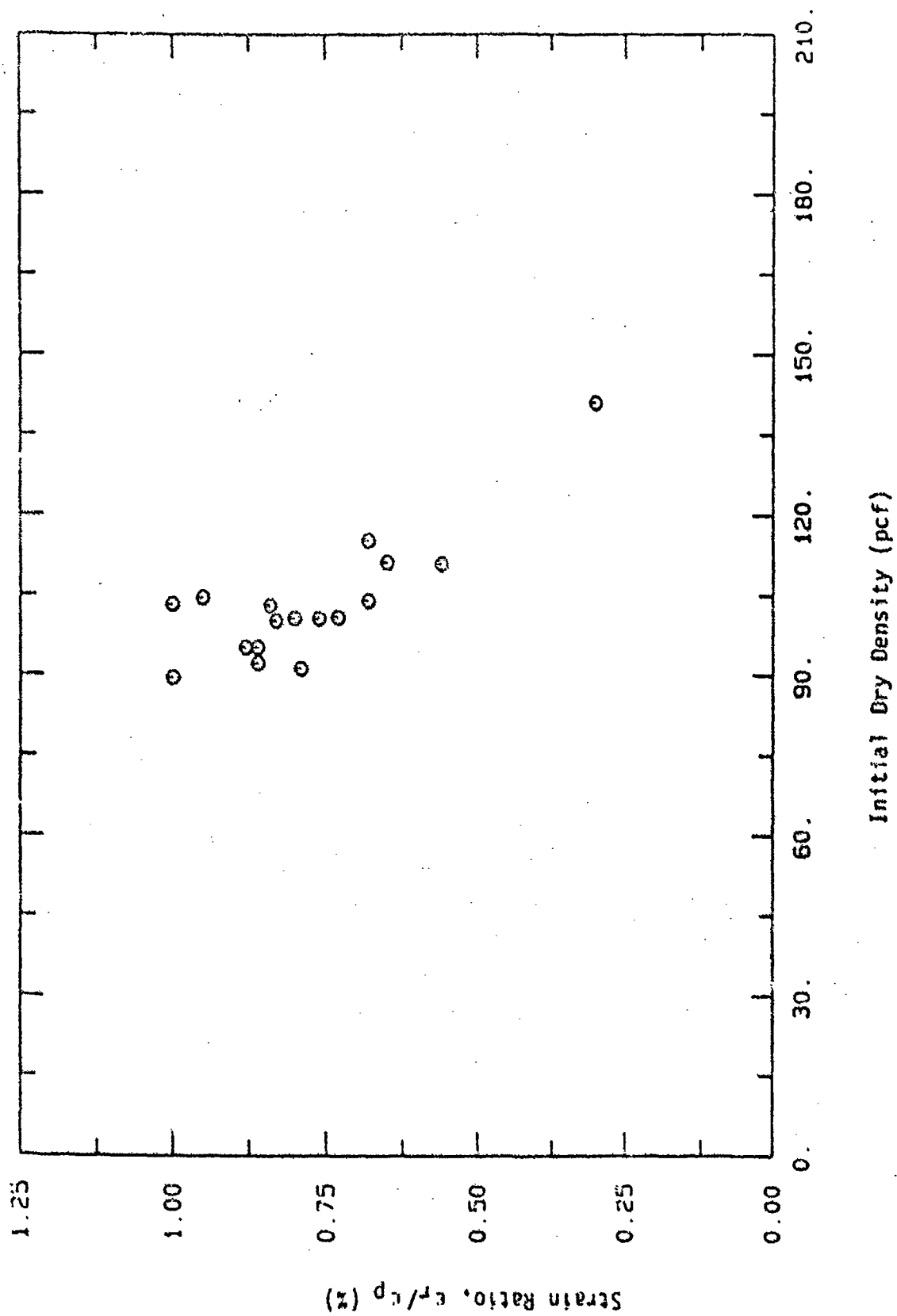


Figure 6.7. Ratio of residual volume strain following consolidation to peak strain during undrained loading from shock consolidation tests.

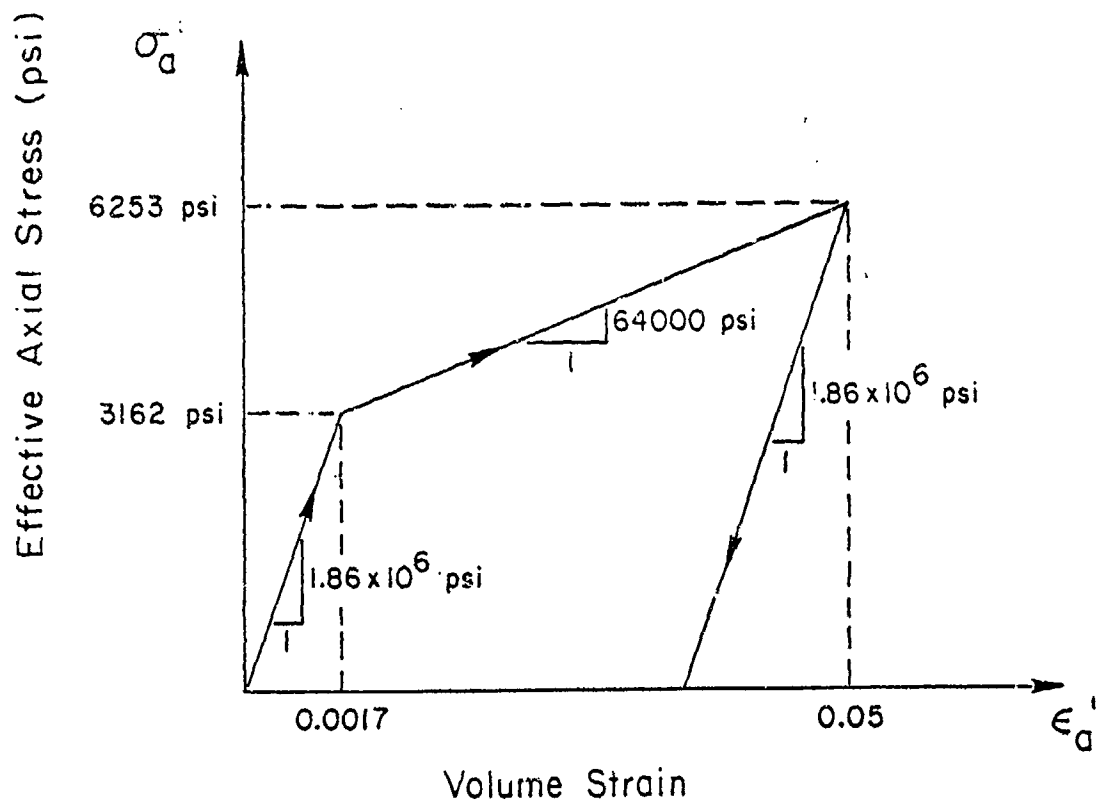


Figure 6.8. Effective uniaxial stress-strain model for calculation of the response of saturated medium strength Enewetak limestone.

# Shock Consolidation (A2A6) KAM-2A Depth = 353.8 ft

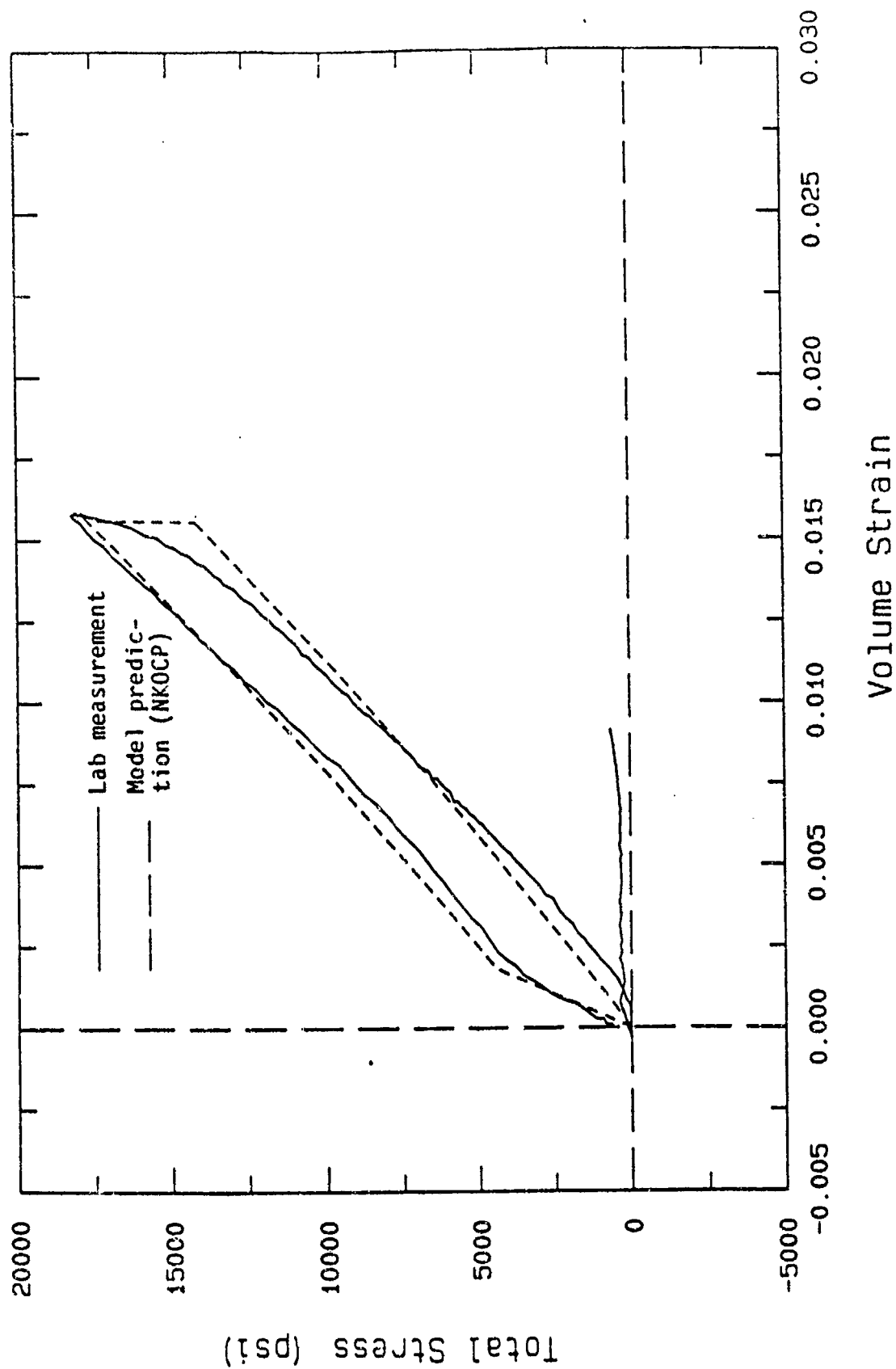


Figure 6.9a. Comparison of total stress response of saturated porous limestone with numerical simulation.



# Shock Consolidation (A2A6) KAM-2A Depth = 353.8 ft

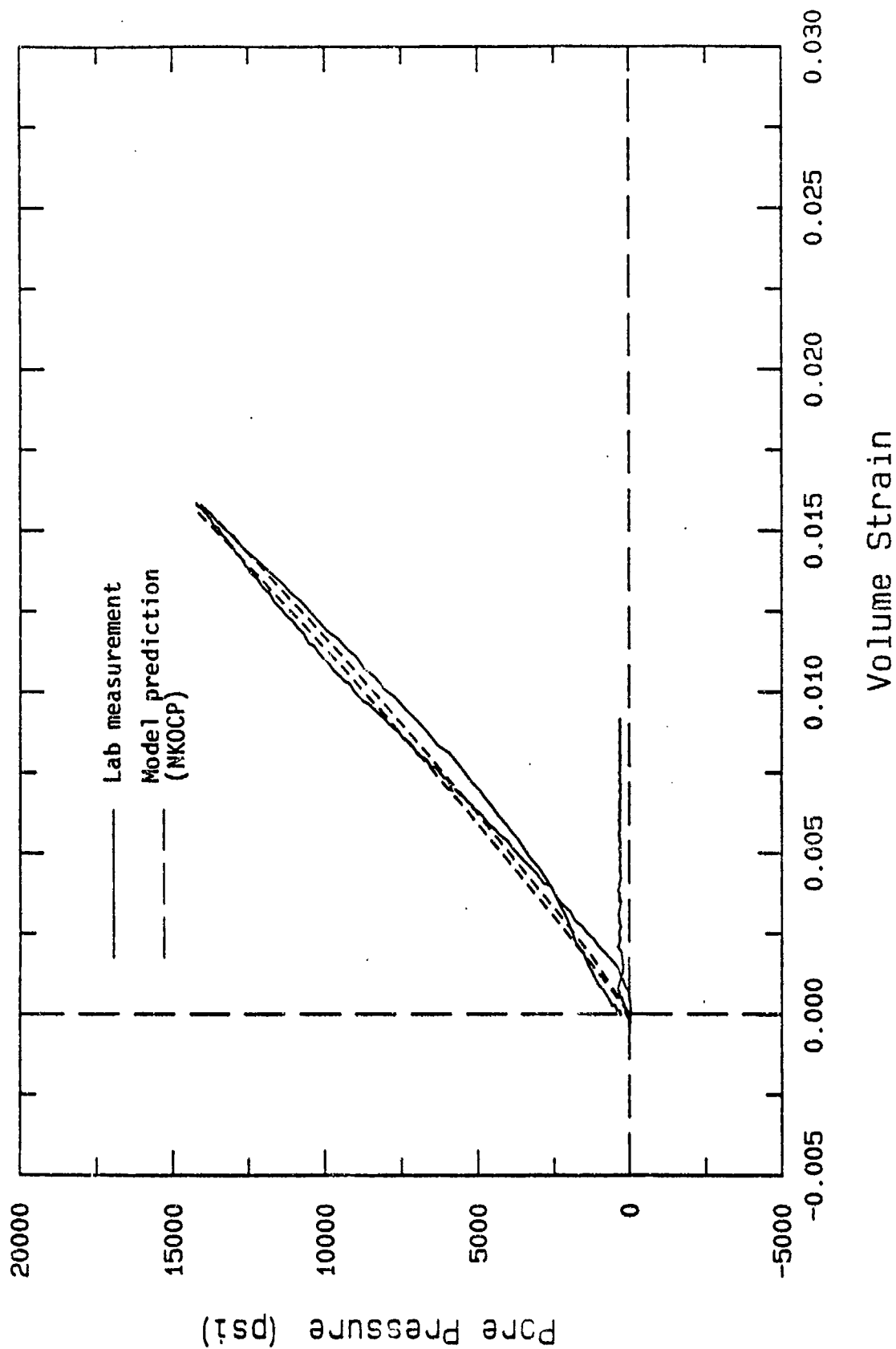


Figure 6.9b. Comparison of pore pressure response of saturated porous limestone with numerical simulation.

# Shock Consolidation (A2A6) KAM-2A

## Depth = 353.8 ft

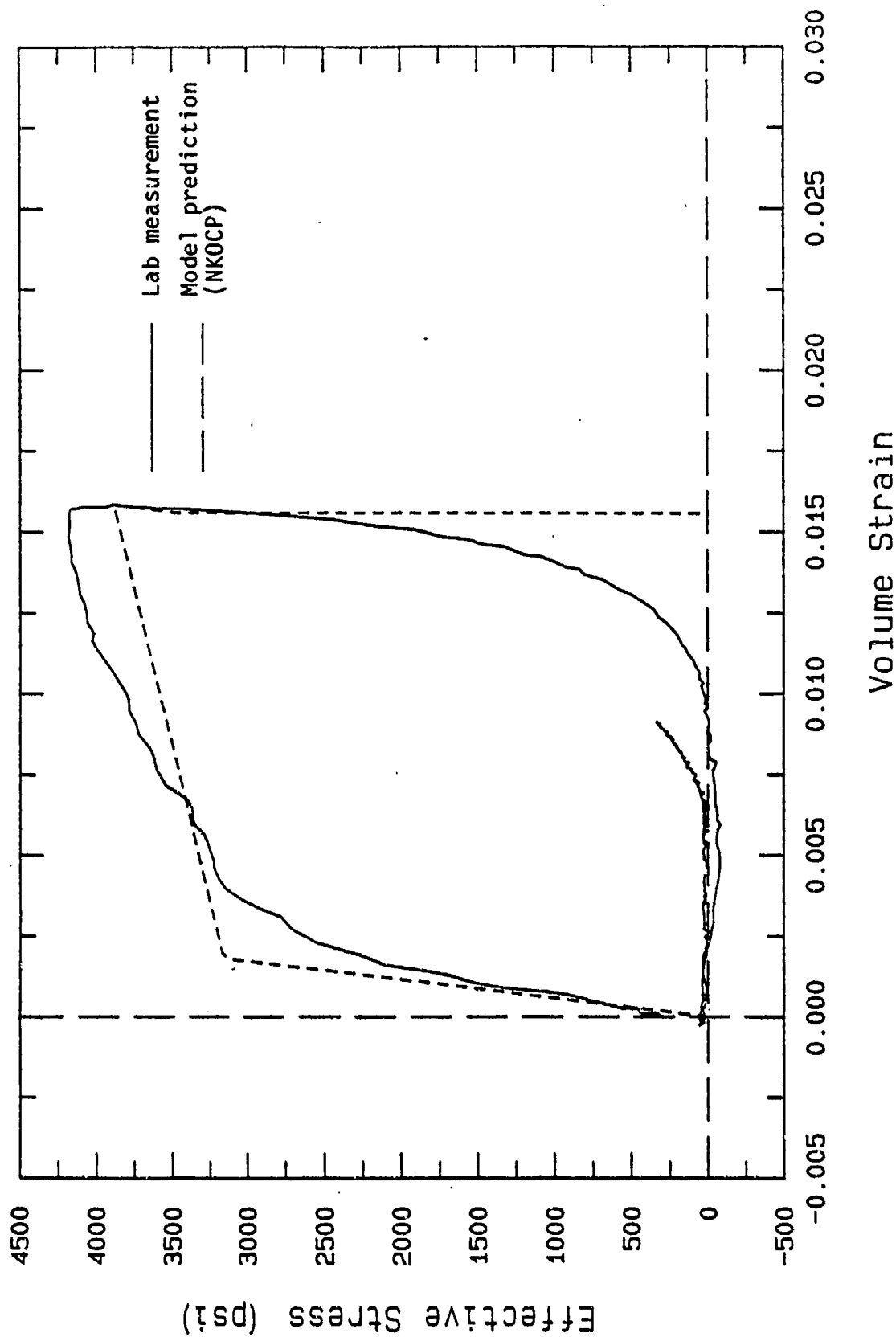


Figure 6.9c. Comparison of effective axial stress response of saturated porous limestone with numerical simulation.

# ROCK

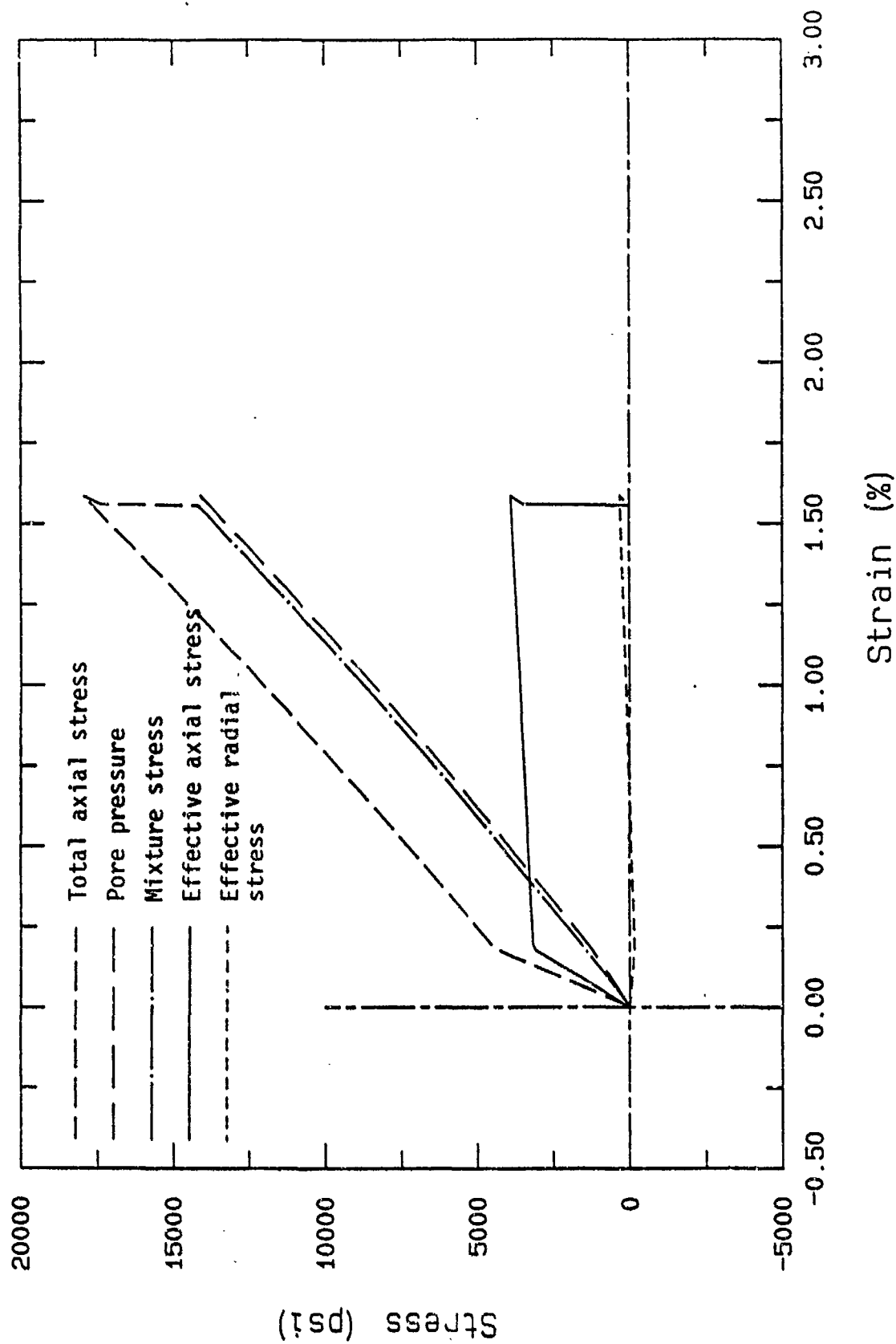


Figure 6.10. Undrained uniaxial strain load-unload response of saturated porous limestone computed using NKCCP.

# Shock Consolidation (A4B6) OAM-2

## Depth = 259.8 ft

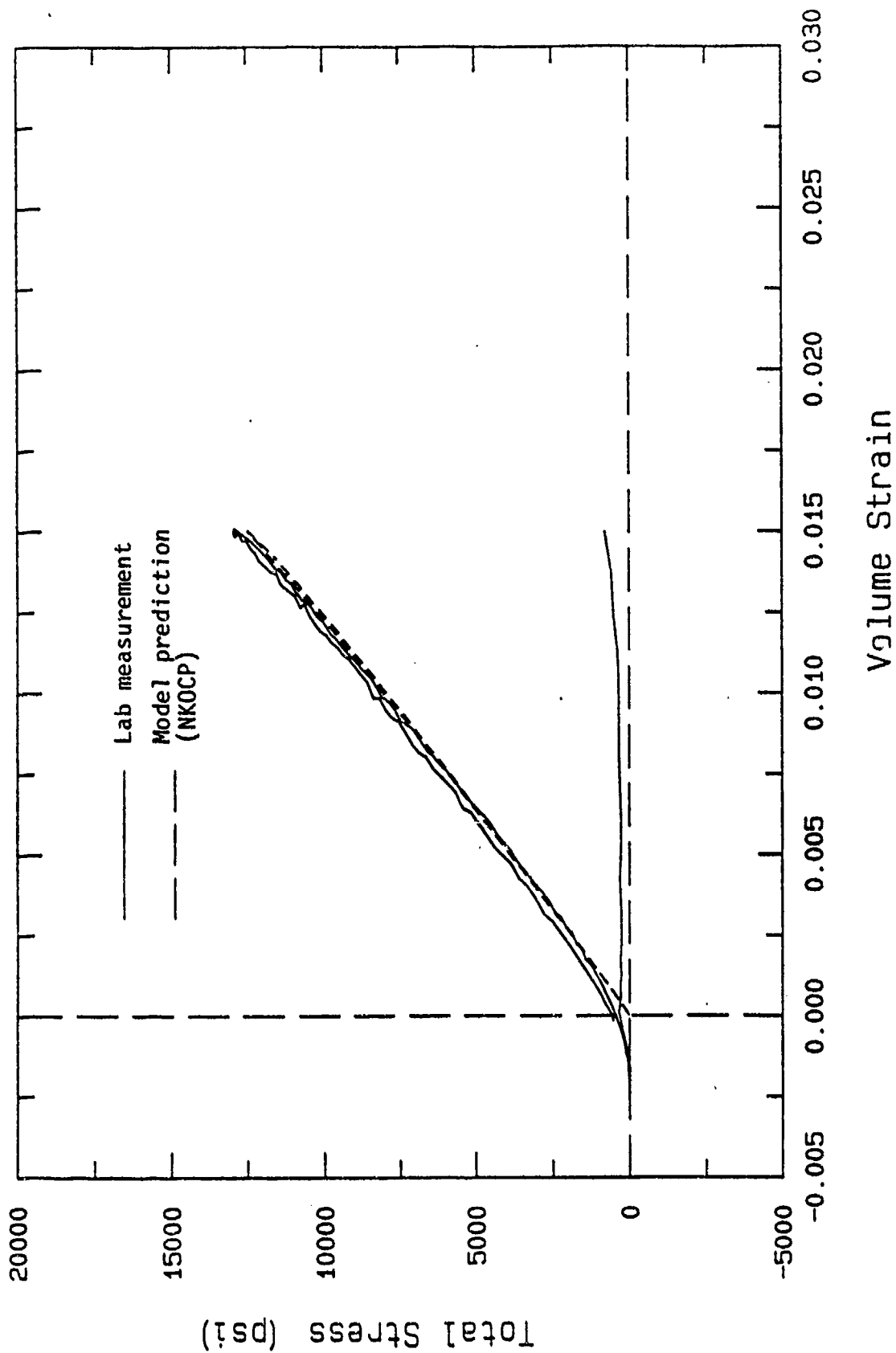


Figure 6.11a. Comparison of total stress response of saturated uncemented silt, sand, gravel with numerical simulation.

Shock Consolidation (A4B6) OAM-2  
Depth = 259.8 ft

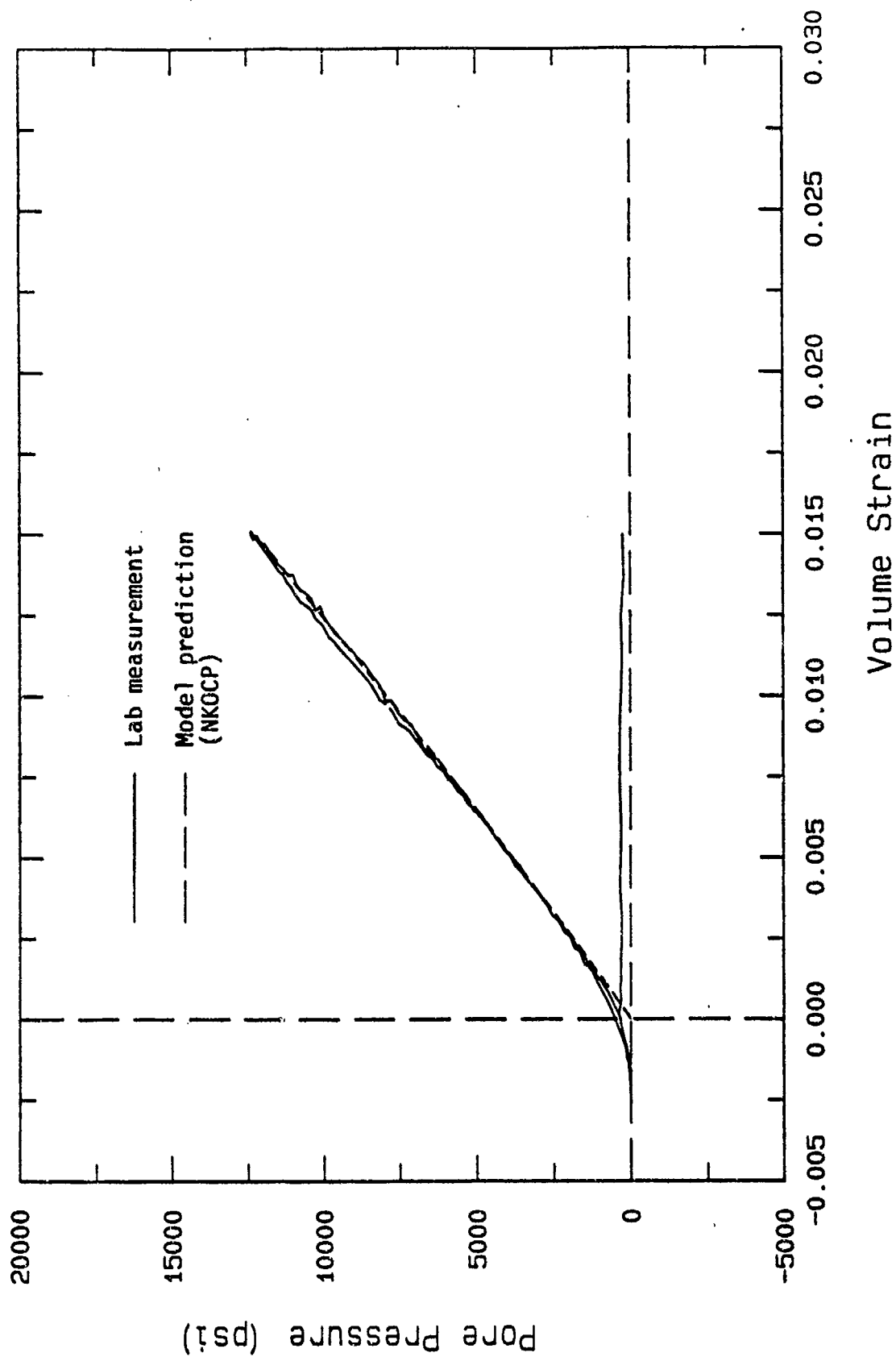


Figure 6.11b. Comparison of pore pressure response of saturated uncemented silt, sand, gravel with numerical simulation.

# Shock Consolidation (A4B6) OAM-2

## Depth = 259.8 ft

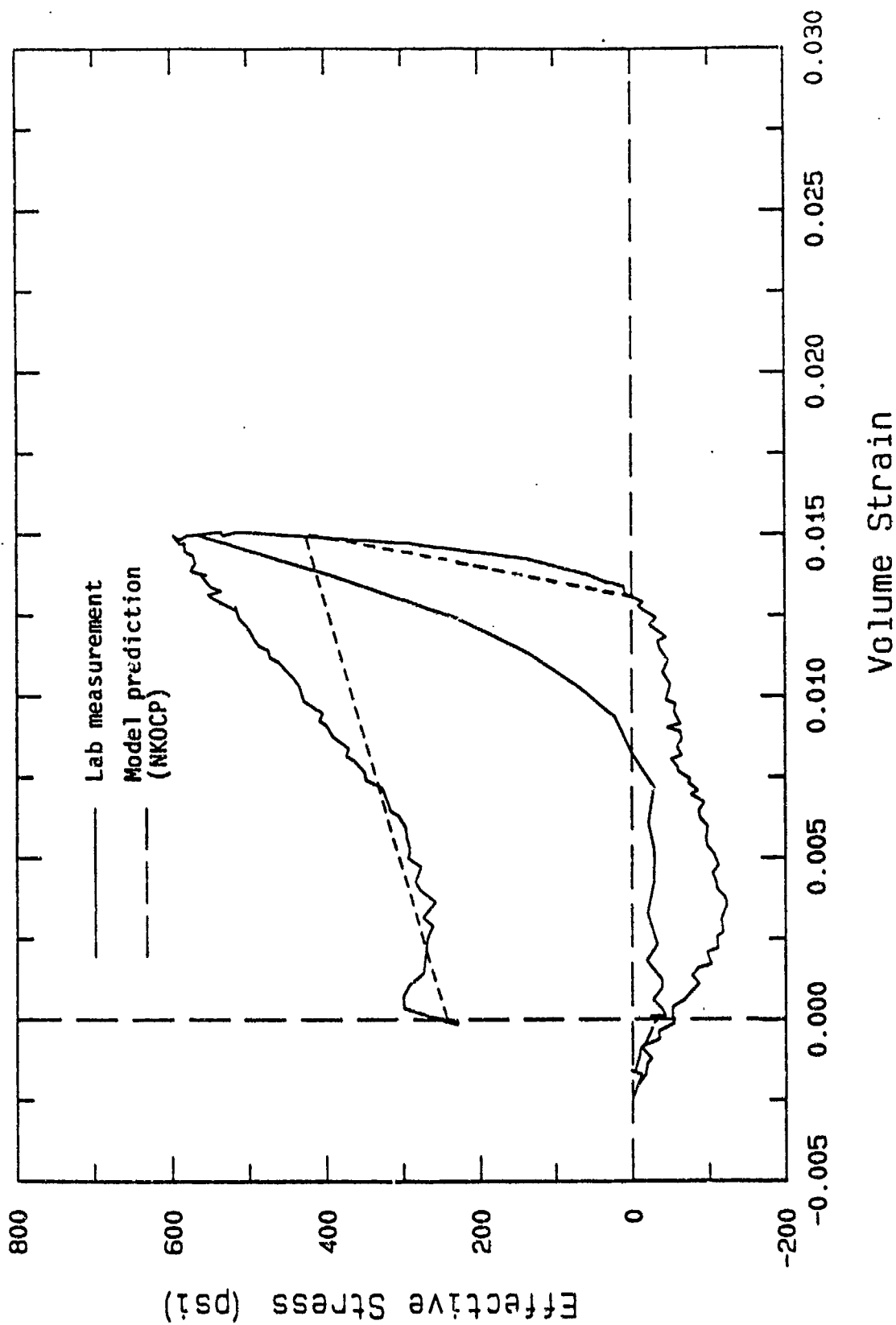


Figure 6.11c. Comparison of effective axial stress response of saturated uncemented silt, sand, gravel with numerical simulation.

## SECTION 7

### GRAIN DAMAGE AS A FUNCTION OF STRESS PATH AND MAGNITUDE

#### 7.1 INTRODUCTION

In Section 2 it was shown that hysteresis in the material skeleton results in liquefaction following both hydrostatic and uniaxial undrained loadings of porous saturated materials. The skeleton hysteresis is actually a measure of the non recoverable plastic work done on the material during the load unload cycle. There are two principal plastic work mechanisms acting during the cycle: frictional energy dissipation and grain breakage. Frictional energy dissipation causes heating of the sample during the load unload cycle, but leaves little in the way of post-test evidence. Grain breakage, however, is easily recognizable and can be documented post-test. Blouin, Martin and McIntosh (1984), observed extensive grain crushing during uniaxial and hydrostatic drained loadings of Enewetak beach sand, a well rounded uniform carbonate sand.

In this section we present test results from a systematic study of grain crushing in a variety of test types and stress paths to several different peak stresses. By relating the measured grain crushing to the stress-strain data from the various tests, it is hoped that we can gain insight into the similarities and differences between the different types of loadings on the microscopic levels, and particularly into the differences and similarities between the microscopic response of granular materials under shear and compressive loadings. The data presented in this section will support our investigation and analysis of grain crushing during the coming year.

#### 7.2 TEST DESCRIPTIONS

A series of nine drained compression tests, listed in Table 7.1, was run on well rounded Enewetak beach sand samples which had been sieved and sorted so that all the pretest material was retained on the number 40 sieve and had a grain size ranging from 0.425 to 0.60 mm. All test samples were cylindrical

with a nominal diameter of 2 in and length of 4 in. All samples were loaded in a triaxial vessel along one of four stress paths:

1. hydrostatic compression (HY) to pressures of 1,000 psi and 10,000 psi;
2. uniaxial strain compression ( $K_0$ ) to mean stresses of approximately 1,000 psi and 10,000 psi;
3. triaxial compression (TXC) to mean stresses of approximately 1,000 psi, 10,000 psi and 15,300 psi; and
4. triaxial shear at constant mean stresses (TXS) of approximately 1,000 and 10,000 psi.

The stress paths are shown on a plot of stress difference vs. mean stress in Figures 7.1a and b. The hydrostatic loading (HY) simply moves along the mean stress axis with no shear stress generated. The  $K_0$  uniaxial loading follows a stress path governed by the sample as it deforms axially with no lateral strain permitted. The triaxial compression test (TXC) follows a prescribed stress path as the sample is loaded axially under a constant confining pressure. The confining pressure (either 630 psi or 8,400 psi) was computed so that the final stress state would approximately equal that from the corresponding  $K_0$  test. Two TXC tests were run at 8,400 psi confining pressure; test G5DE7 to a mean stress of about 10,000 psi and test U23AB7 to a mean stress of 15,350 psi. The triaxial shear tests (TXS) were run at constant mean pressures to approximately the same final stress states as the corresponding  $K_0$  and TXC tests.

### 7.3 TEST RESULTS

Post-test microscopic views of representative grain samples showing the grain damage are presented in Figures 7.2a through c. In Figure 7.2a, a pre-test sample is compared to a post-test sample from test U23AB7, the TXC test to 15,350 psi mean stress. The uniform well rounded nature of the grains is



apparent in the virgin material. Also note the presence of microporosity visible in some of the individual grains. Extensive grain fracturing and crushing is evident in the post-test sample, with only a few grains apparently having survived intact. Most of the post-test material has been broken into a wide variety of grain sizes.

Figure 7.2b shows post-test microscopic views of material from the four tests run to a peak mean stress of about 1,000 psi. Qualitatively, there appears to be little difference between the four samples. In all cases only minor grain damage is apparent, with a modest number of grains broken into large pieces and creation of only a small amount of finer grain sizes.

Microscopic views of the material from the four 10,000 psi mean stress tests are compared in Figure 7.2c. Grain damage is substantially more pervasive than that from the 1,000 psi tests, but again there does not appear to be a significant difference in damage between the four tests. The 10,000 psi results show a more well graded post-test grain distribution than the 1,000 psi tests, with numerous medium sized and small sized grains in evidence.

The post-test grain size distributions from the nine tests are plotted in parts "a" of Figures 7.3 through 7.11, and listed in Table 7.1. The distributions are plotted as percent by weight within a given size interval as a function of the log of the interval. Thus each interval is represented by an equal width and the area within each interval is proportional to the weight of material having grain sizes within the interval. Gradations were not run on material passing the number 200 sieve (smaller than 0.075 mm). For convenience all such material was lumped into a single grain interval equal in width to the others, but delineated by a dashed line such as shown in Figure 7.11a.

Figures 7.12 and 7.13 compare the post-test grain size distributions from the 1,000 psi and 10,000 psi mean stress tests, respectively. The samples loaded to 1,000 psi mean effective stress sustained only minor grain damage, with between 3% and 7% of the pretest grains being broken into a smaller size interval. Most of the broken grains only moved to the next smaller interval,

suggesting that the original grains sustained only one or two fractures. This conclusion is supported qualitatively by the post-test microscopic views of Figure 7.2b. The material loaded in the hydrostatic test received the least amount of damage, with only 2.8% of the grains broken to a smaller size. The three samples loaded in combined hydrostatic and shear stress sustained somewhat more damage (between 5.3% and 6.7% broken to a smaller size). The amount of damage to these three samples is very similar in all cases and appears to be independent of the stress path used to reach the final state of stress.

The comparison of grain damage for the 10,000 psi mean stress tests shown in Figure 7.13 shows a moderate to high degree of damage, 36% to 49% of the grains broken into a smaller size interval. In all cases, grain breakage is much more extensive than breakage from the 1,000 psi loadings, with a well graded distribution of broken grains being created. Again, the material loaded in hydrostatic compression sustained the least damage, with 36.4% of the grains reduced in size. Damage from the combined hydrostatic and shear loadings ranged from 42.2% for the TXC test to 49.1% for the  $K_0$  test. The differences between these three is not thought to be significant, though additional testing would be required to substantiate this.

While the material loaded in hydrostatic compression sustained less damage in both test series, the difference in damage between the hydrostatic tests and the shear tests is quite small. Additional tests at 10,000 psi mean stress but with higher shear stress components are planned to better define the influence of shear stress on grain damage. Severe grain damage was sustained by the triaxial sample loaded under the same 8,400 psi confining pressure as the 10,000 psi mean stress sample, but carried to a maximum mean stress of 15,350 psi and a maximum stress difference of 20,900 psi. Nearly 80% of the grains were reduced in size, with over half the total post-test weight having grain sizes of less than .106 mm.

In order to briefly, but quantitatively, describe the grain damage we developed a technique which uses the pretest and post-test log mean grain sizes to compute a grain damage factor,  $D_f$ , given by

$$D_f = \frac{D_o - D_b}{D_o - D_m} \quad (7-1)$$

where

$D_o$  = pre-test log mean grain size

$D_b$  = post-test log mean grain size

$D_m$  = minimum measured grain size interval

The log mean grain size represents the center of mass of the grain size and weight fraction semi-log histograms in terms of grain size. Thus all of the pretest samples have a mean grain size of 0.50 mm, while the post-test mean grain sizes range from 0.495 mm for the 1,000 psi HY test (Y4A7) to 0.177 mm for the 15,350 psi mean stress TXC test (U23AB7).

The grain damage factor is a measure of both the amount and severity of the grain damage. A sample with most of its grains crushed to a fine powder will have a much larger grain damage factor than a sample with most of its grains broken into only slightly smaller pieces. As shown in Table 7.1, the grain damage factor ranges from 0.011 for the 1,000 psi HY sample to 0.743 for the 15,350 mean stress TXC sample. The maximum grain damage factor is 1.0.

The stress-strain response of the material in the nine loading tests is presented in parts b through h of Figures 7.3 through 7.11. These test results will be used in future analysis to compare the plastic work done on the samples to grain damage, and to evaluate grain damage as a function of other response parameters.



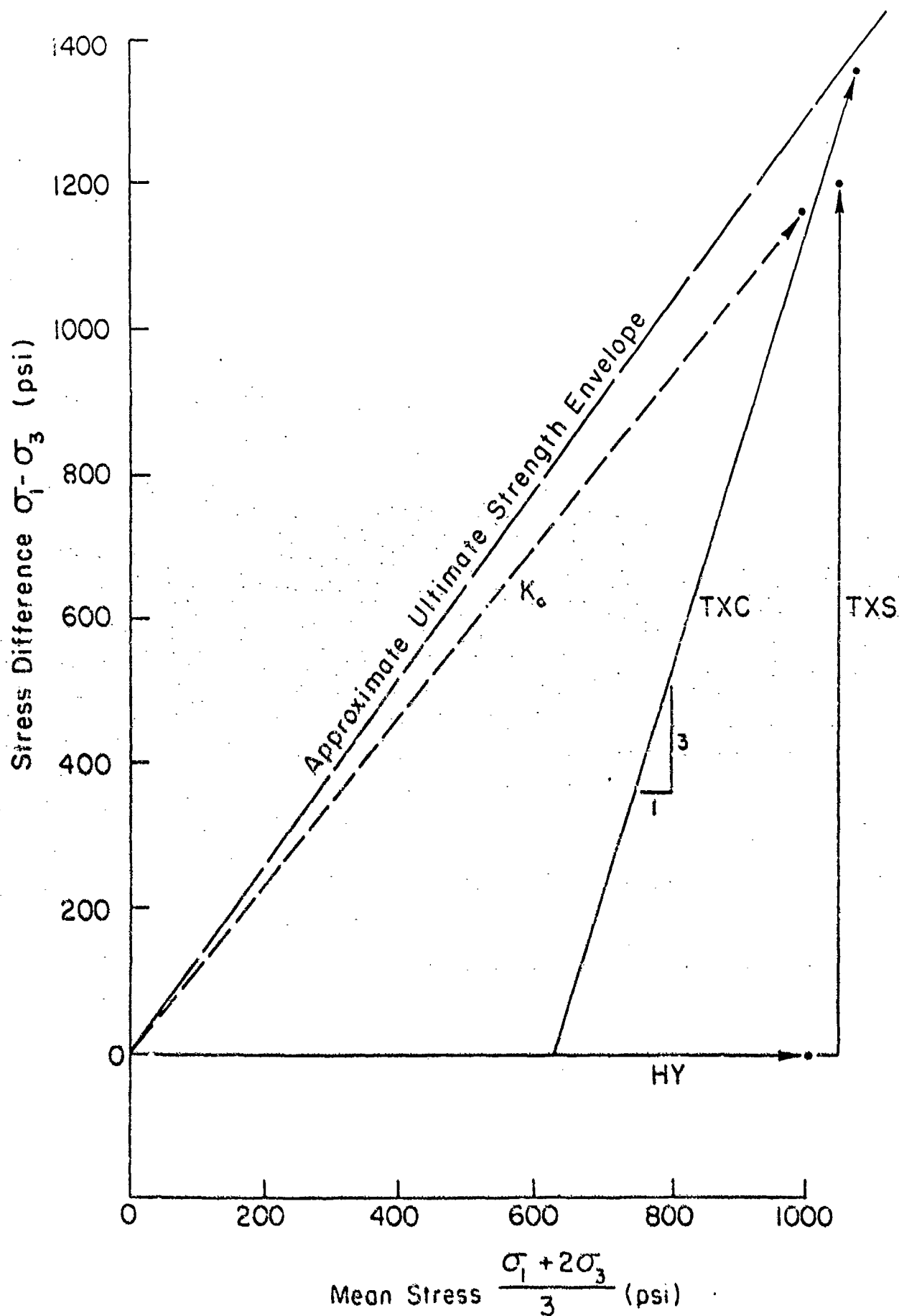


Figure 7.1a. Stress paths to approximate mean stress of 1,000 psi.

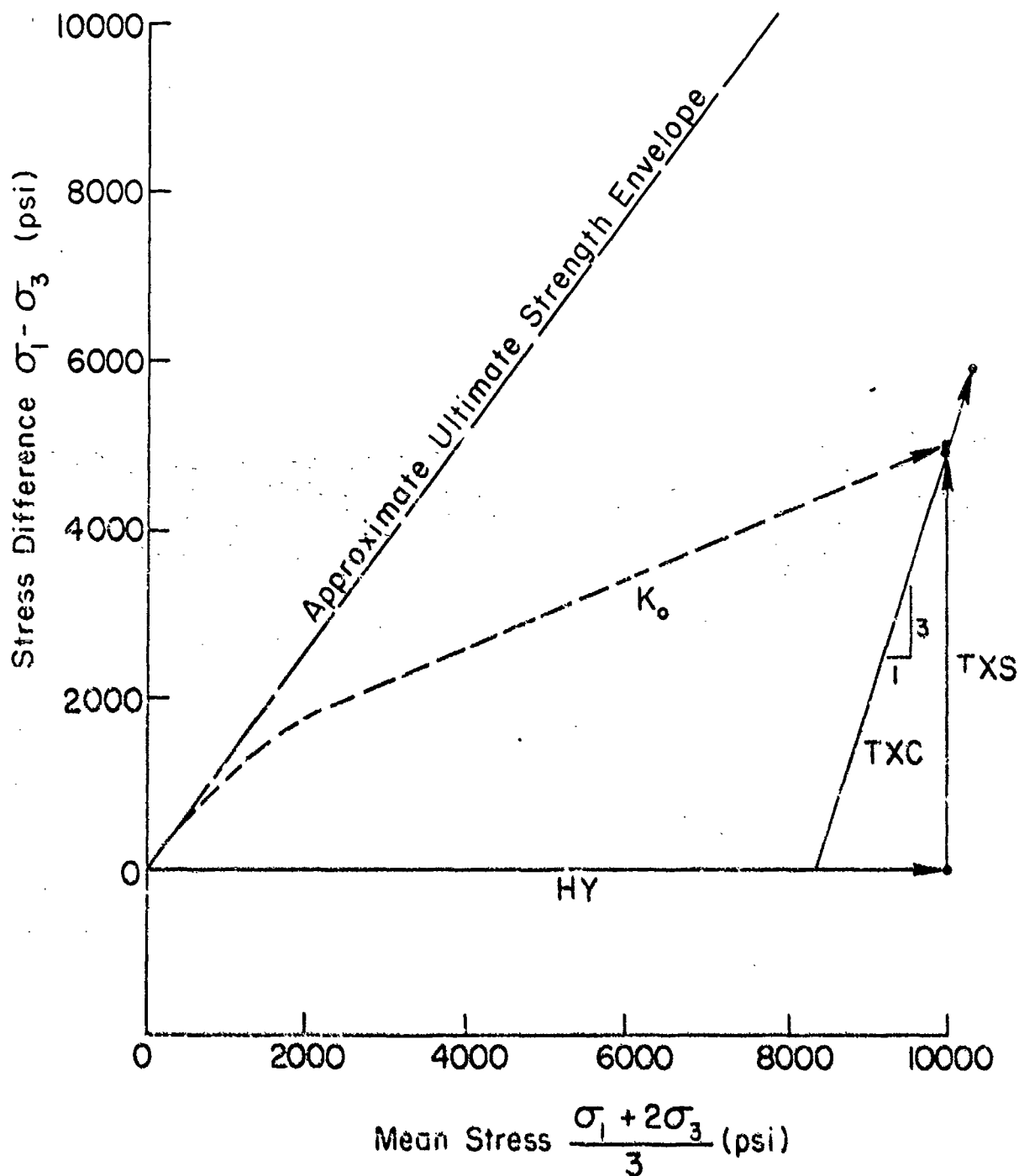
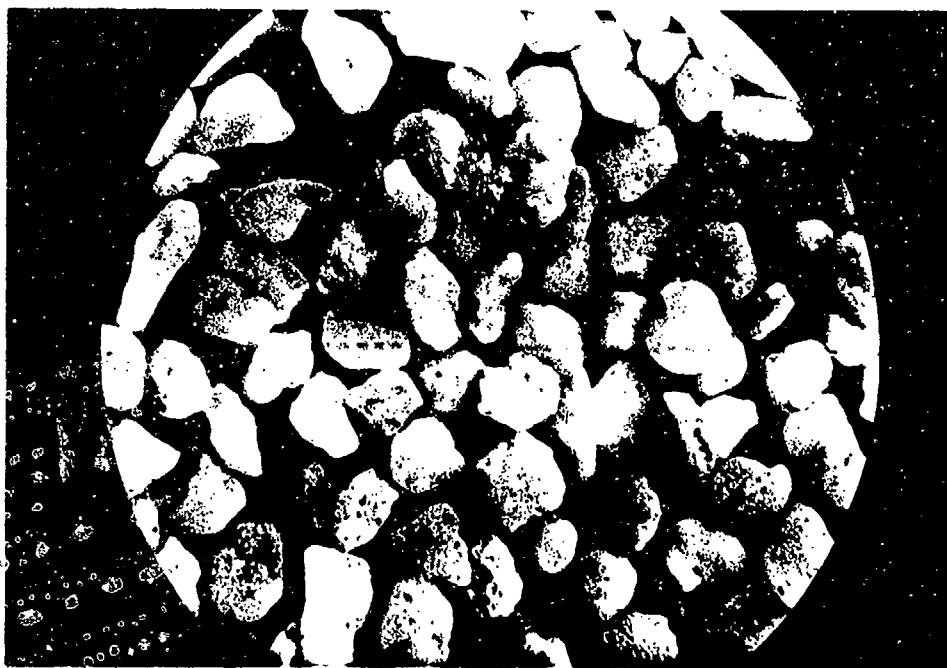
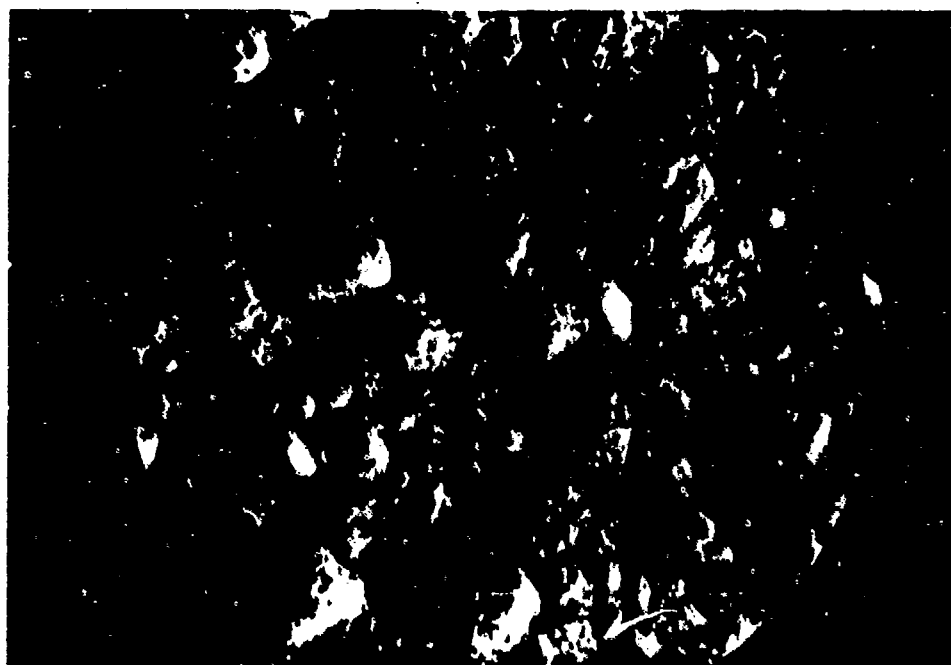


Figure 7.1b. Stress paths to approximate mean stress of 10,000 psi.



a. Virgin sand



b. Post test sand

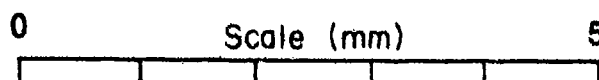
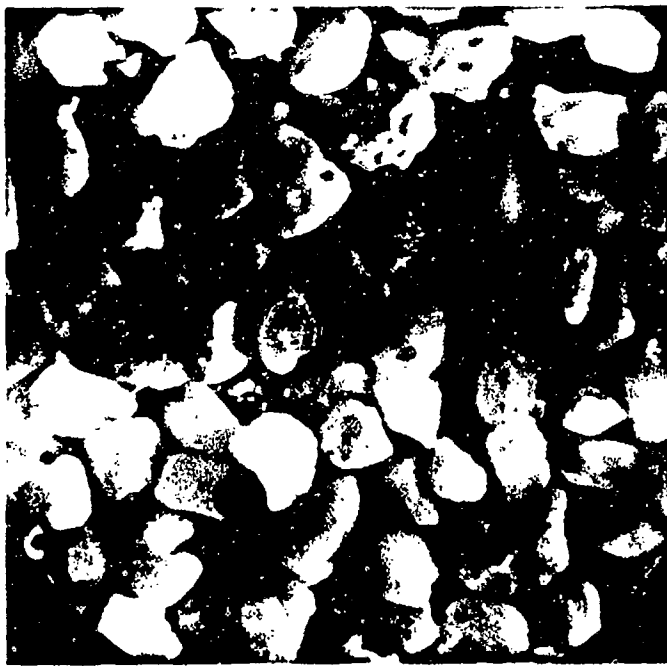


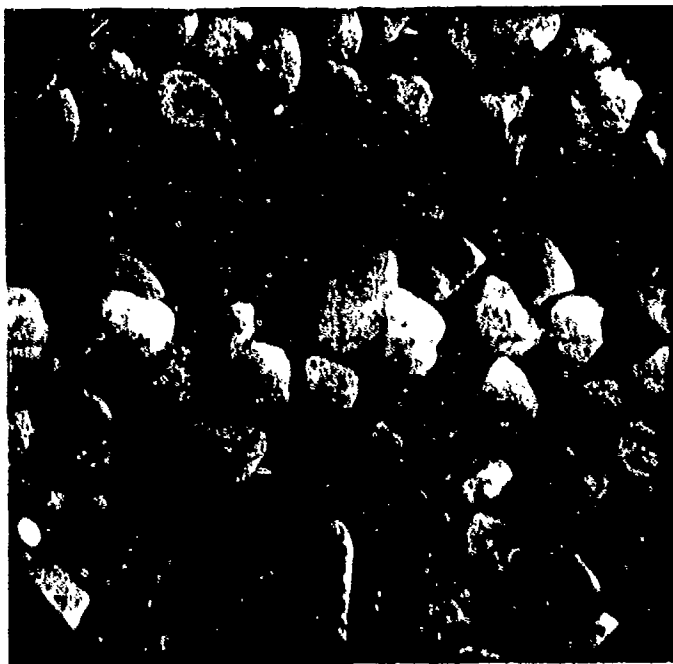
Figure 7.2a. Microscopic comparison of virgin beach sand with post-test sample loaded in triaxial compression to a mean stress of 15,300 psi.



a. Hydrostatic



B.  $K_0$  Triaxial



c. Triaxial compression



d. Triaxial shear at constant mean stress

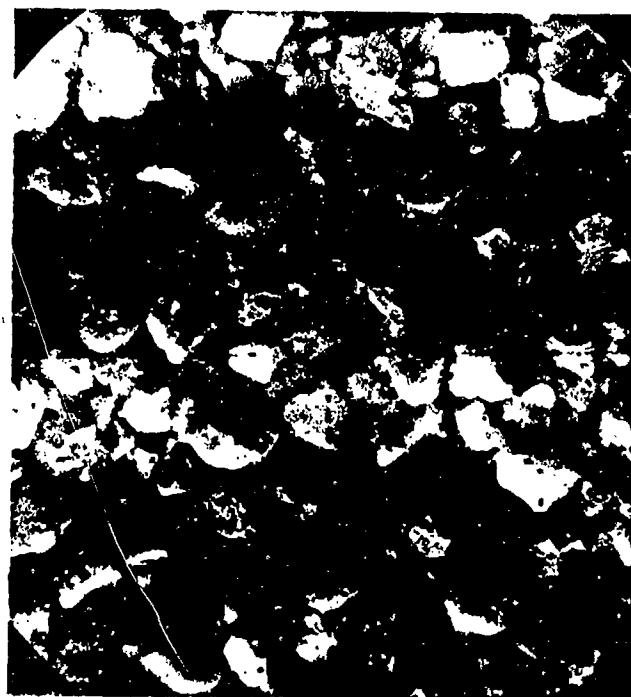
0 Scale (mm) 5

Figure 7.2b. Microscopic comparison of beach sand samples loaded along various stress paths to a mean stress of approximately 1000 psi.





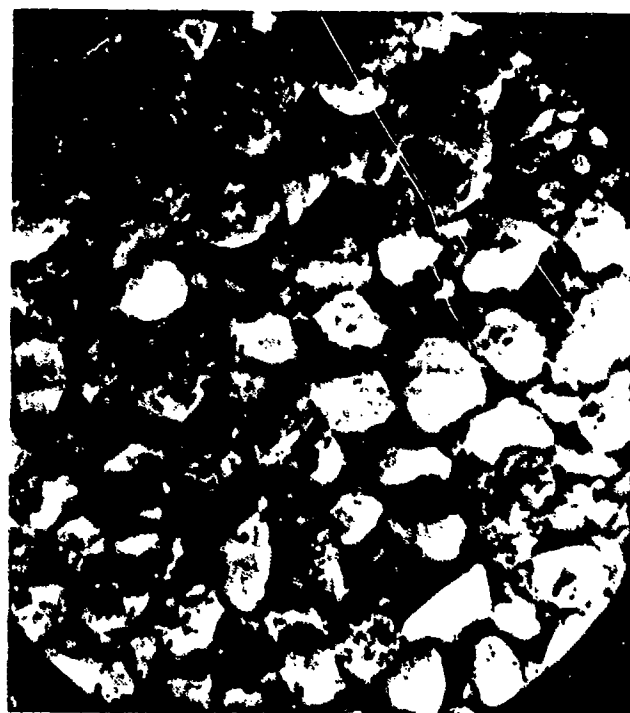
a. Hydrostatic



b.  $K_0$  Triaxial



c. Triaxial compression



d. Triaxial shear at constant mean stress

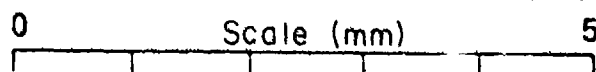


Figure 7.2c. Microscopic comparison of beach sand samples loaded along various stress paths to a mean stress of approximately 10,000 psi.

# Grain Size Distribution Y4A7

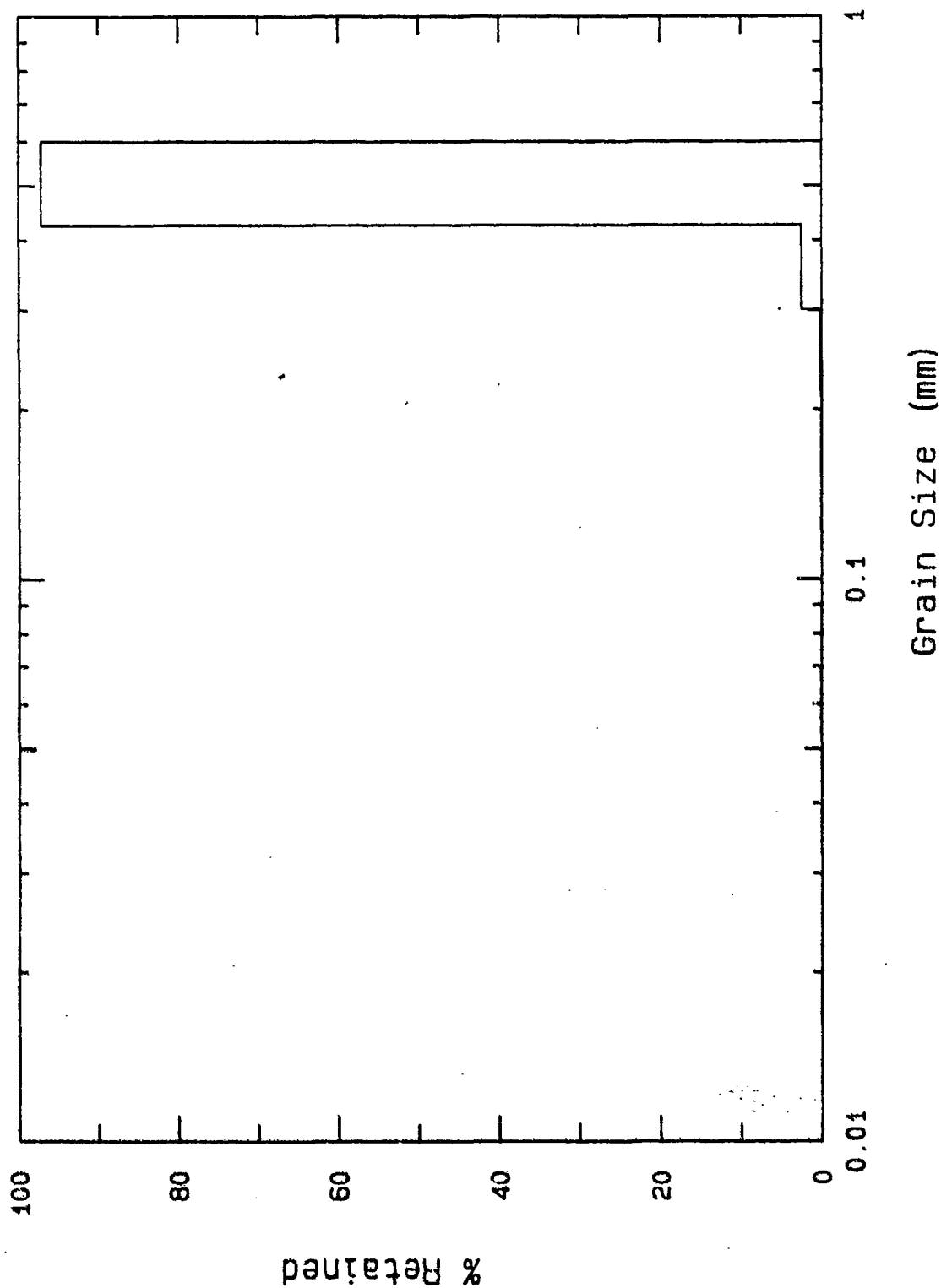


Figure 7.3a. Post-test grain size and weight-fraction distribution following hydrostatic drained loading to 1000 psi.

Hydrostat (Y4A7)  
Beach Sand

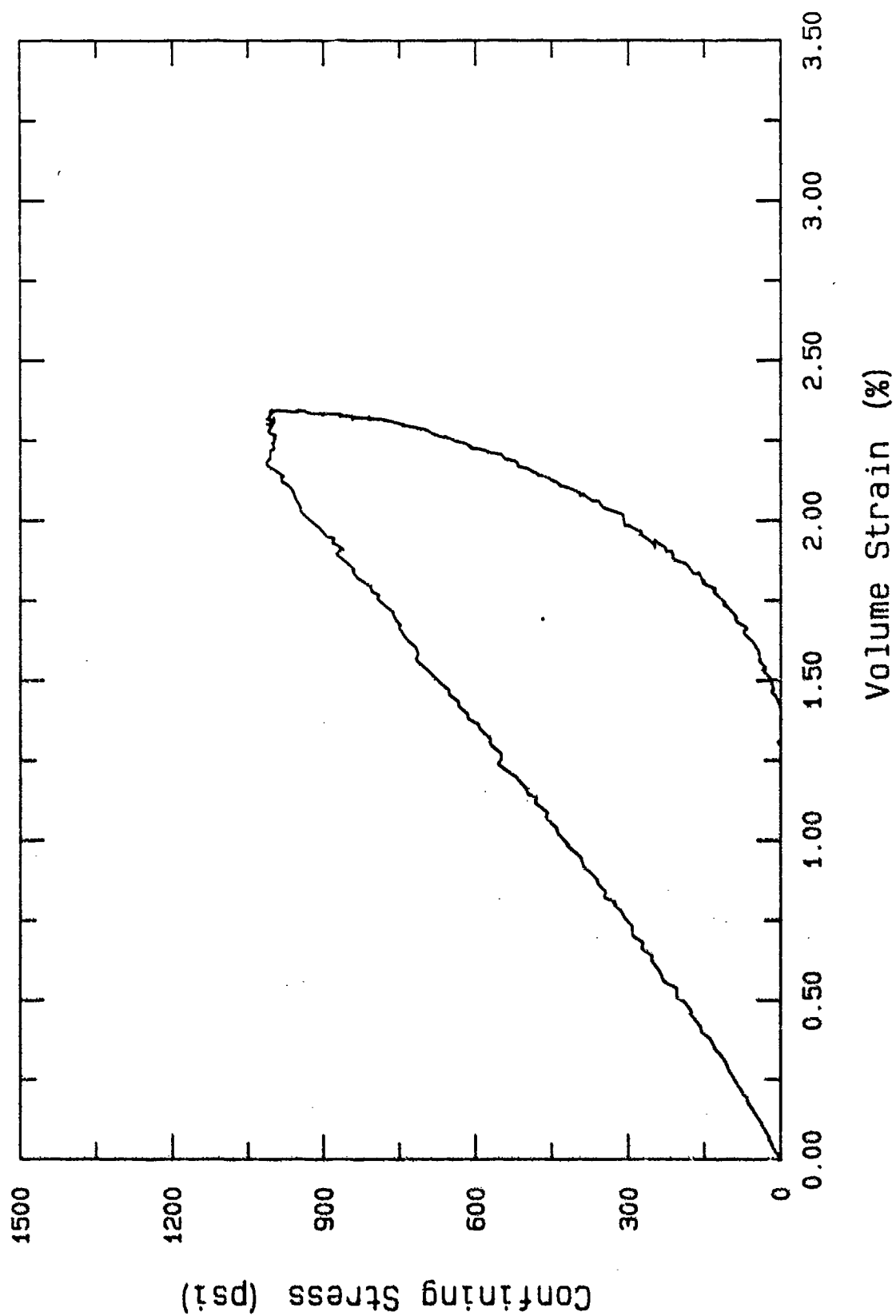


Figure 7.3b. Pressure-volume strain data, hydrostatic loading to 1,000 psi.

# Grain Size Distribution U22A7

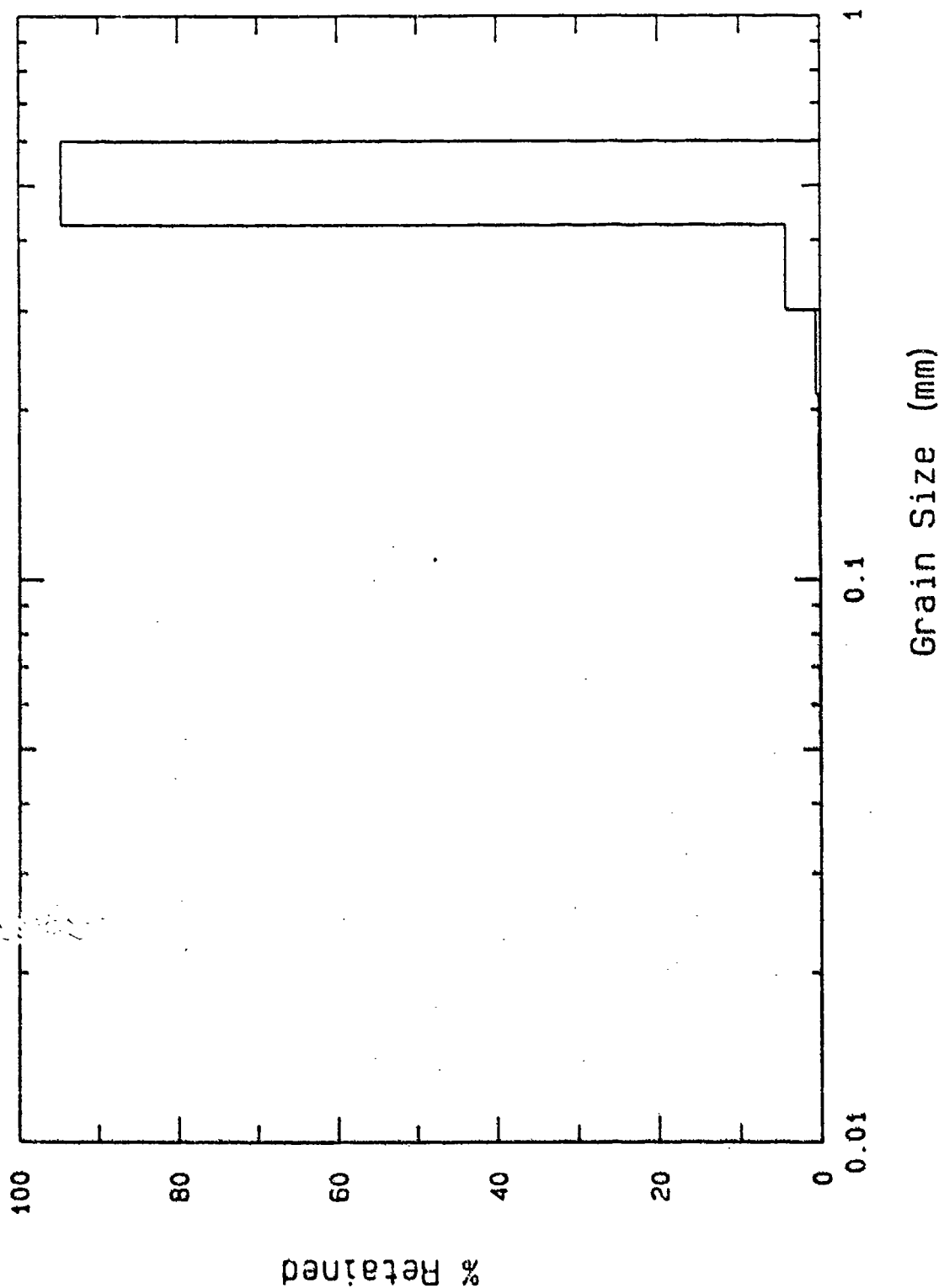


Figure 7.4a. Post test grain size and weight-fraction distribution following  $K_0$  drained loading to approximately 1000 psi mean stress.

K<sub>0</sub> (U22A7)  
Beach Sand

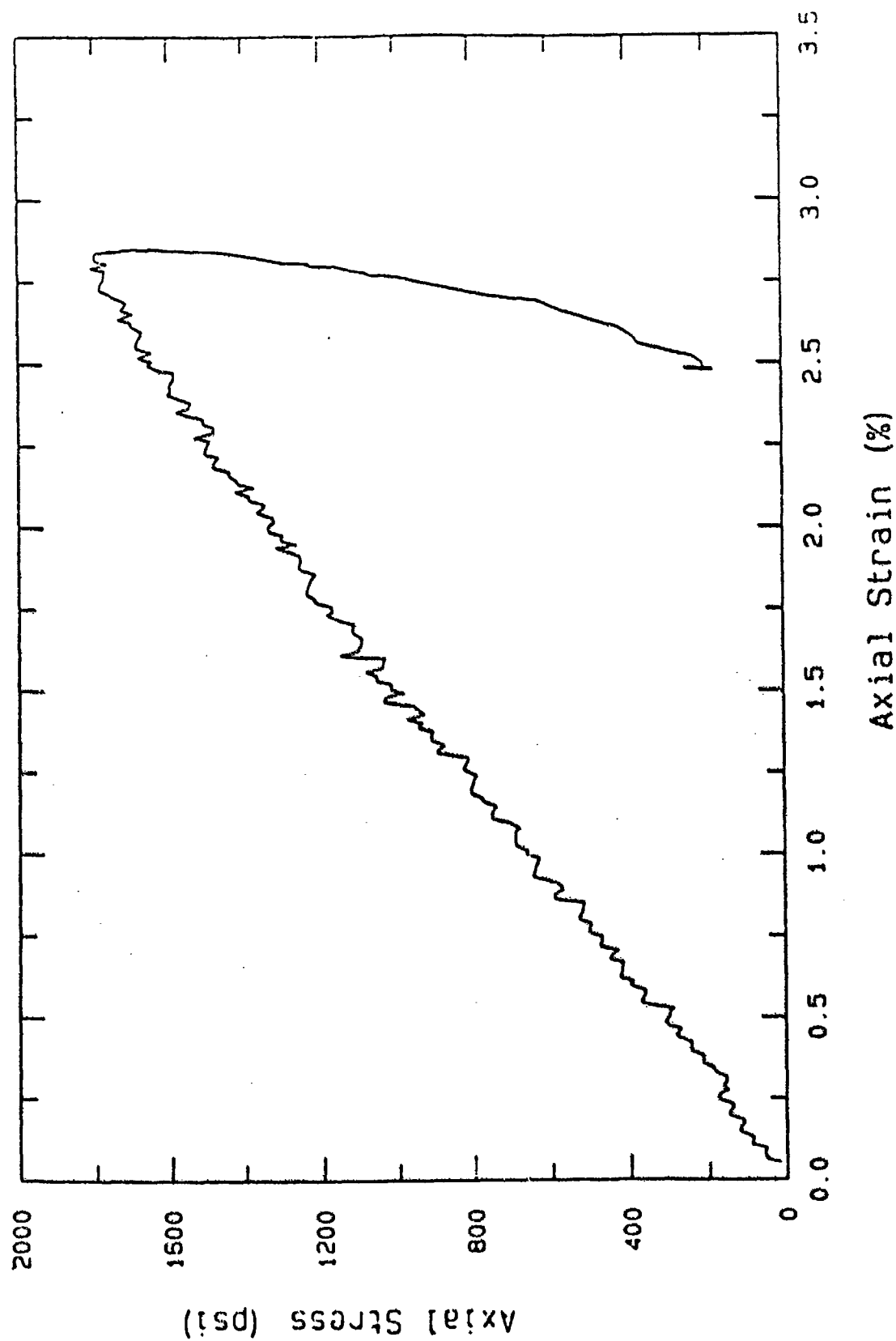


Figure 7.4b. Axial stress-axial strain data, K<sub>0</sub> loading to approximately 1000 psi mean stress.

Ko (U22A7)  
Beach Sand

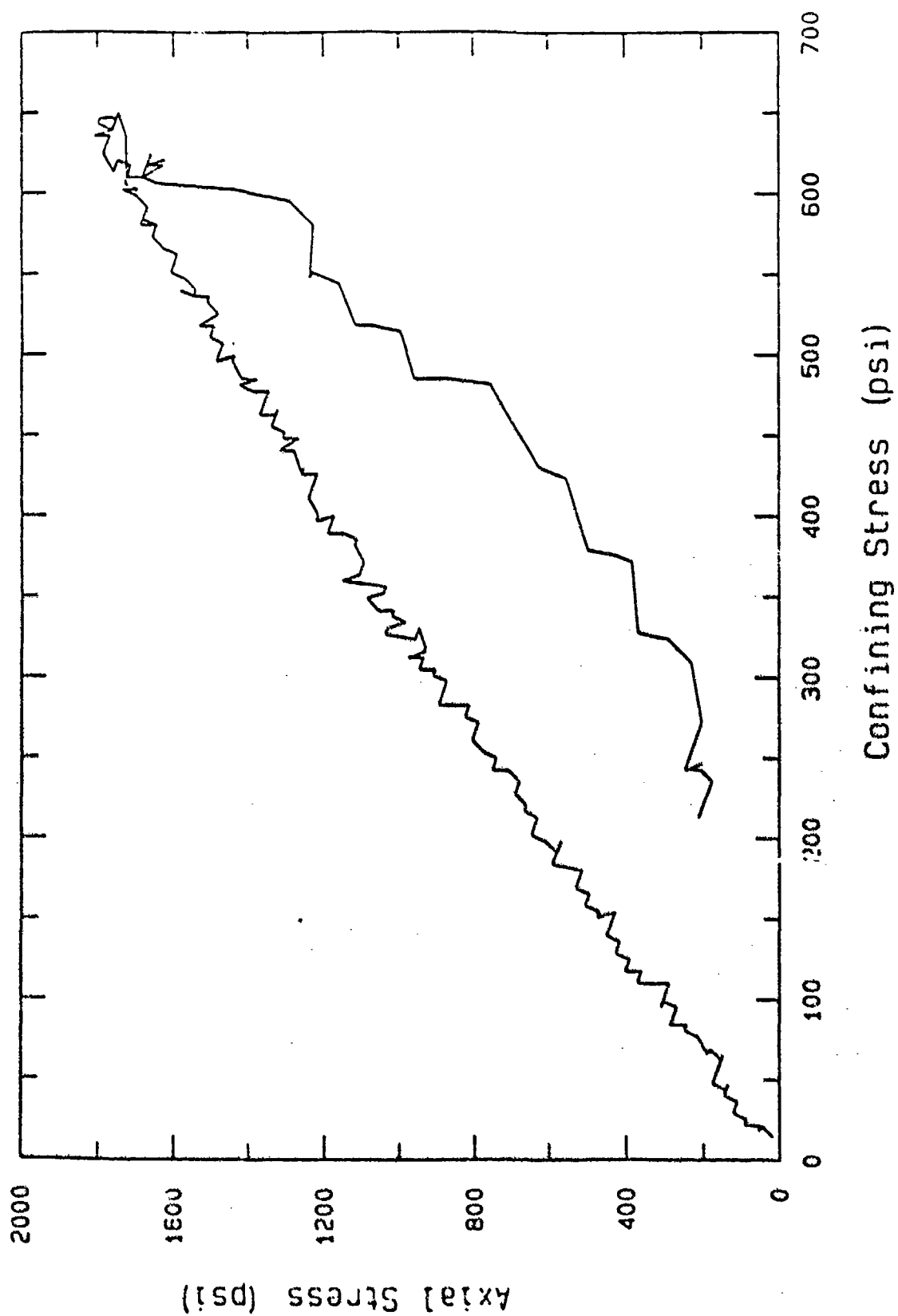


Figure 7.4c. Axial stress-confining stress data,  $K_0$  loading to approximately 1000 psi mean stress.

$K_0$  (U22A7)  
Beach Sand

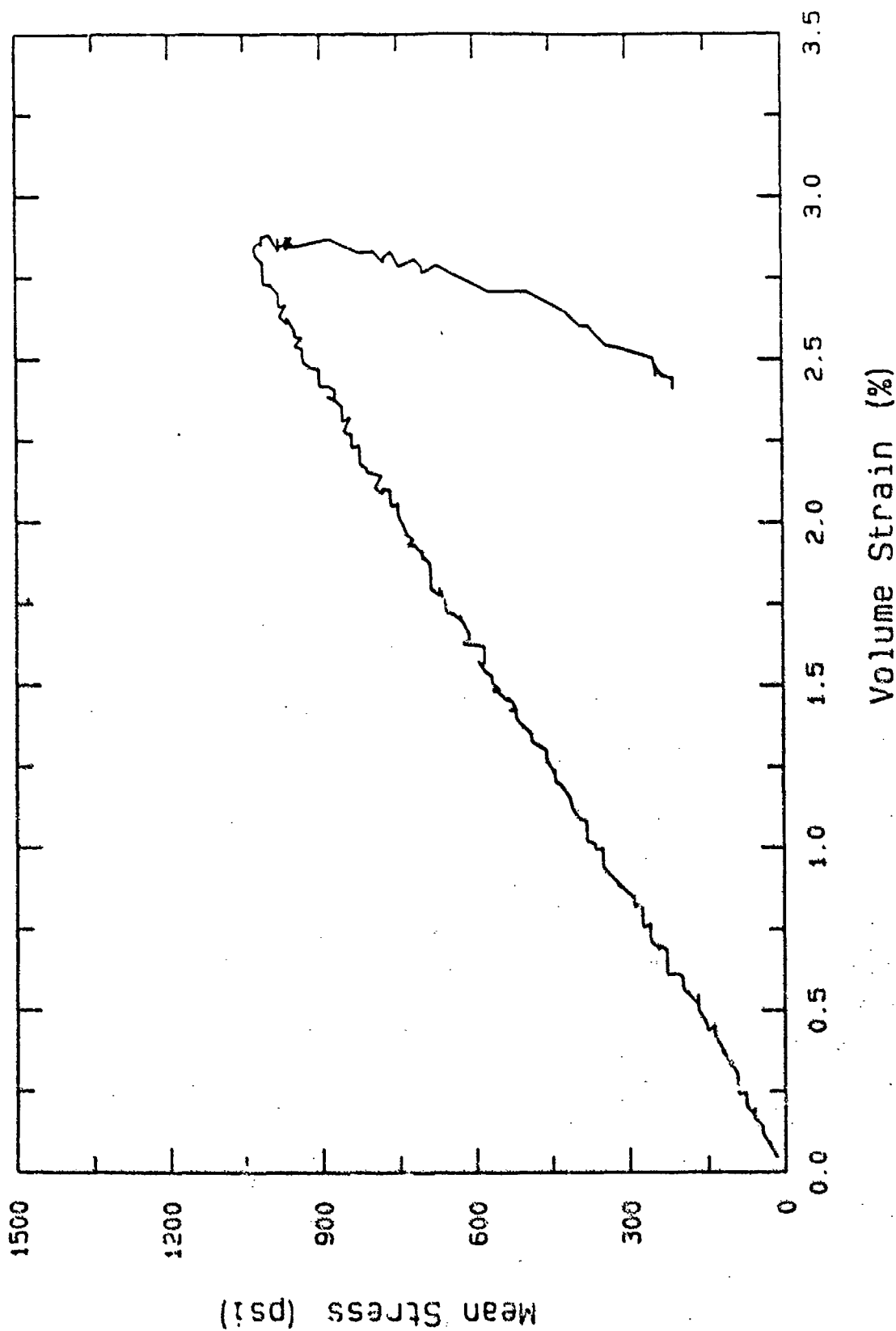


Figure 7.4d. Mean stress-volume strain data,  $K_0$  loading to approximately 1000 psi mean stress.

Ko (U22A7)  
Beach Sand

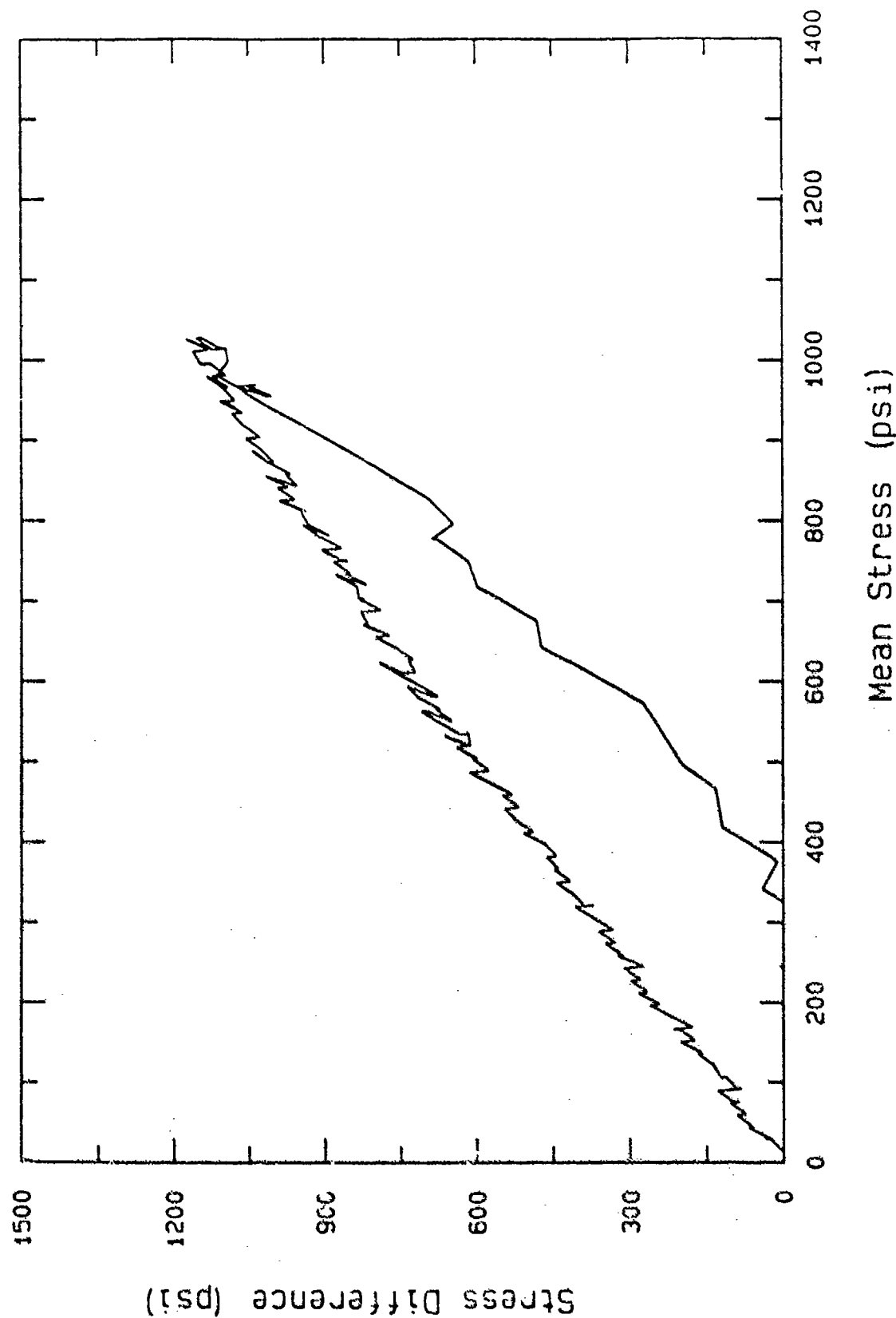


Figure 7.4e. Stress difference-mean stress data,  $K_0$  loading to approximately 1000 psi mean stress.



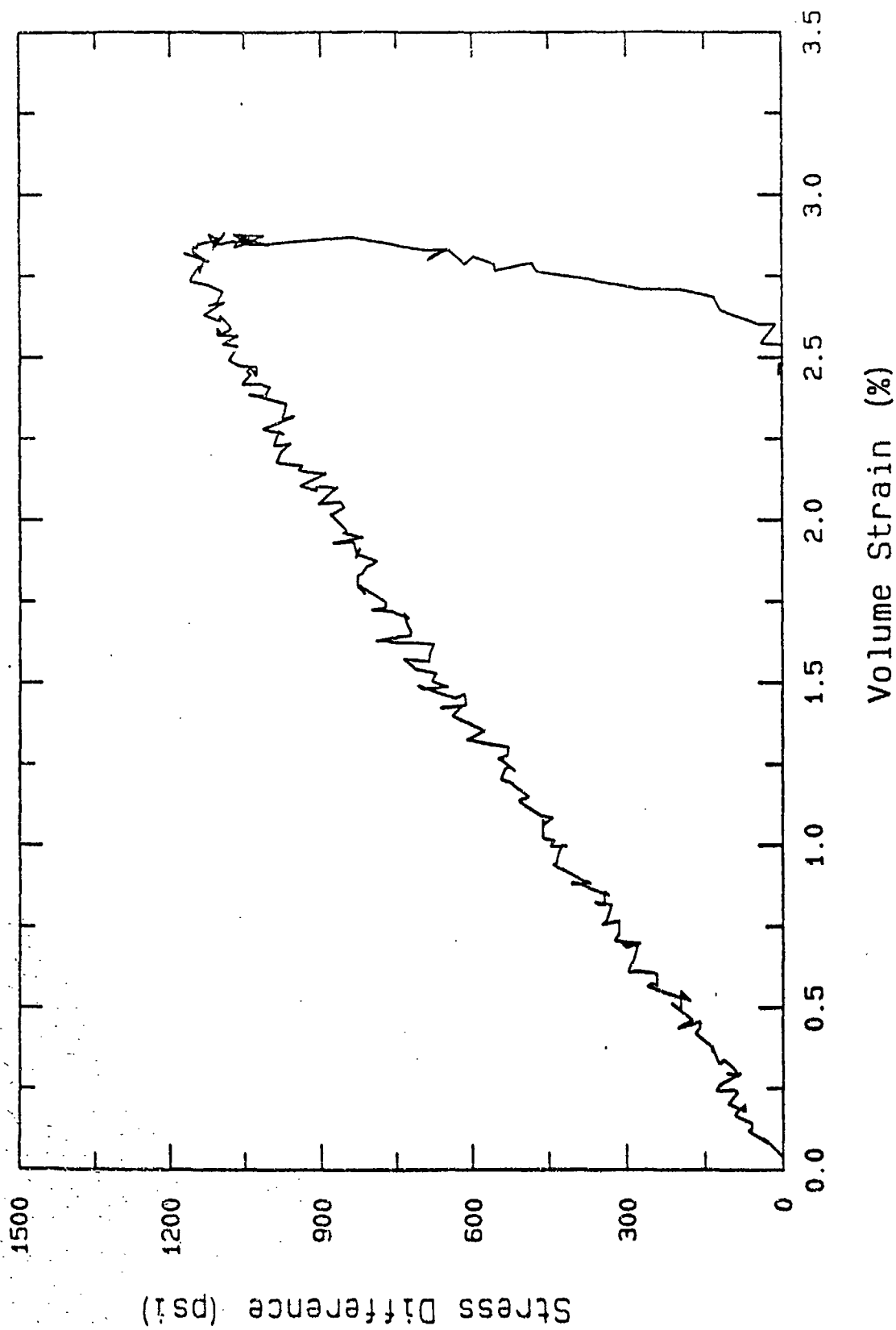


Figure 7.4f. Stress difference-volume strain data,  $K_0$  loading to approximately 1000 psi mean stress.

# Grain Size Distribution G5B&C7

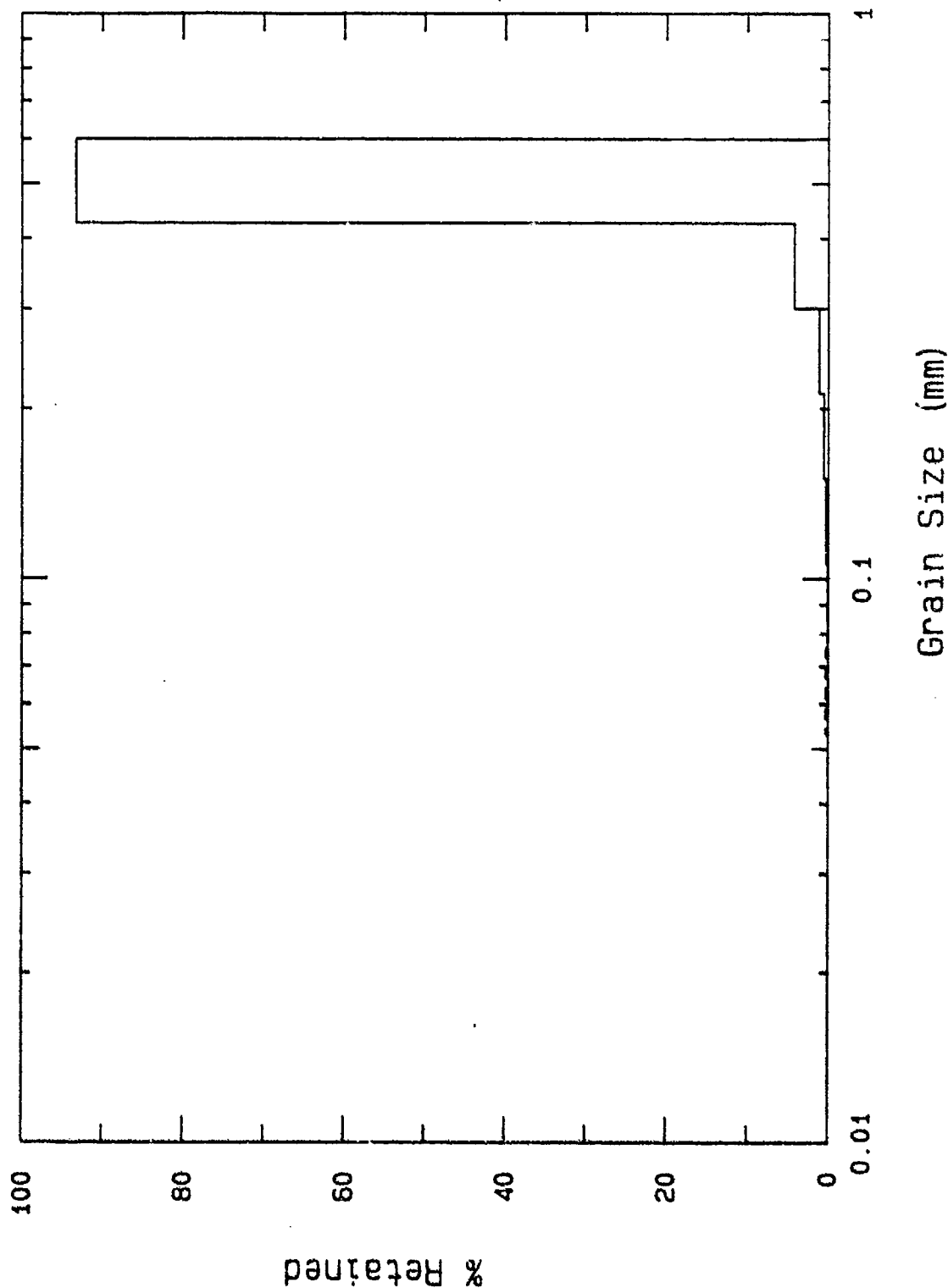


Figure 7.5a. Post-test grain size and weight fraction distribution following triaxial compression to approximately 1000 psi mean stress.

Hydrostat (G587) to 630 psi  
Beach Sand

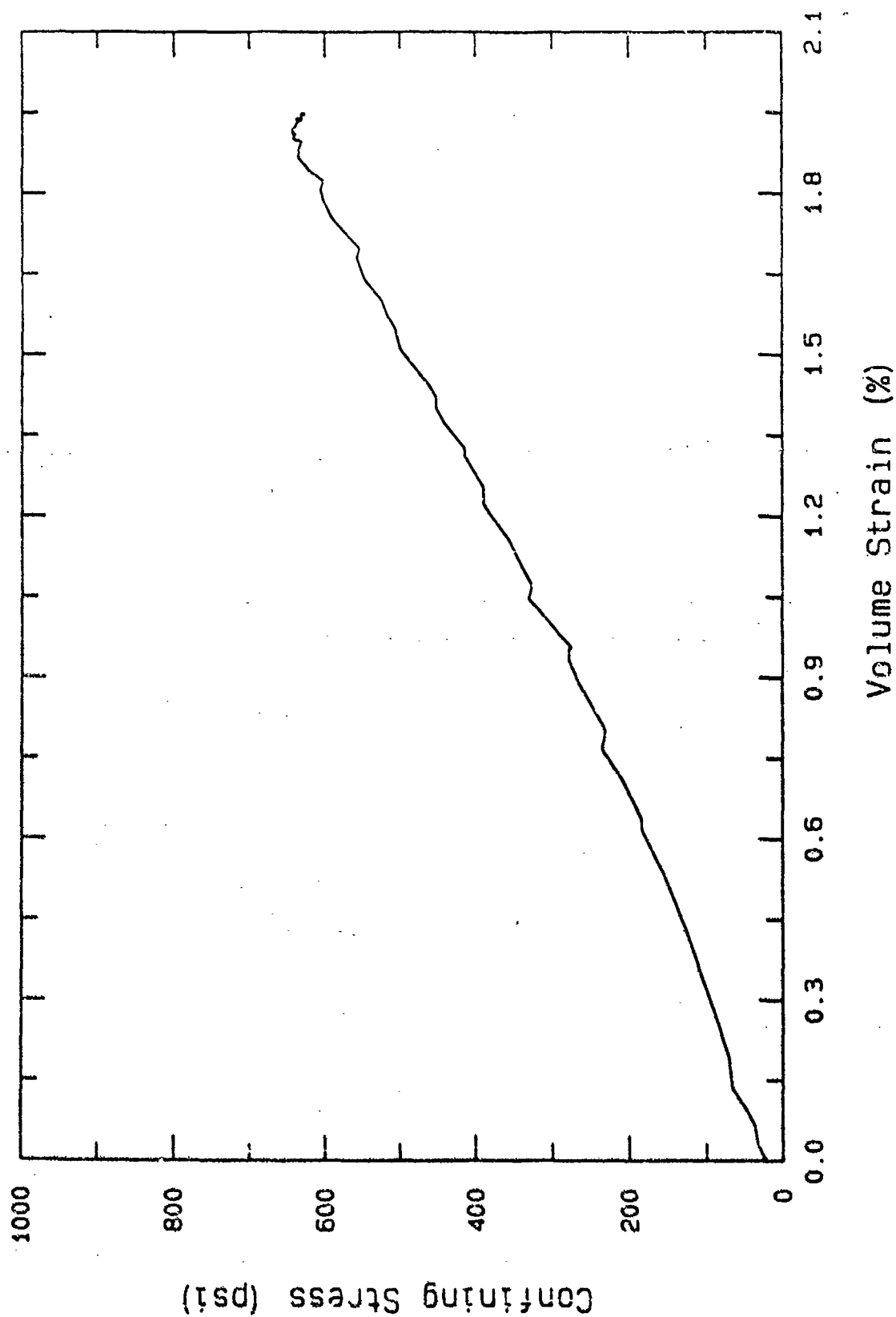


Figure 7.5b. Pressure-volume strain data to 630 psi prior to triaxial compression to approximately 1000 psi mean stress.

# Triax (G5C7) from 630 psi Beach Sand

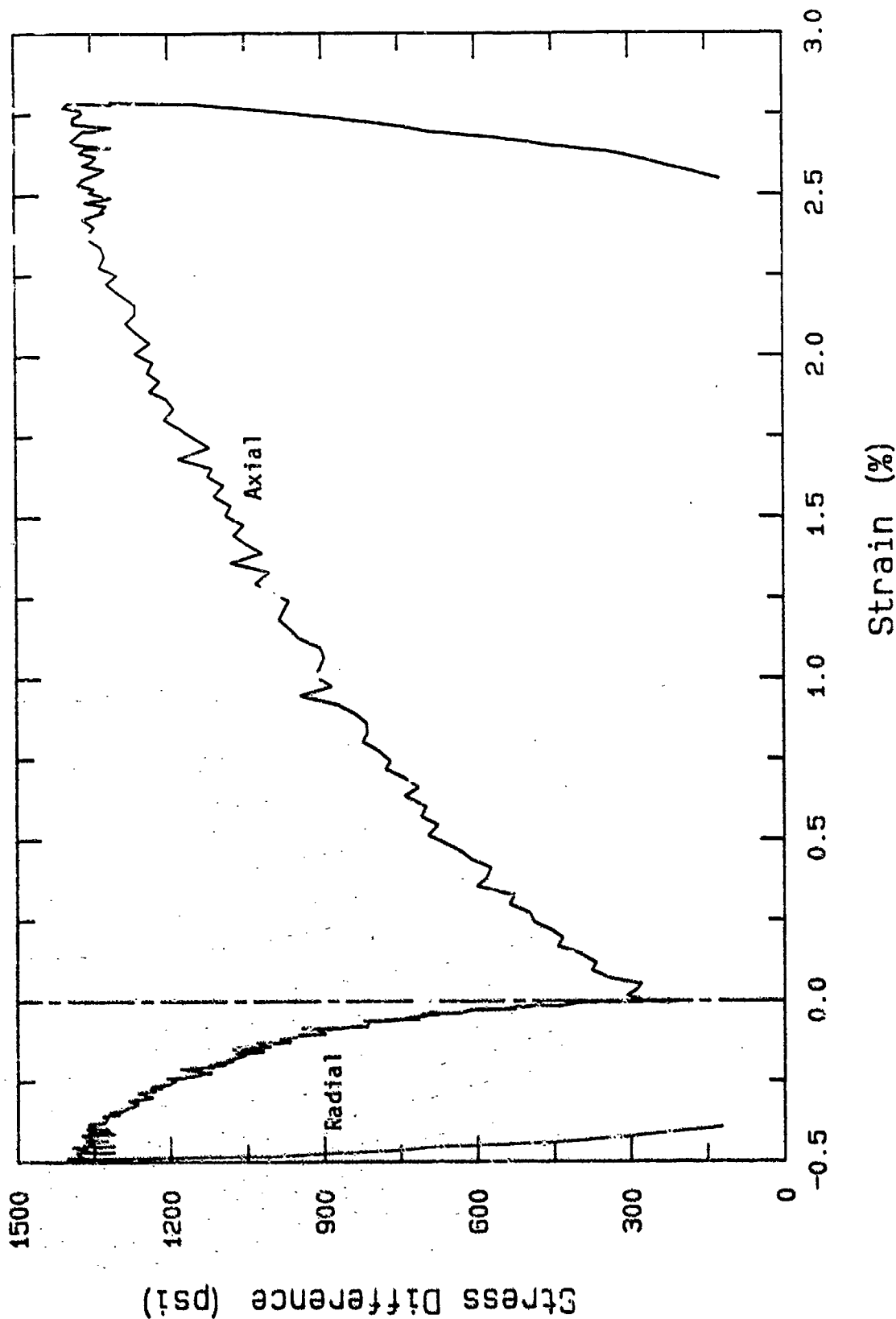


Figure 7.5c. Stress difference-axial and radial strain data, triaxial compression to approximately 1000 psi mean stress.

Triax (65C7) from 630 psi  
Beach Sand

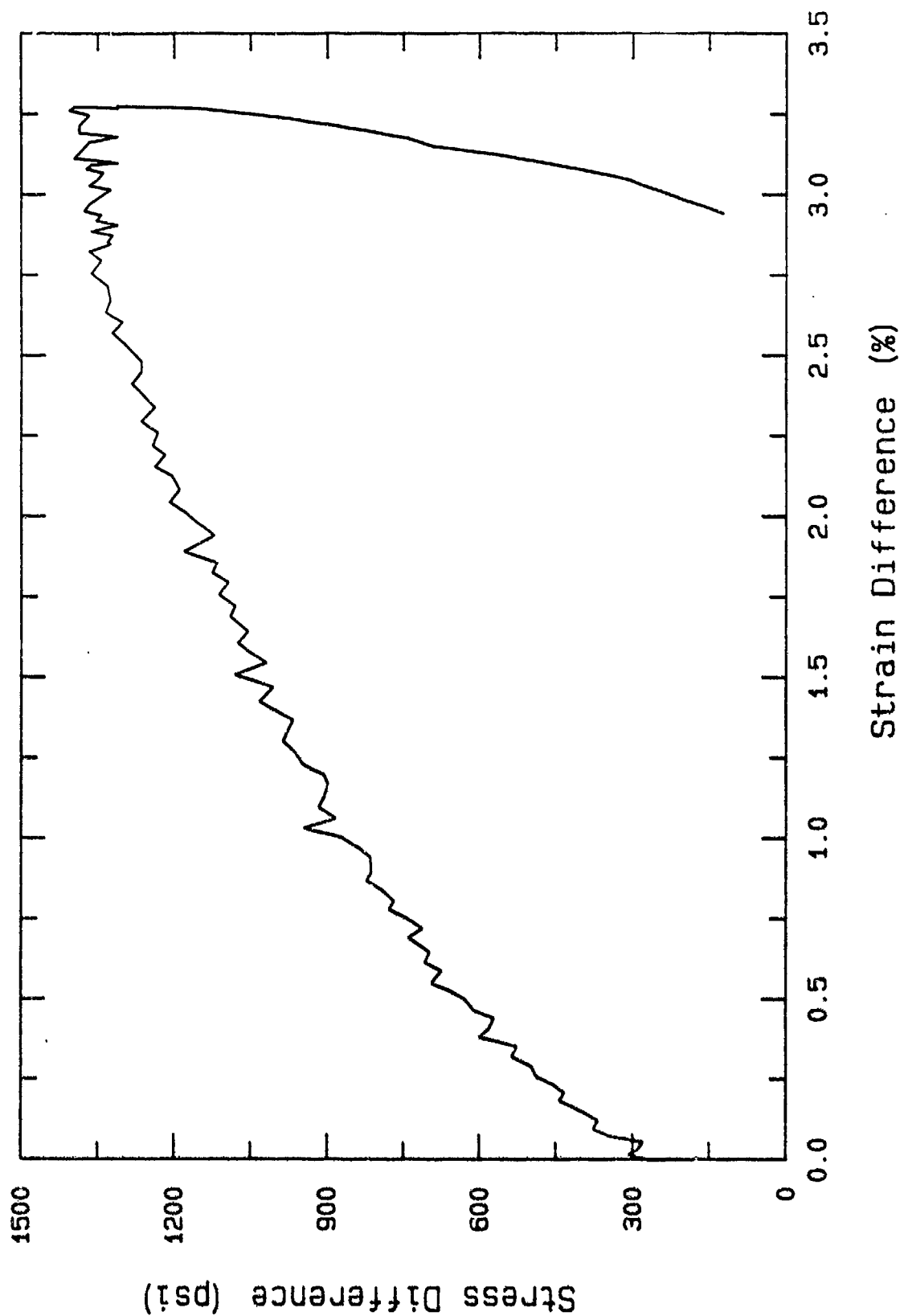


Figure 7.5d. Stress difference-strain difference data, triaxial compression to approximately 1000 psi mean stress.

Triax (G5C7) from 630 psi  
Beach Sand

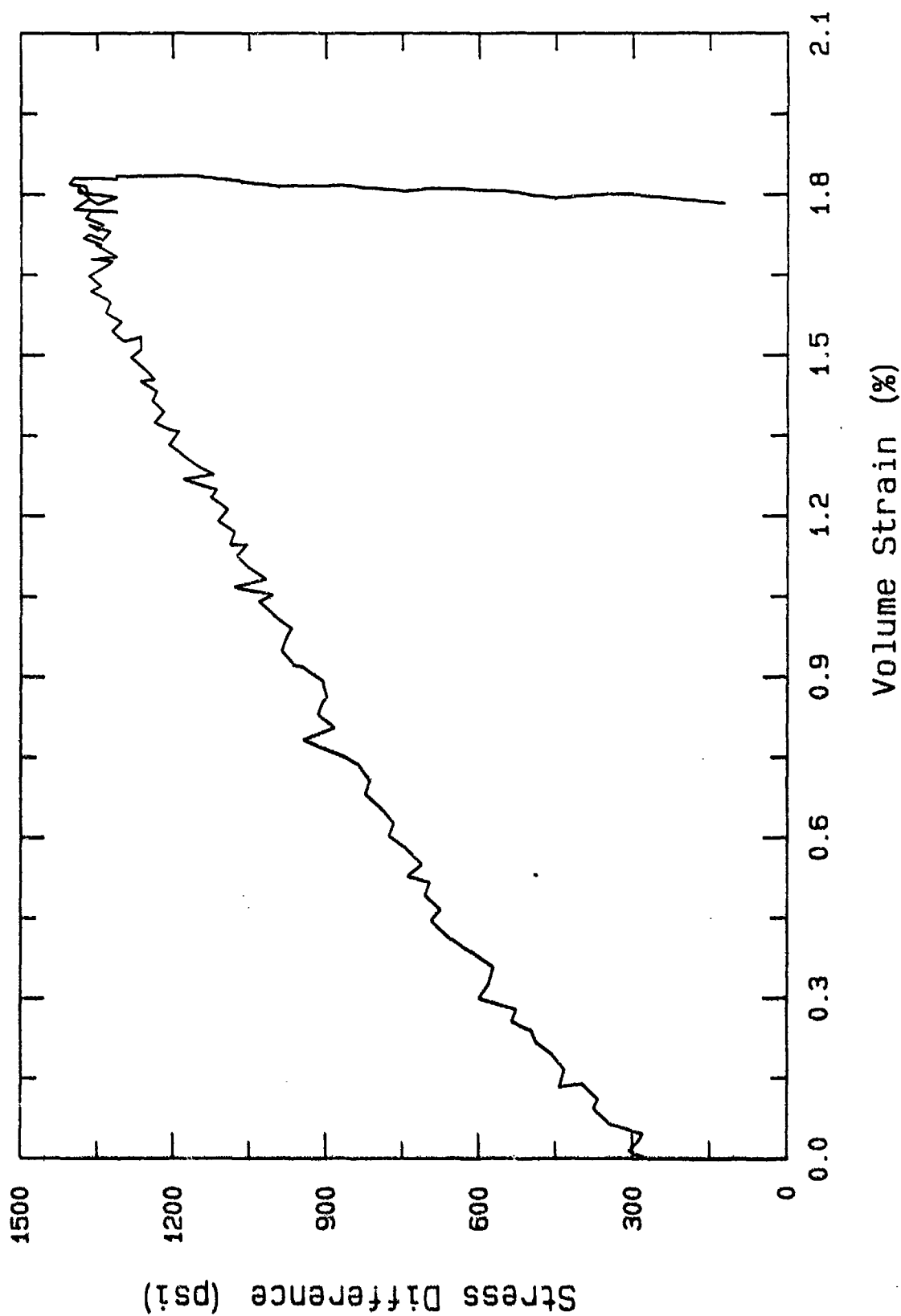


Figure 7.5e. Stress difference-volume strain data, triaxial compression to approximately 1000 psi mean stress.

Triax (G5C7) from 630 psi  
Beach Sand

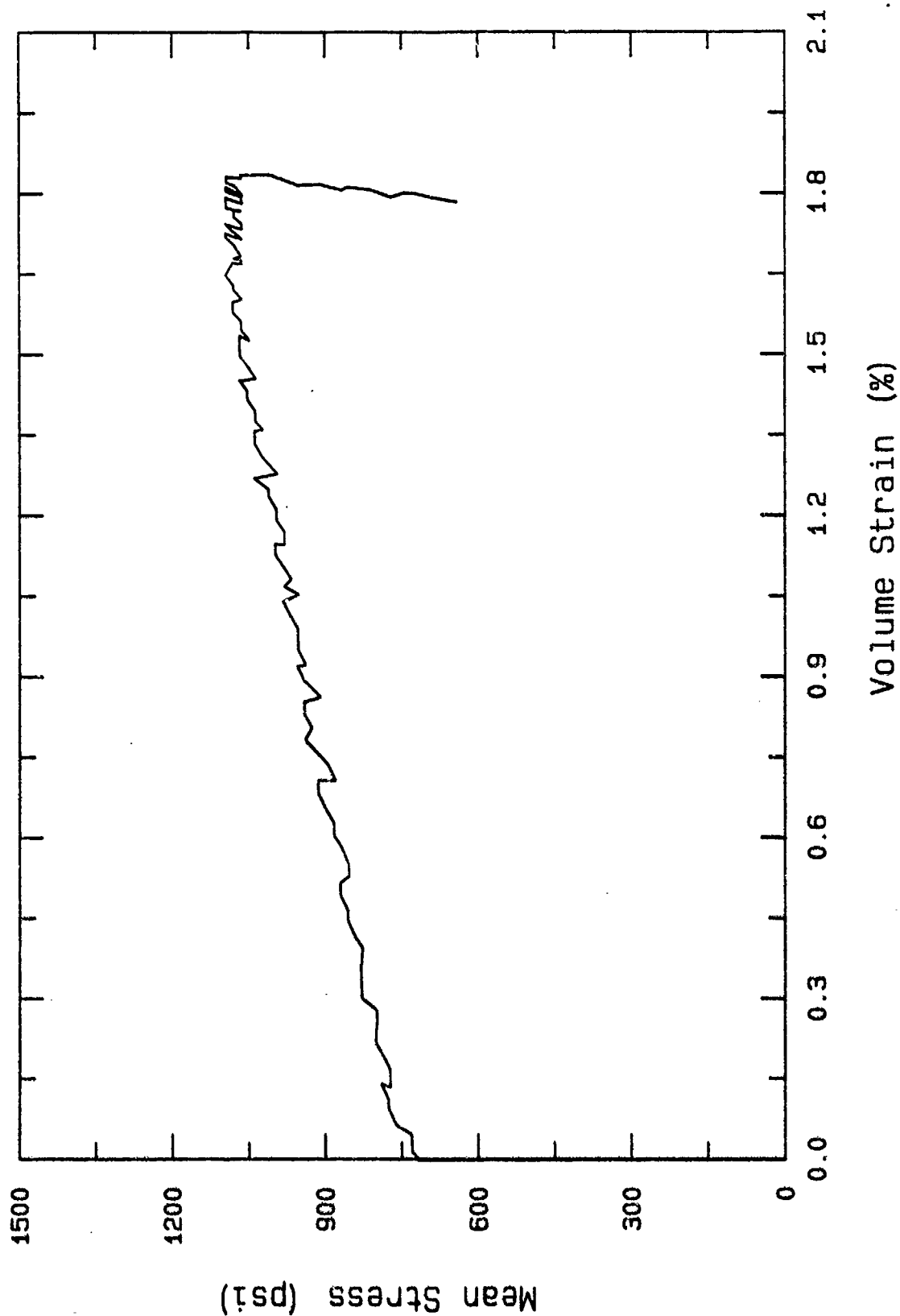


Figure 7.5f. Mean stress-volume strain data, triaxial compression to approximately 1000 psi mean stress.

Triax (G5C7) from 630 psi  
Beach Sand

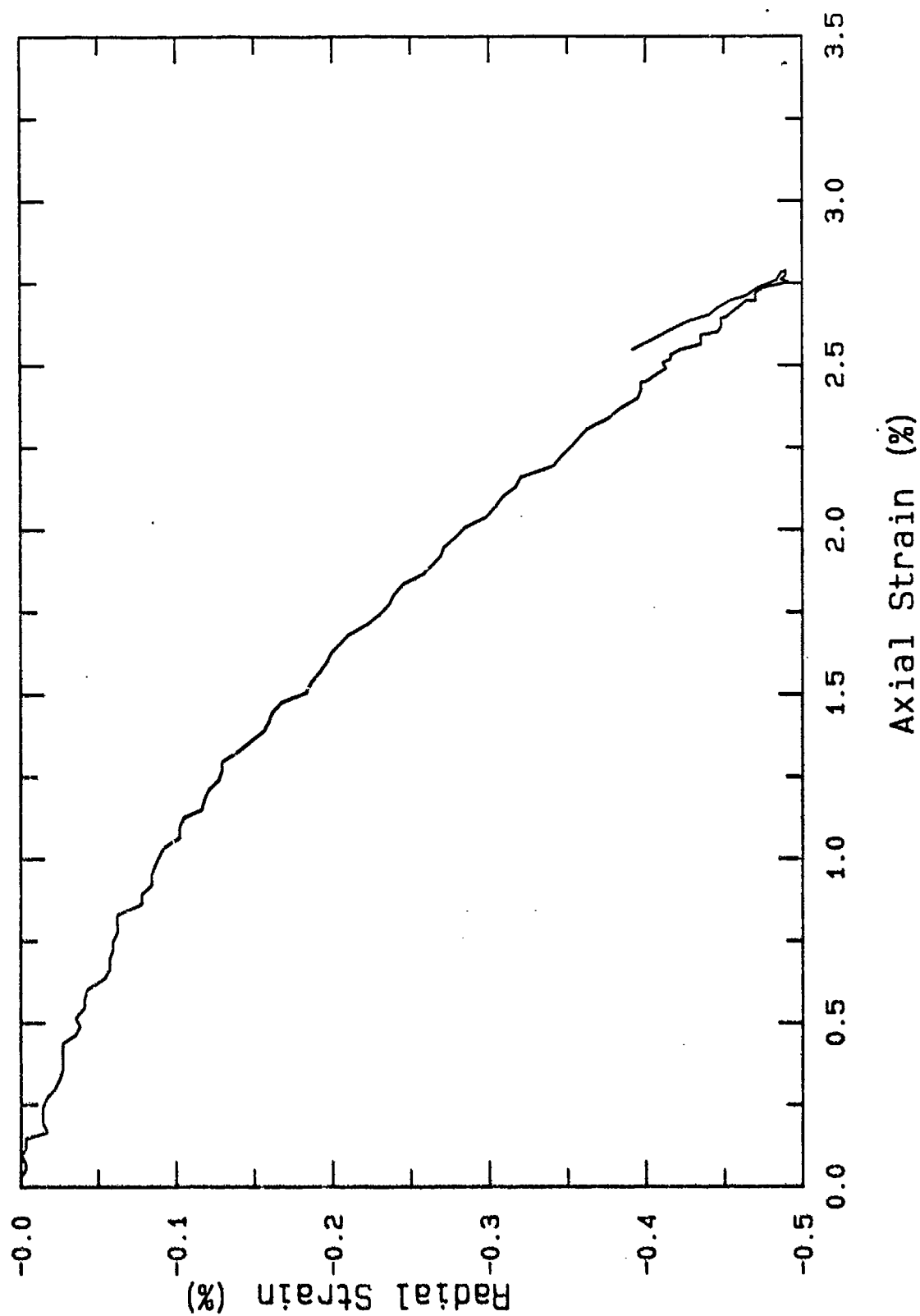


Figure 7.5g. Radial strain-axial strain data, triaxial compression to approximately 1000 psi mean stress.



# Triax (65C7) from 630 psi Beach Sand

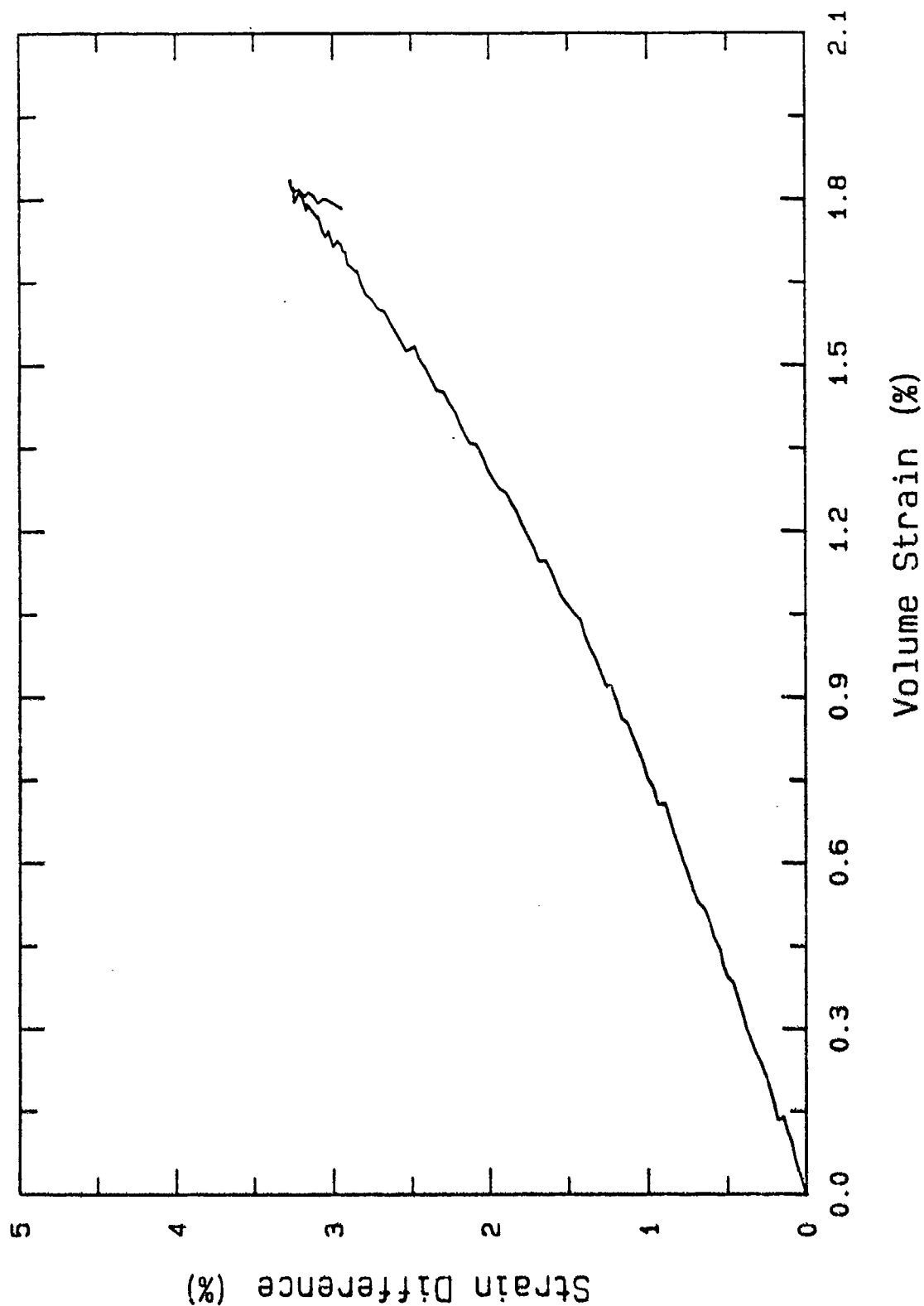


Figure 7.5h. Strain difference-volume strain data, triaxial compression to approximately 1000 psi mean stress.

# Grain Size Distribution G6A7

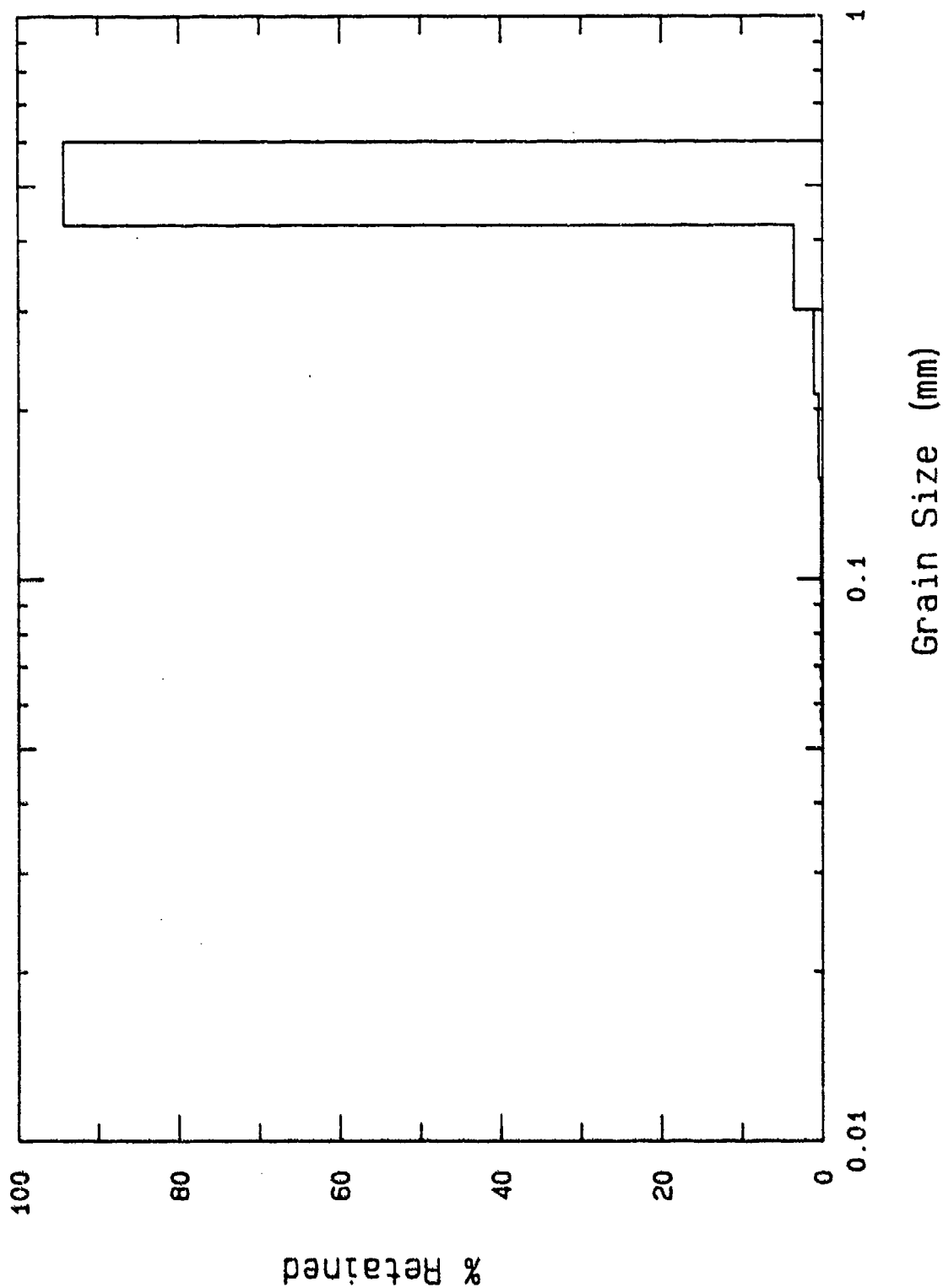


Figure 7.6a. Post test grain size and weight-fraction distribution following triaxial shear at constant mean stress of approximately 1000 psi.

Hydrostat w/ Triax (G6A7) 1000 psi  
Beach Sand

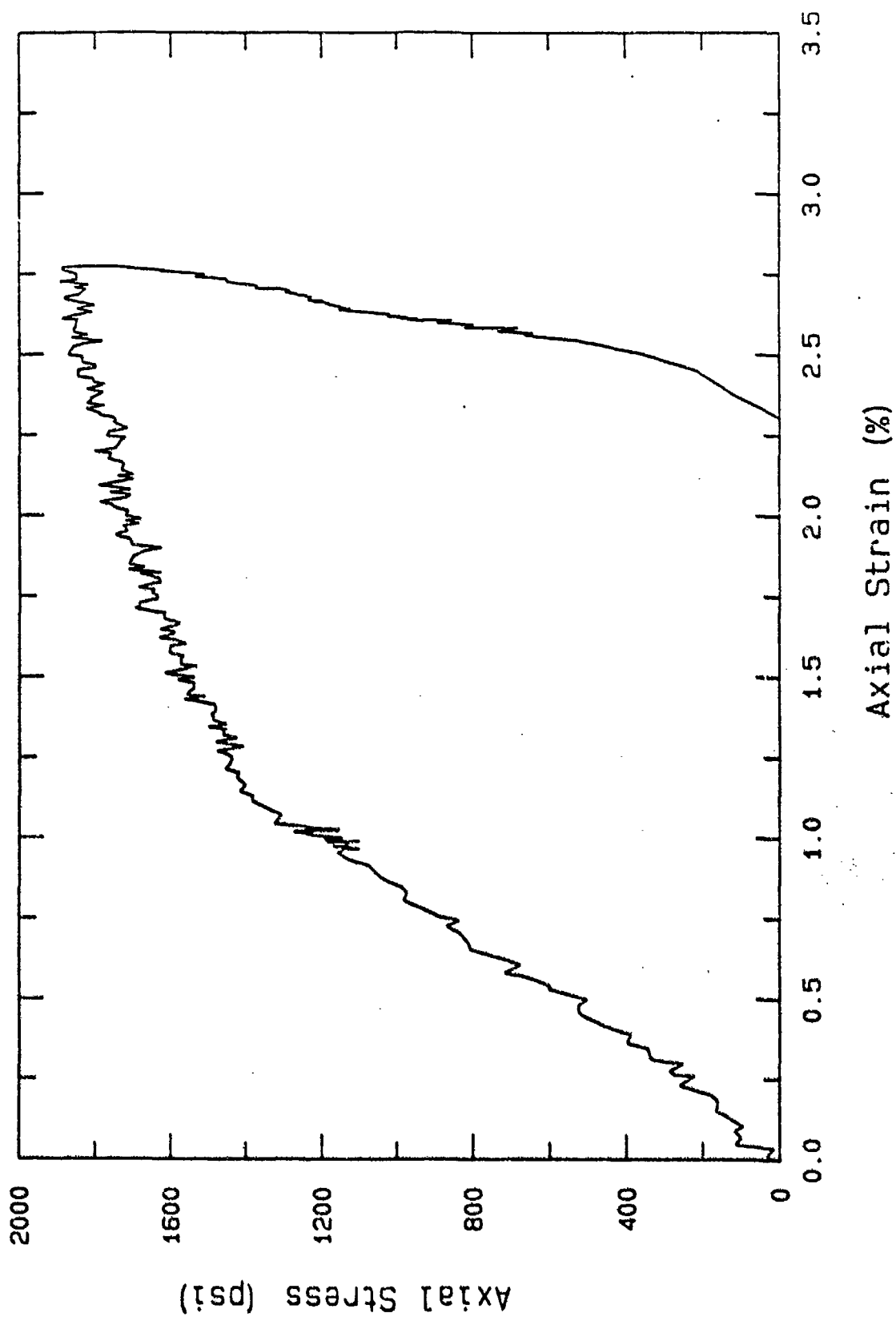


Figure 7.5b. Axial stress - axial strain data, hydrostatic loading and TXS loading at constant mean stress of approximately 1000 psi.

Hydrostat w/ Triax (G6A7) 1000 psi  
Beach Sand

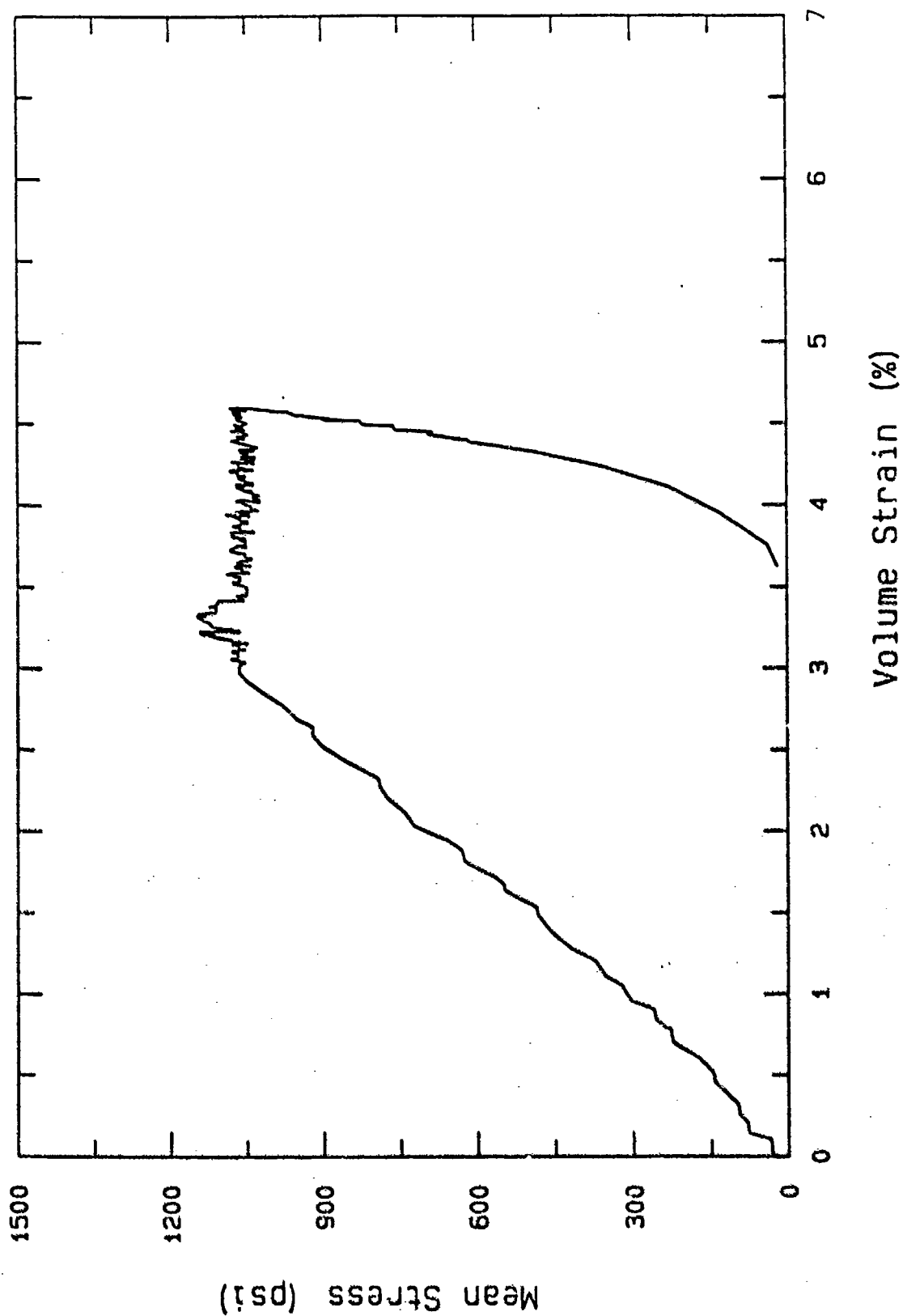


Figure 7.6c. Mean stress-volume strain, hydrostatic loading and TXS loading at constant mean stress of approximately 1000 psi.

# Hydrostat w/ Triax (G6A7) 1000 psi Beach Sand

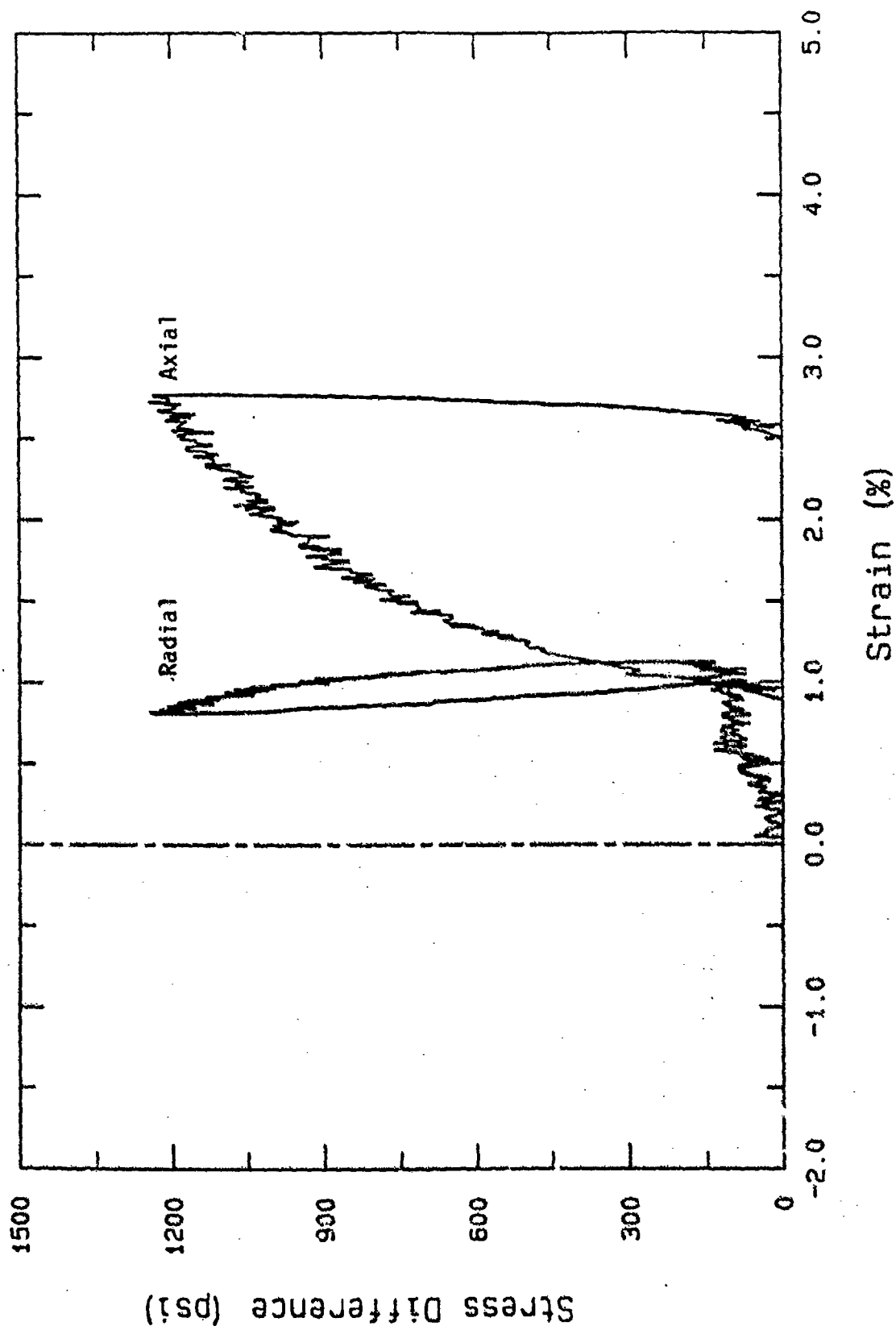


Figure 7.6d. Stress difference-axial and radial strain data, hydrostatic loading and TXS loading at constant mean stress of approximately 1000 psi.

Hydrostat w/ Triax (G6A7) 1000 psi  
Beach Sand

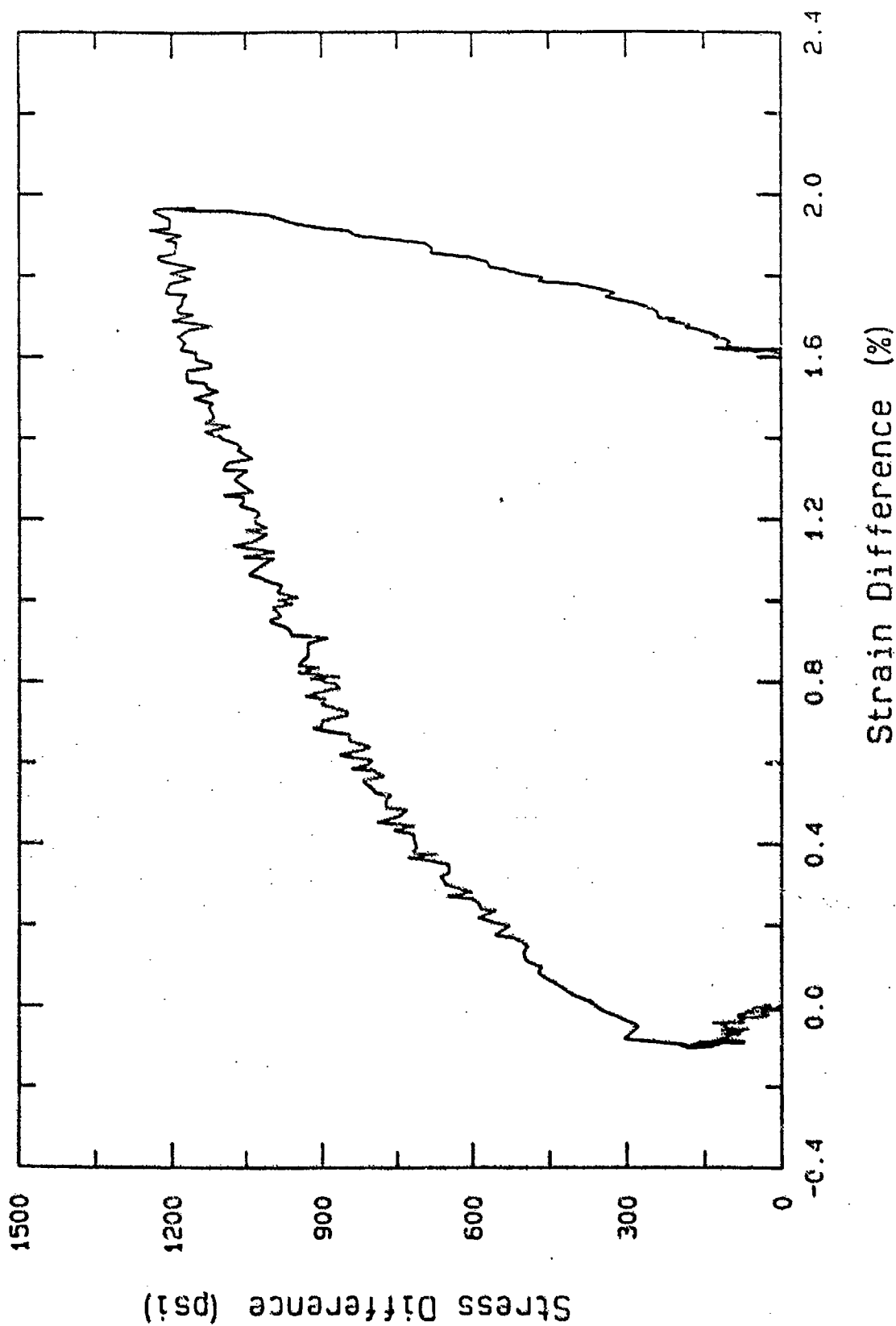


Figure 7.6e. Stress difference-strain difference data, hydrostatic loading and TXS loading at constant mean stress of approximately 1000 psi.

Hydrostat w/ Triax (G6A7) 1000 psi  
Beach Sand

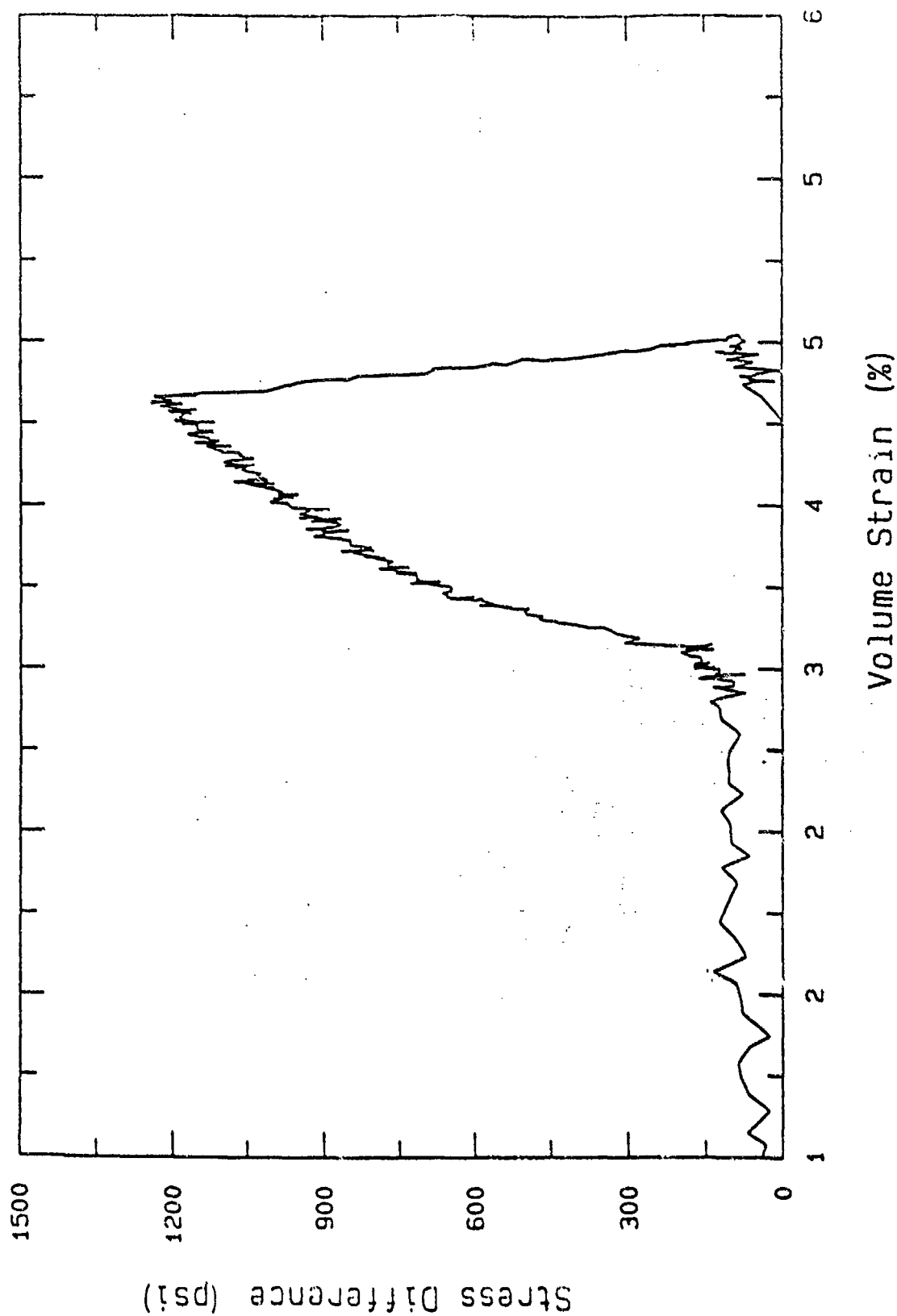


Figure 7.6f. Stress difference-volume strain data, hydrostatic loading and TXS loading at constant mean stress of approximately 1000 psi.

Hydrostat w/ Triax (G6A7) 1000 psi  
Beach Sand

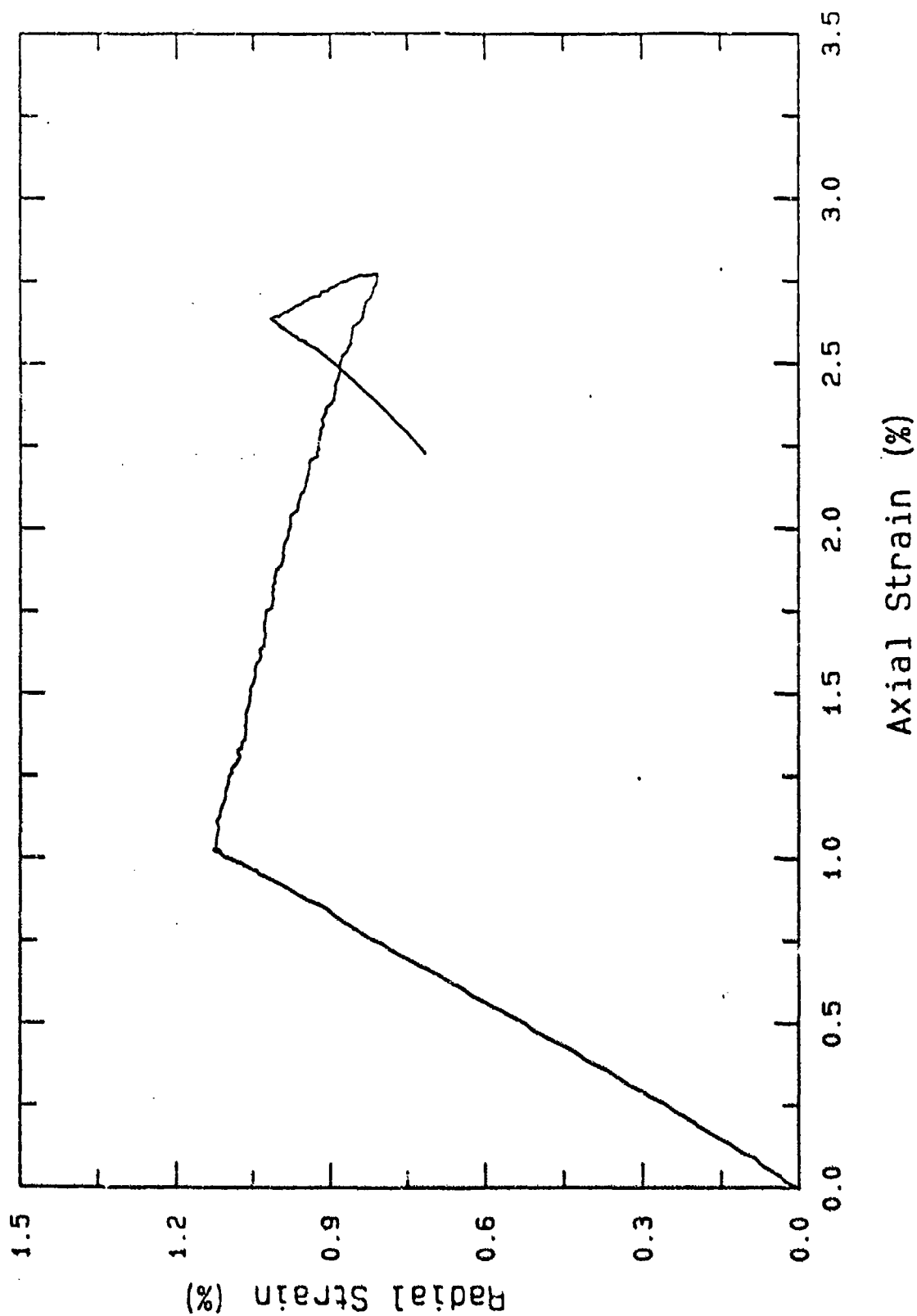


Figure 7.6g. Radial strain-axial strain data, hydrostatic loading and TXS loading at constant mean stress of approximately 1000 psi.



Hydrostat w/ Triax (G6A7) 1000 psi  
Beach Sand

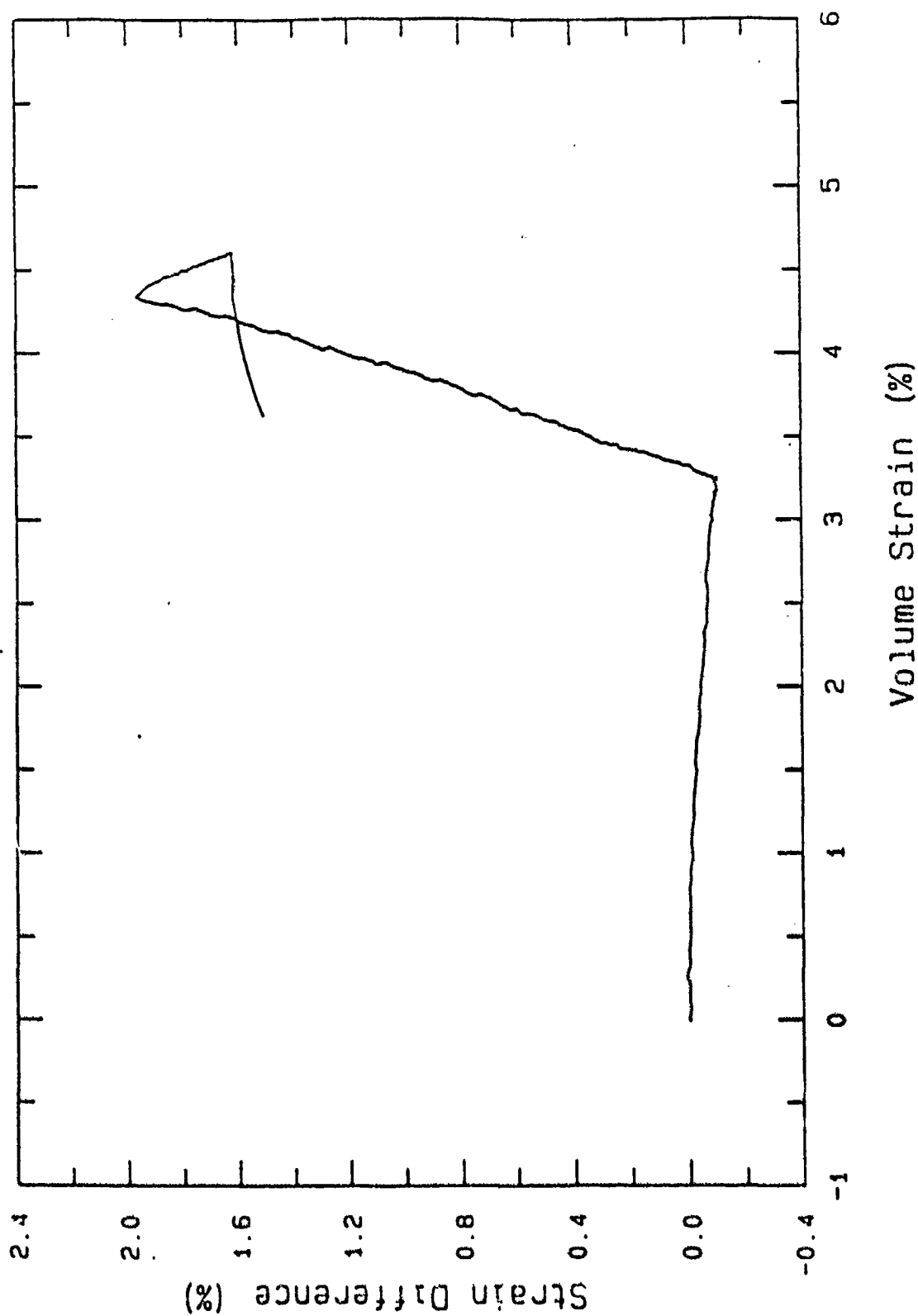


Figure 7.6h. Strain difference-volume strain data, hydrostatic loading and TXS loading at constant mean stress of approximately 1000 psi.

# Grain Size Distribution Y20A7

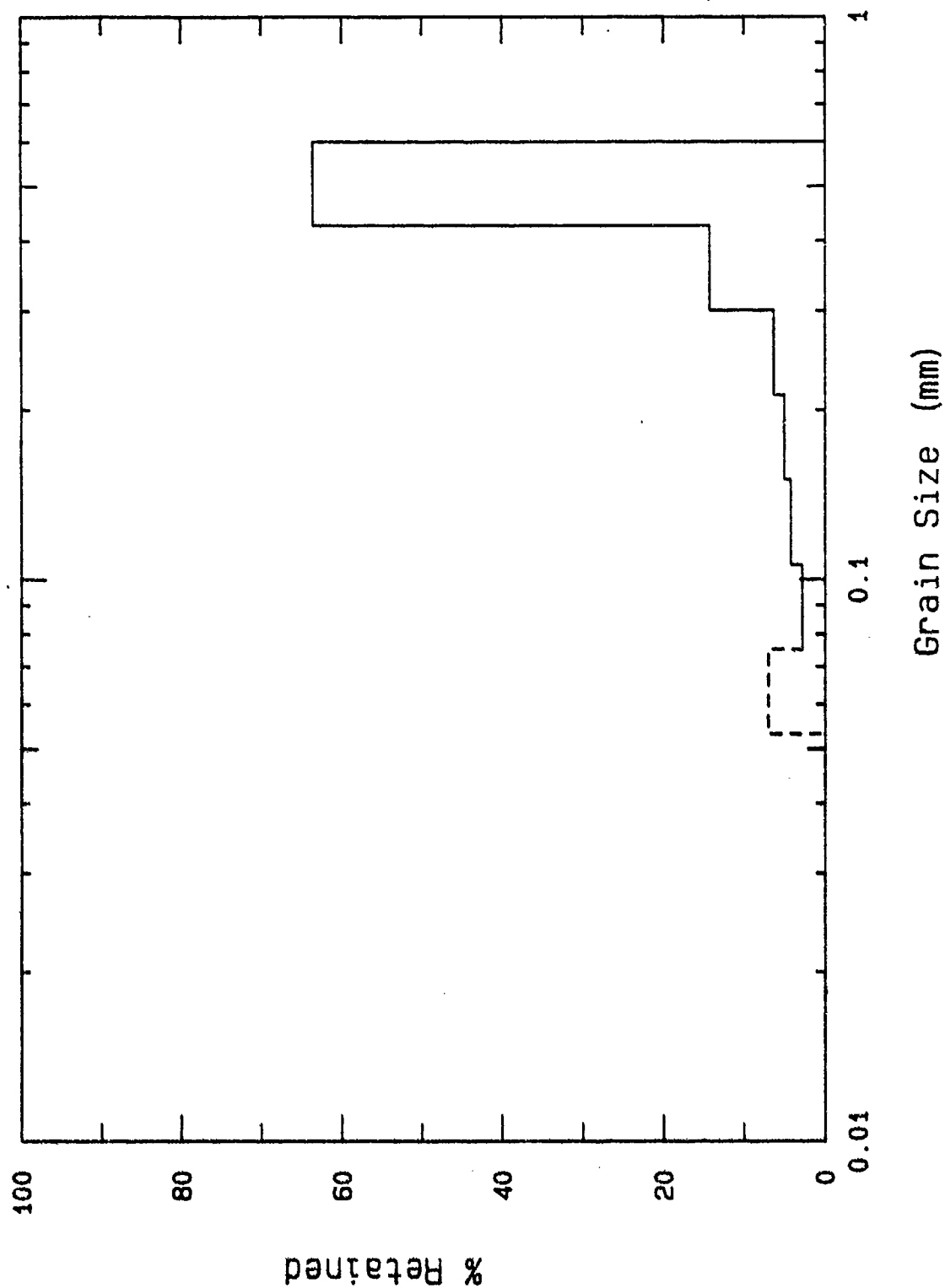


Figure 7.7a. Post test grain size and weight-fraction distribution following hydrostatic drained loading to 10,000 psi.

BEACH SAND (Y20A7)  
HYDRO TO 10KSI

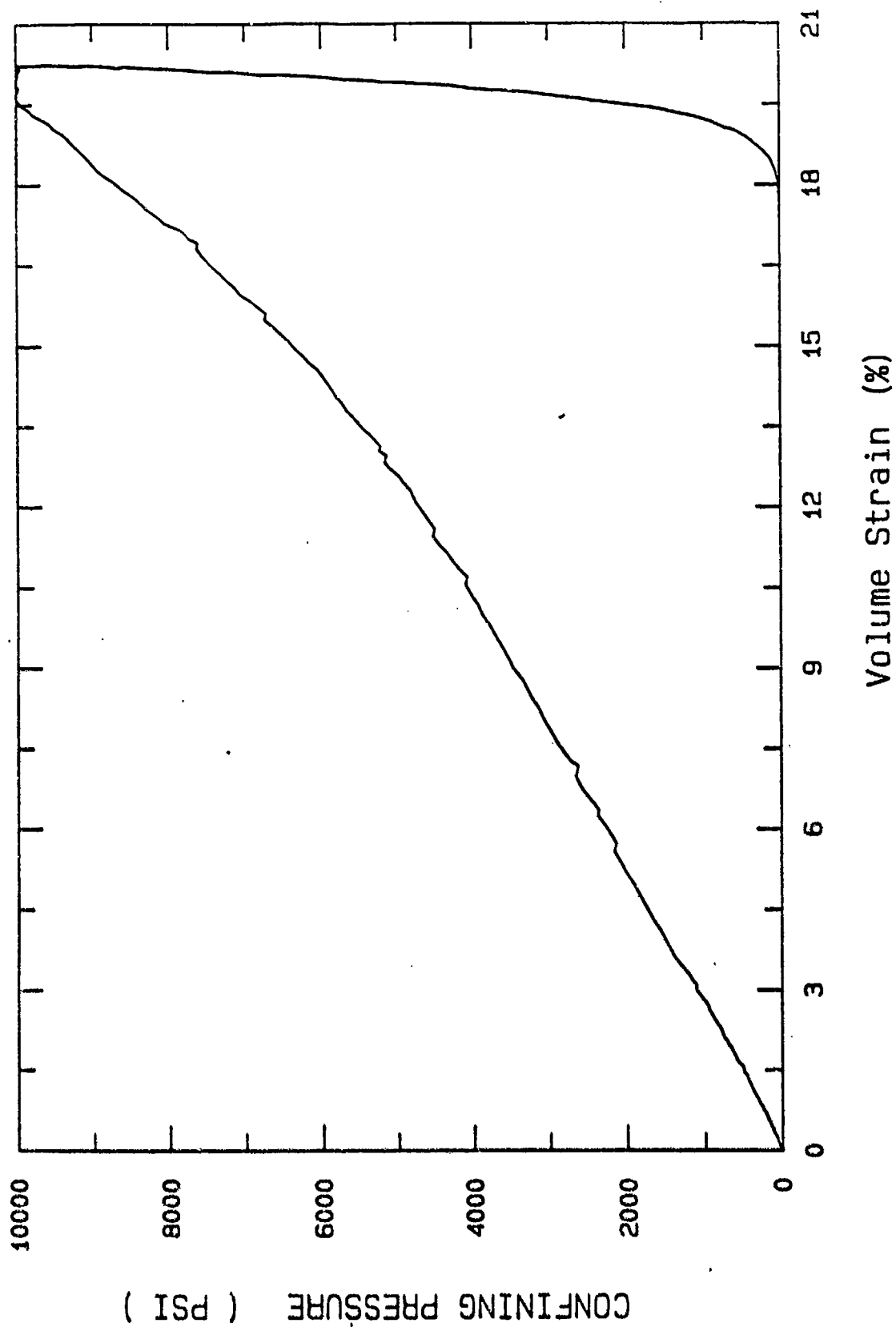


Figure 7.7b. Pressure-volume strain data, hydrostatic loading to 10,000 psi.

# Grain Size Distribution U11A7

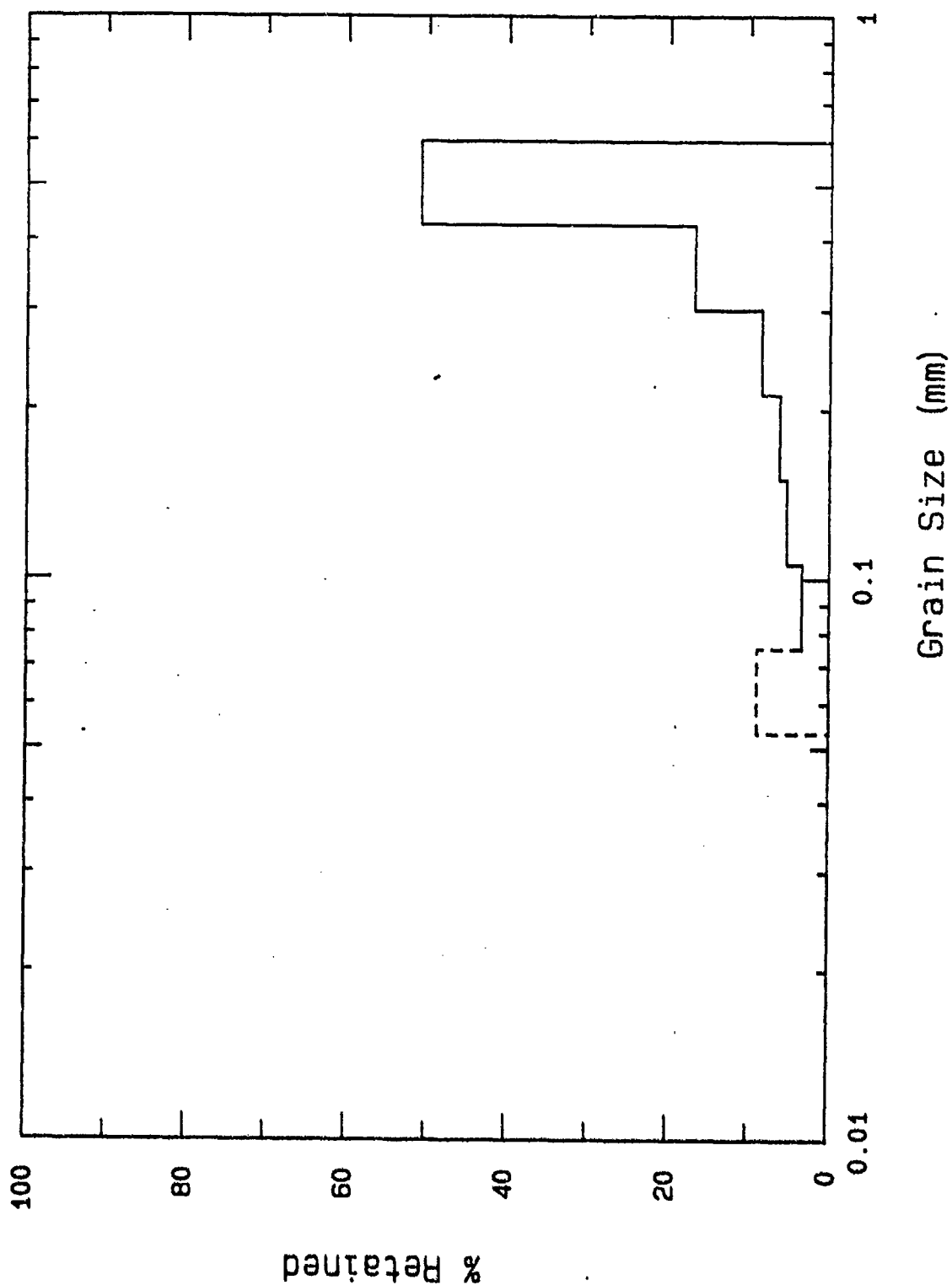


Figure 7.8a. Post test grain size and weight-fraction distribution following  $K_0$  drained loading to 10,000 psi mean stress.

K<sub>0</sub> (U11A7)  
Beach Sand

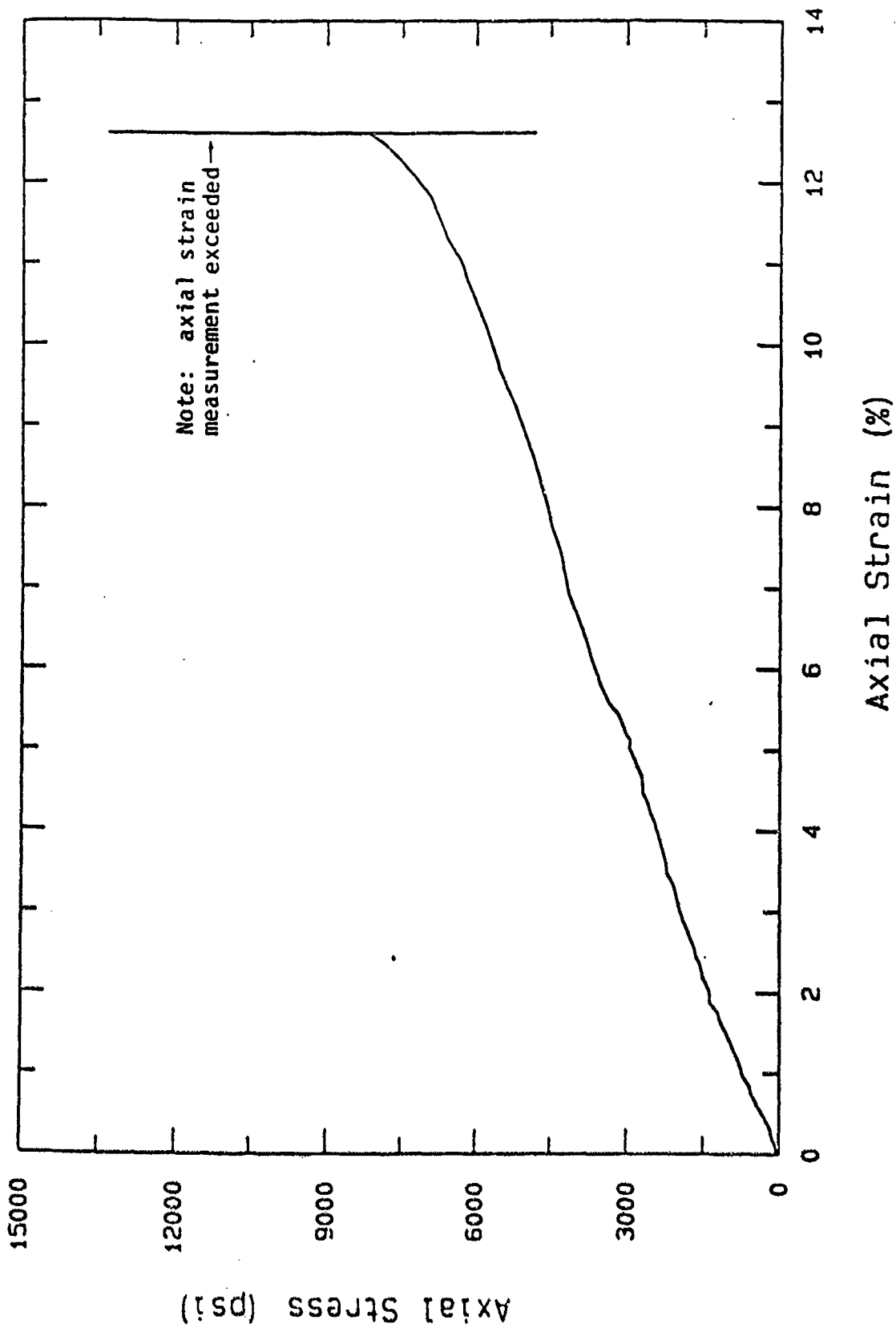


Figure 7.8b. Axial stress-axial strain data, K<sub>0</sub> loading to approximately 10,000 psi mean stress.

K0 (U11A/J)  
Beach Sand

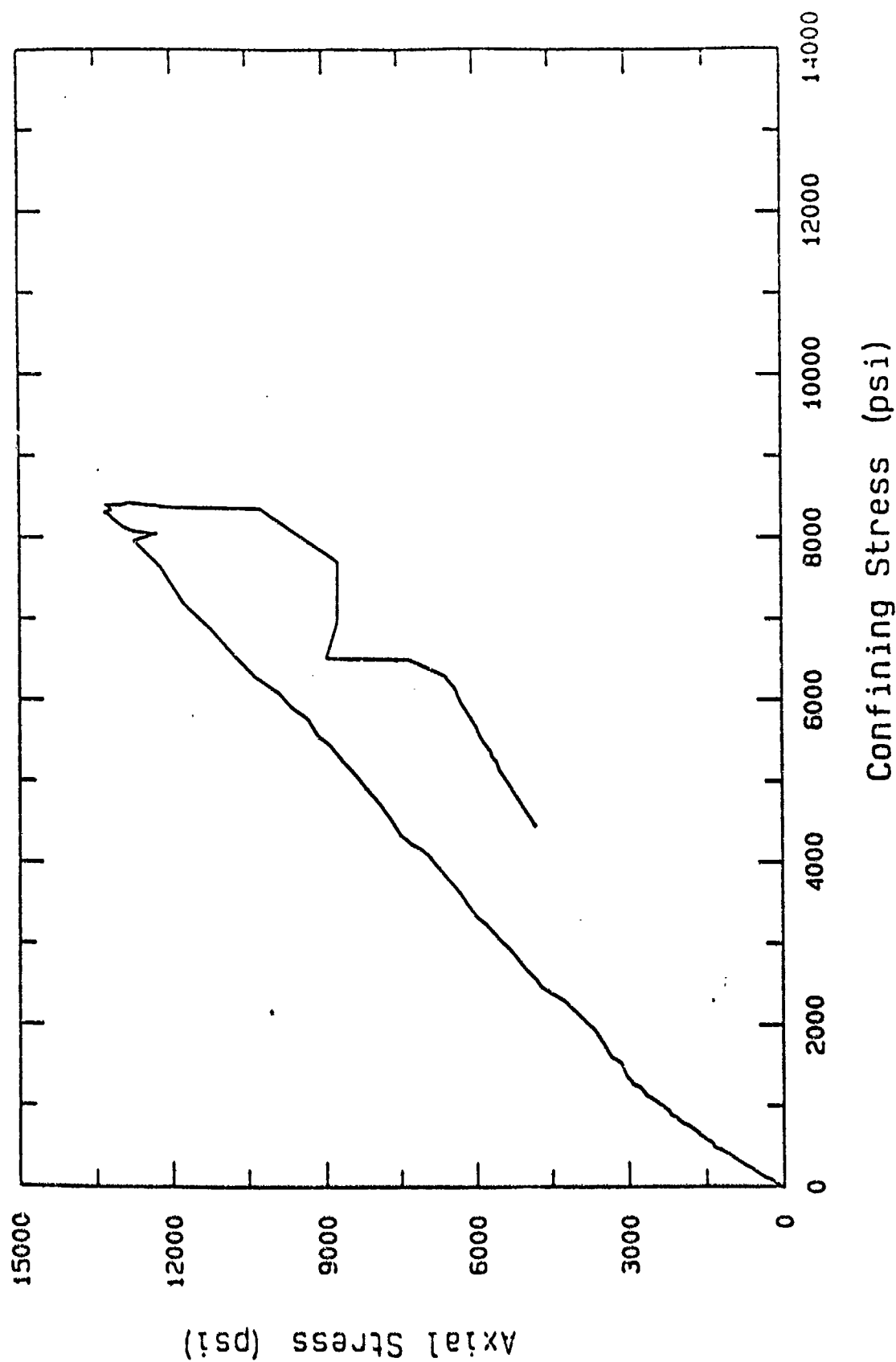


Figure 7.8c. Axial stress-confining stress data,  $K_0$  loading to approximately 10,000 psi mean stress.

K<sub>0</sub> U1 (R7)  
Beach Sand

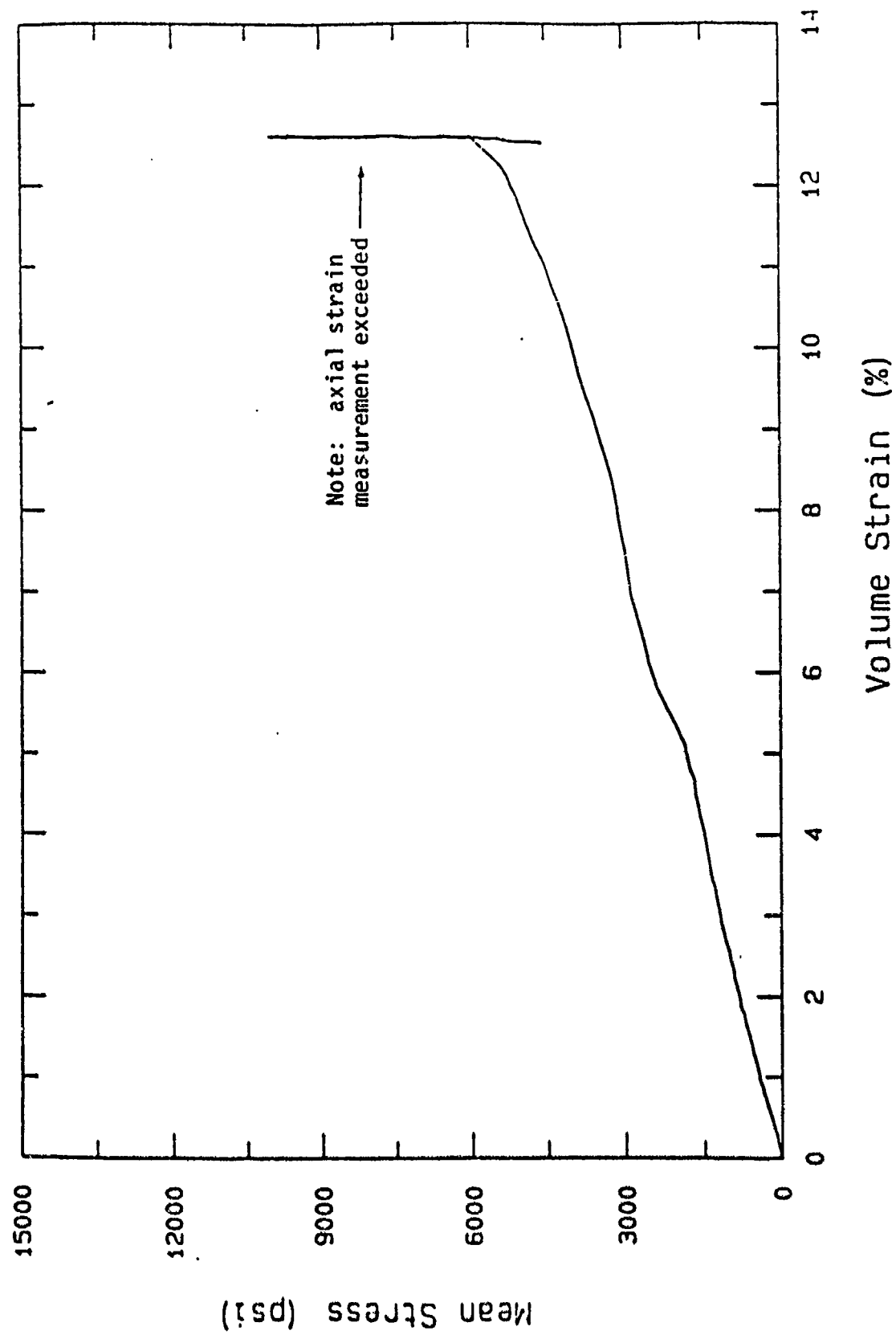


Figure 7.8d. Mean stress-volume strain data,  $K_0$  loading to approximately 10,000 psi mean stress.

$K_0$  (U11A7)  
Beach Sand

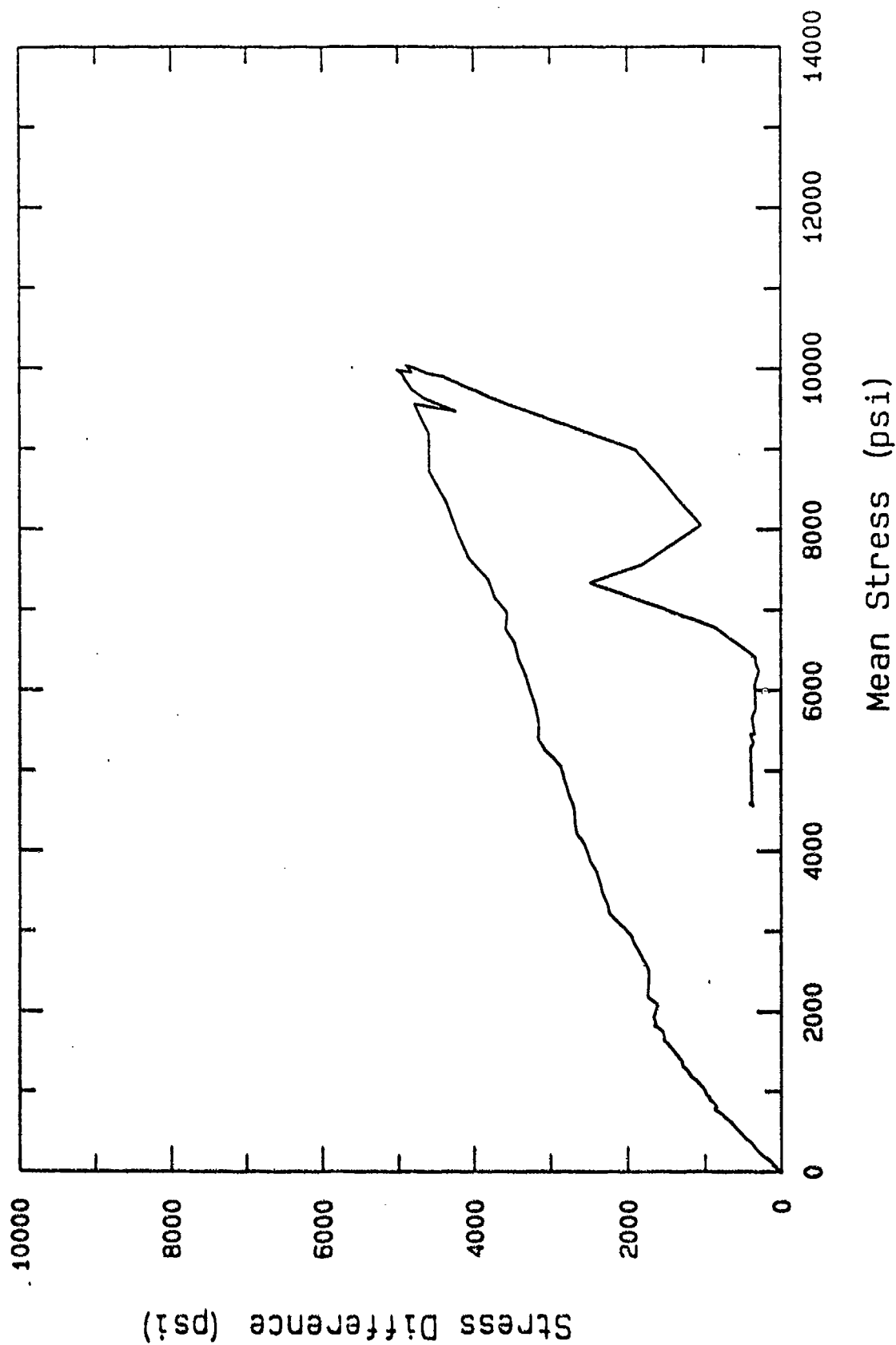


Figure 7.8e. Stress difference-mean stress data,  $K_0$  loading to approximately 10.000 psi mean stress.



K<sub>0</sub> (U11A7)  
Beach Sand

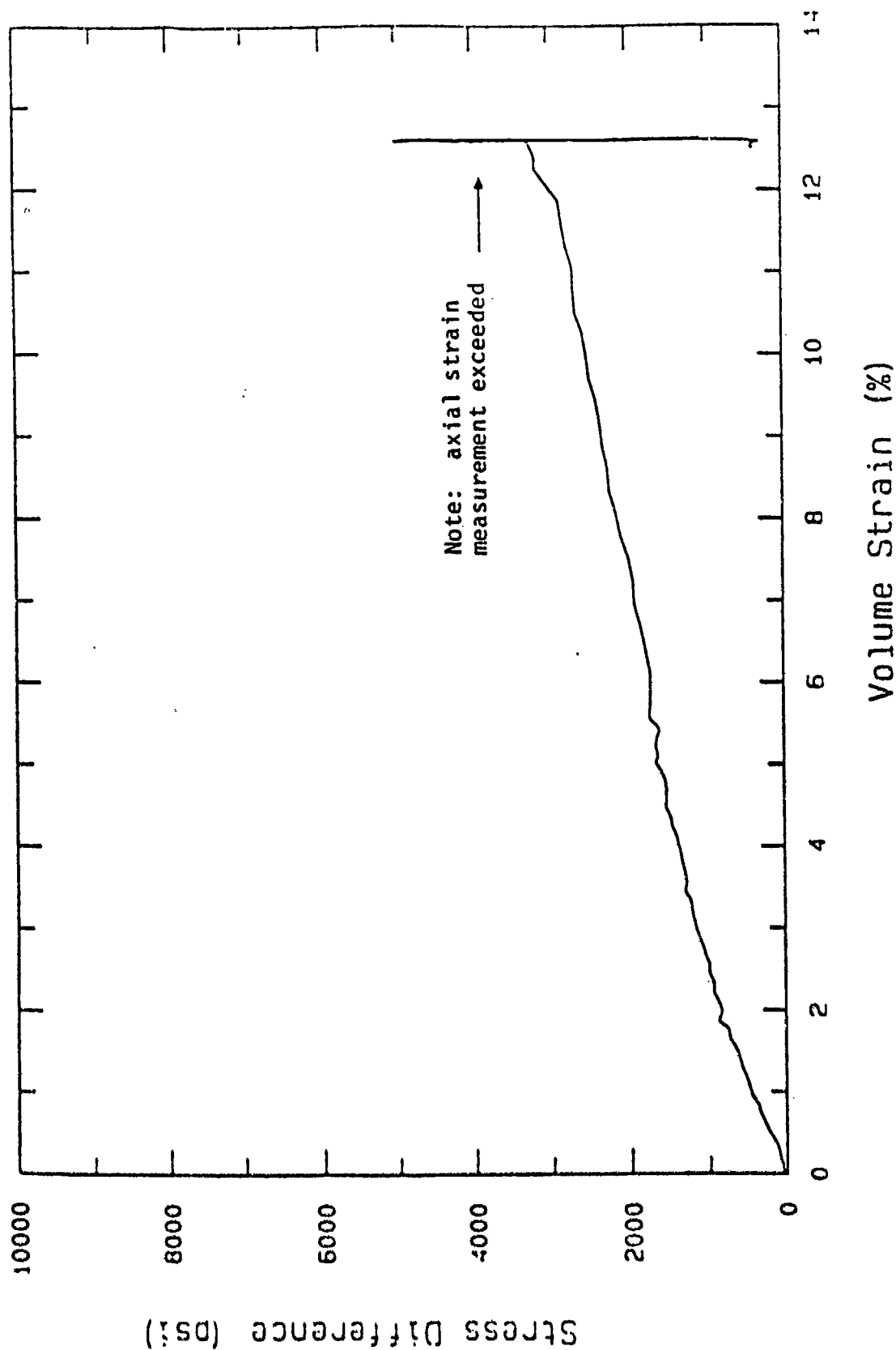


Figure 7.8f. Stress difference-volume strain data, K<sub>0</sub> loading to approximately 10,000 psi mean stress.

# Grain Size Distribution G5D&E7

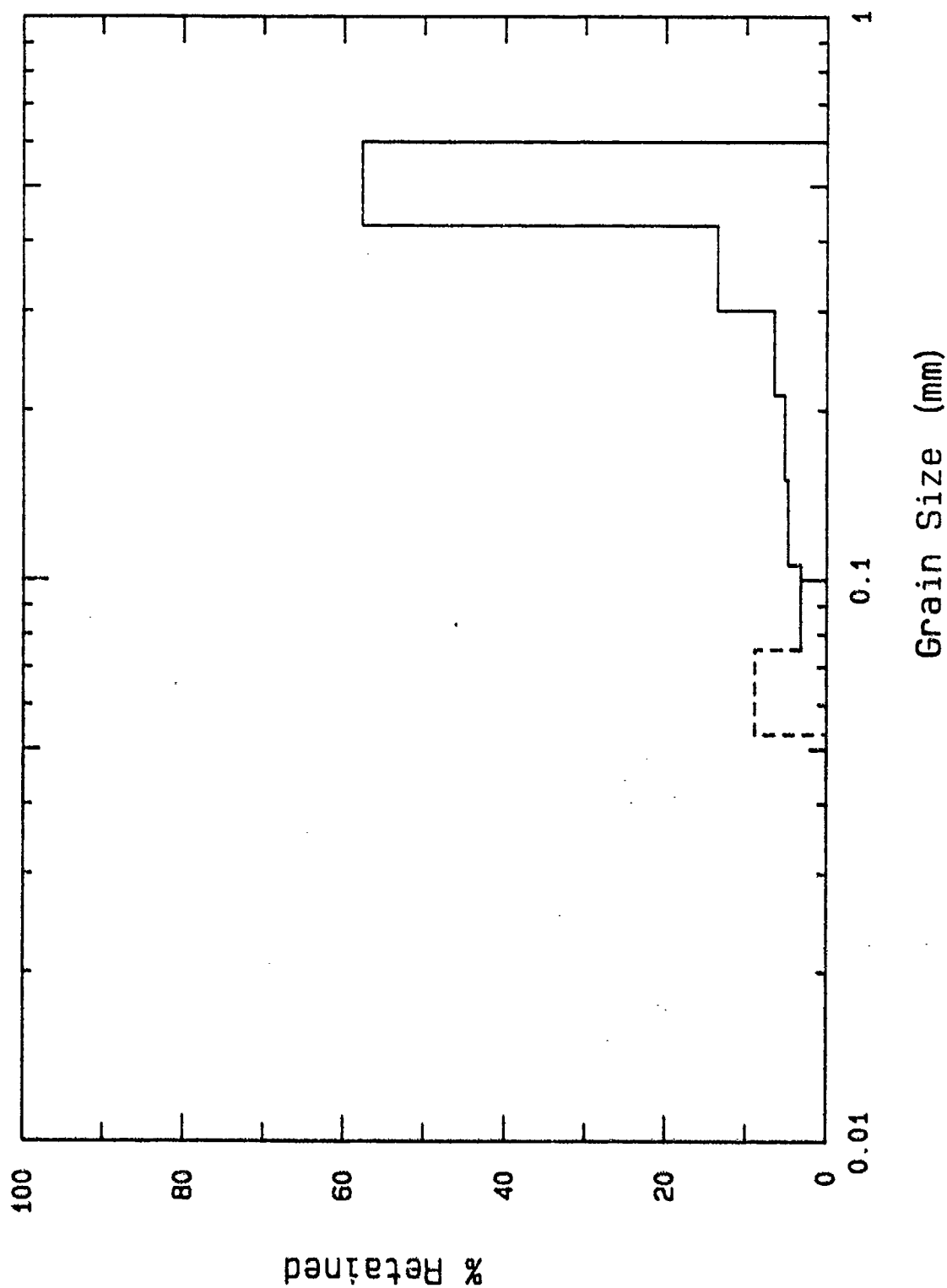


Figure 7.9a. Post test grain size and weight-fraction distribution following triaxial compression to approximately 10,000 psi mean stress.

Hydrostat (G5D7) to 8400 psi  
Beach Sand

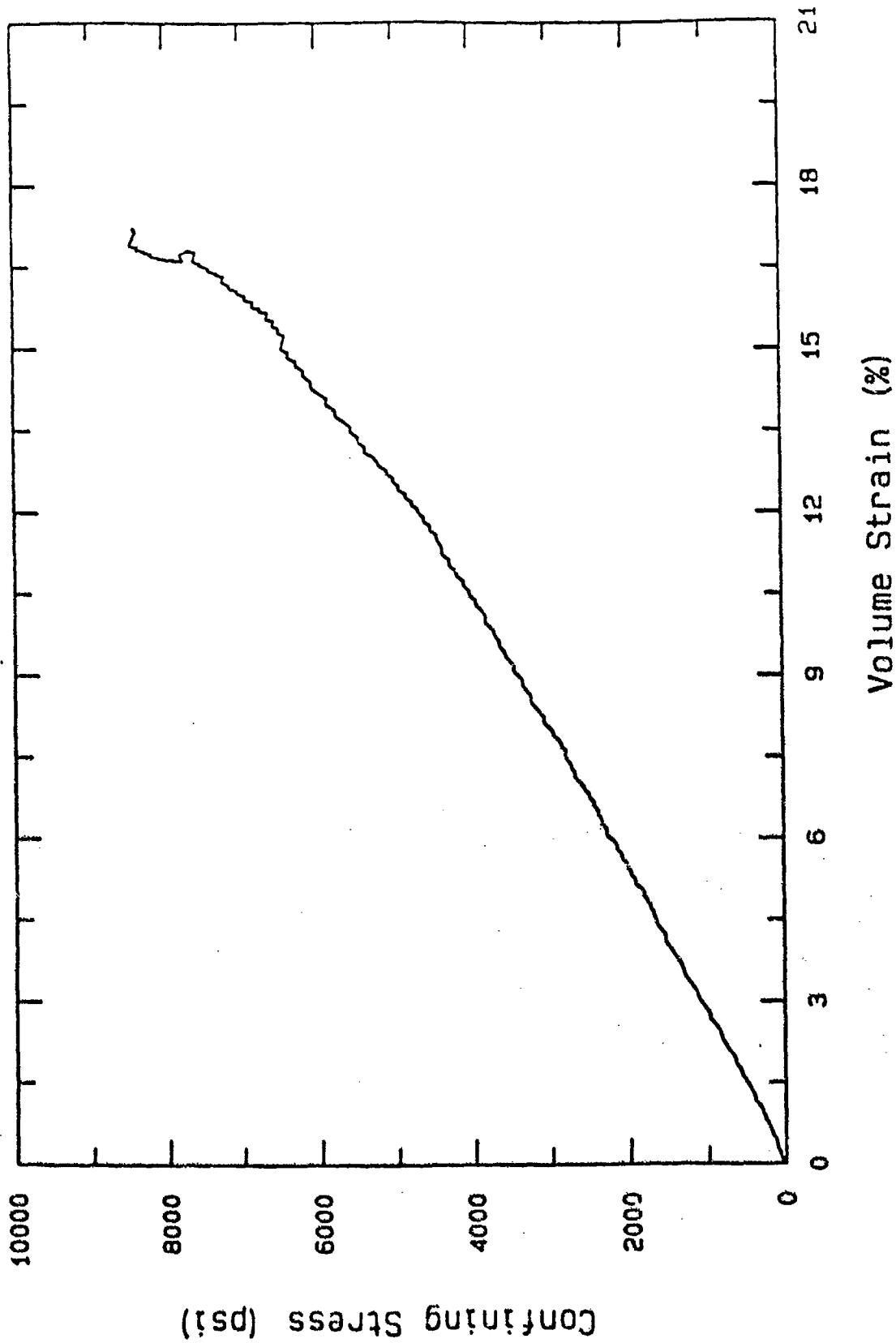


Figure 7.9b. Pressure-volume strain data to 8400 psi prior to triaxial compression to approximately 10,000 psi mean stress.

# Triax (G5E7) from 8400 psi Beach Sand

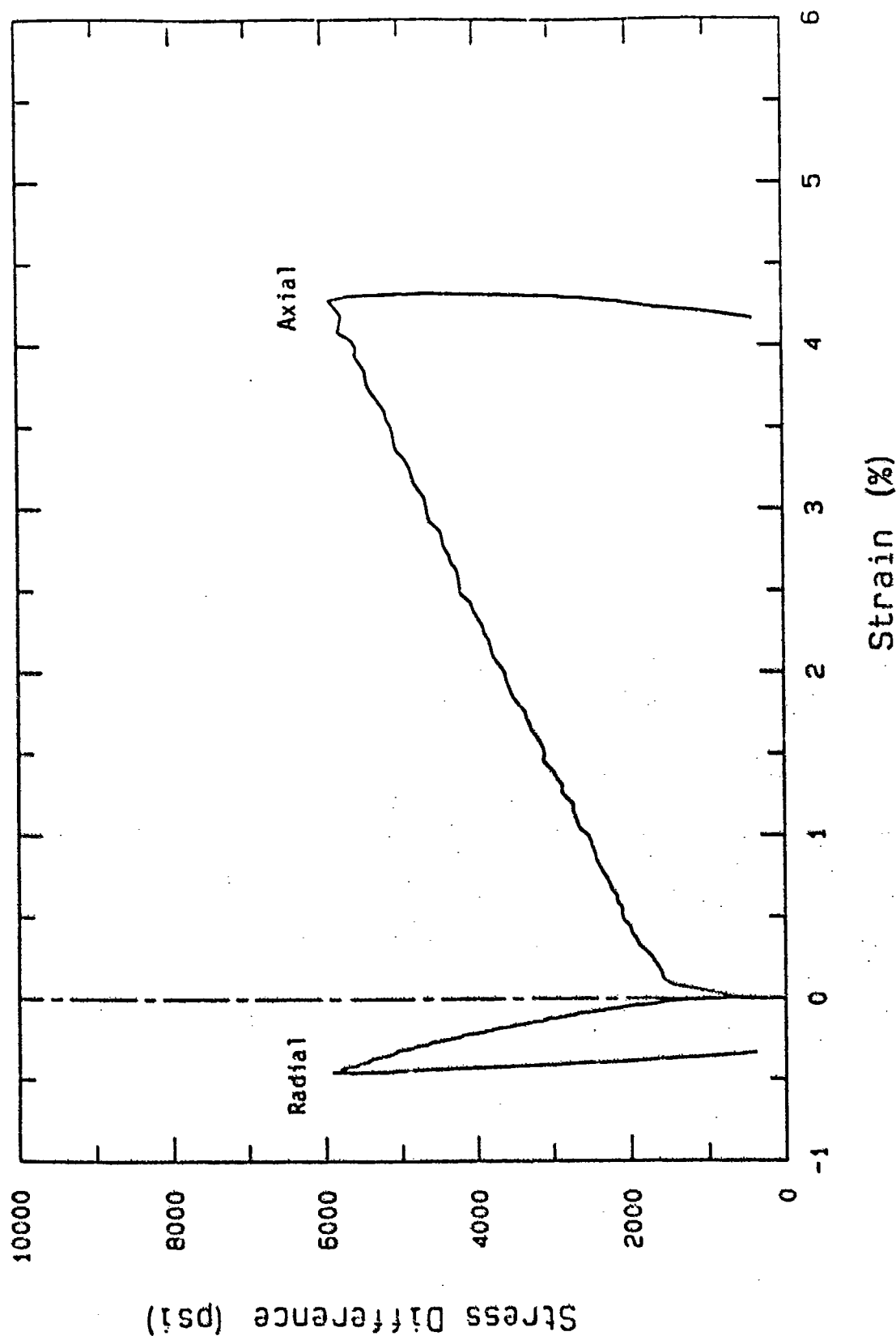


Figure 7.9c. Stress difference-axial and radial strain data, triaxial compression to approximately 10,000 psi mean stress.

Triax (G5E7) from 8400 psi  
Beach Sand

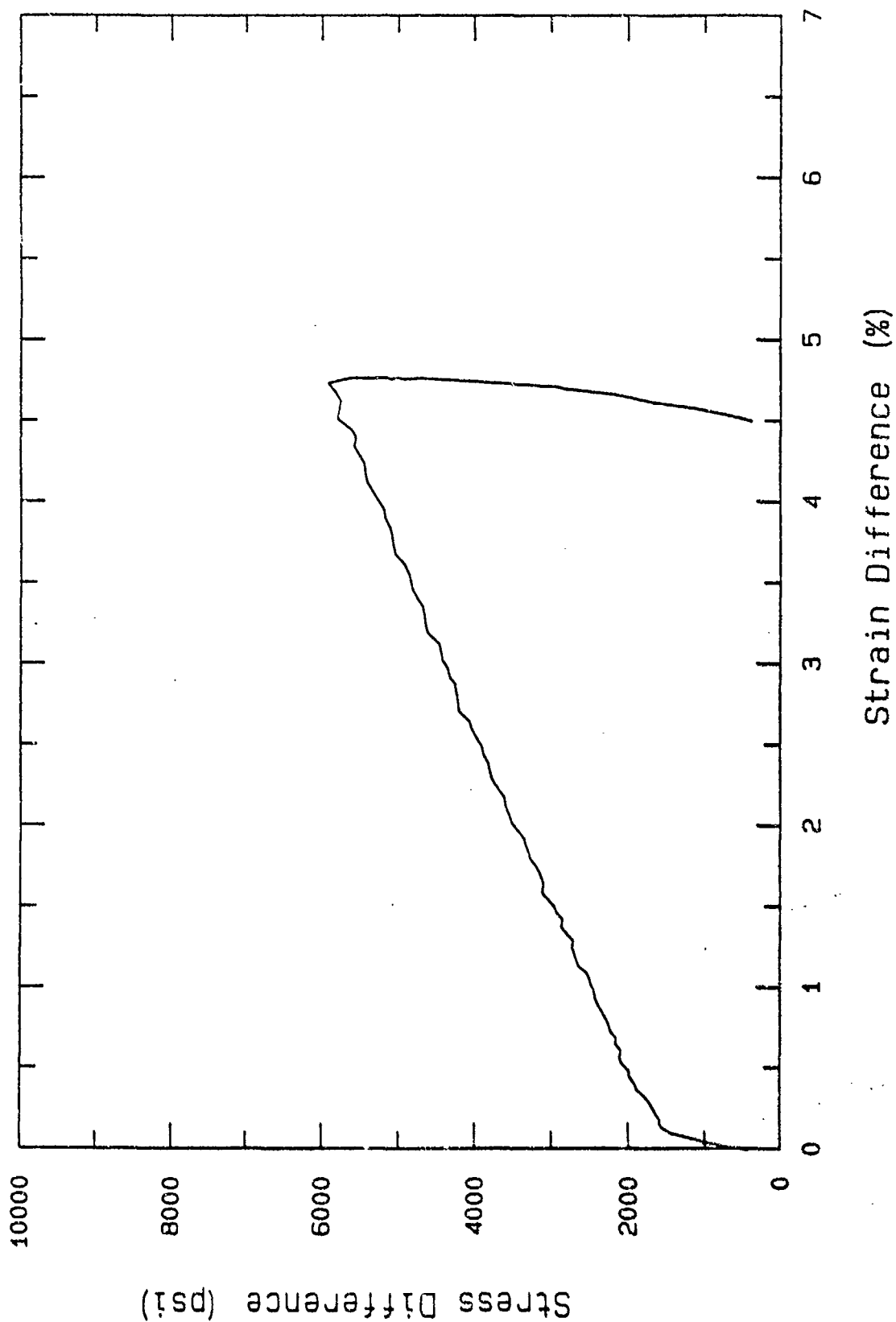


Figure 7.9d. Stress difference-strain difference data, triaxial compression to approximately 10,000 psi mean stress.

Triax (G5E7) from 8400 psi  
Beach Sand

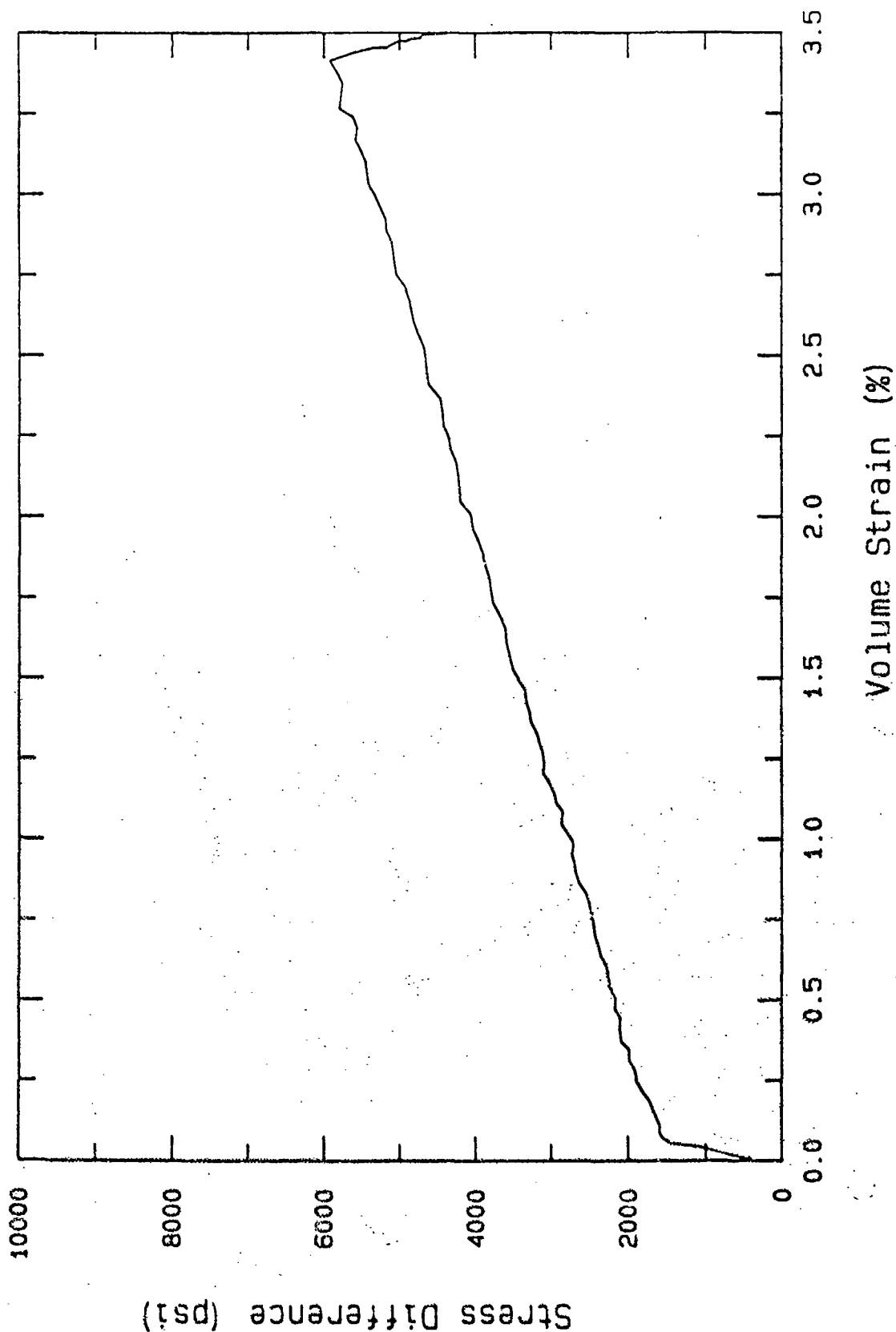


Figure 7.9e. Stress difference-volume strain data, triaxial compression to approximately 10,000 psi mean stress.

Triax (G5E7) from 8400 psi  
Beach Sand

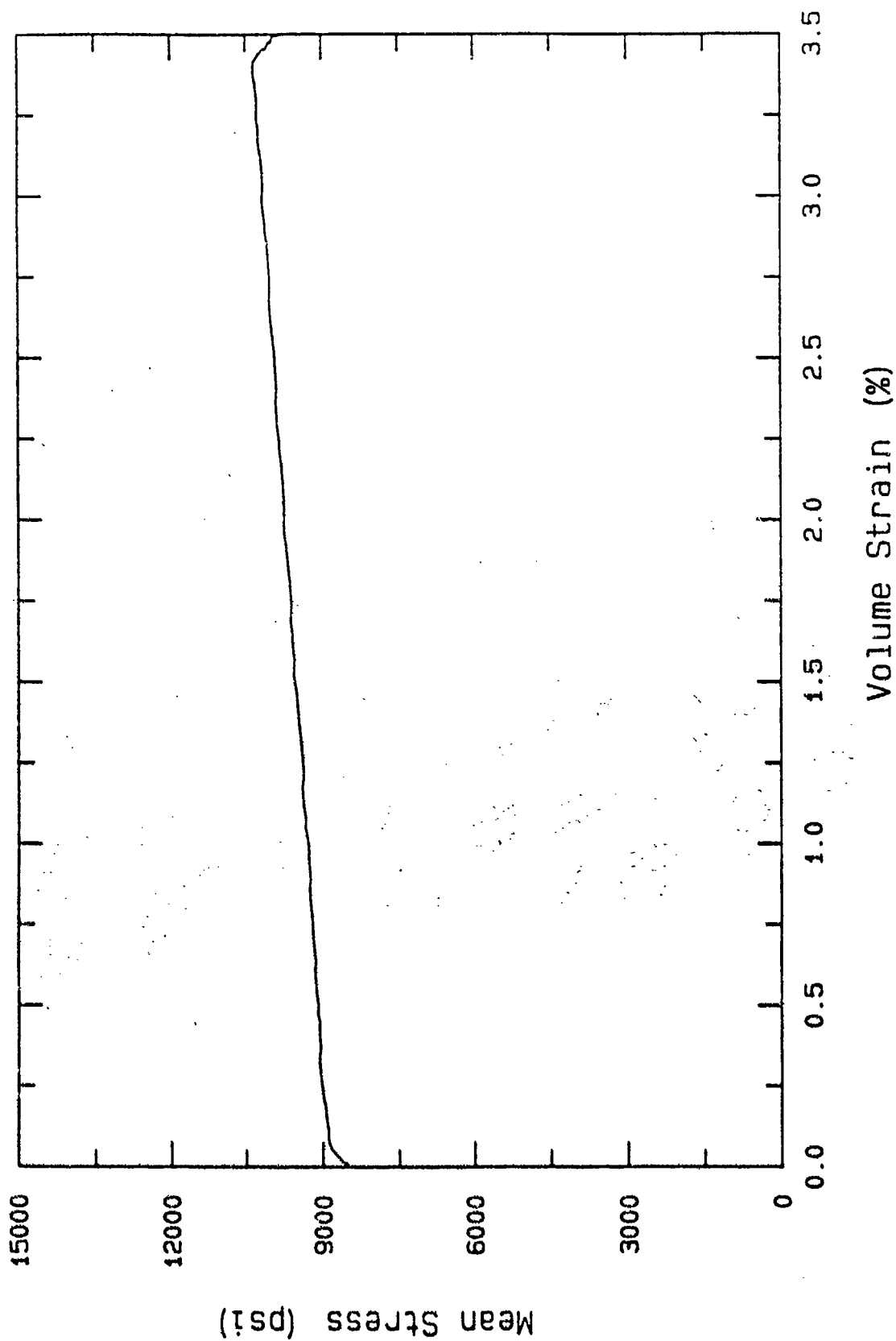


Figure 7.9f. Mean stress-volume strain data, triaxial compression to approximately 10,000 psi mean stress.

Triax (G5E7) from 8400 psi  
Beach Sand

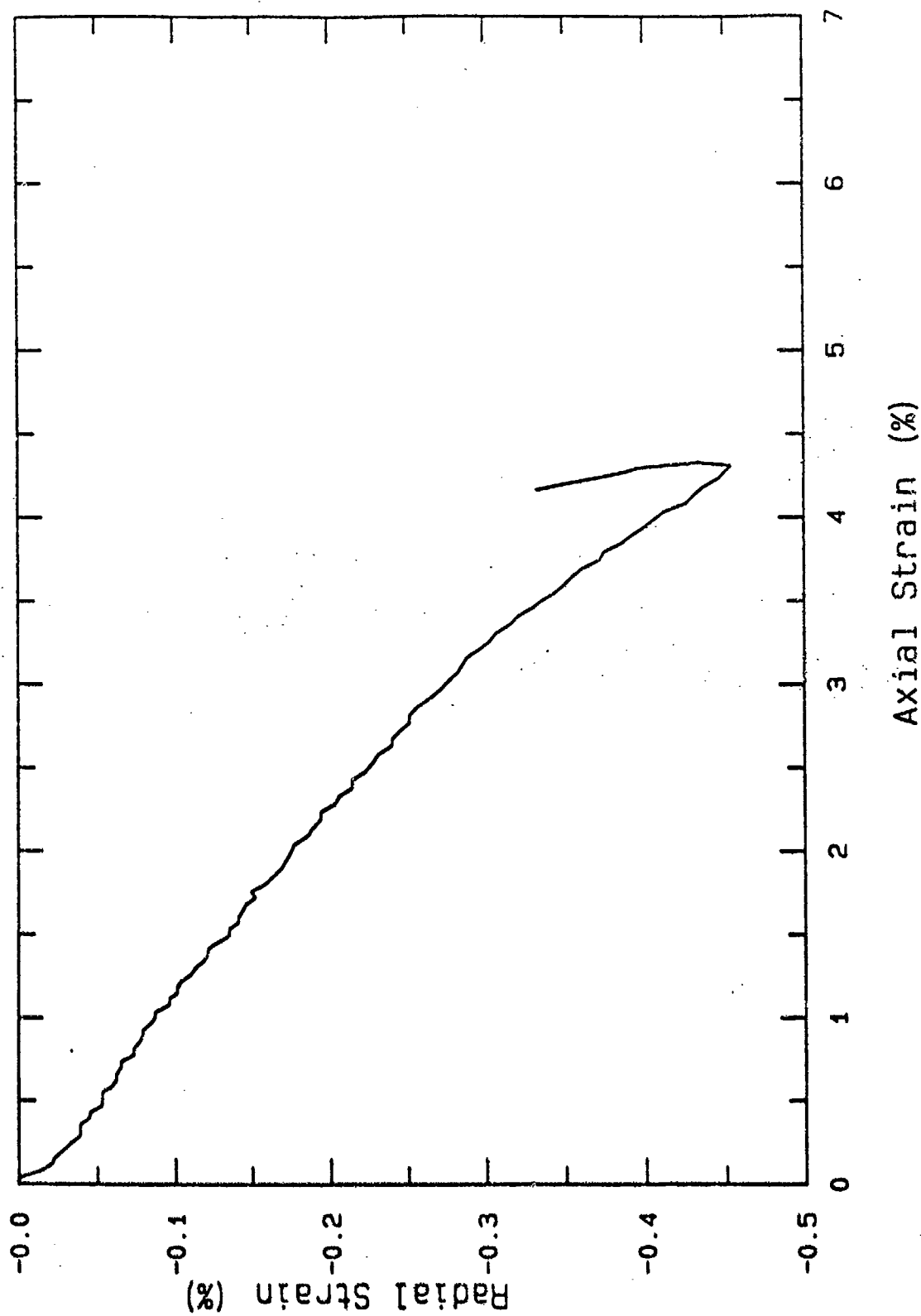


Figure 7.9g. Radial strain-axial strain data, triaxial compression to approximately 10,000 psi mean stress.



Triax (G5E7) from 8400 psi  
Beach Sand

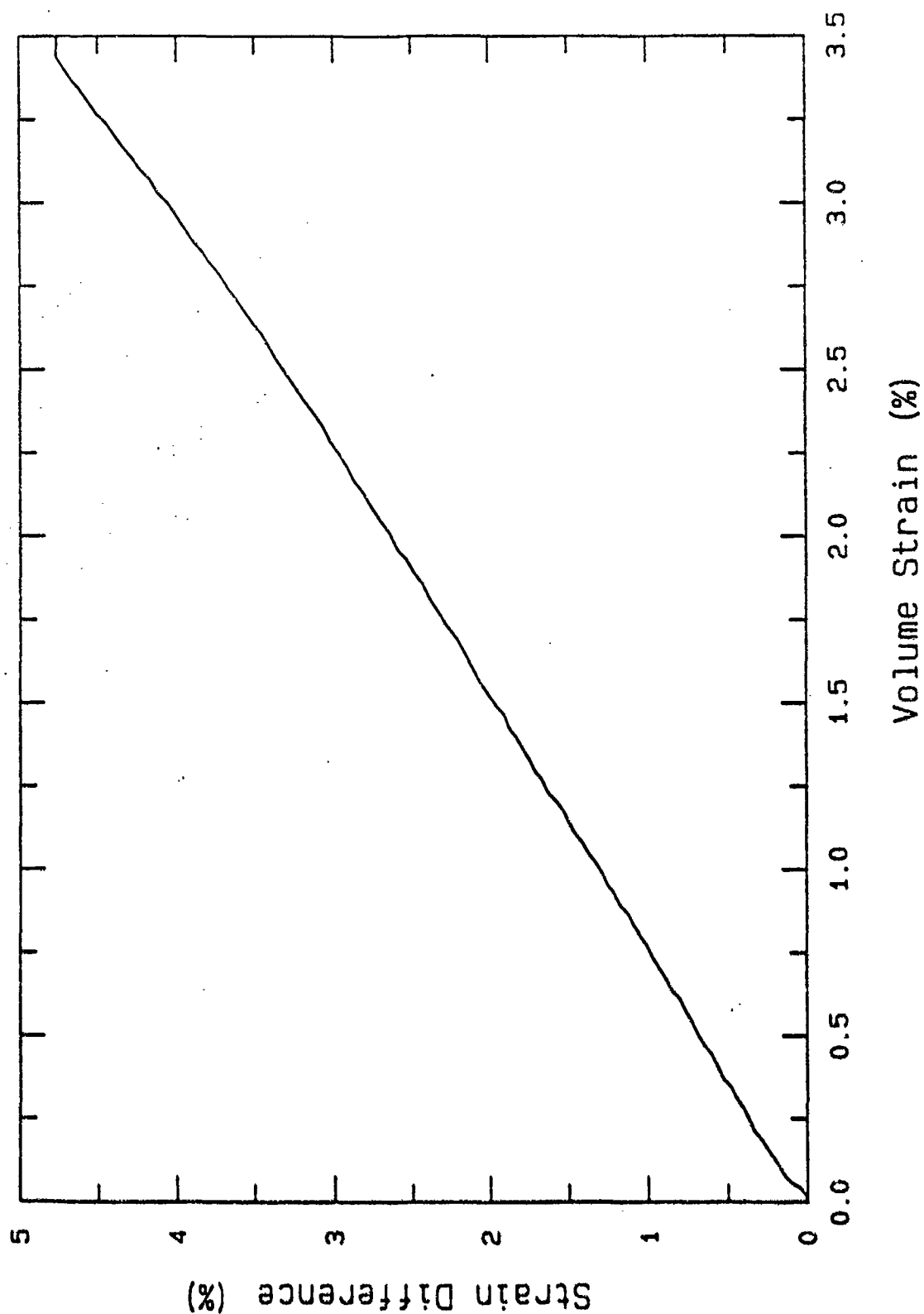


Figure 7.9h. Strain difference-volume strain data, triaxial compression to approximately 10,000 psi mean stress.

# Grain Size Distribution G11C7

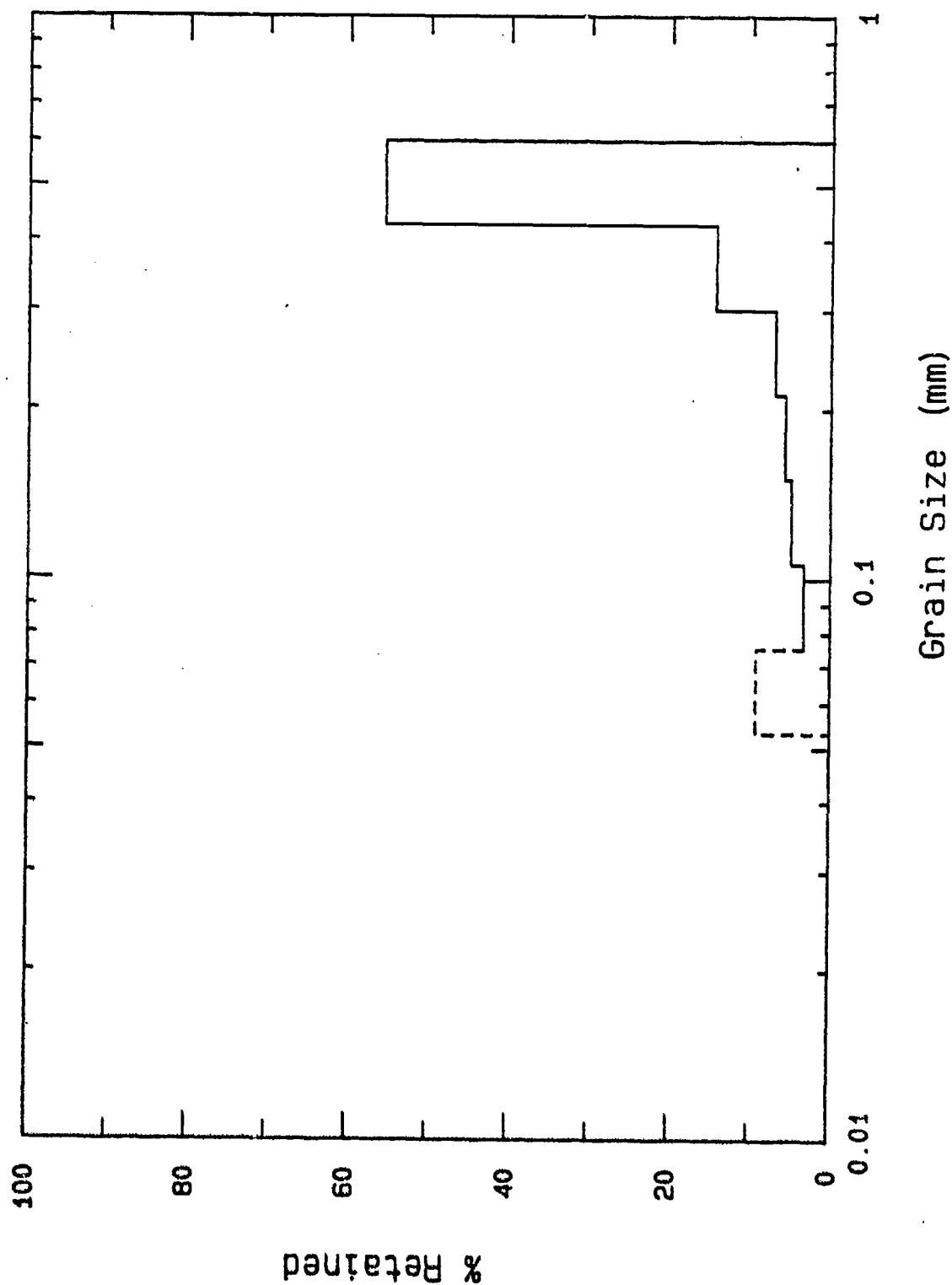


Figure 7.10a. Post test grain size and weight-fraction distribution following triaxial shear at constant mean stress of approximately 10,000 psi.

# Hydrostat w/Triax (G11C7) Beach Sand

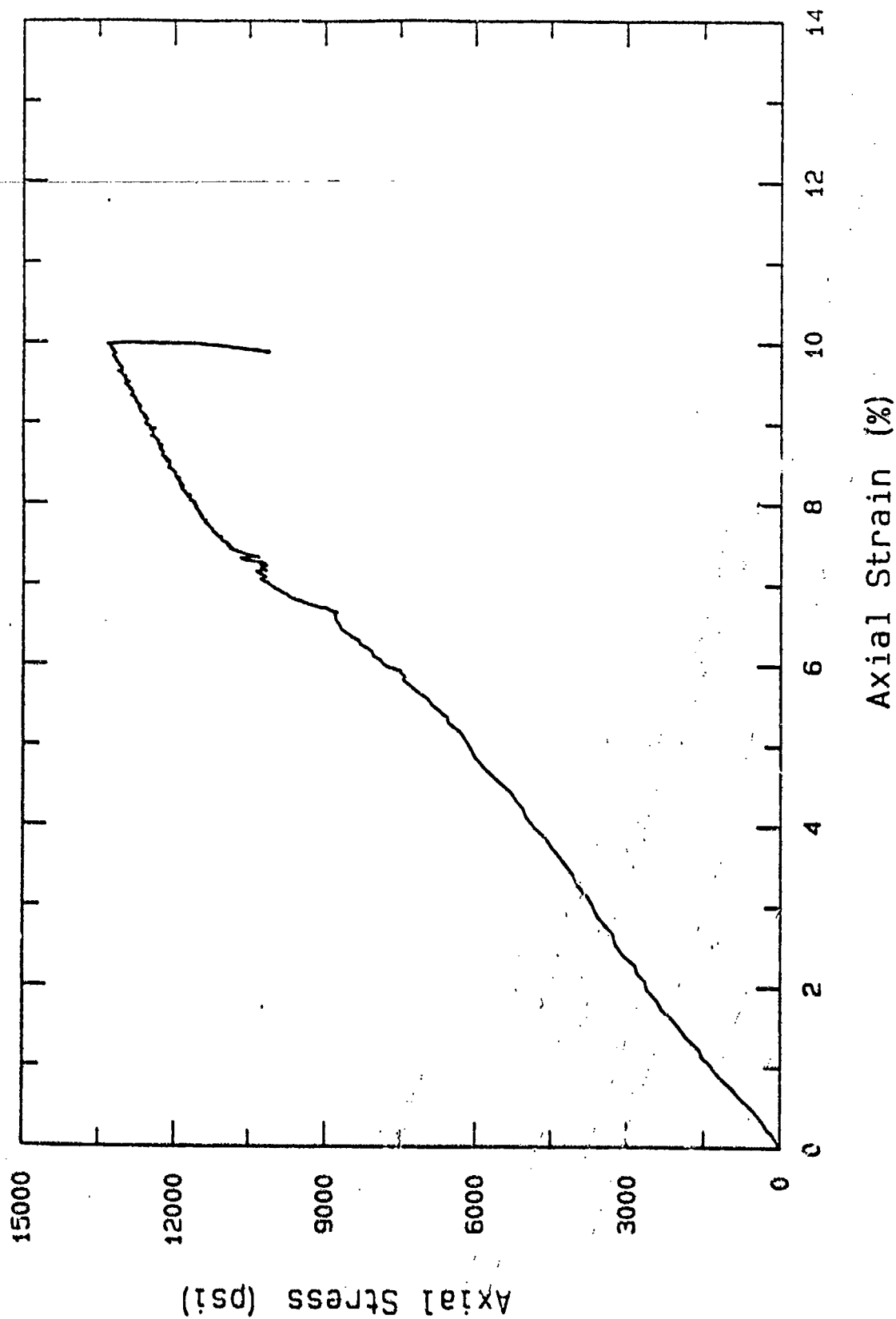


Figure 7.10b. Axial stress-axial strain data, hydrostatic loading and TXS loading at constant mean stress of approximately 10,000 psi.

Hydrostat w/Triax (G11C7)  
Beach Sand

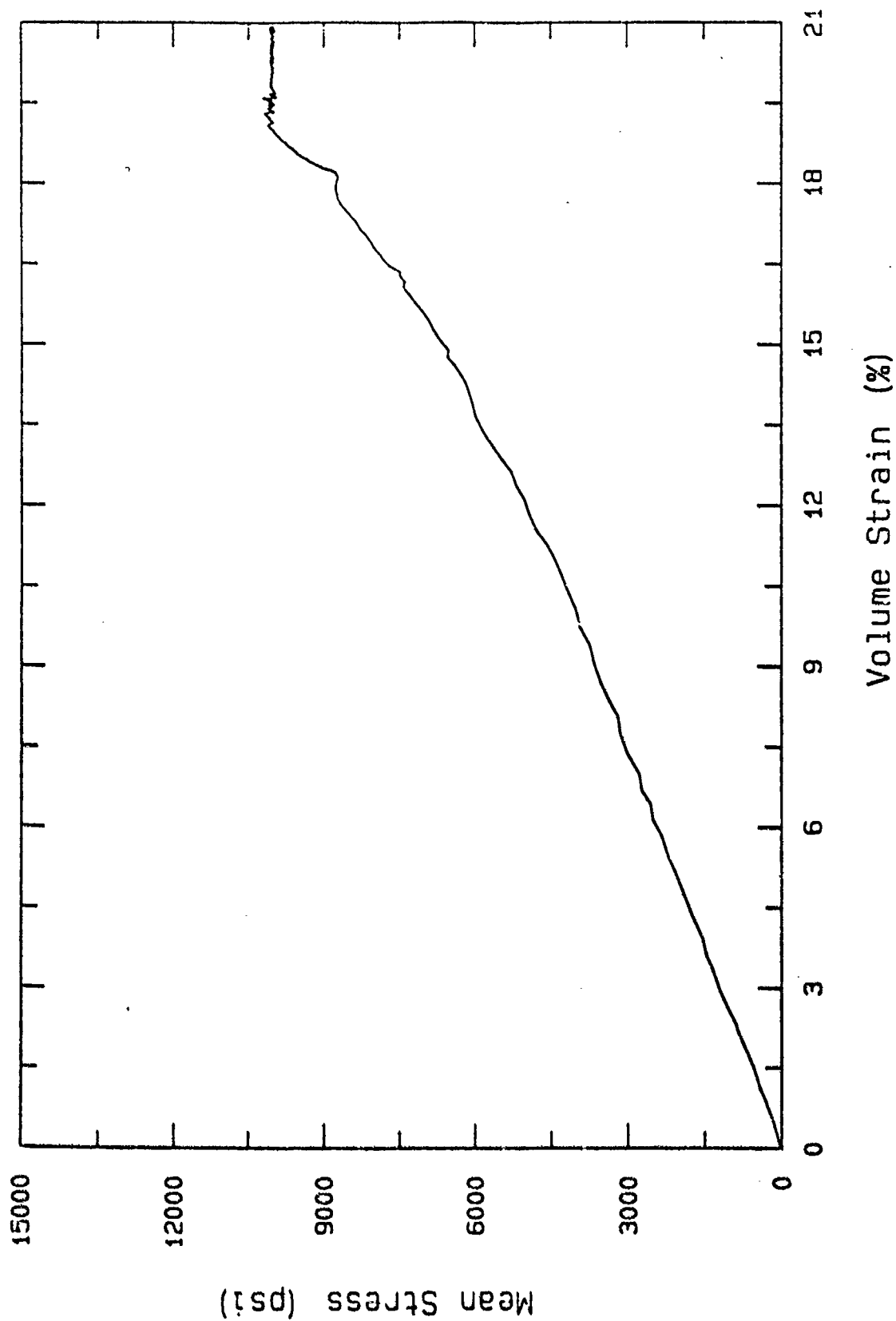


Figure 7.10c. Mean stress-volume strain data, hydrostatic loading and TXS loading at constant mean stress of approximately 10,000 psi.

# Hydrostat w/Triax (G11C7) Beach Sand

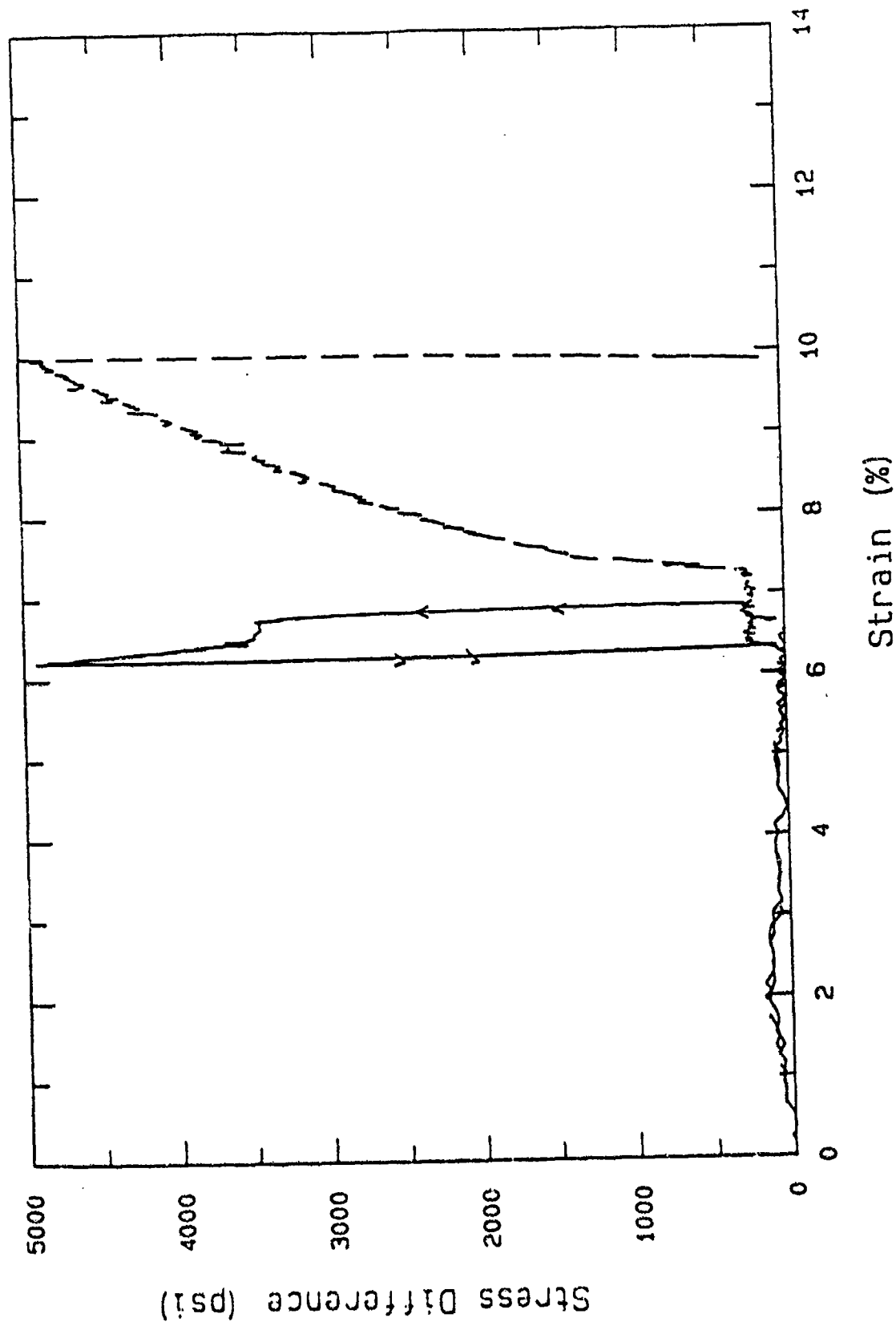


Figure 7.10d. Stress difference-axial and radial strain data, hydrostatic loading and TXS loading at constant mean stress of approximately 10,000 psi.

Hydrostat w/Triax (G11C7)  
Beach Sand

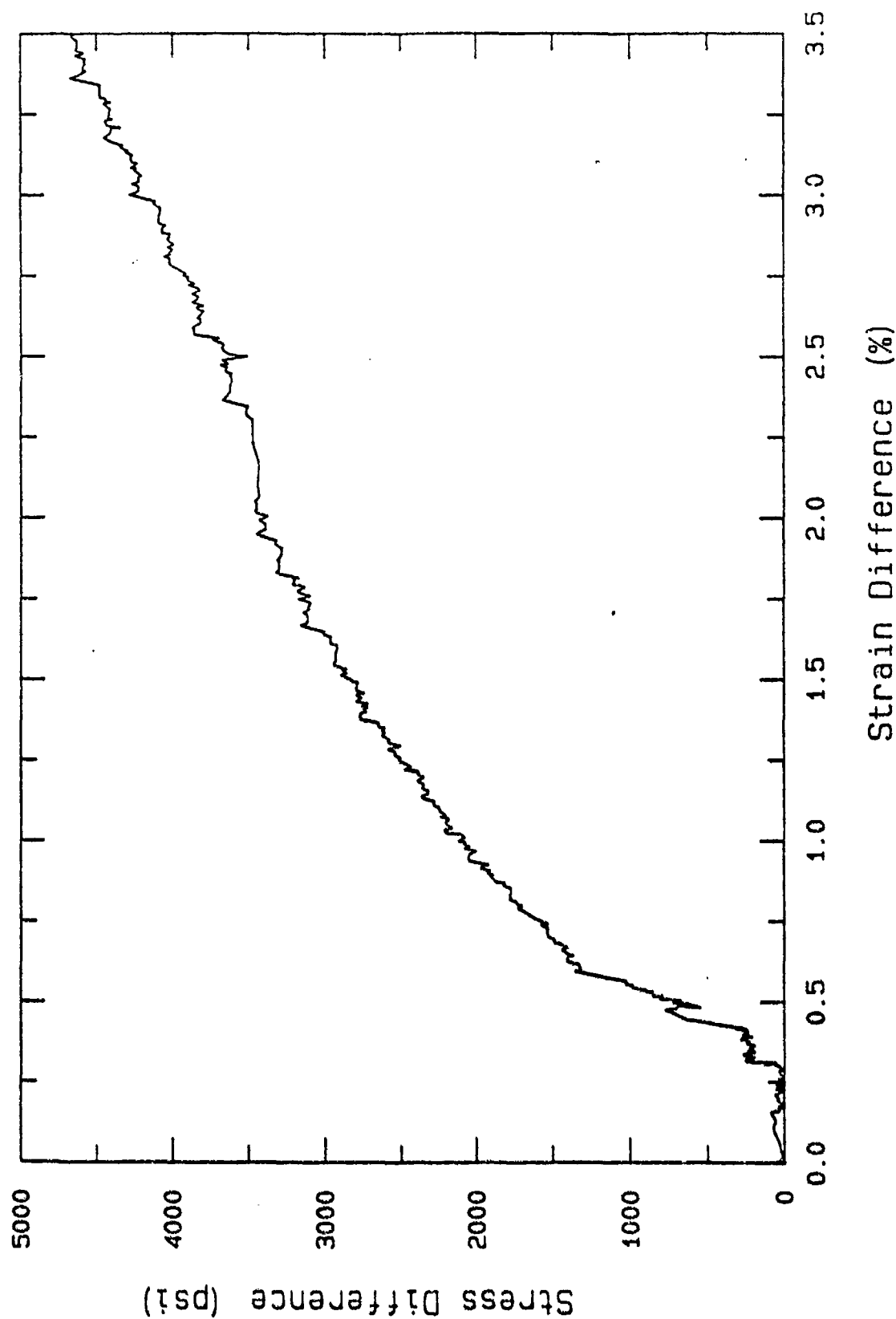


Figure 7.10e. Stress difference-strain difference data, hydrostatic loading and TXS loading at constant mean stress of approximately 10,000 psi.

# Hydrostat w/Triax (G11C7) Beach Sand

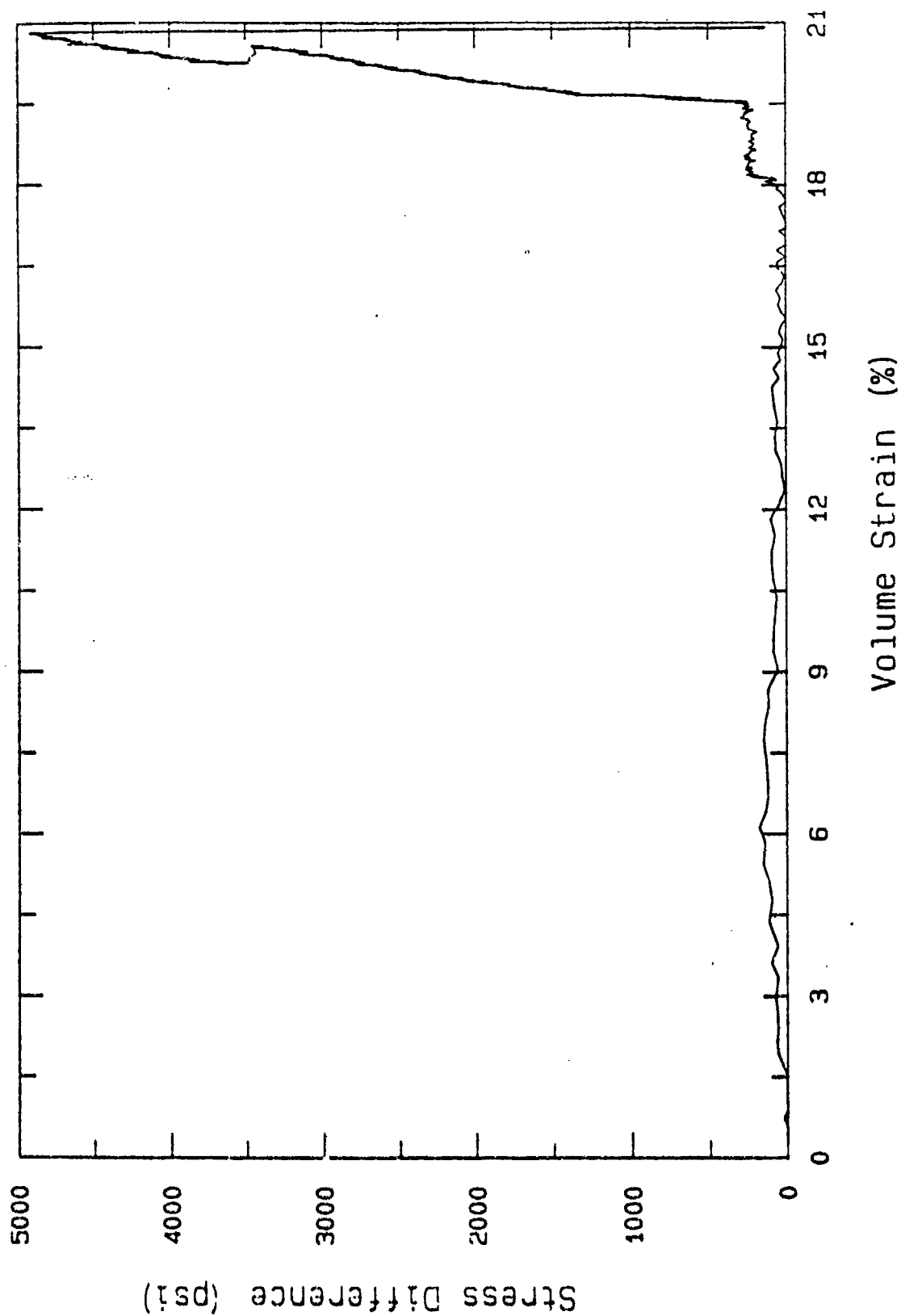


Figure 7.10f. Stress difference-volume strain data, hydrostatic loading and TXS loading at constant mean stress of approximately 10,000 psi.

Hydrostat w/Triax (G11C7)  
Beach Sand

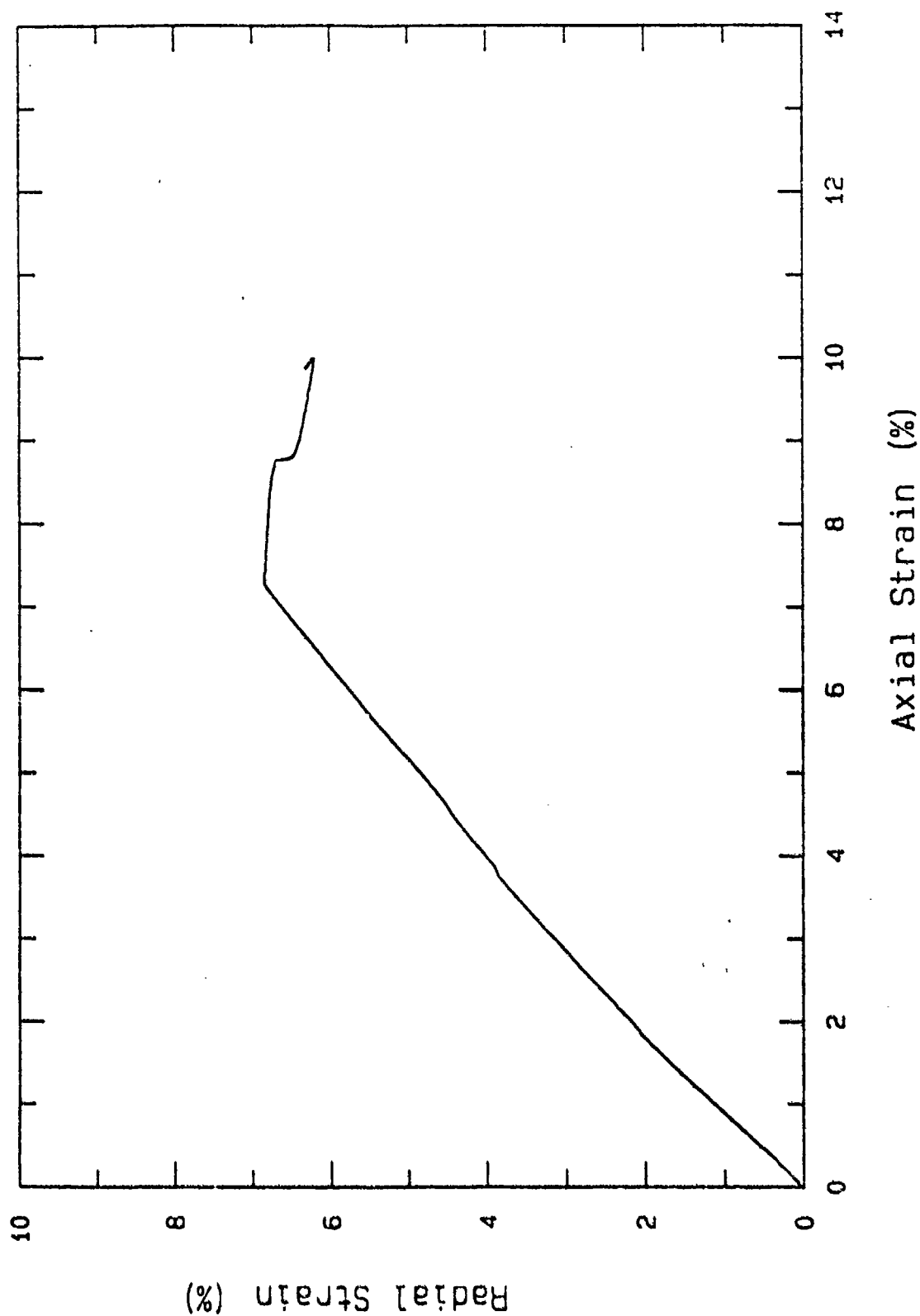


Figure 7.10g. Radial Strain-axial strain data, hydrostatic loading and TXS loading at constant mean stress of approximately 10,000 psi.



# Hydrostat w/Triax (G11C7) Beach Sand

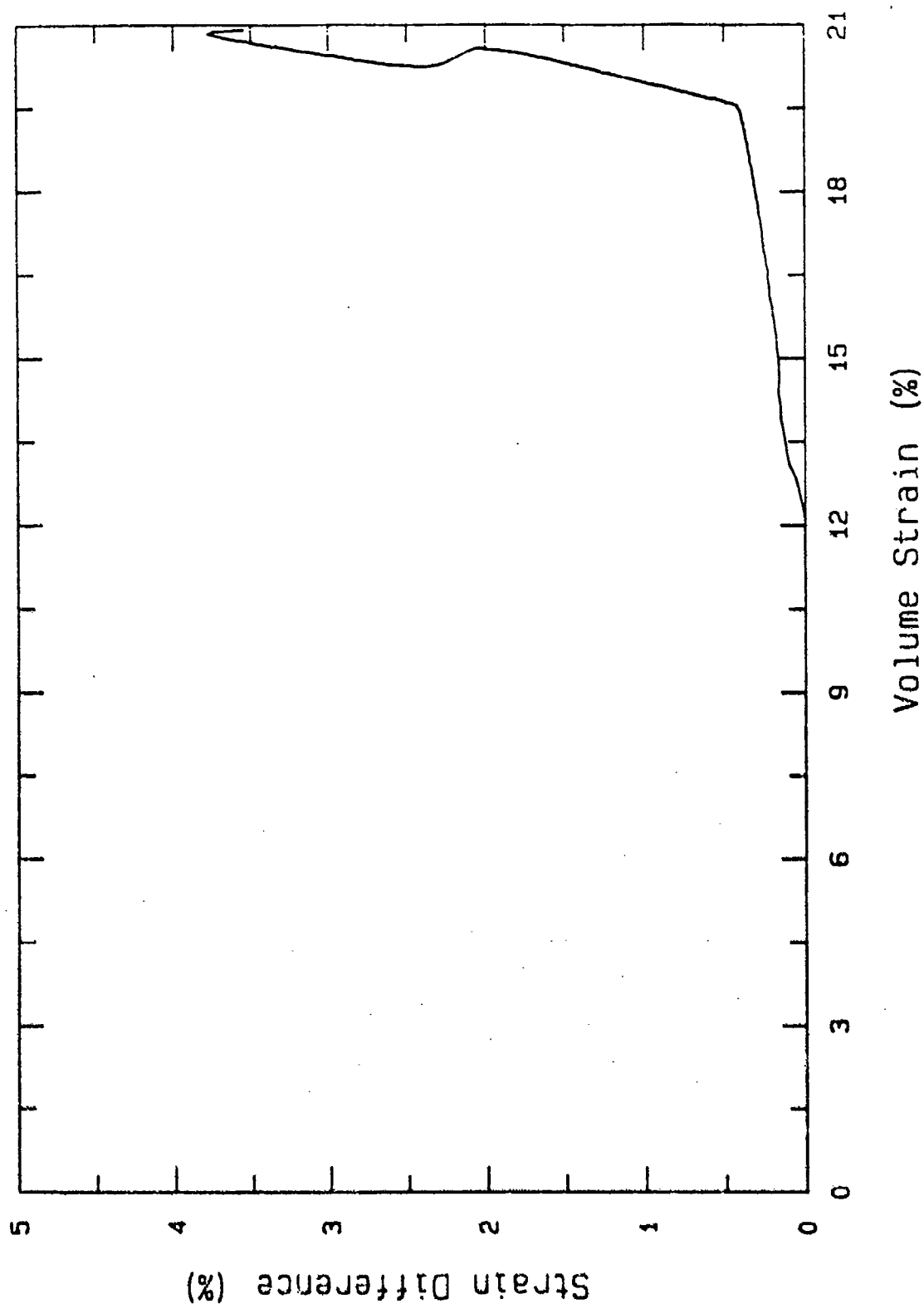


Figure 7.10h. Strain difference-volume strain data, hydrostatic loading and TXS loading at constant mean stress of approximately 10,000 psi.

# Grain Size Distribution U23A&B7

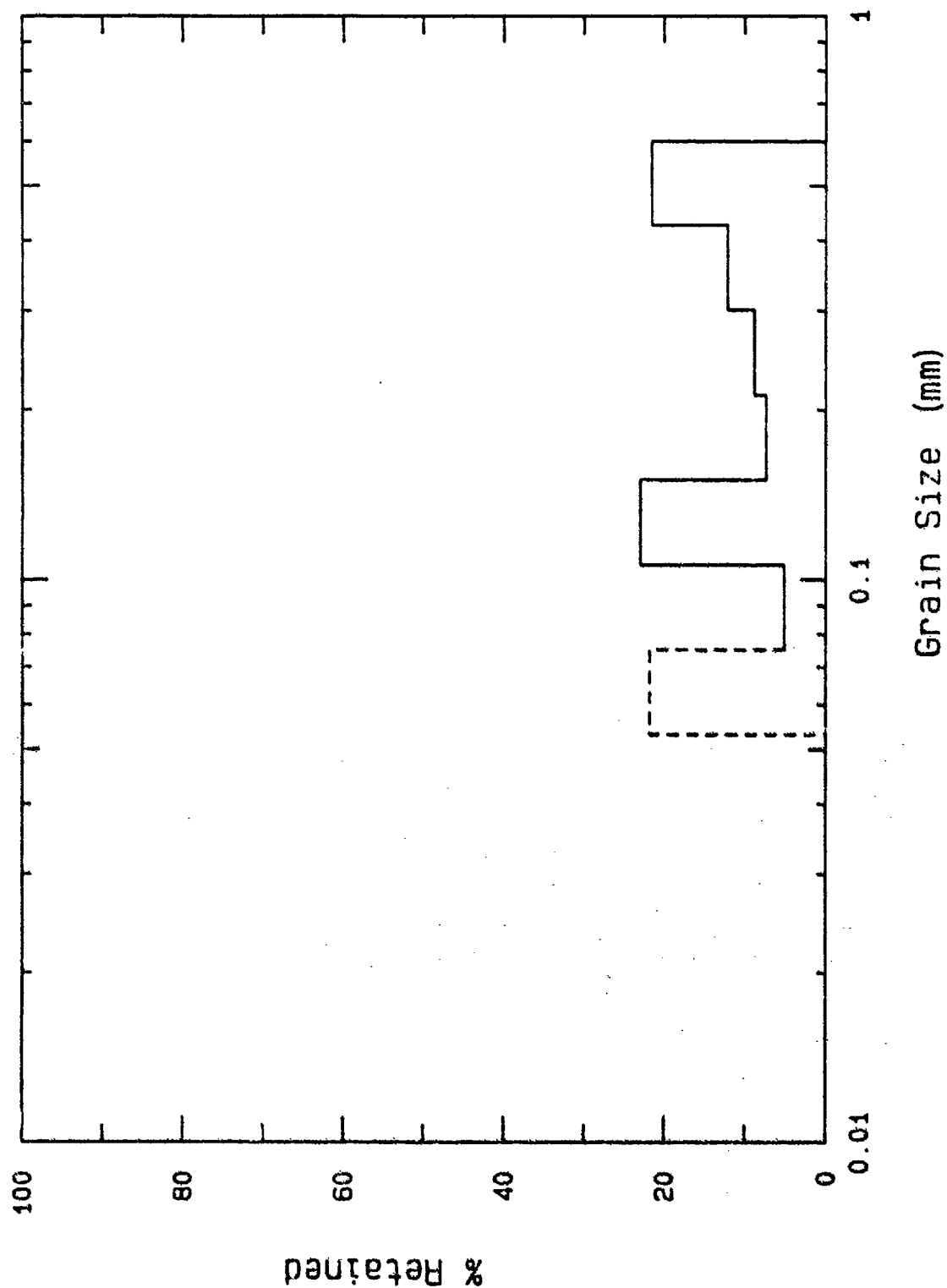


Figure 7.11a. Post test grain size and weight fraction distribution following triaxial compression to 15,350 psi mean stress.

Hydrostat (U23A7)  
Beach Sand

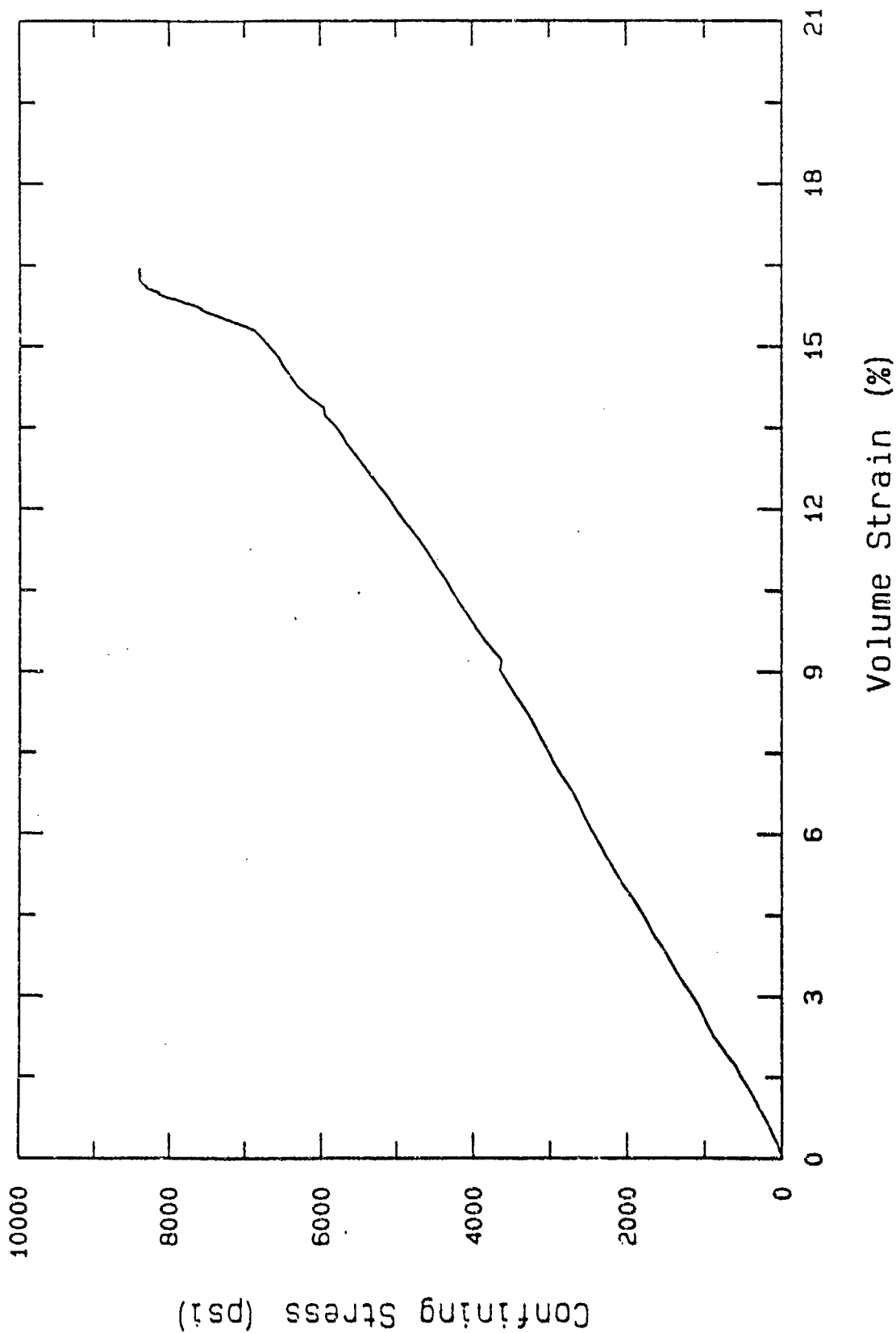


Figure 7.11b. Pressure-volume strain data to 8400 psi prior to triaxial compression to 15,350 psi mean stress.

Triax (U23B7)  
Beach Sand, Confining Pressure = 8400 psi

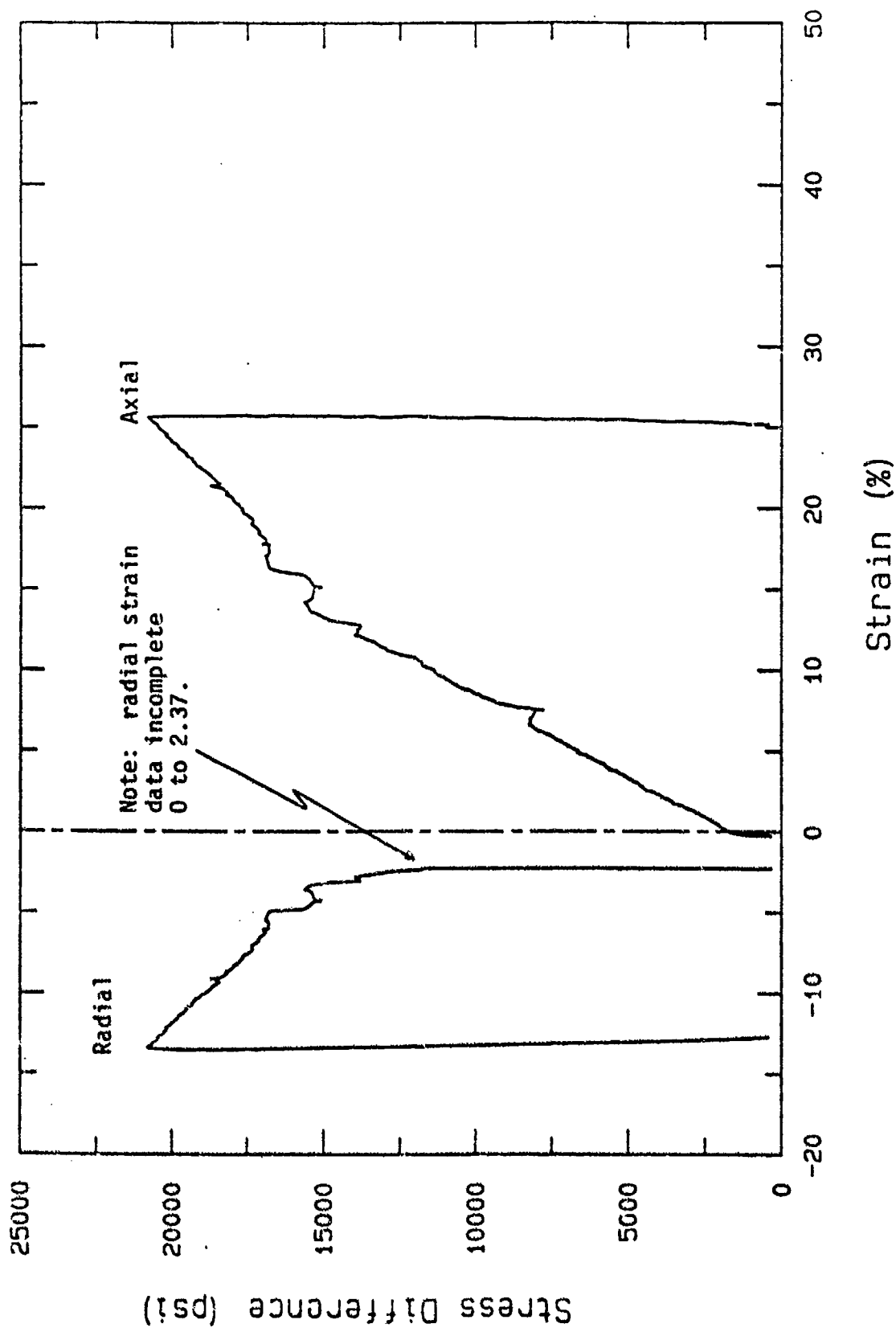


Figure 7.11c. Stress difference-axial and radial strain data, triaxial compression to 15,350 psi mean stress.

Triax (U23B7)  
Beach Sand, Confining Pressure = 8400 psi

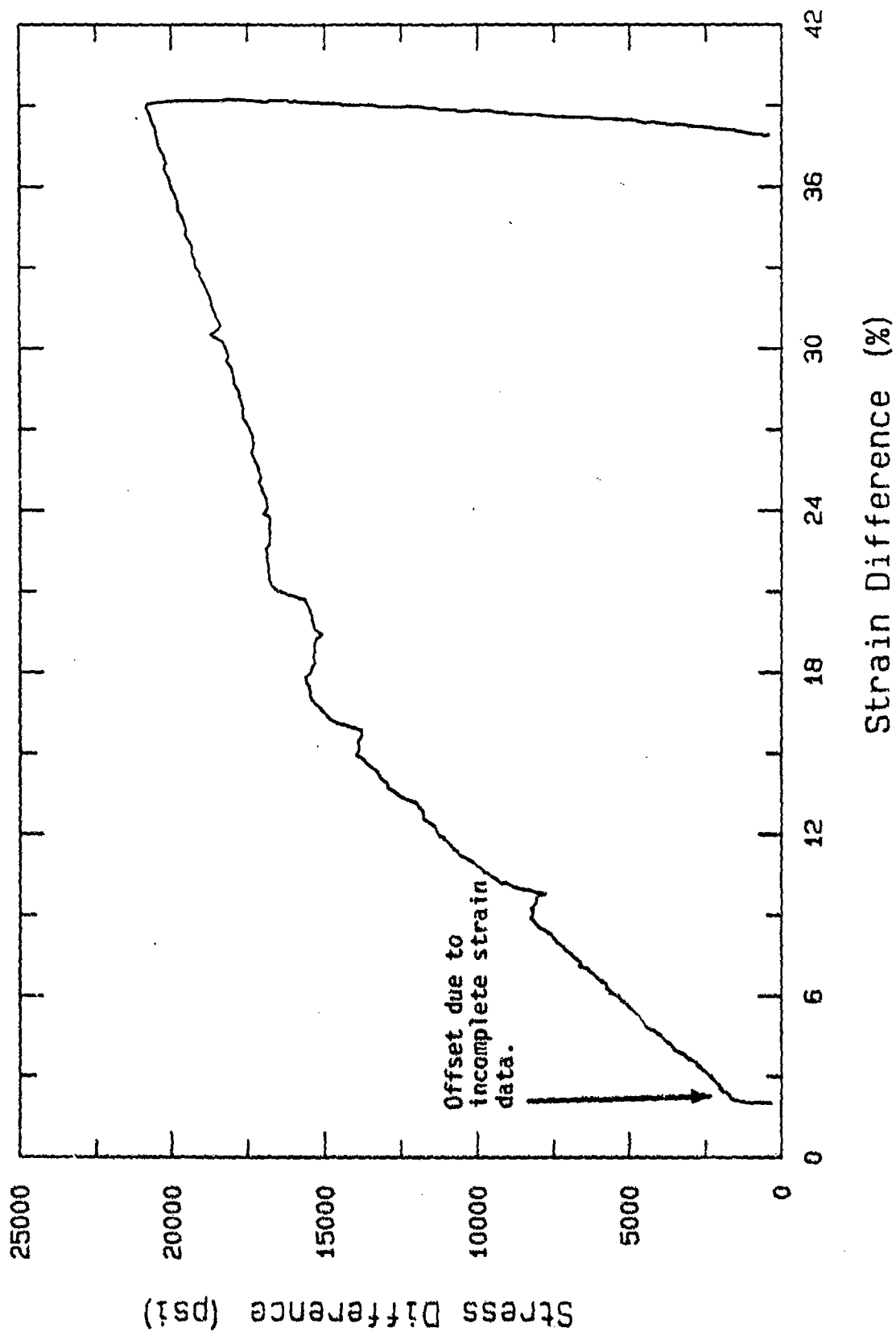


Figure 7.11d. Stress difference-strain difference data, triaxial compression to 15,350 psi mean stress.

Triax (U23B7)  
Beach Sand, Confining Pressure = 8400 psi

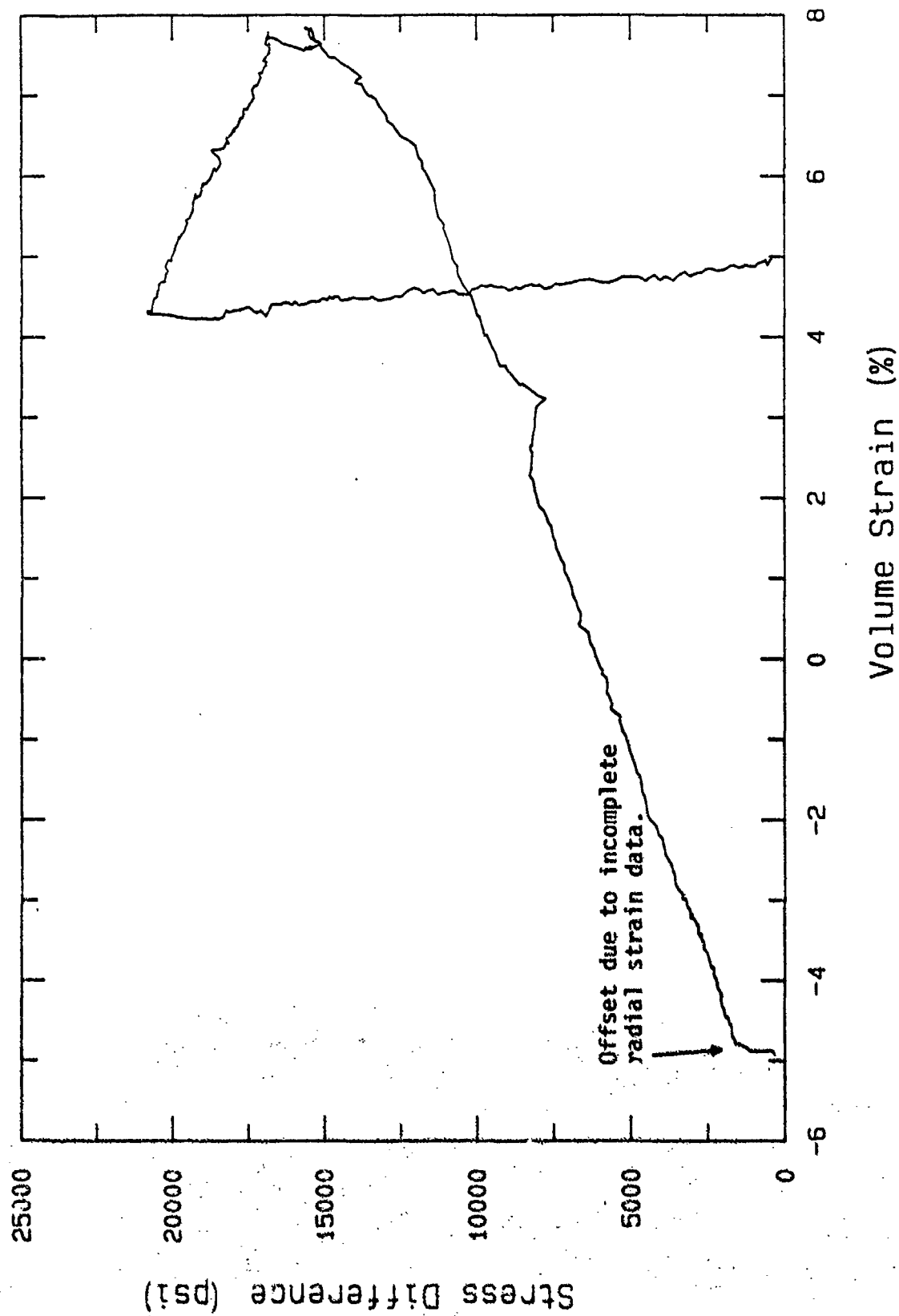


Figure 7.11e. Stress difference-volume strain data, triaxial compression to 15,350 psi mean stress.

Triax (U23B7)  
Beach Sand, Confining Pressure = 8400 psi

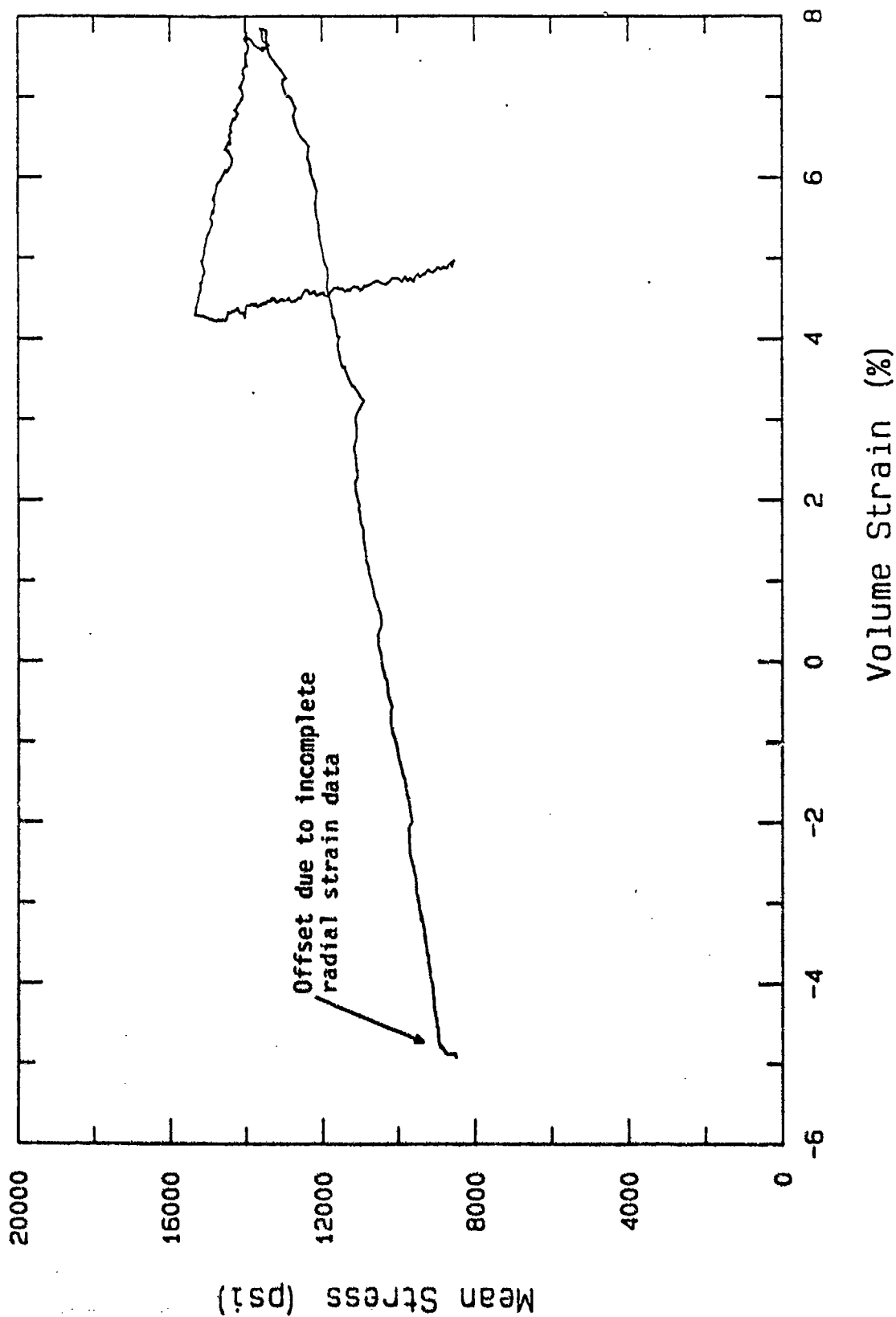


Figure 7.11f. Mean stress-volume strain data, triaxial compression to 15,350 psi mean stress.

Triax (U23B7)  
Beach Sand, Confining Pressure = 8400 psi

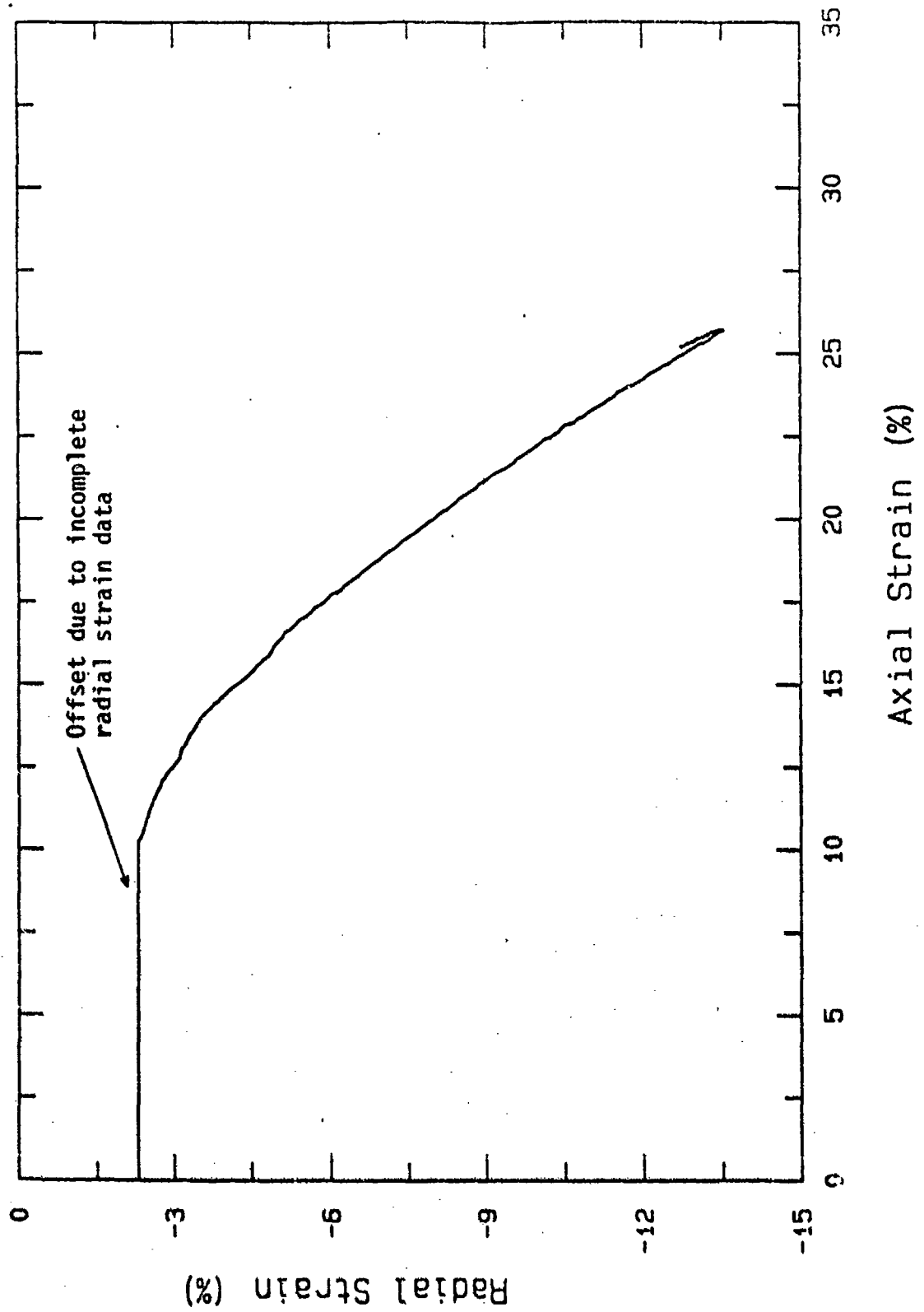


Figure 7.11g. Radial strain-axial strain data, triaxial compression to 15,350 psi mean stress.



Triax (U23B7)  
Beach Sand, Confining Pressure = 8400 psi

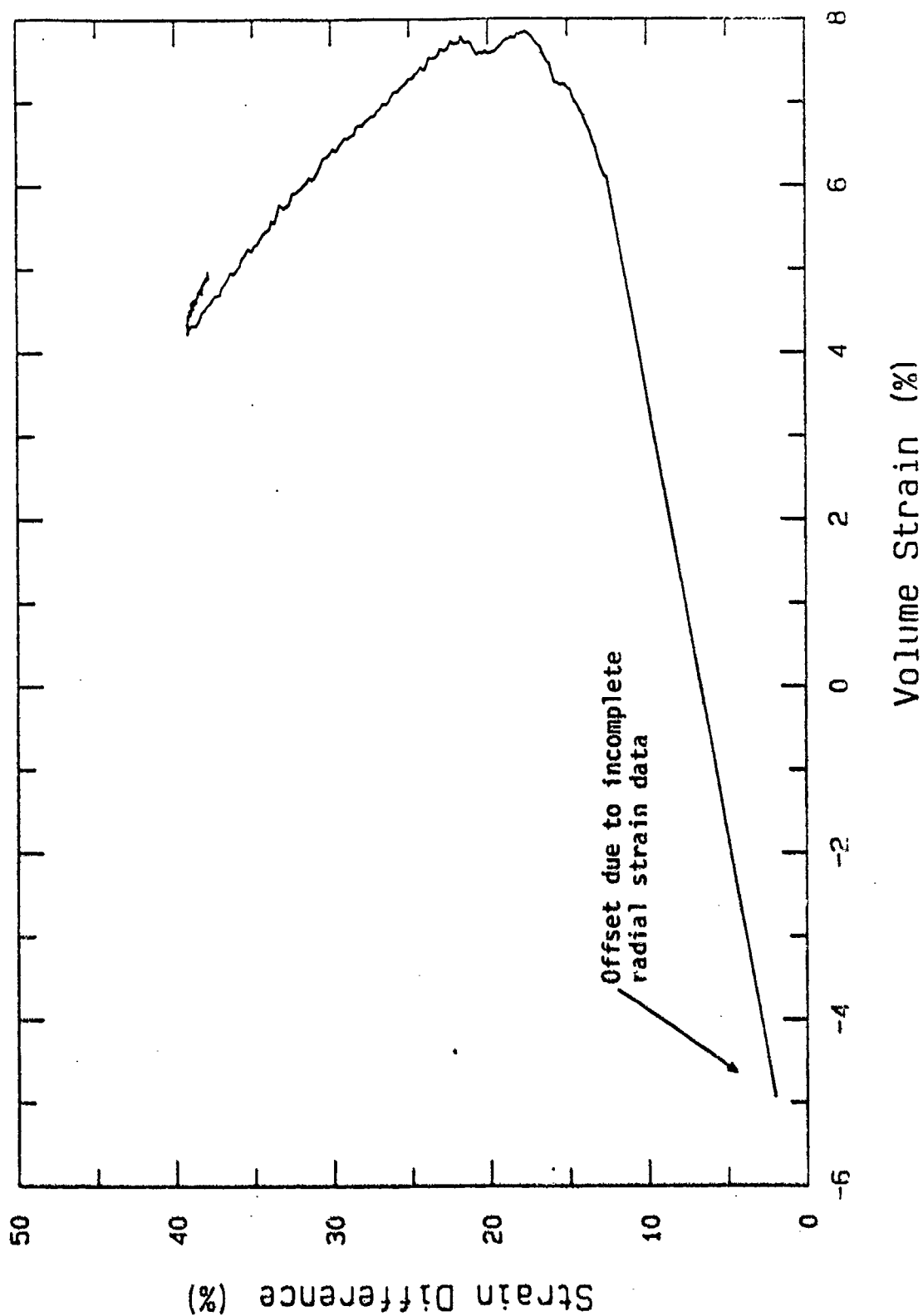


Figure 7.11h. Strain difference-volume strain data. triaxial compression to 15,350 psi mean stress.

# Grain Size Distributions

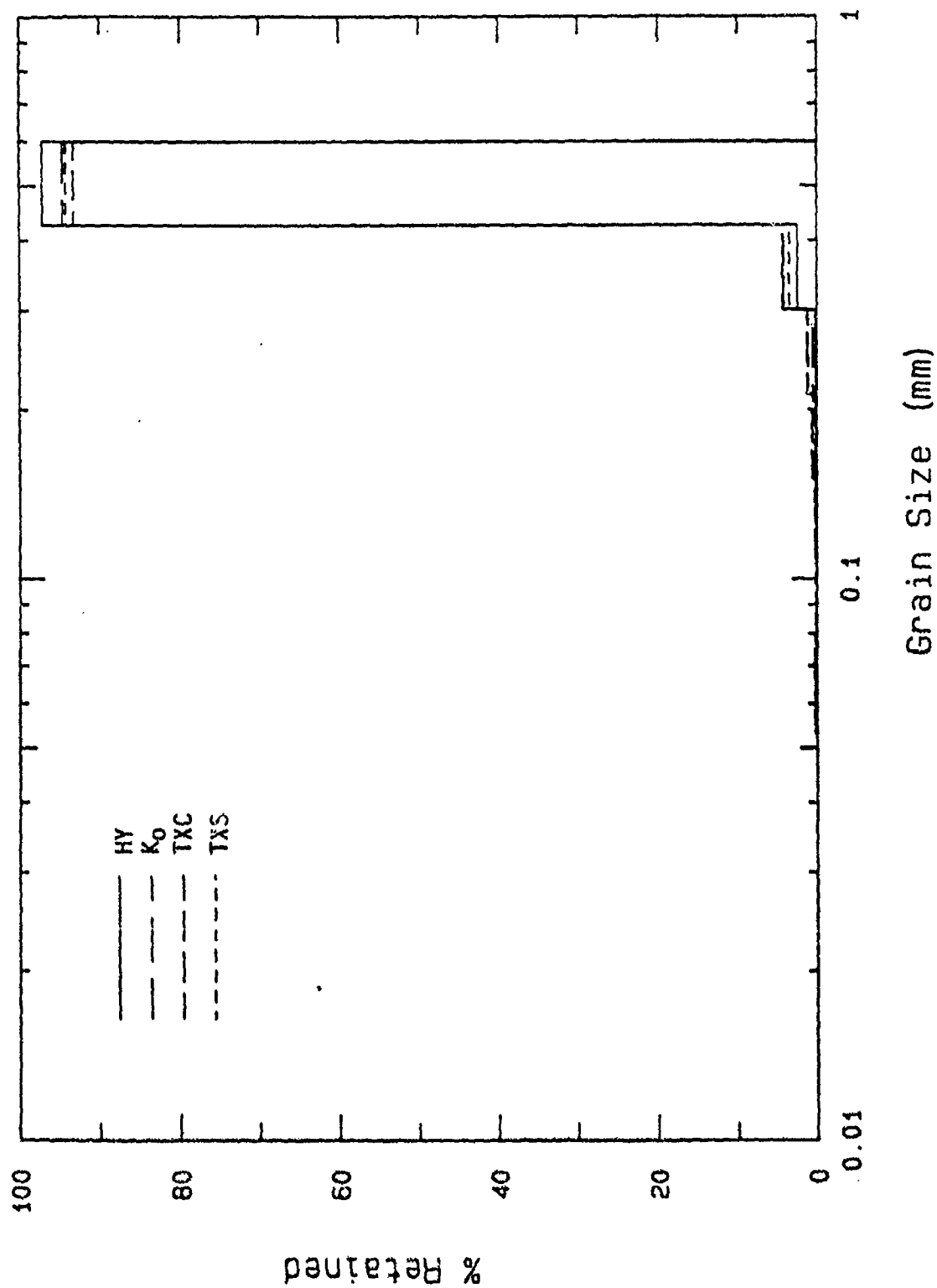


Figure 7.12. Comparison of post test grain size and weight fraction distributions from samples loaded to 1000 psi mean stress.

# Grain Size Distributions

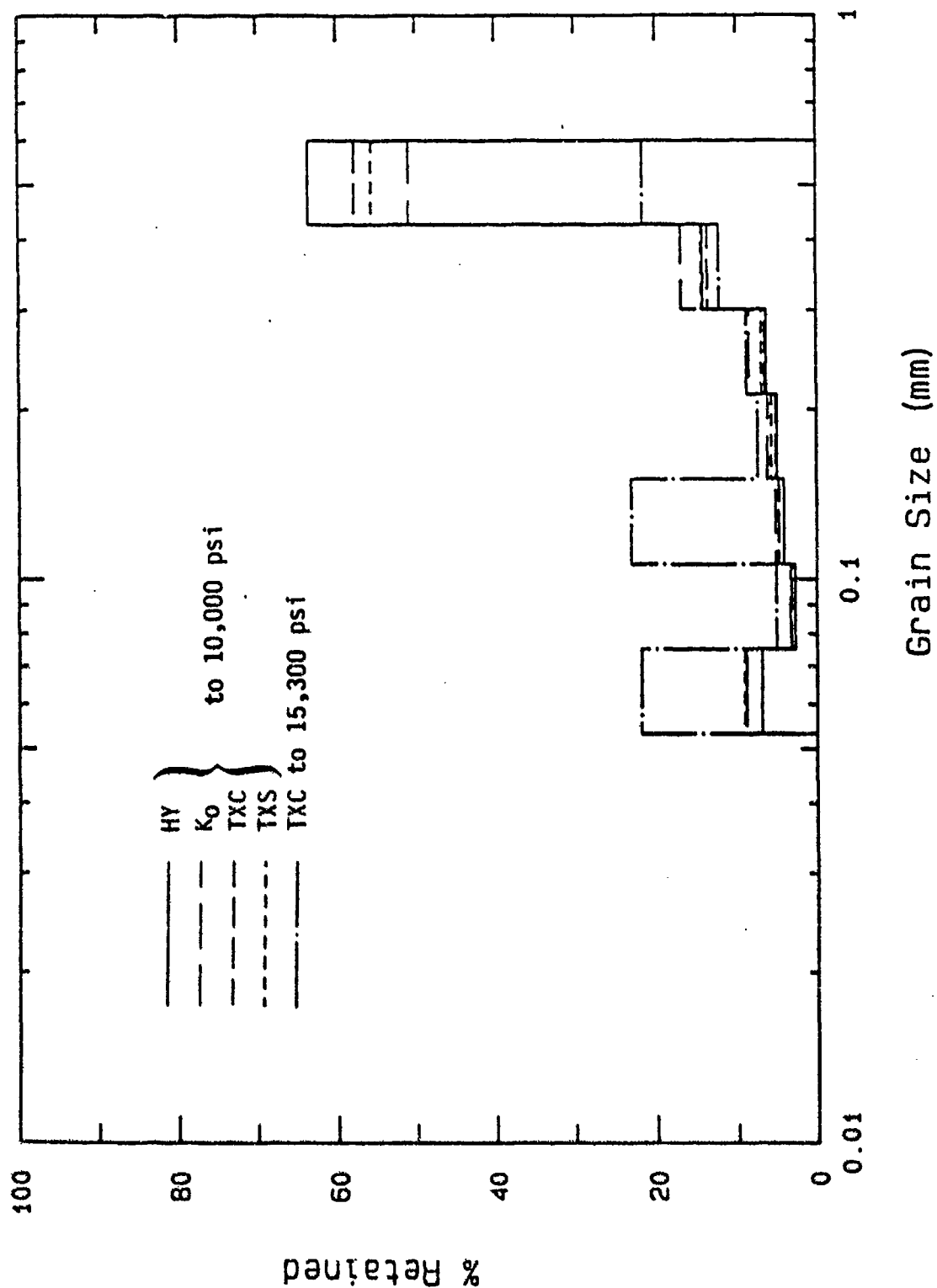


Figure 7.13. Comparison of post test grain size and weight fraction distribution from samples loaded to 10,000 psi and 15,350 psi mean stress.



## SECTION 8

### LABORATORY INVESTIGATION OF FLUID FLOW THROUGH POROUS MEDIA

#### 8.1 INTRODUCTION

A key component of multiphase modeling is the equation of motion of the fluid within the porous skeleton. Nearly all previous work in this area is based on work performed by Biot (1956, 1962a, 1962b). Biot determined theoretical relationships for nonsteady state laminar flow through circular and flat ducts.

Ward (1964) conducted a series of experimental flow tests and based upon analysis of these tests, he proposed an empirical equation which is applicable for both laminar and turbulent flow in porous media. However, Ward's work was limited to steady state flow.

A proposed viscous friction equation combining our generalization of Biot's theoretical equation and Ward's empirical equation is given by:

$$D_i = \frac{\gamma_f}{k} \dot{w}_i + \frac{\beta_f}{k^2} (\dot{w}_i) + \frac{\rho_f}{n} r \ddot{w}_i \quad (8.1)$$

where  $D_i$  = viscous friction force between the pore fluid and the soil skeleton per unit volume of pore fluid

$\gamma_f$  = unit weight of the pore fluid

$\rho_f$  = mass density of the pore fluid

$n$  = porosity

$k$  = coefficient of permeability

$r$  = mass increment factor

$\beta_f$  = Ward's empirical constant which is a function of both skeleton and fluid properties

$\dot{w}_i$  = apparent fluid velocity

$\ddot{w}_i$  = apparent relative fluid acceleration

This equation requires validation and/or modification based on laboratory experiments. The laboratory investigation of fluid friction in nonsteady state flow and in the turbulent regime is an important part of the experimental portion of our research. A research plan was formulated which includes the following goals:

1. Design and fabrication of a high pressure laboratory fluid flow device.
2. Experimental verification of Biot's theoretical equations.
3. Validation of Ward's flow model.
4. Experimental tests to verify and/or modify Equation 8.1.
5. Development of relationships for nonuniform flow paths under steady state flow.
6. Development of relationships for nonsteady state flow through nonuniform paths in the turbulent flow regime.

## 8.2 RESEARCH ACCOMPLISHMENTS

### 8.2.1 Design and Fabrication

The design process for the fluid flow device included determination of equipment and testing criteria to accomplish the goals listed above. These criteria include sample size requirements for both uniform and nonuniform ducts, pressure and pressure gradient conditions, test control and data acquisition requirements.

It was determined that the device must be capable of testing samples 2.0 inches in diameter and 9.0 inches in length. Other capabilities include the ability to pressurize the fluid to 5,000 psi, the ability to measure and

control the rate of flow through the sample, the ability to measure the pressure and temperature on the high and low pressure sides of the sample, and the ability to change either the fluid or sample easily.

Based on the design criteria, a flow device was designed and constructed utilizing components of a 5,000 psi hydraulic cylinder. A schematic of the device is shown in Figure 8.1. A computer controlled servo valve provides hydraulic oil pressure to the rod side of the piston which pressurizes the large fluid reservoir shown. The computer control allows various loading conditions to be programmed including specified steady state conditions and a variety of nonsteady state flow conditions including constant velocity, constant acceleration, and variable acceleration. By monitoring flow under these various conditions the terms of Equation 8.1 can be investigated independently. Flow is measured by monitoring the position of the loading piston. Based on the position of the piston at each time step and the area of the reservoir, a simple calculation yields the flow through the sample. Transducers measure the pressure and temperature on both the high and low pressure sides of the sample from which the pressure and temperature gradients can be calculated.

#### 8.2.2 Steady State Flow Tests, Circular Duct

Steady state flow tests were conducted through both a circular and a flat duct. The circular duct has a diameter of 0.0625 inches and a length of 9.125 inches.

Data output from each of a series of steady state flow tests is in the overall form of displacement and pressure difference time histories. Figures 8.2 and 8.3 show typical output from a circular duct test. A velocity value is measured from the displacement time history by finding the slope of the line. The slope of the line is taken between two time intervals when the pressure difference is constant.

Figure 8.4 shows the results of 36 steady state flow tests using kerosene as the pore fluid. The velocities range in value from 2.5 inches per second

to 2,350 inches per second. The pressure gradient, which is equal to the overall pressure difference divided by the duct length, is plotted as a function of the velocity. Figure 8.5 is an enlargement of Figure 8.4 below 180 in/s. The initial portion of the line defined by the points below about 60 in/s is clearly linear which corresponds to the laminar flow regime. Figure 8.4 shows that the points transition from a linear relationship into a nonlinear relationship where the pressure gradient is proportional to the square of the velocity. The latter corresponds to the turbulent flow regime and the transition region between the linear and turbulent regimes is the transitional flow regime.

The governing equation of motion for pore fluid flow derived from Biot's work (see previous references) expresses the pore pressure gradient,  $\pi_{,i}$ , as

$$\pi_{,i} = \rho_f \ddot{U}_i + D_i \quad (8.2)$$

where

$\pi_{,i}$  = pressure gradient

$\ddot{U}_i$  = acceleration of the pore fluid

For steady state flow through a circular or flat duct, Equation 8.2 can be combined with Equation 8.1 to produce the form

$$\pi_{,i} = \frac{\gamma_f}{k} \dot{w}_i + \frac{\beta_f}{k^{\frac{3}{2}}} \dot{w}_i^2 \quad (8.3)$$

Dividing both sides of  $\dot{w}$  produces an equation of the form

$$y = a + bx$$

where

$$a = \frac{\gamma_f}{k}$$



$$b = \frac{\beta_f}{k^{\frac{1}{2}}}$$

Replotting the steady state data in the form of the pressure gradient divided by the relative fluid velocity vs the relative fluid velocity allows a linear regression to be performed. The intercept can be equated with "a" and the slope is equal to "b".

Knowing the unit weight of the fluid allows the calculation of the coefficient of permeability by

$$k = \frac{\gamma_f}{a} \quad (8.4)$$

Once the coefficient of permeability has been calculated, Ward's constant,  $\beta_f$ , can then be evaluated by solving the equation.

$$\beta_f = k^{\frac{1}{2}} b \quad (8.5)$$

Figure 8.6 shows the steady state data from the circular duct replotted with the pressure gradient divided by the velocity plotted as a function of the velocity. A linear relationship is clearly evident. A regression analysis provides an intercept of  $1.91 \times 10^{-3}$  lbs-s/in<sup>4</sup> and a slope of  $2.069 \times 10^{-5}$  lb-s/in<sup>5</sup>. Knowing the unit weight of kerosene is approximately  $2.914 \times 10^{-2}$  lb/in<sup>3</sup> allows the calculation of the coefficient of permeability from Equation 8.4. For the circular duct, the experimental value of k is 15.26 inches per second. Kim and Blouin (1984) showed that k can also be calculated for the circular duct theoretically from the formula

$$k = \frac{n a^2 \gamma_f}{8\mu} \quad (8.6)$$

where

a = the radius of the duct

$\mu$  = dynamic viscosity of the pore fluid

n = porosity

$\gamma_f$  = unit weight of the pore fluid

Substituting the appropriate values into Equation 8.6 yields a theoretical value of permeability equal to 13.45 in/s. This value is satisfyingly close to the 15.26 in/s measured experimentally.

Ward's constant can also be calculated using Equation 3.5 and the measured coefficient of permeability.  $\beta_f$  works out to be  $8.082 \times 10^{-5} \text{ lb-s}^{1.5}/\text{in}^{4.5}$ .

### 8.2.3 Constant Acceleration Flow Tests, Circular Duct

Figures 8.7 and 8.8 present the displacement and pressure difference time histories for a constant acceleration flow test through the circular duct. An equation describing the displacement curve is

$$w = 4.30 t + .526 t^2 \quad (8.7)$$

which can be differentiated to produce the velocity and acceleration equations. These equations are

$$\dot{w} = 4.30 + 1.05 t \quad (8.8)$$

$$\ddot{w} = 1.05$$

To compare this constant acceleration dynamic test data to steady state test data, we computed flow velocities and pressure gradients at 40 and 80 seconds. As shown in Figure 8.9, the dynamic test data agrees with the steady state data, indicating that the magnitude of the fluid acceleration is too low to produce a measurable influence of fluid inertia and mass increment factor on the fluid friction. Attempts will be made to increase accelerations so that these influences can be measured.

#### 8.2.4 Steady State Flow Tests, Flat Duct

As a parallel effort to the circular duct, we also conducted a set of steady state flow tests through a flat duct. The flat duct, as shown in Figure 8.10a, has a height of 0.04 inches, a width of 0.28 inches, and a length of 8.71 inches. The flat duct dynamic flow equations developed by Biot assume that the width of the duct is infinite so that there will be no influence on fluid friction due to the side walls. Our flat duct, however, has finite width with an aspect ratio of seven. To check the accuracy of the steady state test results, as well as the influence of the side wall friction, we developed the method of calculating the equivalent flow system in Appendix E. A total of 39 steady state flow tests through the flat duct were conducted. These results are plotted in Figure 8.11 in terms of flow velocity vs pressure gradient, with an expanded view of the low velocity region of Figure 8.11 given in Figure 8.12. As with the circular duct, we have replotted the steady state data in terms of the pressure gradient divided by the fluid velocity vs the fluid velocity in Figure 8.13. A least squares fit to data yields the coefficient of permeability,  $k = 11.85 \text{ in/s}$ , and Ward's constant,  $\beta_f = 5.0 \times 10^{-5} \text{ lb-s}^{1.5}/\text{in}^{4.5}$ . The theoretical value of  $k$ , computed in Appendix E, is  $11.92 \text{ in/s}$  which is very close to the experimental value of  $11.85 \text{ in/s}$ .

#### 8.2.5 Constant Acceleration Flow Tests, Flat Duct

Three sets of constant acceleration dynamic flow tests through the flat duct were conducted at three different fluid accelerations. Figures 8.14, 8.15, and 8.16 show the dynamic test results for fluid accelerations of 27.1, 42.7, and 63.1  $\text{in/s}^2$ , respectively. For each test, time histories of actual ram displacements, high pressures at the duct inlet and low pressure at the duct outlet are presented.

To evaluate the influence of fluid inertia and mass increment factor on the fluid friction, we computed flow velocities and pressure gradients at various times and compared them to the steady state data as shown in Figure 8.17. The dynamic data presented in Figure 8.17 are slightly above the fit to

the steady state data in the turbulent flow regime. The deviation of the dynamic data from the steady state fit increases slightly with increasing fluid acceleration, but higher fluid accelerations must be achieved in order to make confident measurements of the inertial and mass increment influences.

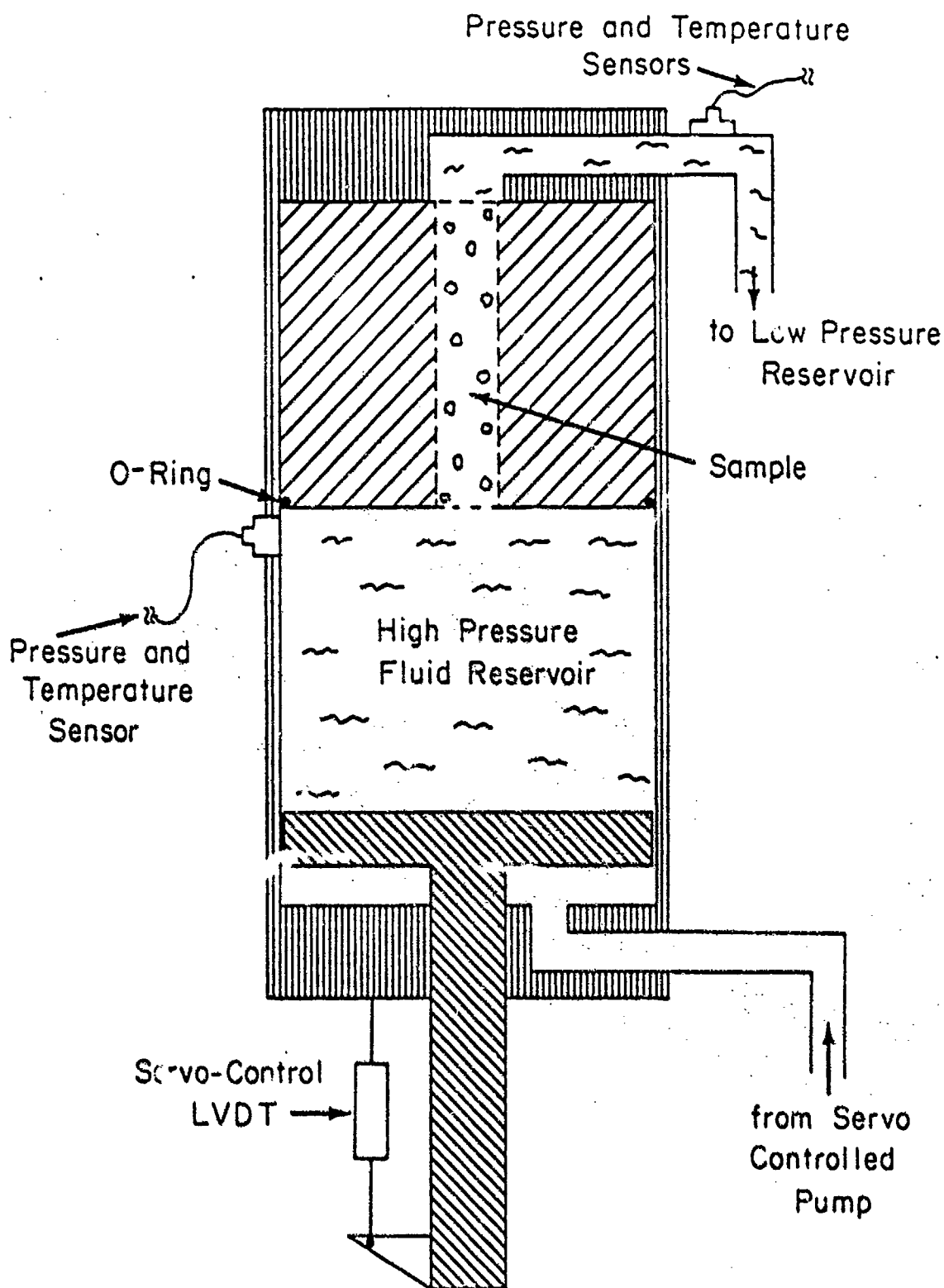


Figure 8.1. Schematic section view of servo controlled fluid flow device.

Test CS25      Diameter = 0.0625 in  
Kerosene

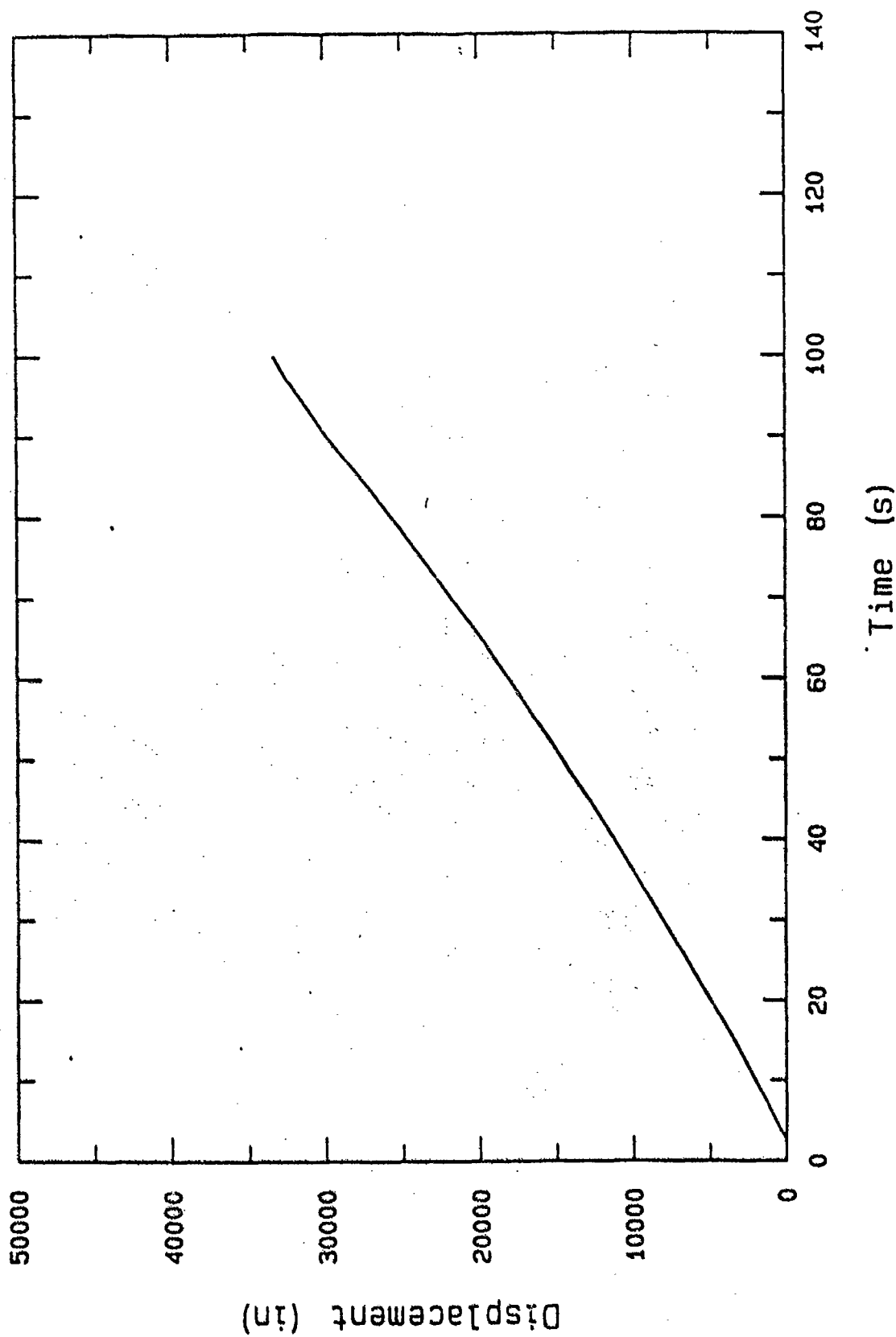


Figure 8.2. Displacement time history for steady state flow through circular duct.

Test CS25      Diameter = 0.0625 in  
Kerosene

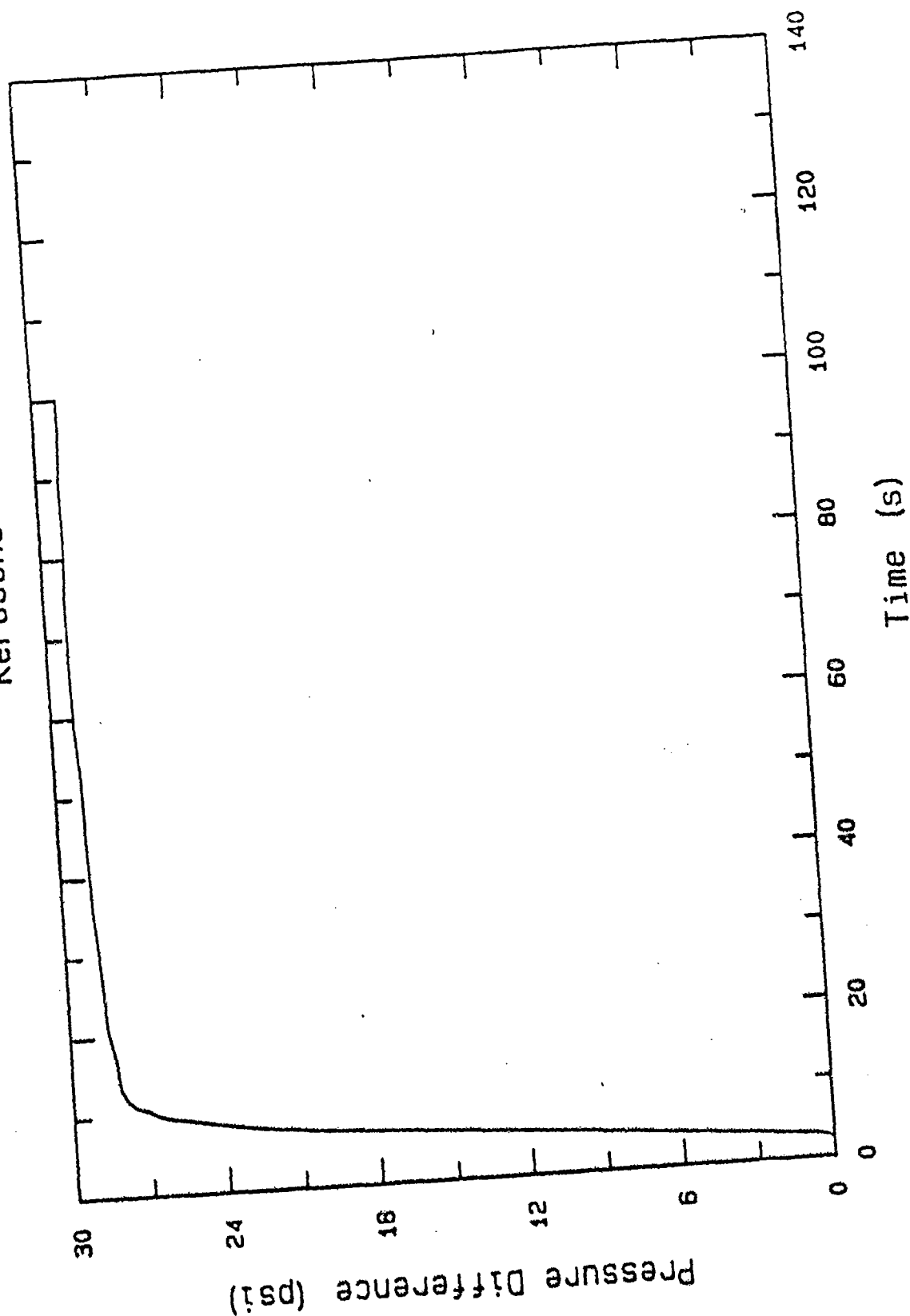
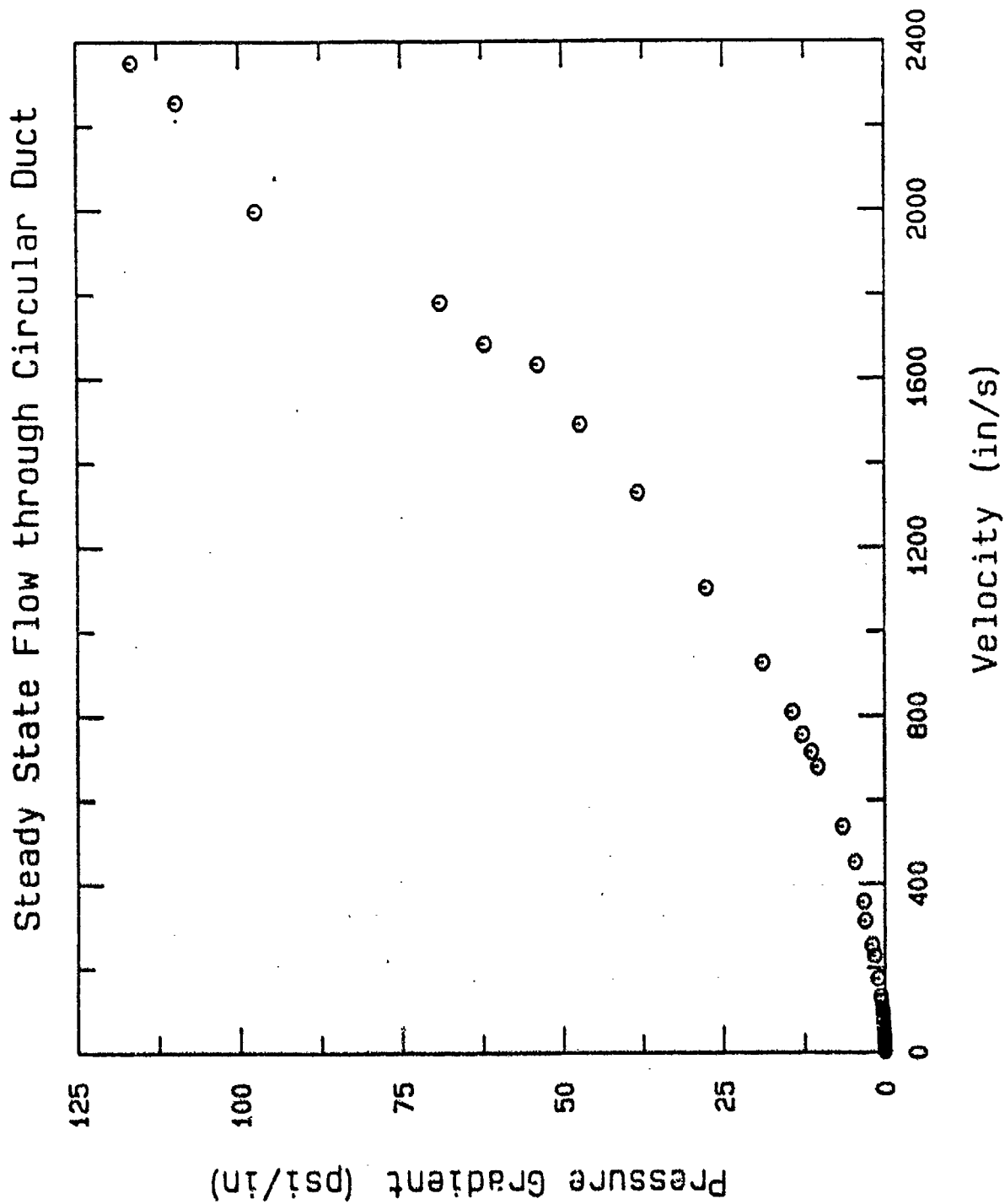


Figure 8.3. Pressure time history for steady state flow through circular duct.





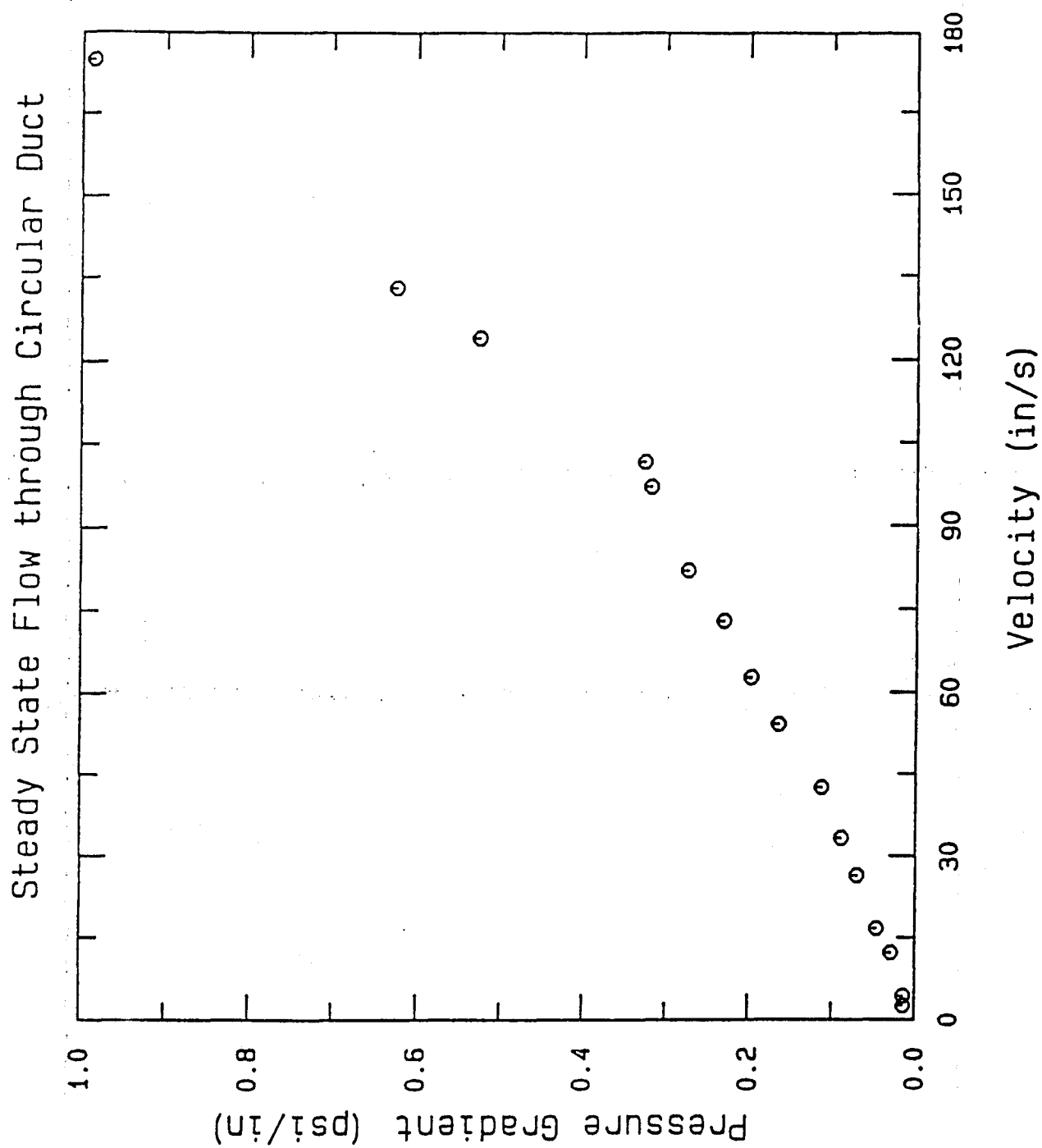


Figure 8.5. Expanded view of Figure 8.4 showing linear relationship in the laminar regime.

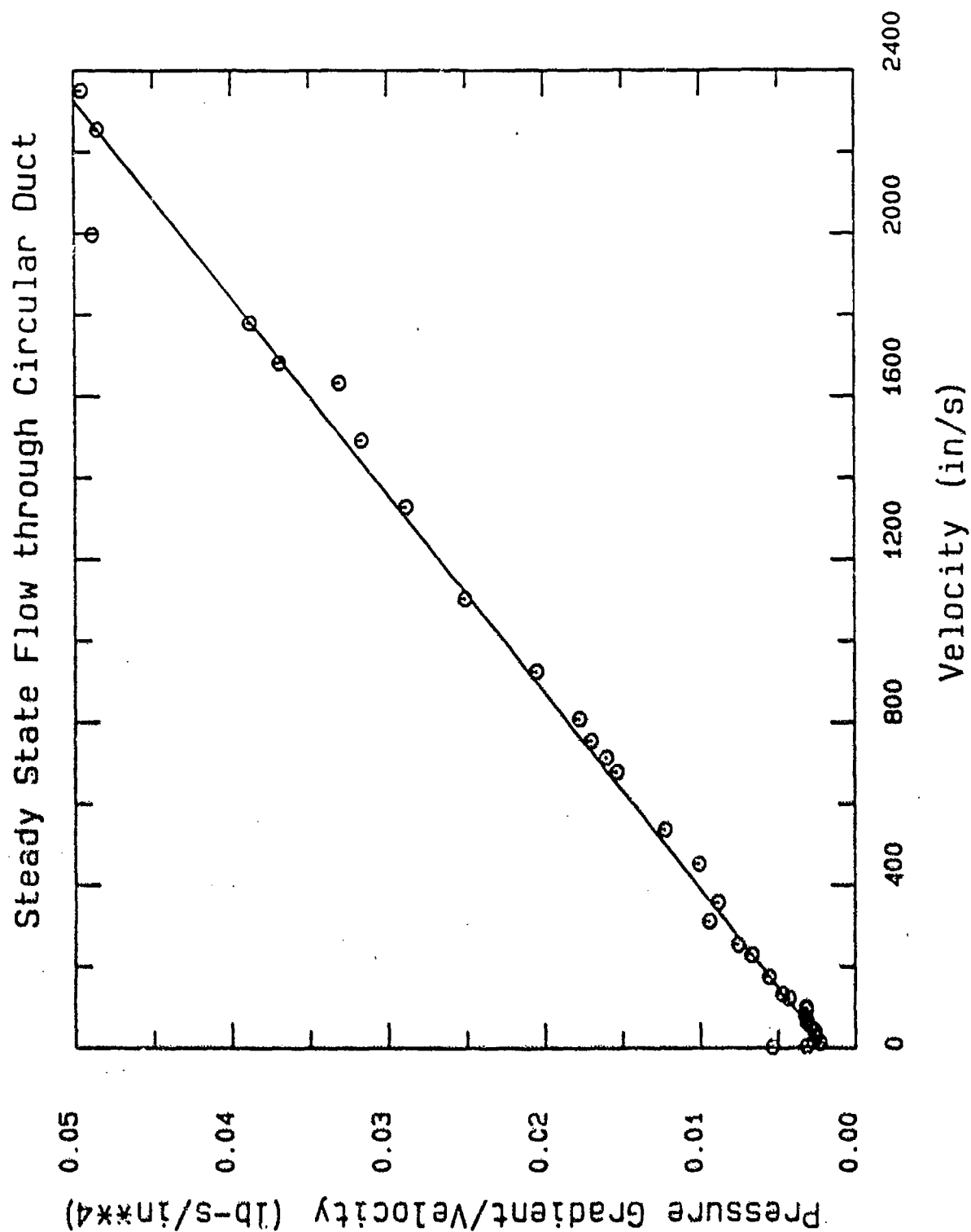


Figure 8.6. Steady state data replotted in order to measure the coefficient of permeability and Hard's constant.

Constant Acceleration Flow through Circular Duct

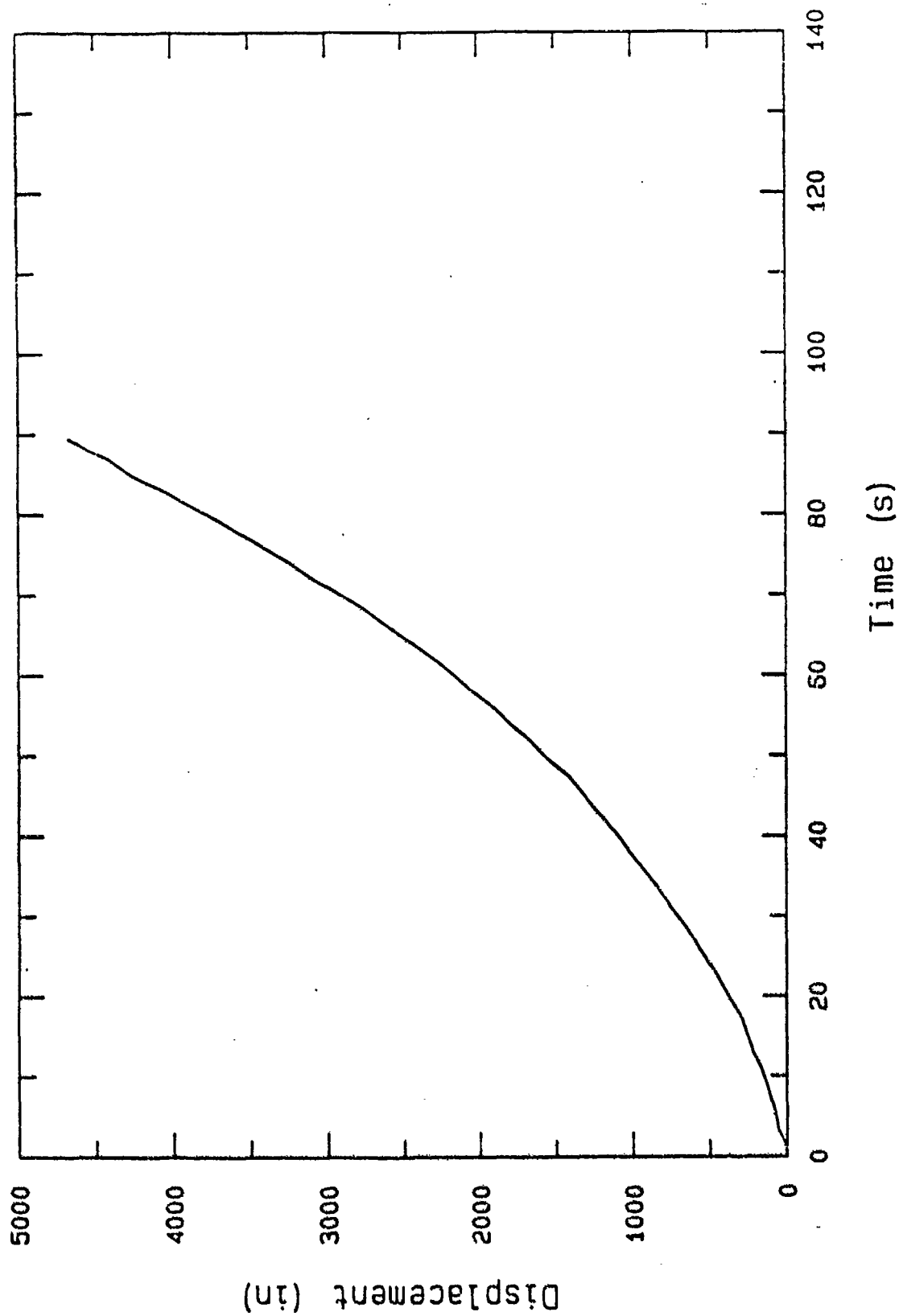


Figure 8.7. Displacement time history from constant acceleration test.

# Constant Acceleration Flow through Circular Duct

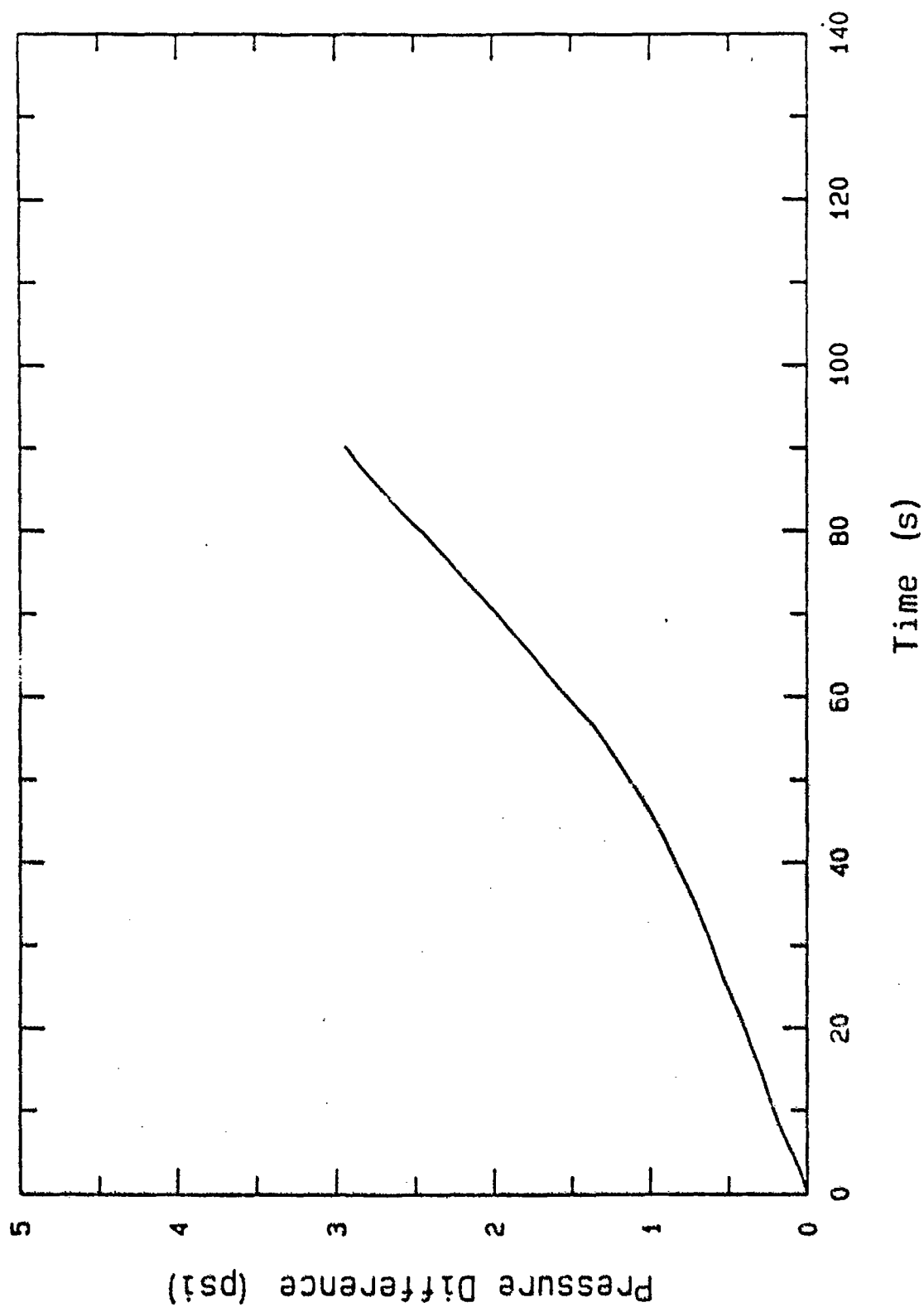


Figure 8.8. Pressure difference time history from constant acceleration test.

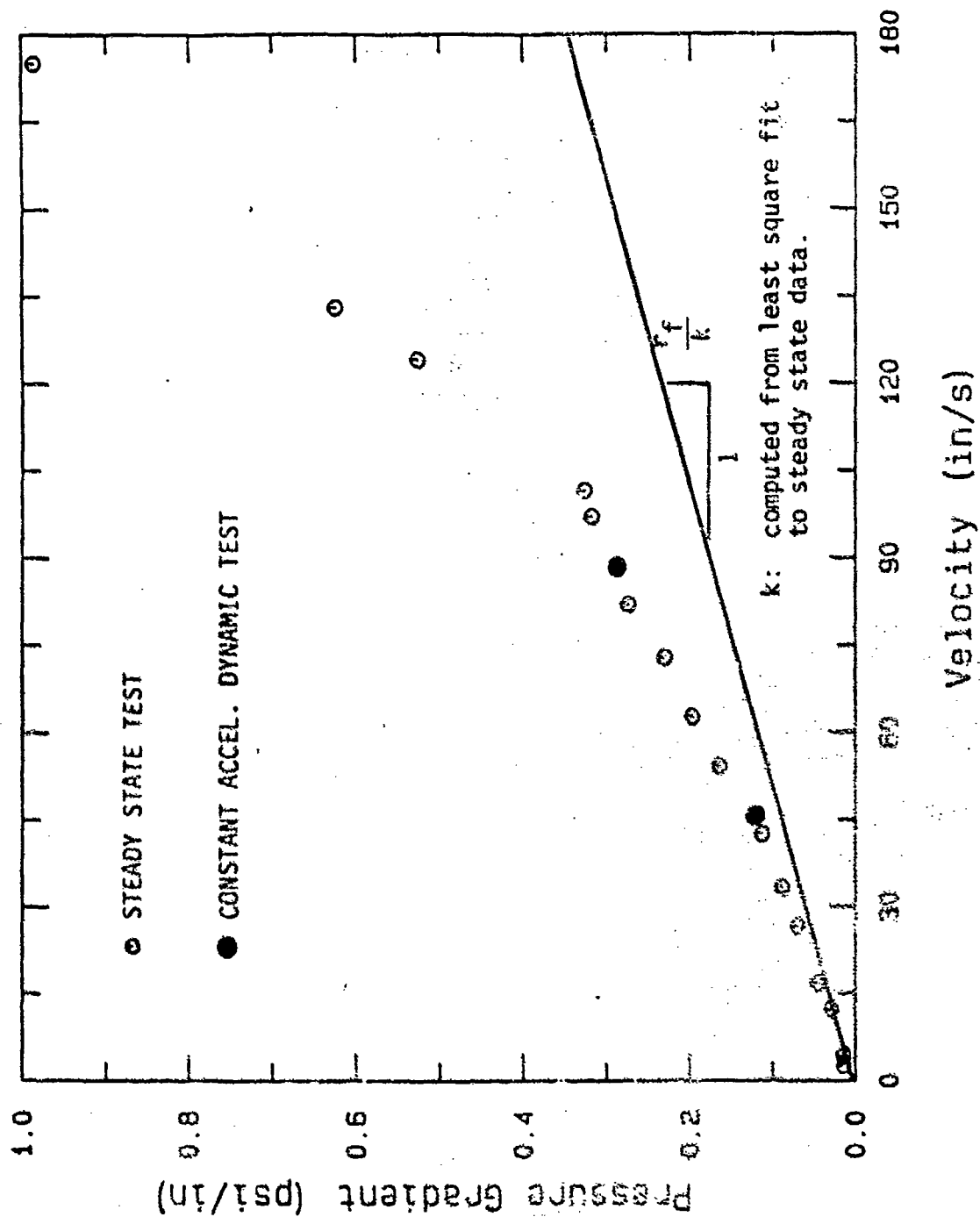
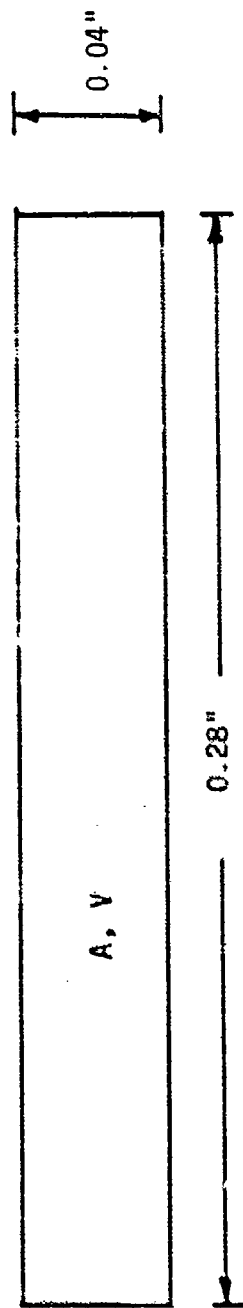


Figure 8.9. Constant acceleration dynamic flow test through a circular duct, compared with steady state flow data.

a. Cross section view of flat duct.



b. Illustration of divided cross section for equivalent coefficient of permeability.

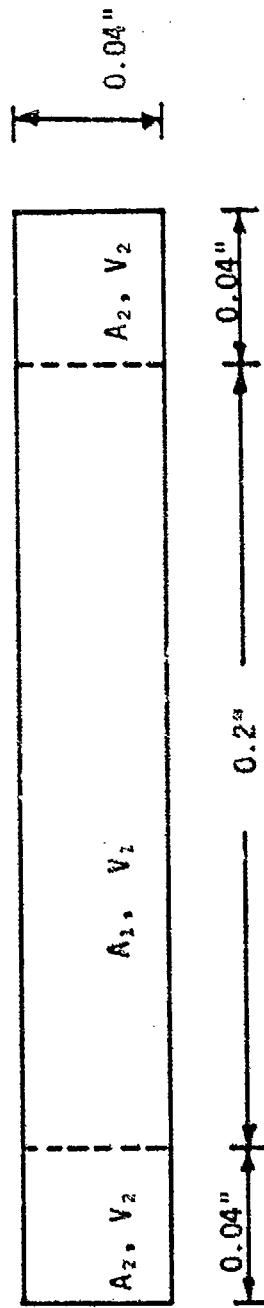


Figure 8.10. Cross section view of flat duct and subdivisions of cross section used to compute equivalent coefficient of permeability.

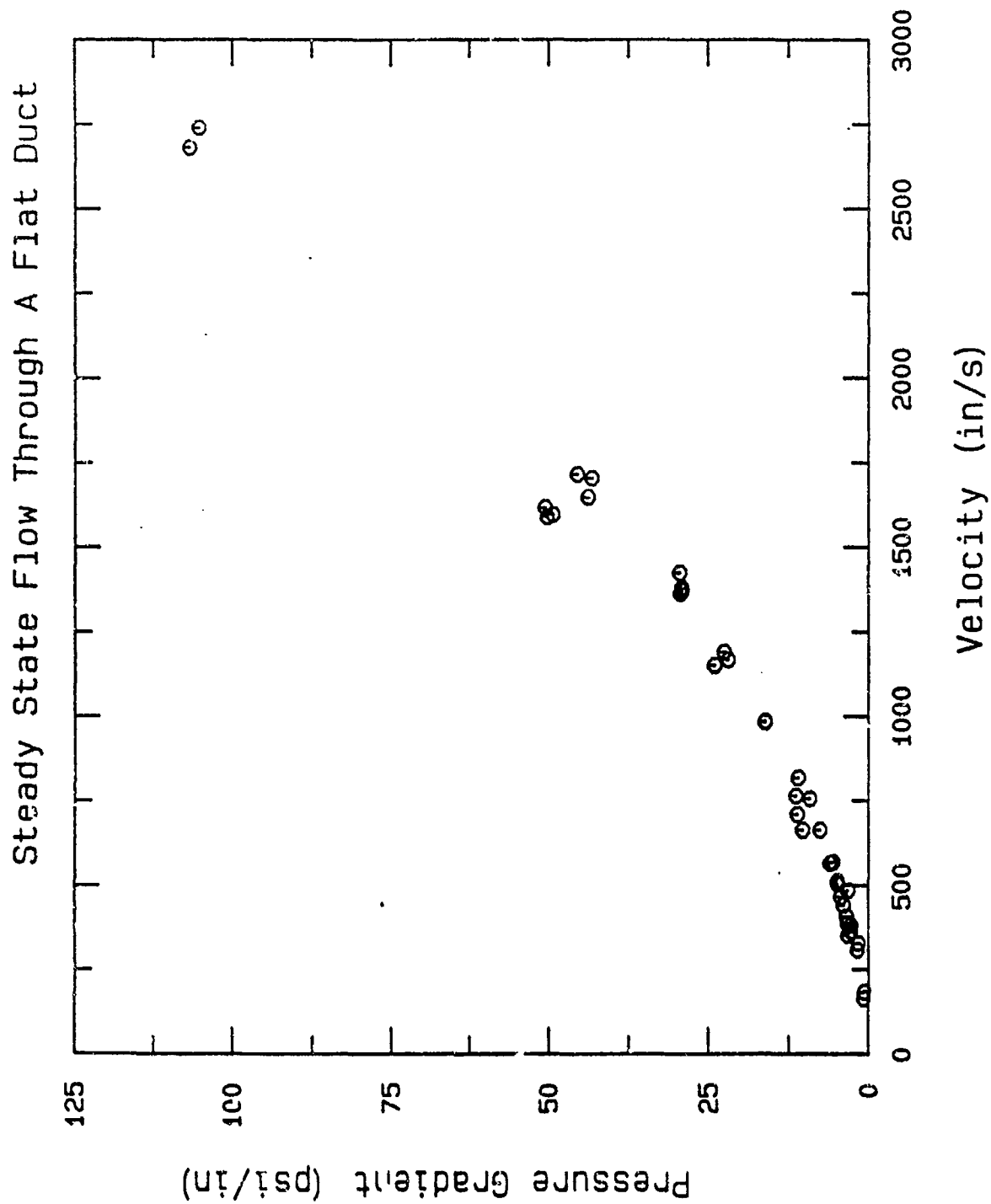


Figure 8.11. Steady state data showing laminar, transition and turbulent regimes, flat duct flow test.

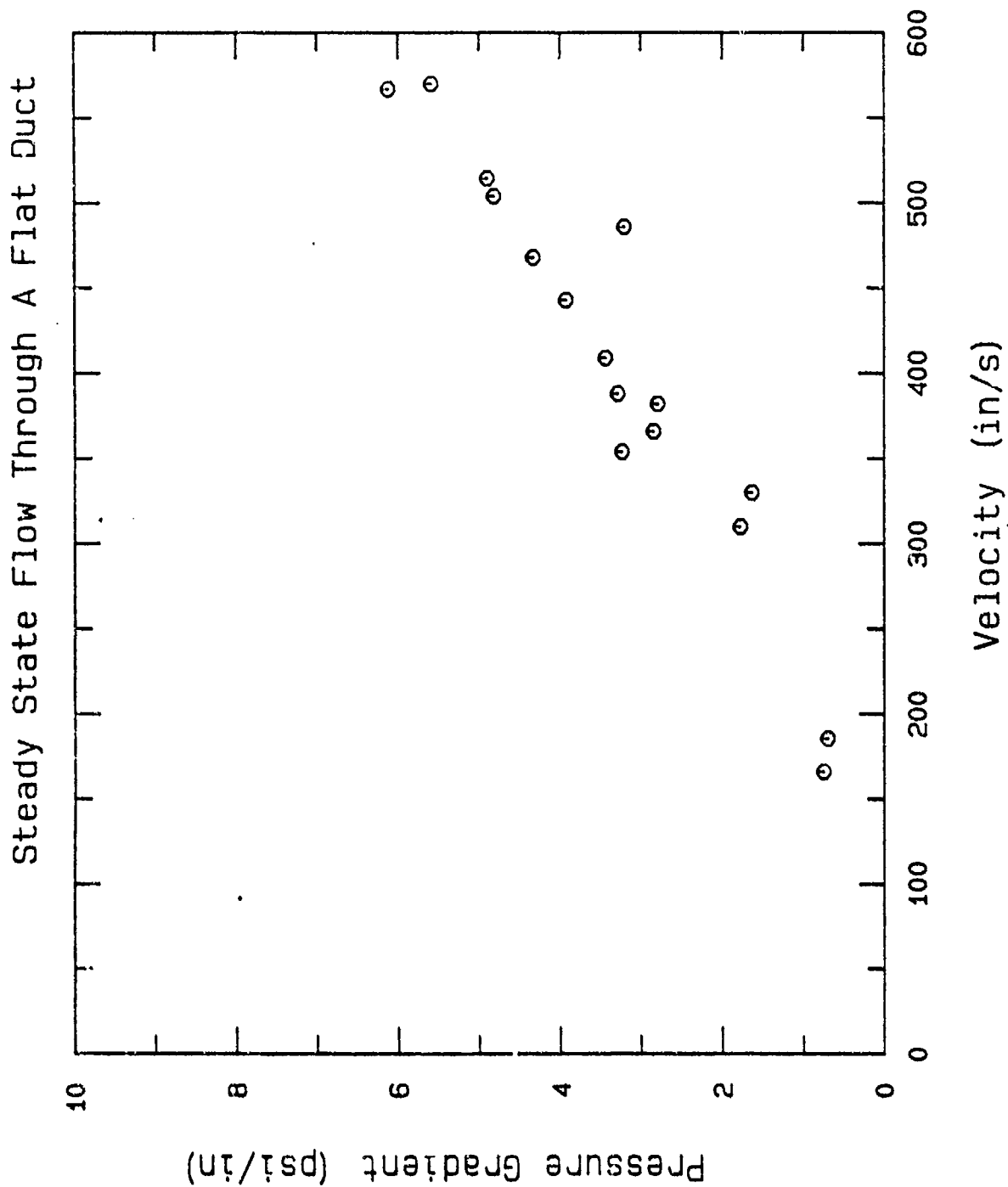


Figure 8.12. Expanded view of Figure 8.11 at the low velocity region, flat duct flow test.



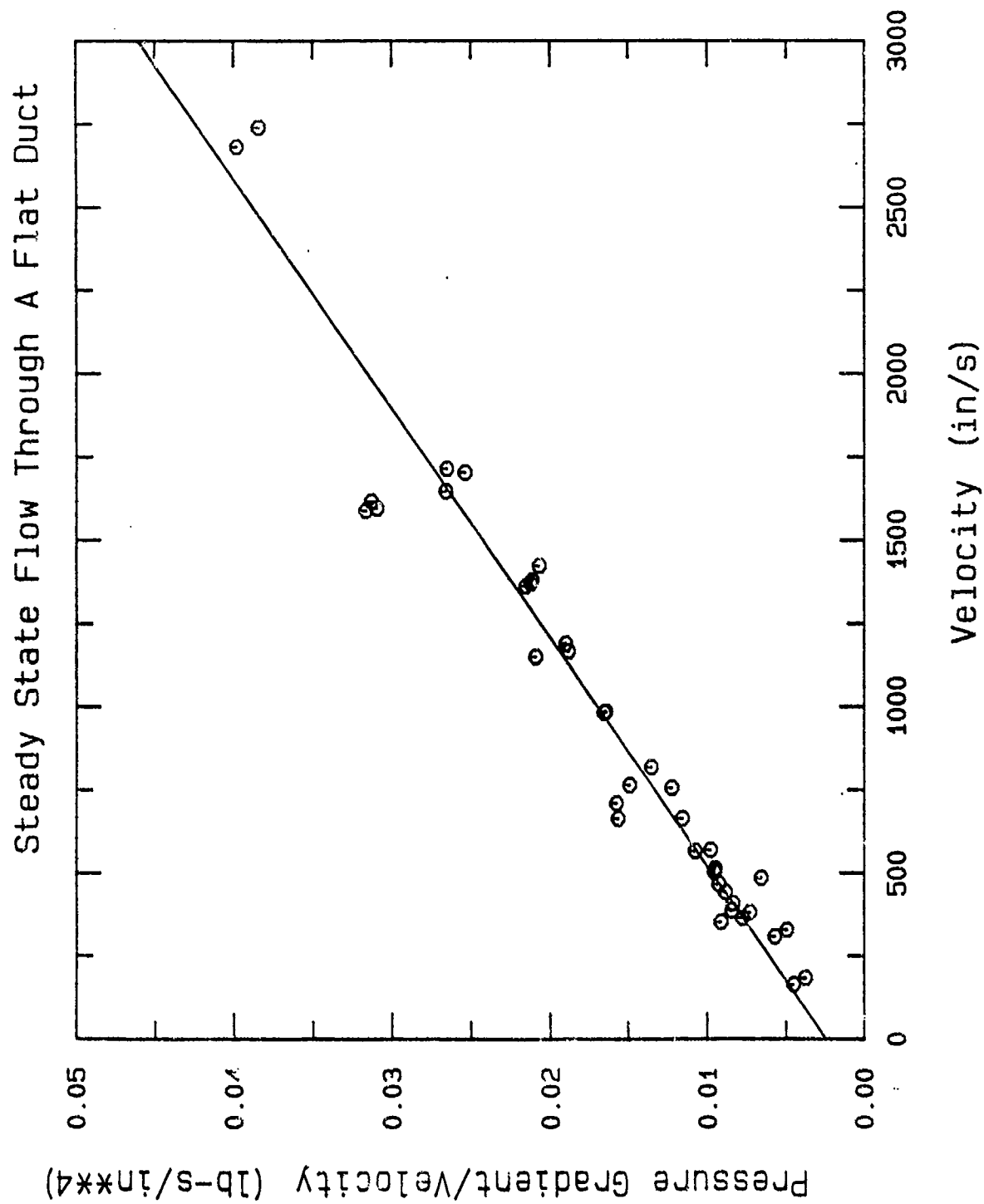


Figure 8.13. Steady state data replotted in order to measure the coefficient of permeability and Ward's constant, flat duct flow test.

U26C7

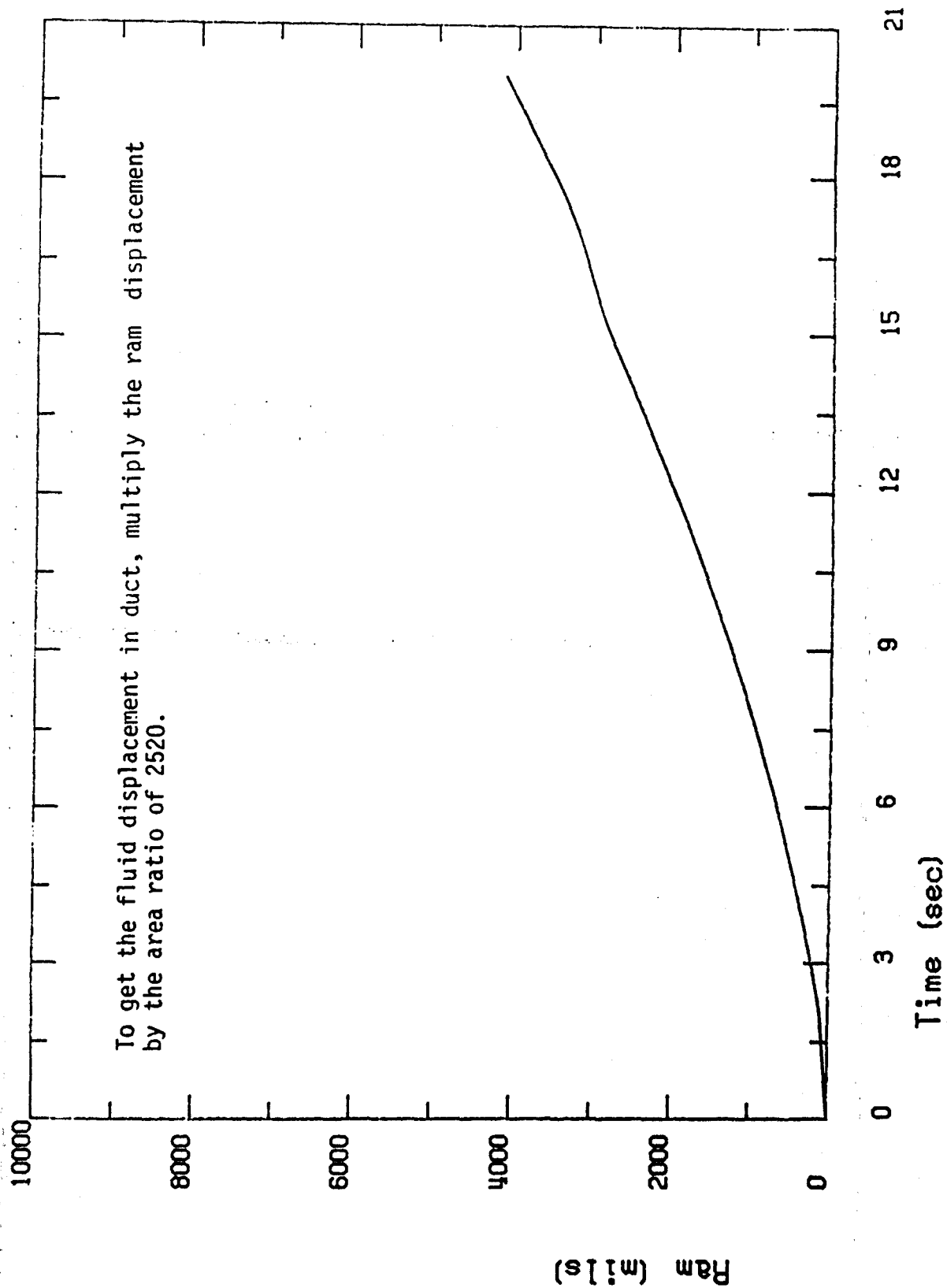


Figure 8.14a. Displacement time history from constant acceleration dynamic flow test through a flat duct, acceleration =  $27.1 \text{ in/sec}^2$ .

U26C7

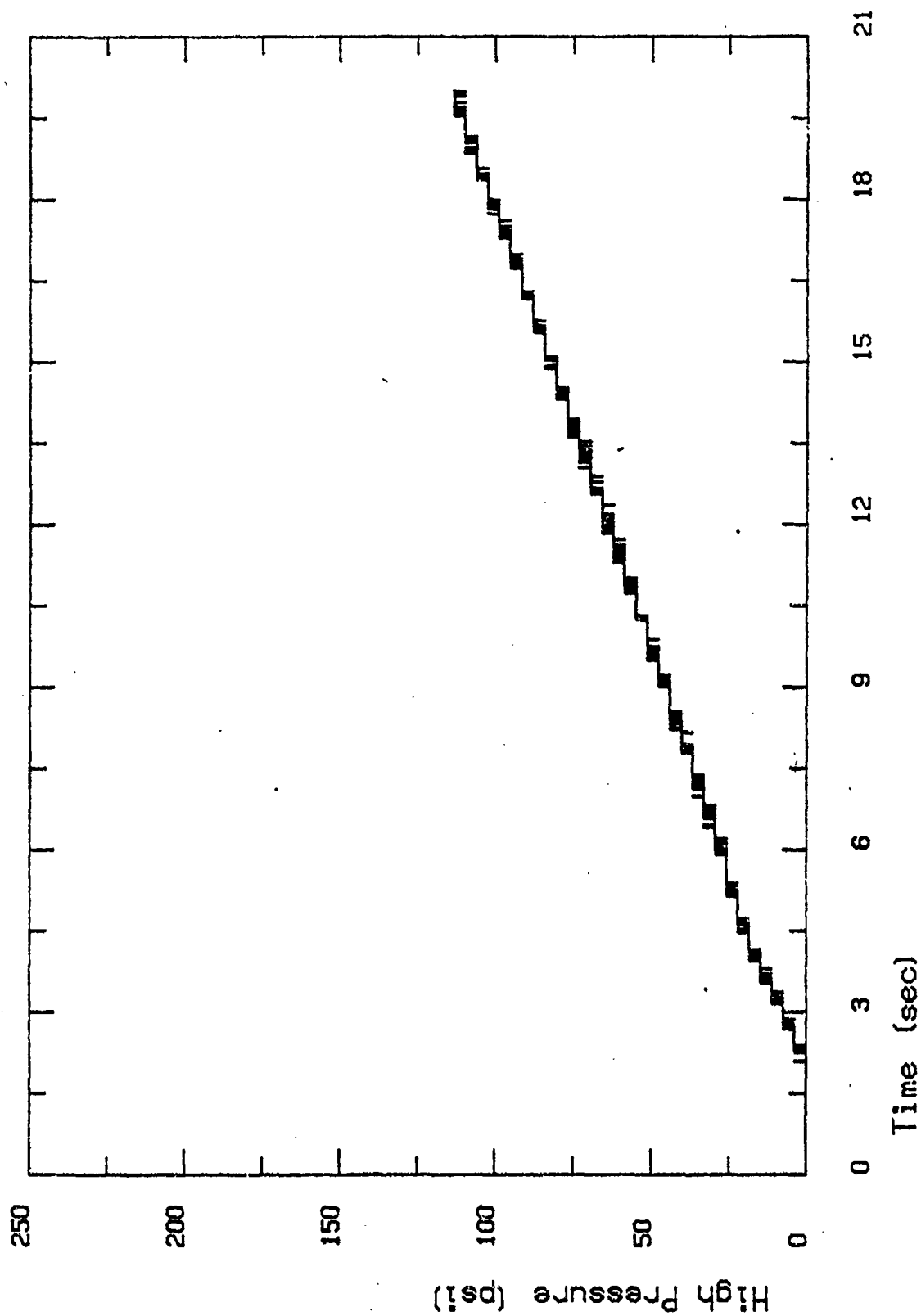


Figure 8.14b. High pressure time history from constant acceleration dynamic flow test through a flat duct, acceleration = 27.1 in/sec<sup>2</sup>.

U26C7

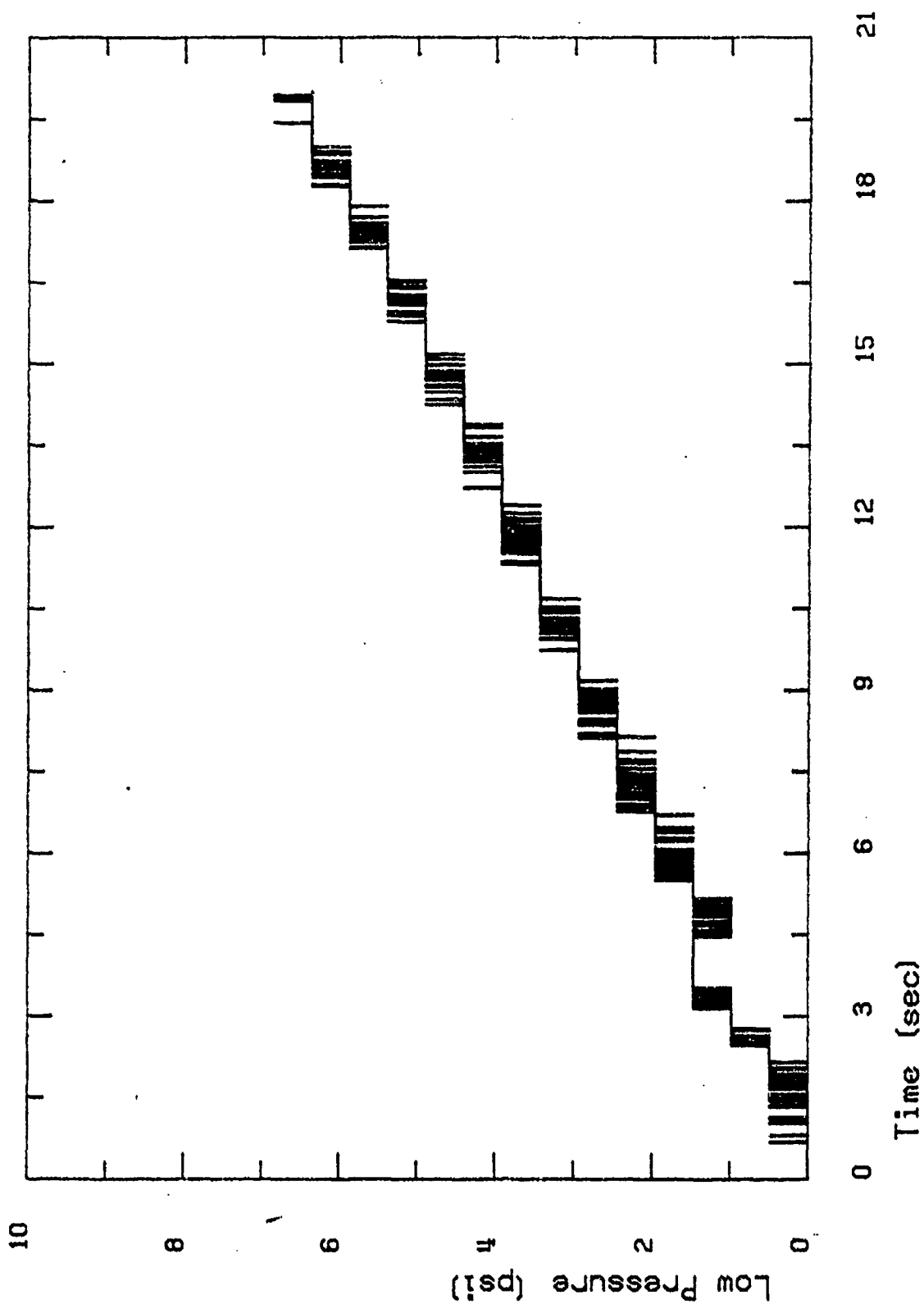


Figure 8.14c. Low pressure time history from constant acceleration dynamic flow test through a flat duct, acceleration =  $27.1 \text{ in/sec}^2$ .

U26A7

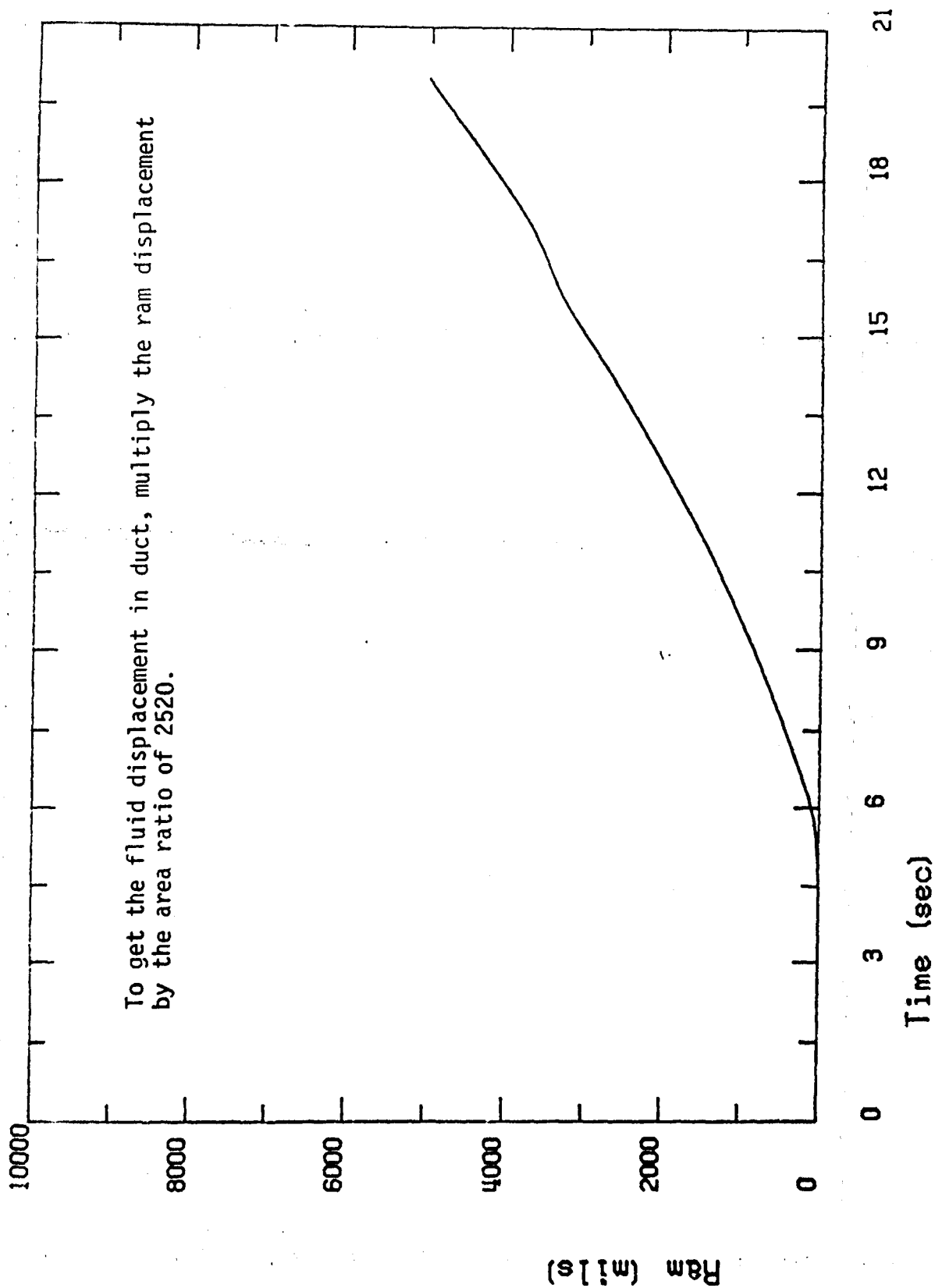


Figure 8.15a. Displacement time history from constant acceleration dynamic flow test through a flat duct, acceleration =  $42.7 \text{ in/sec}^2$ .

U26A7

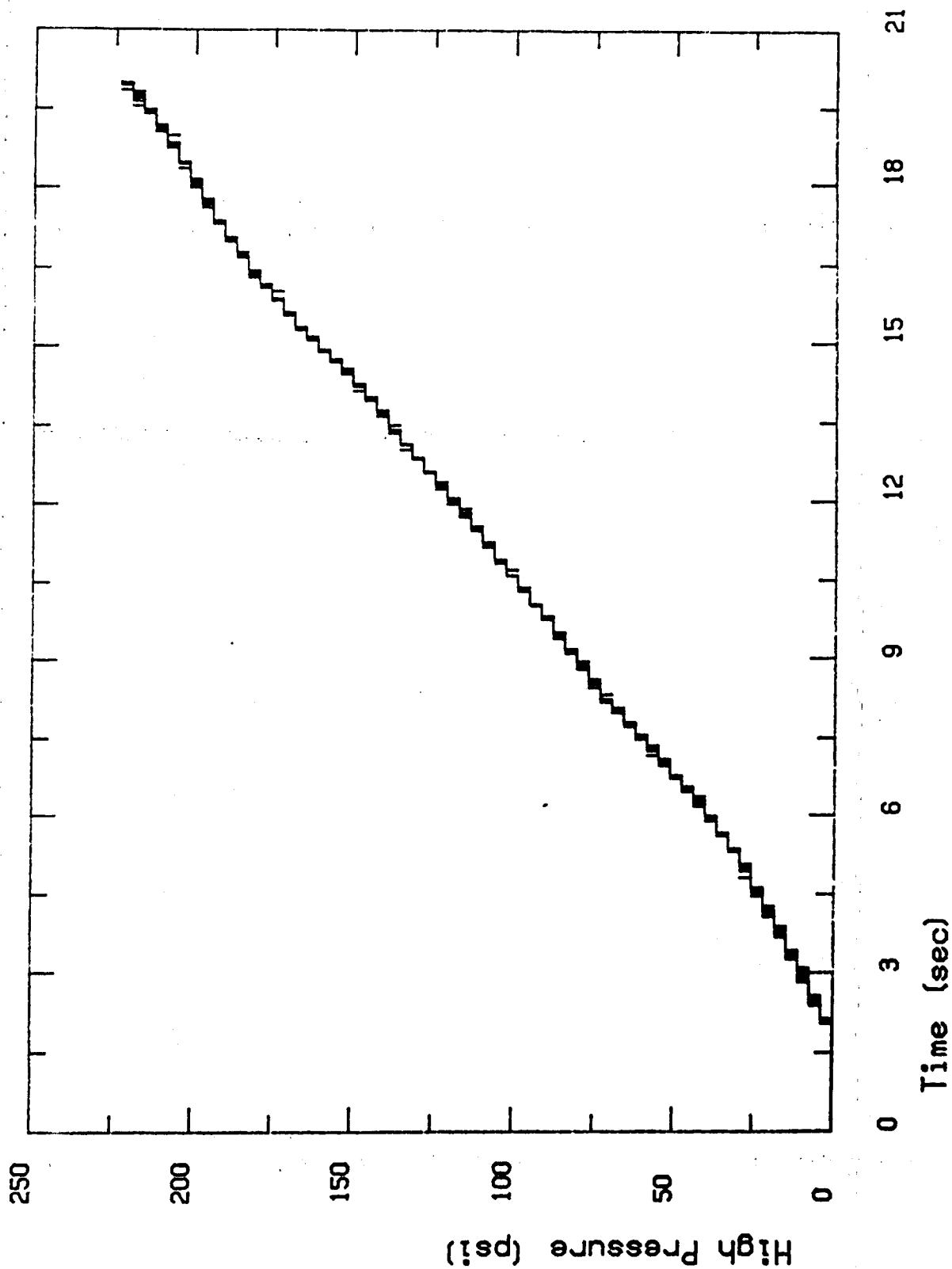


Figure 8.15b. High pressure time history from constant acceleration dynamic flow test through a flat duct, acceleration =  $42.7 \text{ in/sec}^2$ .

U26A7

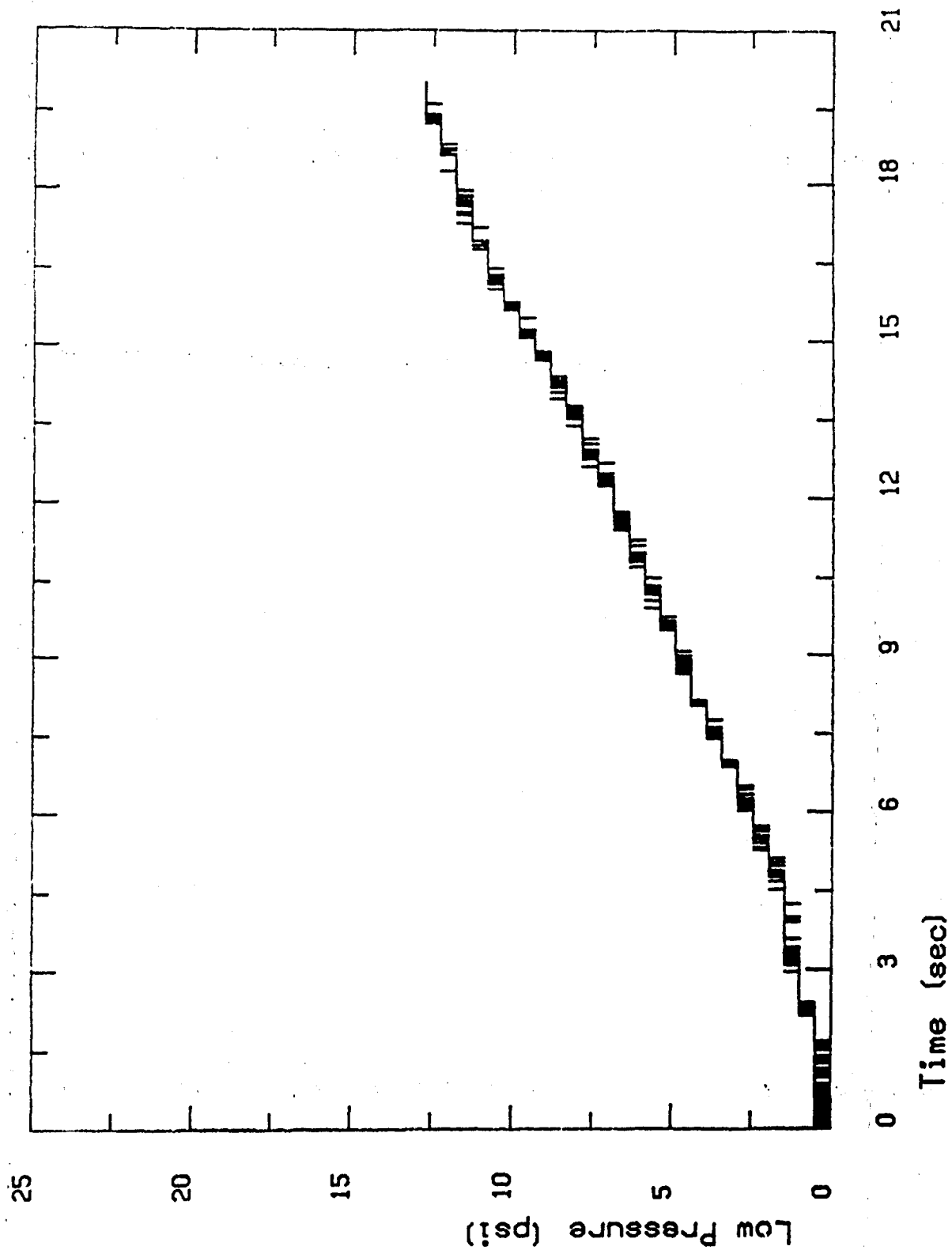


Figure 8.15c. Low pressure time history from constant acceleration dynamic flow test through a flat duct, acceleration =  $42.7 \text{ in/sec}^2$ .

U26B7

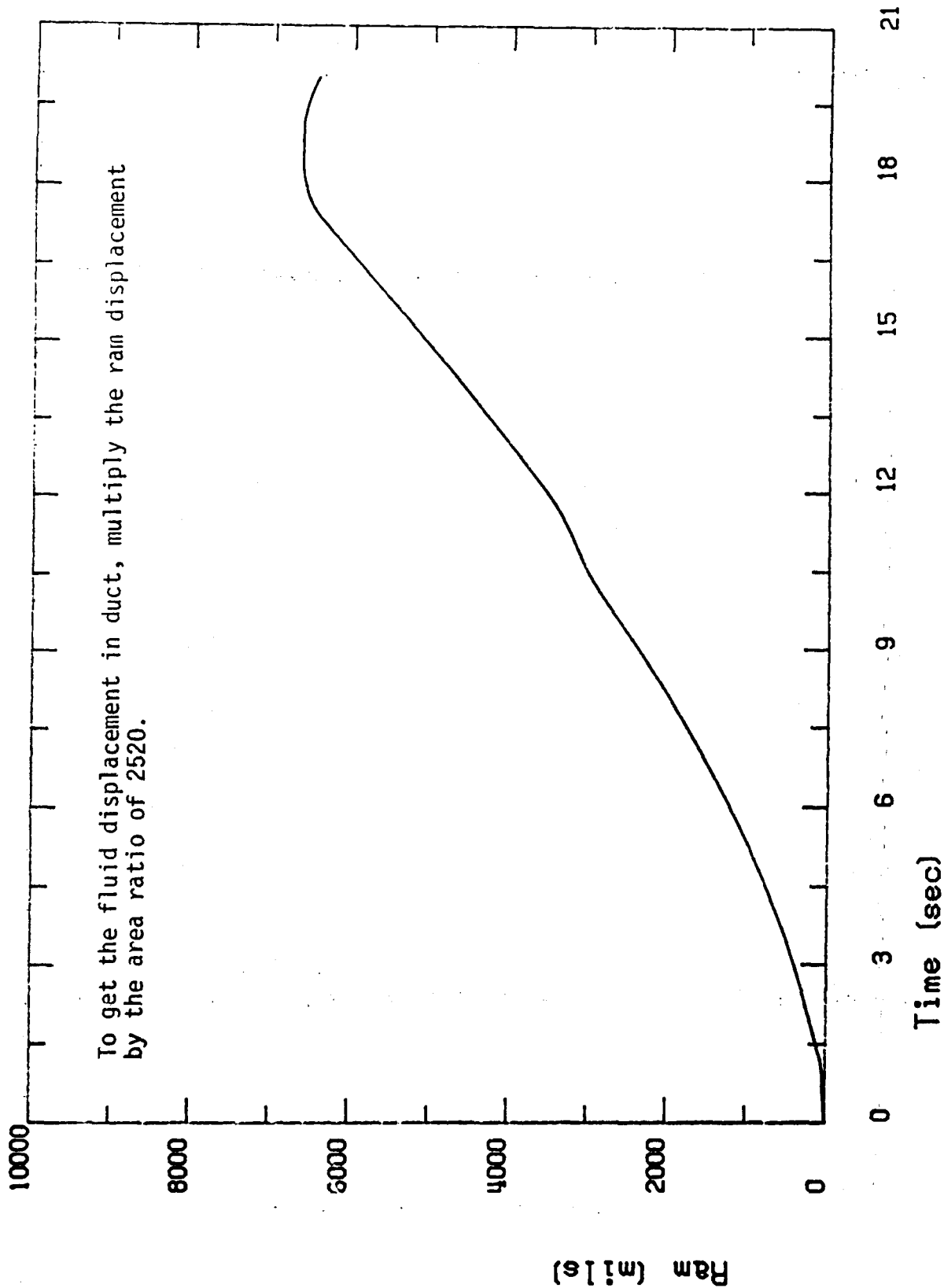


Figure 8.16a. Displacement time history from constant acceleration dynamic flow test through a flat duct, acceleration =  $63.1 \text{ in/sec}^2$ .



U2687

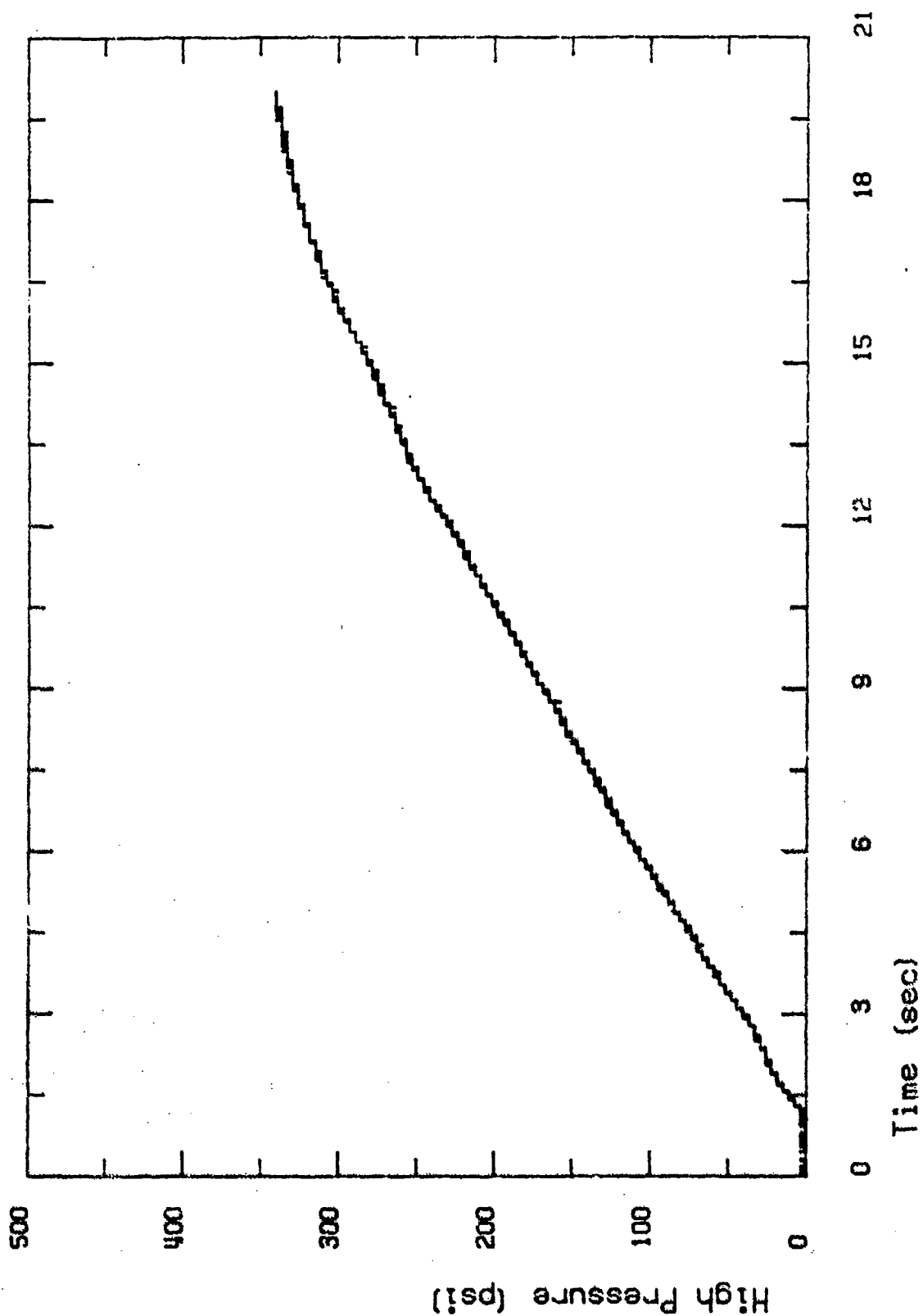


Figure 8.16b. High pressure time history from constant acceleration dynamic flow test through a flat duct, acceleration =  $63.1 \text{ in/sec}^2$ .

U26B7

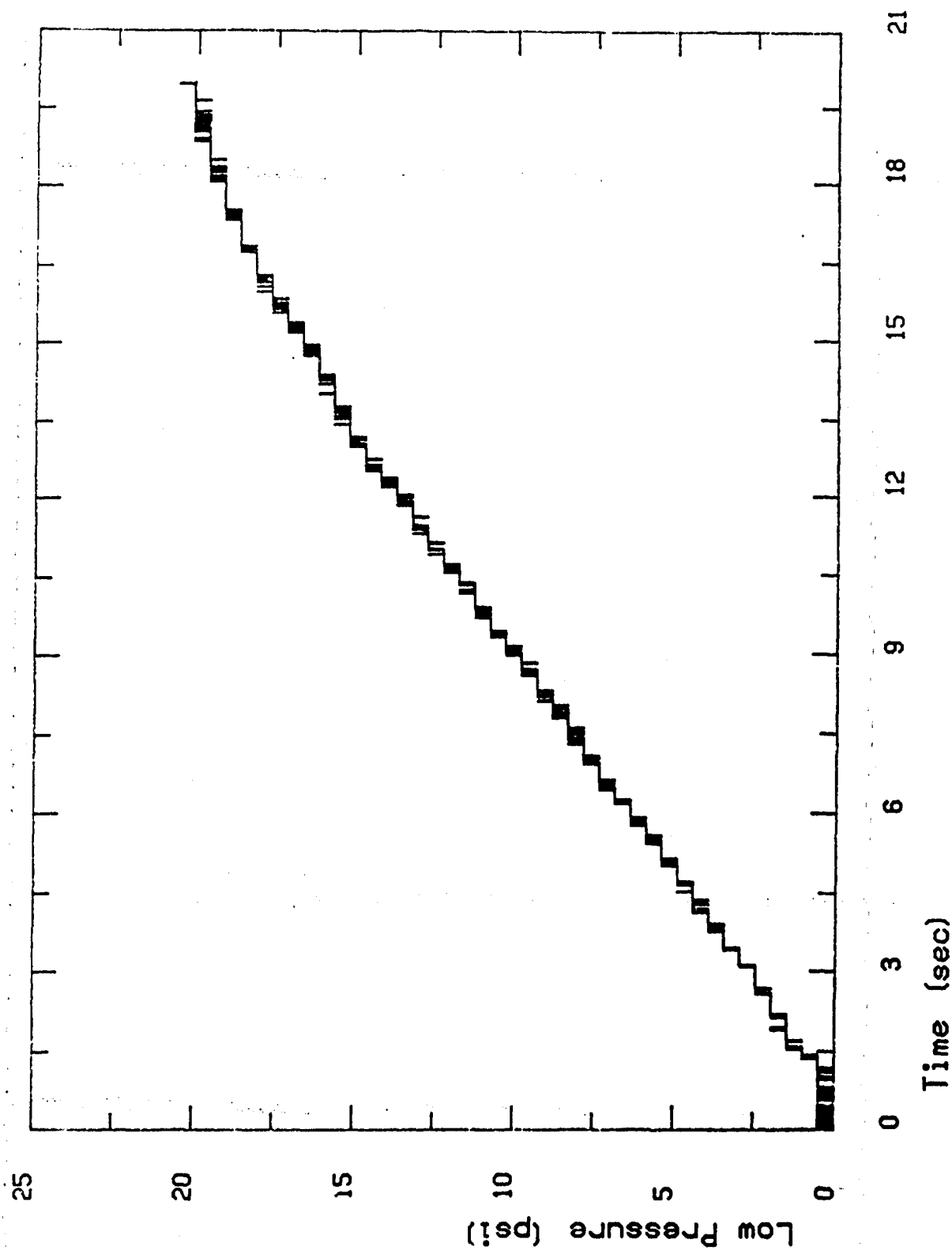


Figure 8.16c. Low pressure time history from constant acceleration dynamic flow test through a flat duct, acceleration =  $63.1 \text{ in/sec}^2$ .

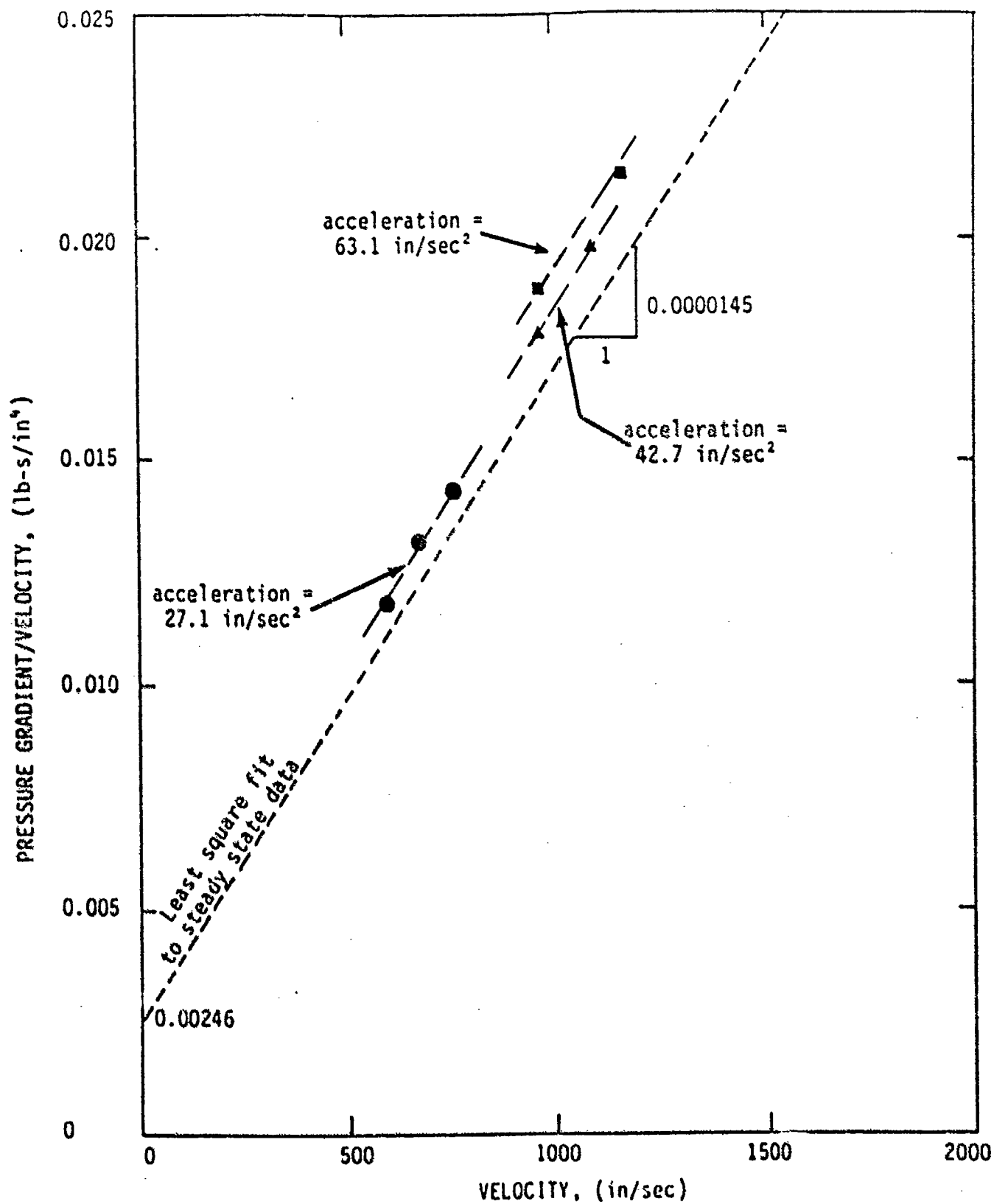


Figure 8.17. Constant acceleration dynamic flow test through a flat duct, compared with steady state flow data.



## SECTION 9

### LIST OF REFERENCES

R.T. Allen, "Equation of State of Rocks and Minerals," Defense Atomic Support Agency, DA49-146-XZ-462, Project No. 532 (March 1967).

M.A. Biot, "Theory of Propagation of Elastic Waves in Fluid Saturated Porous Solid, I, II," Journal of Acoustical Society of America, Vol. 28, pp. 168-191 (1956).

M.A. Biot, "Mechanics of Deformation and Acoustic Propagation in Porous Media," Journal of Applied Physics, Vol. 33, pp. 1482-1498 (1962a).

M.A. Biot, "Generalized Theory of Acoustic Propagation in Porous Dissipative Media," Journal of Acoustical Society of America, Vol. 34, pp. 1254-1264 (1962b).

S.E. Blouin and K.J. Kim, "Undrained Compressibility of Saturated Soil," Draft Report to Defense Nuclear Agency, Washington, DC, (February 1984).

S.E. Blouin, R.J. Martin and K.A. McIntosh, "Laboratory Investigation of the Mechanical Properties of Enewetak Sand," Draft Report to Air Force Office of Scientific Research, Washington, DC (June 1984).

S.E. Blouin and J.D. Shinn II, "Explosion-Induced Liquefaction," Report to Air Force Office of Scientific Research, Washington, DC, (1983).

S.E. Blouin and D.A. Timian, "Material Properties Testing in Support of PEACE Program, Enewetak Atoll," Report to Defense Nuclear Agency, DNA001-95-C-0147, (June 1986).

P.C. Chou and A.K. Hopkins, Dynamic Response of Materials to Intense Impulsive Loading, Air Force Materials Laboratory, Wright Patterson Air Force Base, Ohio (1972).

R.J. Fragaszy and M.E. Voss, "Undrained Compression Behavior of Sand," ASCE Journal of Geotechnical Engineering, Vol. 112, No. 3, pp. 334-347 (March 1986).

K.J. Kim and S.E. Blouin, "Response of Saturated Porous Nonlinear Materials to Dynamic Loadings," Report to Air Force Office of Scientific Research, Washington, DC, F49620-81-C-0014 (May 1984).

K.J. Kim, S.E. Blouin and D.A. Timian, "Experimental and Theoretical Response of Multiphase Porous Media to Dynamic Loads," Report to Air Force Office of Scientific Research, Washington, DC, F49620-85-C-0102 (August 1986).

LIST OF REFERENCES (concluded)

A. Mendelson, "Plasticity: Theory and Application," The MacMillan Company, New York (1968).

D.H. Merkle and W.C. Dass, "Fundamental Properties of Soils for Complex Dynamic Loadings: Development of a Three Invariant Constitutive Model," Report to Air Force Office of Scientific Research, Washington, DC, F49620-80-C-0088 (April 1985).

F. Rischbieter, et.al., "Studies of Soil Liquefaction by Shock Wave Loading," Fifth International Symposium on Military Applications of Blast Simulation, Vol. 3, Royal Swedish Fortifications Administration, Stockholm, Sweden (May 1977).

H. van der Kogel, "Wave Propagation in Saturated Porous Media," Ph.D. thesis, California Institute of Technology (1977).

J. Ward, "Turbulent Flow in Porous Media," ASCE Journal of the Hydraulic Division, American Society of Engineers, HY5, pp. 1-12 (1964).

APPENDIX A  
LISTING OF PROGRAM NKOCF

```

C
C REVISION : JULY 1, 1987 (ALTERED TO RUN ON IBM-PC-AT)
C          INCLUDE INITIAL STRESSES AND UNLOADING
C REVISION : JULY 5, 1987 (NO CHANGES NEEDED TO RUN ON VAX II)
C
COMMON /SKTON/ RR(100),CM(100)
COMMON /KODAT/ EKO(100),RKO(100)
COMMON /UNLDP/ A1,A2,A3,A4,R,XKOI,XKOH,NF
COMMON /UNLDM/ CMI,CMH,SEMAX,EEMAX,EFP,EET
COMMON /GPARM/ RO,CO,GVO,SS,PB
CHARACTER*25 NAM1,NAM2,NAM3,NAM4,NAM5,NAM6

C
C READ INPUT AND OUTPUT FILE NAMES
C
WRITE(*,*) 'Type input file with SKELETON STRAIN-STRESS pairs'
READ(*,*) (A) NAM2
WRITE(*,*) 'Type input file with EFFEC. VER. STRAIN. vs Ko'
READ(*,*) (A) NAM4
WRITE(*,*) 'Type output file for (STRN(%),SE,PF,S,LF)'
READ(*,*) (A) NAM3
WRITE(*,*) 'Type output file for (STRN(%),SEH,SH,BMF,POR)'
READ(*,*) (A) NAM5
WRITE(*,*) 'Type output file for (EV(%),P,BMX,POR)'
READ(*,*) (A) NAM6
OPEN(8,FILE=NAM3,STATUS='NEW')
OPEN(3,FILE=NAM5,STATUS='NEW')
OPEN(66,FILE=NAM6,STATUS='NEW')

C
C READ VARIABLE Ko AS A FUNCTION OF EFFECTIVE VERTICAL STRAIN
C
OPEN(8,FILE=NAM4,STATUS='OLD')
READ(8,*) NK0
DO 50 I=1,NK0
50 READ(8,*) EKO(I),RKO(I)
CLOSE(8)

C
C READ NF      : 0 ---- PRESSURE IN PSI
C              : 1 ---- PRESSURE IN BARS
C              : 2 ---- PRESSURE IN PSI AND Kw = 0.3E6, Kg = 5.E6
C      NW      : 0 ---- FRESH WATER
C              : 1 ---- SEA WATER
C      EMAX    : MAXIMUM STRAIN
C      NDIV    : NUMBER OF DIVISION BETWEEN SKELETON DATA POINTS
C              : DURING LOADING
C      NDIVU   : NUMBER OF DIVISION FOR UNLOAD PRIOR TO LIQUEFACTION
C      NDIVM   : NUMBER OF DIVISION FOR UNLOAD AFTER LIQUEFACTION
C      LPRINT  : OUTPUT PRINT INTERVAL

C      PF      : INITIAL PORE WATER PRESSURE
C      SE      : INITIAL EFFECTIVE VERTICAL STRESS
C      V       : INITIAL POISSON'S RATIO
C      POR     : VIRGIN POROSITY

C
C OPEN(55,FILE=NAM2,STATUS='OLD')
C
C READ(55,*) NF,NW,EMAX,NDIV,NDIVU,NDIVM,LPRINT
C
C READ(55,*) PF,SE,V,POR
C

```

```

C      READ UNLOADING CONSTANTS FOR SKELETON
C      A1,A2 : PARAMETERS FOR RECOVERABLE STRAINS
C      A3,A4 : PARAMETERS FOR INITIAL UNLOADING MODULUS
C      R      : FRACTION OF STRESSES W.R.T. HOOK
C      XKOI   : KO FOR INITIAL PORTION
C      XKOH   : KO FOR HOOK PORTION
C
C      READ(55,*) A1,A2,A3,A4,R,XKOI,XKOH
C
C      READ SOLID GRAIN PROPERTIES
C      RO      : INITIAL GRAIN MASS DENSITY
C      CO      : INITIAL WAVESPEED
C      GVO     : POISSON'S RATIO AT LOW STRESS
C      SS      : SLOPE OF PROPAGATION VELOCITY TO PARTICLE VELOCITY
C      PB      : THRESHOLD PRESSURE
C      note that units are lb, second and inch for grain properties
C
C      READ(55,*) RO,CO,GVO,SS,PB
C
C      READ EFF. STRAIN-STRESS DATA FOR SKELETON
C
C      READ(55,*) NPOINT
C      DO 120 I=1,NPOINT
120  READ(55,*) RR(I),CM(I)
C      CLOSE(55)
C
C      SET INITIAL CONDITIONS
C
C      NFIRST = 0
C      LF = 0
C
C      LF = 0 : VIRGIN LOADING
C      1 : UNLOADING (INITIAL PORTION)
C      2 : UNLOADING (HOOK PORTION)
C      3 : UNLOADING (LIQUEFIED)
C
C      IF(SE.EQ.0.0.AND.PF.EQ.0.0) GO TO 142
C
C      FOR NON-ZERO IN-SITU STRESSES
C
C      COMPUTE INITIAL EFFECTIVE STRAIN (EE)
C
C      I = 1
130  CONTINUE
C      IF(SE.GE.CM(I).AND.SE.LE.CM(I+1)) GO TO 140
C      I = I+1
C      GO TO 130
140  CONTINUE
C      EE = RR(I)+(RR(I+1)-RR(I))*(SE-CM(I))/(CM(I+1)-CM(I))
C      KK = I
C      RR(I) = EE
C      CM(I) = SE
C
C      COMPUTE INITIAL WATER STRAIN (EWI), ASSUME ELASTIC
C
C      CALL BULKW(PF,BKW,NF,NW)
C      EWI = PF/BKW
C
C      COMPUTE GRAIN STRAINS EGI AND EG DUE TO GRAIN PRESSURE(PGI)
C      AND PORE-WATER PRESSURE(PF), ASSUME ELASTIC

```





```

      GO TO 300
200 CONTINUE
      L = LPRINT
      K = 0
      NFIRST = 1
      KK = KK+1
      DDTRN = (RR(KK)-RR(KK-1))/NDIV
300 CONTINUE
C
C      CALCULATE SKELETON CONSTRAINED MODULUS
C
C      CALL CONMS(EE,BMS,LF)
C
C      CALCULATE SKELETON BULK MODULUS
C
C      CALL BULKS(BMS,BKS,EE,LF,AK)
C
C      CALCULATE GRAIN BULK MODULUS
      PORG=POR
      IF(NF.EQ.2) PORG=PORI
C
C      CALL BULKG(PF,PE,PORG,BKG,NF)
C
C      CALCULATE WATER BULK MODULUS
C
C      CALL BULKW(PF,BKW,NF,NW)
C
C      CALCULATE UNDRAINED BULK MODULUS
C
      AA = (1.-PORI)/(1.-POR)
      IF(NF.EQ.2) AA = 1.0
      BMF = BMS+(BKG-AA*BKS)/(1.+PORI*BKG*(BKG-BKW)/
      . (BKW*(BKG-AA*BKS)))
C
C      CALCULATE TOTAL STRAIN INCREMENT
C
C      DSTN = DDTRN*(BKG-BKS)/(BKG-BMF*AK)
C
C      CALCULATE PRESSURE INCREMENTS
C
      DS = BMF*DSTN
      DPF = DSTN*(BMF-BMS)/(1.-BKS/BKG)
      DSE = DS-DPF
      DPE = BKS*(DSTN-DPF/BKG)
C
C      UPDATE PRESSURES
C
      PF = PF+DPF
      PE = PE+DPE
      S = S+DS
      SE = SE+DSE
      SEH = 1.5 * PE- 0.5 * SE
      SH = SEH+PF
C
C      UPDATE STRAINS AND POROSITY
C
      EE = EE+DDTRN
      STRNO = STRN
      PORO = POR
      STRN = STRN+DSTN

```

```

C      DVW = PORO*(1.-STRN0)-PORI*DPF/BKW
      POR = DVW/(1.-STRN)
C
      IF(LF.EQ.0.AND.STRN.GE.EMAX) GO TO 360
      IF(L.NE.LPRINT) GO TO 380
360 L = 0
C
C      WRITE TOTAL VERTICAL STRESS: S
C      TOTAL HORIZONTAL STRESS (SH)
C      UNDRAINED CONSTRAINED MODULUS: BMF
C      EFFECTIVE VERTICAL STRESS: SE
C      EFFECTIVE HORIZONTAL STRESS (SEH)
C      PORE WATER PRESSURE: PF
C      POROSITY: POR
C      AS A FUNCTION OF TOTAL STRAIN: STRN
C
370 CONTINUE
      TEMP = STRN*100.
      WRITE(6,2001) TEMP,SE,PF,S,LF
2001 FORMAT(4E12.4,I5)
      WRITE(3,2002) TEMP,SEH,SH,BMF,POR
2002 FORMAT(5E12.4)
C
380 CONTINUE
C
      IF(LF.EQ.0.AND.STRN.GE.EMAX) GO TO 400
      IF(LF.GT.0.AND.LF.LT.3.AND.SEH.LT.0.0) GO TO 440
      IF(LF.EQ.1.AND.K.EQ.(NDIV-1)) GO TO 420
      IF(LF.EQ.2.AND.K.EQ.(NDIV-1)) GO TO 440
      IF(LF.EQ.3) GO TO 500
      GO TO 150
C
400 CONTINUE
      NDIV = NDIVU
      SEMAX = SE
      EEMAX = EE
      CALL SKUNL
C
      IF(R.GT.0.0.AND.R.LT.1.0) GO TO 414
C
      LF = 2
      RR(KK) = EEMAX
      RR(KK+1) = EEP
      K = NDIV-1
      GO TO 150
C
414 CONTINUE
      LF = 1
      RR(KK) = EEMAX
      RR(KK+1) = EEI
      RR(KK+2) = EEP
      K = NDIV-1
      GO TO 150
C
420 CONTINUE
      LF = 2
      K = NDIV-1
      GO TO 150
C

```

```

440 CONTINUE
    LF = 3
    EVMAX = STRN
    CALL MIXTU(EVMAX,NDIVM,PORI,POR,BMF,PF,NF,LPRINT,NW)
    S = PF
    SH = PF
    SE = 0.0
    SEH = 0.0
    GOTO 370
C
500 CONTINUE
C
    CLOSE(6)
C
    CLOSE(6)
    CLOSE(3)
    CLOSE(66)
    STOP
    END
C *****
    SUBROUTINE BULKG(PF,PE,POR,BKG,NF)
    COMMON /GPARM/ RO,CO,GVO,SS,PB
C
    GRAIN BULK MODULUS
C
    IF(NF.NE.2) GO TO 50
    BKG = 5000000.
    RETURN
C
50 CONTINUE
    P = PF+PE/(1.-POR)
C
    PG = P
    IF(NF.EQ.1) PG = P+14.5
C
    COMPUTE TANGENT CONSTRAINED MODULUS, CG
C
    SROC = SQRT((RO*CO)**2+4.*RO*SS*PG)
    SFP = SROC-RO*CO
    FP = RO*CO*CO*CO*SFP+(SFP*SFP)/(4.*RO)
C
    SFPP = 2.*RO*SS/SROC
    FPP = CO*SFPP*SFP*SFPP/(2.*RO)
C
    CG = (FP*FP)/(FP-PG*FPP)
C
    COMPUTE TANGENT BULK MODULUS, BKG
C
    IF(PG.GT.PB) GO TO 100
    GP=(2./3.)*((1.-2.*GVO)/(1.-GVO))*(PG/PB)+(1.+GVO)/(3.*(1.-GVO))
C
    GO TO 200
C
100 CONTINUE
C
    GP = 1.0
C
200 CONTINUE
C

```

```

      BKG = GP*CG
C
      IF(NF.EQ.1) BKG = BKG/14.5
C
      RETURN
      END
C *****
      SUBROUTINE BULKW(PF,BKW,NF,NW)
C
      IF(NF.NE.2) GO TO 50
      BKW = 300000.
      RETURN
C
50  CONTINUE
C
      P = PF
      IF(NF.EQ.0) P = PF/14.5
C
      PW1 = 10000.
      PW2 = 100000.
C
      IF(NW.EQ.1) GOTO 40
C
      FRESH WATER (NW=0)
C
      C1 = 0.00031775
      C2 = 6.2713
      C3 = 21746.9
C
      C4 = 9.49
      C5 = 21920.
C
      C6 = 0.00000685
      C7 = 1.337
      C8 = 768348.
      GOTO 60
C
      SEA WATER
C
40  CONTINUE
C
      C1 = 0.000342831
      C2 = 6.18393
      C3 = 23806.8
C
      C4 = 9.5546
      C5 = 24758.
C
      C6 = 0.00000291437
      C7 = 3.36508
      C8 = 614918.
C
60  CONTINUE
C
      IF(P.GT.PW1) GO TO 100
C
      BKW = C1*P*P+C2*P+C3
      GO TO 300
100 IF(P.GT.PW2) GO TO 200
C

```

```

      BKW = C4*P+C5
      GO TO 300
C
200 CONTINUE
      BKW = C6*P+P+C7*P+C8
C
300 CONTINUE
C
      IF(NF.EQ.1) RETURN
C
      BKW = BKW*14.5
C
      RETURN
      END
C *****
      SUBROUTINE CONMS(EE,BMS,LF)
      COMMON /SKTON/ RR(100),CM(100)
      COMMON /UNLDM/ CMI,CMH,SEMAX,EEMAX,EEP,EET
      IF(LF.NE.0) GO TO 300
      I = 1
100 CONTINUE
      IF(EE.GE.RR(I).AND.EE.LE.RR(I+1)) GO TO 200
      I = I+1
      GO TO 100
200 CONTINUE
      BMS = (CM(I+1)-CM(I))/(RR(I+1)-RR(I))
      RETURN
300 IF(LF.NE.1) GO TO 400
      BMS = CMI
      RETURN
400 IF(LF.NE.2) GO TO 500
      BMS = CMH
      RETURN
500 CONTINUE
      BMS = 0.0
      RETURN
      END
C *****
      SUBROUTINE BULKS(BMS,BKS,EE,LF,A)
C
C
C
C
      FIND K0
C
      IF(LF.EQ.3) GO TO 400
      CALL CALKO(EE,XK0,LF)
      A = (2.0*XK0+1.0)/3.
      BKS = A*BMS
      RETURN
400 CONTINUE
      BKS = 0.0
      RETURN
      END
C *****
      SUBROUTINE CALKO(EE,XK0,LF)
      COMMON/KODAT/EK0(100),RK0(100)
      COMMON/UNLDP/ A1,A2,A3,A4,B,XK0I,XK0E,NF
      IF(LF.NE.0) GO TO 300
      I = 1
100 CONTINUE
      IF(EE.GE.EK0(I).AND.EE.LE.EK0(I+1)) GO TO 200
      I = I + 1

```

```

      GO TO 100
200  CONTINUE
      XK0 = RK0(I)
      RETURN
300  IF(LF.NE.1) GO TO 400
      XK0 = XK0I
      RETURN
400  IF(LF.NE.2) GO TO 500
      XK0 = XK0H
500  RETURN
      END
C *****
      SUBROUTINE SKUNL
      COMMON/UNLDP/ A1,A2,A3,A4,R,XK0I,XK0H,NF
      COMMON/UNLDM/ CMI,CMH,SEMAX,EEMAX,EFP,EPI
C
C      CALCULATE UNLOADING MODULUS
C
      CMI = A3*(SEMAX**A4)
C
      IF(R.GT.0.0.AND.R.LT.1.0) GO TO 100
C
      EEP = SEMAX/CMI
      EFP = EEMAX-EEP
C
      CMH = CMI
      XK0H = XK0I
      EPI = EFP
C
      RETURN
C
100  CONTINUE
C
      CALCULATE RECOVERABLE (EEP) AND PERMANENT (EFP) STRAINS
C
      EEP = A1*(SEMAX**A2)
      EFP = EEMAX-EEP
C
      CMA = SEMAX/EEP
      EPI = EEMAX-(1.-R)*SEMAX/CMI
      CMH = R*CMA/(1.-(1.-R)*CMA/CMI)
C
      RETURN
      END
C -----
C
      SUBROUTINE MIXTU(EVMAX,NDIVM,PORI,POR,BMX,PF,NF,LPRINT,NW)
C
      L = LPRINT
      EV = 0.0
      P = 0.0
      DEV = EVMAX/NDIVM
      POR = PORI
      DO 100 I=1,NDIVM
          CALL BULK(P,0.0,PORI,BKG,NF)
          CALL BULK(P,BKW,NF,NW)
          BMX=BKG*BKW/(BKW*PORI*(BKG-BKW))
          EP=BMX*DEV
          EVO=EV

```

```

      PORO=POR
      EV=EV+DEV
      DVW=PORO*(1-EVO)-PORI*DP/BKW
      POR=DVW/(1-EV)
      P=P+DP
      IF(I.EQ.NDIVM) GO TO 40
      IF(L.NE.LPRINT) GO TO 50
40    WRITE(66,2000) EV*100,P,BMX,POR
      L = 0
50    L = L+1
100   CONTINUE
2000  FORMAT(4E12.4)
      PF=P
      RETURN
      END

```



APPENDIX B

EXAMPLE PROBLEM USING PROGRAM NKOCF

Table B.1. Listings of input files for example problem.

Input file: TAPE 55

```
2, 0, 0.03, 100, 100, 100, 10
0.0, 0.0, 0.2, 0.1
0.0, 0.0, 4000000., 0.0, 0.0, 0.25, 0.25
0.0, 0.0, 0.0, 0.0, 0.0
3
0.0 , 0.0
0.02 , 20000.
0.04 , 40000.
```

Input file: TAPE 8

```
2
0.0 , 0.25
0.04 , 0.25
```

Table B.2 Listings of output files for example problem.

Output file: TAPE 6

Total axial strain (%)	Effective axial stress (psi)	Pore pressure (psi)	Total axial stress (psi)	Loading Status
0.2446E-01	0.2000E+03	0.4463E+03	0.6463E+03	0
0.2691E-00	0.2200E+04	0.4909E+04	0.7109E+04	0
0.5137E+00	0.4200E+04	0.9372E+04	0.1357E+05	0
0.7583E+00	0.6200E+04	0.1383E+05	0.2003E+05	0
0.1003E+01	0.8200E+04	0.1830E+05	0.2650E+05	0
0.1248E+01	0.1020E+05	0.2276E+05	0.3296E+05	0
0.1492E+01	0.1220E+05	0.2722E+05	0.3942E+05	0
0.1737E+01	0.1420E+05	0.3169E+05	0.4589E+05	0
0.1981E+01	0.1620E+05	0.3615E+05	0.5235E+05	0
0.2226E+01	0.1820E+05	0.4061E+05	0.5881E+05	0
0.2471E+01	0.2020E+05	0.4507E+05	0.6527E+05	0
0.2715E+01	0.2220E+05	0.4954E+05	0.7174E+05	0
0.2960E+01	0.2420E+05	0.5400E+05	0.7820E+05	0
0.3009E+01	0.2480E+05	0.5489E+05	0.7949E+05	0
0.3002E+01	0.2435E+05	0.5479E+05	0.7915E+05	2
0.2930E+01	0.2189E+05	0.5381E+05	0.7570E+05	2
0.2859E+01	0.1943E+05	0.5282E+05	0.7225E+05	2
0.2788E+01	0.1697E+05	0.5183E+05	0.6880E+05	2
0.2718E+01	0.1451E+05	0.5084E+05	0.6535E+05	2
0.2645E+01	0.1205E+05	0.4985E+05	0.6191E+05	2
0.2573E+01	0.9594E+04	0.4886E+05	0.5846E+05	2
0.2552E+01	0.0000E+00	0.4972E+05	0.4972E+05	3

Table B.2. Listings of output files for example problem (concluded).

Output file: TAPE 3

Total axial strain (%)	Effective radial stress (psi)	Total radial stress (psi)	Undrained Modulus (psi)	Current Porosity
0.2448E-01	0.1653E+02	0.4628E+03	0.2642E+07	0.9988E-01
0.2691E+00	0.1818E+03	0.5091E+04	0.2642E+07	0.9883E-01
0.5137E+00	0.3471E+03	0.9719E+04	0.2642E+07	0.9738E-01
0.7583E+00	0.5124E+03	0.1435E+05	0.2642E+07	0.9612E-01
0.1003E+01	0.6777E+03	0.1898E+05	0.2642E+07	0.9485E-01
0.1248E+01	0.8430E+03	0.2360E+05	0.2642E+07	0.9358E-01
0.1492E+01	0.1008E+04	0.2823E+05	0.2642E+07	0.9230E-01
0.1737E+01	0.1174E+04	0.3286E+05	0.2642E+07	0.9102E-01
0.1981E+01	0.1339E+04	0.3749E+05	0.2642E+07	0.8973E-01
0.2226E+01	0.1504E+04	0.4212E+05	0.2642E+07	0.8843E-01
0.2471E+01	0.1669E+04	0.4674E+05	0.2642E+07	0.8713E-01
0.2715E+01	0.1835E+04	0.5137E+05	0.2642E+07	0.8582E-01
0.2960E+01	0.2000E+04	0.5600E+05	0.2642E+07	0.8450E-01
0.3009E+01	0.2033E+04	0.5693E+05	0.2642E+07	0.8424E-01
0.3002E+01	0.2001E+04	0.5679E+05	0.4831E+07	0.8427E-01
0.2930E+01	0.1683E+04	0.5549E+05	0.4831E+07	0.8454E-01
0.2859E+01	0.1364E+04	0.5418E+05	0.4831E+07	0.8432E-01
0.2788E+01	0.1046E+04	0.5287E+05	0.4831E+07	0.8510E-01
0.2718E+01	0.7273E+03	0.5157E+05	0.4831E+07	0.8537E-01
0.2645E+01	0.4088E+03	0.5026E+05	0.4831E+07	0.8565E-01
0.2573E+01	0.9032E+02	0.4895E+05	0.4831E+07	0.8592E-01
0.2552E+01	0.0000E+00	0.4972E+05	0.1948E+07	0.8561E-01

Output file: TAPE 66 (Mixture Response)

Total strain (%)	Pressure (psi)	Undrained Modulus	Current Porosity
0.2552E-01	0.4372E+03	0.1948E+07	0.9988E-01
0.2807E+00	0.5469E+04	0.1948E+07	0.9845E-01
0.5359E+00	0.1044E+05	0.1948E+07	0.9704E-01
0.7911E+00	0.1541E+05	0.1948E+07	0.9562E-01
0.1046E+01	0.2038E+05	0.1948E+07	0.9419E-01
0.1302E+01	0.2535E+05	0.1948E+07	0.9276E-01
0.1557E+01	0.2033E+05	0.1948E+07	0.9131E-01
0.1812E+01	0.3530E+05	0.1948E+07	0.8986E-01
0.2067E+01	0.4027E+05	0.1948E+07	0.8840E-01
0.2322E+01	0.4524E+05	0.1948E+07	0.8694E-01
0.2552E+01	0.4972E+05	0.1948E+07	0.8561E-01

# UNDRAINED UNIAXIAL STRAIN LOAD-UNLOAD RESPONSE OF IDEALIZED SATURATED POROUS MATERIAL

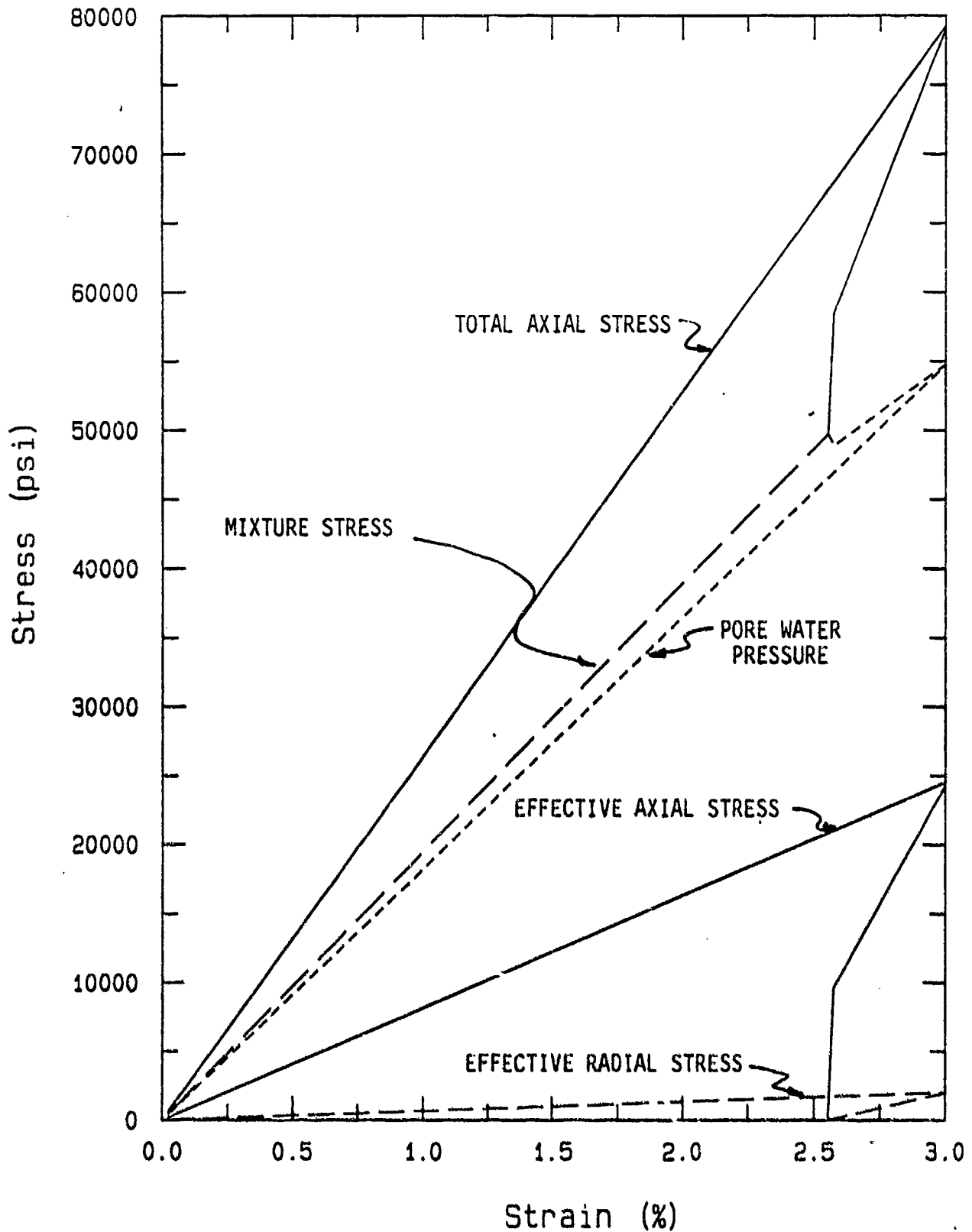


Figure B.1. Example problem using program NKOCp.



# APPENDIX C

## LISTING OF PROGRAM TWAVE

```

PROGRAM TWAVE
C
C   IMPLICIT DOUBLE PRECISION (A - Z)
C
C   PROGRAM TWAVE CALCULATES WAVE SPEEDS AND DAMPING CONSTANTS
C   OF WAVES OF FIRST AND SECOND KIND IN THE POROUS MEDIUM
C   SATURATED BY FLUID
C
C   FOR LOW FREQUENCY-PERMEABILITY PRODUCT ( KAPPA < 2.0 )
C   USE :  RB = 0.0
C   FOR HIGH FREQUENCY-PERMEABILITY PRODUCT ( KAPPA > 2.0 )
C   USE :  R  = 0.0
C
C   NF = 0 : EXCITATION FREQUENCY IS GIVEN
C   1 : COMPUTE APPROXIMATE CRITICAL FREQUENCY AND USE IT
C
C   open(unit=5,file='IWAVE',status='old')
C   open(unit=6,file='OWAVE',status='new')
C
C   CALL RDATA
C
C   CALL WAVE
C
C   CALL OUTPT
C
C   STOP
C   END
C
C   SUBROUTINE RDATA
C   IMPLICIT DOUBLE PRECISION (A - Z)
C   INTEGER NF
C   COMMON /INP/ W,POR,PER,R,RB,GW,G,SGF,SGG,BF,BG,BS,CS,NF
C
C   READ INPUT DATA
C
C   READ (5,1000) NF
C   READ (5,2000) W
C   READ (5,2000) POR,PER,R,RB
C   READ (5,2000) GW,G,SGF,SGG
C   READ (5,2000) BF,BG,BS,CS
C
C   1000 FORMAT(I5)
C
C   2000 FORMAT(4F10.0)
C
C   RETURN
C   END
C
C   SUBROUTINE WAVE
C   IMPLICIT DOUBLE PRECISION (A - Z)
C   INTEGER NF
C   COMMON /INP/ W,POR,PER,R,RB,GW,G,SGF,SGG,BF,BG,BS,CS,NF
C   COMMON /OUT/ CP,CM,ALPHAP,ALPHAM,RK
C
C   ROF = SGF*GW/G

```

```

      ROG = SGG*GW/G
      RO  = POR*ROF+(1.-POR)*ROG
C
      A2 = ROF*(1.+R)/POR
      A3 = POR/BF+(1.-POR)/BG-BS/(BG*BG)
      A4 = 1.-BS/BG
C
      B1 = RO*A2*A3-(ROF**2)*A3
      B3 = 2.*ROF*A4-A2*(A4**2)-A2*A3*CS-RO
C
      IF(NF.EQ.0) GO TO 50
C
      COMPUTE CRITICAL FREQUENCY
C
      B40 = -(A4*A4+A3*CS)
C
      E1 = (B3/CS)**2-4.*(B1/CS)
      E2 = (B40/CS)**2
C
      WC = (GW/PER)*DSQRT(E2/E1)
C
      W = WC
C
50  CONTINUE
C
      COMPUTE WAVE SPEEDS AND DAMPING CONSTANTS
C
      ONE = 1.0
      PIE = 4.0*DATAN(ONE)
C
      A1 = -GW/(PER*W)
      B2 = RO*A1*A3
      B4 = A1*(A4**2)+A1*A3*CS
C
      FRICTION CORRECTION FOR HIGH FREQUENCY MODE ( RB .NE. 0.0 )
C
      IF(RB.EQ.0.0) GO TO 80
C
      RKO = DSQRT(8.*W*PER/(POR*G))
C
      RK = RB*RKO
C
      IF(RK.LT.20.) CALL FKEXC(RK,F1,F2)
      IF(RK.GE.20.) CALL FKAPP(RK,F1,F2)
C
      CALCULATE NEW B1,B2,B3,AND B4
C
      B2B = B2
      B4B = B4
C
      B1 = B1-B2B*F2
      B2 = B2B*F1
C
      B3 = B3+B4B*F2
      B4 = B4*F1

```



```

C
80 CONTINUE
C
  C1 = (B3**2-B4**2)/(CS**2)-4.*B1/CS
  C2 = -4.*B2/CS-2.*B3*B4/(CS**2)
C
  DAPZERO = 1.0D-100
  C1ABS = DABS(C1)
  IF(C1ABS.GE.DAPZERO) GO TO 85
  IF(C2.GE.0.0) T2 = 0.5*PIE
  IF(C2.LT.0.0) T2 = 1.5*PIE
  GO TO 90
C
85 CONTINUE
  C12 = DABS(C2/C1)
  AT2 = DATAN(C12)
  IF(C1.GE.0.0.AND.C2.GE.0.0) T2 = AT2
  IF(C1.LE.0.0.AND.C2.GE.0.0) T2 = PIE-AT2
  IF(C1.LE.0.0.AND.C2.LE.0.0) T2 = PIE+AT2
  IF(C1.GE.0.0.AND.C2.LE.0.0) T2 = -AT2
C
90 CONTINUE
C
  T12 = 0.5*T2
  Z4 = (C1**2+C2**2)**0.25
C
  D1P = -B3/CS+Z4*DCOS(T12)
  D1M = -B3/CS-Z4*DCOS(T12)
  D2P = B4/CS+Z4*DSIN(T12)
  D2M = B4/CS-Z4*DSIN(T12)
  D3 = 2.*B1/CS
  D4 = 2.*B2/CS
C
  COMPUTE WAVE-SPEED
C
  CALL WDAMP(D1P,D2P,D3,D4,W,CP,ALPHAP)
C
  CALL WDAMP(D1M,D2M,D3,D4,W,CM,ALPHAM)
C
  C1 = CP
  A1 = ALPHAP
  IF(CP.GE.CM) GO TO 100
  CP = CM
  ALPHAP = ALPHAM
  CM = C1
  ALPHAM = A1
100 CONTINUE
C
  RETURN
  END
C
  SUBROUTINE OUTPT
  IMPLICIT DOUBLE PRECISION (A - Z)
  INTEGER NF
  COMMON /INP/ W,POR,PER,R,RB,GW,G,SGF,SGG,BF,BG,BS,CS,NF

```

COMMON /OUT/ CP,CM,ALPHAP,ALPHAM,RK

PRINT INPUT DATA WITH LABELS

WRITE(6,2000) NF,W,POR,PER,R,RB,GW,G,SGF,SGG,BF,BG,BS,CS

FORMAT STATEMENT

```
2000 FORMAT(
. ' OPTIONAL FLAG ----- = ',I5 //
. ' .EQ.0 : COMPUTE AT GIVEN FREQUENCY = ' //
. ' .EQ.1 : COMPUTE AT CRITICAL FREQUENCY = ' //
. ' FREQUENCY ----- = ',E13.6 //
. ' POROSITY ----- = ',F12.5 //
. ' COEFFICIENT OF PERMEABILITY ----- = ',E13.6 //
. ' MASS INCREMENT FACTOR ----- = ',F12.7 //
. ' PORE SHAPE FACTOR ----- = ',F12.7 //
. ' UNIT WEIGHT OF STANDARD WATER ----- = ',E13.6 //
. ' GRAVITATIONAL ACCELERATION ----- = ',E13.6 //
. ' SPECIFIC GRAVITY OF PORE FLUID ----- = ',F12.5 //
. ' SPECIFIC GRAVITY OF SOLID GRAIN ----- = ',F12.5 //
. ' BULK MODULUS OF PORE FLUID ----- = ',E13.6 //
. ' BULK MODULUS OF SOLID GRAIN ----- = ',E13.6 //
. ' BULK MODULUS OF SOLID SKELETON ----- = ',E13.6 //
. ' CONSTRAINED MODULUS OF SOLID SKELETON ----- = ',E13.6 //)
```

WRITE COMPUTED WAVE-SPEEDS

WRITE(6,2100) CP,CM,ALPHAP,ALPHAM,RK

```
2100 FORMAT(
. ' SPEED OF FIRST KIND WAVE ----- = ',E13.6 //
. ' SPEED OF SECOND KIND WAVE ----- = ',E13.6 //
. ' DAMPING CONSTANT OF FIRST KIND WAVE ----- = ',E13.6 //
. ' DAMPING CONSTANT OF SECOND KIND WAVE ----- = ',E13.6 //
. ' NON-DIMENSIONAL PARAMETER, KAPPA ----- = ',E13.6 //)
```

RETURN  
END

SUBROUTINE WDAMP(D1,D2,D3,D4,W,C,ALPHA)  
IMPLICIT DOUBLE PRECISION (A - Z)

D34 = D3\*D3+D4\*D4

K3 = (D1\*D3+D2\*D4)/D34

K4 = (D2\*D3-D1\*D4)/D34

SQK34 = DSQRT(K3\*K3+K4\*K4)

```

C      K1 = (1./SQRT(2.))*DSQRT(SQK34+K3)
C      K2 = -(1./SQRT(2.))*DSQRT(SQK34-K3)
C
C      C = K1+K2*K2/K1
C      ALPHA = K2*W/(C*K1)
C
C      RETURN
C      END
C      SUBROUTINE FKEXC(RK,F1,F2)
C      IMPLICIT DOUBLE PRECISION (A - Z)
C
C      CALL BESSL(RK,X1,X2,X3,X4)
C
C      CALL COMPX(X1,X2,X3,X4,T1,T2)
C
C      F1B = 1.-2.*T2/RK
C      F2B = 2.*T1/RK
C      F3B = 0.25*RK*T1
C      F4B = 0.25*RK*T2
C
C      CALL COMPX(F1B,F2B,F3B,F4B,F1,F2)
C
C      RETURN
C      END
C
C      SUBROUTINE BESSL(RK,X1,X2,X3,X4)
C      IMPLICIT DOUBLE PRECISION (A - Z)
C      INTEGER NE,N
C
C      NE = 60
C
C      X1 = 0.0
C      X2 = 0.0
C      X3 = 0.0
C      X4 = 0.0
C
C      FACEV = 1.0
C      N = 0
C      SN = -1.0
C      SIGN = 1.0
C
C      100 CONTINUE
C
C      N = N+1
C
C      FACEV = (2.*N-2.)*FACEV
C      IF(N.EQ.1) FACEV = 1.0
C      FACOD = (2.*N-1.)*FACEV
C
C      P1 = (0.5*RK)**(4.*N-4.)

```

```

P2 = (0.5*RK)**(4.*N-2.)
P3 = (0.5*RK)**(4.*N-5.)
P4 = (0.5*RK)**(4.*N-3.)
C
X1 = X1+SIGN*(P1/FACEV)/FACEV
X2 = X2+SIGN*(P2/FACOD)/FACOD
C
X3 = X3+SIGN*(P3/FACEV)*(2.*N-2.)/FACEV
X4 = X4+SIGN*(P4/FACOD)*(2.*N-1.)/FACOD
C
SIGN = SIGN*SN
FACEV = FACOD
C
IF(N.LT.NE) GO TO 100
C
RETURN
END
C
SUBROUTINE COMPX(E1,E2,E3,E4,Y1,Y2)
IMPLICIT DOUBLE PRECISION (A - Z)
C
DD = E1*E1+E2*E2
C
Y1 = (E3*E1+E2*E4)/DD
C
Y2 = (E1*E4-E2*E3)/DD
C
RETURN
END
C
SUBROUTINE FKAPP(RK,F1,F2)
IMPLICIT DOUBLE PRECISION (A - Z)
C
FA = 2.9213
FB = 1./(4.*SQRT(2.))
C
FBK = (FB*RK)**2
F1 = DSQRT(FA+FBK)
C
F2 = FB*RK
C
RETURN
END

```

## APPENDIX D

### CALCULATION OF EQUIVALENT COEFFICIENT OF PERMEABILITY FOR A FLAT DUCT

Figure 8.10b shows subdivisions of the cross section used to compute the equivalent coefficient of permeability for the flat duct. The total cross section is assumed to be divided into the middle section and two square side sections connecting the parallel faces of the middle section.

For the middle section, we assumed the flow condition as in a theoretical flat duct having infinite width. For the side sections, the flow conditions are assumed to be governed by the equivalent circular duct having the same perimeter as the three wet sides of the square.

Assuming that the flow velocity in the middle section (area  $A_1$ ) is  $V_1$  and the flow velocity in each side section (area  $A_2$ ) is  $V_2$ , then the total flow is given by

$$Q = A_1 V_1 + 2 A_2 V_2 \quad (D-1)$$

Velocities are related to the hydraulic gradient,  $i$ , as

$$V_1 = k_1 i \quad (D-2)$$

and

$$V_2 = k_2 i \quad (D-3)$$

where  $k_1$  and  $k_2$  are the coefficients of permeability for the middle and the side sections, respectively.  $k_1$  is computed from the theoretical flat duct equation as

$$k_1 = \frac{a_1^2 \gamma_f}{3\mu} \quad (D-4)$$

where

$a_1$  = half the height of the duct.

$k_2$  is computed from the circular duct flow (Equation 8.6) with the radius of the duct,  $a$ , given by

$$a = \frac{3}{2} \frac{\sqrt{A_2}}{\pi} \quad (D-5)$$

From Figure 8.10a, the total flow is computed by

$$Q = AV \quad (D-6)$$

where

$$A = A_1 + 2 A_2 \quad (D-7)$$

and

$$V = k_{eq} i \quad (D-8)$$

$k_{eq}$  represents the equivalent coefficient of permeability for the total cross section of the flat duct. Substituting Equation D-2 and D-3 into D-1,

$$Q = (A_1 k_1 + 2 A_2 k_2) i \quad (D-9)$$

and substitution of Equation D-7 and D-8 into D-6 yields

$$Q = (A_1 + 2A_2) k_{eq} i \quad (D-10)$$

From Equations D-9 and D-10, the equivalent coefficient of permeability is computed as

$$k_{eq} = \left( \frac{A_1}{A} \right) k_1 + \left( \frac{2A_2}{A} \right) k_2 \quad (D-11)$$